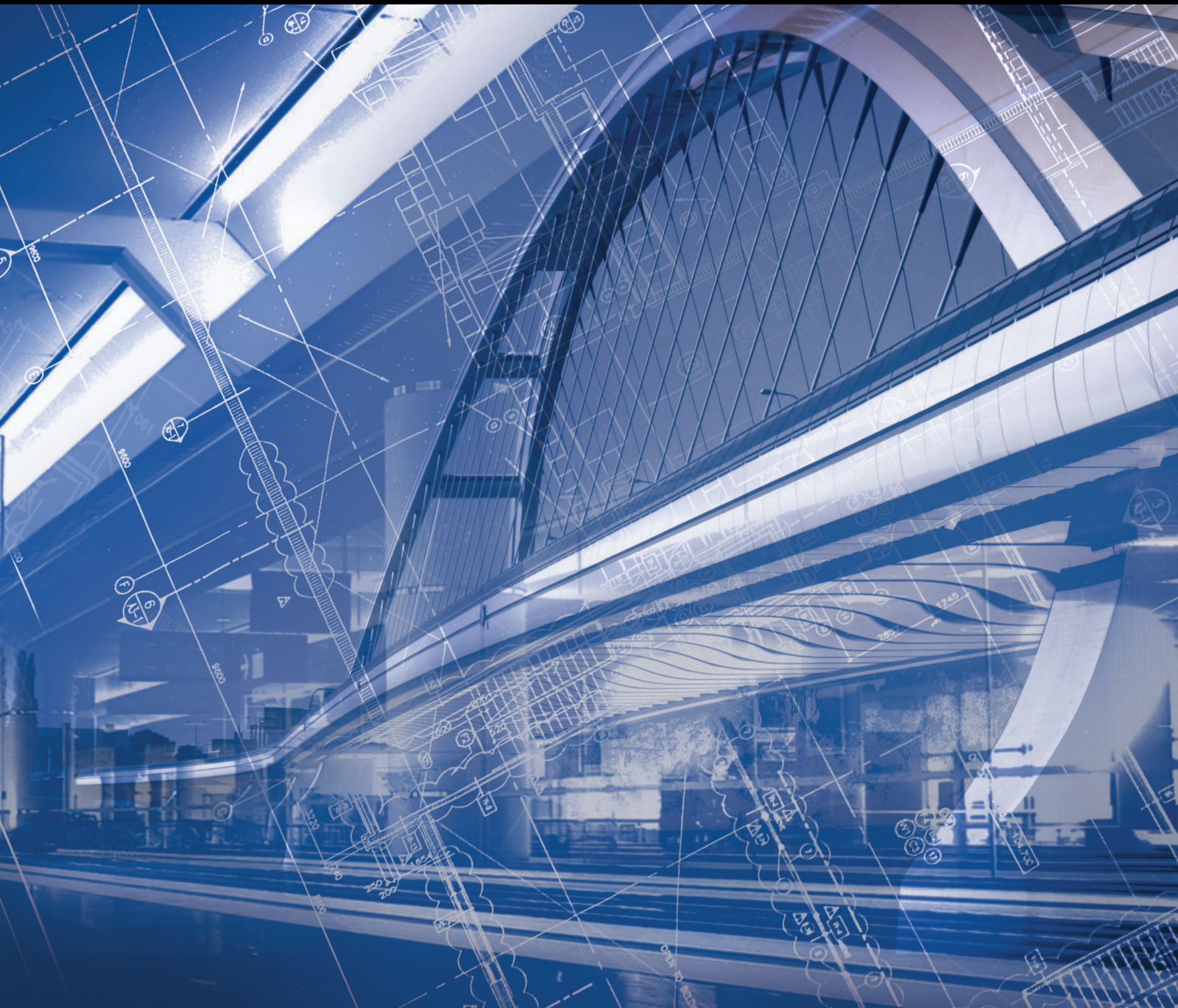


Advances in Civil Engineering

Harmonic Suppression Traction Transformer in Railway Systems

Lead Guest Editor: Lingkun Chen

Guest Editors: Nan Zhang, Qinghua Zhang, and Peng Liu





Harmonic Suppression Traction Transformer in Railway Systems

Advances in Civil Engineering

Harmonic Suppression Traction Transformer in Railway Systems

Lead Guest Editor: Lingkun Chen

Guest Editors: Nan Zhang, Qinghua Zhang, and
Peng Liu



Copyright © 2022 Hindawi Limited. All rights reserved.

This is a special issue published in "Advances in Civil Engineering." All articles are open access articles distributed under the Creative Commons Attribution License, which permits unrestricted use, distribution, and reproduction in any medium, provided the original work is properly cited.





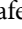
Chief Editor

Cumaraswamy Vipulanandan, USA













Associate Editors

Chiara Bedon , Italy
Constantin Chalioris , Greece
Ghassan Chehab , Lebanon
Ottavia Corbi, Italy
Mohamed ElGawady , USA
Husnain Haider , Saudi Arabia
Jian Ji , China
Jiang Jin , China
Shazim A. Memon , Kazakhstan
Hossein Moayedi , Vietnam
Sanjay Nimbalkar, Australia
Giuseppe Oliveto , Italy
Alessandro Palmeri , United Kingdom
Arnaud Perrot , France
Hugo Rodrigues , Portugal
Victor Yepes , Spain
Xianbo Zhao , Australia

Academic Editors

José A.F.O. Correia, Portugal
Glenda Abate, Italy
Khalid Abdel-Rahman , Germany
Ali Mardani Aghabaglou, Turkey
José Aguiar , Portugal
Afaq Ahmad , Pakistan
Muhammad Riaz Ahmad , Hong Kong
Hashim M.N. Al-Madani , Bahrain
Luigi Aldieri , Italy
Angelo Aloisio , Italy
Maria Cruz Alonso, Spain
Filipe Amarante dos Santos , Portugal
Serji N. Amirkhania, USA
Eleftherios K. Anastasiou , Greece
Panagiotis Ch. Anastasopoulos , USA
Mohamed Moafak Arbili , Iraq
Farhad Aslani , Australia
Siva Avudaiappan , Chile
Ozgur BASKAN , Turkey
Adewumi Babafemi, Nigeria
Morteza Bagherpour, Turkey
Qingsheng Bai , Germany
Nicola Baldo , Italy
Daniele Baraldi , Italy

Eva Barreira , Portugal
Emilio Bastidas-Arteaga , France
Rita Bento, Portugal
Rafael Bergillos , Spain
Han-bing Bian , China
Xia Bian , China
Huseyin Bilgin , Albania
Giovanni Biondi , Italy
Hugo C. Biscaia , Portugal
Rahul Biswas , India
Edén Bojórquez , Mexico
Giosuè Boscato , Italy
Melina Bosco , Italy
Jorge Branco , Portugal
Bruno Briseghella , China
Brian M. Broderick, Ireland
Emanuele Brunesi , Italy
Quoc-Bao Bui , Vietnam
Tan-Trung Bui , France
Nicola Buratti, Italy
Gaochuang Cai, France
Gladis Camarini , Brazil
Alberto Campisano , Italy
Qi Cao, China
Qixin Cao, China
Iacopo Carnacina , Italy
Alessio Cascardi, Italy
Paolo Castaldo , Italy
Nicola Cavalagli , Italy
Liborio Cavaleri , Italy
Anush Chandrappa , United Kingdom
Wen-Shao Chang , United Kingdom
Muhammad Tariq Amin Chaudhary, Kuwait
Po-Han Chen , Taiwan
Qian Chen , China
Wei Tong Chen , Taiwan
Qixiu Cheng, Hong Kong
Zhanbo Cheng, United Kingdom
Nicholas Chileshe, Australia
Prinya Chindaprasirt , Thailand
Corrado Chisari , United Kingdom
Se Jin Choi , Republic of Korea
Heap-Yih Chong , Australia
S.H. Chu , USA
Ting-Xiang Chu , China


Zhaofei Chu , China
Wonseok Chung , Republic of Korea
Donato Ciampa , Italy
Gian Paolo Cimellaro, Italy
Francesco Colangelo, Italy
Romulus Costache , Romania
Liviu-Adrian Cotfas , Romania
Antonio Maria D'Altri, Italy
Bruno Dal Lago , Italy
Amos Darko , Hong Kong
Arka Jyoti Das , India
Dario De Domenico , Italy
Gianmarco De Felice , Italy
Stefano De Miranda , Italy
Maria T. De Risi , Italy
Tayfun Dede, Turkey
Sadik O. Degertekin , Turkey
Camelia Delcea , Romania
Cristoforo Demartino, China
Giuseppe Di Filippo , Italy
Luigi Di Sarno, Italy
Fabio Di Trapani , Italy
Aboelkasim Diab , Egypt
Thi My Dung Do, Vietnam
Giulio Dondi , Italy
Jiangfeng Dong , China
Chao Dou , China
Mario D'Aniello , Italy
Jingtao Du , China
Ahmed Elghazouli, United Kingdom
Francesco Fabbrocino , Italy
Flora Faleschini , Italy
Dingqiang Fan, Hong Kong
Xueping Fan, China
Qian Fang , China
Salar Farahmand-Tabar , Iran
Ilenia Farina, Italy
Roberto Fedele, Italy
Guang-Liang Feng , China
Luigi Fenu , Italy
Tiago Ferreira , Portugal
Marco Filippo Ferrotto, Italy
Antonio Formisano , Italy
Guoyang Fu, Australia
Stefano Galassi , Italy

Junfeng Gao , China
Meng Gao , China
Giovanni Garcea , Italy
Enrique García-Macías, Spain
Emilio García-Taengua , United Kingdom
DongDong Ge , USA
Khaled Ghaedi, Malaysia
Khaled Ghaedi , Malaysia
Gian Felice Giaccu, Italy
Agathoklis Giaralis , United Kingdom
Ravindran Gobinath, India
Rodrigo Gonçalves, Portugal
Peilin Gong , China
Belén González-Fonteboa , Spain
Salvatore Grasso , Italy
Fan Gu, USA
Erhan Güneyisi , Turkey
Esra Mete Güneyisi, Turkey
Pingye Guo , China
Ankit Gupta , India
Federico Gusella , Italy
Kemal Hacıfendioglu, Turkey
Jianyong Han , China
Song Han , China
Asad Hanif , Macau
Hadi Hasanzadehshooiili , Canada
Mostafa Fahmi Hassanein, Egypt
Amir Ahmad Hedayat , Iran
Khandaker Hossain , Canada
Zahid Hossain , USA
Chao Hou, China
Biao Hu, China
Jiang Hu , China
Xiaodong Hu, China
Lei Huang , China
Cun Hui , China
Bon-Gang Hwang, Singapore
Jijo James , India
Abbas Fadhil Jasim , Iraq
Ahad Javanmardi , China
Krishnan Prabhakan Jaya, India
Dong-Sheng Jeng , Australia
Han-Yong Jeon, Republic of Korea
Pengjiao Jia, China
Shaohua Jiang , China

MOUSTAFA KASSEM , Malaysia
Mosbeh Kaloop , Egypt
Shankar Karuppanan , Ethiopia
John Kechagias , Greece
Mohammad Khajehzadeh , Iran
Afzal Husain Khan , Saudi Arabia
Mehran Khan , Hong Kong
Manoj Khandelwal, Australia
Jin Kook Kim , Republic of Korea
Woosuk Kim , Republic of Korea
Vaclav Koci , Czech Republic
Loke Kok Foong, Vietnam
Hailing Kong , China
Leonidas Alexandros Kouris , Greece
Kyriakos Kourousis , Ireland
Moacir Kripka , Brazil
Anupam Kumar, The Netherlands
Emma La Malfa Ribolla, Czech Republic
Ali Lakirouhani , Iran
Angus C. C. Lam, China
Thanh Quang Khai Lam , Vietnam
Luciano Lamberti, Italy
Andreas Lampropoulos , United Kingdom
Raffaele Landolfo, Italy
Massimo Latour , Italy
Bang Yeon Lee , Republic of Korea
Eul-Bum Lee , Republic of Korea
Zhen Lei , Canada
Leonardo Leonetti , Italy
Chun-Qing Li , Australia
Dongsheng Li , China
Gen Li, China
Jiale Li , China
Minghui Li, China
Qingchao Li , China
Shuang Yang Li , China
Sunwei Li , Hong Kong
Yajun Li , China
Shun Liang , China
Francesco Liguori , Italy
Jae-Han Lim , Republic of Korea
Jia-Rui Lin , China
Kun Lin , China
Shibin Lin, China

Tzu-Kang Lin , Taiwan
Yu-Cheng Lin , Taiwan
Hexu Liu, USA
Jian Lin Liu , China
Xiaoli Liu , China
Xuemei Liu , Australia
Zaobao Liu , China
Zhuang-Zhuang Liu, China
Diego Lopez-Garcia , Chile
Cristiano Loss , Canada
Lyan-Ywan Lu , Taiwan
Jin Luo , USA
Yanbin Luo , China
Jianjun Ma , China
Junwei Ma , China
Tian-Shou Ma, China
Zhongguo John Ma , USA
Maria Macchiaroli, Italy
Domenico Magisano, Italy
Reza Mahinroosta, Australia
Yann Malecot , France
Prabhat Kumar Mandal , India
John Mander, USA
Iman Mansouri, Iran
André Dias Martins, Portugal
Domagoj Matesan , Croatia
Jose Matos, Portugal
Vasant Matsagar , India
Claudio Mazzotti , Italy
Ahmed Mebarki , France
Gang Mei , China
Kasim Mermerdas, Turkey
Giovanni Minafò , Italy
Masoomah Mirrashid , Iran
Abbas Mohajerani , Australia
Fadzli Mohamed Nazri , Malaysia
Fabrizio Mollaioli , Italy
Rosario Montuori , Italy
H. Naderpour , Iran
Hassan Nasir , Pakistan
Hossein Nassiraei , Iran
Satheeskumar Navaratnam , Australia
Ignacio J. Navarro , Spain
Ashish Kumar Nayak , India
Behzad Nematollahi , Australia

Chayut Ngamkhanong , Thailand
Trung Ngo, Australia
Tengfei Nian, China
Mehdi Nikoo , Canada
Youjun Ning , China
Olugbenga Timo Oladinrin , United Kingdom
Oladimeji Benedict Olalusi, South Africa
Timothy O. Olawumi , Hong Kong
Alejandro Orfila , Spain
Maurizio Orlando , Italy
Siti Aminah Osman, Malaysia
Walid Oueslati , Tunisia
SUVASH PAUL , Bangladesh
John-Paris Pantouvakis , Greece
Fabrizio Paolacci , Italy
Giuseppina Pappalardo , Italy
Fulvio Parisi , Italy
Dimitrios G. Pavlou , Norway
Daniele Pellegrini , Italy
Gatheeshgar Perampalam , United Kingdom
Daniele Perrone , Italy
Giuseppe Piccardo , Italy
Vagelis Plevris , Qatar
Andrea Pranno , Italy
Adolfo Preciado , Mexico
Chongchong Qi , China
Yu Qian, USA
Ying Qin , China
Giuseppe Quaranta , Italy
Krishanu ROY , New Zealand
Vlastimir Radonjanin, Serbia
Carlo Rainieri , Italy
Rahul V. Ralegaonkar, India
Raizal Saifulnaz Muhammad Rashid, Malaysia
Alessandro Rasulo , Italy
Chonghong Ren , China
Qing-Xin Ren, China
Dimitris Rizos , USA
Geoffrey W. Rodgers , New Zealand
Pier Paolo Rossi, Italy
Nicola Ruggieri , Italy
JUNLONG SHANG, Singapore

Nikhil Saboo, India
Anna Saetta, Italy
Juan Sagaseta , United Kingdom
Timo Saksala, Finland
Mostafa Salari, Canada
Ginevra Salerno , Italy
Evangelos J. Sapountzakis , Greece
Vassilis Sarhosis , United Kingdom
Navaratnarajah Sathiparan , Sri Lanka
Fabrizio Scozzese , Italy
Halil Sezen , USA
Payam Shafigh , Malaysia
M. Shahria Alam, Canada
Yi Shan, China
Hussein Sharaf, Iraq
Mostafa Sharifzadeh, Australia
Sanjay Kumar Shukla, Australia
Amir Si Larbi , France
Okan Sirin , Qatar
Piotr Smarzewski , Poland
Francesca Sollecito , Italy
Rui Song , China
Tian-Yi Song, Australia
Flavio Stochino , Italy
Mayank Sukhija , USA
Piti Sukontasukkul , Thailand
Jianping Sun, Singapore
Xiao Sun , China
T. Tafsirojjaman , Australia
Fujiao Tang , China
Patrick W.C. Tang , Australia
Zhi Cheng Tang , China
Weerachart Tangchirapat , Thailand
Xiixin Tao, China
Piergiorgio Tataranni , Italy
Elisabete Teixeira , Portugal
Jorge Iván Tobón , Colombia
Jing-Zhong Tong, China
Francesco Trentadue , Italy
Antonello Troncone, Italy
Majbah Uddin , USA
Tariq Umar , United Kingdom
Muahmmad Usman, United Kingdom
Muhammad Usman , Pakistan
Mucteba Uysal , Turkey

Ilaria Venanzi , Italy
Castorina S. Vieira , Portugal
Valeria Vignali , Italy
Claudia Vitone , Italy
Liwei WEN , China
Chunfeng Wan , China
Hua-Ping Wan, China
Roman Wan-Wendner , Austria
Chaohui Wang , China
Hao Wang , USA
Shiming Wang , China
Wayne Yu Wang , United Kingdom
Wen-Da Wang, China
Xing Wang , China
Xiuling Wang , China
Zhenjun Wang , China
Xin-Jiang Wei , China
Tao Wen , China
Weiping Wen , China
Lei Weng , China
Chao Wu , United Kingdom
Jiangyu Wu, China
Wangjie Wu , China
Wenbing Wu , China
Zhixing Xiao, China
Gang Xu, China
Jian Xu , China
Panpan , China
Rongchao Xu , China
HE YONGLIANG, China
Michael Yam, Hong Kong
Hailu Yang , China
Xu-Xu Yang , China
Hui Yao , China
Xinyu Ye , China
Zhoujing Ye, China
Gürol Yildirim , Turkey
Dawei Yin , China
Doo-Yeol Yoo , Republic of Korea
Zhanping You , USA
Afshar A. Yousefi , Iran
Xinbao Yu , USA
Dongdong Yuan , China
Geun Y. Yun , Republic of Korea

Hyun-Do Yun , Republic of Korea
Cemal YİĞİT , Turkey
Paolo Zampieri, Italy
Giulio Zani , Italy
Mariano Angelo Zanini , Italy
Zhixiong Zeng , Hong Kong
Mustafa Zeybek, Turkey
Henglong Zhang , China
Jiupeng Zhang, China
Tingting Zhang , China
Zengping Zhang, China
Zetian Zhang , China
Zhigang Zhang , China
Zhipeng Zhao , Japan
Jun Zhao , China
Annan Zhou , Australia
Jia-wen Zhou , China
Hai-Tao Zhu , China
Peng Zhu , China
QuanJie Zhu , China
Wenjun Zhu , China
Marco Zucca, Italy
Haoran Zuo, Australia
Junqing Zuo , China
Robert Černý , Czech Republic
Süleyman İpek , Turkey


Contents

Experimental Study on a Low-Rise Shear Wall with the Built-In Shear Steel Plate

Xingyu Song , Lin Zhao, Lingkun Chen , Yuan Duan, Yehao Jiang, and Yuan Tian


Research Article (10 pages), Article ID 3687475, Volume 2022 (2022)

Deformation Characteristics and Safety Evaluation of the Throw Filling Soft Clay Cofferdam under Super-Historical Flood Conditions

Ping Jiang, Yong Huang, Zhipeng Tao, Junhua Zhu , Ning Wang, and Jianwei Qiao


Research Article (10 pages), Article ID 9578477, Volume 2022 (2022)

The Influence of Water-Level Fluctuation on the Instability and Seepage Failure of Dump-Fill Cofferdam

Yunqing Hu, Jianyu Huang, Zhipeng Tao, Junhua Zhu , Qing Lv, Jianwei Qiao, and Weibin Cai

Research Article (11 pages), Article ID 5845340, Volume 2022 (2022)

The Exploration of New Courtyard Architecture Based on the Guidance of Architectural Culture and Technology

Xi Luo and Jianyun Huang 


Research Article (12 pages), Article ID 5029647, Volume 2022 (2022)

Near-Fault Ground Motion Impacts on High-Speed Rail Large-Span Continuous Girder Bridge considering Pile-Soil Interaction

Yefei Zhou , Gang Wang , Shuyi Yang , and Niu Liu 

Research Article (9 pages), Article ID 7554440, Volume 2022 (2022)

MEMS Dynamic Characteristics Analysis of Electrostatic Microbeams for Building Structure Monitoring

Youping Gong, Hong Bo, Chuanping Zhou, Maofa Wang, and Rougang Zhou 


Research Article (8 pages), Article ID 8355127, Volume 2022 (2022)

Wave Mode Control of Cantilever Slab Structure of T-Beam Bridge with Large Aspect Ratio

Tingting Liu , Chuanping Zhou , Zhigang Yan, and Guojin Chen

Research Article (9 pages), Article ID 6544058, Volume 2021 (2021)

Asymmetric Evolutionary Game Analysis of Building Information Modeling (BIM) Technology Diffusion

Qian Liu 

Research Article (11 pages), Article ID 4464737, Volume 2021 (2021)

Coriolis Force Sliding Mode Control Method for the Rotary Motion of the Central Rigid Body-Flexible Cantilever Beam System in TBM


Chuanlu Zhou, Long Qin , Ming Chen, and Jingxiang Zhang

Research Article (7 pages), Article ID 9866453, Volume 2021 (2021)




An Impact-Echo Experimental Approach for Detecting Concrete Structural Faults

Ya-xun Yang , Wen-hao Chai , De-chuang Liu , Wei-de Zhang , Jia-cheng Lu , and Zhi-kui Yang 
Research Article (8 pages), Article ID 8141015, Volume 2021 (2021)

Study on Deformation Evolution Characteristics of Reverse-Dip Rock Slope under the Influence of Rainfall

Jiabing Zhang, Liangfu Xie , Xuejun Liu, Yongjun Qin, and Liming Wu
Research Article (18 pages), Article ID 8789588, Volume 2021 (2021)

Research Progress on Corrosion of Equipment and Materials in Deep-Sea Environment

Sheng Chen , Liping Qiu , Shaofang Sun, Junyi Yang , Qinghua Meng, and Weibo Yang
Review Article (12 pages), Article ID 7803536, Volume 2021 (2021)

Experimental Investigation on the Influence of Ambient Temperature on the Test Accuracy for the Differential Pressure Hydrostatic Levelling System

Li Bo, Chen Guo, and Wu Qi 
Research Article (10 pages), Article ID 5942838, Volume 2021 (2021)

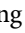


Study on Deep and Large Foundation Pit of a National First-Class Key Tomb Protection Project

Jiagang Zhang , Zhimin Chen , Mingzhu Hu, and Zhaoguo Wu
Research Article (12 pages), Article ID 7158021, Volume 2021 (2021)


Fracture Modeling of the Bi-Block Ballastless Track System Resulting from Early-Aged Relative Humidity during the Construction Process

Shihao Cao , Wang Hui , Shufang Zhai , Kui Hu , Yujing Chen , and Junqi Chen 
Research Article (17 pages), Article ID 2511582, Volume 2021 (2021)

Optimization of VEDs for Vibration Control of Transmission Line Tower

Guoping Huang , Jianhua Hu , Yuzhu He, Haibo Liu , and Xiugui Sun
Research Article (13 pages), Article ID 9060414, Volume 2021 (2021)

Design of Constructive Controller of Nonlinear System Based on Polynomial Function Growth Condition and Its Application in Deep Subsea Energy Mining and Production Control System

Longchuan Guo , Chuanping Zhou, Xiaoqing Tian, Huawei Ji, and Yudong Peng
Research Article (9 pages), Article ID 4788428, Volume 2021 (2021)

Research Article

Experimental Study on a Low-Rise Shear Wall with the Built-In Shear Steel Plate

Xingyu Song ¹, Lin Zhao,¹ Lingkun Chen ^{1,2}, Yuan Duan,³ Yehao Jiang,⁴ and Yuan Tian⁵

¹College of Architectural Science and Engineering, Yangzhou University, Yangzhou 225000, China

²Department of Civil and Environmental Engineering, University of California, Los Angeles 90095, CA, USA

³Shanxi Institute of Chemical Engineering Design, Taiyuan 030000, China

⁴School of Civil Engineering, Yangzhou Polytechnic College, Yangzhou 225009, China

⁵Transportation Technology Development Promotion Center, China Academy of Transportation Sciences, Beijing 100029, China

Correspondence should be addressed to Lingkun Chen; lkchen@yzu.edu.cn

Received 19 November 2021; Revised 27 May 2022; Accepted 13 June 2022; Published 11 July 2022

Academic Editor: Andreas Lampropoulos

Copyright © 2022 Xingyu Song et al. This is an open access article distributed under the Creative Commons Attribution License, which permits unrestricted use, distribution, and reproduction in any medium, provided the original work is properly cited.

In this paper, a new reinforcement scheme is proposed to improve the seismic performance of low-rise shear walls. The new system combines the advantages of slotted and composite shear walls to exhibit a high bearing capacity and good deformation performance. Two low-cycle repeated loading tests with different forms of shear walls were conducted to accurately understand its seismic performance. Seismic performance indexes, such as failure mode, bearing capacity, hysteresis curve, stiffness degradation, and energy dissipation capacity, of the new shear wall under the low-cycle reciprocating load were obtained to verify its reliability. The results show that the newly reinforced shear wall has two clear seismic defense lines. Its deformation and energy-dissipation capacities and lateral stiffness stability are greatly improved compared with traditional low-rise shear walls. Thus, the proposed method can provide a new means for enhancing the seismic performance of shear walls.

1. Introduction

Reinforced concrete shear walls, the prominent lateral force-resisting members used in high-rise structures, have high bearing capacity and stiffness. However, widespread seismic damage and experimental research [1–3] show that the low-rise shear walls with small aspect ratios (height to width ratios) and high axial compression ratios have poor ductility and energy dissipation capacity, which were seriously damaged during strong earthquakes. The failure process has the characteristics of brittle shear failure, which is not conducive to the seismic performance of the structure. Low-rise shear walls always exist in a multistory frame-shear wall at bottom story structures and high-rise large-space in basement structures. However, their ductility is poor and the number and thickness of the shear wall are restricted by architectural function. So it is urgent in the engineering field to develop a new kind of low-rise shear wall which has a better seismic behavior.

To improve the deformation capacity and seismic performance of shear walls, researchers have carried out many studies and proposed many improvement measures. Muto [4] studied the seismic performance and the force mechanism of shear walls with vertical slits, and the results show that the method of opening vertical slits can effectively improve the deformation performance of shear walls. Studies have shown that an appropriate slit setting can change the failure mode of the shear wall and effectively improve the energy dissipation capacity and ductility of low-rise shear walls [5, 6]. Other research studies have studied the seismic behavior of shear walls with diagonal reinforcement, and the results show that oblique reinforcement could improve the deformation capacity of the shear wall, slow down the stiffness degradation, and effectively avoid shear failure [7, 8]. Experimental research on shear walls with concealed bracings was also conducted, and the results show that owing to the existence of bracings, the cracks in the concrete were fully developed; the overall stiffness

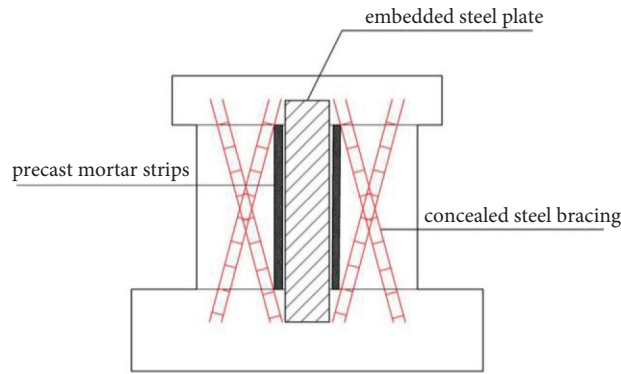
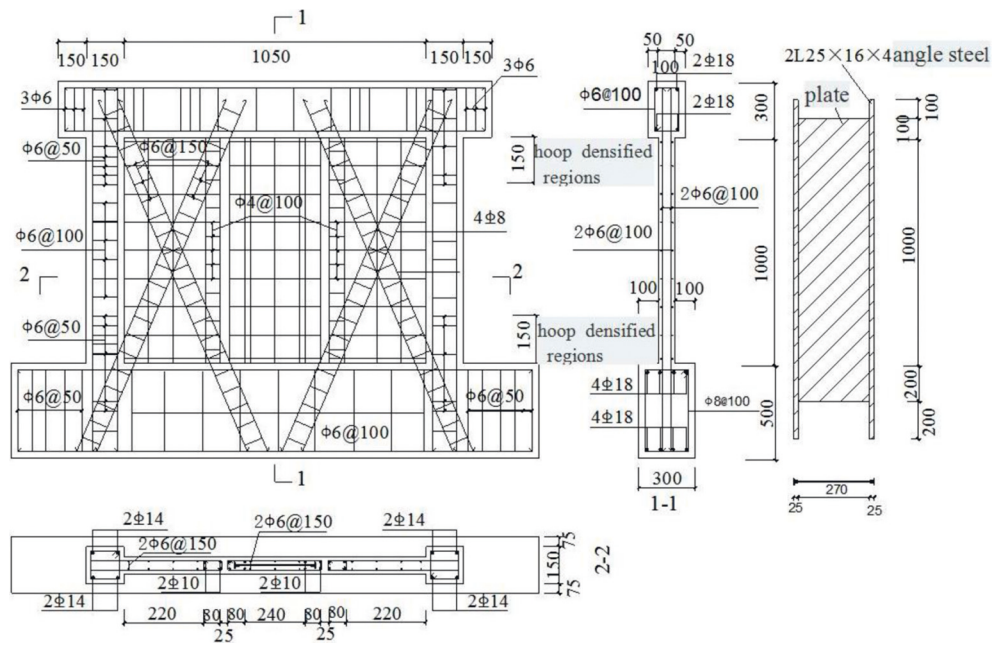


FIGURE 2: HDNLSW structure diagram.



(a)



(b)

FIGURE 3: Reinforcement details and the actual model of HDNLSW. (a) Reinforcement details of HDNLSW. (b) Actual model of HDNLSW.

specimen, and the reinforcement details and the actual model are shown in Figure 1. HDNLSW is a slotted low-rise shear wall with a built-in steel plate proposed in this paper. The structural diagram is shown in Figure 2, and the reinforcement details and actual model are shown in Figure 3.

The production process of HDNLSW mainly includes three steps. Firstly, two vertical slits were opened on the wallboard of the shear wall to divide the low-rise shear wall into three parts. Then, the concealed steel bracings were set on the wallboard on both sides, and the steel plate was embedded in

TABLE 1: Parameters of specimens.

Specimen	Span ratio	Net height of the wallboard (mm)	Net width of the wallboard (mm)	Frame column (mm)	Width of slit (mm)
HDLSW	0.74	1000	1050	150 × 150	—
HDNLSW	0.74	1000	1050	150 × 150	25

TABLE 2: Properties of reinforcing bars and the steel plate.

Specification	Yield strength (MPa)	Ultimate strength (MPa)	Elastic modulus (MPa)
Φ4	270	368	2.02×10^5
Φ6	458	542	2.01×10^5
Φ8	407	477	2.07×10^5
Φ10	416	461	2.03×10^5
Φ14	385	518	2.03×10^5
Φ18	380	527	2.01×10^5
Steel plate	289	415	1.98×10^5

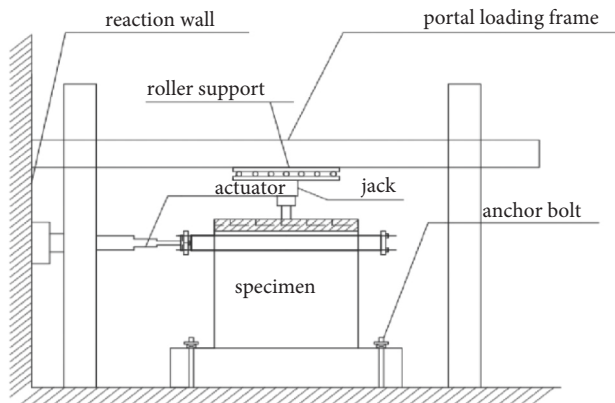


FIGURE 4: Test setup.

the wallboard between the vertical slits. Finally, the cement mortar block was placed at the slits, and then, the concrete was poured as a whole to form the shear wall. The size of the shear walls is summarized in Table 1.

2.2. Material Performance. The concrete cubic compressive strength f_{cu} was determined by the compression test on standard cubic samples (three $150 \times 150 \times 150$ mm cubes were used as test samples in each specimen). In the code for the design of concrete structures in China (GB50010-2010) [17], the average compressive strength of concrete f_c was taken $f_c = 0.76f_{cu}$. The f_c was tested to be equal to 34.1 MPa, and the elastic modulus of the concrete E_c was 3.06×10^4 MPa. Regarding the reinforcement, the average values of the yield strength $f_{y,m}$ and the tensile strength $f_{u,m}$ are shown in Table 2. It should be noted that all bars were hot-rolled plain steel bars except Φ4 mm bars, which were cold-rolled ribbed bars.

2.3. Test Apparatus and the Loading System. The dynamic and quasi-static tests were performed before and after loading to obtain each specimen's change in frequency and damping. Low cyclic reversed loading tests of two shear walls were carried out, and the test device is shown in Figure 4. During the test, the foundation beam was anchored to the test bench by using an anchor beam and an anchor bolt, and



FIGURE 5: Loading site.

the loading beam was connected to the end face of the horizontal jack by using the screw and the end plate. The rigid distribution beam was placed on the top of the specimen to evenly distribute the pressure of the jackshaft to the wall so that the stress state of the model was closer to the engineering practice. The roller was set between the vertical jack and the beam to ensure that the vertical jack could move with the lateral displacement of the specimen top.

The vertical load was first applied in the test, and the vertical load was applied to all the predetermined loads and remained constant during the trial. The horizontal loading process functions under the force-displacement dual control method. Specimens in the elastic phase following the force control are divided into three levels of loading, and each loading cycle is repeated one time; when the horizontal force-displacement curve of the top of the specimen shows an obvious turning point, the displacement control is used to load step-by-step. The displacement increment in each stage was 3 mm, and the load of each stage was cycled twice.

2.4. The Loading System and the Loading Procedure. The counter-force apparatus system is depicted in Figure 4, and all the specimens were fixed on the rigid floor through high-strength screws. The axial load was first applied to the models using a 1000 kN hydraulic jack, and it remained unchanged during the tests. The axial load applied on the two specimens was $0.2 A_c f_c$ (f_c : average compressive strength of concrete; A_c : cross-sectional area of the wall). Because the

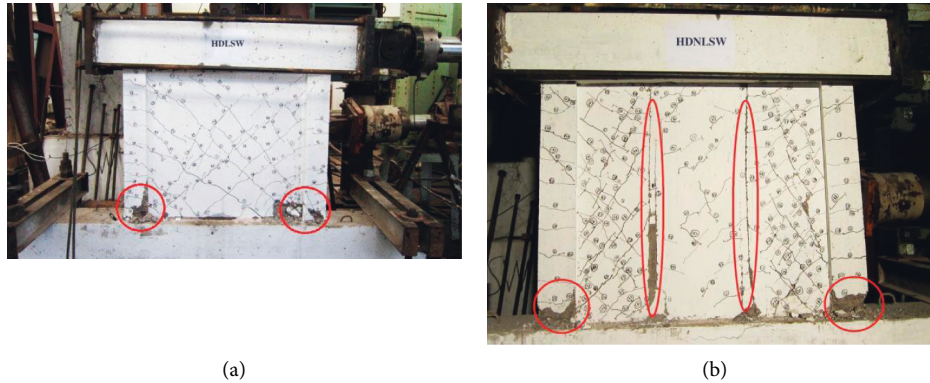


FIGURE 6: Crack development of the two specimens: (a) specimen HDLSW; (b) specimen HDNLSW.

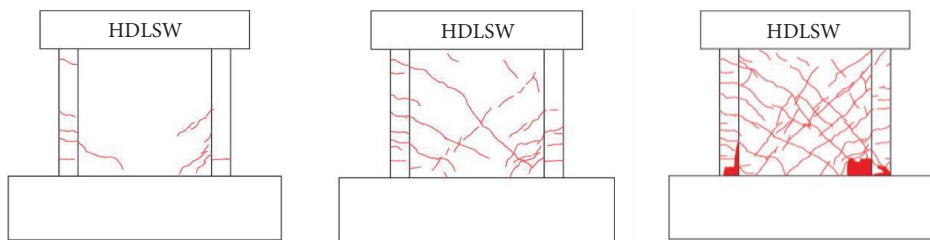


FIGURE 7: Crack development of the shear wall HDLSW.

hydraulic jack was installed on the frictionless rollers, the hydraulic jack could move freely in the lateral loading direction, and the free lateral displacement of the top end of the specimens appeared as a cantilever. A 1000 kN actuator provided the lateral loading. The quasi-static cyclic loading method was adopted for all specimens.

The lateral loading protocol for all specimens was under displacement control, as shown in Figure 5. Each loading cycle was repeated twice, and the experiments were stopped when the load dropped below 85% of the peak load [18].

2.5. Testing Contents. The physical quantities of each specimen were measured during the test, including the load, displacement, relative deformation, and strain. The displacement meter was set at the center of the loading beam to measure the vertex displacement of the tested piece. One horizontal displacement meter and two vertical displacement meters were arranged on the foundation beam to correct the influence of the translation and rotation of the foundation beam on the displacement value of the specimen. The vertical load was monitored frequently to control the specimen's axial compression ratio to keep it constant. In addition, several parallel concrete strain gauges are arranged at the lower part of the wallboard to study the plastic development of the shear wall.

3. Results and Analyses

3.1. Failure Process and Morphology of Specimens. The failure modes of each shear wall are shown in Figure 6. The failure modes of the two low-rise shear walls are entirely different. For the traditional low-rise shear wall HDLSW with

concealed steel bracings, when the cracking load reaches, the horizontal cracks first appear at the bottom of the frame column and extend obliquely to the wallboard with an increase in the load. Upon further loading, multiple diagonal shear cracks appeared on the web and numerous horizontal cracks appeared on the frame column. As the load increased gradually, the original cracks extended and penetrated further, forming multiple shear oblique cracks through the web. The cracks intersect with each other into a mesh and divide the web into several small blocks. During the later loading period, the concrete at the corner of the web peeled off and the concrete at the bottom of the frame column was crushed. The failure mode of the component is mainly shear failure. The crack development diagram of the HDLSW shear wall is shown in Figure 7.

For the slotted low-rise shear wall HDNLSW, cracks first appeared along the two sides of the vertical slits. As the load increased, oblique cracks appeared on the web of the shear wall on both sides of the vertical slits and horizontal cracks appeared on the frame column. There was no crack in the built-in steel plate shear wall between the two vertical slits. With a further increase in the load, the shear walls on both sides of the vertical slits appeared as multiple cross oblique cracks and continued to extend; the frame columns on both sides appeared as multiple horizontal cracks, and oblique cracks began to appear on the middle web. During the later loading period, the shear walls on both sides of the vertical slits were filled with oblique cross cracks and the crack width increased significantly. The transverse reinforcement intersected with the oblique cracks yielded, and the concrete at the corner of the two frame columns was crushed. However, the shear wall between the two vertical slits maintained good integrity. The failure process of

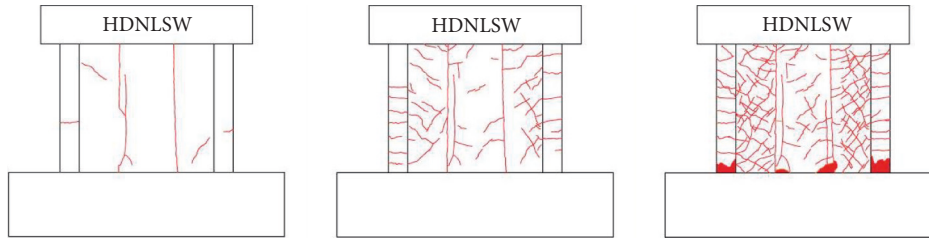


FIGURE 8: Crack development of the shear wall HDNLSW.

TABLE 3: Experimental results of bearing capacity of specimens.

Specimen	F_c/kN		F_y/kN		F_m/kN		μ_{cm} means F_c/F_m	μ_{ym} means F_y/F_m
	Positive	Negative	Positive	Negative	Positive	Negative		
HDLSW	71.2	-72.8	308.5	-297.3	511.6	-503.8	0.14	0.60
HDNLSW	73.7	-70.1	318.6	-302.5	494.8	-480.1	0.15	0.64

TABLE 4: Experimental results of displacements and ductility coefficients of specimens.

Specimen	U_c/mm		U_y/mm		U_d/mm		μ means U_d/U_y
	Positive	Negative	Positive	Negative	Positive	Negative	
HDLSW	0.57	-0.56	8.31	-8.15	30.11	-29.85	3.64
HDNLSW	0.74	-0.70	9.71	-9.26	40.8	-39.48	4.23

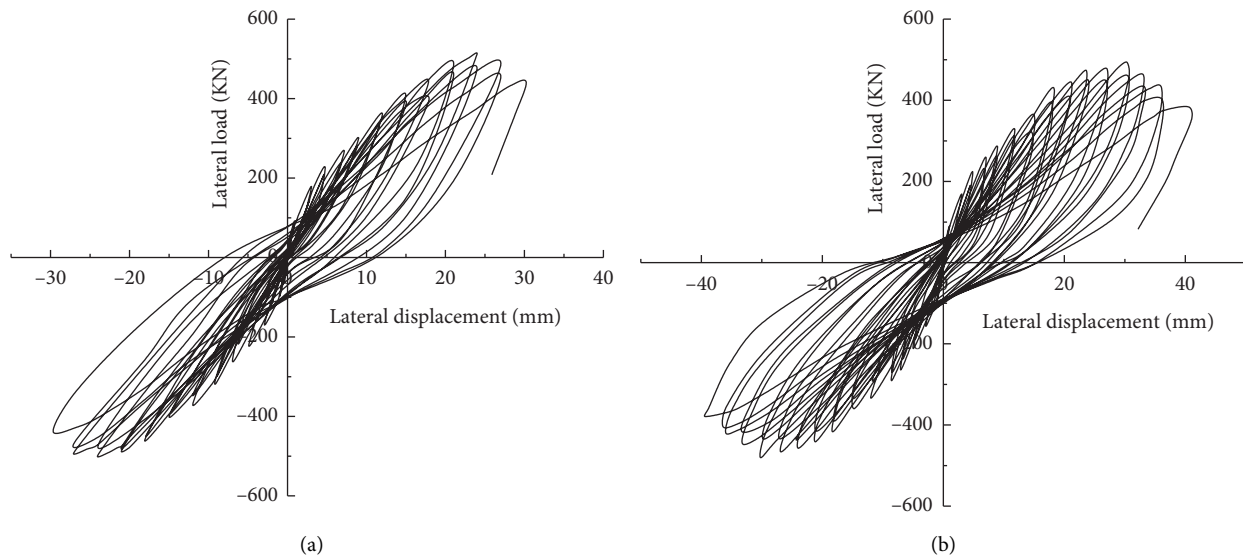


FIGURE 9: Lateral force versus the top displacement hysteretic curve. (a) HDLSW. (b) HDNLSW.

the shear wall shows good ductility. The crack development of the shear wall HDNLSW is shown in Figure 8.

3.2. Bearing Capacity and Ductility Analysis. Table 3 shows the measured values of the cracking, apparent yield, and ultimate loads of the two shear walls in this test. Table 4 shows the measured values of the top displacement and ductility coefficients of the two shear walls, in which F_c and U_c are the specimen's cracking load and cracking displacement, respectively, and the positive and negative mean values are obtained. F_y and U_y are the yield load and the yield

displacement of the specimen, respectively, and their values are calculated using the equal energy principle. F_m is the maximum horizontal load of the specimen, U_d is the maximum elastic-plastic displacement value when the load does not decrease significantly, μ_{cm} is the ratio of the cracking load to the ultimate load, and μ_{ym} is the ratio of the yield load to the ultimate load.

Comparing the test results of the two shear walls, it can be seen that the cracking load and the yield load of the two shear walls are almost the same, but the bearing capacity of the shear wall HDNLSW decreases slightly (by 4%). At the same time, the ultimate displacement and the ductility ratio

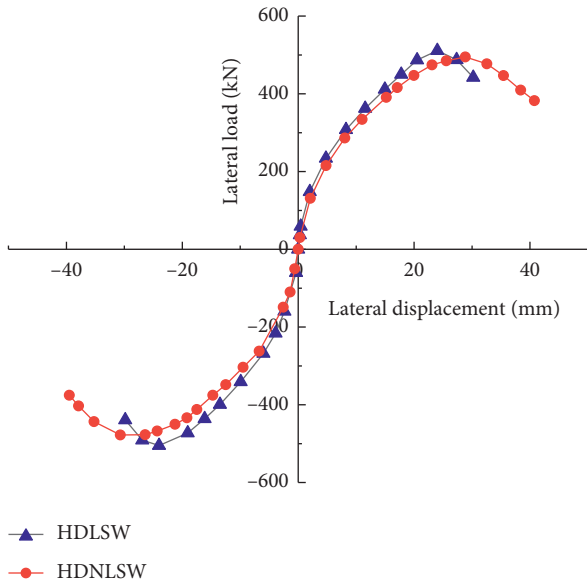


FIGURE 10: Force-displacement skeleton curves of two specimens.

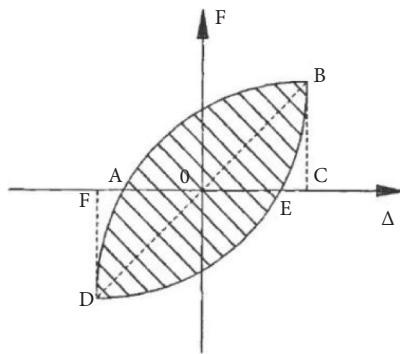


FIGURE 11: Calculation of the equivalent viscosity coefficient.

of the shear wall HDNLSW are also increased by 33.9% and 16.2%, respectively.

3.3. Hysteresis Characteristic Analysis and Skeleton Curve Comparison. The hysteretic curves and skeleton curves of the two shear walls are shown in Figures 9 and 10. The hysteretic curve can comprehensively reflect the shear wall strength, stiffness, deformation capacity, and energy dissipation capacity. It can be seen from Figure 9 that the hysteretic curve of HDNLSW is more plumped than that of HDLSW, indicating that the new shear wall has a better energy dissipation capacity. It can also be seen from the skeleton curve that the bearing capacity of the shear wall HDLSW decreases faster after reaching the peak load Although the maximum bearing capacity of the shear wall HDNLSW decreased slightly, the decrease in the bearing capacity was not evident after the peak load and the bearing capacity was relatively stable and had better deformation performance.

3.4. Energy Dissipation Capability Analysis. The equivalent viscous damping coefficient h_e and the area around the

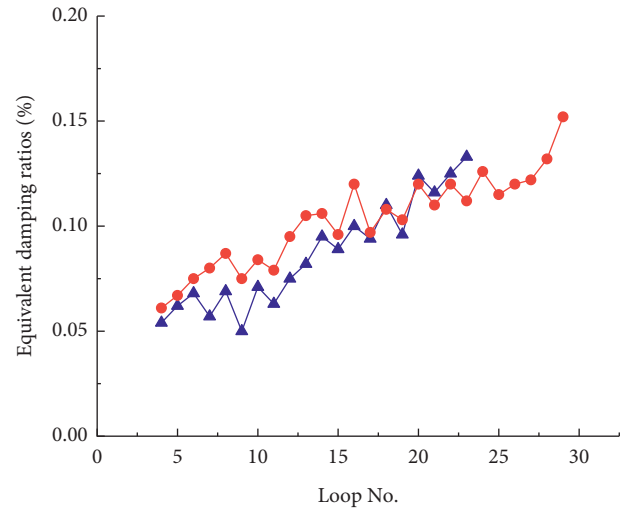


FIGURE 12: Equivalent viscous damping ratios of two specimens.

skeleton curve and the coordinate axis can be used as quantitative indexes to measure the energy dissipation capacity of the component. The equivalent viscous damping coefficient represents the fullness of the hysteresis curve of the structure. The calculation formula is shown in Figure 11. The equivalent viscous damping coefficient was calculated using the following equation. The area (ABE + EDA) represents the dissipation energy at each loading cycle, and the area (OBC + ODF) represents the elastic strain energy at each loading cycle, as depicted in Figure 11.

$$h_e = \frac{1}{2\pi} \frac{\text{Area (ABE + EDA)}}{\text{Area (OBC + ODF)}} \quad (1)$$

The equivalent viscous damping coefficient-loading cycle curve is shown in Figure 12. It can be seen that the equivalent viscous damping coefficient increases with the increase in the number of cycles. Overall, the equivalent viscous damping coefficient h_e of the shear wall HDNLSW is greater than that of the low-rise shear wall HDLSW, indicating that the shear wall HDNLSW has good energy dissipation capacity.

The area enclosed by the skeleton curve and the coordinate axis reflects the total energy consumption of the component. The average calculation results of the area surrounded by each skeleton curve and coordinate axis were as follows: HDLSW energy consumption was 11267.5 kN mm, and HDNLSW energy consumption was 15107.4 kN mm. Therefore, the energy consumption of HDNLSW is 34.1%, which is higher than that of HDLSW.

3.5. Analysis of the Stiffness Degradation Process. The stiffness of the shear wall specimen is related to the stress level and the number of loading cycles. The stiffness is variable during loading. For the needs of seismic response analysis, the change in secant stiffness during loading is given in this

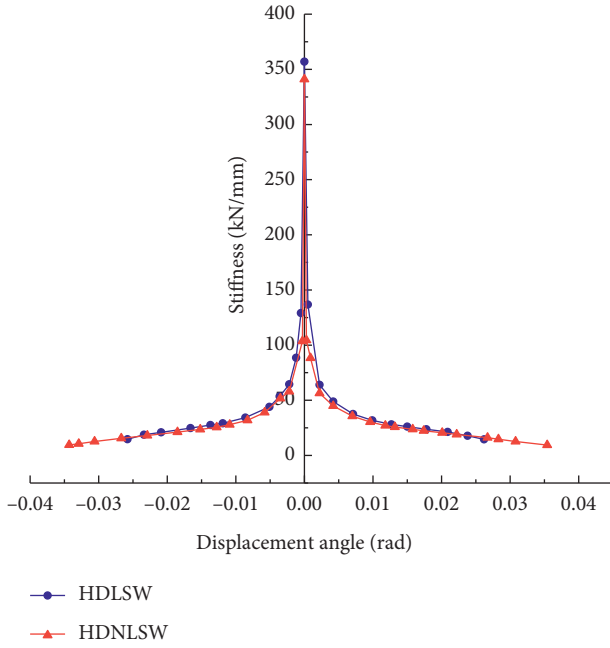


FIGURE 13: The contrast diagram of attenuation curves of rigidity.

TABLE 5: Variance of the frequency and the damping ratio of undamaged and damaged specimens.

Specimen	Before test		After test	
	Frequency/ Hz	Damping ratio/%	Frequency/ Hz	Damping ratio/%
HDLSW	175.4	3.2	82.6	9.4
HDNLSW	173.2	3.4	90.1	12.3

paper. The specific calculation formula for the secant stiffness is shown in the following formula(2):

$$K_i = \frac{|+F_i| + |-F_i|}{|+\Delta_i| + |-\Delta_i|} \quad (2)$$

Here, $\pm F_i$ are the maximum positive and negative loads of the i^{th} loading cycle, respectively, and $\pm \Delta_i$ are the displacements corresponding to $\pm F_i$. The stiffness degradation curves for the two specimens are shown in Figure 13.

Table 5 shows the stiffness at each stage of the two shear walls, where K_0 represents the initial stiffness, K_c represents the cracking stiffness, K_y represents the yield stiffness, β_{c0} represents the stiffness attenuation from the initial stage to the cracking stage, and β_{y0} represents the stiffness attenuation from the initial stage to the yield stage.

The initial stiffness K_0 (corresponding to the elastic stage), cracking stiffness K_c (corresponding to the cracking load), yield stiffness K_y (corresponding to the yield load), and the stiffness degradation coefficient β ($\beta_{y0} = K_y/K_0$, $\beta_{c0} = K_c/K_0$) of the two specimens are computed and are listed in Table 6.

It can be seen that the stiffness of the two shear walls is similar before cracking, indicating that the mortar bars in

TABLE 6: Experimental results of stiffness of specimens.

Specimen	K_0 kN·mm ⁻¹	K_c kN·mm ⁻¹	K_y kN·mm ⁻¹	β_{c0} K_c/K_0	β_{y0} K_y/K_0
HDLSW	357.2	127.46	36.80	0.36	0.10
HDNLSW	341.3	99.87	32.74	0.29	0.10

the HDNLSW vertical slits of the specimen at the beginning stage work together with the wall panels on both sides. After cracking, the stiffness of the HDNLSW decreased rapidly owing to the influence of the vertical slits and the cracking stiffness decreased by 21.6% compared with that of HDLSW. It is worth noting that the stiffness degradation of the HDNLSW shear wall in the early stage is greater than that of HDLSW. Still, the stiffness degradation in the late phase is slow, indicating that it has good residual stiffness, mainly because the built-in steel plate composite wallboard in the middle part maintains good integrity. Meanwhile, it can also be seen that the ultimate displacement angle of the shear wall HDNLSW is larger, indicating that the new low-rise shear wall is safer under severe earthquakes.

3.6. Damping Performance Analysis. The dynamic tests of the two shear walls before and after the tests were carried out using the free attenuation method, and the first-order frequency and the modal damping ratio of each shear wall were measured, as shown in Table 6. The test results show that there was little difference in frequency between the two shear walls before the test, indicating that the stiffness difference between them is small. After failure, the frequency of the shear wall HDNLSW was greater, indicating that its residual stiffness is larger, which was more conducive to structural earthquake resistance.

Damping reflects the attenuation of the vibration energy of an object. The damping ratio is the ratio of the damping force to the critical damping force, representing the damping force's magnitude. In the elastic stage, damping is mainly related to the material. The material and size of the two specimens were the same, so the damping ratios were similar. After the structure enters the plastic stage, damping is mainly related to structural damage. It can be seen that the new shear wall has a more excellent damping ratio after the test, implying that it has a better energy dissipation capacity. This is because the cracks between the mortar strip and the wallboard on both sides increase the friction energy consumption of the wallboard under a reciprocating load, thus improving the structural damping.

4. Discussion

In order to solve the problem of poor deformation capacity of a conventional low-rise shear wall, a new shear wall with an embedded steel plate and vertical slits was proposed in this paper. Through the comparative test of the two shear walls, it can be seen that the function of two vertical slits was to change the original low-rise shear wall into three high-rise shear walls. Thus, the brittle failure of the original low-rise

shear wall was transformed into ductile failure. At the same time, the embedded steel plate can improve the stiffness and bearing capacity of the shear wall with vertical slits and reduce the weakening effect of slit treatment on the low-rise shear wall. This finding provides a basis for the optimized design of shear walls.

This study only completed a comparative test of the two shear walls to verify the rationality of the new shear wall. However, the theoretical calculation and reasonable parameters of the new shear wall, such as the location of the crack and the size of the built-in steel plate, need to be studied further. The next step will be to establish a numerical model for verification and further for the mechanical procedure and parameter analysis.

5. Conclusion

The following findings can be obtained from the experimental research and analysis of two distinct kinds of shear walls:

- (1) Compared with the traditional concealed bracing low-rise shear wall, the deformation capacity and energy dissipation capacity of the new low-rise shear wall are significantly improved and they have a good bearing capacity. The hysteresis loop was more plumped, and the seismic performance was better.
- (2) The traditional low-rise shear wall with concealed bracing is mainly brittle shear failure. In contrast, the new low-rise shear wall exhibits bending loss with good ductility, and the failure is primarily concentrated on the two sides of the vertical slits of the shear wall. The shear wall between the vertical slits was slightly damaged, and the failure mode was more reasonable. Because the shear wall between the vertical slits still has a high bearing capacity after the failure of the shear wall on both sides of the vertical slits, a clear two-way seismic defense line is formed, which can meet the requirements of no collapse under strong earthquakes.
- (3) The new low-rise shear wall can meet different mechanical properties. By adjusting the width of the shear wall between the vertical slits and the size of the steel plate, shear walls with varying capacities of bearing and ductility can be obtained to meet different needs. However, further studies are required for a proper seam position and an economical steel plate size.

Data Availability

The data used to support the findings of this study are available from the corresponding author upon request.

Conflicts of Interest

The authors declare that there are no conflicts of interest.

Acknowledgments

This paper was supported by the Ministry of Housing and Urban-Rural Development of China Research Project (No. 2017-K9-010) and the Science and Technology Program of Yangzhou (YZ2019138).

References

- [1] C. R. Farrar, J. W. Reed, and M. W. Salmon, "Failure modes of low-rise shear walls," *Journal of Energy Engineering*, vol. 119, no. 2, pp. 119–138, 1993.
- [2] T. N. Salonikios, A. J. Kappos, I. A. Tegos, and G. G. Penelis, "Cyclic load behavior of low-slenderness RC walls: failure modes, strength, and deformation analysis, and design implications," *ACI Structural Journal*, vol. 97, no. 1, pp. 132–141, 2000.
- [3] W. Y. Kam, S. Pampanin, and K. Elwood, "Seismic performance of reinforced concrete buildings in the 22 February Christchurch (Lyttelton) earthquake," *Bulletin of the New Zealand Society for Earthquake Engineering*, vol. 44, no. 4, pp. 239–278, 2011.
- [4] K. Muto, *Structural Dynamic Design*, pp. 87–90, China Architecture and Building Press, Beijing, 1984.
- [5] H. J. Jiang, X. L. Lu, and Y. K. Cheung, "Study on a seismic slit shear wall with cyclic experiment and macro-model analysis," *Structural Engineering & Mechanics*, vol. 16, no. 4, pp. 371–390, 2003.
- [6] X. L. Lu, X. L. Dang, J. Qian, Y. Zhou, and H. J. Jiang, "Experimental study of self-centering shear walls with horizontal bottom slits," *Journal of Structural Engineering*, vol. 143, no. 3, 2017.
- [7] C. Sittipunt, S. L. Wood, and P. Lukkunaprasit, "Cyclic behavior of reinforced concrete structural walls with diagonal web reinforcement," *ACI Structural Journal*, vol. 98, no. 4, p. 554, 2001.
- [8] S. Shaingchin, P. Lukkunaprasit, and S. L. Wood, "Influence of diagonal web reinforcement on cyclic behavior of structural walls," *Engineering Structures*, vol. 29, no. 4, pp. 498–510, 2007.
- [9] J. W. Zhang, W. L. Cao, C. Yu, and H. Y. Dong, "Shake table test of reinforced concrete wall structure with concealed bracings," *Proceedings of the Institution of Civil Engineers - Structures and Buildings*, vol. 167, no. 10, pp. 598–609, 2014.
- [10] D. Zhang, Z. Tao, and L. Zhang, "Research on deformation behavior of reinforced concrete composite shear wall with concealed bracings based on performance," *Engineering Review*, vol. 37, no. 2, pp. 111–121, 2017.
- [11] M. Gan, M. Kang, C. Long, and L. R. Li, "Cyclic response of scaled low-rise shear walls with concealed bracings," *Materiali in tehnologije*, vol. 54, no. 4, pp. 447–455, 2020.
- [12] W. Wang, Y. Z. Ren, Z. Lu, K. L. Song, and Y. Zhou, "Experimental study of the hysteretic behaviour of corrugated steel plate shear walls and steel plate reinforced concrete composite shear walls," *Journal of Constructional Steel Research*, vol. 160, pp. 136–152, 2019.
- [13] W. Wang, Y. Wang, and Z. Lu, "Experimental study on seismic behavior of steel plate reinforced concrete composite shear wall," *Engineering Structures*, vol. 160, pp. 281–292, 2018.
- [14] D. Dan, A. Fabian, and V. Stoian, "Nonlinear behavior of composite shear walls with vertical steel encased profiles," *Engineering Structures*, vol. 33, no. 10, pp. 2794–2804, 2011.

- [15] C. J. Gan and L. V. Xilin, "Computational simulation of nonlinearity of steel plate reinforced concrete shear walls," *Journal of Structural Engineering*, vol. 30, no. 5, pp. 97–102, 2009.
- [16] Z. Zhou, J. Qian, and W. Huang, "Numerical study on deformation capacity of steel plate reinforced concrete shear walls," *Advances in Civil Engineering*, vol. 34, 2019.
- [17] *Code for Design of concrete Structures: GB 50010-2010*, China Architecture & Building Press, Beijing, 2015.
- [18] *Specification for Seismic Test of Buildings: JGJ/T 101-2015*, China Architecture & Building Press, Beijing, 2015.

Research Article

Deformation Characteristics and Safety Evaluation of the Throw Filling Soft Clay Cofferdam under Super-Historical Flood Conditions

Ping Jiang,¹ Yong Huang,² Zhipeng Tao,³ Junhua Zhu ,^{4,5,6} Ning Wang,⁵ and Jianwei Qiao⁷

¹Jiangxi Port Group Co., Ltd., Nanchang 330062, China

²Jiangxi Road and Port Engineering Co., Ltd., Nanchang 330062, China

³Jiangxi Transportation Institute Co., Ltd., Nanchang 330062, China

⁴School of Civil Engineering and Architecture, East China Jiaotong University, Nanchang 330013, China

⁵State Key Laboratory of Performance Monitoring Protecting of Rail Transit Infrastructure, East China Jiaotong University, Nanchang 330013, China

⁶Engineering Research & Development Centre for Underground Technology of Jiangxi Province, Nanchang 330013, China

⁷China Jikan Research Institute of Engineering Investigations and Design Co., Ltd., Xi'an 710043, China

Correspondence should be addressed to Junhua Zhu; 3062@ecjtu.edu.cn

Received 6 December 2021; Accepted 29 March 2022; Published 26 April 2022

Academic Editor: Qinghua Zhang

Copyright © 2022 Ping Jiang et al. This is an open access article distributed under the Creative Commons Attribution License, which permits unrestricted use, distribution, and reproduction in any medium, provided the original work is properly cited.

Affected by super-historical flood, the surface deformation of throw filling soft clay cofferdam is obvious and the stability of the cofferdam slope is difficult to ensure. Relying on the cofferdam project of Jiangxi Xinjiang Shuanggang navigation power junction and according to the data of filed investigation and automatic monitoring, the Plaxis infinite element software is used to analyze the deformation characteristics and stabilities of cofferdam during the super-historical flood period, and the effective emergency reinforcement measures are presented. The results show that (1) the stability of cofferdam is controlled by downstream face slope of cofferdam during the super-historical flood period, and there is a most dangerous slide surface interpenetrating through the top to the toe of downstream face slope; (2) the stability of upstream face slope is influenced significantly by the water level fluctuation and it is reduced sharply during the water level decline process; and (3) real-time remote monitoring can effectively reflect the deformation and failure characteristics of cofferdam under the condition of super-historical flood level and provide early warning and prediction in time. The results and analyzing methods can be applied to analyze the similar projects excellently.

1. Introduction

In hydropower and navigation junction projects, the cofferdam is designed according to the diversion flow of design frequency and corresponding water level to carry out construction diversion and ensure the continuous construction of main works [1–5]. At the same time, the year-round cofferdam as a temporary water-blocking building during the river flood season, its stability in flood period is an important premise to protect the construction personnel in the weir and the safety of the project [6, 7].

In the diversion system of earth rock cofferdam, slope instability is not only the most frequent but also the most

loss and the most difficult to make up [8–12]. In addition to the stability of the cofferdam under the action of self weight, the seepage will also lead to the instability of the cofferdam body under the condition of water level difference inside and outside the cofferdam [13–17]. During the flood period, the rise of water level leads to the increase in soil moisture content and the decrease in shear strength, and the pore water pressure in the slope is also in dynamic change with the rise and fall of water level [18, 19]. At the same time, the stress condition and antisliding ability of cofferdam slope will be changed by flood pressure and immersion [20]. In the study by Zhang [21], according to the deformation mechanism of some landslides after the change of water level in

the Three Gorges reservoir, from the analysis, the rise of reservoir water level has limited influence on landslide deformation, but the decline of water level will directly lead to landslide. Luo [22] through integrating on-site investigation, monitoring data, and numerical simulation, the formation mechanism and deformation characteristics of Waitang landslide are revealed, in which rainfall and reservoir water level change are the main factors affecting slope behavior; Xiao et al. [23], using the method of intermittent decline of reservoir water level to trigger landslide, studied the effect of rapid change of water level on landslide stability; the analysis shows that the intermittent drop is beneficial to the dissipation of hole pressure in the landslide body, but when the reservoir water level decreases too fast, there is a lag effect of groundwater fall back beneficial to the reduction of hydraulic gradient.

In the study by Wang et al. [24], through the comparison and analysis of the stability of different processes of flood rise, flood immersion, and flood decline, it is pointed out that the stability of the shore beach is the best during the period of rapid flood rise, followed by the period of slow rise, soak period, and slow decline of flood, and the stability of shore beach is the worst during the period of flood plunge.

From the existing research, most of them are aimed at the deformation characteristics and instability mechanism of earth rock cofferdam, clay core dam, and reservoir bank slope under the condition of water level fluctuation or flood, while there are few studies on soft clay cofferdam formed by the throw filling [25–30]. Due to the shortage of filling materials, the cofferdam of Shuanggang navigation power junction project in Xinjiang, Jiangxi Province, mainly adopted silty clay excavated by diversion channel with low shear strength, low bearing capacity, and high water content and supplemented by outsourcing soil. In the cofferdam operation stage in July 2020, with the water level outside the cofferdam raised to 20.8 m that exceeded the design flood water level, there is certain deformation in the surface of the cofferdam and posed a great threat to the stability of it. This paper lies on this project; according to the data of filed investigation and automatic monitoring, the finite element software named Plaxis is applied to analyze the deformation characteristics and evaluate the safety situation of cofferdam during the super-historical period, presenting the emergency reinforcement measures to provide reference for the similar projects.

2. Background of Project

2.1. General Situation of Cofferdam. The main construction of Jiangxi Xinjiang Shuanggang navigation power junction project is located in the distance of 5 km far away from downstream of Poyang Town, Shangrao City. For providing the drying construction condition for building main structures, a cofferdam should be fabricated. Due to the shortage of filling materials, the perennial cofferdam filling is mainly filled with saturated silty clay mixed with muddy soil from the riverbed excavated by diversion channel, and some outsourcing soil is purchased for the backfilling of the cofferdam dike core to strengthen the cofferdam and form roads. The total length of

the cofferdam is 2454 m, including 450 m length of upstream cofferdam, 1459 m length of longitudinal cofferdam, and 545 m length of downstream cofferdam, with the service life of the cofferdam which belongs to the perennial cofferdams ranging from 2 to 2.5 years. According to the Design Code for Cofferdams of Water Resources and Hydropower Engineering (SL645-2013), the lock level is Class II and the design level of the cofferdam is Class IV. The layout of diversion channel and cofferdam is shown in Figure 1.

The design of lowest water level and flood water level is 13.92 m and 19.94 m. The molding of throw filling soft clay cofferdam is really hard because of the high compressibility and low strength of filling materials. After the stable molding, the actual shape of the cofferdam is different from the design shape that the actual slope ratios of the cofferdam above the horse path whose elevation is 14 m at both of upstream and downstream cofferdam are less than 1 : 5, and the slope ratio of the slope whose elevation is lower than 14 m is less than 1 : 7, and it is more gentle at the center location where the slope ratio is 1 : 31 eventually.

2.2. Automatic Monitoring of Cofferdam. Considering the lack of experience references for this type of cofferdam and because of the low strength, discreteness of mechanical properties, and uncertainties of spatial distribution of filling materials, the automatic monitoring of displacement and seepage force is applied to monitor the real-time deformation and stability of the cofferdam for ensuring the safety operation of it. The arrangement plan of automatic monitoring is shown in Figure 2. According to the results of numerical simulation and field experience, the early warning value and alarm value of horizontal displacement rate of the cofferdam is set as 1.5 mm/d and 2.0 mm/d [31, 32].

2.3. General Situation of Super-Historical Flood. In July 2020, affected by the superposition of continuous heavy rainfall and upstream river water, the water level of Xingzi station which is a landmark hydrological station of Poyang Lake was raised to 22.53 m that it was 0.01 m higher than the historical highest water level of 22.52 m in 1998; the water level of Poyang Lake broke through the historical extreme value since the exist of hydrological record.

Affected by the super-historical flood, the water level outside the cofferdam is reached to 20.8 m that it is 0.86 m higher than the design flood water level of the cofferdam. From June 30 to July 12, the increment of water level outside the cofferdam was 4.91 m, and the maximum water level increasing rate was 0.81 m/d, which was higher than the maximum daily water level increasing rate in 1998. The change curve of water level outside the cofferdam during flood period is shown in Figure 3.

3. Analysis on Deformation Characteristics of Cofferdam in Flood Period

The field investigation shows that under the action of super-historical flood, the cofferdam slope has certain deformation and damage, which is mainly concentrated in the upstream



FIGURE 1: Layout of cofferdam and divert.

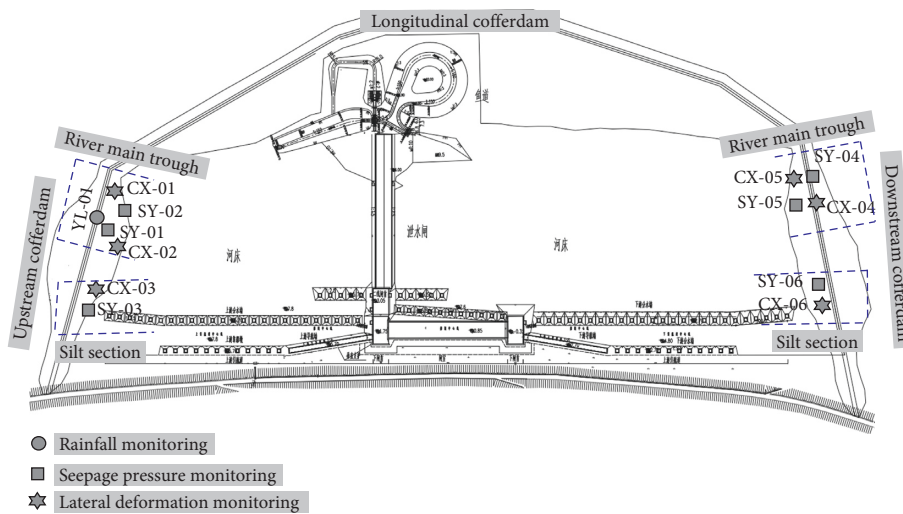


FIGURE 2: Schematic layout of cofferdam slope monitoring points.

cofferdam. According to the data of field investigation and automatic monitoring, the deformation characteristics of cofferdam during the flood rising period and flood decline period are analyzed in this paper.

3.1. Deformation Characteristics of Cofferdam in Flood Rising Period. According to the field investigation, in the flood rising period, the deformation and damage area are located in the riverbed center of upstream cofferdam where the thickness of filling material is maximum. Because the height difference between the flood water level and the top of cofferdam is just 0.2 m, a surcharge load of sand bags whose height and width are 1 m and 2 m is carried out at the upstream side of cofferdam for preventing the cofferdam exceeded by the flood water. However, influenced by the surcharge load, a tensile fissure and meteorism deformation

occurred at the top of cofferdam. The length and width of the tensile fissure are 99 m and 2.0~3.0 cm separately as shown in Figure 4 and the strike almost parallels with the extended direction of road. The height of meteorism deformation is 6.0~8.0 cm generally.

Meanwhile, there is a small sized piping damage occurred at the position of elevation of 11 m which is located in the horse path of downstream face caused by the huge seepage force which is formed by the water head difference between upstream face and downstream face. Fortunately, the filling material of cofferdam almost consists of clay particles whose permeability is small so that the seepage water from the piping is clean and there is a small threat to the stability of cofferdam (as shown in Figure 5).

According to the distribution of deformation area, the real-time monitoring data of measuring points cx-01, cx-02, and sw-01 are selected to comparative analysis. The results

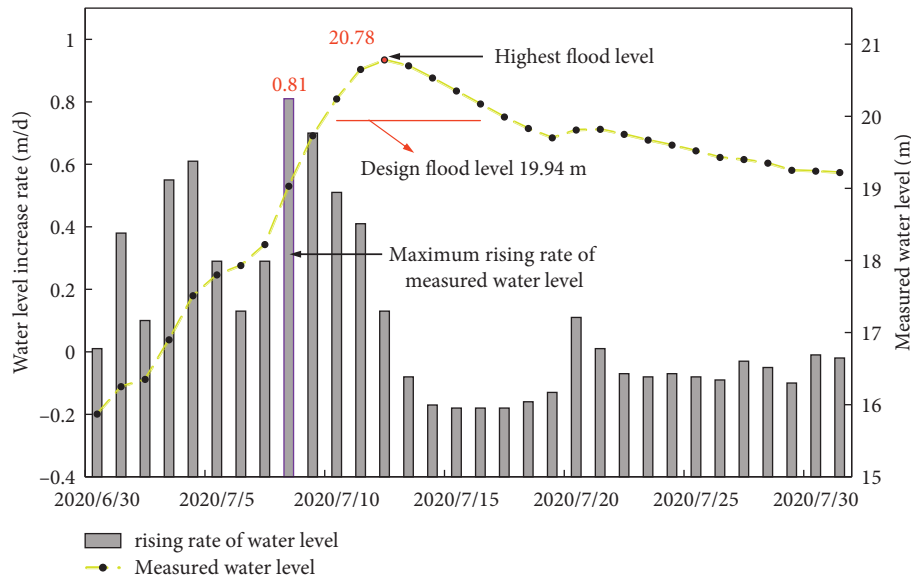


FIGURE 3: Curve of water level change outside the cofferdam during flooding.



FIGURE 4: Tensile fissure at the top of upstream cofferdam.



FIGURE 5: Piping effect at downstream face slope of cofferdam.

show that (Figure 6), during the flood rising period, the soil deformation rate below the path way is small and the state is stable. However, the soil above the path way of the downstream face has an accelerated deformation rate, and the maximum value reaches to 1.95 mm/d that is closing to the alarm value, and there is a potential risk of sliding. The generation and development of tensile cracks are closely related to the displacement of the soil below the cofferdam crest of the downstream face slope.

The growth rate of the water level in the cofferdam lags behind the growth rate of outside water level during the super-historical flood raising period. The high head difference between the flood water level (20.78 m) and the water level in the cofferdam (11 m) is an important reason for the local piping failure. Considering the risk of instability and damage of cofferdam, the emergency treatment measures shall be taken to reinforce the cofferdam as follows: concrete grouting reinforcement is carried out in the tensile fissure area; the height of piping well is increased and the geotextile is laid aside the piping outlet; a flood spillway is set to reduce the water head difference between outside and inside of the cofferdam.

3.2. Deformation Characteristics of Cofferdam in Flood Decline Period. The tensile fissure and meteorism deformation which has been reinforced at the top of cofferdam continue to develop that the width of tensile fissure is increased to 4 cm and the height of meteorism deformation is increased to 10 cm (Figure 7). The scope of piping is not expanding, and its flow rate is reduced benefitting from the reinforcement measure.

The real-time monitoring results show (Figure 6) that the deformation rate of potential sliding area is less than 1.5 mm/d and the situation of deformation rates is

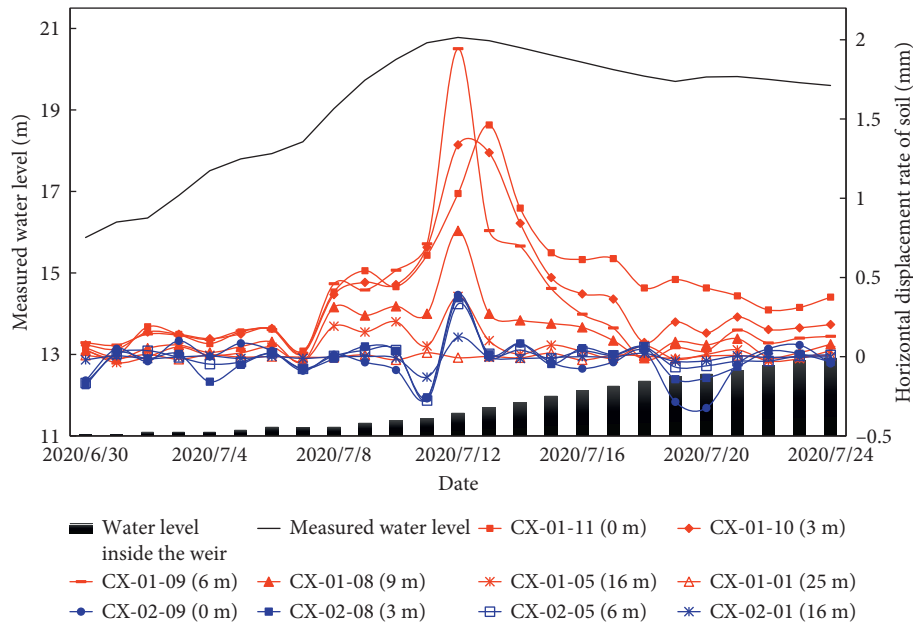


FIGURE 6: The displacement changing rates of CX-01 and CX-02 during the super-historical flooding period.

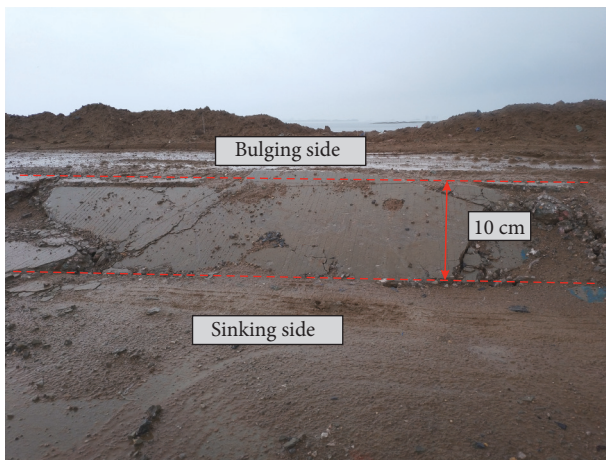


FIGURE 7: Meteorism deformation in the top of upstream cofferdam during flood decline period.

convergent during the super-historical flood decline process. It demonstrates that the emergency reinforcement measurements are effective and the cofferdam tides over the super-historical period safely. Due to the influence of upstream face head pressure and cofferdam foundation drainage, the water level inside the cofferdam gradually rises, and the water level difference inside and outside of the cofferdam is reduced, avoiding the development of piping damage.

4. Stability Evaluation of Cofferdam Slope and Discussion

As mentioned above, the dynamic change of outside flood water level will not only affect the development of cofferdam slope but also change the seepage state of soil inside the

cofferdam, resulting in the increase in soil moisture content and the decrease in shear strength. In addition, influenced by the water head difference between outside and inside of cofferdam, the stability of the cofferdam slope will be reduced caused by the seepage force inside the cofferdam (see Zhang and Hu [33]). For further research and verification, the finite element numerical software named Plaxis is used to analyze the stability state of the cofferdam during the super-historical flood period [34].

4.1. *Computational Model.* According to the field investigation and drilling boring information, a 2-dimensional calculation model is established by the Plaxis software, which represents the most dangerous profile of the cofferdam as shown in Figure 8.

4.2. *Computing Method.* Mohr–Coulomb model is selected to describe the constitutive model of filling materials, and liner-elastic model is selected to describe the impermeable wall [35]. It is assumed that the flow of pore water accords with Darcy’s law, and the coupling effect of seepage field and stress field during the water level fluctuation is considered in the seepage analysis process. Furthermore, a shear strength reduction factor ΣMSF leads to the calculation of stability of the cofferdam that making the strength parameter C and ϕ and the tensile strength decrease gradually until the soil is damaged [36]. The ΣMSF is defined as follows:

$$\sum M_{sf} = \frac{\tan \phi_{input}}{\tan \phi_{reduced}} = \frac{c_{input}}{c_{reduced}} \quad (1)$$

In the formula, ϕ_{input} is the internal friction angle of soil mass; c_{input} is the initial cohesion; $\phi_{reduced}$ is the internal friction angle of soil mass after the strength

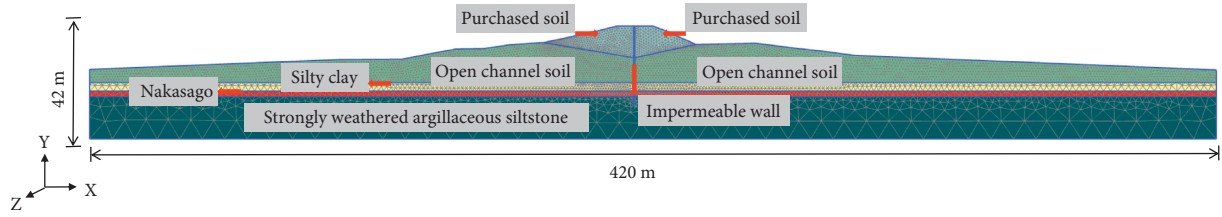


FIGURE 8: Cofferdam structure and filling distribution.

TABLE 1: Properties of soils/rocks of the cofferdam and foundation.

Cofferdam material	Cohesion (kPa)	Internal friction angle (°)	Permeability coefficient (cm·s ⁻¹)	Natural bulk density (kN·m ⁻³)	Saturated bulk density (kN·m ⁻³)	Elastic modulus (kPa)	Poisson's ratio	Thickness (m)
Outsourcing soil	34.1	13.4	6.17×10^{-5}	18.40	19.30	11260	0.30*	6.0~8.0
Outsourcing soil soaked in flood (upstream face)	30.1	13.4	6.17×10^{-5}	18.40	19.30	11260	0.30*	6.0~8.0
Open channel backfill (upstream face)	19.0	9.0	6.17×10^{-5}	18.00	18.30	10580	0.35*	13.0~15.0
Open channel backfill (downstream face)	12.5	7.0	6.17×10^{-5}	18.00	18.30	10580	0.35*	13.0~15.0
Silty clay	20.0	13.0	7.0×10^{-5}	18.80	20.00	8840*	0.30*	1.5
Medium sand	0.0	28.0	1.0×10^{-3}	18.00	19.00	12000*	0.30*	0.5
Strongly weathered argillaceous siltstone	100.0	35.0	1.0×10^{-4}	20.00	21.00	300000*	0.30*	—
Impermeable wall	—	—	5.0×10^{-6}	22.00	23.00	300000*	0.20*	—

reduction; and c_{reduced} is the cohesion after the strength reduction.

Assume that if the calculation model does not converge during the numerical analysis, it indicates that the cofferdam or its foundation reaches completely destruction, and the corresponding safety factor is as follows:

$$SF = \frac{\text{usable strength}}{\text{failure strength}} = \sum M_{sf} = (\text{at failure}). \quad (2)$$

According to «Design code for cofferdam of water resources and hydropower engineering» (SL645-2013), when the design level of cofferdam is IV, the safety factor of antisliding stability of cofferdam slope is $k \geq 1.05$.

4.3. Parameter Selection. The silty clay and outsourcing soils disturbed by both excavation and throw filling are filled as the main structure of the cofferdam, causing the huge discreteness on the physical and mechanical parameters of the filling materials that are hard to determine. Therefore, an antianalysis method is applied to analyze the mechanical parameters of the filling materials in different conditions based on the data of automatic monitoring, laboratory tests, and experience. As the length limitation of this paper, the specific analysis process would not be mentioned. The final physical and mechanical parameters of rock and soil are shown in Table 1.

4.4. Calculating Conditions. Combined with the water level monitoring data outside the cofferdam and considering the flood change time history, the measured water level from March 24 to November 1, 2020, is selected to simulate the whole process of flood operation situation of the cofferdam in flood season and analyze the change of cofferdam slope stability coefficient under the change of water level. Calculation working conditions include stable operation stage of cofferdam before flood (working condition A1), flood rising stage (working condition B2), pile-loading sandbags on weir crest at upstream side, stable seepage stage of flood level (working condition C3), and flood falling stage (working condition D4), as shown in Table 2.

4.5. Calculation Results Analysis and Discussion. The cofferdam stability safety factor obtained under all the above working conditions is listed in Table 3; it indicates that

- (1) The safety factors of cofferdam are greater than 1.05 entirely during the whole process of super-historical flood season, and the overall stability of cofferdam is controlled by the downstream face slope, and the condition of flood water decline is the most unfavorable working condition, and the minimum safety factor is 1.58 in D4 condition. The cofferdam is in a stable state.

TABLE 2: Load combinations for cofferdam stability analysis.

Calculation conditions	Illustrate	Measured water level outside of the cofferdam	Cofferdam top loading
A1	Stable operation of the cofferdam before the flood	March 24–June 30, 2020	—
B2	Flood rising period	July 01–July 11, 2020	—
C3	Loaded sand bags, stable seepage at flood level (20.78 m)	July 12, 2020	20 kN/m ²
D4	Flood decline period	July 12–November 1, 2020	20 kN/m ²

TABLE 3: Factor of safety (FOS) of cofferdam stability for all load conditions.

Calculation working condition	Upstream face side slope Minimum safety factor	Downstream face side slope Minimum safety factor	Entirety cofferdam Minimum safety factor	Destabilization side
A1	2.04	1.64	1.65	Downstream face
B2	3.12	1.60	1.61	Downstream face
C3	2.92	1.62	1.62	Downstream face
D4	1.94	1.57	1.58	Downstream face

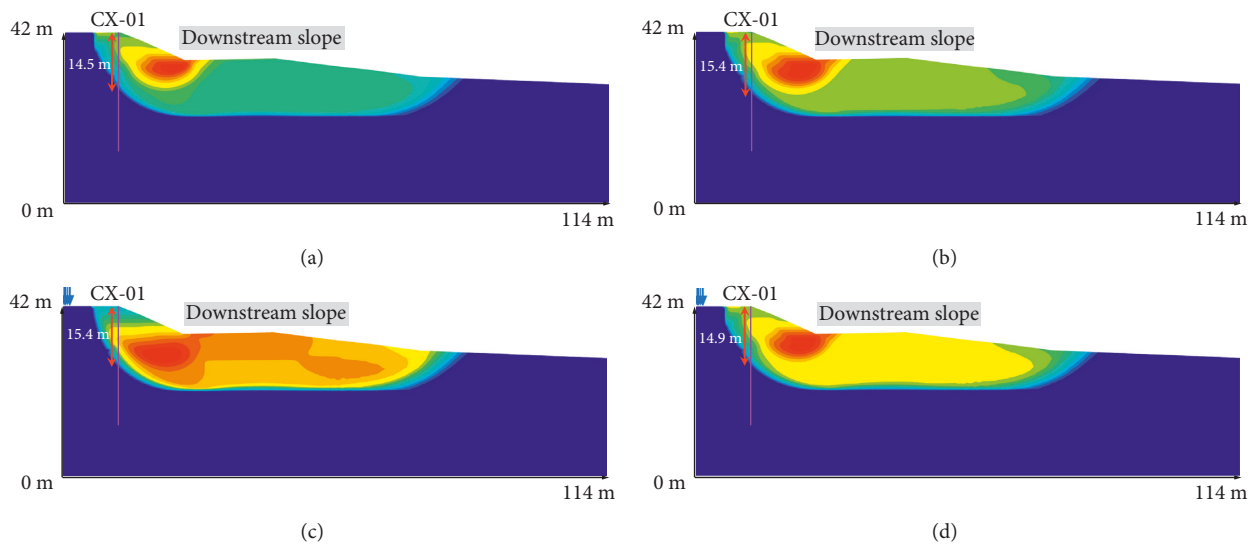


FIGURE 9: Horizontal displacement clouds of the backwater slope hazardous slip surface: (a) working condition A1; (b) working condition B2; (c) working condition C3; (d) working condition D4.

- (2) The change of water level significantly affects the stability of the upstream face slope, and the stability safety factor decimated in the process of flood declines that the reduction rate of safety factor between the maximum and minimum value is 37.8%.
- (3) During the whole process, the surcharge load at the top of cofferdam has a positive effect to the stability of whole cofferdam, but it will reduce the stability of upstream face slope and the reduction rate is 6.4%. Therefore, we suggest that the surcharge load of sand bags should be loaded at the axis of the top of the cofferdam.
- (4) As shown in Figure 9, the minimum safety factors of actual slope types in all conditions are located in the downstream face entirely, and the displacement value and the scope of sliding area simulated by the

numerical method are consistent with the automatic monitoring data that the potential sliding region is transfixion from the toe to the top of downstream face slope.

- (5) Figure 10 shows the horizontal displacement of calculated and measured at the position of CX-01, and we can see that the value and regulation of them are consistent ultimately. The result indicates that the actual situation of the cofferdam engineering can be reflected excellently by the numerical simulation of Plaxis.

As shown in Figure 11 that the safety factors of cofferdam in each condition are reduced, the reduction rates are really small. It is because that the actual slope ratio of cofferdam is much more gentle than the design slope ratio and the permeability coefficient of filling materials is really

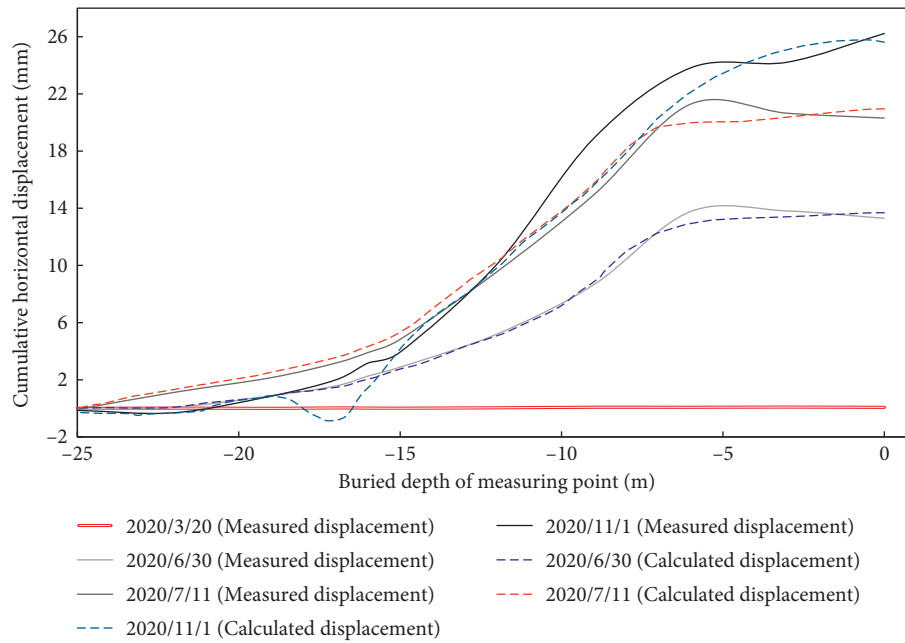


FIGURE 10: Cofferdam slope soil horizontal displacement fitting curve.

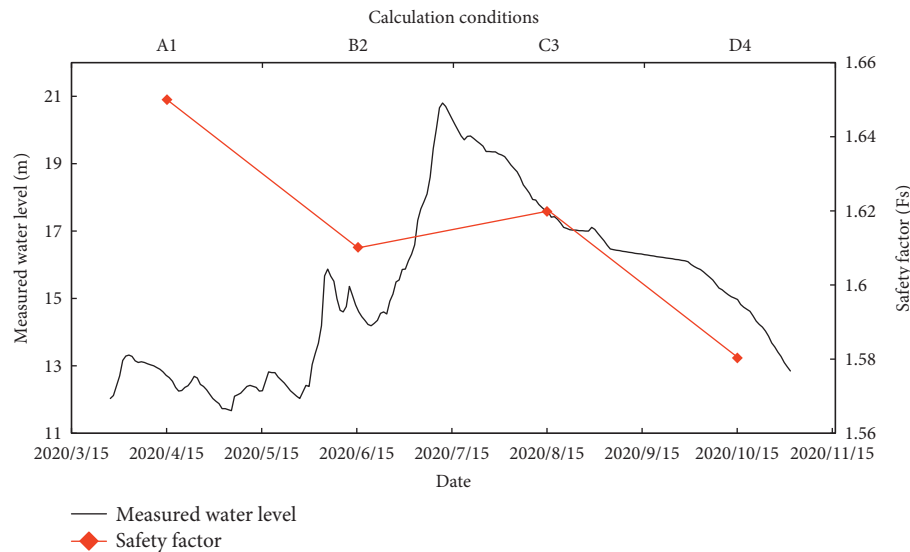


FIGURE 11: Variation of safety factors under different operating conditions.

small so that the change of seepage pressure in the downstream face slope is tiny during the transient seepage state of high flood water level.

5. Conclusion

According to the results of field investigation, automatic monitoring, and numerical simulation analysis, the conclusion can be obtained as follows:

- (1) The generation of tensile fissure on the top of cofferdam is closely related to the soil deformation of the downstream face slope. In addition, the rise of flood accelerates the growth of soil deformation rate

within 15 m below the cofferdam crest, which directly leads to the continuous development of fissure.

- (2) According to the monitoring data, the water level variation inside the cofferdam is lagging to the rise of water level in flood season, and the high head difference between the flood level (20.78 m) and the cofferdam internal body water level (11 m) is an important reason for the local piping failure.
- (3) For the throw filling soft clay cofferdam which is constructed in a gentle slope ratio type, the stability is controlled by the downstream face and the most dangerous situation is performed in the flood water decline process.

- (4) The internal deformation of cofferdam can be reflected effectively by the real-time automatic monitoring method, and the early warning can be presented to ensure the stable operation of cofferdam.

Data Availability

The data are generated from experiments and can be available from the corresponding author upon request.

Conflicts of Interest

The authors declare that they have no conflicts of interest.

Acknowledgments

This research was funded by Key Engineering Science and Technology Projects of Jiangxi Provincial Department of Transportation 2019C0010 and 2019C0011 and the National Natural Science Foundation of China, 51868021, and supported by the National Natural Science Foundation of China, 52168047; Jiangxi Provincial Natural Science Foundation, 20202BABL20405; High Speed Railway Joint Fund of NSFC, U1934208; and the Natural Science Foundation of Jiangxi Province 20212BAB214009.

References

- [1] X. Li, Z. Cao, and Y. Xu, "Characteristics and trends of coal mine safety development," *Energy Sources, Part A: Recovery, Utilization, and Environmental Effects*, vol. 12, pp. 1–19, 2020.
- [2] S. Liu, X. Li, and D. Wang, "Investigations on the Mechanism of the Microstructural Evolution of Different Coal Ranks under Liquid Nitrogen Cold Soaking," *Energy Sources, Part A: Recovery, Utilization, and Environmental Effects*, vol. 7, pp. 1–17, 2020.
- [3] X. L. Li, S. J. Chen, Q. M. Zhang, X. Gao, and F. Feng, "Research on theory, simulation and measurement of stress behavior under regenerated roof condition," *Geomechanics and Engineering*, vol. 26, no. 1, pp. 49–61, 2021a.
- [4] X. L. Li, S. J. Chen, S. M. Liu, and Z. H. Li, "AE waveform characteristics of rock mass under uniaxial loading based on Hilbert-Huang transform," *Journal of Central South University*, vol. 28, no. 6, pp. 1843–1856, 2021b.
- [5] X. L. Li, S. J. Chen, and S. Wang, "Study on in situ stress distribution law of the deep mine taking Linyi Mining area as an example," *Advances in Materials Science and Engineering*, vol. 9, no. 4, p. 5594181, 2021c.
- [6] Yu Yang, G.-liang Feng, C.-jie Xu, B.-R. Chen, Da-X. Geng, and Bi-T. Zhu, "Quantitative Threshold of Energy Fractal Dimension for Immediate Rock-Burst Warning in Deep Tunnel: A Case Study," *Lithosphere*, vol. 2022, Article ID 1699273, 2022.
- [7] F. Zhang, *Study on the Stability of Weir Slopes of High Soil and Rock Weirs with Deep Overburden*, China Three Gorges University, Yichang, China, 2015a.
- [8] W. L. Shen, G. C. Shi, Y. G. Wang, J. B. Bai, R. F. Zhang, and X. Y. Wang, "Tomography of the dynamic stress coefficient for stress wave prediction in sedimentary rock layer under the mining additional stress," *International Journal of Mining Science and Technology*, vol. 31, pp. 653–663, 2021.
- [9] X. G. Kong, D. He, X. F. Liu et al., "Strain characteristics and energy dissipation laws of gas-bearing coal during impact fracture process," *Energy*, vol. 242, Article ID 123028, 2022.
- [10] X. G. Kong, S. G. Li, E. Y. Wang et al., "Experimental and numerical investigations on dynamic mechanical responses and failure process of gas-bearing coal under impact load," *Soil Dynamics and Earthquake Engineering*, vol. 142, Article ID 106579, 2021.
- [11] Z. Li, X. Zhang, and Y. Wei, "Experimental study of electric potential response characteristics of different lithological samples subject to uniaxial loading," *Rock Mechanics and Rock Engineering*, vol. 54, pp. 397–408, 2021d.
- [12] Y. Niu, E. Wang, and Z. Li, "Identification of coal and gas outburst-hazardous zones by electric potential inversion during mining process in deep coal seam," *Rock Mechanics and Rock Engineering*, vol. 2022, 2022.
- [13] Y. Gao, Y. Yin, and B. Li, "Failure process simulation analysis of the Shenzhen "12.20" CDW landfill landslide: a case study," *Arabian Journal of Geosciences*, vol. 14, no. 12, pp. 1–12, 2021.
- [14] Y. Gao, Y. Yin, and B. Li, "Investigation and dynamic analysis of the long runout catastrophic landslide at the Shenzhen landfill on December 20, 2015, in Guangdong, China," *Environmental Earth Sciences*, vol. 76, no. 1, pp. 1–16, 2017.
- [15] T. Vitaly, N. Aleksandr, B. Vladimír, G. Inna, V. Yulia, and S. Olga, "Modeling of hydrophysical properties of the soil as capillary-porous media and improvement of mualem-van genuchten method as a part of foundation arrangement research," *Advances in Civil Engineering*, vol. 2016, Article ID 8176728, 7 pages, 2016.
- [16] B. Wang, *The Influence of Water on the Management of Large Mounded Landslides*, Shijiazhuang Tiedao University, Shaoxing, China, 2014.
- [17] C. Zhang, "Analysis of slope instability risk of high soil and rock but water cofferdams," *Chinese Journal of Rock Mechanics and Engineering*, vol. 34, no. S2, pp. 4157–4163, 2015b.
- [18] H. Wu, G. Zhao, and S. Ma, "Failure behavior of horseshoe-shaped tunnel in hard rock under high stress: phenomenon and mechanisms," *Transactions of Nonferrous Metals Society of China*, vol. 32, no. 2, pp. 639–656, 2022a.
- [19] G. Han, Yu Zhou, R. Liu, Q. Tang, X. Wang, and L. Song, "Influence of surface roughness on shear behaviors of rock joints under constant normal load and stiffness boundary conditions," *Natural Hazards*, vol. 2, pp. 1–18, 2022.
- [20] Li Zhan, *Research on Multi-Conditions Test and Numerical Simulation Calculation of High Water Level Long-Term Inundation Embankment Project*, Heilongjiang University, Harbin, China, 2018.
- [21] Y. Zhang, "Stability analysis of a typical landslide mass in the Three Gorges Reservoir under varying reservoir water levels," *Environmental Earth Sciences*, vol. 79, no. 1, pp. 243–254, 2020a.
- [22] S. Luo, "Reactivation of a huge, deep-seated, ancient landslide: formation Mechanism, deformation characteristics, and stability," *Water*, vol. 12, no. 7, 2020.
- [23] Z. Xiao, H. Deng, and J. Li, "Influence of intermittent decline in reservoir water level on the stability of mounded landslides," *Journal of Yangtze River Scientific Research Institute*, vol. 33, no. 8, pp. 114–119, 2016.
- [24] Y. Wang, S. Kuang, and C. Yin, "Influence of flood level changes on shore beach stability," *Journal of Hydraulic Engineering*, vol. 46, no. 12, pp. 1398–1405, 2015.
- [25] X. Wang, Y. Xiao, W. Shi et al., "Forensic Analysis and Numerical Simulation of a Catastrophic Landslide of

- Dissolved and Fractured Rock Slope Subject to Underground Mining,” *Landslides*, vol. 18, no. 5, 2022.
- [26] J. B. Yan, Z. X. Zou, R. Mu et al., “Evaluating the stability of Outang landslide in the Three Gorges Reservoir area considering the mechanical behavior with large deformation of the slip zone,” *Natural Hazards*, vol. 2022, 2022.
- [27] Z. Li, J. Chen, and C. Tan, “Debris flow susceptibility assessment based on topo-hydrological factors at different unit scales: a case study of Mentougou district, Beijing,” *Environmental Earth Sciences*, vol. 80, p. 365, 2021e.
- [28] X. Zhang, W. Li, and B. Zeng, “Design and construction of double-wall steel cofferdam in deep water foundations. IOP Conference Series,” *Earth and Environmental Science*, vol. 631, no. 1, Article ID 012054, 2021.
- [29] F. Yuan and W. Chen, “Stability analysis of temporary cofferdam of a ship lock construction project in coastal area. IOP Conference Series,” *Earth and Environmental Science*, vol. 768, no. 1, Article ID 012118, 2021.
- [30] Z. Huang, S. Yang, N. Yang, M. Zhou, and A. Li, “Optimized design for large geotextile mats over soft soil,” *Advances in Civil Engineering*, vol. 2021, no. 4, Article ID 4084961, 13 pages, 2021.
- [31] H. Wu, M. A. Trigg, W. Murphy, and R. Fuentes, “A new global landslide dam database (raglad) and analysis utilizing auxiliary global fluvial datasets,” *Landslides*, vol. 19, no. 3, pp. 555–572, 2022b.
- [32] P. Amatya, D. Kirschbaum, and T. Stanley, “Rainfall-induced landslide inventories for lower mekong based on planet imagery and a semi-automatic mapping method,” *Geoscience Data Journal*, pp. 1–13, 2022.
- [33] S. Zhang and M. Hu, “Seepage and slope stability analysis of Kauswagan power station embankment in the Philippines during flooding,” *Port and Waterway Engineering*, vol. 5, pp. 55–60, 2020b.
- [34] Y. G. Zhang, J. Tang, Y. M. Cheng et al., “Prediction of landslide displacement with dynamic features using intelligent approaches,” *International Journal of Mining Science and Technology*, vol. 2, no. 1, pp. 1–11, 2022.
- [35] W. Zhong, J. Ouyang, D. Yang, X. Wang, Z. Guo, and K. Hu, “Effect of the in situ leaching solution of ion-absorbed rare earth on the mechanical behavior of basement rock,” *Journal of Rock Mechanics and Geotechnical Engineering*, vol. 2, no. 1, pp. 39–51, 2022.
- [36] X. Tang, Y. Zheng, and A. Wu, “Slope stability analysis under seepage action using PLAXIS finite element program,” *Journal of Yangtze River Scientific Research Institute*, vol. 4, pp. 13–16, 2006.

Research Article

The Influence of Water-Level Fluctuation on the Instability and Seepage Failure of Dump-Fill Cofferdam

Yunqing Hu,¹ Jianyu Huang,² Zhipeng Tao,³ Junhua Zhu ,⁴ Qing Lv,⁵ Jianwei Qiao,⁶ and Weibin Cai⁷

¹Jiangxi V&T College of Communications, Nanchang 330062, China

²Nanchang Longxing Port Group Co., Ltd., Nanchang 330062, China

³Jiangxi Transportation Institute Co., Ltd., Nanchang 330062, China

⁴School of Civil Engineering and Architecture, East China Jiaotong University, Nanchang 330013, China

⁵Research & Development Centre for Underground Technology of Jiangxi Province, Nanchang 330013, China

⁶China Jikan Research Institute of Engineering Investigations and Design Co., Ltd., Xi'an 710043, China

⁷Sichuan Highway Planning, Survey, Design and Research Institute Ltd., Chengdu 610047, China

Correspondence should be addressed to Junhua Zhu; 3062@ecjtu.edu.cn

Received 1 December 2021; Accepted 18 March 2022; Published 12 April 2022

Academic Editor: Lingkun Chen

Copyright © 2022 Yunqing Hu et al. This is an open access article distributed under the Creative Commons Attribution License, which permits unrestricted use, distribution, and reproduction in any medium, provided the original work is properly cited.

Due to the double disturbance effect of dredging and filling, there will be a problem with weir slope stability after the formation of a fill type saturated clay weir. In order to study the influence of water-level fluctuation on the instability and seepage failure of the dump-fill cofferdam, the saturated-unsaturated seepage theory and strength reduction method are embedded into the finite element system such that the fluid-solid coupling stability of the dump-fill cofferdam is analyzed. The results show that the influence of water-level fluctuation on the instability and seepage failure of the dump-fill cofferdam can be revealed by the coupling analysis excellently. The variation of the saturation line of the cofferdam is consistent with the variation of water-level rising, but the change response of the saturation line of the cofferdam has a lag property during the water-level decline process in that the water level changes faster. The maximum displacement of the cofferdam can be approximated as two stages, namely, the stable growth stage and the accelerated growth stage (slip initiation), in which the influence of the water-level fluctuation on the displacement of stable growth stage is more obvious. Based on the fluid-solid coupling analysis, the most dangerous sliding surface of the cofferdam is located at the position of the horse path, with a critical strength reduction coefficient of approximately 1.475. The possibility of seepage failure of the cofferdam will be increased if the water level exceeds the height of the impermeable wall.

1. Introduction

With the development of society, the construction of water conservancy and shipping projects in China is gradually increasing and the scale of construction is expanding. The construction of water conservancy and shipping engineering plays an important role in national economic development and social stability [1–4]. At the same time, the safety of the cofferdam is also crucial, which not only relates to the safety and progress of the whole construction diversion project and the main project but also involves the downstream ecological problems. After nearly 30 years of practice in the

construction of large- and medium-sized water conservancy and hydropower projects in China, from the successful interception of the Yangtze River Gezhouba project using the vertical plugging method ([5], [6]) to the construction of the world-renowned Yangtze River Three Gorges project deep-water high earth and stone cofferdam, the design and construction level of diversion and cofferdam engineering has rapidly improved ([7,8]). However, with the continued construction of large and mega hydraulic pivot projects, the scale of cofferdams has increased and the difficulty has grown day by day. The safety and stability of cofferdams are of great concern to researchers and engineers.

As the cofferdams are temporary structures, most of them are made from local materials, generally filled with sand, pebbles, piled stones, and transitional materials, and the more common forms of damage are instability slips and infiltration damage. Therefore, slope stability and seepage stability are two important indicators for evaluating the safety of cofferdams. In terms of research on the stability of cofferdam slopes, Zhao Shangyi et al [9] applied the strength reduction method to slope stability analysis, using the reduction factor when the finite element calculation did not converge as the safety factor, and the analysis results showed that the safety factor of slope stability obtained by this method was quite close to the calculation results of the traditional method. Luo Hongming et al [2] carried out research on the influence of periodic fluctuations of water level on the stability of landslides and proposed a polynomial constrained optimisation model of the soil-water characteristic curve of the polynomial constraint optimisation model applied to actual projects. Yang Jin et al. [10] took the Three Gorges reservoir area loess slope landslide as the research object, carried out the influence of reservoir water rise and fall on the groundwater level of the landslide combined with field monitoring data, and analyzed the influence of the change of the reservoir bank landslide infiltration line on the stability of the landslide under the rise and fall of reservoir water. Xiao Zhiyong et al. [11] took a Three Gorges mound landslide as an example and used Geostudio to analyze the stability of the landslide of a reservoir water-level accumulation body under two factors of multistage descent and different intermittent time periods, and the results showed that the use of intermittent descent was beneficial to the dissipation of pore pressure in the landslide body, while when the reservoir water level decreased rapidly, there was a hysteresis effect of groundwater fall back on the reduction of the hydraulic gradient. Zhang Deng et al. [12] took a tailing pond project as an example and used a time-varying analysis model to study the safety coefficient of the slope, and the results showed that with the change of slope safety coefficient lags behind the change of reservoir water level, the rising speed of water level slowed down the lagging effect, and the falling speed accelerated the lagging effect. And, the decrease in rising rate reduced the lagging effect, and the coupling of rainfall and water level would accelerate the weakening of the tailing reservoir safety coefficient.

This paper relies on the project of Xinjiang River Shuanggang Shipping Hub Project on Poyang Lake in Jiangxi Province. The cofferdam belongs to the dump-fill saturated clay cofferdam, which has the characteristics of high water content of the soil, heterogeneous internal structure, and complex changes in reservoir water level. It is observed that most of the research studies on slope instability of cofferdams are concentrated on mixed types of cofferdams such as soil, rock, and sand and barely concentrated on the research of seepage process and stability of the saturated clay cofferdam. Therefore, there has been an important guiding significance for engineering safety assessment to research the stability and seepage failure of the dump-fill cofferdam caused by water-level fluctuation.

2. Materials and Methods

2.1. Background of the Project. The main construction of this project is located in Poyang Town, Shangrao City, and the width of the riverbed in the dam site area is about 150~450 m. It is a comprehensive hub mainly for navigation. The hub layout is shown in Figure 1, with a total length of 496.5 m along the dam axis. In order to provide dry land construction conditions for the main structure, a diversion canal and a cofferdam should be constructed. The total length of the cofferdam is 2454 m, including 450 m length of the upstream cofferdam, 1459 m length of the longitudinal cofferdam, and 545 m length of the downstream cofferdam, with the service life of the cofferdam which belongs to the perennial cofferdams ranging from 2 to 2.5 years. According to the Design Code for Cofferdams of Water Resources and Hydropower Engineering (SL645-2013), the lock level is Class II and the design level of the cofferdam is Class IV. The weir is protected against seepage by a combination of bagged sand slope protection and geotextile fabric on the headwater side and grass slope protection on the backwater side. The weir body above 19.5 m height is protected against seepage by outsourcing soil filling, and the upstream and downstream weir closed air structure is a high-pressure rotary pile structure; the weir body below 19.5 m height is protected against seepage by a single row of high-pressure rotary pile seepage wall.

2.2. Geological and Hydrological Conditions. According to ground investigation and drilling, the riverbed stratigraphy at the dam site is mainly composed of the Holocene Alluvium of the Fourth Series and the Xinyu Group of the Third Series. The lithology of the original riverbed is divided into chalky clay, thick silty chalky clay medium sand, gravelly sand, rounded gravel, and strong and medium weathered muddy siltstone in order from the top to bottom. The daily water level at the dam site is obtained by interpolation from the water-level stations at Poyang upstream and Longkou downstream of the dam site. Considering the influence of river training before and after 1978 and sand dredging in the lake area and river channel on water-level undercutting in recent years as well as the continuity of the data, the measured water level and the projected flow data of the Shuanggang dam site from Poyang and Longkou stations in the same period after 1991 are used for water level and flow relationship analysis.

2.3. Mechanical Properties of Cofferdam Filling Materials. The saturated clay with silty soil excavated from the diversion channel is the main filling material of the cofferdam, and it has the characteristics of high saturation, high compressibility, and low shear strength because of the double disturbance of excavation and dump-fill so that the cofferdam with a large thickness of 21 m in the upstream and downstream cannot be stable for a long time. In order to construct a stable cofferdam, the outsourcing soil is chosen to fill the upper layer of the cofferdam.



FIGURE 1: The project overview: layout of the cofferdam diversion channel.

The soil samples are obtained by drilling after the cofferdam was completed, and the physical and mechanical parameters of filling materials are obtained by laboratory tests as shown in Table 1.

3. Seepage Calculation Models

3.1. Saturated-Unsaturated Seepage Theory. The soil of the cofferdam is lying in a complex state of saturation and unsaturation during the water-level fluctuation such that the area which lies below the saturation line can be regarded as saturated and the fluid seepage satisfies Darcy's law and the area which lies above the infiltration line can be regarded as unsaturated and the fluid flow law cannot be given based on Darcy's law. Therefore, the fluid seepage equation should describe both saturated and unsaturated seepage behavior. The continuity equation of the fluid medium during seepage is obtained by taking a volume microelement dV and performing a fluid mass conservation analysis on it [13,14].

$$\int_V \frac{\partial(\rho\theta)}{\partial t} dV + \int_V (\rho \cdot u)_{i,i} dV = \int_V \rho q dV, \quad (1)$$

where θ denotes the volumetric water content, ρ denotes the fluid density, u denotes the fluid percolation velocity, and q denotes the flow rate.

Assuming that the fluid is incompressible during percolation, the previous equation can be evolved as follows:

$$\frac{\partial\theta}{\partial t} + u_{i,i} = q. \quad (2)$$

For a fluid in the saturated zone, the equation of motion is in accordance with Darcy's law:

$$u = -K\nabla h, \quad (3)$$

where K denotes the hydraulic conductivity (coefficient of permeability) and ∇h is the hydraulic gradient.

For fluids in the unsaturated zone, the volumetric water content can be described by the van Genuchten equation [15,16]:

$$\theta = \theta_r + \frac{\theta_s - \theta_r}{[1 + (\alpha h)^n]^m}, \quad (4)$$

where θ_s and θ_r denote the saturated volumetric water content and residual volumetric water content, respectively, α, m , and n are the basic model parameters, and h is the pressure head which is taken as a positive value.

Substituting equations (3) and (4) into (2), respectively, gives the final form of the equation for fluid seepage continuity in saturated-unsaturated soil.

$$(\theta_s - \theta_r) \cdot \frac{\partial[1 + (\alpha h)^n]^m}{\partial t} = q + K\nabla h. \quad (5)$$

Equation (5) is a partial differential equation for the pressure head h , which integrates the relationship between the seepage velocity and the matrix suction. However, the partial differential equation is currently difficult to solve analytically and coupled with the dynamic boundary conditions of water-level fluctuation poses a challenge to the solution of the equation. Therefore, it is necessary to solve the equation discretely with the aid of numerical calculations to obtain a numerical solution, so that the seepage state and deformation characteristics of the cofferdam during the water-level fluctuation can be revealed [17].

3.2. Establishment of a Coupled Seepage Model. The model is established based on the closure section of the upstream cofferdam which is regarded as the most dangerous section [18–20]. The height of the cofferdam is 21 m, and the width of the top is 8 m. The length of the upstream face is 43 m, and the ratio of the slope is 1 : 5; the length of the downstream face is 40 m, and the ratio of the slope is 1 : 4~1 : 5. The soil types from the top to the bottom are gravelly silty clay, fill material, silty clay, medium sand, rounded gravel, and strongly weathered muddy siltstone (as shown in Figure 2). To prevent infiltration damage to the cofferdam and ensure its stability, two rows of interlocking high-pressure jet grouting piles were installed 1.5 m below the top of the cofferdam, with a width of 0.8 m and a depth of 2 m inside the strongly weathered rock, providing good

TABLE 1: Basic physical and mechanical parameters of cofferdam, rock, and soil.

Cofferdam materials	Cohesion (kPa)	Angle of internal friction (°)	Coefficient of permeability (cm/s)	Natural gravity (kN/m ³)	Saturated bulk weight (kN/m ³)	Modulus of elasticity (kPa)	Poisson's ratio
Outsourced soil	21.23	10.03	6.63×10^{-5}	18.40	19.30	10240	0.3
Fill material	13.47	7.40	9.27×10^{-8}	19.70	19.70	8820	0.3
Powdery clay	20.00	13.00	7.0×10^{-5}	18.80	20.00	8640	0.3
Medium sand	0.00	28.00	1.0×10^{-3}	18.00	19.00	12000	0.3
Round gravel	0.00	35.00	1.0×10^{-2}	18.60	19.60	36000	0.3
Impregnating wall	/	/	5.0×10^{-9}	22.00	23.00	300000	0.2
Strongly weathered rock	100.00	35.00	1.0×10^{-4}	20.00	21.00	300000	0.3

impermeability. The basic physical and mechanical parameters of the materials are detailed in Table 1.

The COMSOL Multiphysics software is used to analyze the seepage and stability of the cofferdam, and the model is established as shown in Figure 3. The analysis of saturated-unsaturated seepage can be accomplished based on the PDE module which embedded Equation (5). The Mohr–Coulomb ontology model is used for the geotechnical materials, the effects of fluid osmotic pressure and the self-weight of the geotechnical materials are considered, and the coupling calculation is accomplished as follows:

$$\begin{cases} F = \lambda\sqrt{J_2} + \omega I_1 - \chi \\ \omega = \sin \varphi/3, \chi = c/\cos \varphi \end{cases}, \quad (6)$$

where F denotes the Mohr–Coulomb yield function, c and φ denote the cohesion and internal friction angle of the geotechnical materials, and J_2 and I_1 denote the second invariant of partial stress and the first invariant of stress, respectively.

In order to carry out the subsequent stability analysis of the cofferdam, a shear strength reduction factor (Equation (7)) is introduced to discount the mechanical parameters of the geotechnical materials until the destruction occurs [21].

$$\begin{cases} C = \frac{c}{\xi} \\ \Phi = a \tan \left(\frac{\tan \varphi_u}{\xi} \right)_{p < 0} + a \tan \left(\frac{\tan \varphi_s}{\xi} \right)_{p \geq 0} \end{cases}. \quad (7)$$

Here, ξ denotes the strength discount factor, φ_u and φ_s are the internal friction angles of unsaturated and saturated geotechnical bodies, p denotes the pore pressure, and C and Φ are the cohesion and internal friction angles after considering the strength discount.

3.3. Boundary Conditions of Displacement and Pressure.

The bottom of the model is constrained by fixed displacement with zero displacement boundary; the model is surrounded by roller displacement constraint with zero normal displacement.

$$\text{for } \begin{cases} z = z_b: & U_x = U_y = 0 \\ z \neq z_b: & U_x = 0. \end{cases} \quad (8)$$

The boundary condition of water pressure at the upstream face is related to the water level which changed with time. For this reason, we research the water-level fluctuation data of Poyang Lake in the last 40 years and find that the water-level fluctuation rates of 1998 are the most drastic. The highest flood level is 20.76 m, which is only 0.24 m away from the top of the cofferdam; the lowest water level is 11.60 m, the difference between flood and dry water level reaches 9.16 m, and the pressure difference is 90.16 kPa, which has a huge impact on the cofferdam of the throw-fill type powder clay with silt soil. It is necessary to carry out a destabilization and infiltration damage study for the upstream cofferdam where the water-level difference is large.

Figure 4(a) shows the water-level variation of the lake in 1998. The flooding season lasts from June to August each year, while winter and spring are the low-water-level seasons. Considering the large discreteness of the actual data that the calculation speed and astringency of the model would be impacted significantly, the highest water level of each month is taken as the reference value (the most dangerous case) and interpolated for analysis, resulting in the water-level change curve shown in Figure 4(b). The similarity index of them is 90%, and the timing of the flood and dry water levels coincide exactly, which has an approximately negligible effect on the model calculations.

3.4. Calculation Parameters and Simulation Conditions.

The physical and mechanical parameters and infiltration parameters of the cofferdam are detailed in Table 1, and the water-level depth and fluctuation rates are given in Figure 4(b). In terms of numerical analysis, three groups of scenarios are set up, which are the steady-state simulations at the lowest and highest water levels and the transient simulations at the dynamic fluctuation of the water level over a year; the detailed simulation scenarios are shown in Table 2.

In particular, for the transient coupling calculation under the dynamic rise and fall of the water level, the initial seepage field of the weir body needs to be given. Here, the water level of the first day in 1998 (12.92 m) is taken as the initial seepage condition, the initial seepage field and stress field conditions are obtained through the steady-state

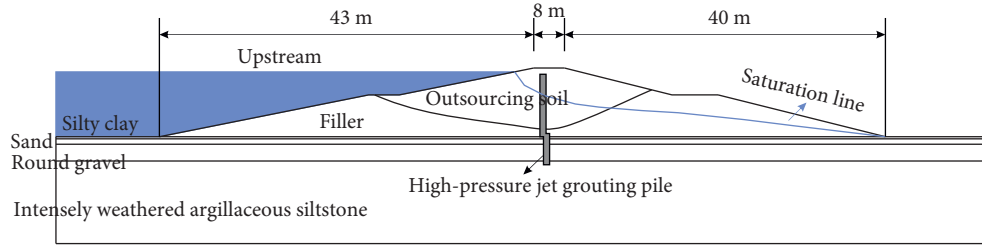


FIGURE 2: Lateral section of the upstream closure section of the cofferdam.

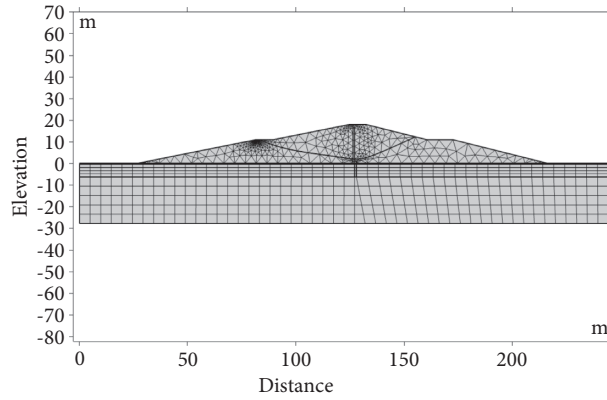


FIGURE 3: Fluid-solid coupling numerical analysis model.

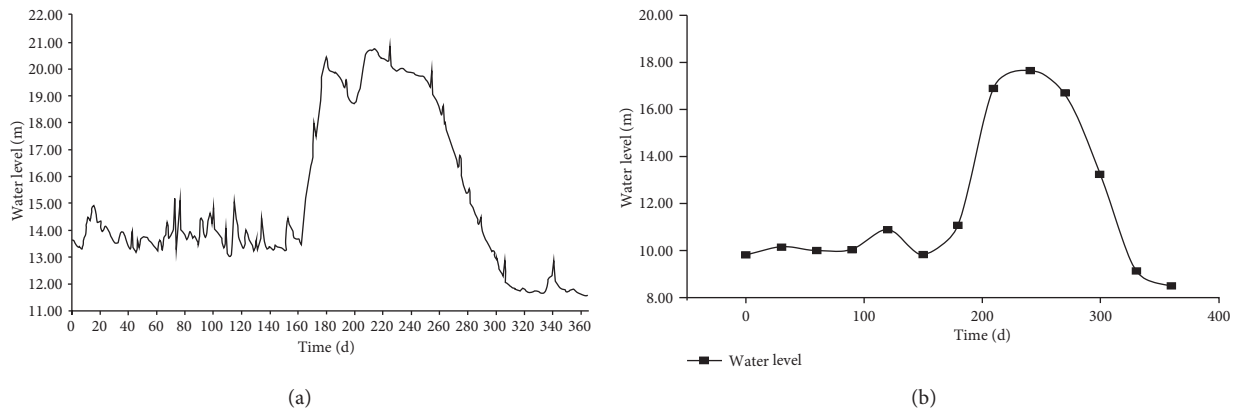


FIGURE 4: Change trend of water level of the cofferdam: (a) actual water-level change; (b) simplified water level based on interpolation.

TABLE 2: Simulation conditions.

Simulation program	Water-level position (m)	Water level in foundation pit (m)	Computational simulation
Minimum water level	11.60	Pit bottom-1 m	Steady-state coupling
Maximum water level	20.76	Pit bottom-1 m	Steady-state coupling
Dynamic water level	11.60~20.76	Pit bottom-1 m	Transient coupling

coupling calculation, and then, the purpose of the transient coupling calculation is achieved [22].

4. Analysis of Results and Discussion

4.1. Influence of Water-Level Fluctuation on the Saturation Line of the Cofferdam. The variation of pore water pressure

and saturation line in the cofferdam can be obtained by steady-state coupling and a transient coupling according to different simulation conditions. Figures 5 and 6 show the variation of pore water pressure and saturation line in the cofferdam at the lowest and highest water levels, respectively. The comparative analysis shows that the water level has a significant influence on the seepage rate, pore water

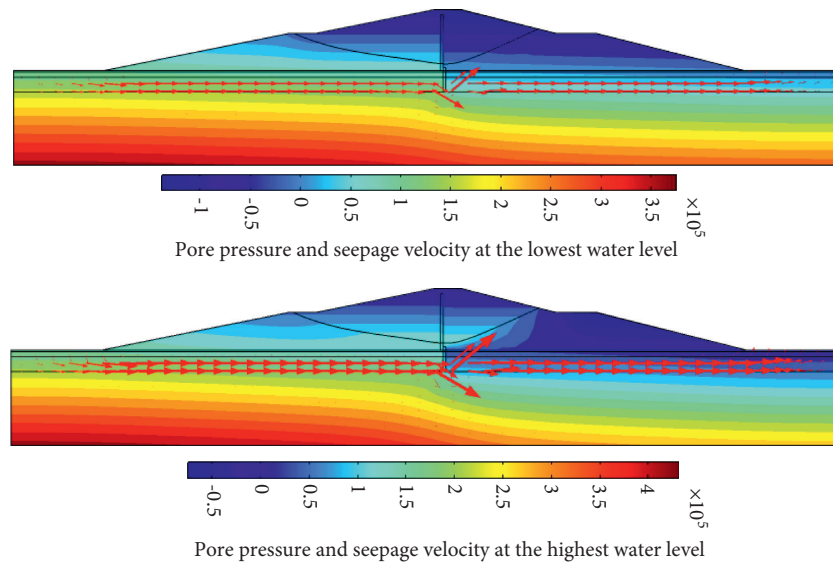


FIGURE 5: Contour map of pore pressure and seepage velocity in the cofferdam.

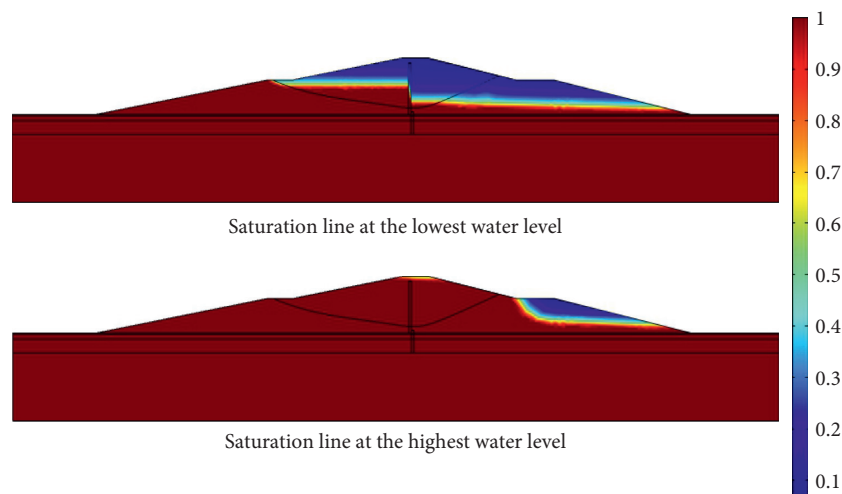


FIGURE 6: Contour map of the seepage line in the cofferdam.

pressure, and infiltration line in the cofferdam. The higher the water level is, the more saturated the areas (red areas) are, the faster the seepage rate (flow rate arrows) is, and the more drastic the pore pressure change will be. Due to the setting of the high-pressure cyclone wall, there are obvious sudden changes in pore water pressure and regional saturation between the different sides of the impermeable wall, the seepage area is mainly concentrated in the medium sand and round gravel layer, and the phenomenon of bypass flow exists at the bottom of the wall, which has a positive seepage prevention effect. With the gradual increase in water level, the water pressure gradient in the cofferdam is increased, and when the water level exceeds the impermeable wall, the effect of seepage prevention and flow blocking of the impermeable wall is gradually weakened and the stability of the cofferdam will be decreased.

The variation of the saturation line of the cofferdam under the dynamic water-level fluctuation condition is

shown in Figure 7, and the variation regulation of the saturation line is similar to the water-level fluctuation regulation which is shown in Figure 4(b), illustrating that the migration of moist sharp in the cofferdam is controlled by the water-level fluctuation. During the flood period from June to August, the water level rises rapidly and fluid flow occurs along the outsourcing soil of the cofferdam, resulting in an increase in the saturated zone on the right side, with the unsaturated zone only existing near the bottom of the slope inside the cofferdam. In addition, due to the saturated-unsaturated soil seepage theory model used, the saturation line that migrates in the cofferdam has significant lagging characteristics during the water-level decline process; for example, the water level in September is lower than the water level in July, but its saturation zone is larger than that in July, which is not consistent with the water-level rising regulation; the water level in November is the same as the water level in May, but the saturation line in the cofferdam does not

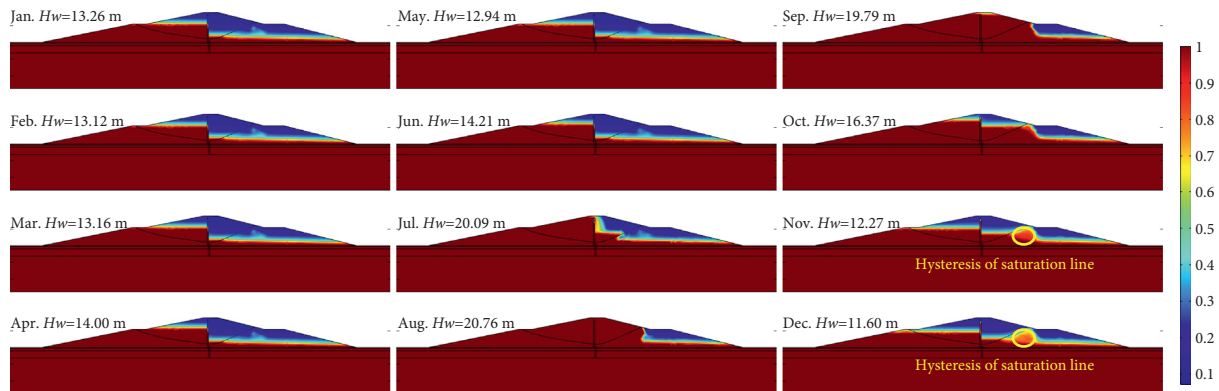


FIGURE 7: Change of the seepage line in the cofferdam under water-level fluctuation.

exactly overlap either. The results show that there are different effects on the saturation line caused by water-level rising and decline and the effect caused by the water-level decline process is more significant.

4.2. Influence of Water-Level Fluctuation on the Displacement of Cofferdam. The analysis points of displacement in the cofferdam model are selected as shown in Figure 8, where Section 1-1 indicates the downstream face, Section 2-2 indicates the intersection between the outsourcing soil and the fill material, Section 3-3 indicates the vertical section at the top of the cofferdam, and Section 4-4 indicates the vertical section at the horse path. The blue points shown in Figure 8 are the key points for slide damage that locate on the surface or at the intersection of different geotechnical materials.

The deformation results of the four sections of the cofferdam are shown in Figure 9. The results indicate that the water-level fluctuation has a light influence on the deformation of the top of the cofferdam, which remains at 17.16 mm. But it has an obvious influence on the deformation of the intersection of geotechnical materials. For example, during the flood period, the displacements of the intersection of outsourcing soil and filler (points B, J, and E), the intersection of medium sand and round gravel (points C and H), and the intersection of round gravel and strongly weathered muddy siltstone (point D and I) show significant increase such that the maximum displacement increment is about 11.62 mm which is located in point J. In general, the deformation values of the cofferdam meet the safety requirements and the probability of seepage damage is slight. But special attention needs to be paid to the deformation between the intersection of the outsourced soil and the filler, which is the potential slip surface of the cofferdam.

4.3. Influence of Water-Level Fluctuation on the Stability of the Cofferdam. The highest and lowest water-level conditions and the shear strength reduction method are used to analyze the stability of the cofferdam. The evaluation of whether the

cofferdam has slide damage is relied on the shear strength reduction factor, and there is no convergence of elastic-plastic analysis of geotechnical materials as the referee condition. The analysis results show that the maximum displacement of the cofferdam increases slowly as the strength reduction factor gradually increases, and when the reduction factor reaches a certain threshold value, the maximum displacement rises sharply, which means that slip damage begins. The reduction factor that causes the sudden increase in the maximum displacement is named the critical strength reduction factor (CSRF).

The variation curves of the maximum displacement of the cofferdam with the strength reduction factor under the highest and lowest water-level conditions are shown in Figure 10. The curves can be divided into two stages. During the first stage, the maximum displacement is increasing stably and the displacement in the highest water-level condition is a little larger than that in the lowest water-level condition. The maximum displacement in the second stage is increasing rapidly, and the curves in two different conditions are coincident such that the slide is forming. The result means that the water level has almost no effect on the critical strength reduction factor of the cofferdam, which is about 1.475.

Figure 11 shows the effective plastic strain of the cofferdam before the destruction at the highest and lowest water levels, respectively, which is another representation of the cofferdam damage mechanism. The effective plastic strain variation of the two different conditions are consistent, and this result is consistent with the results of the critical strength discount factor analysis. Figure 12 shows the slide surface of the cofferdam under the highest and lowest water-level conditions, respectively, with the most dangerous slide surfaces being located at the horse path and the arrows indicating the direction of displacement of the soil particles. The most dangerous slide surface for both conditions is also in general agreement and also coincides with the results of the effective plastic strain and critical strength reduction factor analysis.

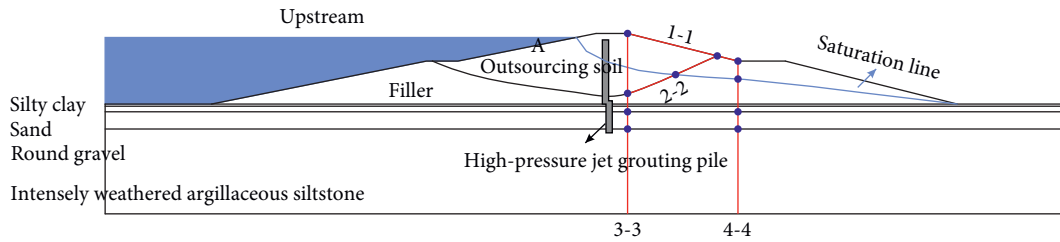


FIGURE 8: Schematic diagram of selection of cofferdam deformation analysis points under water-level fluctuation.

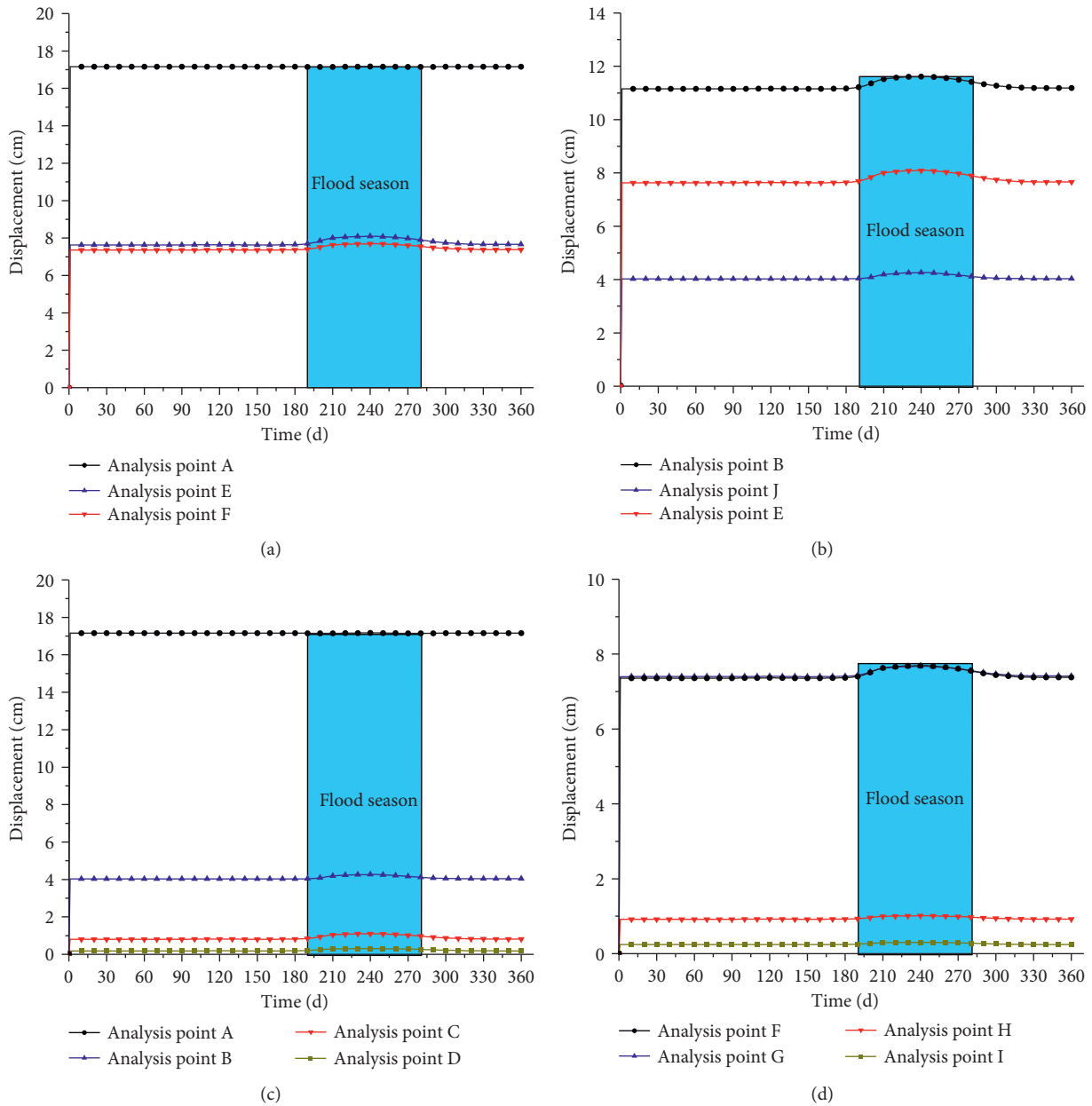


FIGURE 9: Schematic diagram of selection of cofferdam deformation analysis points under water-level fluctuation: (a) deformation of the backwater slope of the cofferdam; (b) deformation of the interface between outsourcing oil and the filler; (c) vertical section deformation at the top of the cofferdam; (d) vertical section deformation at the horse track.

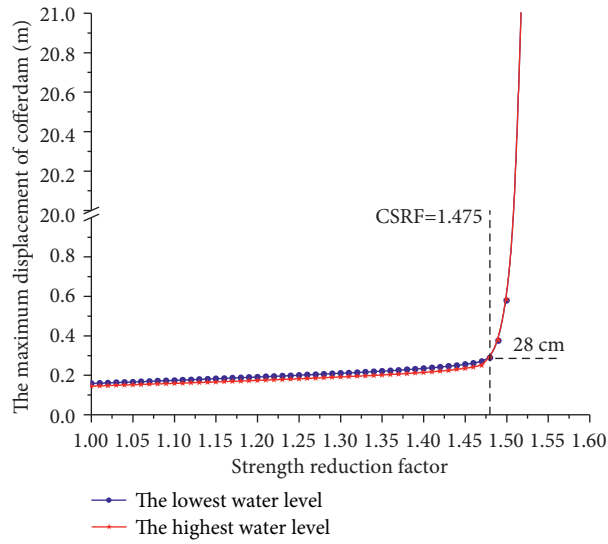


FIGURE 10: The variation law of the maximum displacement of the cofferdam with the strength reduction factor.

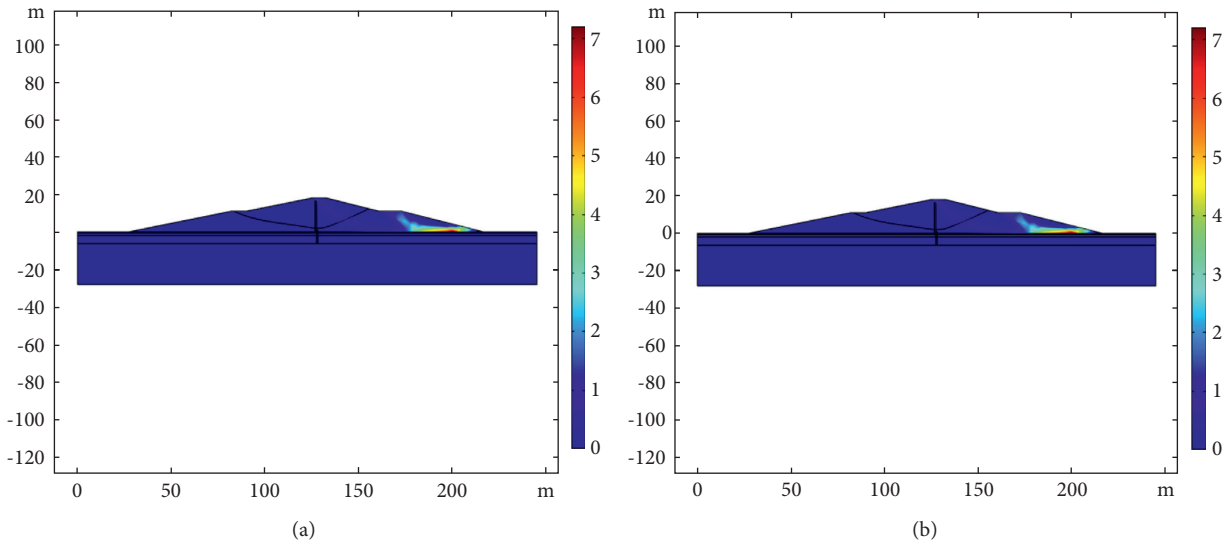


FIGURE 11: The effective plastic strain before the cofferdam failure under (a) flood level and (b) low water level.

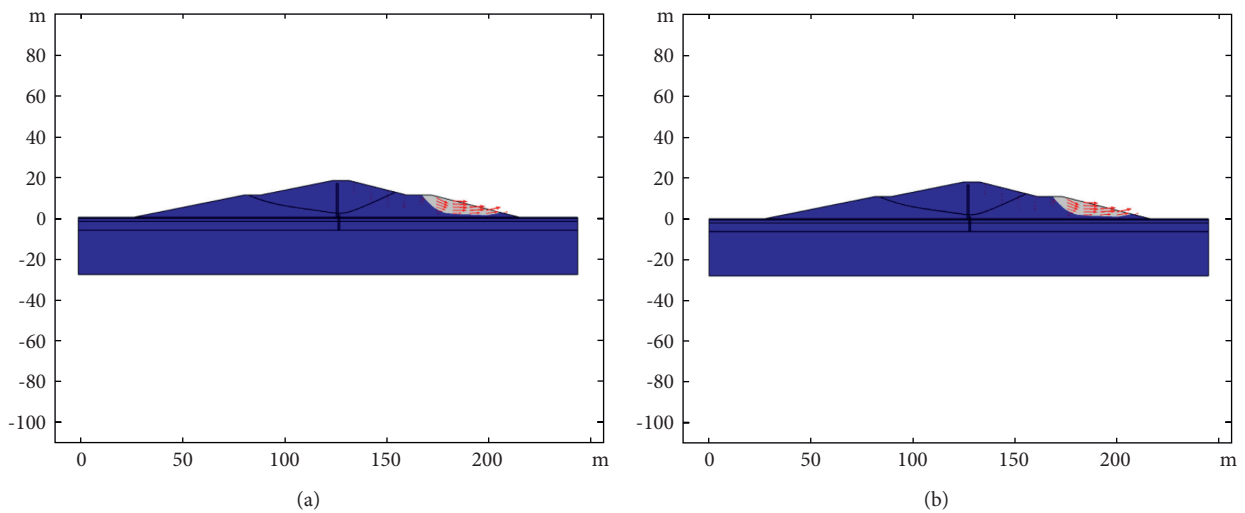


FIGURE 12: The most dangerous slip surface of the cofferdam under (a) flood level and (b) low water level.

5. Conclusion

- (1) The influence of water-level fluctuation on the deformation and stability of the cofferdam can be analyzed excellently by finite element simulation which embedded the saturated-unsaturated seepage theory.
- (2) With the rise of water level, the saturation zone in the cofferdam increases and the value of pore water pressure changes sharply. The prevention effect of the impermeable wall will be reduced while the water level exceeds the top of the impermeable wall, and the saturation zone of the downstream face will be enlarged, causing the decrease in stability of the cofferdam.
- (3) The variation regulation of the saturation line is similar to the water-level fluctuation regulation, and the migration of moist sharp in the cofferdam is controlled by the water-level fluctuation. Because of the use of saturation-unsaturation seepage theory, the saturation line in the cofferdam lags to the water-level fluctuation and the lag time is more obvious during the water-level decline process.
- (4) The maximum displacement of the cofferdam can be divided into two stages: stable increasing stage and sharp increasing stage. The maximum displacement in the second stage is increasing rapidly, and the curves in two different conditions are coincident such that the slide is forming. The result shows that the water level has almost no effect on the critical strength reduction factor of the cofferdam, which is about 1.475.

Data Availability

The data reported in this article are available from the corresponding author upon request.

Conflicts of Interest

The authors declare that they have no conflicts of interest.

Acknowledgments

This work was supported by Key Engineering Science and Technology Projects of Jiangxi Provincial Department of Transportation (2019C0010 and 2019C0011); National Natural Science Foundation of China (51868021 and 52168047); Jiangxi Provincial Natural Science Foundation (20202BABL20405); High Speed Railway Joint Fund of NSFC (U1934208); and Natural Science Foundation of Jiangxi Province (20212BAB214009).

References

- [1] X. Bai, *Research on the Evaluation of China's Soft Power of Shipping*, Dalian Maritime University, Dalian, 2013.
- [2] H. Luo, H. Tang, and G. Zhang, "Influence of reservoir water level rise and fall on the stability of reservoir bank landslides," *Earth Science*, vol. 33, no. 5, pp. 687–692, 2008.
- [3] B. Wang, D. Huang, and H. Jian, "Social stability risk assessment and empirical study of water conservancy project construction," *China Population Resources and Environment*, vol. 25, no. 4, pp. 149–154, 2015.
- [4] H. Xie, W. Xu, and C. Liu, "Strategic concept and key technology outlook for underground hydraulic engineering," *Journal of Rock Mechanics and Engineering*, vol. 37, no. 4, pp. 781–791, 2018.
- [5] H. Guo, J. Ning, and W. Jiang, "Experimental research and engineering practice on the protection (mat) bottom of the interceptor dragon mouth of large water conservancy projects," *Journal of China Three Gorges University*, vol. 29, no. 6, pp. 481–485, 2007.
- [6] D. M. Liu, D. Y. Wang, and X. M. Wang, "Experimental study and basic conclusions of some hydraulics problems of the Grand River cut-off of Gezhouba project," *Chinese Science (Series A) Mathematics Physics Astronomy Technology Science*, vol. 10, pp. 951–962, 1982.
- [7] H. Dai and L. Wang, "Study of seepage in the Three Gorges deep-water high earth and rock weir project," *Advances in Water Science*, vol. 16, no. 6, pp. 849–852, 2005.
- [8] Si Zhaole, "Science and technology of deep water high earth and rock cofferdam of Three Gorges Project Phase II and its practical test," *Journal of Yangtze River Scientific Research Institute*, vol. 21, no. 6, pp. 1–6, 2004.
- [9] S. Zhao, Y. Zheng, and W. Shi, "Coefficient of safety for slope stability using finite element strength reduction," *Chinese Journal of Geotechnical Engineering*, vol. 3, pp. 343–346, 2002.
- [10] Y. A. N. G. Jin, W. Jian, and H. Yang, "Study on the dynamic change of infiltration line of loess slope in Three Gorges reservoir area," *Rock and Soil Mechanics*, vol. 33, no. 3, pp. 853–858, 2012.
- [11] Z. Xiao, H. Deng, and J. Li, "Influence of intermittent decline in reservoir water level on the stability of mounded landslides," *Journal of the Yangtze River Academy of Sciences Scientific Research Institute*, vol. 33, no. 8, pp. 114–119, 2016.
- [12] D. Zhang, W. B. Jian, and Q. Ye, "Time-varying analysis model of tailings pond slope and its application," *Rock and Soil Mechanics*, vol. 35, no. 3, pp. 835–840, 2014.
- [13] X. Kong, *Higher Seepage Mechanics*, Press of University of Science and Technology of China, Hefei, 2010.
- [14] Q. W. Zhan and R. D. Liu, "Research on slope instability during rainfall," *Yangtze River*, vol. 42, no. 11, pp. 103–106, 2011.
- [15] H. Li, J. Q. Wu, and R. Hou, "Experimental study on the application of one-step flow method for rapid determination of soil-water characteristic curve," *Yangtze River*, vol. 51, no. 2, pp. 160–165, 2020.
- [16] Z. Tian, D. Kool, T. Ren, R. Horton, and J. L. Heitman, "Approaches for estimating unsaturated soil hydraulic conductivities at various bulk densities with the extended Mualem-van Genuchten model," *Journal of Hydrology*, vol. 572, pp. 719–731, 2019.
- [17] Y. G. Zhang, J. Tang, Y. M. Cheng et al., "Prediction of Landslide Displacement with Dynamic Features Using Intelligent Approaches," *International Journal of Mining Science and Technol.*, vol. 2, no. 1, pp. 1–11, 2022.
- [18] G. Han, Y. Zhou, R. Liu, Q. Tang, X. Wang, and L. Song, "Influence of surface roughness on shear behaviors of rock joints under constant normal load and stiffness boundary conditions," *Natural Hazards*, vol. 2, no. 1, pp. 1–18, 2022.
- [19] L. XL, C. SJ, Z. QM, and G. X. Feng F., "Research on theory, simulation and measurement of stress behavior under

- regenerated roof condition,” *Geomechanics and Engineering*, vol. 26, no. 1, pp. 49–61, 2021.
- [20] H. Wu, G. Zhao, and S. Ma, “Failure behavior of horseshoe-shaped tunnel in hard rock under high stress: Phenomenon and mechanisms,” *Transactions of Nonferrous Metals Society of China*, vol. 32, no. 2, pp. 639–656, 2022.
- [21] S. Li, Y. G. Zhang, M. Cao, and Z. N. Wang, “Study on excavation sequence of pilot tunnels for a rectangular tunnel using numerical simulation and field monitoring method,” *Rock Mechanics and Rock Engineering*, vol. 12, pp. 1–16, 2022.
- [22] B. Yang, M. He, Z. Zhang, J. Zhu, and Y. Chen, “A New Criterion of Strain Rockburst in Consideration of the Plastic Zone of Tunnel Surrounding Rock,” *Rock Mechanics and Rock Engineering*, vol. 14, pp. 1–15, 2022.

Research Article

The Exploration of New Courtyard Architecture Based on the Guidance of Architectural Culture and Technology

Xi Luo and Jianyun Huang 

School of Design, Shanghai Jiao Tong University, Shanghai 200240, China

Correspondence should be addressed to Jianyun Huang; jianyunhuang@sjtu.edu.cn

Received 1 December 2021; Accepted 5 March 2022; Published 24 March 2022

Academic Editor: Lingkun Chen

Copyright © 2022 Xi Luo and Jianyun Huang. This is an open access article distributed under the Creative Commons Attribution License, which permits unrestricted use, distribution, and reproduction in any medium, provided the original work is properly cited.

The paper interprets the “shape” and “meaning” of the new courtyard-style building from the two dimensions of architectural culture and architectural technology, as well as three levels of interpretation, construction, and cooperation. At the same time, it takes the building of “Waterside Cube” in Solar Decathlon China Competition as an example, which puts forward the concept of “Re-Traditional” and analyzes the generation logic and possibility of development of the new courtyard-style building which is combined with architectural culture and architectural aesthetics. Meanwhile, it puts forward the application of building technology and coping methods for rapid construction problems and finally summarizes the new ideas for the development of new courtyard-style buildings.

1. Introduction

With the deepening influence of world architecture style on China, more and more high-rise buildings or Western-style buildings are popular in China’s large-sized and medium-sized cities, and buildings with Chinese local culture are not fashionable compared with those which have modern urban atmosphere, and this is the majority of aesthetic concepts. The problem to be solved in the new courtyard-style building is how to regenerate the culture and fit the modern lifestyle, and make the culture livable and feasible, so that it can be adaptive to different groups. In the design, its concept inherits the traditional culture, but the applied techniques and the form and experience of creating a new space are more in line with the characteristics of the times [1].

The embodiment of architectural language in the architectural system has an internal connection with the architectural culture, which is preserved in the development of people’s life needs [2]. For example, people’s need for “combination” in family life can be represented as defensive outside and warm inside. This is not in contradiction with the creation of modern urban life and public communication space. The type of courtyard building can be constructed in a

modular manner, such as misaligning, opposing, interspersing, or superimposing one or more functional unit modules to create different space for internal and external environment. This is also the advantage of a new courtyard-style building which is more satisfied with the characteristics of future lifestyle.

The courtyard-style building is a well-known architectural system and representative of traditional residential buildings. In Solar Decathlon China Competition, the building “Waterside Cube” designed and built by Shanghai Jiao Tong University and the University of Illinois at Urbana-Champaign is an exploration and practice of the construction of contemporary new courtyard buildings in cities and villages. It combines all aspects of humanities, art, and technology in architectural design through modular construction methods, providing innovative ideas for the development of new courtyard-style buildings in the future urban development.

“Waterside Cube” is a new type of courtyard-style building. Its design analyzes and extracts the architectural style and architectural elements of traditional courtyard-style buildings, as well as the “shape” and “meaning” that have been preserved in the process of continuous evolution.

In order to meet the requirements of 20 days to complete the construction of the competition, the design adopts the construction method of prefabricated buildings and uses a combination of passive and active technical methods to fit modern livability. The new courtyard-style building is also different from the construction mode of the traditional courtyard-style building which is easy to be popularized and used in contemporary life.

2. Architectural Culture and New Courtyard Buildings

2.1. Overview. The courtyard-style building is a traditional Chinese architectural form, which is based on the architectural style of the courtyard [3, 4]. In the north, it is represented by the courtyard of Beijing, the courtyard in the south of Jiangsu and Zhejiang Province, and the courtyard of the Huizhou-style building.

The courtyard-style building carries the “shape” and “meaning” of the architectural culture. Starting from the early and most complete courtyard house represented by the ruins of Fengqi Village in Qishan, Shanxi Province, during the Western Zhou Dynasty, to scenes of people living in the inner court in the Han Dynasty portraits, as well as the performance of the courtyard-style buildings in “Riverside Scene at Qingming Festival” (“Riverside Scene at Qingming Festival” is a famous Chinese painting created by Zeduan Zhang in Song Dynasty; this painting describes the prosperous scene of Bianjing, the capital of the Song Dynasty) of the Song Dynasty; they all reflect the status of the courtyard-style architecture in the early Chinese society. Nowadays, there are still courtyard-style buildings in the north and south of China, some of which still have the function of living. However, some of the architectural functions that have been transformed into historic buildings, commercial and cultural centers, and art and creative workshops are more in line with modern needs, and this means that the spirit of the heritage of the courtyard-style buildings should be continued [5].

Architectural culture is the same as culture, which includes entities, norms, ideas, and symbolic culture. It affects the development of architectural systems from different dimensions, such as material form, architectural technology, architectural art, and architectural language.

2.2. Basic Characteristics of Courtyard Buildings. The courtyard-style building has the concept of overall building environment management. Starting from the courtyard house represented by the ruins of Fengqi Village, the prototype of the courtyard-style building was completed, and then people began to gradually improve the structure of the courtyard-style building in the Han Dynasty, including the use of building materials. During the Wei Jin Southern and Northern dynasties, the type of courtyard-style buildings began to diversify, including the “日” shape, the triple courtyard, the quadrangle courtyard, and other flat layouts. These layouts are centered on the inner courtyard and are generally centrally axisymmetric, and they develop

longitudinally and laterally along the axis. The architectural function is arranged as “the hall is in front of the bedroom” and “east and west wing layout” [6] (Figure 1).

As the core of the whole building, the courtyard space is not only an important place for daily life and family gatherings, but also the spirit of the family. Geomantic culture plays an important role in the courtyard-style building, and the concept of harmony between man and nature makes people pay more attention to the location and construction of the building, and pay attention to the harmony between man and nature. In southern regions, the conception of “*Si Shui Gui Tang*” (in south of China, sloping rain eaves are built in the inner courtyard surrounded by four rooms, and they allow rainwater to flow into the inner courtyard from all four sides; this phenomenon is called “*Si Shui Gui Tang*” and means gathering wealth and bringing good luck) in the courtyard reflects the low-key introversion and modesty of Confucianism [7] (Figure 2).

The emergence of the courtyard-type building system in the southern and northern regions is not only the inheritance of culture, but also an optimized architectural form that creates a livable space to adapt to the environment and climate, and isolates the internal and external environment [8]. The courtyard regulates the microclimate inside the building and creates passive ventilation. In the north of China, the courtyard is spacious and easy to receive sunlight, so that the climate is fairly mild in winter and rather cool in summer while resisting wind and sand [9]. The courtyard can collect rainwater and optimizes the built environment [10]. Meanwhile, the courtyard-style building form has the characteristics of clear internal streamlines, clear functional division, and livability environment.

2.3. Development of New Courtyard-Style Buildings. Nowadays, excellent architectural design not only is compatible with urban characteristics in terms of function and form, but also fits regional culture and humanistic environment. Architectural design in the contemporary context can use modern technical methods to inherit and preserve the traditional architectural forms and space creation, especially the courtyard structure design in the courtyard design, so that modern architecture can more closely link the relationship between nature, society, and people. At the same time, the inheritance of two ideas of “harmony between man and nature,” and “combination of nihility and reality” makes the spirit of the culture passed down in contemporary life [11].

In traditional construction, the form and function of the courtyard-style building are mostly based on courtyard-style residential buildings. However, in order to adapt to the needs of different geographical environment and urban life, modularized building forms can be used to customize the functions of every single module according to needs and then spatially combine and optimize. In this way, the inheritance of the courtyard-style buildings will not be constrained by the traditional building construction techniques, and the “shape” and “meaning” of the courtyard-style buildings will be better preserved. The new courtyard-style

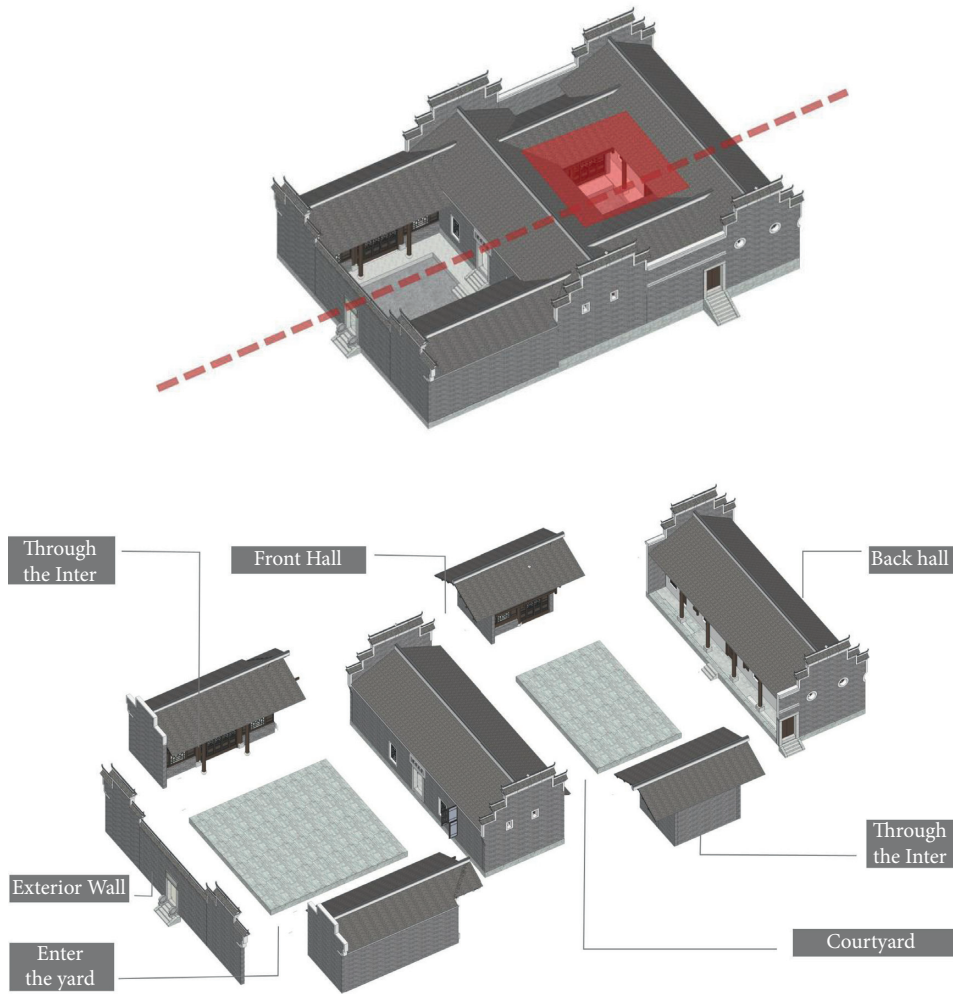


FIGURE 1: Traditional courtyard-style building layout.



FIGURE 2: Inner courtyard and community layout.

architecture is the heritage of the culture and an update of the design and construction techniques. Meanwhile, it can be established by using contemporary techniques through the combination of humanity, art, and technology.

In Solar Decathlon China Competition, the architectural design of Shanghai Jiao Tong University was named “Waterside Cube,” and the two elements of “water” and “square” were embedded in the design and practice. This not only

inherits the culture but also extracts the elements of traditional courtyard-style architecture and applies it to modern architectural design techniques and space construction. It is a new practice and exploration of courtyard-style architecture in the contemporary context.

3. “Waterside Cube”: The Practice and Exploration of the New Courtyard-Style Building

Each architectural design has its unique soul, which is different from the morphological generation of the building or the physical and spatial levels such as regional and functional aspects. It is also different from the technical background under the adaptive demand to make the building achieve better economic, applicable, and beautiful needs. This is a kind of exploration under the background of roots and culture. The meaning of architectural culture is higher than culture. It includes but not limited to multi-dimensional culture such as material, system, spirit, and symbol. It only transmits culture through the expression of architecture.

The “Waterside Cube” takes architectural culture as its context and takes traditional Chinese courtyard-style buildings as its prototype. It puts forward the design concept of “R-T,” which is named as Re-Traditional. And “Re-” means that people can extract the core concepts of traditional architectural culture and integrate them into modern architectural culture for conceptual improvement. This is also a new exploration of combining architectural culture and architectural technology in “Waterside Cube.”

“Waterside Cube” interprets the generation logic of the new courtyard-style building under the influence of architectural culture. This paper will analyze the redesign of architectural culture in architecture, the application of architectural technology in practice, and the response of construction mode to competition issues from the three dimensions of interpretation, construction, and consistency. Such a traditional and modern courtyard-style architecture exploration is the new practice to break the traditional courtyard-style construction.

3.1. Design: Design Concept and Layout

3.1.1. Layout. “Waterside Cube” is a courtyard-style house under the influence of architectural culture, which takes the layout of the two-in-one courtyard as the basic type of design. At the same time, the use of traditional architectural elements in design is preserved, which is interpreted and expressed in architectural language, and is realized through modern technological methods. Thus, it enhances the space and experience sense of the building. Considering the coordination between the building and the venue, as well as the experience needs of the customer groups that the competition will face, the design is optimized for the layout of the two-in-one courtyard. In the design, the inner courtyard of the first entrance is opened as an open outer courtyard space, which strengthens the combination of architecture and

natural environment, and at the same time has the functions of landscape and recreation. At the same time, the organizational structure of the inner courtyard is retained as a core part of the building, providing space for family activities (Figure 3).

The concept of “Waterside Cube” interprets the innovation and feasibility of architectural culture in contemporary architectural design through the use of the two elements of “water” and “square.” In traditional culture, the water element satisfies the needs of people’s life and also has the meaning of fortune. And the concept of “square” is not only the intuitive feeling of the whole building, but also an interpretation of the reproduction of the courtyard-style architectural elements and the modular construction technology.

3.1.2. Modular Construction. Taking the 20-day construction completion requirements into account in the competition, the design broke the traditional courtyard-style building construction model and adopted prefabricated containers for modular construction to meet the needs of family life. Customization of the module divides the building into four parts: the public area module, the rest module, the sanitary module, and the kitchen module. The inner courtyard is the core of “Waterside Cube,” and four functional modules are arranged around to form a courtyard-style building unit. Such a flexible customization model and rapid construction method also provide the possibility for future popularization (Figures 4–6).

3.1.3. Architectural Elements and Expression of Intention. The inheritance of architectural culture in courtyard-style buildings requires the expression of architectural elements, architectural aesthetics, and architectural systems in the design of new courtyard-style buildings. Buildings in cultural development can neither copy all the construction models of traditional buildings nor create models that do not fit the law of development.

“Waterside Cube” optimizes the space elements of the traditional courtyard-style building’s outer corridors, overhangs and inner courtyards, and material elements such as black tiles, white walls, partition windows, and landscapes and retains these architectural elements in the inner courtyard. Rectangular wooden partition windows are retained on the facade of the building, and the surface is covered with perforated aluminum panels to enhance the privacy of family life inside the building (Figure 7).

The courtyard-style architecture has been preserved during so many years of evolution in that its unique cultural qualities conform to the public’s aesthetic and value orientation. The design of the inner courtyard in “Waterside Cube” follows the traditional concept of “Harmony between Man and Nature” and the expression of the spirit of the courtyard. We planted green landscapes and expressive images of dry landscapes in the inner courtyard and transplanted a fruit tree in the courtyard as the visual center of the inner courtyard. At the same time, it can create a sense of place with the changes of four seasons. Brick carvings,

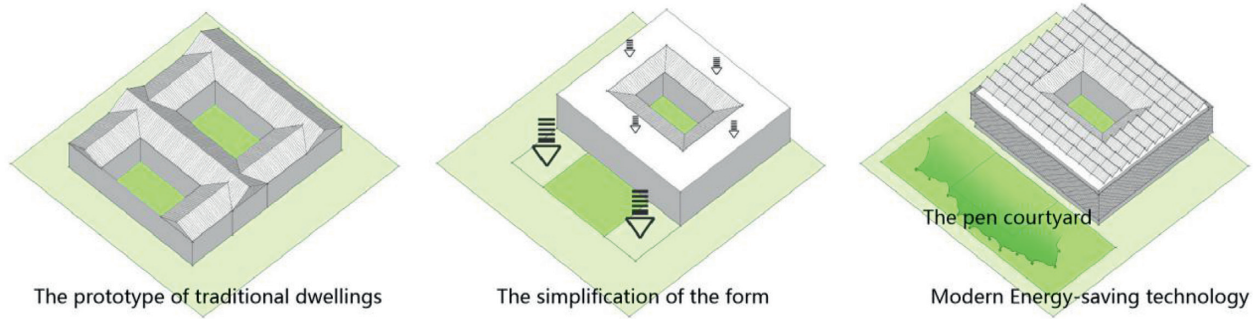


FIGURE 3: The extraction of elements.

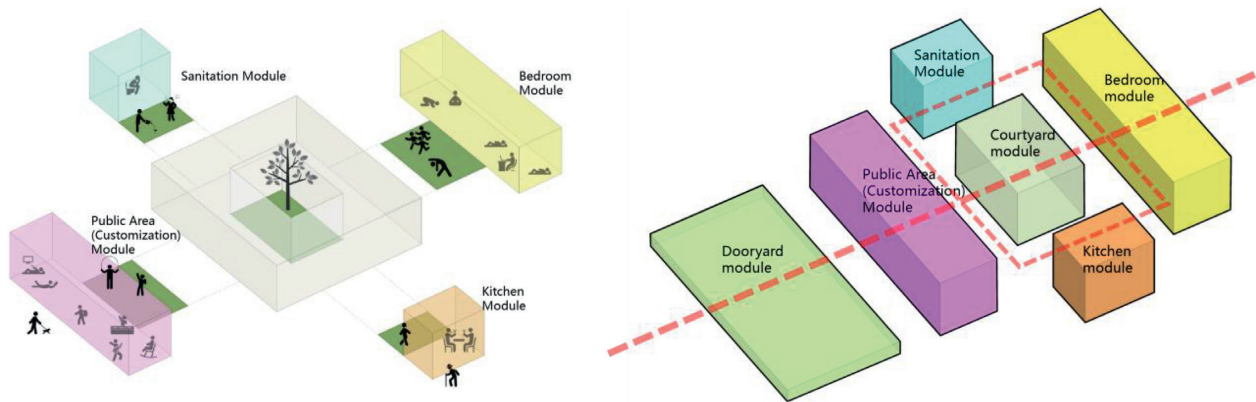


FIGURE 4: Function modules.



FIGURE 5: Exterior courtyard and inner courtyard.

stone carvings, and wood carving elements are used in the detailed design of the building to combine nature and design art to interpret the beauty of humanity. The spatial layout and functional layout of the entire building inherited the traditional Chinese architectural system. At the same time, container-style building modules are superior to traditional buildings in space and are suitable for modern lifestyles.

Water plays an indispensable role in traditional culture and family life. The perforated aluminum plate used on the building's facade applies its characteristics of ventilation,

shading, and cooling to increase light refraction, so that the effects of heat preservation and heat insulation can be achieved. In addition, the wave shape of perforated aluminum plate can also be applied as an image expression of a traditional water curtain. Therefore, the spray system and the "water curtain" are combined to interpret the water element in an interactive way (Figure 8).

At the same time, the traditional culture is used in the landscape design of the outer courtyard with modern techniques. "Qu Shui Liu Shang" (which means that a

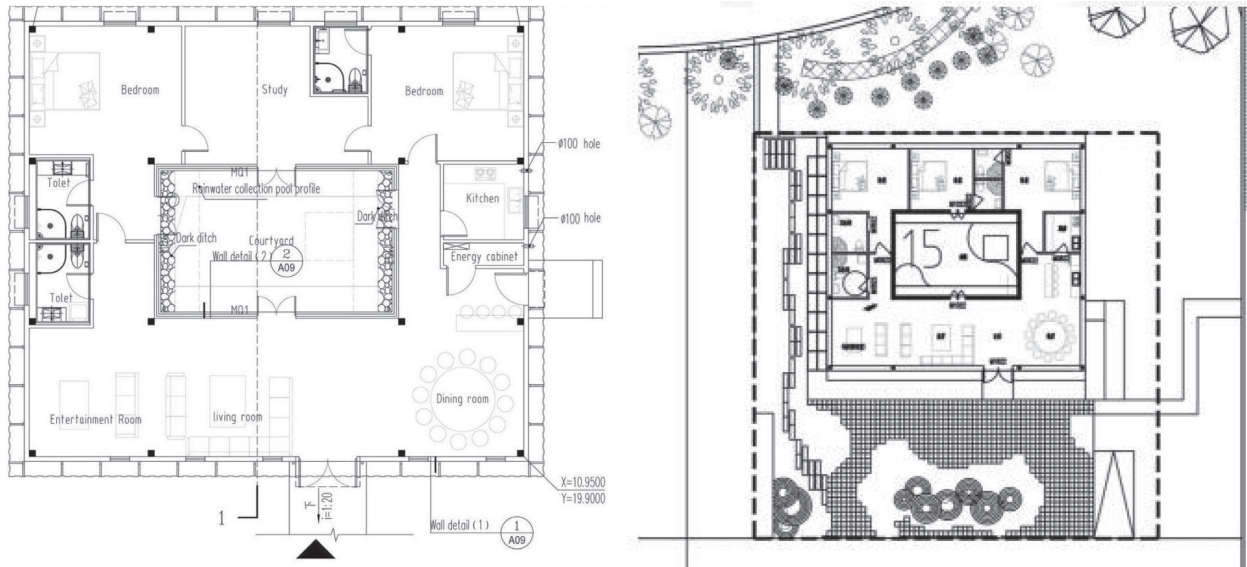
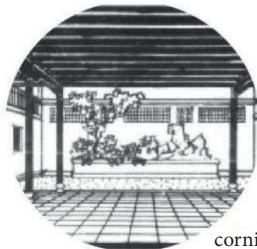


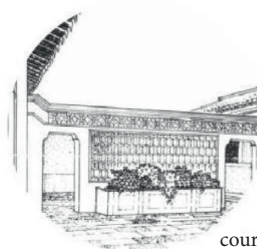
FIGURE 6: Layout.



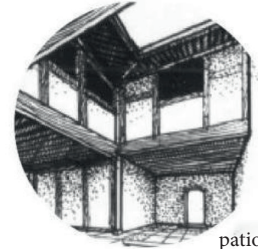
corridor



cornice



courtyard



patio



black tiles



white wall



shutters



landscape

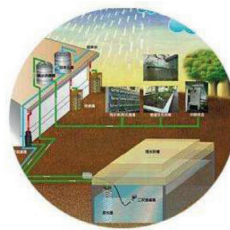
FIGURE 7: Traditional space elements and material elements.



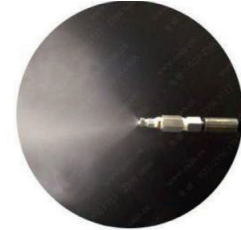
perforated aluminium panel



photovoltaic panel



rainwater collection



spray cooling

FIGURE 8: Modern element placement.

gathered crowd drink water from a winding canal with one wine cup floating on it to wash away ominousness) is an elegant cultural custom in the Chinese folk. It comes from the preface of the calligrapher Wang Xizhi's "The Preface of the Lanting Pavilion" and has two major functions: celebration and praying for disaster prevention. Considering the hot and dry weather in Dezhou, China, PC bricks were laid on the curve instead of water in the traditional sense. In this way, the combination of PC bricks and light strips at night can better create the artistic conception of "Qu Shui Liu Shang." The light strip in the outer courtyard, the light and shadow of the building, and the surrounding environment are more suitable for modern gatherings. This landscape has inherited the context of Chinese history and allowed the rebirth of cultural classics here. In addition, we use steel pipes to simulate the shape of mountains and rocks to show the beauty of classical gardens and use modern technology to express traditional landscape shapes.

3.2. Construction: Architectural Technology and Livable Experience. "Waterside Cube" uses a combination of active and passive technologies, including the introduction of passive energy-saving design methods, to create a more comfortable and livable living environment. This is also the advantage of the combination of new courtyard-style architecture and architectural technology. The passive design strategy in "Waterside Cube" is a unique design direction in the new courtyard-style building, which reduces the use of active equipment and achieves the best energy-saving effect.

First of all, in the site, we arranged this square building in a north-south orientation. The building is composed of a central inner courtyard and four container modules around. The functional design follows the layout pattern of a traditional courtyard-style building to ensure the lighting and sunshine of the building.

Secondly, the inner courtyard enclosed by the four modules not only functions as a landscape and family gathering, but also has the functions of ventilation, lighting, and shading. When we open the grilles on both sides of the courtyard, the courtyard space and the living room and study space can be combined inside and outside, and passive ventilation enhances air circulation, acting as a "large living room" and enhancing the flexibility of the space (Figure 9).

Thirdly, in terms of building shading, we adopted a combination of wooden grilles and full floor glass around the inner courtyard to enhance the connection between users and the inner courtyard. At the same time, the wooden grilles are combined with the traditional sloping roof canopy of the inner courtyard to enhance the shading effect. It is worth mentioning that the perforated aluminum plate design on the building envelope has special functions; due to the particularity of the material, its wavy surface not only increases the three-dimensional effect, but also refracts and reflects light to play a role in shading. The use of perforated aluminum panels on the outer protective structure and the placement of the spray system break the heavy feeling of the building block. Meanwhile, the combination of virtual and

real facade design and the material properties of perforated aluminum plates make the interface of the building rich in rhythm.

Fourthly, the use of buffer space is a more comprehensive design technique in passive energy-saving design strategies. Through the use of buffer space, the building microenvironment is improved. In the new courtyard-style building, we also added some detailed designs to the inner courtyard.

Water is the core element of the building, so we incorporated natural rainwater into the design of the courtyard. In the inner courtyard, the meaning of "Si Shui Gui Tang" carries the cultural context, and considering the arid climate in the north, so we hope that rainwater can be used. Therefore, the rainwater harvesting module is placed below the inner courtyard surface to allow it to absorb water, store water, seep through water, and then purify the water for domestic water and landscape irrigation in the outer courtyard (Figure 10).

In the landscape construction, a spray system is added between the perforated aluminum plate on the outer facade and the box to create a misty rain effect and a different mood. This system also has a cooling function. The principle is that the liquid state is converted into gaseous mist by a physical high-pressure method, and the gaseous mist is formed after atomization, whose particle diameter is less than 4 micrometres with the probability of 70%. Afterwards, the gaseous mist can quickly take away the air heat, and the combination of gaseous mist and radiation-proof thermal energy coating on the external wall has the effect of cooling down 3–7°C. At the same time, it can produce a large number of negative ions which are known as "airborne vitamins" to create a unique "forest oxygen bar" in the city and improve the air quality that is good for health. Its unique moisturizing function can better protect the plant landscape in outer garden.

Fifthly, for the envelope structure, we can conclude that walls, roofs and windows account for 76.6% of the total heat loss through thermal analysis. Therefore, high-density rock wool and extruded board (the density is 120 kg/m³) are finally used in the design. Their heat transfer coefficient is less than or equal to 0.028 W/(m·K), and the heat transfer coefficient of light weight foamed concrete is 0.052 W/(m·K) in general light steel fabricated houses, and the thermal insulation effect of foamed concrete is the best. In the selection of glass, vacuum glass is used in all buildings to enhance heat preservation, sound insulation, and noise reduction.

Effective use of energy is a key issue for solar homes. At the same time, in order to cope with the possible impact of extreme weather in the future, active technology has been added to the house to ensure the overall operation of the house. Based on geographical location and solar elevation angle of Dezhou, Shandong Province, we calculated the optimal slope, azimuth, and distance between the two solar panels, so that the photovoltaic system can achieve the best results. It has resulted in an installed capacity of 22.770 kW with sixty photovoltaic panels placed on top of the building and nine panels on the garage. According to the actual



FIGURE 9: Principle of air flow in the inner courtyard.

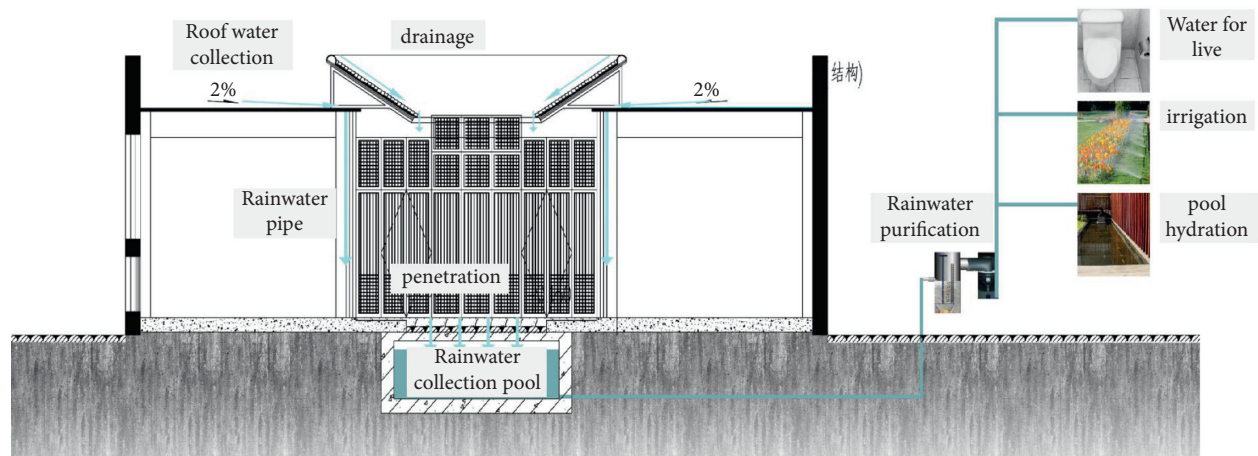


FIGURE 10: Principle of rainwater harvesting module.

measurement on the site, the power generation per week is 700 kWh, and the power generation per day can reach 125.7 kWh when the radiation is good. The whole system uses high-efficiency photovoltaic panels and microinverters. The photovoltaic panels use N-type single-crystal double-sided double-glass, and the efficiency can reach more than 20% under STC conditions. The advantage of using a microinverter is that each of the four photovoltaic panels is easy to repair and has an efficiency up to 97%, and the power generation inspection fault can be detected in real time from the APP. The house uses a mode of self-use of surplus power to access the Internet. To improve the quality of photovoltaic power generation and reduce the interaction with the power grid, we added a battery to form a photovoltaic battery system, sold the electricity at the highest price, and stored it at a low price to improve economic efficiency.

In order to make users feel more comfortable, the use of water-cooled central air conditioners in buildings can keep the temperature difference at about one degree in winter and summer, and the air supply is more uniform, which is better than traditional air conditioners. It is worth mentioning that the water circulation structure can reduce the use of refrigerants, together with the passive energy-saving technology in the inner courtyard design, as well as the spray system and perforated aluminum panels for the building's

climate regulation, and can reduce the load throughout the year.

Whether it is livable or not is an important criterion for judging residential buildings [12, 13]. The application of the smart home system in this building enhances the user's comfort. With the continuous improvement of intelligent systems, such integrated design has improved the past living and operating modes. Its intelligent central control system serves as the wisdom center of the family. The Zigbee Center integrated with the smart host interacts with each front-end device, server platform, and mobile phone client, enabling users to use the mobile APP to view and control indoor conditions (e.g., lighting, scene panels, smart appliances, smart air conditioners, smart air detection, smart door locks, smart security, and family music). It is convenient for different users to make personalized adjustments (Figure 11). During the competition in Dezhou from August 2nd to 15th, the measuring index curve diagram of the competition house under the combined influence of active and passive construction technology is listed as follows. This is to calculate the score according to the scoring curve in the rules and then select the lowest value as the curve of temperature, humidity, PM2.5, and CO₂ in the house obtained by recording. It can be seen that these values are stable and in line with the competition requirements (Figures 12–15).

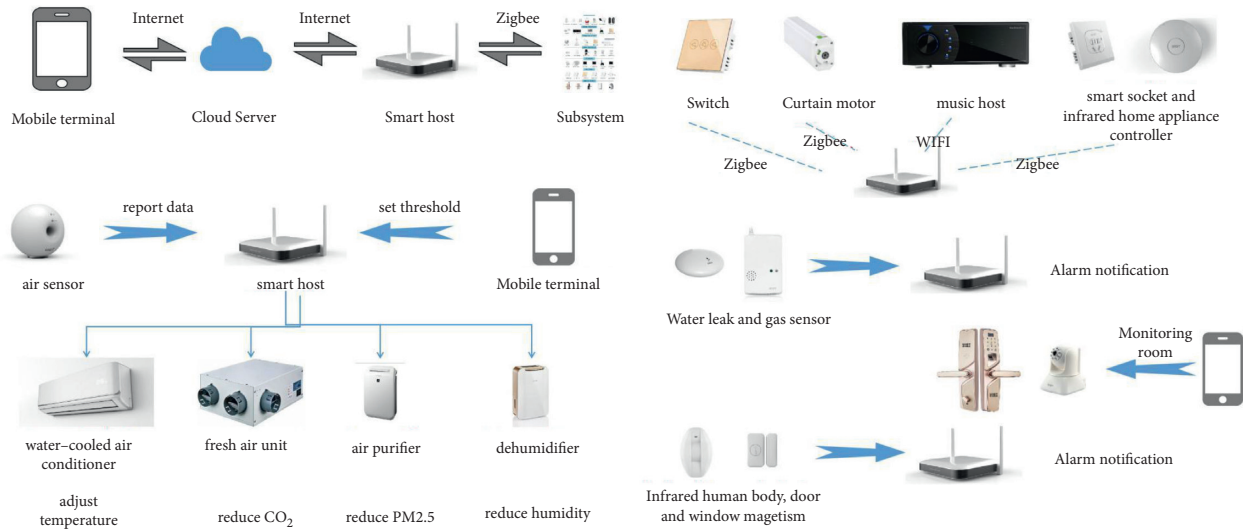


FIGURE 11: Smart home system application.

3.3. Consistency: Construction Mode and Results Feedback. According to the requirements of the competition, the building must be completed and put into operation within 20 days. Considering the requirements of rapid construction, our design adopts a highly prefabricated container construction model. The “Waterside Cube” consists of four containers. Except for the perforated aluminum panels, wooden grids, steel roof truss, solar panels, and other architectural structures on the facade, the rest are processed and installed in the factory, and then the box splicing and decoration are completed in the site. During the construction, the same assembly was completed in only 2 days, which improved the construction efficiency (Figure 16).

Compared with traditional containers, our architectural design has been improved in terms of structure and size, and at the same time, the public area module and the rest module have been adjusted to a length of 15.7 meters. Meanwhile, the height of the four container modules is 3.6 meters, and the indoor net height is 2.95 meters, which guarantees the comfort of the building space. Compared with light steel fabricated houses, the container has fewer splicing nodes, stronger structural integrity, and less construction waste and environmental noise. This construction mode has the characteristics of convenience, environmental protection, and low cost. If mass production is promoted in the future, it can meet the needs of a wider group of people.

At the same time, the container body can be customized according to the location of the building and can be flexibly transformed in space and form, which has strong adaptability and popularization. In terms of the positioning for target customer groups, the container model also has more potential. Whether it is a young family of three, or a group of elderly customers, this problem can be handled through a combination of module stacking and space. In the future development, people can go to the market to purchase and customize different module functions according to their personal preferences and combine them as needed to create an interesting space. This will promote the future

development and popularization of new courtyard-style buildings.

In terms of the height prefabrication of the box, the structural insulation wall panels and embedded pipelines of each standardized module, and even most of the interior decoration, the interior surface of the wall, floor paving and skirting have been prefabricated in the factory, and then the soft decoration and furniture laying are carried out on site. Some flexible wall panels in the box can be removed or installed in a customized manner to allow flexible division of functional areas.

In order to get better feedback from users, many on-site visitors were investigated during the open visit time. These visitors included elderly people, middle-aged people, and children of different ages, covering different social classes. Finally, it is concluded that more than 80% of the customers have more demand for the inner patio than the outer courtyard. At the same time, the architectural form of the inner patio is also a combination of traditional architectural forms and modern lifestyles, which is more conducive to the creation of the family atmosphere. From the perspective of traditional culture, the family lifestyle of four generations living under the same roof is more inclined to the “回” shaped single-family house, rather than the “C” shaped or “L” shaped layout structure. It has more privacy and fits the needs of users which can be interpreted as warm inside and defensive outside.

4. New Courtyard Architecture and Urban Development

The inheritance of architectural culture emphasizes the protection of its historical features and forms, while the cultural significance of the new courtyard-style building emphasizes not only the characteristics of times, but also the livable space created by the contemporary architecture combined with new technologies. In modern life, the new courtyard-style building is not only the reproduction of

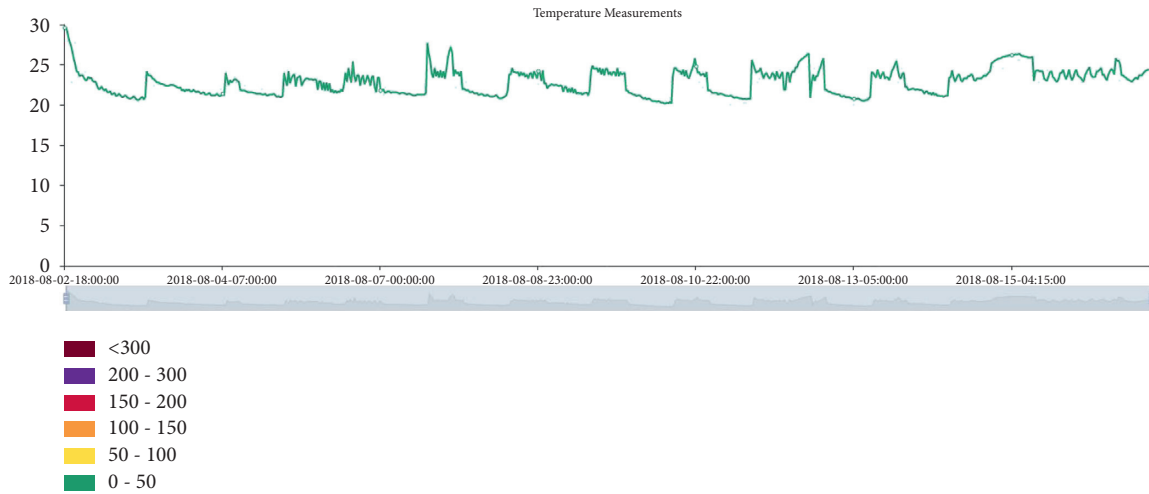


FIGURE 12: Air temperature during the competition indoors.

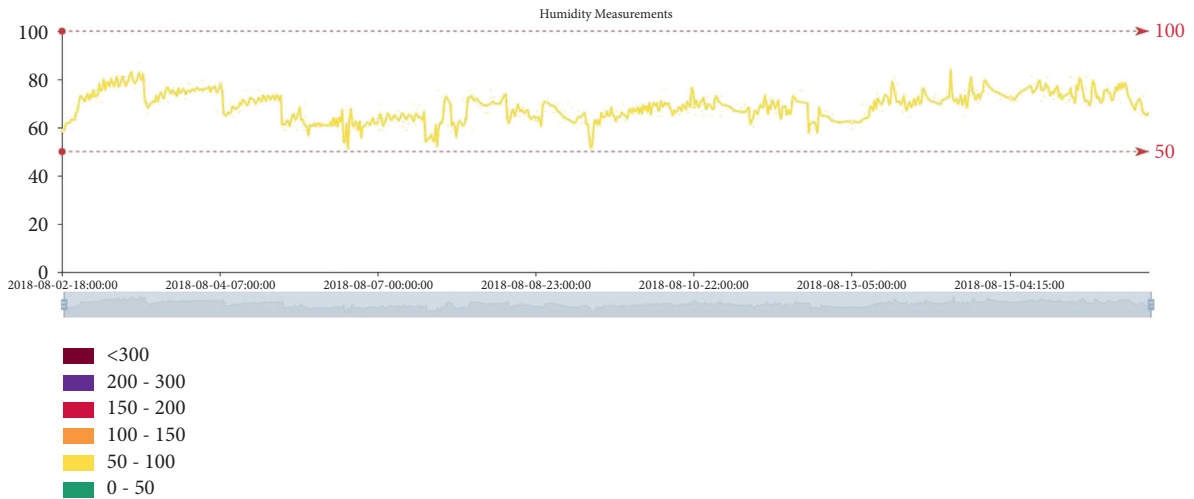


FIGURE 13: Humidity during the competition.

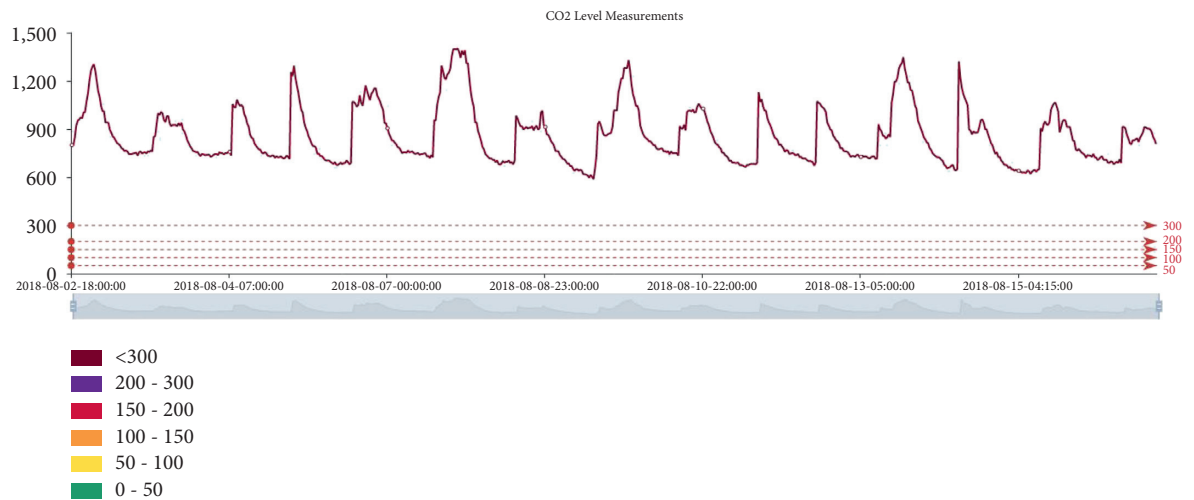


FIGURE 14: CO₂ level during the competition.

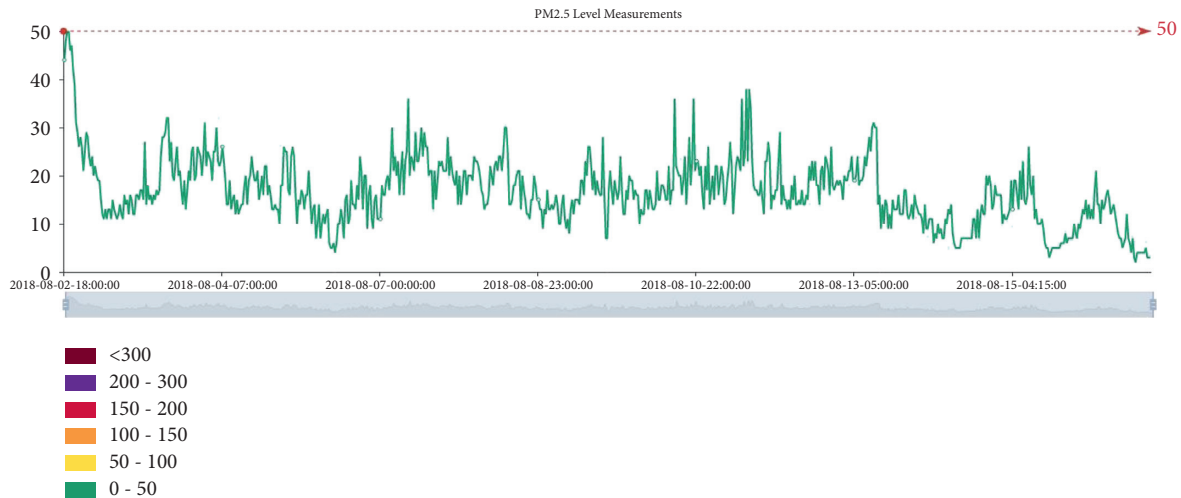


FIGURE 15: PM2.5 level during the competition.



FIGURE 16: Building layout and container hoisting and splicing.

architectural culture, but also the continuation of national culture and the concept of harmony between man and nature, as well as the implementation of the sustainable development concept of harmony between man and nature.

With the rapid development of the city, new buildings have gradually replaced old buildings, and the influence of foreign culture on cities has become increasingly apparent. The preservation of traditional cultural architecture should not only protect the building as a heritage, but also apply the architecture and urban texture under the influence of this context to the contemporary society. The main form of contemporary protection for ancient buildings lies in both in situ protection and off-site restoration, and this protection is only aimed at a single building, which lacks the protection for its architectural community and natural environment. Due to the current situation of modern urban development, especially in large- and medium-sized cities, there is a phenomenon of tension in land use. In order to achieve a larger floor area ratio, the building continues to develop at a high altitude, and the traditional courtyard house cannot be realized in such a city background. However, the inheritance

of architectural culture is not the copying of the entire architectural system, but the application of language and construction to modern life. For example, the “courtyard” elements of a courtyard house not only allow people in urban life to approach nature and experience the semiprivate environment in a unique house, but also improve the environmental microclimate within the building [14].

At the same time, in “Waterside Cube,” the modules of the courtyard-style building can be combined and customized, and the single module can be taken as a unit for horizontal and vertical development to be staggered and opposed. In this way, it not only continues the building layout system of traditional courtyard, but also generates diversified space, and this method has certain development potential [15, 16].

Since the competition includes the inspection for subjective and objective indexes, some local Chinese residents can evaluate different competition buildings after the completion of “Waterside Cube.” “Waterside Cube” has obtained the acceptance from most residents in type system and experience of this new courtyard-style building, even

though there is a wide range of visitors and the differences of occupations and ages are obvious. In China, some residents enjoy high-rise residential communities, but they are also fond of the inner courtyard simultaneously. Therefore, in future research and further exploration, the type systems of inner courtyard or such courtyard building can be superposed and constructed in different ways. In this way, the possibility and practice of application in diversified cultural background and architectural type system are also the issues for future in-depth research.

5. Conclusion

The “Waterside Cube” is an exploration of the new courtyard-style buildings under the influence of architectural culture. It utilizes the construction mode of the container to make the building’s composition and use functions flexible and also provides many possibilities for the future development of architectural design and development. This building is also an exploration of combining traditional culture with modern technology in the new era which satisfies the requirements of architectural culture, architectural aesthetics, construction technology, and so on and thus has great promotion value. The biggest feature of “Waterside Cube” is to use the expression of modern technology to interpret the “shape” and “meaning” in the courtyard-style architectural culture.

The new type of courtyard-style architecture is a practice in the contemporary context and an exploration of the response to the disappearing traditional architectural culture model. As a practical construction case, the “Waterside Cube” is built not only as a competition in Dezhou, Shandong Province, but also as the inheritance of its courtyard-style architectural form and culture. It will be applied to China through the extraction of different elements and the inheritance of regional culture in the southern and northern regions. The architectural culture will continue to be inherited, and the exploration of this new courtyard-style building is only the beginning.

Data Availability

The data used to support the findings of this study are included within the article.

Conflicts of Interest

The authors declare that they have no conflicts of interest.

References

- [1] L. Zhang, *Research on the Inheritance and Development of Courtyard-Style Residential Buildings in Modern Urban Space*, Shandong University, Jinan, China, 2015.
- [2] K. Z. Zheng, *Research on the Aesthetic Culture Spirit in the Courtyard House—Taking Beijing, Shaanxi and Shanxi as Examples*, Xi’an University of Architecture, Xi’an, China, 2009.
- [3] Y. Liu and Q. Ning, “Triple understanding of Guanzhong narrow courtyard and its house space,” *Journal of Housing and the Built Environment*, vol. 36, no. 2, pp. 521–537, 2021.
- [4] S. Yu, “Courtyard in conflict: the transformation of Beijing’s Siheyuanduring revolution and gentrification,” *The Journal of Architecture*, vol. 22, no. 8, pp. 1337–1365, 2017.
- [5] K. Lynch, *The Image of the City*, Thread-Binding Books Publishing House Press, Beijing, China, 2006.
- [6] X. Guo, *An Analysis of the Assimilation of Residential Buildings and its Impact on Urban Construction*, Qingdao Technological University, Qingdao, China, 2018.
- [7] M. C. Zhang, *Morphological Analysis of Traditional Quadrangle Space*, Hebei University, Baoding, China, 2011.
- [8] H. Yang, *The Research of Construction Mode and Development of Quadrangle in Beijing*, North China University of Water Resources and Electric Power, Zhengzhou, China, 2017.
- [9] H. Huang, *Tianjing’ Deciphering—The Study on Tianjing Space of China’s Traditional Residences and Contemporary Architecture*, Chongqing University, Chongqing, China, 2016.
- [10] C. Zhang, *Architectural Courtyard Space*, Tianjin Science and Technology Press, Tianjin, China, 1986.
- [11] J. F. Chen, *Heaven and Man-Concept and Chinese Cultural Tradition*, Sanlian Bookstore, Shanghai, China, 1996.
- [12] İ. Ayçam, S. Akalp, and L. S. Görgülü, “The application of courtyard and settlement layouts of the traditional Diyarbakır houses to contemporary houses: a case study on the analysis of energy performance,” *Energies*, vol. 13, p. 587, 2020.
- [13] R. Hasehzadeh, M. Khakzand, and M. Ojaghlo, “Optimal thermal characteristics of the courtyard in the hot and arid climate of Isfahan,” *Buildings*, vol. 8, no. 12, p. 166, 2018.
- [14] Y. T. Wang, *To the Understanding of the Chinese Traditional “Home” Culture and its Significance to Explore*, Tianjin University, Tianjin, China, 2016.
- [15] J. Ma, X. L. Li, J. G. Wang et al., “Experimental study on vibration reduction technology of hole-by-hole presplitting blasting,” *Geofluids*, vol. 20, 2021.
- [16] J. Wang, T. Zuo, X. Li, Z. Tao, and J. Ma, “Study on the fractal characteristics of the pomegranate biotite schist under impact loading,” *Geofluids*, vol. 22, 2021.

Research Article

Near-Fault Ground Motion Impacts on High-Speed Rail Large-Span Continuous Girder Bridge considering Pile-Soil Interaction

Yefei Zhou ¹, Gang Wang ², Shuyi Yang ², and Niu Liu ²

¹The 4th Construction Co., Ltd. of China 15th Corporation, Zhengzhou 450051, China

²College of Transportation Engineering, Nanjing Tech University, Nanjing 210009, China

Correspondence should be addressed to Gang Wang; swjtu_wg@163.com

Received 3 December 2021; Accepted 12 February 2022; Published 21 March 2022

Academic Editor: Lingkun Chen

Copyright © 2022 Yefei Zhou et al. This is an open access article distributed under the Creative Commons Attribution License, which permits unrestricted use, distribution, and reproduction in any medium, provided the original work is properly cited.

This paper examines and discusses the dynamic response of a high-speed train-bridge-soil-pile foundation system to near-fault earthquakes. A 72 + 120 + 72 m continuous girder bridge of a high-speed railroad was selected as the model for calculation. Based on the p-y model for simulating pile-soil interaction, the moment-curvature analysis program XTRACT is used to calculate the moment and curvature of bridge piers and pile foundation sections, and the finite element (FE) software is used to establish two nonlinear global bridge models under seismic effects in the high-intensity zone, one considering pile-soil interaction and one without considering pile-soil interaction. The A_p/V_p parameter, the ratio of peak acceleration to peak velocity of transverse ground shaking, is used to reflect the impulse characteristics of earthquakes and the effect of the A_p/V_p parameter on the dynamic response of bridges to earthquakes was studied. The elastic-plastic response of the bridge system was calculated under lateral and vertical near-fault (NF) impulse/NF nonimpulse/far-field (FF) ground motions (GMs). The study shows that the structural displacement increases, and the internal force decreases after considering the pile-soil interaction. The results show that the bridge piers enter the elastoplastic phase under rare earthquakes. The NF ground shaking couples with the bridge into the elastoplastic phase with a more significant impulse period than the FF ground shaking intensifies the dynamic response of the bridge structure.

1. Introduction

A high-speed railroad has the advantages of high speed, high density, all-weather, large capacity, comfort, safety, and reliability compared with other means of transport. It has become the trend of railroad development in the world. It is considering that the construction of railroads will inevitably pass through some densely populated urban areas and soft soil areas in the plains or other geological conditions. Therefore, ensuring the overall safety of the bridge structure and the safety of the trains on the bridge has become an urgent problem for the bridge designers to solve, which is because high-speed railroad bridges are subjected to forced vibration due to the powerful impact of the upper high-speed trains and structural fatigue under the long-term, high-density effect of this power, which reduces the stability

and strength. This vibration of the bridge structure, in turn, affects the safety and smoothness of the running vehicles on the bridge. Therefore, the study must consider the dynamic response of the vehicle-bridge coupling.

Pile foundations are widely used for their high bearing capacity, good stability, low settlement, and ability to adapt to various geological conditions and loading situations. Due to multiple factors such as superstructure, overlying infinite foundation, and far-field ground motion, the pile-soil-structure dynamic interaction is one of the most complex topics in structural dynamics and soil dynamics and has received wide attention.

Erhan and Dicleli [1] developed a soil-bridge nonlinear model considering SSI and calculated the seismic response of bridges under different earthquake intensities and found the influence of SSI on the seismic response of bridges under

design. Khoshnoudian et al. [2] established SSI by building a simplified vertebral soil model and studying impulsive earthquakes' effect on dynamic structural stability. For SSI can cause lateral displacement of the structure, Khoshnoudian and Ahmadi [3] investigated the impact of the impulsive earthquake on the displacement ratio of the structure and pointed out that a smaller structural length to slenderness ratio as Timoshenko type piers may offset part of the lateral displacement response. Wang et al. [4] and Chotesuwan et al. [5] investigated the effect of SSI on the seismic response of bridges based on experiments. Moghaddasi et al. [6] investigated the effect of bending properties of pile foundations on the seismic response of structures by using a robust Monte Carlo method to develop an equivalent linear model of soil-pile foundation-bridge. Xie et al. [7] studied the SSI effect on the seismic response of a typical bridge in California. Durucan and Dicleli M [8] and Liu and Zhang [9] investigated the impact of A_p/V_p parameters on the seismic response of seismically isolated structures.

The study by Wang et al. [10] analyzed the effect of soil-structure interaction SSI (SSI) on the seismic response of bridges due to vertical earthquakes, including liquefaction potential. The study results indicate that the SSI effect tends to reduce the amount of response to certain ground motions and increase the demand for other ground motions relative to the fixed base case. This phenomenon can be explained by the frequency components of ground motions, the drift of the vertical self-oscillation period, and the generalization of the vertical spectral acceleration for higher modes. In addition, the liquefaction mechanism of nonliquefied soils is isolated concerning the SSI effect, revealing the impact of liquefaction on the bridge response. Li et al. [11] developed a three-dimensional nonlinear vibration isolation finite element model of a prototype California High-Speed Rail (CHSR) bridge under NF earthquakes by considering soil-structure and track-structure interactions and calculating the seismic response of the bridge. The study did not compare the seismic response of the bridge before and after considering SSI. Galvín et al. [12] proposed a method for calculating the dynamic response of railroad bridges considering soil-structure interactions. The technique uses the substructure method to decompose the problem into two coupled interactions: the soil-foundation and the soil-foundation-bridge systems. The foundation and surrounding soil are discretized using the finite element method and filled with perfectly matched layers to avoid boundary reflections. The benefit of the technique is that as the complexity of the problem increases, the technique allows access to specialized analysis tools to deal with both the soil-foundation and superstructure domains. Bhure et al. [13] studied the dynamic response of a subway bridge under moving loads. Track unevenness and train inertia effects were not considered. Moving load analysis was performed for the fixed foundation and the full pile models. It was shown that the resonance phenomenon of the full pile model was lower than that of the fixed foundation model in both loading cases.

Through the investigation and comparison of different research results at home and abroad, it can be found that the

study of the vehicle-bridge coupling dynamics of high-speed railroad continuous girder bridges under the action of earthquakes is of great significance to the design of both high-speed railroad bridges and high-speed trains in the future, so this research topic has gradually received extensive attention from various researchers. However, the existing research still has many shortcomings, mainly in the following points.

Firstly, the continuous girder bridges have received wide attention for their structural stiffness, small deformation, good dynamic performance, and benefits to high-speed traffic. So far, the leading research at home and abroad has been limited to simply supported girder bridges, and the vibration response of continuous girder bridges lacks systematic analysis. Therefore, the seismic response of large-span continuous girder bridges for high-speed railroads needs to be studied in depth.

Secondly, the existing domestic studies on the elastic-plastic seismic response analysis of high-speed railroad continuous girder bridges are few and limited to the elastic-plastic analysis of supported girder bridges. Still, the dynamic characteristics of the two are different. Therefore, the elastic-plastic seismic response analysis of high-speed railroad continuous girder bridges is needed.

Again, most of the studies at this stage only establish the train-bridge model and ignore or simplify other system elements, such as not considering the influence of the soil on the structure. Therefore, a more detailed model to analyze the pile-soil-structure interaction should be established.

This paper selects the research object of a $72 + 120 + 72$ m continuous girder bridge of high-speed railroad. The nonlinear model of the soil-pile foundation is established with the SHAKE91 program. P-y curve, t-z curve, and q-z curve and the hysteresis characteristics of bridge piers and pile foundation are simulated with the bilinear model to establish the dynamic responses railroad bridge-soil-pile foundation continuous girder bridge system in the wrong geological development area. The dynamic calculation of the train large-span bridge system under velocity impulse NF earthquake is carried out. The study analyzes the elastic-plastic seismic response of the bridge pile foundation system under NF earthquakes. It reveals the dynamic performance of railroad bridges in poorly developed geological areas under multidimensional seismic action. The research aims to promote the preliminary research results to the application by solving the core scientific problems behind the technical bottlenecks.

2. Power p-y (t-z and q-z) Curve Method

In recent years, the simulation of soil confining action around piles under intense earthquake action has been a complex problem and a hot research topic. Due to the complexity of pile-soil interaction, in this paper, based on the Winkler foundation assumption that the response of each soil layer is independent of the adjacent soil layers, an analytical model with dynamic p-y (t-z and q-z) curves is shown in Figure 2(e), which consists of three main parts: free-field soil, structural, and pile units. Among them, the

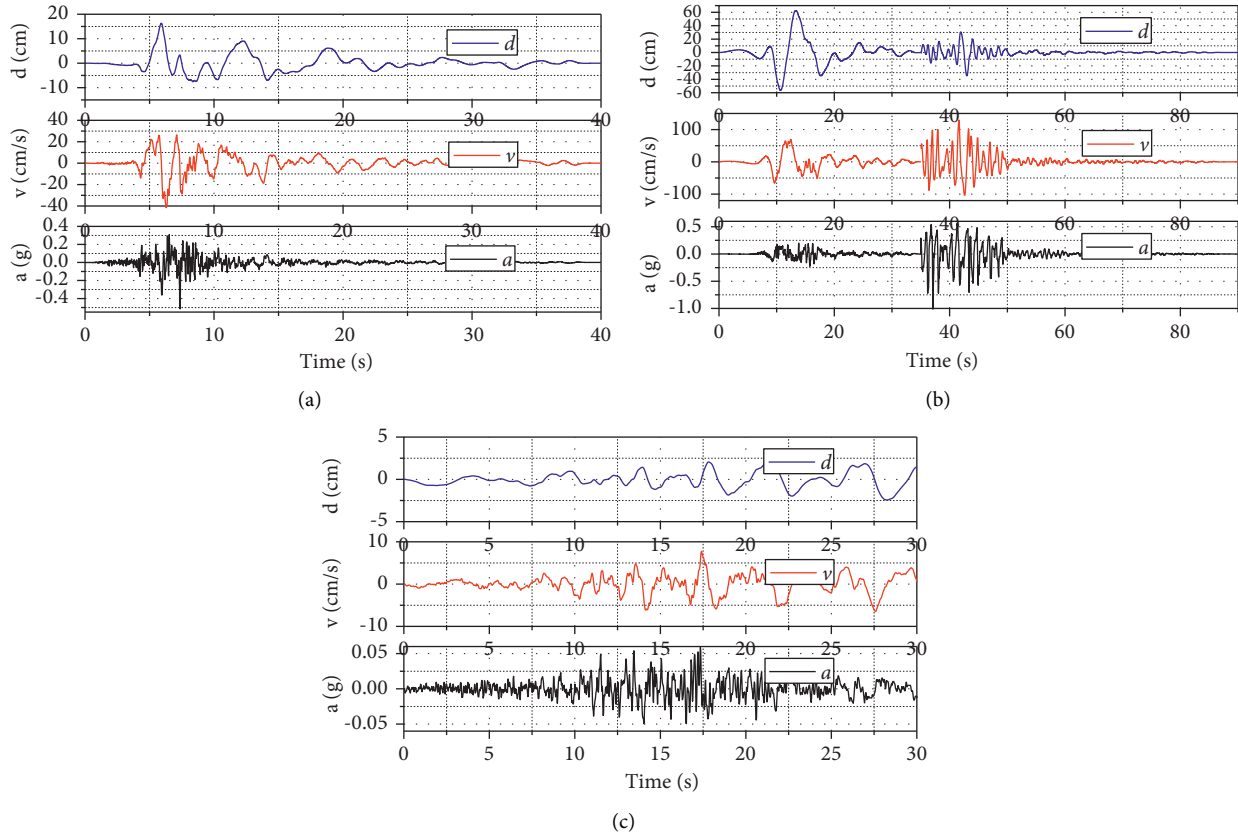


FIGURE 1: Time-history curves of ground motions: (a) Loma Prieta STG000; (b) Kocaeli_Yarimca; (c) Hector Mine BRS090.

TABLE 1: Impulse-type NF ground vibration information table.

Earthquake name	Stations	Magnitude	Time	Amount	PGA(g)	Ap/Vp	V/H	Fault distance (km)	V_{s30} (m/s)
Irpinia Italy	Sturno (STN)	6.9	1980	STU270	0.321	4.47	0.73	10.84	382
				STU-UP	0.235				
Loma Prieta	Saratoga-Aloha Ave	6.93	1989	STG000	0.514	12.37	0.77	8.5	380
				STG-UP	0.396				
Cape Mendocino	Petrolia	7.01	1992	PET090	0.662	7.48	0.25	8.18	422
				PET-UP	0.165				
Landers	Lucerne	7.28	1992	LCN260	0.725	5.44	1.14	2.19	369
				LCN-UP	0.823				
Northridge	Sylmar-Olive View Med FF	6.69	1994	SYL360	0.843	6.52	0.64	5.3	440
				SYL-UP	0.536				
Kocaeli Turkey	Izmit	7.51	1999	IZT090	0.230	6.01	0.63	7.21	811
				IZT-UP	0.145				

pile is simulated with a beam unit. The nonlinear soil is simulated with three indifferent dynamic units: the active p-y unit acts as the horizontal resistance of the Earth, the dynamic t-z unit simulates the vertical frictional force of the soil, and the dynamic q-z unit simulates the vertical support of the ground, and the free field is part of the pile-soil interaction, and the springs used are not one, but multiple springs in series.

The load transfer (T-Z) method models the pile as a series of cells supported by discrete nonlinear springs representing the frictional resistance at the soil surface (T-Z springs) and nonlinear springs at the pile ends, meaning the end-bearing springs (Q-Z springs). The soil spring is a

nonlinear representation of the soil reaction force T (or Q at the pile end) versus the displacement Z , as shown in Figure 2(e). With known T-Z and Q-Z curves, the axial load-settlement response can be obtained using the computer program.

Appropriate T-Z and Q-Z curves are necessary to obtain reliable settlement and axial monopile load transfer calculations. Such load transfer curves were initially obtained empirically. Coyle and Sulaiman [14] received T-Z curves based on models and experience with full-size sand pile loading tests. Vijayvergiya [15] and API [16], based on this work and other empirical results, made general recommendations for estimating T-Z and Q-Z curves for sandy

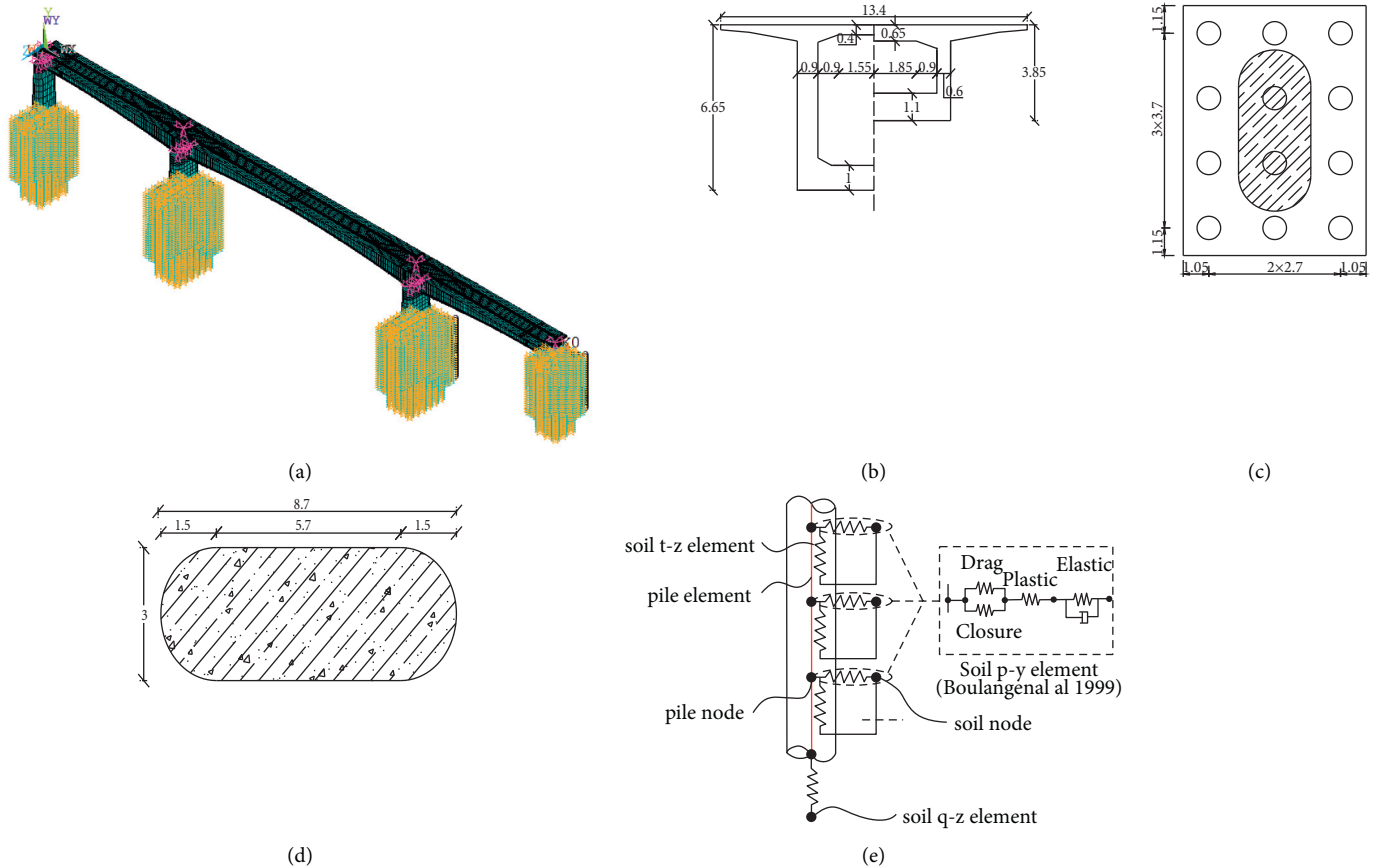


FIGURE 2: Typical bridge sections. (a) Bridge structure, (b) girder section, (c) bearing section, (d) pier section, and (e) pile-soil interaction model.

soils. The load transfer curves can also be satisfactorily constructed using theoretical methods related to the shear stiffness of the soil around the pile [17, 18].

The dynamic p - y (t - z and q - z) curve approach is a nonlinear foundation response method that takes into consideration soil nonlinearity, soil stratification, soil type, load type, soil interface slip and detachment, and far-field soil radiation damping, among other factors. It overcomes the shortcomings of the single parameter method (such as the 6-spring method) for calculating the deflection, angle of rotation, and maximum bending moment of the pile by horizontal load-bearing pile, which cannot be well-matched with the actual measured data and boundary conditions at the same time, and resolves the issue that the linear soil pressure and displacement solution method is not applicable to the actual soil nonlinear reaction when large deformation occurs.

3. Ground Vibration Selection

In this paper, based on PEER strong seismic records, concerning the recommendations of FEMA-P695 Quantification of Performance and Response Parameters for Building Systems (ATC-63 Project) [19], and according to the USGS code, according to the difference of the average shear wave velocity (V_{s30}) within 30 m below the ground surface, the

average shear wave velocity of 360 m/s was used as the boundary.

The type of site ground shaking with shear wave velocity more significant than 360 m/s was selected. The ground vibrations were chosen from six groups of the near-fault (NF) impulse ground motions (GMs), six NF nonimpulse GMs, and six far-field (FF) GMs, each group including one horizontal ground vibration and one vertical ground vibration. Figure 1 depicts the time-history curves of selected ground movements, such as the Loma Prieta earthquake that struck STG000, the Kocaeli earthquake that struck Yarimca, and the Hector Mine earthquake that struck BRS090. Data on the characteristics of each ground vibration may be found in Tables 1 through 3.

4. Vibration Analysis of Railroad Bridges under near (Span) Fault Seismic Action

4.1. Project Overview. This paper uses a section of $48\text{ m} + 80\text{ m} + 48\text{ m}$ stubble-free cast-in-place prestressed concrete continuous girder bridge (double line) on the high-speed rail as the research background. Among them, the bridge structure schematic diagram is shown in Figure 2.

The girder adopts the form of a single-box single-cell section with variable cross section, and the bottom curve of

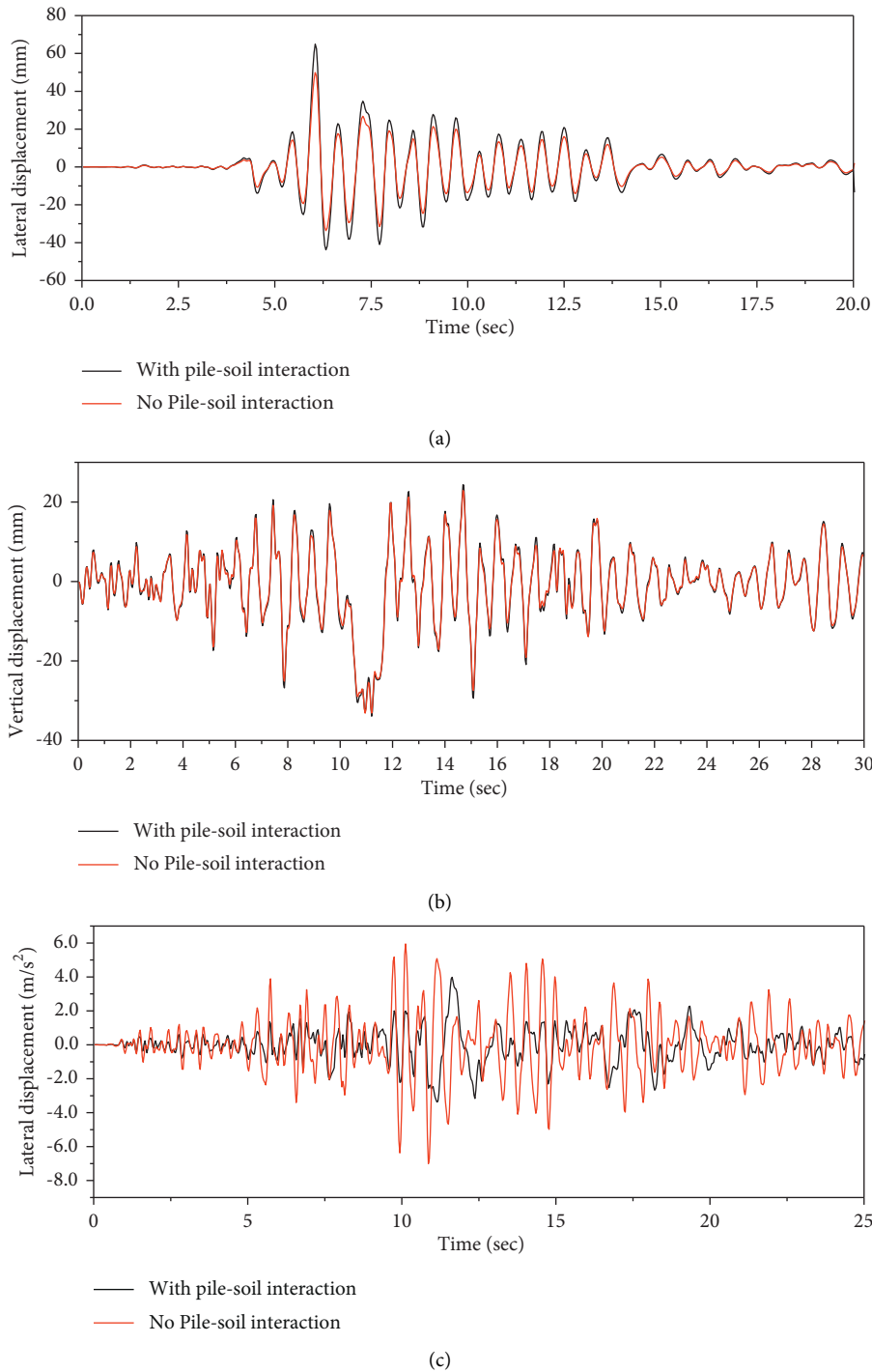


FIGURE 3: Time-history curves of the comparison of two models considering pile-soil interaction and without interaction: (a) Loma Prieta 1989 lateral displacement of beams in span under earthquake action; (b) Hector Mine 1999 Vertical mid-span displacement of beams under seismic action; (c) Kocaeli Turkey 1999 transverse acceleration in the span of a beam under seismic action.

the beam varies in a quadratic curve; the height of the cross section girder varies from 3.85 m to 6.65 m in the middle of the span; the thickness of the web differs from 0.6 m to 0.9 m; the thickness of the top plate varies from 0.4 m to 0.65 m; the thickness curve of the bottom plate varies from 0.4 m to 0.9 m; the typical cross section of the bridge is shown in Figure 2(b). The concrete material used in the girder is C40.

The bridge pier is around an end-shaped hollow pier with variable cross sections. The pier abutment is made of C35 concrete, and the pile foundation is made of concrete (C25) infill pile with 1 m diameter and 26 m pile length, and the foundation bearing is rigid and does not contact the soil. Standard reinforcement adopts HPB235 and HRB335 steel bars.

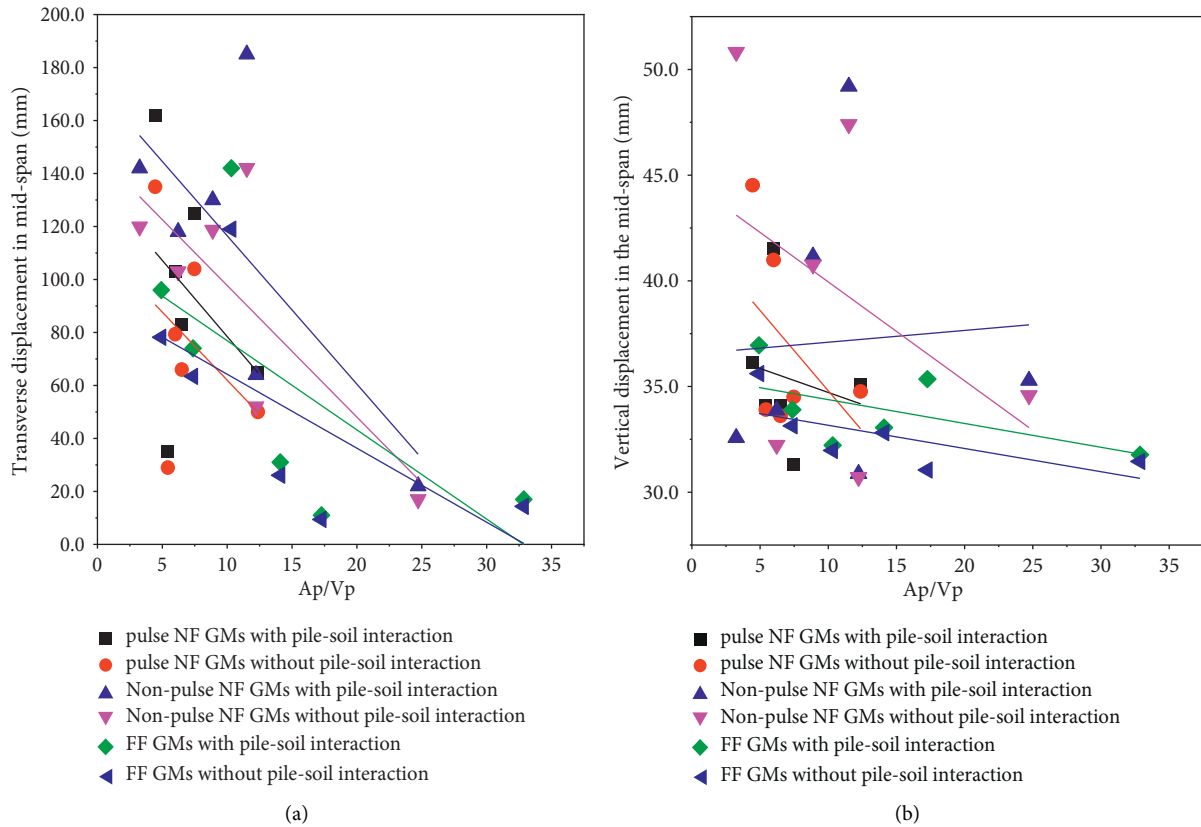


FIGURE 4: A_p/V_p values and seismic dynamic response. (a) Transverse displacement in the beam span. (b) Vertical displacement in the beam span.

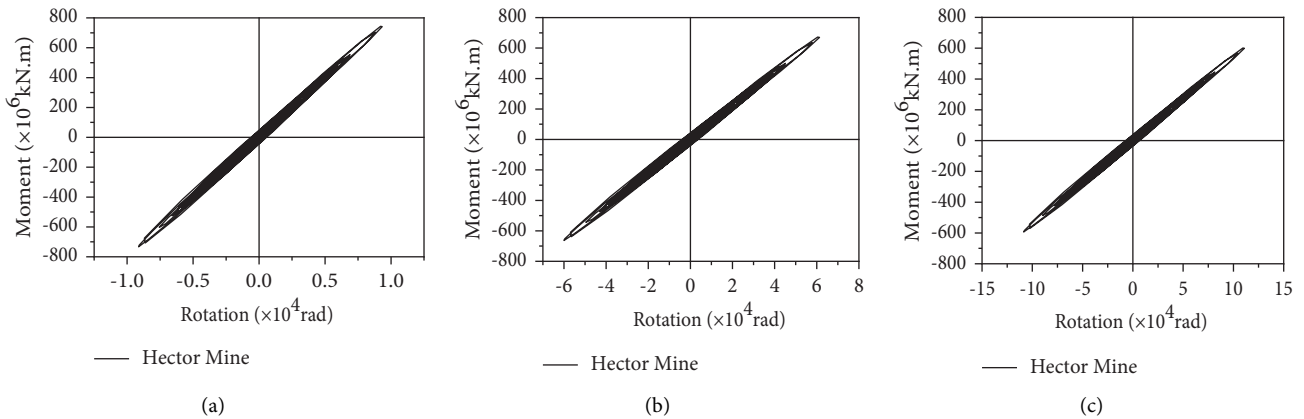


FIGURE 5: Moment-curvature relationship of pier bottom element under seismic action of Hector Mine earthquake. (a) First element. (b) Second element. (c) Third element.

4.2. Moment-Curvature Analysis of Bridge Pier Section. In this paper, XTRACT software is applied to perform the section bending-curvature analysis, and the bridge pier section is discretized into various fiber unit models. Then the section moment-curvature calculation is performed. The specific implementation process is as follows: after defining the ground vibration input, the plastic hinge is formed through the centralized plastic model for nonlinear time-history analysis. Using the FE program to calculate the average axial pressure at the bottom of the pier when the train crosses the bridge, according to the actual cut-off and

size, the arrangement position of various types of reinforcement, based on the Mander restrained concrete stress-strain relationship, the section fiber unit is established. Calculate the yield curvature and yield bending moment, ultimate curvature, and ultimate bending moment of the pier section under the action of axial force. Table 4 shows the values of the characteristic points of the equivalent bifurcation moment-curvature relationship of the cross section. In order to realize the nonlinear analysis of piers and piles, firstly, the parameters of mass density, axial strain, moment-curvature, and torsional and shear modulus of

TABLE 2: Nonimpulse type NF ground vibration information table.

Earthquake name	Stations	Magnitude	Time	Amount	PGA(g)	Ap/Vp	V/H	Fault distance (km)	V_{s30} (m/s)
Loma Prieta	BRAN	6.93	1989	BRN000 BRN-UP	0.456 0.506	8.88	1.10	10.72	476
Loma Prieta	Corralitos	6.93	1989	CLS090 CLS-UP	0.483 0.458	10.16	0.94	3.85	462
Cape Mendocino	Cape Mendocino	7.01	1992	CPM090 CPM-UP	1.039 0.739	24.51	0.71	6.96	567
Northridge-01	LA-Sepulveda VA Hospital	6.69	1994	SVP360 SVP-UP	0.932 0.318	12.23	0.34	8.44	380
Chi-Chi_ Taiwan	TCU067	7.62	1999	TCU067- N	0.319	6.22	0.74	0.62	433
Kocaeli_ Turkey	Yarimca	7.51	1999	YPT060 YPT-UP	0.394 0.242	3.25	0.61	4.83	297

TABLE 3: Far-fault general earthquake information sheet.

Earthquake name	Stations	Magnitude	Time	Amount	PGA(g)	Ap/Vp	V/H	Fault distance (km)	V_{s30} (m/s)
Friuli Italy-01	Tolmezzo	6.5	1976	TMZ270 TMZ-UP	0.315 0.277	10.33	0.88	15.82	505
Cape Mendocino	Shelter Cove Airport	7.01	1992	SHL000 SHL-UP	0.229 0.0543	33.10	0.24	28.78	518
Northridge -01	Featherly Park-Main	6.69	1994	FEA000 FEA-UP	0.101 0.0243	13.23	0.24	82.32	367
Kobe_Japan	Chimayo	6.9	1995	CHY000 CHY-UP	0.0921 0.0752	17.30	0.82	49.91	609
Kocaeli Turkey	Iznik	7.51	1999	IZN090 IZN-UP	0.124 0.0754	4.91	0.61	30.73	467
Hector Mine	Barsto	7.13	1999	BRS090 BRS-UP	0.0589 0.0445	7.60	0.76	61.2	370

TABLE 4: Equivalent bifurcation moment-curvature relationship of bridge pier section.

	Equivalent yield		Equivalent limit	
	Curvature (rad/m)	Bending moment (kN • m)	Curvature (rad/m)	Bending moment (kN • m)
Longitudinal	0.002310	5051	0.04705	6142
Lateral	0.002310	5051	0.04705	6142

piers and piles are defined, and the above parameters can realize the nonlinearity of piers; when the moment response of piers and piles cross section exceeds the yield moment of cross section, the turning spring will be activated. The nonlinear properties, such as the abovementioned moment-curvature relationship, are assigned to the bridge pier and pile units, and the bending moment and turning angle of each element of the bridge pier are calculated.

4.3. Dynamic Response of the Bridge. The combination of horizontal and vertical earthquake high-level seismic action is taken following the bridge design instructions and the site classification on which the bridge is built. The peak acceleration of ground vibration is considered to be 0.4 g following GB5011-2006 "Code for Seismic Design of Railway Engineering" [20]. All earthquakes are specified in the calculation to the fortification earthquake level. The train

passes at 350 kilometers per hour across the bridge structure. The peak elastic-plastic seismic response of two models of high-speed railroad reinforced concrete continuous girder bridges with and without pile-soil is computed in this article after lengthy computations.

Under rare earthquakes, the dynamic response of the bridge should be calculated by the nonlinear time-response analysis method, and the train travels over the bridge structure at 350 km/h. The peak elastic-plastic seismic response of two models of high-speed railroad reinforced concrete continuous girder bridge considering pile-soil and not considering pile-soil is calculated, which is shown in Table 5, with the NF impulse/NF nonimpulse/FF typical earthquake Loma Prieta 1989 earthquake, Hector Mine 1999, and Kocaeli Turkey 1999 as examples, and the corresponding time-history curves for the comparison of the two models considering pile-soil and not considering pile are shown in Figure 3.

TABLE 5: Summary of peak seismic response of continuous girder bridge of high-speed railroad under the action of rare impulse-type NF earthquake.

Earthquake type	Earthquake	Model type	Transverse displacement in the span/m	Vertical displacement in the span/m	Transverse acceleration in the span/(m/s ²)	Vertical moment in the span (10 ³ N • m)
Impulse NF GMs	Irpinia Italy-01 1980 Sturno (STN)	With pile-soil interaction	0.162	0.036	3.324	1.678
		No pile-soil interaction	0.135	0.044	6.621	2.098
	Loma Prieta 1989 Saratoga-Aloha Ave	With pile-soil interaction	0.065	0.035	3.532	0.921
		No pile-soil interaction	0.050	0.034	6.751	1.940
	Landers 1992 Lucerne	With pile-soil interaction	0.125	0.031	3.552	1.452
		No pile-soil interaction	0.104	0.035	12.62	2.074
	Northridge-01 1994 Sylmar-Olive	With pile-soil interaction	0.035	0.034	2.713	3.142
		No pile-soil interaction	0.029	0.031	4.073	4.189
	Northridge-01 1994 Sylmar-Olive	With pile-soil interaction	0.083	0.034	3.414	1.703
		No pile-soil interaction	0.066	0.033	9.226	2.129
	Kocaeli Turkey 1999 Izmit	With pile-soil interaction	0.103	0.042	3.403	4.091
		No pile-soil interaction	0.079	0.041	7.707	5.842

As shown in Table 5 and the time-history curves in Figure 3, the mid-span horizontal and vertical displacements and vertical bending moment response of the bridge under NF ground shaking are more significant than those under FF ground were shaking, which is due to the high amplitude effect of NF ground shaking. Thus the increased energy demand of the bridge under the impact of NF ground shaking should be considered.

4.4. Effect of A_p/V_p on Seismic Response. A_p/V_p is the ratio of peak lateral acceleration to peak lateral velocity (see equation (1)), whose value has a strong connection with the seismic dynamic response of the structure.

$$\frac{A_p}{V_p} = \frac{2\pi}{T_g}, \quad (1)$$

where A_p and V_p are the peak lateral acceleration and the velocity, respectively; T_g is the remarkable period of ground shaking.

It is shown in Figure 4 that the A_p/V_p values and dynamic seismic reaction are linked. The dynamic response values of the two bridge structural models that include pile-soil and do not consider pile-soil are decreasing under the action of NF impulse-type ground shaking, NF no-impulse ground shaking, and FF ground shaking, as can be seen from the scattering trend.

According to the calculated value of the moment-curvature skeleton curve response of the pier, as shown in Figure 5, the top moment of the first unit of the pier bottom

is 7.65×10^5 kN m at 350 km/h, which is larger than the yield moment and beyond the yield moment into the elastic-plastic phase. The moment of the third element of the pier bottom is 6.38×10^4 kN m, which is smaller than the yield moment; the element is in an elastic state. The study shows that the pier needs more excellent ductility and reinforcement under impulse-type NF earthquakes.

From the moment-angle relationship of the pier bottom unit in the above figure, it can be seen that the pier bottom is in the elastic-plastic stage under the action of NF impulsive ground shaking, NF nonimpulsive ground shaking, and far-fault ground shaking, and the bridge structure has different responses under different ground shaking excitation. In the case of pulsed NF ground shaking, the moment response of the pier bottom unit under the action of pulsed NF earthquake is larger than the other two types of earthquakes because of its long-held high amplitude pulsed action characteristics.

5. Conclusion

An earthquake-induced model of the dynamic interaction between trains and bridges is presented in this work. The high-speed train-bridge model is chosen. The finite element software is used to study the continuous girder bridge's self-vibration characteristics, which are then used to conduct the dynamic analysis of the bridge. This model was used to determine the elastic-plastic response of the bridge piers to transverse and vertical seismic stresses. That is evident from the findings.

- (1) Based on the finite element software, two nonlinear analytical models of a large-span continuous girder bridge for high-speed railroad without considering pile-soil interaction (i.e., pier bottom consolidation) and considering pile-soil interaction are established, and the bridge response corresponding to ground shaking is obtained by inputting eighteen groups of ground shaking effects. The structural displacement increases, and the internal force decreases after considering the pile-soil interaction. Hence, the internal structural force decreases, but the extended period will lead to a more significant structural displacement.
- (2) With the increase of A_p/V_p , the dynamic response values of the two bridge structure models, considering pile-soil and not considering pile-soil, under the action of NF impulsive ground shaking, NF nonimpulsive ground shaking, and FF ground shaking, all show a decreasing trend in the eight taken in this paper. For the 18 ground vibrations studied in this paper, the most pronounced structural response is found for A_p/V_p between 0 and 10.
- (3) Due to the brief duration of high amplitude pulsed action during pulsed NF ground shaking, substantial displacements of the bridge structure and the bottom unit of the piling are caused. This indicates that structural requirements are increased during pulsed NF seismic activity.

Data Availability

The data used to support the findings of this study are available from the corresponding author upon request.

Conflicts of Interest

The authors declare that there are no conflicts of interest regarding the publication of this paper.

References

- [1] S. Erhan and M. Dicleli, "Effect of dynamic soil-bridge interaction modeling assumptions on the calculated seismic response of integral bridges," *Soil Dynamics and Earthquake Engineering*, vol. 66, pp. 42–55, 2014.
- [2] F. Khoshnoudian, E. Ahmadi, M. Kiani, and M. Hadikhani Tehrani, "Collapse capacity of soil-structure systems under pulse-like earthquakes," *Earthquake Engineering & Structural Dynamics*, vol. 44, no. 3, pp. 481–490, 2015.
- [3] F. Khoshnoudian and E. Ahmadi, "Effects of inertial soil-structure interaction on inelastic displacement ratios of SDOF oscillators subjected to pulse-like ground motions," *Bulletin of Earthquake Engineering*, vol. 13, no. 6, pp. 1809–1833, 2015.
- [4] S.-C. Wang, K.-Y. Liu, C.-H. Chen, and K.-C. Chang, "Experimental investigation on seismic behavior of scoured bridge pier with pile foundation," *Earthquake Engineering & Structural Dynamics*, vol. 44, no. 6, pp. 849–864, 2015.
- [5] A. Chotesuwan, H. Mutsuyoshi, and T. Maki, "Seismic behavior of bridges with pier and foundation strengthening: PsD tests and analytical study," *Earthquake Engineering & Structural Dynamics*, vol. 41, no. 2, pp. 279–294, 2012.
- [6] M. Moghaddasi, M. Cubrinovski, J. G. Chase, S. Pampanin, and A. Carr, "Probabilistic evaluation of soil-foundation-structure interaction effects on seismic structural response," *Earthquake Engineering & Structural Dynamics*, vol. 40, no. 2, pp. 135–154, 2011.
- [7] Y. Xie, Y. Huo, and J. Zhang, "Development and validation of p-y modeling approach for seismic response predictions of highway bridges," *Earthquake Engineering & Structural Dynamics*, vol. 46, no. 4, pp. 585–604, 2017.
- [8] C. Durucan and M. Dicleli, "AP/VP specific inelastic displacement ratio for seismic response estimation of structures," *Earthquake Engineering & Structural Dynamics*, vol. 44, no. 7, pp. 1075–1097, 2015.
- [9] T. Liu and Q. Zhang, "AP/VP specific equivalent viscous damping model for base-isolated buildings characterized by SDOF systems," *Engineering Structures*, vol. 111, pp. 36–47, 2016.
- [10] X. Wang, Z. Li, and A. Shafieezadeh, "Seismic response prediction and variable importance analysis of extended pile-shaft-supported bridges against lateral spreading: exploring optimized machine learning models," *Engineering Structures*, vol. 236, Article ID 112142, 2021.
- [11] Y. Li and J. P. Conte, "Effects of seismic isolation on the seismic response of a California high-speed rail prototype bridge with soil-structure and track-structure interactions," *Earthquake Engineering & Structural Dynamics*, vol. 45, no. 15, pp. 2415–2434, 2016.
- [12] P. Galvín, A. Romero, E. Moliner, D. P. Connolly, and M. D. Martínez-Rodrigo, "Fast simulation of railway bridge dynamics accounting for soil-structure interaction," *Bulletin of Earthquake Engineering*, pp. 1–19, 2021.
- [13] H. Bhure, G. Sidh, and A. Gharad, "Dynamic analysis of metro rail bridge subjected to moving loads considering soil-structure interaction," *International Journal of Advanced Structural Engineering*, vol. 10, no. 3, pp. 285–294, 2018.
- [14] H. M. Coyle and I. H. Sulaiman, "Skin friction for steel piles in sand," *Journal of the Soil Mechanics and Foundations Division*, vol. 93, no. 6, pp. 261–278, 1967.
- [15] V. N. Vijivergiya, "Load-movement characteristics of piles," in *Proceedings of the 4th Symp. of Waterway, Port, Coastal and Ocean Div*, vol. 2, pp. 269–284, New York, NY, USA, March 1977.
- [16] API, *Recommended Practice for Planning, Designing and Constructing Fixed Offshore Platforms—Working Stress Design*, American Petroleum Institute, Washington, DC, USA, 20th edition, 1993.
- [17] J. T. Chin and H. G. Poulos, "A "T-Z" approach for cyclic axial loading analysis of single piles," *Computers and Geotechnics*, vol. 12, no. 4, pp. 289–320, 1991.
- [18] H. G. Poulos, "Settlement of single piles in nonhomogeneous soil," *Journal of the Geotechnical Engineering Division*, vol. 105, no. 5, pp. 627–641, 1979.
- [19] FEMA, *Quantification of Building Seismic Performance Factors, Rep. FEMA P695*, Federal Emergency Management Agency, Washington, DC, USA, 2009.
- [20] C. P. Press, *Code for Seismic Design of Railway Engineering (GB 50111-2006)*, Chinese Standard, Beijing, China, 2009.

Research Article

MEMS Dynamic Characteristics Analysis of Electrostatic Microbeams for Building Structure Monitoring

Youping Gong, Hong Bo, Chuanping Zhou, Maofa Wang, and Rougang Zhou 

School of Mechanical Engineering, Hangzhou Dianzi University, Hangzhou 310018, China

Correspondence should be addressed to Rougang Zhou; zjlhzz@163.com

Received 3 October 2021; Revised 25 November 2021; Accepted 11 December 2021; Published 19 January 2022

Academic Editor: Lingkun Chen

Copyright © 2022 Youping Gong et al. This is an open access article distributed under the Creative Commons Attribution License, which permits unrestricted use, distribution, and reproduction in any medium, provided the original work is properly cited.

Building structure health monitoring is essential for modern buildings, sensors related to building structure health monitoring are often made with microelectrostatic cantilever beam (MECB), and the performance of this kind of devices is often affected by instability, which affects the measurement results and accuracy. Therefore, it is necessary to study the nonlinear dynamic characteristics of the MECB in the process of bending and pull-in. In this paper, based on the energy principle and fluid pressure film damping effect, the dynamic equation mathematical model of MECB is established and then the dynamic characteristics of the pull-in and lift-off voltage of the MECB and the harmonic motion characteristics under the bias voltage are obtained, which provides guidance for the design of the electrostatic driving sensor.

1. Introduction

Building structure health monitoring is essential for modern buildings. Due to the action of various external forces (i.e., loads), building structures will produce certain damage. Therefore, a method that can monitor the structural health for a long time and make safety early warning is needed [1–4]. Sensors related to building structure health monitoring technology have become a research hotspot. Electrostatic-driven multilayer cantilever beams are widely used in building structure monitoring sensors. Fatigue effect, material aging, accidental load, and other factors have great influence on the structure. In recent years, there are numerous examples of loss of life and properties caused by structural instability [5, 6]. This makes the building structure health monitoring become an urgent need. The research of building structure monitoring systems based on MEMS has become a cutting-edge topic in the field of civil engineering. As the basic structural devices of many MEMS devices, microelectrostatic cantilever beams (MECBs) are widely used in RF switches, low-light switches, and pressure sensors, as well as MEMS devices in building structure monitoring systems [7–10]. However, due to the inherent instability of electromechanical coupling, that is, the so-called pull-in phenomenon, the performance of these

devices is often affected by instability. In addition, due to the multicoupling and nonlinear characteristics of the MECB cantilever beam, the multiparameter simulation design method has the disadvantages of high cost, slow speed, and insufficient accuracy. Therefore, in the process of device-level design of building monitoring MEMS, it is increasingly important to find a high-precision, high-economic and fast optimization method for MECB.

At present, the most accurate method for solving the device-level dynamic characteristics of MEMS is to establish an effective partial differential equation (PDES) to describe the nonlinear dynamic characteristics of the system in mathematical form through the analysis of its working principle and coupled physical model and then solve it by finite element method (FEM), boundary element method (BEM), finite difference method (FDM), and other methods after selecting effective control parameters. To improve the accuracy of the calculation, the model needs to be divided into a very detailed grid to solve, the refinement of the grid will inevitably lead to the allocation of a large number of resources, which cannot meet the solution under multiparameters and multiexcitation, so the optimization efficiency of the parameter design space is very low, and it is even more difficult to deal with the MEMS devices of multidevices

[11–16]. In this paper, according to the principle of conservation of energy, the MECB model of the building monitoring MEMS is constructed. The model is solved in Simulink, and the dynamic characteristics of the MECB under pull-in and lift-off voltage and the harmonic motion characteristics under bias voltage are obtained. The research results of this paper will greatly improve the development and application of building monitoring MEMS system.

2. Construction of Dynamic Characteristic Model of MECB Based on Energy Method

As shown in Figure 1, the MEMS electrostatic microbeam's length is l , width is w , and thickness is h , and the x axis is established on the neutral axis of the beam, and the y axis is located at the left end of the beam. In this case, it is assumed that the material of the microbeam is homogeneous, Young's modulus is E , and Poisson's ratio is δ . The initial in-plane load of the beam is affected by N_{ox} or residual stress s .

Then, the relationship between stress and strain of the microbeam can be expressed by the following equation:

$$\sigma_x = \frac{E}{(1 - \delta^2)} \varepsilon_x + \frac{1}{wh} N_{ox}. \quad (1)$$

In formula (1), E is the equivalent modulus, and axial strain force of the beam can be expressed as the following equation:

$$\varepsilon_x = \frac{\partial \hat{u}}{\partial \hat{x}} - \frac{\partial^2 \hat{y}}{\partial \hat{x}^2} \hat{y} + \frac{1}{2} \left(\frac{\partial \hat{y}}{\partial \hat{x}} \right)^2. \quad (2)$$

The elastic deformation energy in the beam volume can be expressed as the following equation:

$$\begin{aligned} U_{st} = & \frac{1}{2} \iiint_V \varepsilon_x \sigma_x dV = \frac{EA}{2} \int_0^l \left(\frac{\partial \hat{u}}{\partial \hat{x}} \right)^2 d\hat{x} \\ & + \frac{EI}{2} \int_0^l \left(\frac{\partial^2 \hat{y}}{\partial \hat{x}^2} \right)^2 d\hat{x} + \frac{EA}{2} \int_0^l \left(\frac{\partial \hat{u}}{\partial \hat{x}} \right) \left(\frac{\partial^2 \hat{y}}{\partial \hat{x}^2} \right)^2 d\hat{x} \\ & + \frac{EA}{2} \int_0^l \sigma_0 \left(\frac{\partial \hat{u}}{\partial \hat{x}} \right) d\hat{x} + \frac{EA}{4} \int_0^l \sigma_0 \left(\frac{\partial \hat{y}}{\partial \hat{x}} \right)^2 d\hat{x}. \end{aligned} \quad (3)$$

In equation (3), $I = wh^3/12$, which is moment of inertia, ρ is the density of material, and the third term is the geometric nonlinear coupling term due to large deformation. The axial force on the neutral plane can be expressed as $\partial \hat{u} / \partial \hat{x} = 1/2l \int_0^l (\partial \hat{y} / \partial \hat{x})^2 d\hat{x}$. Equation (4) can be obtained by substituting it into equation (3):

$$U_{st} = \frac{EI}{2} \int_0^l \left(\frac{\partial^2 \hat{y}}{\partial \hat{x}^2} \right)^2 d\hat{x} + \frac{1}{2} N_{ox} \int_0^l \left(\frac{\partial^2 \hat{y}}{\partial \hat{x}^2} \right)^2 d\hat{x} + \frac{Ewh}{8l} \left[\left(\frac{\partial^2 \hat{y}}{\partial \hat{x}^2} \right)^2 d\hat{x} \right]^2. \quad (4)$$

2.1. MECB Energy Equation. The electrostatic common energy of the above system can be expressed as the following equation:

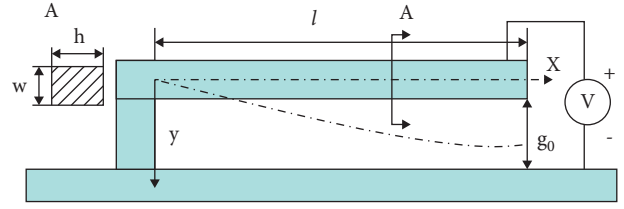


FIGURE 1: Structural diagram of microcantilever.

$$U_E = -\frac{\varepsilon w V^2}{2} \int_0^l \frac{1}{(g_0 - \hat{y})} d\hat{x}. \quad (5)$$

In equation (5), the formula of parallel plate capacitor is adopted. At this time, the edge effect of the electrostatic field is not considered. In some cases, the influence of edge effect needs to be considered. The correction formula is as follows:

$$U_E = -\frac{\varepsilon w V^2}{2} \int_0^l \frac{1}{(g_0 - \hat{y})} \left[1 + \frac{(g_0/l)^2}{3} \cdot \frac{1}{g_0^2} \left(\frac{\partial}{\partial x} (g_0 - \hat{y}) \right)^2 \right] d\hat{x}. \quad (6)$$

2.2. Deformation Equation of MECB. The deformation equation of the beam can be derived by using the Lagrangian equation as follows:

$$EI \frac{\partial^4 \hat{y}}{\partial \hat{x}^4} - \left[N_{ox} + \frac{Ewh}{2l} \int_0^l \left(\frac{\partial \hat{y}}{\partial \hat{x}} \right) d\hat{x} \right] \frac{\partial^2 \hat{y}}{\partial \hat{x}^2} = f_{elec}(\hat{x}, t) - wh\rho \frac{\partial^2 \hat{y}}{\partial \hat{t}^2}, \quad (7)$$

where $f_{elec}(x, t)$ is the expression of electrostatic load on the parallel plate beam as follows:

$$f_{elec}(x, t) = \frac{1}{2} \frac{\varepsilon w V^2}{(g_0 - \hat{y})}. \quad (8)$$

According to the energy principle of the system, the equation describing its dynamics can be obtained as the following equation:

$$\begin{aligned} EI \frac{\partial^4 \hat{y}}{\partial \hat{x}^4} - \left[N_{ox} + \frac{Ewh}{2l} \int_0^l \left(\frac{\partial \hat{y}}{\partial \hat{x}} \right) d\hat{x} \right] \frac{\partial^2 \hat{y}}{\partial \hat{x}^2} = & f_{elec}(\hat{x}, t) \\ & + f_{air}(\hat{x}, y, t) - wh\rho \frac{\partial^2 \hat{y}}{\partial \hat{t}^2}. \end{aligned} \quad (9)$$

The dimensionless displacement of the beam can be expressed by the product expansion of the spatial and time-dependent modal coordinates and the global function $\{\phi_k(x)\}$ as the following equation:

$$y(x, t) = \sum_{i=1}^{Mv} q_i(t) \phi_i(x). \quad (10)$$

In equation (10), basis function $\{\phi_i(x)\}$ can be expressed as the set of functions satisfying any boundary condition. Here, Mv is the number of basis functions. Through the transformation of the above formula, the displacement of the beam in the original physical coordinate system can be

transformed into the expression in the generalized state $q_i(t)$. The number of modes Mv is usually much smaller than the number of dimensions obtained by the common grid method, so the reduced order model can be obtained, and the accuracy can be controlled by selecting the number of modes. Through this method, the calculation consumption of the model can be reduced and the calculation speed can be improved. The dimensionless displacement y of the beam can be expressed in the product expansion form of spatial and time-dependent modal coordinates and global function.

Substituting formula (9) into (10) and making the residual as zero, then the following expression can be obtained:

$$\begin{aligned} & \sum_{i=1}^{Mv} q_i(t) \int_0^1 \phi_j \phi_i dx + \sum_{i=1}^{Mv} q_i(t) \int_0^1 \phi_j'' \phi_i'' dx + N_0 \sum_{i=1}^{Mv} q_i(t) \\ & \cdot \int_0^1 \phi_j' \phi_i' dx + \alpha_1 \sum_{m,n,i=1}^{Mv} q_m(t) q_n(t) q_i(t) \\ & \cdot \int_0^l \phi_m' \phi_n' dx \int_0^1 \phi_m' \phi_n' dx = \alpha_2 V^2 \\ & \cdot \int_0^1 \frac{\phi_j}{\left(1 - \sum_{i=1}^{Mv} q_i(t) \phi_i\right)} dx, (j = 1, 2, \dots, Mv). \end{aligned} \quad (11)$$

In equation (11), the third term is related to the axial tension, and the electrostatic force load term is on the right of the formula. It can be obtained by transforming it into matrix form as follows:

$$M\ddot{q} + (K + N_0 S)q + \alpha_1 q^T S q + f = 0. \quad (12)$$

In equation (12), $M = [M_{ij}]$ is mass matrix, $K = [K_{ij}]$ is bending stiffness matrix, and $N_0 S = N_0 [S_{ij}]$ is the stiffness matrix resulting from the initial axial load. Now, consider the solution result of the model in the case of single degree of freedom and make $Mv = 1$; here, $y(x, t) = g(t) \phi_1(x)$; from (11), we can obtain the following equation:

$$\begin{aligned} & \ddot{g} \int_0^1 \phi_1^2 dx + g \left(\int_0^1 (\phi_1'')^2 dx + N_0 \int_0^1 (\phi_1')^2 dx \right) \\ & + g^3 \alpha_1 \left(\int_0^1 (\phi_1')^2 dx \right)^2 \\ & = V^2 \alpha_2 \int_0^1 \left(\frac{\phi_1}{(1 - g \phi_1)} \right) dx. \end{aligned} \quad (13)$$

The simulation model of the MECB is established according to formula (13), and it can be dynamically simulated and solved, as shown in Figure 2.

2.3. Study on the Dynamic Process of MECB Pull-In and Lift-Off. The pull-in and lift-off process of the MECB is studied. The detailed parameters are listed in Table 1.

By adding a triangular wave voltage described in the simulation model established in the above process and taking

the damping coefficient as $B = 2$, the relationship between the end point of the micro cantilever and the voltage can be obtained, as shown in Figure 3. With the linear increase in the input voltage, the end displacement of the microcantilever does increase nonlinearly. When the pull-in voltage is exceeded, the beam end point suddenly accelerates and pulls down and pulls in to the substrate, resulting in the pull-in voltage. With the decrease in the voltage, when it falls below the pull-in voltage, it will not be separated immediately, because the electrode spacing after the pull-in is very small and the electrostatic load is very large, so it will not separate immediately even if it drops below the pull-in voltage. It can be observed from the figure that when the voltage drops to about 3.2 V, the deformation recovery force of the beam is greater than the electrostatic attraction, and the lift-off phenomenon occurs at this time. It can be found that the lift-off voltage is much smaller than the pull-in voltage and has a lag phenomenon, which is of great significance for the research of sensors and actuators working with pull-in voltage.

The pull-in the curve can be obtained from the single-mode model established by Simulink, as shown in Figure 4; it can be observed that the pull-in voltage is about 8.75 v.

The working mode of microresonance is to apply DC voltage and alternating driving voltage to the upper plate of the fixed microbeam. The DC voltage can make it reach an equilibrium position, and the alternating current can make it simple harmonic vibration up and down at this equilibrium position. In this process, the equilibrium state is curved, and there is a gap between the modal vibration mode and the straight beam. At this time, using the modal vibration mode of the straight beam as the basis function will have the possibility of error, resulting in the inaccuracy of the calculated dynamic characteristics [17]. Therefore, to verify that the reduced order model has sufficient accuracy to simulate and calculate the dynamic characteristics of MEMS microbeam under resonant voltage, at this time, the dynamic characteristics of the device model based on the above data are simulated and calculated when the input voltage signal of the device is v . The steady-state response diagram of the end displacement of the beam calculated by the reduced order model is shown in Figure 5. To verify the correctness of the above model verification, the same simulation is done in ConventorWare, and the result is shown in Figure 6.

From Figure 5, it can be seen that the equilibrium center point of the results calculated by the simulation model is $-0.647 \mu\text{m}$, the upper limit change displacement after stabilization is $-0.748 \mu\text{m}$, and the lower limit displacement is $-0.546 \mu\text{m}$, while the analysis results in ConventorWare show that the equilibrium point position is stable at $-0.643 \mu\text{m}$, the upper limit displacement after stabilization is $-0.748 \mu\text{m}$, and the lower limit is $-0.565 \mu\text{m}$, as shown in Figure 6. The results show that the two analysis results are consistent which verifies the effectiveness of our proposed model and can calculate the dynamic characteristics of the beam under bias voltage. We established the physical simulation model of the electrostatic microbeam in ConventorWare software. The specific parameters are shown in the simulation model. Voltage is applied continuously to it to obtain its lift-off voltage diagram. The results are shown in Figure 7.

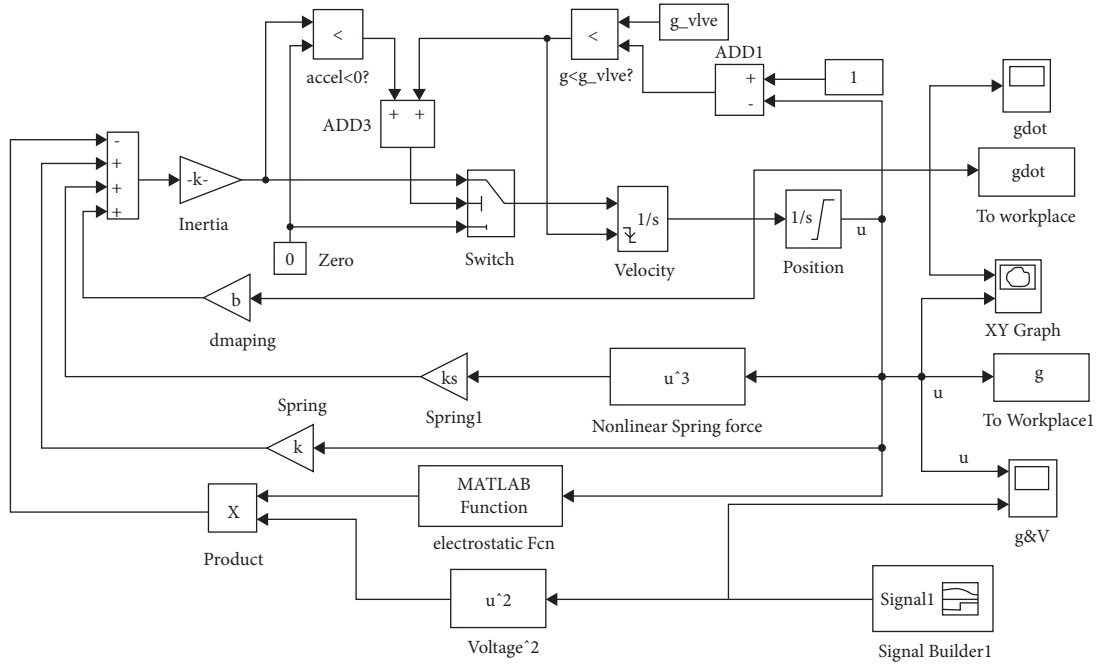


FIGURE 2: The simulation model of the MECB device.

TABLE 1: Multilayer microbeam parameters.

Type	Symbol	Data
Length	L	600 μm
Width	w	40 μm
Thickness	H	2.4 μm
Young modulus	E	150 GPa
Air viscosity	U	$1.82 \cdot 10^{-5} \text{ kg}/(\text{m} \cdot \text{s})$
Residual stress	S	-3.7 MPa
Density	$V(t) = 8 + 0.3 \sin(2\pi f)V$	2330 kg/m^3
Air pressure	P_0	$1.013 \cdot 10^5 \text{ pa}$

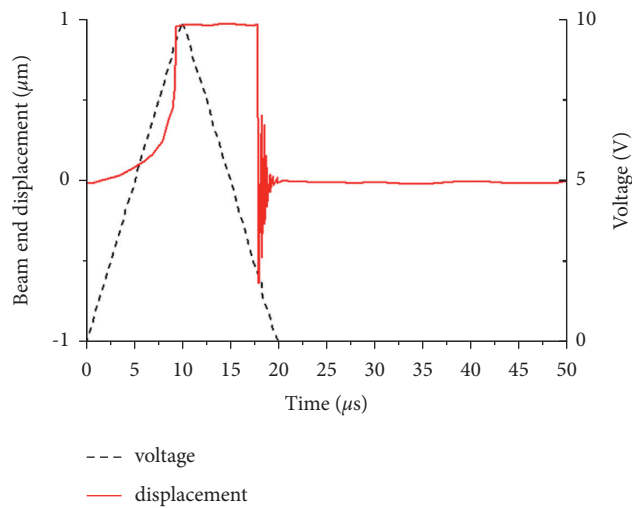


FIGURE 3: Variation diagram of voltage and displacement from pull-in to lift-off.

From Figure 7, the lift-off voltage is 3.1875 v–3.375 v, which is consistent with the result of 3.2 V obtained in the price reduction process of the above model. We can also learn that

before the pull-in phenomenon, the deformation of MEMS microcantilever is relatively small and the deformation force is relatively small. At this time, it can be observed in Figure 7 that

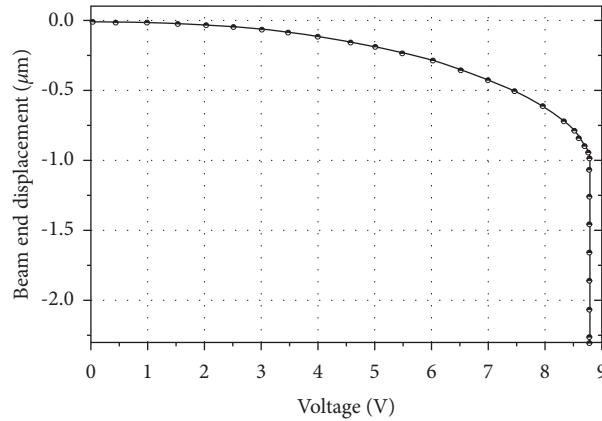


FIGURE 4: Pull-in process.

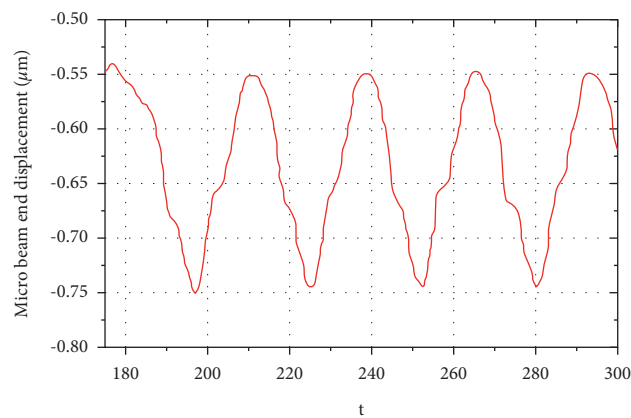


FIGURE 5: Steady-state response diagram of resonant motion under the action of bias voltage and superimposed sinusoidal voltage.

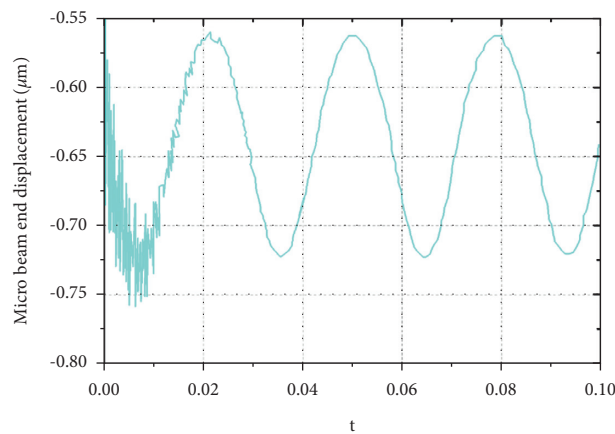


FIGURE 6: Steady-state response curve under ConvectorWare analysis.

the linear spring restoring force is much larger than the nonlinear restoring force, which plays a leading role. With the increase in voltage, the nonlinear spring restoring force increases sharply; at this time, the nonlinear spring restoring force and linear restoring force act on the microcantilever at the same time. At this time, if the research on the nonlinear spring restoring force is ignored, it will have a great impact on the lift-off voltage. It is verified again that the microcantilever has very

strong nonlinear characteristics under the coupling field. Therefore, the large deformation geometric nonlinearity must be considered in the research of pull-in process.

2.4. Study on the Instability of MECB. The quasi-static pull-in and lift-off characteristic analysis of the MECB cannot accurately express the stability of the microcantilever at the equilibrium position. Under the working conditions, the

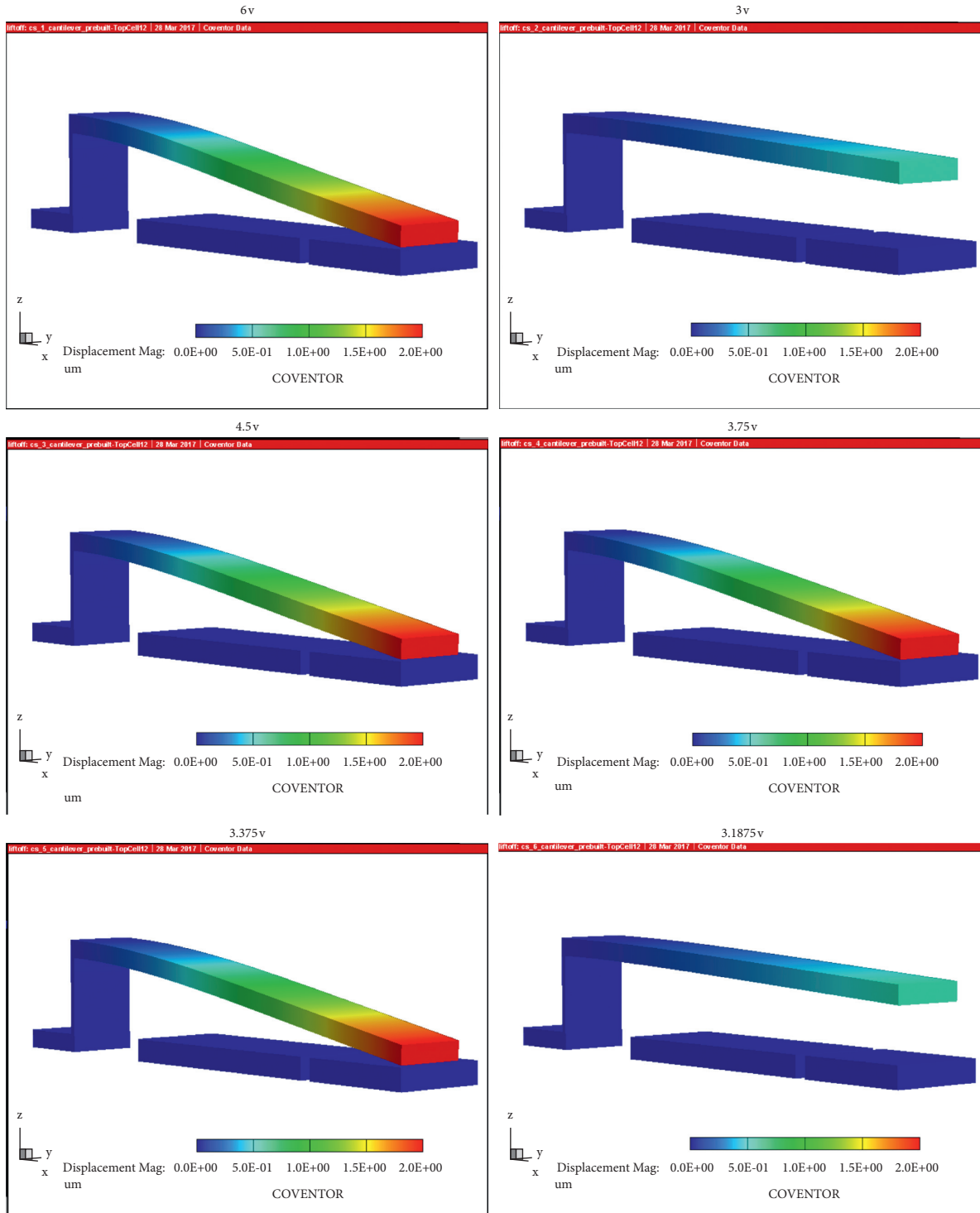


FIGURE 7: Iterative solution of lift-off voltage in CoventorWare: (a) 6 v; (b) 3 v; (c) 4.5 v; (d) 3.75 v; (e) 3.375 v; (f) 3.1875 v.

instability of the electrostatic microbeam will be caused by the action of step voltage and inertial force in advance. The stable position of the microbeam can be obtained by solving the changes of the dynamic characteristics of the microbeam under different step voltages in the initial state [18, 19]. Figure 8(a) shows the change history of microbeam end displacement with time under different step voltages without damping, and Figure 8(b) is its corresponding phase plan. It

can be observed from the figure that there is an overshoot phenomenon in the microbeam under the step voltage; that is, the pull-in phenomenon also occurs when the pull-in voltage calculated by the steady state has not been reached. The pull-in voltage at this time is called the dynamic pull-in voltage. It can be observed that the calculated voltage is about 8.1 v, which is only 91.3% of the static voltage at this time. When it is lower than the dynamic pull-in voltage,

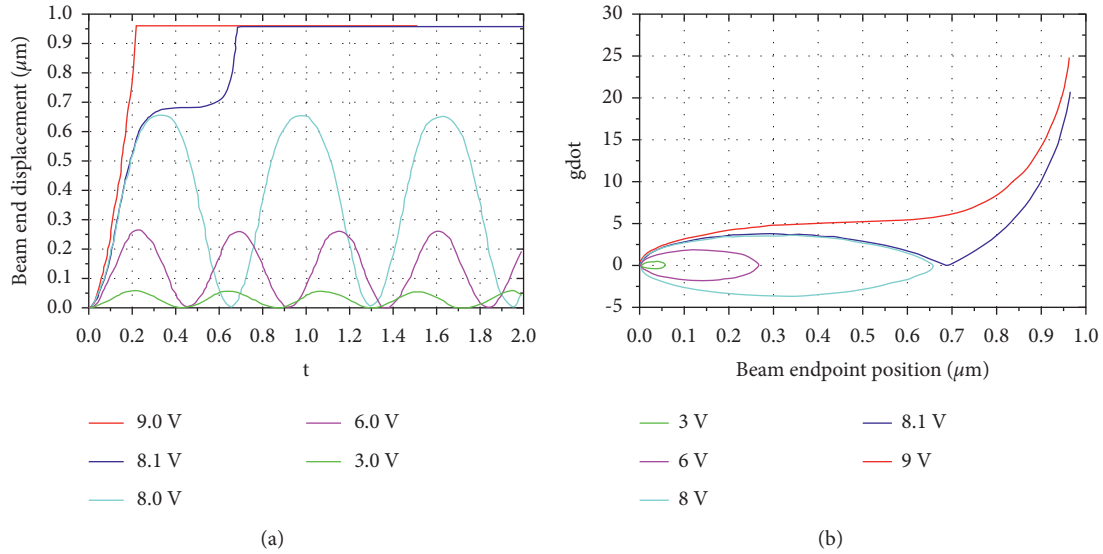


FIGURE 8: Different step voltages without damping: (a) time history diagram; (b) phase plan.

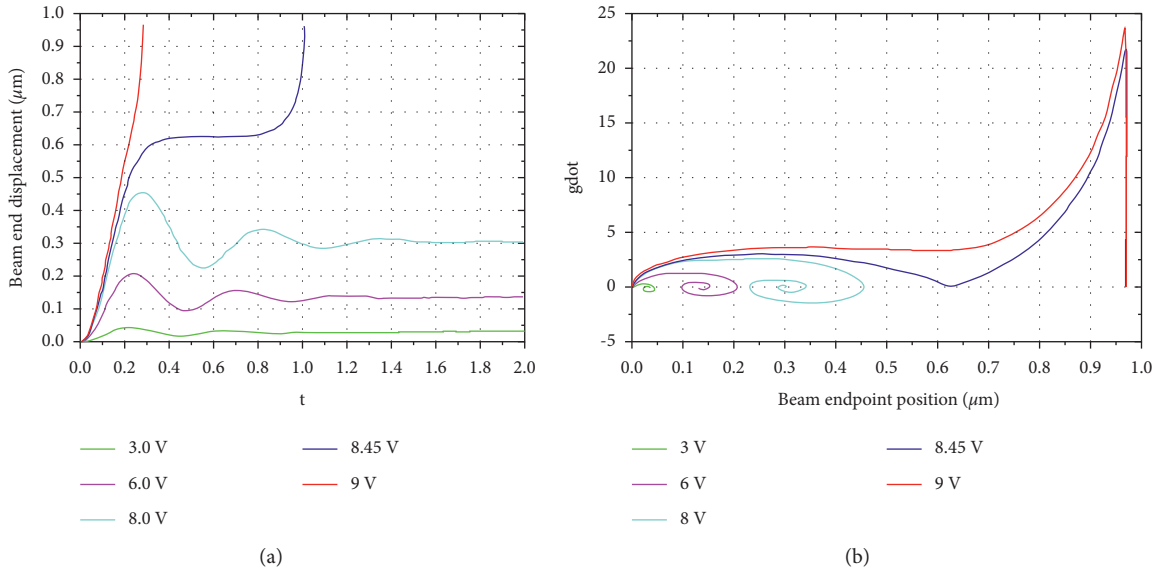


FIGURE 9: Different step voltages with damping: (a) time history diagram; (b) phase plan.

because it is set to be undamped at this time, the microbeam makes a fixed simple harmonic vibration at a certain frequency at the equilibrium position. It can be observed in the figure that as the voltage increases, the amplitude increases, but its vibration frequency decreases. When the input voltage is greater than the dynamic pull-in voltage, there is a bifurcation phenomenon in the phase plan, which indicates a pull-in phenomenon.

Figures 9(a) and 9(b) show the displacement diagram and phase plan of the end point of the microbeam with different step voltages under the condition of damping. It can be observed from the figure that V_{DPI} is about 8.45 v with damping, which is different from that without damping but lower than the static pull-in voltage. It can be seen that the damping will also affect the dynamic pull-in voltage. When it is lower than the microbeam V_{DPI} at an equilibrium

position, the attenuation motion is made. When it is higher than the microbeam V_{DPI} , the phase plan bifurcation occurs. At this time, the microbeam is pulled down quickly. When the voltage is close to the critical point, the small voltage change will affect the response of MEMS microbeam. Therefore, the research on the pull-in voltage of MEMS is of great significance, and the dynamic pull-in voltage stability of microbeam has a certain relationship with damping, which should be further studied.

3. Conclusion

In this paper, a method for calculating the MECB model is proposed. The main parameters of the beam model are equivalent to those of the single-layer cantilever beam, and then the dynamic model of the electrostatic microbeam was

constructed. Aiming at the characteristics of multifield coupling and strong nonlinearity in the process of solving microbeam, the solution method is proposed to express the solution system as a set of global orthogonal spatial basis functions with finite number, so that the simulation process of the dynamic model of microbeam structure can be realized with certain accuracy, fast solution.

Data Availability

The data used to support the findings of this study are included within the article.

Conflicts of Interest

The authors declare that they have no conflicts of interest.

Acknowledgments

The work was financially supported by the National Natural Science Foundation of China (51805475, 51475129, 51275141, and 51305113), Key Discipline of the Ocean Technic Equipment's Technology, Nature Science Foundation of Zhejiang Provinces Technology (51475129), and 3D Assembly of Complex Biological Structure (LY14E050026).

References

- [1] A. Norris, M. Saafi, and P. Romine, "Temperature and moisture monitoring in concrete structures using embedded nanotechnology/microelectromechanical systems (MEMS) sensors," *Construction and Building Materials*, vol. 22, no. 2, pp. 111–120, 2008.
- [2] K. Hong-Jin, "System identification of a building structure using wireless MEMS system," *Transactions of the Korean Society for Noise and Vibration Engineering*, vol. 18, no. 4, pp. 458–464, 2008.
- [3] P. Ragam and N. Devidas Sahebraoji, "Application of MEMS-based accelerometer wireless sensor systems for monitoring of blast-induced ground vibration and structural health: a review," *IET Wireless Sensor Systems*, vol. 9, no. 3, pp. 103–109, 2019.
- [4] Č. Kristýna, V. Lukáš, V. Jan, D. Milan, and Š. Ladislav, "Environmental testing of a FBG sensor system for structural health monitoring of building and transport structures," *Procedia Structural Integrity*, vol. 17, pp. 726–733, 2019.
- [5] G. J. Yun, S.-G. Lee, J. Carletta, and T. Nagayama, "Decentralized damage identification using wavelet signal analysis embedded on wireless smart sensors," *Engineering Structures*, vol. 33, no. 7, pp. 2162–2172, 2011.
- [6] T. Torfs, T. Sterken, S. Brebels et al., "Low power wireless sensor network for building monitoring," *IEEE Sensors Journal*, vol. 13, no. 3, pp. 909–915, 2013.
- [7] M. Moghimi Zand and M. T. Ahmadian, "Application of homotopy analysis method in studying dynamic pull-in instability of microsystems," *Mechanics Research Communications*, vol. 36, no. 7, pp. 851–858, 2009.
- [8] G. De Pasquale and A. Somà, "Dynamic identification of electrostatically actuated MEMS in the frequency domain," *Mechanical Systems and Signal Processing*, vol. 24, no. 6, pp. 1621–1633, 2010.
- [9] B. Krijnen and D. M. Brouwer, "Flexures for large stroke electrostatic actuation in MEMS," *Journal of Micromechanics and Microengineering*, vol. 24, p. 1, Article ID 015006, 2013.
- [10] G. C. Brown and R. J. Pryputniewicz, "Experimental and computational determination of dynamic characteristics of microbeam sensors," *Proceedings of SPIE - The International Society for Optical Engineering*, vol. 2545, pp. 108–119, 1995.
- [11] N. Dumas, C. Trigona, P. Pons, L. Latorre, and P. Nouet, "Design of smart drivers for electrostatic MEMS switches," *Sensors and Actuators A: Physical*, vol. 167, no. 2, pp. 422–432, 2011.
- [12] R. Lewandowski and P. Wielentejczyk, "Analysis of dynamic characteristics of viscoelastic frame structures," *Archive of Applied Mechanics*, vol. 90, no. 1, pp. 147–171, 2020.
- [13] L. Zhang, X. Zhang, J. Song, and H. Zheng, "Thermo-induced curvature and interlayer shear stress analysis of MEMS double-layer structure," *Continuum Mechanics and Thermo-dynamics*, vol. 32, no. 4, pp. 1127–1139, 2020.
- [14] Y. Kessler, A. Liberzon, and S. Krylov, "Flow velocity gradient sensing using a single curved bistable microbeam," *Journal of Microelectromechanical Systems*, vol. 99, pp. 1–6, 2020.
- [15] L. Ruzziconi, N. Jaber, L. Kosuru, M. L. Bellaredj, and M. I. Younis, "Internal resonance in the higher-order modes of a MEMS beam: experiments and global analysis," *Nonlinear Dynamics*, vol. 103, no. 3, pp. 2197–2226, 2021.
- [16] M. Mousavi, M. M. Zand, and S. Siahpour, "Effect of added mass distribution on the dynamic PI and frequency shifting in MEMS and NEMS biosensors," *Microsystem Technologies*, vol. 27, no. 5, pp. 1–10, 2020.
- [17] M. Rezaee and N. Sharafkhani, "Nonlinear dynamic analysis of an electrostatically actuated cylindrical micro-beam subjected to cross fluid flow," *International Journal of Applied Mechanics*, vol. 11, no. 6, pp. 745–755, 2019.
- [18] D. M. Lancaster, C. H. Allen, K. Jersey, and T. Lancaster, "Electrostatic guiding of the methylidyne radical at cryogenic temperatures," *The European Physical Journal D*, vol. 74, no. 6, 2020.
- [19] R. K. Godara, A. K. Sharma, N. Joshi, and M. Joglekar, "A novel capacitive mass sensor using an open-loop controlled microcantilever," *Microsystem Technologies*, vol. 26, no. 4, 2020.

Research Article

Wave Mode Control of Cantilever Slab Structure of T-Beam Bridge with Large Aspect Ratio

Tingting Liu , Chuanping Zhou , Zhigang Yan, and Guojin Chen

School of Mechanical Engineering, Hangzhou Dianzi University, Hangzhou 310018, China

Correspondence should be addressed to Chuanping Zhou; zhoucp@hdu.edu.cn

Received 15 November 2021; Accepted 16 December 2021; Published 30 December 2021

Academic Editor: Nan Zhang

Copyright © 2021 Tingting Liu et al. This is an open access article distributed under the Creative Commons Attribution License, which permits unrestricted use, distribution, and reproduction in any medium, provided the original work is properly cited.

The cantilever plate structure in a T-beam bridge with a large aspect ratio will cause vibration under the influence of environmental disturbance and self-stress, resulting in fatigue damage of the plate structure. Wave control based on elastic wave theory is an effective method to suppress the vibration of the cantilever plate structure in a beam bridge. Based on the classical thin plate theory and the wave control method, the active vibration control of the T-shaped cantilever plate with a large aspect ratio in the beam bridge is studied in this paper. The wave mode control strategy of structural vibration is analyzed and studied, the controller is designed, the vibration mode function of the cantilever plate is established, and the control force/sensor feedback wave control is implemented for the structure. The dynamic response of the cantilever plate before and after applying wave control force is analyzed through numerical examples. The results show that the response of the structure is intense before control, but after wave control, the structure increases damping, absorbs the energy carried by the elastic wave in the structure, weakens the sharp response, and changes the natural frequency of the structure to a certain extent.

1. Introduction

The bridge structure in working condition will bear its static load and dynamic load caused by peripheral vibration. There are a large number of T-cantilever extended plate structures in beam bridge structures, mostly T-cantilever plate structures with a large aspect ratio. These structures carry their static load and the static load and dynamic load of surrounding vehicles in the beam bridge. At the same time, the environmental disturbance and dynamic rotation of the beam bridge structure will also cause structural vibration [1, 2]. The abovementioned will cause the vibration of the bridge structure. If effective vibration suppression measures are not taken, the vibration will decay very slowly, which will not only affect the position of the beam bridge structure, but also cause the vibration of the plate structure, cause fatigue damage, and have a serious impact on the safety and service life of the beam bridge [3].

The traditional passive control methods, such as adding damping, often only increase the additional weight of the structure and reduce the service efficiency of the plate

structure and cannot get satisfactory results [4]. Therefore, wave control based on elastic wave theory to suppress the vibration of the cantilever plate structure in the beam bridge is a new method to solve this problem.

At present, in the research of wave control, the research object is mostly simplified as a flexible beam, and some literature are simplified as plate structure to implement the bending wave control [5, 6]. The wave control method can be used to control the propagation of waves in one-dimensional structures, such as bending waves in beams, and axial waves in rods.

Halkyard studied the feedback adaptive control of bending vibration of beam structure by the wave control method [7]. EL-Khatib employs a tuned vibration absorber to investigate the bending wave suppression in beams [8]. Krushynska studied the propagation characteristics of curved edge waves in semi-infinite isotropic elastic plates and found that the velocity of edge waves is essentially independent of Poisson's ratio [9]. Jones, IS used the same method to analyze and experiment with the active control of semi-infinite simply supported rib [10]. Kaplunov studied

the propagation of a three-dimensional edge wave along the edge of a semi-infinite elastic plate under mixed boundary conditions and found that the cut-off frequency of the edge wave is consistent with the natural frequency of the semi-infinite strip [11]. In this paper, based on the research of the abovementioned documents, a large number of cantilever plate structures existing in the girder bridge structure are controlled by the sliding film variable structure control method which is different from the conventional control method.

The vibration of the structure can be regarded as the superposition of the waves propagating in the structure, which are reflected and transmitted at the discontinuity of the structure [12, 13]. By controlling the transmitted or absorbed wave energy from one side to the other side of the structure, the structural vibration can be suppressed.

Based on the classical thin plate theory and the wave control method, the active vibration control of T-cantilever plate with a large aspect ratio in beam bridge is studied in this paper. The wave mode control strategy of structural vibration is analyzed and studied. The controller is designed to control the force/sensor feedback wave of the structure.

2. Vibration Equation and Solution of Thin Plate

According to the classical thin plate theory, the expression of displacement component u v in the rectangular coordinate system is [14, 15]

$$\begin{aligned} u(x, y, z, t) &= -z \frac{\partial w(x, y, t)}{\partial x}, \\ v(x, y, z, t) &= -z \frac{\partial w(x, y, t)}{\partial y}, \end{aligned} \quad (1)$$

where $w(x, y, t)$ represents the transverse displacement of the plate, $u(x, y, z, t)$ and $v(x, y, z, t)$ represent the displacement in x and y directions in the plane, respectively, which is linearly distributed along the thickness direction.

The bending moment and shear force in the plate can be described as follows:

$$M_x = -D \left(\frac{\partial^2 w}{\partial x^2} + \nu \frac{\partial^2 w}{\partial y^2} \right), \quad (2a)$$

$$M_y = -D \left(\frac{\partial^2 w}{\partial y^2} + \nu \frac{\partial^2 w}{\partial x^2} \right),$$

$$\begin{aligned} M_{xy} &= M_{yx} \\ &= -D(1 - \nu) \frac{\partial^2 w}{\partial x \partial y}, \end{aligned} \quad (2b)$$

$$\begin{aligned} Q_x &= -D \frac{\partial}{\partial x} \nabla^2 w, \\ Q_y &= -D \frac{\partial}{\partial y} \nabla^2 w, \end{aligned} \quad (2c)$$

where D is the bending stiffness of the plate, $D = Eh^3/12(1 - \nu^2)$, $\nabla^2 = \partial^2/\partial x^2 + \partial^2/\partial y^2$ is the Laplace operator, and ν is the Poisson's ratio.

The cantilever plate structure studied in this paper is shown in Figure 1. The equilibrium equation of plate microelement is

$$\frac{\partial M_x}{\partial x} + \frac{\partial M_{yx}}{\partial y} - Q_x = 0, \quad (3a)$$

$$\frac{\partial M_{xy}}{\partial x} + \frac{\partial M_y}{\partial y} - Q_y = 0, \quad (3b)$$

$$\frac{\partial Q_x}{\partial x} + \frac{\partial Q_y}{\partial y} + \bar{q} - \rho h \frac{\partial^2 w}{\partial t^2} = 0, \quad (3c)$$

where ρ is the mass of the plate per unit area and \bar{q} is the external load on the plate per unit area.

Substituting equation (2a) in (3a), the vibration differential equation of the thin plate is

$$\frac{\partial^4 w}{\partial x^4} + 2 \frac{\partial^4 w}{\partial x^2 \partial y^2} + \frac{\partial^4 w}{\partial y^4} + \frac{\rho h}{D} \frac{\partial^2 w}{\partial t^2} = \frac{\bar{q}(x, y, t)}{D}, \quad (4a)$$

$$\nabla^2 \nabla^2 w + \frac{\rho h}{D} \frac{\partial^2 w}{\partial t^2} = \frac{\bar{q}(x, y, t)}{D}. \quad (4b)$$

The displacement expression of modal expansion form of thin plate is

$$w(x, y, t) = \sum_{i=1}^m \sum_{j=1}^n W_{i,j}(x, y) q_{i,j}(t), \quad (5)$$

where $W_{i,j}(x, y)$ is the vector modal function, $q_{i,j}(t)$ is the modal coordinate, and m, n are the modal truncation numbers.

Substitute equation (5) in (4a) to obtain

$$\sum_{i=1}^m \sum_{j=1}^n \nabla^4 W_{i,j} q_{i,j} + \sum_{i=1}^m \sum_{j=1}^n \frac{\rho h}{D} W_{i,j} \frac{\partial^2 q_{i,j}}{\partial t^2} = \frac{\bar{q}(x, y, t)}{D}, \quad (6)$$

where $W_{i,j}(x, y)$ shall satisfy the following equation:

$$\nabla^4 W_{i,j} - \omega_{i,j}^2 \frac{\rho h}{D} W_{i,j} = 0, \quad (7)$$

where $\omega_{i,j}$ is the natural frequency of the plate.

Substitute equation (7) in (6) to obtain

$$\sum_{i=1}^m \sum_{j=1}^n (\rho h) W_{i,j} \frac{\partial^2 q_{i,j}}{\partial t^2} + \sum_{i=1}^m \sum_{j=1}^n (\rho h) \omega_{i,j}^2 W_{i,j} q_{i,j} = \bar{q}. \quad (8)$$

Multiply both ends of equation (8) by the vibration mode function $W_{r,s}(x, y)$, it is integrated on the area domain Ω of the thin plate, and the orthogonality of the structural vibration mode shape function is used.

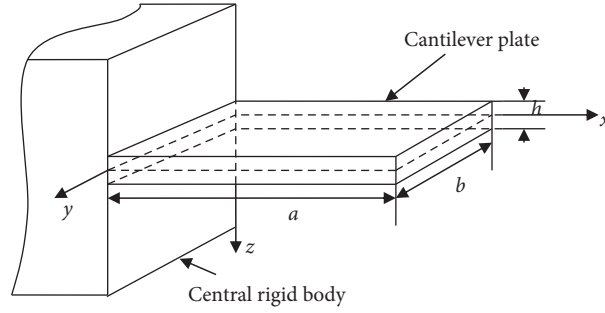


FIGURE 1: Model of the cantilever plate.

$$\frac{1}{m_{i,j}} \iint_{\Omega} W_{i,j}(\rho h) W_{r,s} dx dy = \begin{cases} 0 & i \neq r, j \neq s \quad i, r = 1, 2, \dots, m \quad j, s = 1, 2, \dots, n, \\ 1 & i = r, j = s \quad i, r = 1, 2, \dots, m \quad j, s = 1, 2, \dots, n. \end{cases} \quad (9)$$

The result is as follows:

$$\iint_{\Omega} \sum_{i=1}^m \sum_{j=1}^n W_{i,j}(\rho h) W_{r,s} \frac{\partial^2 q_{i,j}}{\partial t^2} dx dy + \iint_{\Omega} \sum_{i=1}^m \sum_{j=1}^n \omega_{i,j}^2 W_{i,j}(\rho h) W_{r,s} q_{i,j} dx dy = \iint_{\Omega} W_{r,s} \bar{q}(x, y, t) dx dy. \quad (10)$$

Therefore, there are

$$\frac{\partial^2 q_{i,j}(t)}{\partial t^2} + \omega_{i,j}^2 q_{i,j}(t) = p_{i,j}(t), \quad i = 1, 2, \dots, m; \quad j = 1, 2, \dots, n. \quad (11)$$

Among them, the external disturbing force $p_{i,j}(t) = 1/m_{i,j} \iint_{\Omega} \bar{q}(x, y, t) W_{i,j}(x) dx dy$, equation (11) is the modal coordinate equation of the plate.

The lateral displacement of the points on the plate is expanded into the form of modal superposition. For cantilever rectangular plates, the modal function can usually be decomposed into the product of two beam functions [16], that is, the product of cantilever beam in x -direction and free beam at both ends in y -direction. Therefore, the deflection of the plate can be expressed as

$$w(x, y, t) = \sum_{i=1}^m \sum_{j=1}^n W_i(x) W_j(y) q_{i,j}(t), \quad (12)$$

where $W_i(x)$ is the mode function of the transverse displacement of the cantilever beam in the x -direction of the plate and $W_j(y)$ is the modal function of the free beam in the y -direction of the plate.

2.1. Vibration Mode Function of Cantilever Plate in x -Direction. Based on Euler Bernoulli beam theory, the i -order modal function of transverse displacement in x -direction can be expressed as

$$W_i(x) = D_1 e^{-ik_{0i}x} + D_2 e^{ik_{0i}x} + D_3 e^{-k_{0i}x} + D_4 e^{k_{0i}x}. \quad (13)$$

Applying Euler formula,

$$\left. \begin{aligned} e^{\pm ikx} &= \cos(kx) \pm i \sin(kx) \\ e^{\pm kx} &= \cosh(kx) \pm \sinh(kx) \end{aligned} \right\}. \quad (14)$$

By substituting (14) in (13), another expression of the vibration mode function can be obtained.

$$\begin{aligned} W_i(x) &= A_1 \cos(k_{0i}x) + A_2 \sin(k_{0i}x) \\ &\quad + A_3 \cosh(k_{0i}x) + A_4 \sinh(k_{0i}x). \end{aligned} \quad (15)$$

Considering the boundary conditions at both ends of the cantilever Euler Bernoulli beam, it can be obtained that

$$\cos(k_{0i}a) \cdot \cosh(k_{0i}a) + 1 = 0. \quad (16)$$

Equation (16) is the dispersion equation of cantilever vibration [17].

Combined with the frequency equation, equation (15) can be expressed as

$$\begin{aligned} W_i(x) &= \cos h(k_{0i}x) - \cos(k_{0i}x) \\ &\quad + a_i [\sin h(k_{0i}x) - \sin(k_{0i}x)], \end{aligned} \quad (17)$$

where a is the length in the x -direction, $k_{0i} = (\rho h \omega^2 / D)^{1/4}$ is the elastic wave number in the classical plate; $a_i = -\cosh(k_{0i}a) + \cos(k_{0i}a) / \sinh(k_{0i}a) + \sin(k_{0i}a)$, this coefficient is determined according to the boundary conditions at both ends of the cantilever Euler Bernoulli beam. Equation (17) is the vibration mode function of the cantilever plate in the x -direction.

2.2. *Vibration Mode Function of Cantilever Plate in y-Direction.* In the same way as the derivation of the mode shape function in the x -direction, the j -order mode shape function of the transverse displacement in the y -direction of the cantilever plate is

$$W_j(y) = C_1 e^{-ik_{0j}y} + C_2 e^{ik_{0j}y} + C_3 e^{-k_{0j}y} + C_4 e^{k_{0j}y}. \quad (18)$$

Using Euler formula (14), change x into y and substitute it in (18)

$$W_j(y) = B_1 \cos(k_{0j}y) + B_2 \sin(k_{0j}y) + B_3 \cosh(k_{0j}y) + B_4 \sinh(k_{0j}y) \quad (19)$$

Considering the boundary conditions at both ends of the Euler Bernoulli beam with free ends, it can be obtained that

$$\cos(k_{0j}b) \cdot \cosh(k_{0j}b) - 1 = 0. \quad (20)$$

Equation (20) is the dispersion equation of the vibration of free beams at both ends [18, 19].

Combined with the frequency equation, equation (20) can be expressed as

$$W_j(y) = \cosh(k_{0j}y) + \cos(k_{0j}y) + b_j [\sinh(k_{0j}y) + \sin(k_{0j}y)], \quad (21)$$

where b is the length in the y -direction, $k_{0j} = (\rho h \omega^2 / D)^{1/4}$ is the elastic wave number in the classical plate; $b_j = -\cosh(k_{0j}b) - \cos(k_{0j}b) / \sinh(k_{0j}b) - \sin(k_{0j}b)$, this coefficient is determined according to the boundary conditions of Euler Bernoulli beams with free ends.

It should be emphasized here that when $j \geq 3$, the mode function of the Euler Bernoulli beam with free ends is equation (21), which is determined by the dispersion equation of vibration of free beams at both ends. And, W_j ($j = 1, 2$) is in the following form:

$$W_1 = 1, \quad (22)$$

$$W_2 = 1 - \frac{2y}{b}.$$

It can be seen that equations (21) and (22) are vibration mode functions in the y -direction of the cantilever plate.

The maximum kinetic energy of the plate during vibration is [20]

$$T_{\max} = \frac{1}{2} \iint_{\Omega} \rho h W^2(x, y) dx dy. \quad (23)$$

The maximum potential energy of the plate during vibration is

$$U_{\max} = \frac{1}{2} \iint_{\Omega} D \left\{ \left(\frac{\partial^2 W}{\partial x^2} + \frac{\partial^2 W}{\partial y^2} \right)^2 + 2(1 - \nu) \left[\left(\frac{\partial^2 W}{\partial x \partial x} \right)^2 - \frac{\partial^2 W}{\partial x^2} \frac{\partial^2 W}{\partial y^2} \right] \right\} dx dy. \quad (24)$$

According to the Rayleigh-Ritz principle, the natural frequency of the plate is

$$\omega^2 = \frac{U_{\max}}{T_{\max}}. \quad (25)$$

3. Feedback Wave Control of Cantilever Plate

Consider the presence of an excitation in the beam structure where a train of wave control forces is applied to a line parallel to the y -axis. At this point, the point discontinuity on the beam is the line discontinuity here. According to the traveling wave theory, the incident elastic wave will be reflected and transmitted at discontinuities [21, 22]. Assuming a column of forward propagating waves is incident at $x = 0$, where the incident attenuation wave is ignored and the time factor is not considered, the displacements of the beam at $x < 0$ and $x > 0$ are respectively as follows:

$$\omega_-(x, y) = a^+ e^{-ikx} W(y) + a^- e^{ikx} W(y) + a_N^- e^{kx} W(y),$$

$$\omega_+(x, y) = b^+ e^{-ikx} W(y) + b_N^+ e^{-kx} W(y). \quad (26)$$

Make

$$\begin{bmatrix} b^+ \\ b_N^+ \end{bmatrix} = \begin{bmatrix} t_1 \\ t_2 \end{bmatrix} a^+, \quad (27)$$

$$\begin{bmatrix} a^- \\ a_N^- \end{bmatrix} = \begin{bmatrix} r_1 \\ r_2 \end{bmatrix} a^+,$$

where a^+ is the mode coefficient of the incident propagation wave, a^- is the mode coefficient of the reflected propagation wave, a_N^- is the mode coefficient of the reflected attenuation wave, b^+ is the mode coefficient of the transmitted propagation wave, and b_N^+ is the mode coefficient of the transmitted attenuation wave.

In feedback wave control, sensors and actuators are positioned in an area of the structure to control the propagation of elastic waves, where the position of the control force is discontinuous. In the frequency domain, the control force of the feedback wave is taken as

$$F(\omega) = -H(\omega)W(\omega), \quad (28)$$

where $H(\omega)$ is the transfer function of the controller, which can be determined by calculating the reflection coefficient and transmission coefficient of the solution wave.

Considering the continuity and balance of the beam at $x = 0$, there are

$$\begin{aligned} w_+(0, y) &= w_-(0, y), \\ \frac{\partial w_-(0, y)}{\partial x} &= \frac{\partial w_+(0, y)}{\partial x}, \end{aligned} \quad (29a)$$

$$\begin{aligned} Hw_+ &= Q_+(0, y) - Q_-(0, y), \\ M_+(0, y) &= M_-(0, y), \end{aligned} \quad (29b)$$

where H is the transfer function of the wave controller. Substitute equation (26) in (29a)

$$\begin{bmatrix} 1 \\ -i \end{bmatrix} a^+ + \begin{bmatrix} 1 & 1 \\ i & 1 \end{bmatrix} \begin{bmatrix} a^- \\ a_N^- \end{bmatrix} = \begin{bmatrix} 1 & 1 \\ -i & -1 \end{bmatrix} \begin{bmatrix} b^+ \\ b_N^+ \end{bmatrix}, \quad (30a)$$

$$\begin{bmatrix} i \\ -1 \end{bmatrix} a^+ + \begin{bmatrix} -i & 1 \\ -1 & 1 \end{bmatrix} \begin{bmatrix} a^- \\ a_N^- \end{bmatrix} = \begin{bmatrix} i & -1 \\ -1 & 1 \end{bmatrix} \begin{bmatrix} b^+ \\ b_N^+ \end{bmatrix} + \begin{bmatrix} \bar{H} & \bar{H} \\ 0 & 0 \end{bmatrix} \begin{bmatrix} b^+ \\ b_N^+ \end{bmatrix}, \quad (30b)$$

where $\bar{H} = H/EIk^3$.

Substitute equation (27) in (30a),

$$\begin{bmatrix} 1 \\ -i \end{bmatrix} a^+ + \begin{bmatrix} 1 & 1 \\ i & 1 \end{bmatrix} \begin{bmatrix} r_1 \\ r_2 \end{bmatrix} a^+ = \begin{bmatrix} 1 & 1 \\ -i & -1 \end{bmatrix} \begin{bmatrix} t_1 \\ t_2 \end{bmatrix} a^+, \quad (31a)$$

$$\begin{bmatrix} i \\ -1 \end{bmatrix} a^+ + \begin{bmatrix} -i & 1 \\ -1 & 1 \end{bmatrix} \begin{bmatrix} r_1 \\ r_2 \end{bmatrix} a^+ = \begin{bmatrix} i & -1 \\ -1 & 1 \end{bmatrix} \begin{bmatrix} t_1 \\ t_2 \end{bmatrix} a^+ + \begin{bmatrix} \bar{H} & \bar{H} \\ 0 & 0 \end{bmatrix} \begin{bmatrix} t_1 \\ t_2 \end{bmatrix} a^+. \quad (31b)$$

By solving this equation

$$\begin{aligned} t_1 &= 1 + \frac{\bar{H}i}{4 - (1+i)\bar{H}}, \\ r_1 &= \frac{\bar{H}i}{4 - (1+i)\bar{H}} \end{aligned} \quad (32)$$

The energy carried by the propagating wave is proportional to the square of the wave amplitude [23]. Therefore, the reflection energy and transmission energy per unit incident energy is $E = |t_1|^2 + |r_1|^2$, if there is no energy dissipation at $x = 0$, then $|t_1|^2 + |r_1|^2 = 1$. In this paper, a controller for absorbing incident energy is designed by adding damping to the structure.

In particular, if we let $\bar{H}(\omega) = \sqrt{2}(1+i)\omega g$, then

$$E = |t_1|^2 + |r_1|^2 = \left| 1 - \frac{(1+i)g\omega}{2g\omega + 2\sqrt{2}i} \right|^2 + \left| \frac{(1+i)g\omega}{2g\omega + 2\sqrt{2}i} \right|^2. \quad (33)$$

We assume that the wave is incident from one side of the control region to seek the optimal control gain g and make it absorb the energy of the incident wave as much as possible, in other words, minimize $E = |r|^2 + |t|^2$ (maximize the energy absorbed by the controller). In this case, let $\partial E/\partial \omega = 0$, and the control gain is

$$g = \frac{\sqrt{2}}{\omega}. \quad (34)$$

Therefore, the transfer function of the wave controller is

$$\bar{H}(\omega) = 2(1+i). \quad (35)$$

Typically, the tuned PD (proportional plus differential control) feedback wave control is used so that it has the same effect as the optimal controller at a particular frequency ω_d . The frequency response of the controller is

$$\bar{H}_w(\omega) = c_1 + c_2(i\omega), \quad (36)$$

where $c_1 = 2, c_2 = 2/\omega_d$.

When the controller in the frequency domain is converted to the time domain, the inverse Fourier transform is performed on the control law, and the PD control in the time domain is obtained [24, 25]. If the wave control force is applied at (x_w, y_w) , it becomes

$$f_w(x, y, t) = -[c_1 w(x, t) + c_2 \dot{w}(x, t)] \delta(x - x_w) \delta(y - y_w). \quad (37)$$

At this time, the wave control force (37) is applied to the original vibration system, and the matrix form of the system motion equation is

$$\bar{M}_w \ddot{q} + \bar{C}_w \dot{q} + \bar{K}_w q = \bar{p}, \quad (38)$$

where $\tilde{P} = [p_{11} \ p_{12} \ \dots \ p_{N}]^T$, $p_{i,j}(t) = 1/m_{i,j} \iint_{\Omega} \bar{q}(x, y, t) W_{i,j}(x) dx dy$, \tilde{M}_w , \tilde{C}_w , \tilde{K}_w are mass matrix,

damping matrix, and stiffness matrix, respectively, in the form of

$$\begin{aligned} \tilde{M}_w &= I, \\ \tilde{C}_w &= c_2 \hat{\Psi}_w, \end{aligned} \quad (39a)$$

$$\tilde{K}_w = \omega^2 + c_1 \hat{\Psi}_w, \quad (39b)$$

$$\hat{\Psi}_w = \begin{bmatrix} W_1(x_w)W_1(y_w)W_1(x_w)W_1(y_w) & \dots & W_1(x_w)W_m(y_w)W_1(x_w)W_n(y_w) \\ W_1(x_w)W_1(y_w)W_2(x_w)W_1(y_w) & \dots & W_1(x_w)W_m(y_w)W_2(x_w)W_n(y_w) \\ \vdots & \vdots & \vdots \\ W_m(x_w)W_1(y_w)W_n(x_w)W_1(y_w) & \dots & W_m(x_w)W_m(y_w)W_n(x_w)W_n(y_w) \end{bmatrix}_{(m \cdot n) \times (m \cdot n)}$$

And it should be emphasized that in the later programming calculation, c_1, c_2 will also be matrices.

When there is no wave control force, the mass matrix M is the unit matrix of $(m \cdot n) \times (m \cdot n)$, C is the zero matrix of $(m \cdot n) \times (m \cdot n)$, and K is the diagonal matrix of the square of natural frequency. However, the wave control force couples the vibration modes of the uncontrolled original

system together, and the modes of the wave control system change accordingly.

The state vector $X(t) = [q^T(t); \dot{q}^T(t)]^T$ is introduced, and equations (2a)–(35) are written as

$$\dot{X}(t) = AX(t) + B\tilde{p}, \quad (40)$$

where the coefficient matrix is

$$\begin{aligned} A &= \begin{bmatrix} 0 & I \\ -\tilde{M}_w^{-1}\tilde{K}_w & -\tilde{M}_w^{-1}\tilde{C}_w \end{bmatrix}, \\ B &= \begin{bmatrix} 0 \\ \tilde{M}_w^{-1}\hat{\Psi}_d \end{bmatrix}, \\ \hat{\Psi}_d &= \begin{bmatrix} W_1(x_1)W_1(y_1)W_1(x_2)W_1(y_2) & \dots & W_1(x_N)W_1(y_N) \\ W_1(x_1)W_2(y_1) & \dots & W_1(x_N)W_2(y_N) \\ \vdots & \vdots & \vdots \\ W_m(x_1)W_n(y_1) & \dots & W_1(x_N)W_2(y_N) \end{bmatrix}_{(m \cdot n) \times N} \end{aligned} \quad (41)$$

4. Numerical Examples and Analysis Discussion

The dynamic response of thin plates before and after applying wave control force is analyzed and studied by using feedback wave control. The characteristic length is taken as the length b of the beam, and the following dimensionless quantity is adopted: Poisson ratio $\nu = 0.30$; $a/b = 2$; $\bar{\omega}_{i,j} = \omega_{i,j}/\omega_{1,1}$ ($i = 1, 2, 3$; $j = 1, 2$). The first 6 dimensionless frequencies of the cantilever plate are shown in Table 1.

Figures 2–7 show the frequency response of the structure before and after applying wave control forces. In Figure 2, the unit disturbance force is applied at the point $(x_d, y_d) = (0.30a, 0.20b)$, while the wave control force and the measuring response position are at the point $(x_w, y_w) = (0.40a, 0.40b)$ and $(x_s, y_s) = (0.40a, 0.70b)$, respectively. In Figure 3, the unit disturbance force is applied at the point

$(x_d, y_d) = (0.40a, 0.20b)$, the wave control force and the measured response position are $(x_w, y_w) = (0.40a, 0.40b)$ and $(x_s, y_s) = (0.70a, 0.80b)$, respectively. The unit disturbance force is applied at the point $(x_d, y_d) = (0.30a, 0.30b)$ in Figure 4, the wave control force and the measured response position are $(x_w, y_w) = (0.45a, 0.45b)$ and $(x_s, y_s) = (0.70a, 0.60b)$, respectively.

In Figure 5, the unit disturbance force is applied at the point $(x_d, y_d) = (0.40a, 0.30b)$, the wave control force and the measured response position are $(x_w, y_w) = (0.45a, 0.45b)$ and $(x_s, y_s) = (0.40a, 0.60b)$, respectively. In Figures 6 and 7, the unit disturbance force is applied at the point $(x_d, y_d) = (0.30a, 0.20b)$, and the wave control force positions are $(x_w, y_w) = (0.40a, 0.40b)$, $(x_w, y_w) = (0.45a, 0.45b)$, respectively, the measured response positions are $(x_s, y_s) = (0.40a, 0.60b)$ and $(x_s, y_s) = (0.40a, 0.70b)$, respectively. In the approximation of tuned PD control, the

TABLE 1: The first 6 dimensionless frequencies of the cantilever plate.

Modal order	1	2	3	4	5	6
Natural frequency	1.00	51	5.51	12.90	15.43	23.73

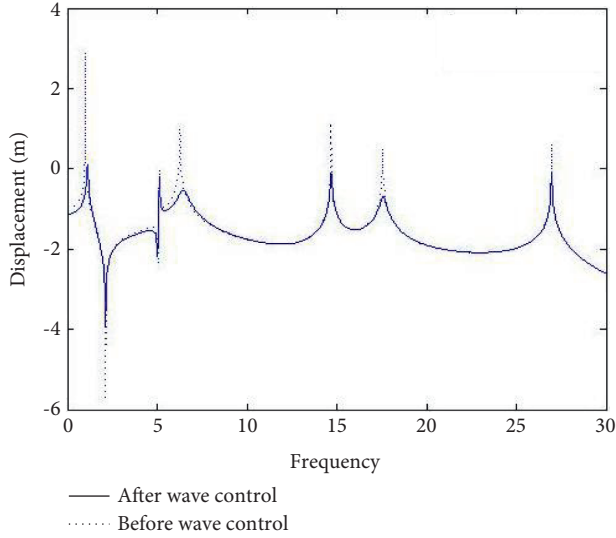


FIGURE 2: Frequency response before and after wave control.

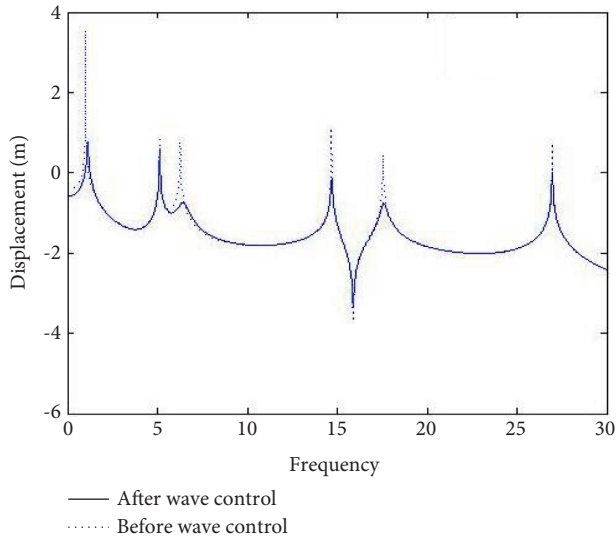


FIGURE 3: Frequency response before and after wave control.

controller is tuned to the optimum at the third natural frequency. Through analysis, the following are discussed:

It can be seen from Figures 2–7 that the frequency responses before and after different wave controls. The transverse coordinates are dimensionless frequency values, while the longitudinal coordinates are the common logarithmic values of frequency responses. Figures 2–7 show the frequency response of the front and rear structures using wave controllers. The response of the structure is rapid before control, while wave control can be regarded as adding damping to the structure and absorbing the energy carried

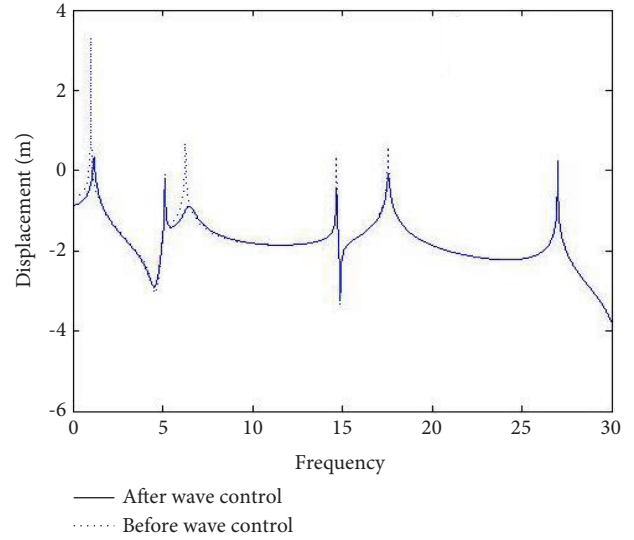


FIGURE 4: Frequency response before and after wave control.

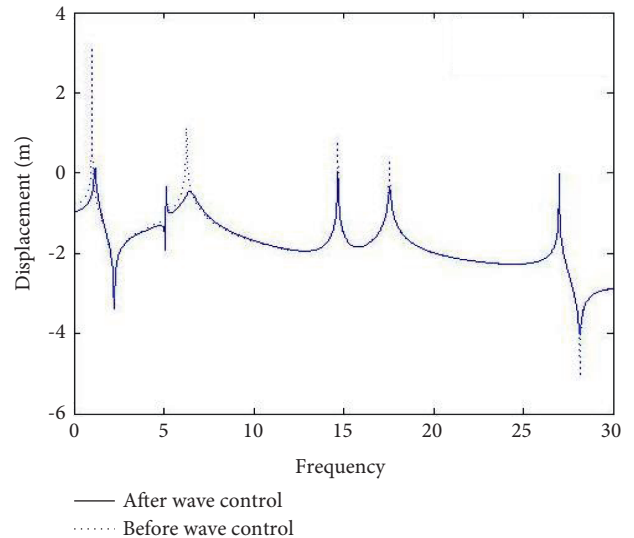


FIGURE 5: Frequency response before and after wave control.

by the elastic wave in the structure. After the wave control, the sharp response is weakened; in addition, the frequency response before and after the wave control also reflects that the modal characteristics of the whole structure have changed after the wave control, the natural frequency of the structure has been changed to a certain extent. Finally, from Figures 2–7, it can be seen that the position of the wave controller is different and the control effect of each order mode is different. At the third natural frequency, the absolute output amplitude of the controller is reduced to about 31.8% of the original value, and the controller is tuned to the optimum value at the third natural frequency, so the control effect is the best at the third natural frequency.

From the comparison of Figures 2–5, it can be seen that when the wave control position is the same, but the disturbance is different. And when the dynamic response position is different, although the sharp response is

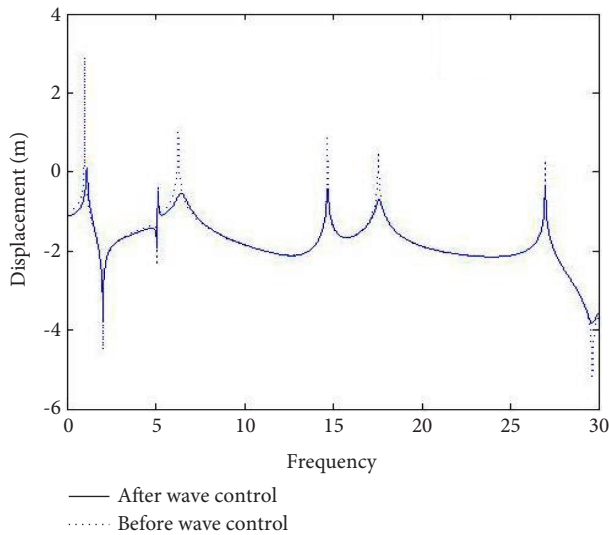


FIGURE 6: Frequency response before and after wave control.

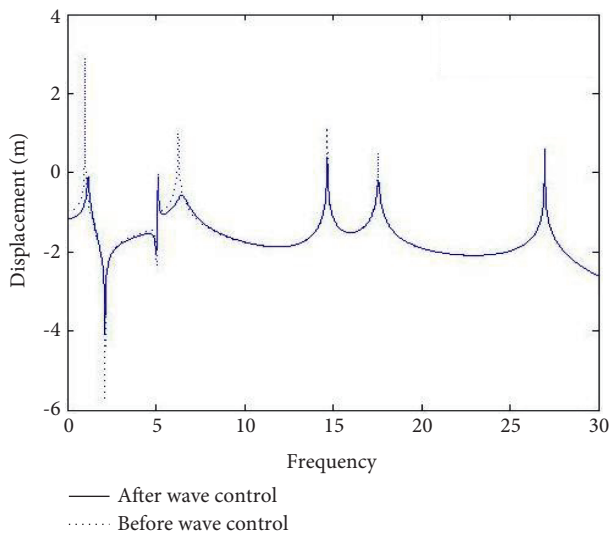


FIGURE 7: Frequency response before and after wave control.

weakened, the control effect is not identical. It can be seen from the comparison between Figures 6 and 7 that when the disturbance position is the same, the wave control force is different, and the dynamic response position is different, the control effect is also different. The influence of the application position of the wave controller on the control effect is also very important. The application point of the wave controller should avoid the node of the mode as far as possible. Otherwise, the active control will not get good results, and may even lead to system instability.

5. Conclusions

Based on the classical thin plate theory and the wave control method, the active vibration control of the cantilever plate is studied in this paper. In this paper, the wave control method widely used in the one-dimensional waveguide is applied to classical thin plates, and a series of active vibration control

examples of cantilever plates are given. The following conclusions can be drawn:

The mode shape function of a cantilever rectangular plate is decomposed into the product of two functions, that is, the product of the mode shape function of a cantilever beam only dependent on the direction, and the mode shape function of a free beam at both ends only dependent on the direction. The problem of solving the vibration mode function of the thin plate is effectively solved.

When a series of wave control forces are applied to the plate, the point discontinuity on the beam is where the line discontinuity is. The wave control force is determined by using the equilibrium condition and continuity condition at the line discontinuity.

With wave control, a controller is designed to absorb the incident vibration energy by adding damping to the structure, which corresponds to a tuned spring and damper in the time domain. It can be seen from the control output that the control gain can achieve the optimal design at a certain tuning frequency. Therefore, when the applied position of wave control is different, the control effect of each order mode is different due to the distance between the applied position and the node of each order mode. For better control, the wave controller can be applied at several different locations, while avoiding instability of the system, the application point of the wave controller should avoid the modal nodes as far as possible.

Data Availability

The data used to support this study are available from the corresponding author upon reasonable request.

Conflicts of Interest

The authors declare that there are no conflicts of interest regarding the publication of this paper.

Acknowledgments

The project was supported by China's National Natural Science Foundation (Program No. 51275142).

References

- [1] H. Moradi, M. Sadighi, and F. N. Bakhtiari, "Optimum design of a tuneable vibration absorber with variable position to suppress vibration of a cantilever plate," *International Journal of Acoustics and Vibration*, vol. 16, no. 2, pp. 55–63, 2011.
- [2] M. Iqbal and F. U. Khan, "Hybrid vibration and wind energy harvesting using combined piezoelectric and electromagnetic conversion for bridge health monitoring applications," *Energy Conversion and Management*, vol. 172, pp. 611–618, 2018.
- [3] A. Kodhanda, N. Ali, M. M. Sucheendran, and S. Talole, "Robust control of nonlinear resonance in a clamped rectangular plate," *Journal of Vibration and Control*, vol. 24, no. 18, pp. 4176–4194, 2018.
- [4] J. Ma and H. J. Maris, "Localized vibrational modes in bars and plates," *Journal of Applied Physics*, vol. 107, no. 10, Article ID 104904, 2010.

- [5] B. Ni and C. Hu, "Dynamics of cantilever plates and its hybrid vibration control," *Acta Mechanica Sinica*, vol. 29, no. 5, pp. 738–748, 2013.
- [6] A. S. M. Alzaidi, J. Kaplunov, and L. Prikazchikova, "Elastic bending wave on the edge of a semi-infinite plate reinforced by a strip plate," *Mathematics and Mechanics of Solids*, vol. 24, no. 10, pp. 3319–3330, 2019.
- [7] C. R. Halkyard, "Sensor array design for wave decomposition in the presence of coupled motion," *Journal of Sound and Vibration*, vol. 259, no. 4, pp. 935–953, 2003.
- [8] H. M. El-Khatib, B. R. Mace, and M. J. Brennan, "Suppression of bending waves in a beam using a tuned vibration absorber," *Journal of Sound and Vibration*, vol. 288, no. 4-5, pp. 1157–1175, 2005.
- [9] A. A. Krushynska, "Flexural edge waves in semi-infinite elastic plates," *Journal of Sound and Vibration*, vol. 330, no. 9, pp. 1964–1976, 2011.
- [10] I. S. Jones, N. V. Movchan, and A. B. Movchan, "Blockage and guiding of flexural waves in a semi-infinite double grating," *Mathematical Methods in the Applied Sciences*, vol. 40, no. 9, pp. 3265–3282, 2017.
- [11] J. Kaplunov and A. Nobili, "The edge waves on a Kirchhoff plate bilaterally supported by a two-parameter elastic foundation," *Journal of Vibration and Control*, vol. 23, no. 12, pp. 2014–2022, 2017.
- [12] S. H. Mirafza, A. M. Khorasani, and A. H. Ghasemi, "Optimizing time delay feedback for active vibration control of a cantilever beam using a genetic algorithm," *Journal of Vibration and Control*, vol. 22, no. 19, pp. 4047–4061, 2016.
- [13] Z. Q. Jiang, C. Dou, and Y. X. Wu, "Experimental study on earthquake-resilient prefabricated cross joints with L-shaped plates," *Engineering Structures*, vol. 184, pp. 74–84, 2019.
- [14] B. Ni and C. Hu, "Dynamics of the Mindlin plate and its modal vibration control," *Journal of Vibration and Control*, vol. 18, no. 13, pp. 2039–2049, 2012.
- [15] T. Chen, C. Hu, and W. H. Huang, "Vibration control of cantilevered Mindlin-type plates," *Journal of Sound and Vibration*, vol. 320, no. 1-2, pp. 221–234, 2009.
- [16] J. S. Bae, J. S. Park, J. H. wang, and J. H. Roh, "Vibration Suppression of a Cantilever Plate Using Magnetically Multimode Tuned Mass Dampers," *Shock and Vibration*, vol. 2018, Article ID 3463528, 2018.
- [17] Y. Cao, M. M. Li, and Z. Z. Gao, "Dynamic testing and analysis of Poisson's ratio of lumbars based on the cantilever-plate bending mode shape method," *Journal of Testing and Evaluation*, vol. 47, no. 4, pp. 2540–2550, 2019.
- [18] E. Omidi and S. N. Mahmoodi, "Vibration suppression of distributed parameter flexible structures by Integral Consensus Control," *Journal of Sound and Vibration*, vol. 364, pp. 1–13, 2016.
- [19] Z. C. Qiu, H. X. Wu, and D. Zhang, "Experimental researches on sliding mode active vibration control of flexible piezoelectric cantilever plate integrated gyroscope," *Thin-Walled Structures*, vol. 47, no. 8-9, pp. 836–846, 2009.
- [20] R. Li, P. C. Wang, and L. H. Tong, "On new analytic free vibration solutions of rectangular thin cantilever plates in the symplectic space," *Applied Mathematical Modelling*, vol. 53, pp. 310–318, 2018.
- [21] Z. C. Qiu, T. X. Wang, and X. M. Zhang, "Sliding mode predictive vibration control of a piezoelectric flexible plate," *Journal of Intelligent Material Systems and Structures*, vol. 21, no. 1, pp. 65–81, 2021.
- [22] P. Khandagale, G. Bhakar, and S. S. Joshi, "Modelling time-domain vibratory deflection response of thin-walled cantilever workpieces during flank milling," *Journal of Manufacturing Processes*, vol. 33, pp. 278–290, 2018.
- [23] P. X. Sun, H. Yang, and Y. Zhao, "Time-domain calculation method of improved hysteretic damped system based on frequency-dependent loss factor," *Journal of Sound and Vibration*, vol. 488, Article ID 115658, 2020.
- [24] H. J. Kim, "A study on the design of a double cantilever structure friction tester for precision friction measurement," *Tribology and Lubricants*, vol. 34, no. 4, pp. 125–131, 2018.
- [25] I. Chenini, R. Nasri, C. Mrad, and Y. Abdelli, "Kinematics effect on honeycomb sandwich beams vibration," *Mechanics & Industry*, vol. 18, no. 3, Article ID 2016039, 2017.

Research Article

Asymmetric Evolutionary Game Analysis of Building Information Modeling (BIM) Technology Diffusion

Qian Liu 

CCCC Fourth Highway Engineering Co. Ltd., Beijing 100022, China

Correspondence should be addressed to Qian Liu; qianliang33152@163.com

Received 22 October 2021; Accepted 26 November 2021; Published 29 December 2021

Academic Editor: Lingkun Chen

Copyright © 2021 Qian Liu. This is an open access article distributed under the Creative Commons Attribution License, which permits unrestricted use, distribution, and reproduction in any medium, provided the original work is properly cited.

Building Information Modeling (BIM) technology plays a pivotal role in the process of building process informatization. In the context of extensive promotion by all parties, how to effectively evaluate the promotion value of countries and enterprises is particularly important. In order to better analyze the promotion trend of the BIM technology diffusion system in China, a noncooperative evolutionary game model of BIM technology diffusion between the government and enterprises is constructed, and Vensim PLE software is used for simulation analysis in this paper. The model includes government subsidy cost and penalty, social benefit and loss, and income payment matrix of BIM technology input income and cost. The results show that enterprises need not only direct cost subsidy from the government but also indirect cost subsidy in the process of BIM technology diffusion. Appropriate government penalties can effectively promote the initiative of enterprises to adopt BIM technology; BIM has a great impact on the input income and cost of enterprises. In view of this, it is suggested that the first task for enterprises to promote the diffusion of BIM technology is to clarify the definition of BIM's high investment cost and do a good financial impact analysis.

1. Introduction

Building Information Modeling (BIM) is generally understood as a general term describing various activities of objects in computer-aided design (CAD), which supports the use of 3D geometric and nongeometric functional attributes and relationships to represent architectural elements and describe the characteristics of the object in 3D. Therefore, BIM is considered a series of technologies and solutions [1]. The diffusion of BIM technology can solve the technical problems in the process of engineering construction, strengthen the collaborative work among organizations, promote the efficiency of engineering construction, increase productivity, and improve and optimize design, construction, and maintenance of construction products. At present, China's formulation of the "Building Information Model Construction Application Standards" and the new policies issued by most provinces and cities where "BIM technology is required for large public buildings of more than 20,000 square meters" have all promoted the application of BIM technology in China to a certain

extent. However, there are no mandatory regulations for private investment construction projects, and the lack of BIM consulting agencies, the constraints of BIM maturity, deep-rooted traditional construction ideas, and a series of problems caused by information asymmetry have greatly hindered China's BIM proliferation of technology. At the same time, as a low-carbon environment-friendly technology, BIM technology's diffusion quality and efficiency [2] are of great significance for sustainable development and are also the focus of attention of scholars at home and abroad [3].

Diffusion is a process in which individuals, societies, or organizations adopt innovation over a period of time [4]; it is generally believed that technology diffusion is a social phenomenon [5]. Chen et al. [6] extended technology diffusion research to the organizational environment and introduced factors such as critical quality and knowledge barriers. Grover et al. [7] combined Twitter analysis and academic literature analysis to provide better diffusion insights for the diffusion of blockchain technology than a single data source. As a cross-organization collaboration

technology, BIM is not aware of the application value of BIM, and the value-added effect brought by BIM application [8] is considered to be the key factor restricting the diffusion and development of BIM in China. The market behavior of enterprises is the essence of technology diffusion, and government departments play a leading role [9]. The proliferation of BIM technology cannot rely solely on government policies but, more importantly, the independent choice of enterprises. The adoption of BIM technology by enterprises requires payment of the huge cost of the BIM technology system, and if enterprises want to gain a cost-leading advantage, then enterprises should focus on innovative activities that minimize costs [10]. Some scholars use the DOI method to explain the spread of BIM within organizations [11, 12] and the spread of BIM in the industry [13]. Reference [14] used a set of diffusion factors determined by Peansupap and Walker (V. Peansupap and D. H. T. Walker, 2005) to study the diffusion of BIM. Ma et al. [15] applied evolutionary game theory to the research of industrial common technology diffusion model and analyzed the main behavior and influence mechanism of technology diffusion in different evolution stages. Laciana and Rovere [16] found that the behavior of early adopters of technology had the most significant impact on the speed of technology diffusion by simulating the dynamic process of technology diffusion. The diffusion of BIM technology in the construction industry is still in the early adopter stage of technology adoption, and the overall diffusion rate is still very slow [17]. Sun et al. [18], based on the agent model and evolutionary game theory, simulated the technology diffusion under different relationships. The above research provides ideas and enlightenment for constructing the BIM technology diffusion model in this paper [15, 19–30].

At present, academic research on the diffusion of BIM mostly focuses on diffusion factors, barriers, and diffusion in the entire technical field. However, there are few research results on the diffusion of BIM technology. Existing research mainly includes the description of the current status of BIM diffusion and the factors affecting the diffusion identification, driving the proliferation strategy. In addition, China adheres to the basic principle of “enterprise dominance, industry services, and policy promotion” for the diffusion of BIM technology [31]. However, few existing studies consider the diffusion of BIM technology from the perspective of government and enterprises. In view of this, this article uses evolutionary game theory to establish the BIM technology diffusion evolution game model based on the analysis of the relationship between the game subjects of the building information model (BIM) technology diffusion and analyzes the evolution process of government and enterprise behavior during the BIM technology diffusion process. And the evolutionary stability strategy, through numerical simulation, analyzes the influence of government reward and punishment system, enterprise risk attitude, and other factors on government and enterprise strategy choices, so as to put forward policies and suggestions to promote the diffusion of BIM technology in China.

2. Analysis of Game Subject Relationship of BIM Technology Diffusion

The process of technology diffusion is a game process, and the decisions made by the participants will not only consider their own interests but also consider the impact of the decision on other participants [32]. However, in the process of BIM technology diffusion, due to the asymmetry of information among the participating entities, the imperfection of BIM related standards, norms, and laws, and the inequality of the benefits of applying BIM technology (the biggest beneficiary of applying BIM technology is units, followed by construction units, design units, etc.) and the huge differentiation of BIM investment (the largest investor investing in BIM technology is the construction unit, followed by the design unit, construction unit, etc.), making it difficult for BIM to pass the mutual interaction between them realizes the widespread adoption and application of BIM technology. Therefore, to achieve the full spread of BIM technology, enterprise adoption is a prerequisite, and the government’s active promotion is a necessary means [33]. The proliferation of BIM technology has accelerated, and the government will reap regulatory costs for quality, safety, environmental protection, and waste of resources. The influence of government agencies on the spread of BIM technology is mainly reflected in accelerating the adoption of BIM application enterprises through regulations, policies, guidelines, and other measures, by calling on local governments to actively promote the application of BIM technology, and training major qualified enterprises to learn BIM knowledge through the organization with skills, etc. In order to implement the government’s policy requirements, enterprises will also face pressures from insufficient investment funds, shortage of BIM comprehensive talents, difficulty in project management, and poor adaptability of management personnel. At the same time, the entire set of optimization programs in BIM technology has changed the traditional construction industry. The current situation of high energy consumption, high danger, many quality accidents, slow progress, low efficiency, and poor personnel coordination also allows enterprises to effectively control investment, progress, quality, safety, environmental protection, etc. and ultimately achieve huge project success income.

It can be seen from the prospect theory [34, 35] that individual strategy choice preferences depend on their individual subjective psychological feelings when gaining and losing strategies and are manifested as loss aversion. Therefore, BIM application companies are confronted with the high cost of adoption and government guarantees. Insufficient, unclear, or obvious benefits, lack of successful implementation cases, etc. often adopt a risk avoidance strategy and put themselves in a wait-and-see state; the government is facing the high R&D costs of BIM and the current status of traditional construction methods. And under the circumstance that enterprises are not enthusiastic about independent research and development and adoption,

the government tends to adopt a conservative strategy, mostly based on encouraging policies, and the most intuitive performance is that there are few subsidies to enterprises. At the same time, due to the slow diffusion of BIM in China, there are still many obstacles in the application of BIM in technology, management, law, contracts, etc. As a limited rational person, the government and enterprises are cautious in the strategy selection process. Therefore, the diffusion process of BIM technology is still very slow, and it will take a long time to diffuse in the entire construction industry, and it is necessary to explore effective ways to accelerate the diffusion of BIM technology in China.

3. Evolutionary Game Analysis of BIM Technology Diffusion

The evolutionary game model is mainly established on the basis of mutation mechanisms and selection mechanisms. In the process of BIM technology adoption, the selection mechanism refers to the strategy that the government and enterprises can obtain higher benefits at the current stage, which will be adopted by more players through learning and imitation in the next stage; mutation refers to the fact that some participants in the adoption of BIM technology choose strategies in a random manner, so the mutation strategy may get lower gains or higher gains. The former will become popular after selection, and the latter will naturally go away. The essence of BIM technology diffusion is a process of the multisubject mutual game, which belongs to the evolutionary game model with social strategy changes. The strategic combination of the game subject through adaptive adjustment and continuous evolution, that is, the “good” strategy becomes more popular [36], thus providing reference and reference for the choice of gamers strategy.

3.1. Evolutionary Game Model Construction

Hypothesis 1. There are two completely different limited rational groups in the BIM technology diffusion system: BIM application companies (including construction units, design units, construction units, operating units, and consulting units) and government agencies (departments representing government agencies, associations, etc.). The strategies that the government can choose are {actively promote; passively promote}, the strategies that the enterprise can choose are {actively adopt BIM technology; passively adopt BIM technology}, and the two parties will form an evolutionarily stable strategy through the dynamic repeated game. Probability of government strategy choice = {probability of positive advancement, probability of negative advancement} = $\{\alpha, 1-\alpha\}$, and probability of enterprise strategy choice = {probability of actively adopting BIM technology, probability of passively adopting BIM technology} = $\{\beta, 1-\beta\}$, where $\alpha, \beta \in [0, 1]$ are all functions of time t .

Hypothesis 2. The government is the main body of market supervision, and the enterprise is the most important body

in the market. The two companies have different total benefits in the process of BIM technology diffusion. Enterprises tend to pay more attention to economic benefits, while the government pays more attention to BIM technology. Social benefits are brought by diffusion. Use R to indicate that the government actively promotes the social benefits brought by the diffusion of BIM technology, and use B and B' , respectively, to indicate the profit before and after the adoption of BIM technology. At the same time, the government and enterprises will also pay a corresponding price. In this paper, the government will actively promote the diffusion of BIM technology and the cost of subsidy management for enterprises will be represented by C_1 and represents the subsidy coefficient; then, the government subsidy for enterprises will be γC_1 . A series of costs for adopting and using BIM technology is denoted by C_2 ; the excess operating costs paid by enterprises for passive adoption are denoted by G . At the same time, the government's passive promotion and passive adoption of enterprises will cause a certain social loss L , which will be borne by the government.

Hypothesis 3. With the increasing demands on production, economy, and quality, BIM brings a set of organizational solutions for the construction industry to increase productivity. BIM technology can bring core competitiveness to enterprises. Those who have not been adopted or passively adopted BIM technology companies will lose their advantages in the competition in the entire construction market. At the same time, if the government actively promotes BIM technology, enterprises will be punished for choosing passive strategies; if the government passively promotes BIM technology, enterprises will lose the value-added benefits that BIM can bring. Therefore, there are risks of profit and loss in the diffusion of BIM technology. We make the government passively promote the enterprise to adopt the impairment loss value of D , and the government actively promotes the passive penalty of the enterprise to be K ; then, the risk profit and loss values of the two are D and K , respectively.

Based on the above assumptions, we construct a revenue payment matrix for both the government and the enterprise (Table 1).

3.2. Evolutionary Game Stability Strategy Analysis.

According to the income payment matrix of government and enterprises in the process of BIM technology diffusion in Table 1, the profit function of pure strategy and mixed strategy and the dynamic differential equation of replication of the BIM technology diffusion system can be obtained as follows.

The revenue function that the government chooses to actively promote the strategy is

$$U_{11} = \beta(R - C_1 - \gamma C_1) + (1 - \beta)(-C_1 + K). \quad (1)$$

The return function of the government's choice of passive promotion strategy is

TABLE 1: The revenue payment matrix of both the government and the enterprise.

Government	Enterprise	
	Actively adopting BIM technology (β)	Passively adopting BIM technology ($1-\beta$)
Positive advancement (α)	$R-C_1-\gamma C_1; B'-C_2+\gamma C_1$	$-C_1+K; B-G-K$
Negative advancement ($1-\alpha$)	$R; B'-C_2-D$	$-L; B-G$

$$U_{12} = \beta R + (1 - \beta)(-L). \quad (2)$$

The average government revenue is

$$\bar{U}_1 = \alpha U_{G1} + (1 - \alpha)U_{G2}. \quad (3)$$

From equations (1)–(3), the government's replication dynamic differential equation is

$$\begin{aligned} F_1(\alpha) &= \frac{d\alpha}{dt} = \alpha(U_{11} - \bar{U}_1) = \alpha(1 - \alpha)(U_{11} - U_{12}) \\ &= \alpha(1 - \alpha)[- \beta(L + \gamma C_1 + K) + K - C_1 + L]. \end{aligned} \quad (4)$$

The profit function of an enterprise's choice to actively adopt a strategy is

$$U_{21} = \alpha(B' - C_2 + \gamma C_1) + (1 - \alpha)(B' - C_2 - D). \quad (5)$$

The income function for enterprises to choose passive adoption strategies is

$$U_{22} = \alpha(B - G - K) + (1 - \alpha)(B - G). \quad (6)$$

The average expected additional benefit of the enterprise is

$$\bar{U}_2 = \beta U_{E1} + (1 - \beta)U_{E2}. \quad (7)$$

From equations (5)–(7), the replication dynamic differential equation of an enterprise is

$$J = \begin{pmatrix} (1 - 2\alpha)[\beta(L + \gamma C_1 + K) - K + C_1 - L] & \alpha(1 - \alpha)(L + \gamma C_1 + K) \\ \beta(1 - \beta)(D + \gamma C_1 + K) & (1 - 2\beta)[\alpha(D + \gamma C_1 + K) - B + G - D - C_2 + B'] \end{pmatrix}. \quad (9)$$

According to evolutionary game theory, when $\det(J) > 0$ and $\text{tr}(J) < 0$, the equilibrium point will approach a local progressive stable state, also known as evolutionary equilibrium state; when $\det(J) > 0$ and $\text{tr}(J) > 0$, the equilibrium point will not approach the local progressive stable state, that is, in an unstable state; when $\det(J) < 0$ and $\text{tr}(J) = 0$ or uncertain, the equilibrium point is a saddle point, also. That is, the equilibrium point is stable in one direction and unstable in the other direction. The basis for judging whether the three parties in the game are in an evolutionary equilibrium state is whether $\det(J) > 0$ and $\text{tr}(J) < 0$ are true. The judgment results are shown in Table 2. It can be seen from the game theory that when $\det(J) > 0$ and $\text{tr}(J) < 0$, the equilibrium point will approach a locally asymptotically stable state; that is, it will reach an evolutionary equilibrium state. By calculating the $\det(J)$ and $\text{tr}(J)$ of the 5 equilibrium points, it can be judged whether the game system has evolved

$$\begin{aligned} F_2(\beta) &= \frac{d\beta}{dt} = \beta(U_{E1} - \bar{U}_E) = \beta(1 - \beta)(U_{E1} - U_{E2}) \\ &= \beta(1 - \beta)[\alpha(\gamma C_1 + D + K) - B + G - D - C_2 + B']. \end{aligned} \quad (8)$$

From equations (4) and (8), the steady state of the replication dynamics is (0, 0), (0, 1), (1, 0), (1, 1), and (α^*, β^*) ; among them, $\alpha^* = (B - G + D + C_2 - B') / (\gamma C_1 + D + K)$ and $\beta^* = (K - C_1 + L) / (L + \gamma C_1 + K)$.

One basic concept of evolutionary game theory is the evolutionarily stable strategy (ESS), which means that when all members of a group adopt this strategy; then, under the influence of natural selection, no mutation strategy will invade this group [36]. The traditional game theory is premised on the assumption of rational people, while the evolutionary game theory is based on limited rationality, through adjustment, comparative analysis, learning, and other strategies between two or more players in the game, after many repeated and dynamic long-term games, to find a stable state, that is, the evolutionarily stable strategy between game players. According to the method proposed by Friedman [37], the system's evolutionarily stable strategy (ESS) can be obtained through the local stability of the Jacobian matrix. Therefore, from equations (4) and (8), the Jacobian matrix of the game between the government and the enterprise can be obtained as follows:

to a stable state. The expressions of the determinant and traces of each equilibrium point are shown in Table 2.

It can be seen from Table 2 that the sizes of $\det(J)$ and $\text{tr}(J)$ corresponding to the equilibrium point and $-B + G - D - C_2 + B'$, $K - C_1 + L$, $\gamma C_1 + K - B + G - C_2 + B'$ are positive and negative related, so the stability of the five equilibrium points is analyzed by considering the size of these three expressions, as follows:

- (1) When $-B + G - D - C_2 + B' > 0$ and $K - C_1 + L > 0$, that is, when the government chooses to actively promote BIM technology, the net income of the company's active adoption of BIM technology is greater than 0, and when the company chooses to passively adopt BIM technology, the net income actively promoted is greater than 0, and the evolutionary stabilization point of the government and

TABLE 2: $\det(J)$ and $\text{tr}(J)$ corresponding to the equilibrium point.

Equilibrium point	Determinants and trace expressions	
(0, 0)	$\det(J)$	$(-K + C_1 - L)(-B + G - D - C_2 + B')$
	$\text{tr}(J)$	$(-K + C_1 - L) + (-B + G - D - C_2 + B')$
(0, 1)	$\det(J)$	$(\gamma C_1 + C_1)[-(-B + G - D - C_2 + B')]$
	$\text{tr}(J)$	$(\gamma C_1 + C_1) + [(-B + G - D - C_2 + B')]$
(1, 0)	$\det(J)$	$[(-K + C_1 - L)](\gamma C_1 + K - B + G - C_2 + B')$
	$\text{tr}(J)$	$[(-K + C_1 - L)] + (\gamma C_1 + K - B + G - C_2 + B')$
(1, 1)	$\det(J)$	$[-(\gamma C_1 + C_1)][-(\gamma C_1 + K - B + G - C_2 + B')]$
	$\text{tr}(J)$	$[-(\gamma C_1 + C_1)] + [-(\gamma C_1 + K - B + G - C_2 + B')]$
(α^*, β^*)	$\det(J)$	$[(-B + G - D - C_2 + B')(D + \gamma C_1 + K) + (-B + G - D - C_2 + B')^2][(K - C_1 + L)(L + \gamma C_1 + K) - (K - C_1 + L)^2]$
	$\text{tr}(J)$	$(D + \gamma C_1 + K)(L + \gamma C_1 + K)$

enterprises tends to be (1, 1). The evolutionary stabilization strategy is for the government to choose to actively promote BIM technology, and the enterprise chooses to actively adopt BIM technology (Table 3).

- (2) When $-B + G - D - C_2 + B' > 0$, $K - C_1 + L < 0$, that is, when the government chooses to actively promote BIM technology, the net income of the company's active adoption of BIM technology is greater than 0, and when the company chooses to passively adopt BIM technology, the net income actively promoted is less than 0, and the evolutionary stabilization point of the government and enterprises tends to be (1, 1). The evolutionary stabilization strategy is for the government to choose to actively promote BIM technology, and the enterprise chooses to actively adopt BIM technology (Table 3).
- (3) When $-B + G - D - C_2 + B' < 0$, $\gamma C_1 + K - B + G - C_2 + B' > 0$, and $K - C_1 + L > 0$, that is, when the government chooses to actively promote BIM technology, the net income of BIM technology is less than 0. When the government chooses to actively promote BIM technology, the net income of enterprises actively adopting BIM technology is greater than 0. When the company chooses to passively adopt BIM technology, the net income actively promoted by the government chooses to be greater than 0. (0, 0) or (1, 1): the evolutionary stabilization strategy is that the government chooses to promote passively BIM technology, enterprises choose to passively adopt BIM technology, or the government chooses to actively promote BIM technology, and enterprises choose to actively adopt BIM technology (Table 3).
- (4) When $-B + G - D - C_2 + B' < 0$, $\gamma C_1 + K - B + G - C_2 + B' > 0$, and $K - C_1 + L < 0$, that is, when the government chooses to actively promote BIM technology, the net income of BIM technology is less than 0. When the government chooses to actively promote BIM technology, the net income of enterprises actively adopting BIM technology is greater than 0. When the company chooses to passively adopt BIM technology, the net income actively promoted by the government chooses to be less than

0. (1, 1): the evolutionary stabilization strategy is actively promoted by the government, and enterprises choose to actively adopt BIM technology (Table 3).

- (5) When $-B + G - D - C_2 + B' < 0$, $\gamma C_1 + K - B + G - C_2 + B' < 0$, and $K - C_1 + L > 0$, that is, when the government chooses to actively promote BIM technology, the net income of BIM technology is less than 0. When the government chooses to actively promote BIM technology, the net income of enterprises actively adopting BIM technology is less than 0. When the company chooses to passively adopt BIM technology, the net income actively promoted by the government chooses to be greater than 0. (0,0): the evolutionary stabilization strategy is for the government to choose passive advancement, and enterprises choose to passively adopt BIM technology (Table 3).
- (6) When $-B + G - D - C_2 + B' < 0$, $\gamma C_1 + K - B + G - C_2 + B' < 0$, and $K - C_1 + L < 0$, that is, when the government chooses to actively promote BIM technology, the net income of BIM technology is less than 0. When the government chooses to actively promote BIM technology, the net income of enterprises actively adopting BIM technology is less than 0. When the company chooses to passively adopt BIM technology, the net income actively promoted by the government chooses to be less than 0. (1, 0): the evolutionary stabilization strategy is actively promoted by the government, and enterprises choose to adopt BIM technology passively (Table 3).

According to the above stability analysis results, the strategic dynamic evolution diagram (Figure 1) of the government and enterprises in promoting BIM technology diffusion can be obtained.

4. Simulation Analysis

Large real estate companies such as Vanke, Evergrande, Country Garden, and Sunac have played a leading role in the diffusion of BIM technology and have demonstrated the characteristics of high BIM application frequency, wide

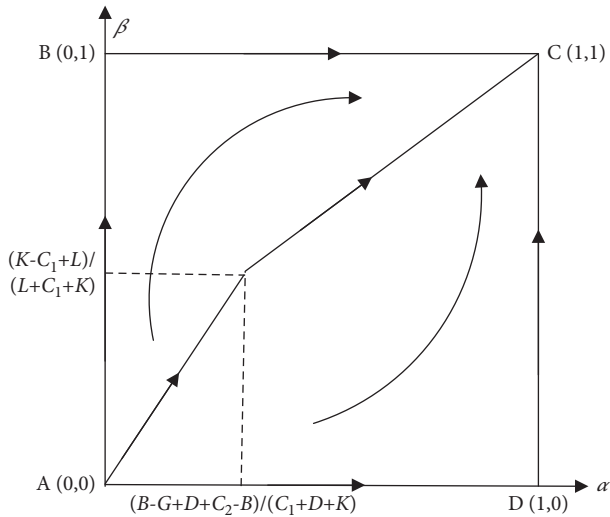


FIGURE 1: The dynamic evolution of government and enterprise strategy.

application range, and many successful BIM application cases. Accelerating the spread of BIM technology is also constantly improving the BIM standards and norms suitable for China’s scenarios and promulgating relevant policies, laws, guidelines, and opinions. In the BIM technology diffusion game model, K , C_1 , L , C_2 , B' , and other parameters affect the strategic choices of the government and enterprises and also affect the evolution process. This article uses the software Vensim PLE (system dynamics software) to simulate the dynamic evolution process that affects the strategic choices of both parties in the diffusion of BIM technology. Vensim PLE type simulation generally follows the following steps: create a new model → check whether the model structure is correct → simulate operation → check whether the model behavior is normally → change the value for simulation test → output the model and its behavior. The focus of system dynamics simulation is the overall system behavior trends and the impact of policy changes. It does not have strict requirements for the accuracy of the results [38]. Yuan Yijun et al. [39] also pointed out that the correctness of the model structure is more important than the choice of parameters. In order to further analyze the strategic relationship between the government and enterprises in the game, we use the assignment method in [39, 40], consider that the status quo of China’s BIM technology is still in its infancy, and assign parameters to the BIM diffusion system. The assignments are $\alpha=0.6$, $\beta=0.5$, $R=16$, $C_1=10$, $C_2=15$, $B=20$, $B'=35$, $L=7$, $D=4$, $K=5$, $G=6$, $\gamma=0.5$, simulation period $T=120$, initial time = 0, final time = 120, and time step = 0.5.

- (1) The sensitivity analysis of the government and enterprises to the fine K : the parameter K is the penalty that the government actively promotes the passive adoption of enterprises, and it has a certain reference value for the government’s policy. Let $K=5, 9, 20$; the

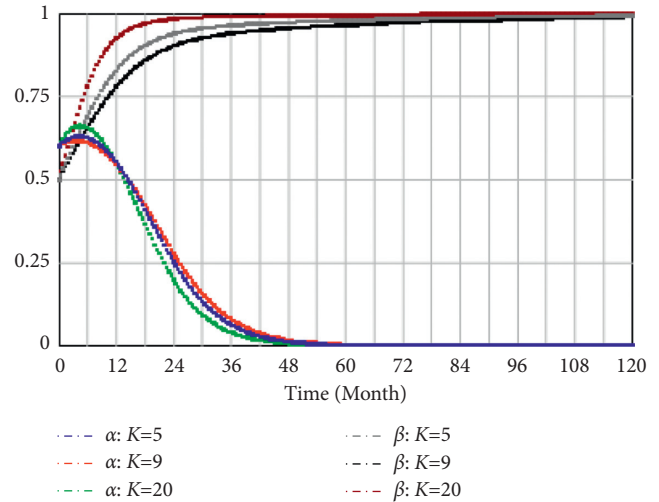


FIGURE 2: The sensitivity analysis of government and enterprises to (K) value.

evolution of the BIM technology diffusion game system is illustrated in Figure 2.

It can be observed from Figure 2 that the spread of BIM technology between the government and enterprises is affected by government fines. When $K=5, 9, 20$, it is obvious that the government adopts a strategy of actively advancing, and enterprises also choose to actively adopt the strategy. At this time, the BIM technology diffusion game system evolves steadily toward $C(1, 1)$. The purpose of the government to impose fines on enterprises is to urge enterprises to actively adopt BIM technology. As can be seen in Figure 2, when the fines continue to increase, the initiative of enterprises to adopt BIM also increases, and they tend to adopt strategies earlier. When the penalties $K=5, 9$, the enterprise has a longer time to stabilize the strategy. At the same time, with the increasing awareness and enthusiasm of enterprises to adopt BIM technology, the government has achieved the purpose of promotion, and its strategy of adopting penalty measures to actively promote BIM technology has gradually turned to the strategy of passive promotion; that is, the game system is going to the stable point $B(0, 1)$ evolution. Therefore, judging from the simulation results, the necessary fines have a positive effect on enterprises’ active adoption of BIM technology. The amount of government fines has little effect on the time to reduce their tendency to passive strategies, but companies are very sensitive, especially when the fine $K=20$. Companies will soon tend to actively adopt stable strategies in this case. Therefore, the government plays an active role in the diffusion of BIM technology, and the implementation of reasonable fines can effectively promote the adoption of BIM technology. In addition, the fines of government for enterprises should take into account the size of the

enterprise, and the fines for extra large and large enterprises should be relatively high, which can be relatively reduced for small- and medium-sized enterprises, thereby enhancing the effectiveness of the fines.

- (2) The sensitivity analysis of government and enterprises to subsidy management cost C_1 (C_1 is both the cost of the government and the benefit of the enterprise) is necessary because of the government's active initiative to promote BIM technology. The initiative of the government is an effective means for diffusing and developing new technology and also has a positive effect on the choice of enterprise strategy. Let $C_1 = 10, 15, 20$; the evolution of the BIM technology diffusion game system is shown in Figure 3.

It can be seen from Figure 3 that when $C_1 = 10, 15, 20$, the higher the government's subsidies to enterprises at this time, the higher the government's stability, and the sensitivity of enterprises to government subsidies is not high, the time for the three C_1 values to stabilize is basically the same, and the time is later, but in the end, the strategies of the government and enterprises have evolved to the stable point B (0, 1). The government has to pay a certain amount of subsidies for enterprises. From the simulation results, with the increase of subsidies, the government will move toward a strategy of negative advancement earlier. Since BIM technology itself is a social technology system, enterprises adopt BIM technology; they not only consider the direct cost of BIM technology but also need to pay more attention to the indirect cost after adoption [41]. Government subsidies for enterprises are often a small part of the direct costs and do not include high indirect costs such as BIM talent training, BIM expert introduction, and BIM system operation and maintenance. Therefore, government subsidies will promote the active adoption of enterprises, but they cannot make enterprises. Soon, it will tend to a stable state. Therefore, the government's subsidies for enterprises are indispensable, which can increase the enthusiasm of enterprises to actively adopt BIM technology. The government should also consider the indirect costs after the enterprises adopt them and give them corresponding subsidies, which will greatly increase the effect of subsidies.

- (3) The sensitivity analysis of government and enterprise on input cost C_2 : input cost is one of the important factors that affect the promotion of BIM technology diffusion by enterprises, and it is also the basis of government subsidies and incentives to promote voluntary adoption by enterprises. Let $C_2 = 15, 10, 30$; the evolution of the BIM technology diffusion game system is shown in Figure 4.

As can be seen from Figure 4, the government and enterprises are highly sensitive to BIM technology

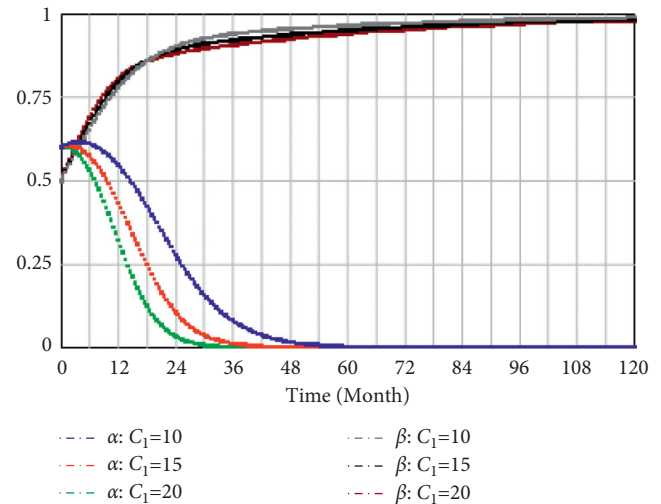


FIGURE 3: Government and enterprise sensitivity analysis of (C_1) value.

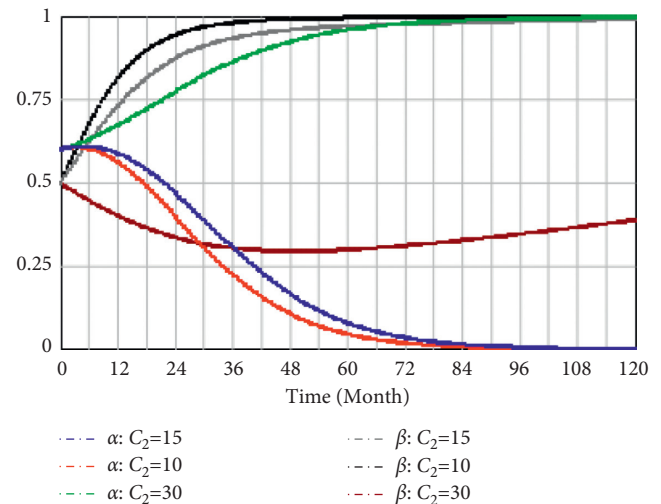


FIGURE 4: The sensitivity analysis of government and enterprises to (C_2) value.

input costs. When the input cost is not high, the strategy of the government and enterprises chooses to evolve to the stable point B (0, 1); when the input cost is high and the profit is not much different, the BIM technology diffusion game system goes to D (1, 0) stable evolution and then to C (1, 1) stable evolution. The simulation results show that when $C_2 = 30$, the enterprise chooses a passive adoption strategy, and the government chooses an active promotion strategy to promote the diffusion of BIM technology; with the enhancement of the government's promotion role, the enterprise gradually evolves into an actively adopted strategy. In practice, the reason why enterprises adopt BIM technology is because of its high economic benefits. When the benefits are small and the cost is large, enterprises usually ignore it; however, the purpose of government to promote the diffusion of BIM

technology is not only to promote economic benefits such as economic development and accelerating informatization construction but also to include ecological benefits such as environmental protection and resource conservation. When the cost of BIM technology is low, the enterprise itself can accept it, and the government often adopts a passive promotion strategy; once the cost of BIM technology is high when the enterprise refuses to adopt it, the government will adopt a series of positive strategies to encourage enterprises to adopt BIM technology. Therefore, when promoting the diffusion of BIM technology, enterprises should actively understand the successful cases of applying BIM to avoid a large number of controllable costs when applying BIM technology, so as to obtain higher profits, and enterprises will also promote BIM technology more actively. The research and development of BIM technology should be increased, and the improvement of BIM standards and specifications should be accelerated to reduce the cost and efficiency of enterprise applications and promote the diffusion of BIM technology.

- (4) The sensitivity analysis of the government and enterprises to the input income B : the income from investing in BIM technology is the second important factor that affects the diffusion of BIM technology, and it also affects the government's strategic choices. Let $B' = 35, 20, 50$; the evolution of the BIM technology diffusion game system is shown in Figure 5.

It can be seen from Figure 5 that the BIM technology diffusion game system has a high sensitivity to the BIM technology investment income. The strategy of government and enterprise tends to be stable point $B(0, 1)$ when the return on input is high; when the input income is low and the cost is not much different, the BIM technology diffusion game system goes to $D(1, 0)$ stable evolution and then to $C(1, 1)$ stable evolution. Compared with Figure 4, the input cost is higher and the input income is smaller. The strategic choices for the government and the enterprise are the same, and eventually, all evolve steadily toward $C(1, 1)$. From the numerical simulation results, when $B' = 35, 50$, the government and enterprises' strategy selection rate is very high in a relatively short period of time, and the strategies of passive promotion and active adoption are evolved; when $B' = 20$, both the government and enterprises will evolve at a relatively slow pace to actively promote and passively adopt strategies. The government will reach a stable state much faster than enterprises. It can be seen from the prospect theory that when the prospects for the development of BIM technology are unknown or there are many uncertainties, decision-makers often adopt a conservative strategy, that is, a risk-avoidance strategy. Therefore, it will take a long time for companies to shift from the concept of lower returns to BIM technology to the concept of higher returns. As shown in Figure 5, it will take a long period for companies to reach a stable state. But when the enterprise reaches a stable state, the government and the enterprise will evolve to the stable point $B(0, 1)$. In order to avoid the above situation, the

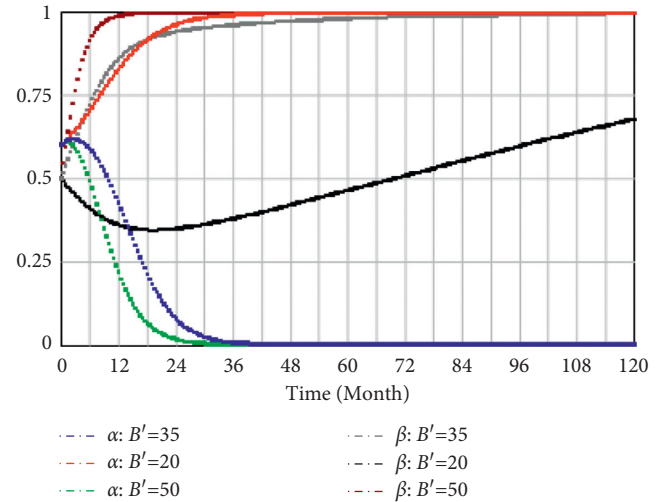


FIGURE 5: The sensitivity analysis of government and enterprises to $(B)'$ value.

government should actively do BIM publicity work, training work, incentive work, subsidy work, etc., and companies should also strengthen the understanding and learning of BIM, conduct BIM seminars and exchanges, at the same time, make a clear definition of the high investment cost of BIM technology, and do a financial impact analysis.

5. Conclusions and Recommendations

BIM technology diffusion evolution game model is constructed and system dynamics software simulation analysis is carried out in this paper. The research shows that the two most sensitive factors of BIM technology diffusion are input income and input cost. The government's penalty on enterprises has a positive impact on the diffusion of BIM technology, while the subsidy cannot promote the effective diffusion of BIM technology among enterprises quickly. The game system eventually evolves to the stable point $(0, 1)$, when the time for the government to reach the stable strategy is shortened.

Based on the above research results, the following suggestions are proposed to improve the diffusion level of BIM technology in China:

- (1) The subsidy should pay more attention to the indirect costs after the adoption of BIM. While providing direct cost subsidies to adopting enterprises, the government should also pay attention to indirect costs such as talent training, expert introduction, and system maintenance that enterprises need to pay after adopting BIM technology; at the same time, they should take the lead in organizing BIM technology and management personnel training to ensure the successful application of BIM. The project will issue bonuses and certificates to accelerate the adoption and application of BIM technology by enterprises.
- (2) Improving the punishment mechanism and highlighting the pertinence of punishment: in the slow

stage of the proliferation of BIM technology, the government should improve the penalty mechanism as soon as possible to distinguish between enterprises of different sizes; the scope of mandatory application of BIM technology is not limited to large public buildings but should also be applied to residential buildings and industrial buildings. The government should make corresponding regulations and requirements, set up corresponding punishment regulations, and promote the proliferation of BIM technology.

- (3) Clarifying the definition of high BIM investment cost and doing a good job of financial impact analysis: enterprises should have a clear understanding of the high investment cost of BIM technology, make clear definitions, and do a good job of financial analysis, so as to increase the willingness and enthusiasm of enterprises to adopt BIM technology.

Data Availability

The data are generated from experiments and can be available upon request to the author.

Conflicts of Interest

The author declares that there are no conflicts of interest.

References

- [1] E. Alreshidi, M. Mourshed, and Y. Rezgui, "Requirements for cloud-based BIM governance solutions to facilitate team collaboration in construction projects," *Requirements Engineering*, vol. 23, no. 1, pp. 1–31, 2018.
- [2] H. Xiao and H. Wang, "Asymmetric evolutionary game study on low-carbon environmentally friendly technological innovation diffusion," *China Science and Technology Forum*, vol. 8, pp. 20–27, 2017.
- [3] Z. Liu, G. Pu, Y. Shi, J. Yan, and J. Hu, "Simulation analysis and evaluation of carbon emission reduction scenarios in the iron and steel industry," *China Population, Resources and Environment*, vol. 22, no. 3, pp. 77–81, 2012.
- [4] M. Rogers Everett, *Diffusion of Innovations*, vol. 12, New York, US, 1995.
- [5] V. Singh and J. Holmström, "Needs and technology adoption: observation from BIM experience," *Engineering Construction and Architectural Management*, vol. 22, no. 2, pp. 128–150, 2015.
- [6] Y. Chen, K. D. Ruikar, and P. M. Carrillo, "Strategic e-business framework: a holistic approach for organisations in the construction industry," *Journal of Information Technology in Construction*, vol. 18, pp. 306–320, 2013.
- [7] P. Grover, A. K. Kar, and M. Janssen, "Diffusion of blockchain technology," *Journal of Enterprise Information Management*, vol. 32, 2019.
- [8] Y. Le, X. Zheng, Y. Li, Y. Lu, and J. Bai, "Research on application value stream and driving path of BIM technology based on SVN," *Journal of Management in Engineering*, vol. 32, no. 1, pp. 71–78, 2018.
- [9] J. Cao, X. Wu, G. Zhou, and Q. Hu, "Game analysis in the process of green product innovation and diffusion in manufacturing enterprises," *Journal of Systems Engineering*, vol. 27, no. 5, pp. 617–625, 2012.
- [10] T. Frohwein and B. Hansjürgens, "Chemicals regulation and the porter hypothesis – a critical review of the new European chemical regulation," *Journal of Business Chemistry*, vol. 2, no. 1, pp. 19–36, 2005.
- [11] V. Peansupap and D. H. T. Walker, "Factors enabling information and communication technology diffusion and actual implementation in construction organizations," *Journal of Information Technology in Construction*, vol. 10, no. 14, pp. 193–218, 2005.
- [12] V. Peansupap and D. H. T. Walker, "Innovation diffusion at the implementation stage of a construction project: a case study of information communication technology," *Construction Management & Economics*, vol. 24, no. 3, pp. 321–332, 2006.
- [13] K. Panuwatwanich and R. A. Stewart, "Evaluating innovation diffusion readiness among architectural and engineering design firms: empirical evidence from Australia," *Automation in Construction*, vol. 27, pp. 50–59, 2012.
- [14] C. Merschbrock and B. E. Munkvold, "Effective digital collaboration in the construction industry – a case study of BIM deployment in a hospital construction project," *Computers in Industry*, vol. 73, pp. 1–7, 2015.
- [15] J. Ma, X. Li, J. Wang et al., "Experimental study on vibration reduction technology of hole-by-hole presplitting blasting," *Geofluids*, vol. 18, 2021.
- [16] C. E. Lacia and S. L. Rovere, "Ising-like agent-based technology diffusion model: adoption patterns vs. seeding strategies," *Physica A: Statistical Mechanics and its Applications*, vol. 390, no. 6, pp. 1139–1149, 2011.
- [17] P. Wang, G. Wang, and D. Tan, "Research on the diffusion and application obstacles of BIM technology," *Construction Economy*, vol. 39, no. 4, pp. 12–16, 2018.
- [18] B. Sun, X. Su, and X. Xu, "Research on technology diffusion and evolution based on new technology adoption decision game," *Industrial Technology and Economics*, vol. 38, no. 6, pp. 10–19, 2019.
- [19] C. Mark, "An updated empirical model for ground control in U.S. multiseam coal mines," *International Journal of Mining Science and Technology*, vol. 31, no. 02, pp. 163–174, 2021.
- [20] H. Rafezi and F. Hassani, "Drilling signals analysis for tricone bit condition monitoring," *International Journal of Mining Science and Technology*, vol. 31, no. 02, pp. 187–195, 2021.
- [21] X. Liu, S. Song, Y. Tan et al., "Similar simulation study on the deformation and failure of surrounding rock of a large section chamber group under dynamic loading[]," *International Journal of Mining Science and Technology*, vol. 31, no. 3, pp. 495–505, 2021a.
- [22] X. Liu, D. Fan, Y. Tan et al., "New detecting method on the connecting fractured zone above the coal face and a case study []," *Rock Mechanics and Rock Engineering*, vol. 54, 2021b.
- [23] X. Liu, D. Fan, Y. Tan et al., "Failure evolution and instability mechanism of surrounding rock for close-distance parallel chambers with super-large section in deep coal mines[]," *International Journal of Geomechanics*, vol. 21, no. 5, Article ID 04021049, 2021c.
- [24] J. Wang, T. Zuo, X. Li, Z. Tao, and J. Ma, "Study on the fractal characteristics of the pomegranate biotite schist under impact loading," *Geofluids*, vol. 21, 2021.
- [25] K. Ranjan, P. K. Mandal, A. Narayan, and A. Jyoti Das, "Evaluation of load transfer mechanism under axial loads in a novel coupler of dual height rock bolts," *International Journal of Mining Science and Technology*, vol. 31, no. 02, pp. 225–232, 2021.

- [26] J. Yang, H. Lian, and L. Li, "Investigating the effect of confining pressure on fracture toughness of CO₂-saturated coals," *Engineering Fracture Mechanics*, vol. 242, no. 6266, Article ID 107496, 2020.
- [27] J. Yang, H. Lian, and V. P. Nugyen, "Study of mixed mode I/II cohesive zone models of different rank coals," *Engineering Fracture Mechanics*, vol. 246, Article ID 107611, 2021.
- [28] W. Hou, H. Wang, L. Yuan, W. Wang, X. Yang, and Z. Ma, "Experimental research into the effect of gas pressure, particle size and nozzle area on initial gas-release energy during gas desorption," *International Journal of Mining Science and Technology*, vol. 31, no. 02, pp. 253–263, 2021.
- [29] W. Tang, Z. Cheng, J. Xu, Y. Sun, Y. Cong, and Y. Zheng, "The influence of borehole arrangement of soundless cracking demolition agents(SCDAs) on weakening the hard rock," *International Journal of Mining Science and Technology*, vol. 31, no. 02, pp. 197–207, 2021.
- [30] Y. Zhou, D. Zhao, B. Li, Q. Tang, and Z. Zhang, "Fatigue damage mechanism and deformation behaviour of granite under ultrahigh-frequency cyclic loading conditions," *Rock Mechanics and Rock Engineering*, vol. 54, pp. 4723–4739, 2021.
- [31] R. Guan, "The ministry of housing and urban-rural development issued the "guiding opinions on promoting the application of building information models"," *Construction Workers*, vol. 36, no. 8, p. 50, 2015.
- [32] K. Kang, *Theory and Model of Technological Innovation Diffusion*, Tianjin University Press, Tianjin, China, 2004.
- [33] Y. Ma, X. Su, and Y. Zhao, "Evolutionary game analysis of industrial common technology diffusion," *Control Theory & Applications*, vol. 36, no. 1, pp. 22–31, 2019.
- [34] G. Heutel, "Prospect theory and energy efficiency," *Journal of Environmental Economics and Management*, vol. 96, pp. 236–254, 2019.
- [35] Li Yu, B. Wu, and C. Wang, "Evolutionary game analysis of behavior decision of crowdsourcing logistics distributor based on prospect theory—based on the perspective of shipper," *Operations Research and Management*, vol. 6, pp. 129–135, 2019.
- [36] R. Fan, *Game Theory*, Wuhan University Press, Wuhan, China, 2011.
- [37] D. Friedman, "On economic applications of evolutionary game theory," *Journal of Evolutionary Economics*, vol. 8, no. 1, pp. 15–43, 1998.
- [38] Y. Hu and Q. Shen, "A system dynamics study on the development of Hong Kong housing industry," *System Engineering Theory and Practice*, vol. 7, pp. 32–37, 2001.
- [39] Y. Yuan, Y. Tian, and J. Sun, "System dynamics modeling and simulation of the stability of industry-university-research technology alliance," *Science Science and Technology Management*, vol. 34, no. 4, pp. 3–9, 2013.
- [40] K. Li, Y. Zhang, G. Jin, S. Yuebin, and X. Ge, "System dynamics analysis of high-speed rail operation safety supervision game evolution," *Journal of Southwest Jiaotong University*, vol. 54, no. 3, pp. 579–586, 2019.
- [41] P. E. D. Love, I. Simpson, A. Hill, and C. Standing, "From justification to evaluation: building information modeling for asset owners," *Automation in Construction*, vol. 35, pp. 208–216, 2013.

Research Article

Coriolis Force Sliding Mode Control Method for the Rotary Motion of the Central Rigid Body-Flexible Cantilever Beam System in TBM

Chuanlu Zhou,¹ Long Qin ,^{1,2} Ming Chen,¹ and Jingxiang Zhang¹

¹China Railway 14th Bureau Group Mega Shield Construction Engineering Co., Ltd, Nan Jing 210000, China

²School of Mechanical Engineering, Hangzhou Dianzi University, Hangzhou 310018, China

Correspondence should be addressed to Long Qin; wzw3049972460@hdu.edu.cn

Received 22 October 2021; Revised 15 November 2021; Accepted 18 November 2021; Published 23 December 2021

Academic Editor: Qinghua Zhang

Copyright © 2021 Chuanlu Zhou et al. This is an open access article distributed under the Creative Commons Attribution License, which permits unrestricted use, distribution, and reproduction in any medium, provided the original work is properly cited.

Beam slab structure is often encountered in a complex tunnel boring machine. Beam slab structure is subject to dynamic load, which is easy to cause fatigue damage and affect its service life. Therefore, it is necessary to control the vibration of this kind of beam slab structure. In this study, the central rigid body-flexible beam model is established for the rotating beam and plate rotating around the y -axis. Based on the Hamilton variational principle, the dynamic equation of the central rigid body-flexible beam system is established, and the dynamic model of the central rigid body-flexible beam system considering the influence of Coriolis force and centrifugal force is given. The vibration control of the central rigid body-flexible beam system is studied. The vibration mode of the rotating Euler Bernoulli beam is determined by using the elastic wave and vibration mode theory. The influence of the rotating motion on the beam vibration is analyzed, and the variable structure control law is designed to suppress the beam vibration. Numerical simulation results show that the control method can effectively suppress the first-order and second-order vibration of the beam and verify the effectiveness of the control strategy.

1. Introduction

With the development of shield technology, superlarge diameter tunnel boring machine (TBM) is frequently used in civil construction and production. However, various vibrations during operation and tunneling have caused damage to the components in the TBM and difficult maintenance, which has increased safety during construction. Risks delay in the construction period. TBM usually has large flexible attachments. These flexible attachments have the characteristics of large span, light weight, low rigidity, weak structural damping, and low rigidity of the connection between the plates [1, 2]. During the operation of the TBM and the tunneling process, certain disturbance can easily arouse the vibration of the structure. Such vibration is not easy to be found in the complex underground environment, and the vibration may last for a long time [3–5]. This will not only directly affect the normal operation of the shield but also cause fatigue of such

structures in the TBM, affect the service life of the structure, and even cause structural damage. Therefore, the attitude adjustment of the TBM and the suppression of the lateral vibration of the flexible attachment have extremely important engineering significance.

The precise dynamic modeling of the structural system is directly related to the motion control strategy and control effect of the system. At present, in the dynamic analysis and vibration control of mechanical arms and rotating machinery, when the flexible beam plate rotates as shown in Figure 1, the central rigid body-flexible beam model [6–8] is widely used. The effects of Coriolis force and centrifugal force are not considered in the state analysis, which will cause large errors in the calculation and analysis. Therefore, the study of active vibration control of rotating beams and plates and the establishment of a more accurate model that reflects the vibration state of the structure is an important way to optimize the control method.

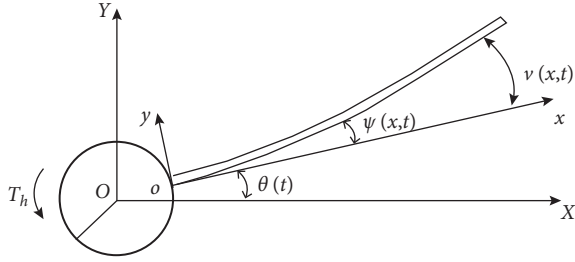


FIGURE 1: Model of the flexible hub-beam.

On the other hand, the coupling of rigid body rotation and flexural vibration of the flexible attachment will cause the system to be affected by centrifugal force and Coriolis force, which will cause the entire motion system to have time-varying and nonlinear characteristics. Look for a robust control strategy. It has become a hot issue in the vibration control of the central rigid body-flexible beam plate model [9–11]. The sliding mode variable structure control strategy is a robust control method, and it is currently widely used in active vibration control based on a central rigid body-flexible beam model [12–15].

Based on the Hamilton variational principle, this study adopts the Euler–Bernoulli beam theory to establish the dynamic equation of the central rigid body-flexible beam system for the rotating plate in which the rotating motion shown in Figure 1 occurs, and the centrifugal force and Coriolis force are considered in the modeling of the flexible attachment. Using elastic wave and vibration mode theory, the vibration mode of Euler–Bernoulli beam affected by Coriolis force is determined. The method of constant velocity approaching law is adopted to design the variable structure control law, and the control force is designed on the flexible attachment to suppress its lateral vibration.

2. Dynamic Model System

According to the movement state of the rotating plate, the model of the central rigid body-flexible beam system is shown in Figure 1. In the figure, $O-XY$ is a fixed inertial coordinate system, and $o-xy$ is a conjoined noninertial coordinate system. The radius of the central rigid body is R_h . The moment of inertia is J_h . The length, height, and mass density of the beam are L , h , and ρ . The load density of the control force is $f(x, t)$. The control torque is T_h . The angular displacement of the rigid body is θ . The lateral displacement of the beam is $v(x, t)$. The Euler–Bernoulli beam theory is used in the dynamic analysis of the system, ignoring the influence of gravity and external disturbances.

During the rotational movement, the displacement of any point $(x, 0)$ on the beam relative to the fixed inertial coordinate system $O-XY$ can be described as

$$p = [-v \sin \theta - (R_h + x)(1 - \cos \theta)]i + [v \cos \theta + (R_h + x)\sin \theta]j. \quad (1)$$

When calculating the kinetic energy, the longitudinal deformation of the beam in motion is ignored. The total kinetic energy of the structure is the sum of the rotational

kinetic energy of the central rigid body and the kinetic energy of the beam. Therefore, the total kinetic energy of the structural system is

$$\begin{aligned} E_k &= \frac{1}{2}\rho h \int_0^L \dot{p}^2 dx + \frac{1}{2}J_h \dot{\theta}^2 \\ &= \frac{1}{2}\rho h \int_0^L \left\{ (-\dot{\theta}v)^2 + [\dot{v} + \dot{\theta}(R_h + x)]^2 \right\} dx + \frac{1}{2}J_h \dot{\theta}^2. \end{aligned} \quad (2)$$

The bending strain energy of the structure is

$$E_p^{(1)} = \frac{1}{2}D \int_0^L \psi'^2 dx, \quad (3)$$

where $D = EI_b$ is the bending stiffness of the beam. I_b is the moment of inertia of the beam. ψ is the corner of the beam section, and ψ' is the derivative of space variable x .

When the flexible beam vibrates under the action of centrifugal force, it must overcome the centrifugal force to do work. When the beam vibrates, any cell dm on the beam moves Δx to the center O . For different microelement segments, Δx is different. Therefore, the deformation energy generated by the centrifugal force on the beam is

$$E_p^{(2)} = \int \Delta x df_{ce} = \rho h \dot{\theta}^2 \int_0^L \Delta x (R_h + x) dx, \quad (4)$$

where $df_{ce} = \rho h \dot{\theta}^2 (R_h + x) dx$ is the centrifugal force received by the microelement, and Δx is the amount of shortening of the structure in the axial direction caused by the lateral displacement.

$$\Delta x = \frac{1}{2} \int_0^x \left(\frac{\partial v}{\partial \zeta} \right)^2 d\zeta. \quad (5)$$

The deformation energy of the Coriolis force on the beam is

$$E_p^{(3)} = \int v df_{c1} + \int \Delta x df_{c2} = 2\rho h \dot{\theta} \int_0^L (v \Delta \dot{x} + \dot{v} \Delta x) dx, \quad (6)$$

where $df_{c1} = -2\rho h \dot{\theta} \Delta \dot{x} dx$ is the Coriolis force that the infinite element receives in the tangential direction, and $df_{c2} = -2\rho h \dot{\theta} \Delta \dot{v} dx$ is the Coriolis force received by the infinite element in the axial direction.

The work done by the external control force is

$$W = T_h \theta + \int_0^L f(x, t) v(x, t) dx + \int_0^L (R_h + x) f(x, t) \theta dx, \quad (7)$$

where $f(x, t)$ is the distributed load density of the beam, which can be expressed as

$$f(x, t) = \sum_{i=1}^k F_i(t) \delta(x - x_i), \quad (8)$$

where F_i is the concentrated force on the beam where the abscissa is x_i .

The Hamilton principle of the system is

$$\int_{t_0}^{t_f} \delta(E_k - E_p + W) dt = 0. \quad (9)$$

Substituting (2)–(8) into (9), the dynamic equation of the central rigid body-flexible beam system is obtained as follows:

$$\int_0^L \rho h [\theta v^2 + (R_h + x)^2 \ddot{\theta} - 2(R_h + x) \ddot{\theta} \Delta x + (R_h + x) \dot{v} - 2\dot{v} \Delta x + 2\dot{\theta} v \dot{v} + 2(R_h + x) \dot{\theta} \Delta \dot{x} + 2v \Delta \ddot{x}] dx + J_h \ddot{\theta} = T_h + \sum_{i=1}^k F_i(t)(R_h + x)_i, \quad (10a)$$

$$\int_0^L (J_b \ddot{\psi} - D \psi'') dx = 0, \quad (10b)$$

$$\int_0^L \left\{ \rho h [(R_h + x) \ddot{\theta} - 2\ddot{\theta} \Delta x + \dot{v} - \dot{\theta}^2 v - 4\dot{\theta} \Delta \dot{x}] + \frac{\partial}{\partial x} \left[v' \int_x^L D_0(x, t) dx \right] + D \psi''' - f(x, t) \right\} dx = 0, \quad (10c)$$

where

$$D_0(x, t) = -\rho h [(R_h + x) \dot{\theta}^2 + 4\dot{\theta} \dot{v} + 2\dot{\theta} v]. \quad (11)$$

The boundary conditions of the flexible beam are the lateral displacement of any point on the beam that can be written as

$$v(x, t) = \sum_{i=1}^n \varphi_i(x) q_i(t) = \Phi \mathbf{q}, \quad (12)$$

where $\Phi = [\varphi_1 \ \varphi_2 \ \dots \ \varphi_n]$, $\mathbf{q} = [q_1 \ q_2 \ \dots \ q_n]^T$, and $\varphi_i(x)$ and $q_i(t)$ are the i^{th} modal function and modal coordinates corresponding to the lateral displacement of the flexible beam.

Therefore, the dynamic equation of the central rigid body-flexible beam system can be further written as

$$\begin{bmatrix} M_{\theta\theta} & \mathbf{M}_{\theta q} \\ \mathbf{M}_{q\theta} & \mathbf{M}_{qq} \end{bmatrix} \begin{bmatrix} \ddot{\theta} \\ \ddot{\mathbf{q}} \end{bmatrix} + \begin{bmatrix} 0 & \mathbf{0} \\ \mathbf{0} & \mathbf{K}_{qq} \end{bmatrix} \begin{bmatrix} \theta \\ \mathbf{q} \end{bmatrix} + \begin{bmatrix} \mathbf{Q}_\theta \\ \mathbf{0} \end{bmatrix} = \begin{bmatrix} T_1 \\ T_2 \end{bmatrix}, \quad (13)$$

where $M_{\theta\theta} \in R^1$ is the total moment of inertia of the system; $\mathbf{M}_{q\theta} \in R^{n \times 1}$, $\mathbf{M}_{\theta q} \in R^{n \times 1}$ is the nonlinear inertial coupling between the rotational movement of the system and the lateral movement of the beam; $\mathbf{M}_{qq} \in R^{n \times n}$ is the mass matrix of the flexible beam; $\mathbf{K}_{qq} \in R^{n \times n}$ is the stiffness matrix; and $\mathbf{Q}_\theta \in R^1$ is the inertial force term generated by the coupling of the rotation of the microelement and the lateral movement of the beam. Their specific expression forms are as follows:

$$M_{\theta\theta} = J_h + J_0 + \mathbf{q}^T \mathbf{M}_1 \mathbf{q} - \mathbf{q}^T \mathbf{M}_2 \mathbf{q}, \quad (14a)$$

$$\mathbf{M}_{q\theta}^T = \mathbf{M}_{\theta q} = \mathbf{M}_3 \quad (14b)$$

$$\mathbf{M}_{qq} = \mathbf{M}_1 \quad (14c)$$

$$\mathbf{K}_{qq} = -\dot{\theta}^2 (\mathbf{M}_1 - \mathbf{M}_2) + \mathbf{M}_4 \quad (14d)$$

$$\tilde{\mathbf{Q}}_\theta = 2\dot{\theta} \dot{\mathbf{q}}^T (\mathbf{M}_1 - \mathbf{M}_2) \dot{\mathbf{q}} \quad (14e)$$

$$\tilde{T}_1 = \tilde{T}_h + \sum_{i=1}^k \tilde{F}_i(\tilde{t})(\tilde{R}_h + \tilde{x}_i), \quad \tilde{T}_2 = \sum_{i=1}^k \tilde{F}_i(\tilde{t}) \tilde{\Phi}^T(\tilde{x}_i), \quad (14f)$$

where $J_0 = \int_0^L \rho h (R_h + x)^2 dx$, $\mathbf{M}_1 = \int_0^L \rho h \Phi^T \Phi dx$, $\mathbf{M}_2 = \int_0^L \rho h (R_h + x) \mathbf{D}_1 dx$, $\mathbf{M}_3 = \int_0^L \rho h (R_h + x) \Phi dx$, $\mathbf{M}_4 = \int_0^L D \Phi^T \Phi''' dx$, $\Delta x = 1/2 \int_0^x v'^2(x, t) dx = 1/2 \mathbf{q}^T \mathbf{D}_1 \mathbf{q}$, $\mathbf{D}_1 = \int_0^x \Phi'^T \Phi' dx$.

Define the dimensionless parameters $\tilde{t} = t \sqrt{EI/\rho h}/L^2$, $\tilde{j}_h = j_h/\rho h L^3$, $\tilde{\theta} = \dot{\theta} L^2 \sqrt{\rho h/EI}$, $\tilde{T}_1 = LT_1/EI$, $\tilde{T}_2 = L^2 T_2/EI$, $\tilde{x} = x/L$, $\tilde{R}_h = R_h/L$, $\tilde{h} = h/L$, and $\tilde{\mathbf{q}} = \mathbf{q}/L$. Then, the dynamic equation of the system in dimensionless form can be expressed as

$$\begin{bmatrix} \tilde{M}_{\theta\theta} & \tilde{\mathbf{M}}_{\theta q} \\ \tilde{\mathbf{M}}_{q\theta} & \tilde{\mathbf{M}}_{qq} \end{bmatrix} \begin{bmatrix} \ddot{\tilde{\theta}} \\ \ddot{\tilde{\mathbf{q}}} \end{bmatrix} + \begin{bmatrix} 0 & 0 \\ 0 & \tilde{\mathbf{K}}_{qq} \end{bmatrix} \begin{bmatrix} \tilde{\theta} \\ \tilde{\mathbf{q}} \end{bmatrix} + \begin{bmatrix} \tilde{\mathbf{Q}}_\theta \\ \mathbf{0} \end{bmatrix} = \begin{bmatrix} \tilde{T}_1 \\ \tilde{T}_2 \end{bmatrix}. \quad (15)$$

The expression for the dimensionless parameter is

$$\tilde{M}_{\theta\theta} = \tilde{j}_h + \tilde{j}_0 + \tilde{\mathbf{q}}^T \tilde{\mathbf{M}}_1 \tilde{\mathbf{q}} - \tilde{\mathbf{q}}^T \tilde{\mathbf{M}}_2 \tilde{\mathbf{q}}, \quad (16a)$$

$$\begin{aligned} \tilde{\mathbf{M}}_{q\theta}^T &= \tilde{\mathbf{M}}_{\theta q} \\ &= \tilde{\mathbf{M}}_3, \end{aligned} \quad (16b)$$

$$\tilde{\mathbf{M}}_{qq} = \tilde{\mathbf{M}}_1, \quad (16c)$$

$$\tilde{\mathbf{K}}_{qq} = -\dot{\tilde{\theta}}^2 (\tilde{\mathbf{M}}_1 - \tilde{\mathbf{M}}_2) + \tilde{\mathbf{M}}_4, \quad (16d)$$

$$\tilde{\mathbf{Q}}_\theta = 2\dot{\tilde{\theta}} \dot{\tilde{\mathbf{q}}}^T (\tilde{\mathbf{M}}_1 - \tilde{\mathbf{M}}_2) \dot{\tilde{\mathbf{q}}}, \quad (16e)$$

$$\tilde{T}_1 = \tilde{T}_h + \sum_{i=1}^k \tilde{F}_i(\tilde{t})(\tilde{R}_h + \tilde{x}_i), \quad \tilde{T}_2 = \sum_{i=1}^k \tilde{F}_i(\tilde{t}) \tilde{\Phi}^T(\tilde{x}_i), \quad (16f)$$

where $\tilde{J}_0 = \int_0^1 (\tilde{R}_h + \tilde{x})^2 d\tilde{x}$, $\tilde{M}_1 = \int_0^1 \tilde{\Phi}^T \tilde{\Phi} d\tilde{x}$, $\tilde{M}_2 = \int_0^1 (\tilde{R}_h + \tilde{x}) \tilde{D}_1 d\tilde{x}$, $\tilde{M}_3 = \int_0^1 (\tilde{R}_h + \tilde{x}) \tilde{\Phi} d\tilde{x}$, $\tilde{M}_4 = \int_0^1 \tilde{\Phi}^T \tilde{\Phi} d\tilde{x}$, $\Delta \tilde{x} = 1/2 \tilde{q}^T \tilde{D}_1 \tilde{q}$, and $\tilde{D}_1 = \int_0^{\tilde{x}} \tilde{\Phi}^T \tilde{\Phi}' d\tilde{x}$.
Let $\mathbf{Y} = \begin{bmatrix} \theta \\ \tilde{\mathbf{q}}^T \end{bmatrix}^T$; then, there is

$$\begin{bmatrix} \tilde{M}_{\theta\theta} & \tilde{M}_{\theta q} \\ \tilde{M}_{q\theta} & \tilde{M}_{qq} \end{bmatrix} \ddot{\mathbf{Y}} + 2\dot{\theta} \begin{bmatrix} 0 & \tilde{\mathbf{G}}_{\theta q} \\ 0 & 0 \end{bmatrix} \dot{\mathbf{Y}} + \begin{bmatrix} 0 & 0 \\ 0 & \tilde{\mathbf{K}}_{qq} \end{bmatrix} \mathbf{Y} = \begin{bmatrix} \tilde{T}_1 \\ \tilde{T}_2 \end{bmatrix}, \quad (17)$$

where $\tilde{\mathbf{G}}_{\theta q} = \tilde{\mathbf{q}}^T (\tilde{\mathbf{M}}_1 - \tilde{\mathbf{M}}_2)$. Let $\mathbf{X} = \begin{bmatrix} \mathbf{Y}^T & \dot{\mathbf{Y}}^T \end{bmatrix}^T$, $\tilde{\mathbf{M}} = \begin{bmatrix} \tilde{M}_{\theta\theta} & \tilde{M}_{\theta q} \\ \tilde{M}_{q\theta} & \tilde{M}_{qq} \end{bmatrix}$, $\tilde{\mathbf{G}} = \begin{bmatrix} 0 & \tilde{\mathbf{G}}_{\theta q} \\ 0 & 0 \end{bmatrix}$, $\mathbf{K} = \begin{bmatrix} 0 & 0 \\ 0 & \tilde{\mathbf{K}}_{qq} \end{bmatrix}$, $\tilde{\mathbf{F}} = \begin{bmatrix} 1 & \tilde{R}_h + \tilde{x}_1 & \dots & \tilde{R}_h + \tilde{x}_k \\ 0 & \tilde{\Phi}^T(\tilde{x}_1) & \dots & \tilde{\Phi}^T(\tilde{x}_k) \end{bmatrix}$.

Then, the above formula can be further expressed as

$$\dot{\mathbf{X}} = \begin{bmatrix} \mathbf{0} & \mathbf{I} \\ -\tilde{\mathbf{M}}^{-1} \tilde{\mathbf{K}} & -2\dot{\theta} \tilde{\mathbf{M}}^{-1} \tilde{\mathbf{G}} \end{bmatrix} \mathbf{X} + \begin{bmatrix} \mathbf{0} \\ \tilde{\mathbf{M}}^{-1} \mathbf{U} \tilde{\mathbf{F}} \end{bmatrix}, \quad (18)$$

where $\tilde{\mathbf{F}}$ is the actuator distribution matrix, $\mathbf{U} = \begin{bmatrix} \tilde{T}_h & \tilde{F}_1 & \dots & \tilde{F}_k \end{bmatrix}^T$.

3. Modal Analysis of Central Rigid Body-Flexible Beam

When solving the beam mode, ignore the axial shortening caused by the lateral displacement and the external force $f(x,t)$ of the system, and consider the uniform rotation stage of the spacecraft's attitude adjustment, that is, the case where $\dot{\theta} = \Omega$ is a constant. From (10b), the dynamic equation of Euler-Bernoulli beam considering the influence of Coriolis force is

$$\rho h (-\Omega^2 v + \ddot{v}) + D \psi'''' = 0. \quad (19)$$

Let $v(x,t) = \varphi(x)e^{i\omega t}$ bring in the above data to get

$$D \frac{\partial^4 \varphi}{\partial x^4} - \rho h (\omega^2 + \Omega^2) \varphi = 0. \quad (20)$$

According to the elastic wave propagation theory and (20), the spatial wave number of the mode function $\varphi(x)$ should satisfy the following equation:

$$k^4 - \frac{\rho h}{D} (\omega^2 + \Omega^2) = 0. \quad (21)$$

When the elastic wave number $k_i^2 \geq 0$ ($i = 1, 2$), it means that there are two pairs of propagating waves in the structural beam, and its phase velocity is $c = \omega/k$; when the elastic wave number $k_1^2 > 0$ and $k_2^2 < 0$, it means that there are a pair of propagating waves and a pair of attenuating waves in the structural beam. Since the structural vibration can be regarded as the superposition of multiple reflections of various elastic wave modes, the propagating wave can form the overall vibration in the limited area of the structure, and the attenuated wave can form the localized vibration in the limited area of the structure.

Therefore, the j^{th} order vector mode function $\varphi_j(x)$ in the structure can be expressed as

$$\varphi_j(x) = a_1 \cos k_1 x + a_2 \sin(k_1 x) + a_3 \cos(k_2 x) + a_4 \sin(k_2 x). \quad (22)$$

The mode coefficient that satisfies the cantilever beam boundary condition is

$$a_2 = -\frac{[k_1^2 \cos(k_1 l) - k_2^2 \cos(k_2 l)]}{[k_1^2 \sin(k_1 l) - k_1 k_2 \sin(k_2 l)]} a_1, \quad (23a)$$

$$a_4 = \frac{[k_1^2 \cos(k_1 l) - k_2^2 \cos(k_2 l)]}{[k_2 k_1 \sin(k_1 l) - k_2^2 \sin(k_2 l)]} a_1, \quad (23c)$$

where k_i is the wave number of beam elastic vibration, which is determined by (21).

Satisfy the boundary conditions at both ends of the cantilever beam to obtain the following equation:

$$\begin{aligned} k_1^4 \sin^2(k_1 l) + k_2^4 \sin^2(k_2 l) - (k_1^2 + k_2^2) \times k_1 k_2 \sin(k_1 l) \sin(k_2 l) \\ + k_1^4 \cos^2(k_1 l) + k_2^4 \cos^2(k_2 l) - 2k_1^2 k_2^2 \cos(k_1 l) \cos(k_2 l) = 0. \end{aligned} \quad (24)$$

Combining (21) and (24) together can determine the dispersion relation of vibration in the structure.

4. Design of the Variable Structure Control Method

The design of variable structure control mainly includes selecting the sliding mode and obtaining the control method. When the variable structure control strategy is adopted, the form of the switching function is as follows:

$$\begin{aligned} S &= \mathbf{C} \mathbf{X} \\ &= \begin{bmatrix} 0 & 0 & 0 & 0 & 0 & 0 \\ 0 & c_1 & 0 & 0 & 1 & 0 \\ 0 & 0 & c_2 & 0 & 0 & 1 \end{bmatrix} \mathbf{X}, \end{aligned} \quad (25)$$

where \mathbf{C} is the coefficient matrix, $\mathbf{X} = \begin{bmatrix} \theta & q_1 & q_2 & \dot{\theta} & \dot{q}_1 & \dot{q}_2 \end{bmatrix}^T$, $S = 0$, and these constitute the switching surface in variable structure control design. In the study of dynamics and control in this study, the first two vibration modes of the flexible attachment when rotating at a constant speed are considered.

Therefore, the specific form of the two switching surfaces is as follows:

$$s_1 = c_1 q_1 + \dot{q}_1, \quad (26a)$$

$$s_2 = c_2 q_2 + \dot{q}_2, \quad (26b)$$

where q_1 and q_2 are the first-order and second-order modal coordinates of the flexible attachment, respectively.

Use the following method of equal velocity approach

$$\dot{s}_i = -P_i \text{sgn}(s_i), \quad (27)$$

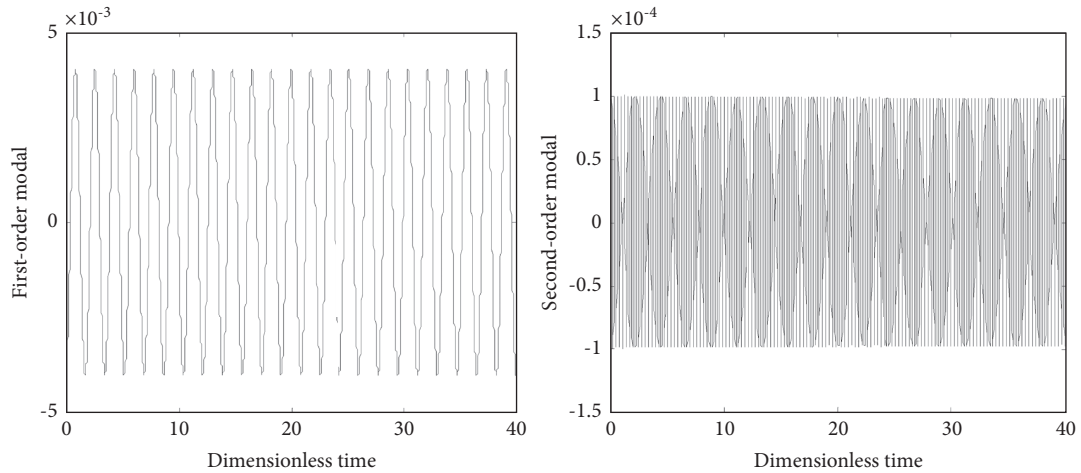


FIGURE 2: The response of the first two modes of the beam before variable structure control.

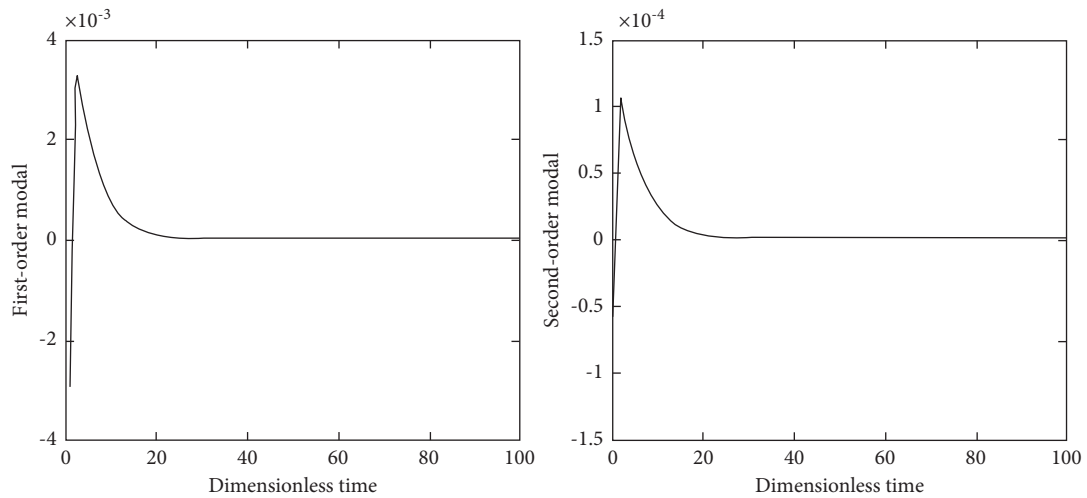


FIGURE 3: The response of the first two modes of the beam after variable structure control.

where $P_i > 0$, $\text{sgn}(s_i) = \begin{cases} 1 & s_i > 0 \\ -1 & s_i < 0 \end{cases}$. It is easy to verify that $\dot{s}_i s_i < 0$ is established, and the reaching condition is satisfied.

Taking the derivation of (25) and considering (17) and (27), the equation satisfied by the variable structure control method is

$$\mathbf{C} \begin{bmatrix} \mathbf{0} \\ \tilde{\mathbf{M}}^{-1} \mathbf{U} \tilde{\mathbf{F}} \end{bmatrix} = \begin{bmatrix} 0 \\ -P_1 \text{sgn}(s_1) \\ -P_2 \text{sgn}(s_2) \end{bmatrix} - \mathbf{C} \begin{bmatrix} \mathbf{0} & \mathbf{I} \\ -\tilde{\mathbf{M}}^{-1} \tilde{\mathbf{K}} & -2\theta \tilde{\mathbf{M}}^{-1} \tilde{\mathbf{G}} \end{bmatrix} \mathbf{X}. \quad (28)$$

Equation (17) becomes

$$\mathbf{C} \dot{\mathbf{X}} = \begin{bmatrix} 0 \\ -P_1 \text{sgn}(s_1) \\ -P_2 \text{sgn}(s_2) \end{bmatrix}. \quad (29)$$

From equation (29), the solution at $P_i > 0$ is stable, so the variable structure system is stable.

5. Numerical Simulation

In the calculation, the beam length L is taken as the characteristic length. $\nu = 0.30$, $\tilde{J}_h = 10\tilde{J}_1$, $\tilde{R}_h = 0.3$; consider the control when the rotation is at a constant speed, and take parameters $P_1 = |q_1|$, $P_2 = |q_2|$, $c_1 = 0.2$, and $c_2 = 0.2$.

In this study, only the first two modes of the system are considered, but the control accuracy is good enough. The control force applied by the two actuators suppresses the vibration of the first-second mode of the flexible attachment, and the applied positions are $x_1 = 0.48L$ and $x_2 = 0.96L$, respectively.

Figure 2 shows the response of the first two-order transverse vibration mode coordinates of the flexible beam when the initial state of the system is $x = [0 \ -0.004 \ -0.0001 \ 1 \ 0.002 \ 0.0001]$. It can be seen from the figure that before the variable structure control, the lateral vibration of the beam is severe.

Figure 3 shows the change rule of the coordinate of the first second-order transverse vibration mode of the flexible

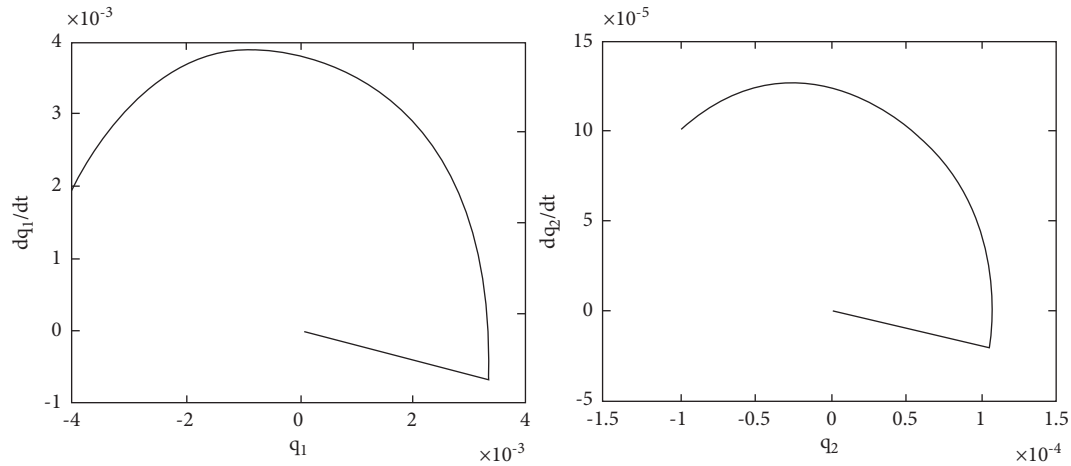


FIGURE 4: The response of the phase trajectory of the first two modes of the beam after variable structure control.

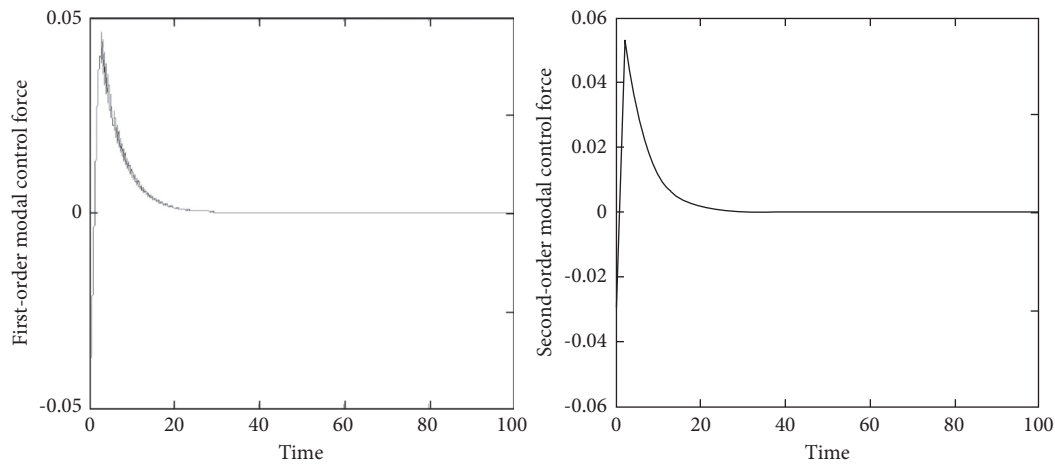


FIGURE 5: The time history of control inputs of the first two modes.

beam after variable structure control. It can be seen from the figure that the dimensionless time for the first stage to reach the desired position is about 17, and the dimensionless time for the second stage to reach the desired position is about 18. The control effect is significant.

Figure 4 shows the change rule of the phase trajectory of the first two modes after the variable structure control. It can be clearly seen from the figure that the variable structure control makes the system enter the sliding mode and moves the modal coordinates along the sliding mode. Convergence is reached.

Figure 5 shows the changing law of the control force required by the system to reach the desired position. It can be seen from the figure that after the system reaches the desired position, the required control force tends to stabilize, which shows that the control strategy is effective.

6. Conclusion

Aiming at the vibration and Coriolis force during the operation and tunneling of the TBM, this study simulates the rotating beam plate rotating around the Y axis as a

central rigid body-flexible beam model for research. In the modeling process of the central rigid body-flexible beam system, the longitudinal shortening caused by the lateral displacement of the flexible beam is considered, and the influence of centrifugal force and Coriolis force is further improved, thereby, further improving the dynamic model. Based on the application of elastic wave and vibration mode theory, the vibration mode of the Euler-Bernoulli beam rotating at a constant speed is determined, and the influence of the rotation motion on the system is fully considered.

In this study, the innovation point is that the variable structure control strategy is applied to the active vibration control of the central rigid body-flexible beam model. The comparison of the simulation results shows that when the system vibrates, the system vibrates severely without active control. After adopting variable structure control, the stability of the system can be ensured, and the vibration of the flexible beam can be suppressed. The dynamic analysis and control method in this study can provide analysis methods and reference data for the dynamic analysis and control of the rotating beam structural components in the TBM.

Data Availability

The data generated or analyzed during this research are included in this paper.

Conflicts of Interest

The authors declare that they have no conflicts of interest.

Acknowledgments

This work was supported by the National Natural Science Foundation of China (51875146).

References

- [1] Z. Yang, Z. Sun, K. Fang, J. Yusheng, and B. Zhiqiang, "Cutting tool wear model for tunnel boring machine tunneling in heterogeneous grounds," *Bulletin of Engineering Geology and the Environment*, vol. 80, no. 7, pp. 5709–5723, 2021.
- [2] Z. H. Zhang, M. Aqeel, C. Li, and F. Sun, "Theoretical prediction of wear of disc cutters in tunnel boring machine and its application," *Journal of Rock Mechanics and Geotechnical Engineering*, vol. 11, no. 1, pp. 111–120, 2019.
- [3] Y. Shi, Y. Xia, Q. Tan, and Y. Zhang, "Distribution of contact loads in crushed zone between tunnel boring machine disc cutter and rock," *Journal of Central South University*, vol. 26, no. 9, pp. 2393–2403, 2019.
- [4] J. P. Ou, *Structural Vibration Control: Active, Semi-active and Intelligent Control*, Science Press, Beijing, China, (in Chinese), 2003.
- [5] Z. Qiu, M. Shi, B. Wang, and Z. Xie, "Genetic algorithm based active vibration control for a moving flexible smart beam driven by a pneumatic rod cylinder," *Journal of Sound and Vibration*, vol. 331, no. 10, pp. 2233–2256, 2012.
- [6] H. Diken, "Vibration control of a rotating Euler-Bernoulli beam," *Journal of Sound and Vibration*, vol. 232, no. 3, pp. 541–551, 2000.
- [7] J. B. Yang, L. J. Jiang, and D. C. Chen, "Dynamic modeling and control of a rotating Euler Bernoulli beam," *Journal of Sound and Vibration*, vol. 274, no. 3-5, pp. 863–875, 2004.
- [8] N. Shafiei, M. Kazemi, and M. Ghadiri, "Comparison of modeling of the rotating tapered axially functionally graded Timoshenko and Euler-Bernoulli microbeams," *Physica E: Low-Dimensional Systems and Nanostructures*, vol. 83, pp. 74–87, 2016.
- [9] I. Z. M. Darus and M. O. Tokhi, "Soft computing-based active vibration control of a flexible structure," *Engineering Applications of Artificial Intelligence*, vol. 18, no. 1, pp. 93–114, 2005.
- [10] J. Lin and W.-Z. Liu, "Experimental evaluation of a piezoelectric vibration absorber using a simplified fuzzy controller in a cantilever beam," *Journal of Sound and Vibration*, vol. 296, no. 3, pp. 567–582, 2006.
- [11] S. S. Ge, T. H. Lee, G. Zhu, and F. Hong, "Variable structure control of a distributed-parameter flexible beam," *Journal of Robotic Systems*, vol. 18, no. 1, pp. 17–27, 2001.
- [12] Q. Hu and G. Ma, "Variable structure control and active vibration suppression of flexible spacecraft during attitude maneuver," *Aerospace Science and Technology*, vol. 9, no. 4, pp. 307–317, 2005.
- [13] S. Choi, C. Cheong, and H. Shin, "Sliding mode control of vibration in a single-link flexible arm with parameter variations," *Journal of Sound and Vibration*, vol. 179, no. 5, pp. 737–748, 1995.
- [14] T. Chen, C. Hu, and W. H. Huang, "Variable structure control and vibration suppression of spacecraft during attitude maneuver," *Journal of Astronautics*, vol. 28, no. 5, pp. 1199–1204, 2007.
- [15] H. Bang and C. Ha, "Flexible spacecraft attitude maneuver by application of sliding mode control," *Acta Astronautica*, vol. 57, no. 11, pp. 841–850, 2005.

Research Article

An Impact-Echo Experimental Approach for Detecting Concrete Structural Faults

Ya-xun Yang ^{1,2} Wen-hao Chai ¹ De-chuang Liu ¹ Wei-de Zhang ¹ Jia-cheng Lu ¹
and Zhi-kui Yang ³

¹School of Highway, Chang'an University, Xi'an, Shaanxi 710064, China

²The Engineering Design Academy of Chang'an University Company Limited, Xi'an, Shaanxi 710064, China

³School of Civil Engineering, Shaanxi Vocational and Technical College, Xi'an, Shaanxi 710100, China

Correspondence should be addressed to Ya-xun Yang; yyx@chd.edu.cn

Received 7 November 2021; Accepted 3 December 2021; Published 20 December 2021

Academic Editor: Lingkun Chen

Copyright © 2021 Ya-xun Yang et al. This is an open access article distributed under the Creative Commons Attribution License, which permits unrestricted use, distribution, and reproduction in any medium, provided the original work is properly cited.

For the current problem of detection of grouting defects in posttensioned prestressed concrete members, the paper takes a single-layer arrangement of prestressed pipes as the object of study. The influence law of the main factors such as pipe material, defect size, defect critical surface location, and prestressing reinforcement location on the results of the impact-echo method for detecting concrete grouting defects was studied. Firstly, the ABAQUS finite element software was used to simulate these factors to obtain the influence law on the detection results, and a modal test was conducted to verify them. The results show that the impact-echo method can effectively test the location of defects and the degree of burial depth, and the pipe material influences the test results, and the impact of corrugated metal pipe is smaller and more accurate than the PVC pipe. In addition, the greater the plate thickness frequency drift rate, the larger the transverse size of the defect, so the plate thickness frequency drift rate and the measured defect depth are combined to quantitatively determine the depth of the defect.

1. Introduction

With the extensive use of posttensioned prestressed concrete bridges, the compactness of posttensioned prestressing duct grouting has become a major problem affecting the performance of bridges. Poor grouting results in the corrosion of prestressing steel bars, and consequently, the collapse of bridge structures has occurred frequently in the past decades. There have been publicly watched bridge collapses in recent years, including the Ynys-y-gwas in South Wales [1], Malle Bridge in Belgium [2], and Tian Zhuang Tai Bridge across the Daliao River on U.S. Route 305 [3]. The investigation shows that the lack of compactness of grouting causes the collapse. To solve this problem, the commonly used methods of grouting compactness detection such as rebound method, ultrasonic method, ground penetrating radar (GPR), acoustic scattering tracking method, endoscopy method, thermal infrared imaging method, and impact-echo (IE) method are used [4–7].

The IE method is a standard nondestructive testing method for detecting the surface and subsurface defects in concrete structures. The technique is widely used in practical engineering because of its convenient and straightforward testing process. It is also known as the most promising inspection method. The impact-echo method was first proposed by Cornell University in the 1980s and used the method to detect defects in prestressed pipes [8].

Hill et al. carried out an experimental study on the quality of prestressed pipe grouting using the impact-echo method of detection. They found that the technique could effectively identify signals of grout defects in square beam pipes [9]. Liu et al. [10] and Kang et al. [11] found that defects in reinforced concrete structures could be accurately detected using the shock-echo method through an indoor experimental study. Jiang et al. [12] used the IE method to detect the concrete emptying problem, and the results showed that the technique was feasible. The impact-echo method analyzes IE data and requires user expertise to define the analysis parameters, hindering comprehensive field implementation.

The feasibility of using deep learning models (DLMs) to detect concrete structural defects has been recently investigated [13]. In this paper, based on this research, the factors affecting the detection results of the impact-echo method are numerically simulated using ABAQUS and validated by indoor tests.

2. Principle of IE Method

The impact-echo method is a method to detect defects using low-frequency stress waves generated by transient shock. In practical engineering, a small steel ball is usually used to tap the surface of the concrete. At this time, a stress wave will be generated on the surface of the concrete. The stress wave (mainly P wave) propagates to the structure, and the reflection phenomenon will occur at different media interfaces. The back-and-forth reflection between other interfaces produces transient resonance. The stress wave formed by transient resonance changes the surface displacement of the concrete structure. Then, the displacement signal is received by the sensor placed near the impact point. The displacement signal received by the sensor is transformed into a frequency domain signal after fast Fourier transform (FFT). Finally, the time-domain signal is transformed into a frequency-domain signal according to the received signal. Frequency-domain signals are used to determine the size and density of defects in the structure. The schematic diagram of the detection principle is shown in Figure 1.

According to the principle of the impact-echo method [14–17], the equations for calculating thickness and frequency are different for different impedance materials when analyzing frequency signals. For compact flawless concrete slabs, the thickness frequency (F_T) can be determined by equation (1), and for reinforced concrete, the reflection frequency (F_s) can be determined by equation (2) as follows:

$$F_T = \alpha_s \frac{V_p}{2T}, \quad (1)$$

$$F_s = \alpha_s \frac{V_p}{4d}, \quad (2)$$

where α_s represents the shape coefficient of the slab; for concrete slab, it is generally 0.96; V_p represents the wave velocity of stress wave in concrete when propagating; T represents the thickness of the slab; d represents the depth of the channel.

Based on equation (2), the impact-echo signals collected from the nonprestressing pipe section, grouting channel, and nongrout channel specimens in the concrete slab will show different characteristics when the grouting compactness of the channel is tested (Figure 2).

3. Finite Element Simulation

3.1. Introduction to Simulation. The impact response under different working conditions is simulated and analyzed by using the finite element software, ABAQUS display solver. The impact-echo method studied the specific influence of various typical factors on the accurate positioning and

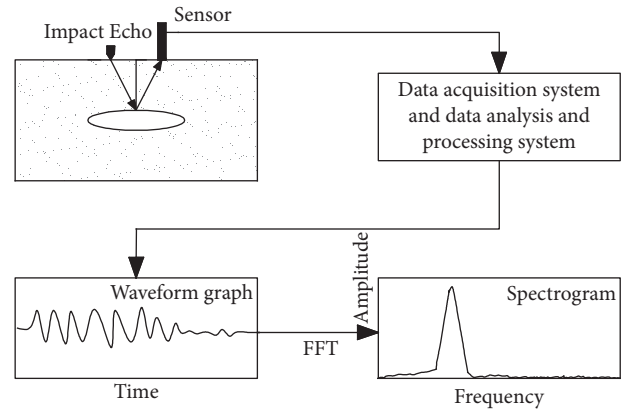


FIGURE 1: Schematic diagram of the shock-echo method.

quantitative detection of grouting defects in prestressed concrete structures. In the study, the impact load generated by steel ball impact is simplified to a semiperiodic simple harmonic force directly. It is inspected at a distance of 5 cm near the impact point. Acceleration/displacement of the measured surface is used to obtain the response signal of the stress wave propagating in concrete. Finally, the received time-domain signal is transformed into a frequency-domain signal through fast Fourier transform (FTT), and the spectrum chart is drawn.

3.2. Simulation Parameters. For the ABAQUS simulation, the material parameters are selected, as shown in Table 1.

In the experimental study, C40 concrete is selected; the meshing accuracy is 10 mm; the impact steel ball with a diameter of 6 mm is used; the impact load is regarded as a half-period sinusoidal load, in which the maximum concentrated force is 30 N, and the impact duration is 30 μ s. The concrete relationship is shown in the following equation:

$$F = F_{\max} \sin\left(\frac{\pi t}{t_c}\right). \quad (3)$$

In the above equation, F is the action force of t at a specific time, F_{\max} is the maximum load of 30 N, t is the action time range of 1–30 μ s, and t_c is the impact duration.

3.3. Simulated Working Conditions. To study the typical influence factors of pipeline material, defect size, defect critical plane position, and prestressing steel bundle, the following working conditions were set up as follows: (1) different grouting degrees was arranged to simulate different defect sizes; the hollow four working conditions such as compactness, 1/3 grouting, 1/2 grouting, and 2/3 grouting were set (see model 1–4 in Table 2), and the other conditions were the same. (2) Parallel and vertical working conditions of critical defect surface and test surface were arranged (see model 5–6 in Table 2), (3) To study the influence of the position of prestressing tendons and tendons on test results, two working conditions of prestressing tendons are set up at the top of the pipeline and the bottom of the pipeline, respectively (see model 7–10 in Table 2).

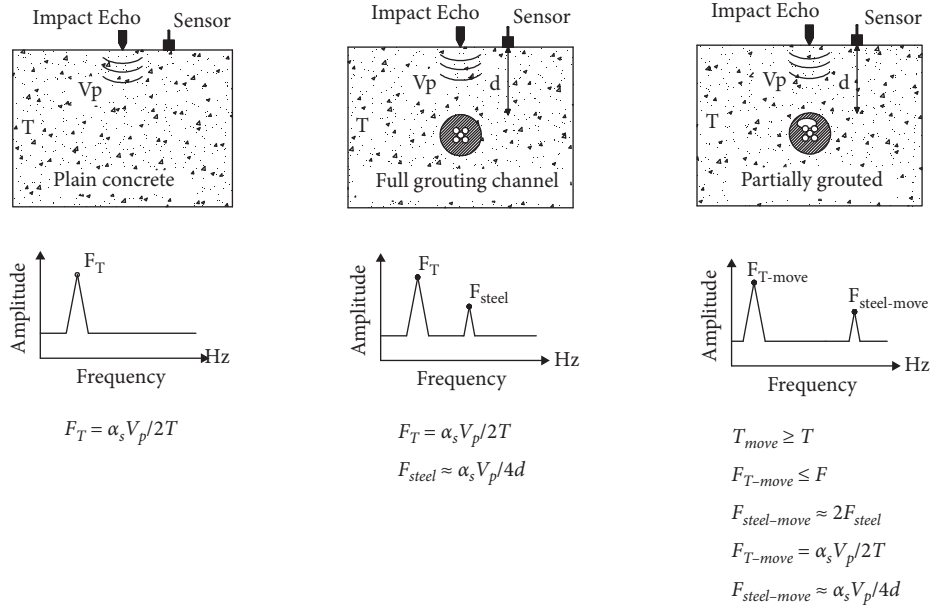


FIGURE 2: Response spectrum analysis diagram of different channels.

TABLE 1: Material parameters.

Material	Density (Kg/m ³)	Elastic modulus (Pa)	Poisson's ratio
Steel	7.8×10^3	2.1×10^{11}	0.3
Concrete	2.4×10^3	3.25×10^{10}	0.2
Mortar	1.74×10^3	8.71×10^9	0.2
PVC	1.1×10^3	4×10^9	0.2

Note. PVC, polyvinyl chloride.

TABLE 2: Summary of working condition model parameters.

Model number	Corrugated pipe material	Grouting compactness	Position of the critical surface of the defect (and the test surface)	Prestressed tendons and their position
1	Metal/PVC	Not grouted	Parallel	None
2	Metal/PVC	1/3Grouting	Parallel	None
3	Metal/PVC	2/3Grouting	Parallel	None
4	Metal/PVC	Compact	Parallel	None
5	Metal	1/3Grouting	Vertical	None
6	Metal	2/3Grouting	Vertical	None
7	Metal	Compact	Parallel	Exist (pipe top)
8	Metal	Compact	Parallel	Exist (pipe bottom)
9	Metal	1/2Grouting	Parallel	Exist (pipe top)
10	Metal	1/2Grouting	Parallel	Exist (pipe bottom)

Note. In Table 2, the location of the defective critical surface is parallel to the test surface that is “top and bottom plate conditions” and vertical that is “web condition.”

Figure 3 is a partial model diagram. The finite element model is 1.6 m in length, 0.4 m in width, and 0.3 m in height. The pipes are arranged in the central position. The diameter of the pipes is 80 mm, the thickness of the metal wave tube wall is 2 mm, the thickness of the PVC pipe wall is 3 mm, and the diameter of the prestressed steel bar bundle is approximately simulated with a 4 cm steel bar. The working conditions are summarized in Table 2.

3.4. *Simulation Results.* The set working conditions are simulated numerically. The time-domain signal data of test points are collected. The time-domain signal data are converted into frequency-domain signals by fast Fourier transform with MATLAB data processing software.

The spectrum of each working condition is obtained. Some of the spectrum results are shown in Figure 4. The peak values in the spectrum of all operating conditions are

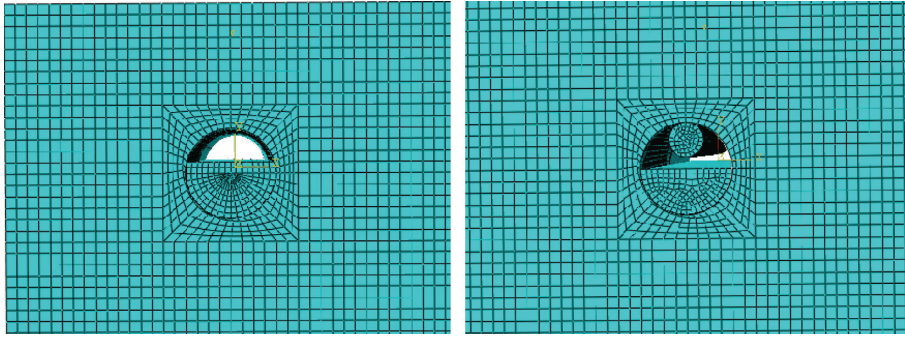


FIGURE 3: Schematic diagram of the finite element model.

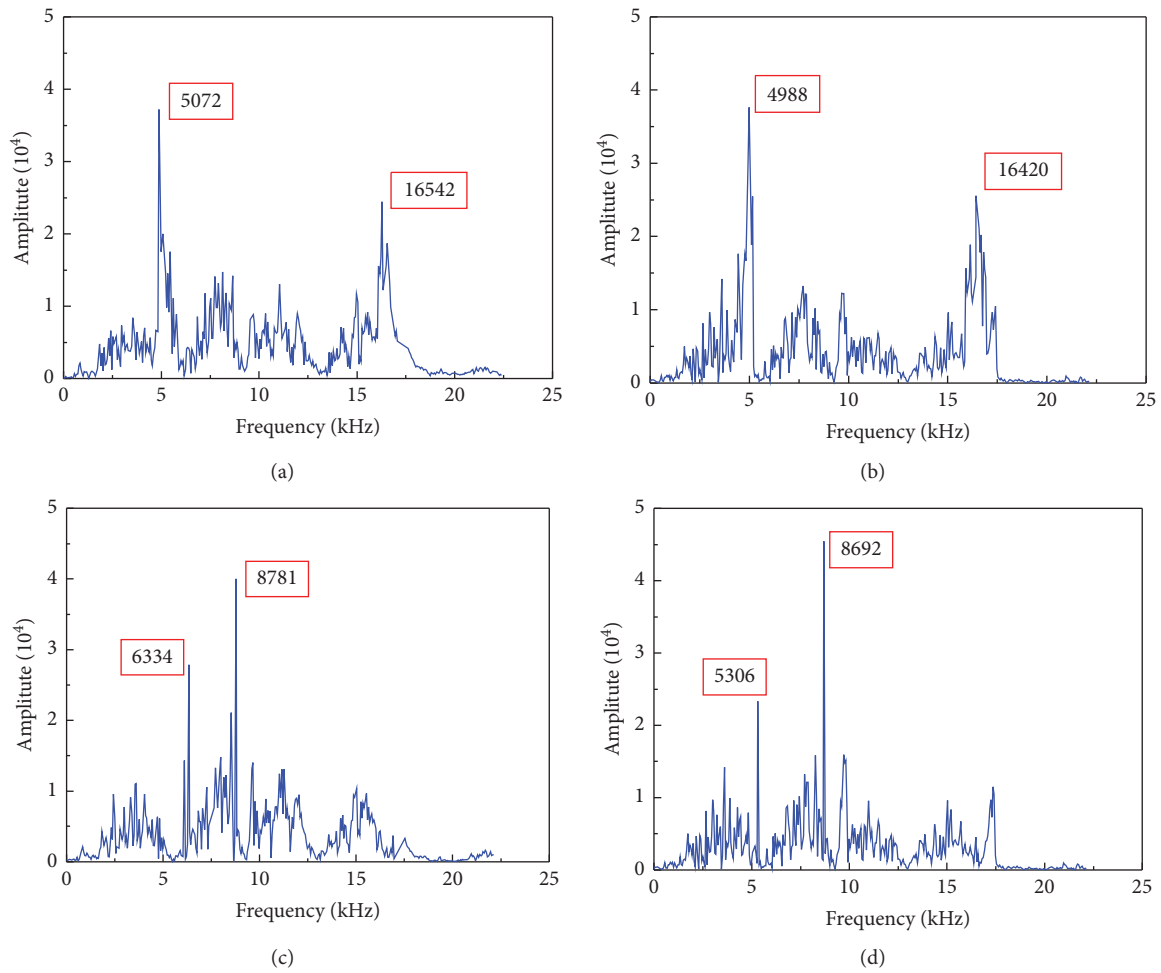


FIGURE 4: Parts of the spectrogram. (a) 3-spectrogram of metal bellows; (b) 4-spectrogram of metal bellows; (c) 7-spectrogram of metal bellows; (d) 9-spectrogram of metal bellows.

counted, and the corresponding thickness frequency values, defect thickness frequency values, and drift rates (Δf and ΔF) are calculated according to equation (1) or equation (2). The peak frequency results are shown in Table 3.

By comparing the results of 1-1~4-2 in Table 3, it can be seen that when the pipe grouting is defective, the corresponding plate thickness frequency drifts to the low frequency, and the drift rate increases gradually with the

increase of the defect size; this point can be used as a basis for judging whether there are defects in the prestressed pipeline. The drift rate of metal bellows increased from 2.1% to 19.6%; the drift rate of PVC pipe increased from 2.5% to 24.7%, and the error of corresponding defect reflection frequency of metal pipe was smaller than that of PVC pipe, which shows that the material bellows have an effect on the test results. Under the same conditions, the obstruction of metal bellows

TABLE 3: Peak frequency.

Number	Plate thickness frequency			Defect frequency		
	f_{theory}	$f_{calculate}$	Δf (%)	F_{theory}	$F_{calculate}$	ΔF (%)
1-1		4988.0	19.6	16296.4	16420	3.0
2-1		5072.0	18.3	16296.4	16542	2.3
3-1		5233.0	15.7	16296.4	16485	2.6
4-1		6080.0	2.1	/	/	/
1-2		4673.0	24.7	16296.4	16180	4.4
2-2		4821.0	22.3	16296.4	16277	4.1
3-2		4904.0	20.9	16296.4	16331	3.5
4-2	6206.3	6053.0	2.5	/	/	/
5		5581.0	10.1	16477	16025	2.7
6		5883.0	5.2	16477	15810	4.1
7		6334.0	-2.1	/	/	/
8		6334.0	-2.1	/	/	/
9		5306.0	14.5	13299.2	12768.5	3.8
10		5306.0	14.5	16926.4	16255.0	3.9

Notes. (1) 1-1 in the table is a corrugated metal pipe; 1-2 is the PVC corrugated pipe; the rest are similar. The rest of the number corresponds to the working conditions in Table 2. (2) “/” in the table indicates that there is no such content, and the above frequency unit is kHz. (3) $\Delta f = (f_{theory} - f_{calculate}) / f_{theory}$; $\Delta F = (F_{theory} - F_{calculate}) / F_{theory}$; ΔF takes absolute value.

is less than that of PVC pipes, and the results are closer to the theoretical values. Therefore, metal pipes can be used as grouting channels.

By comparing the results of 1-1 ~ 4-1, 5, and 6 in Table 3, it can be seen that, under the condition of the web, the frequency drift rate of plate thickness measured under the condition of the same defect size as that of the top and the bottom plates is smaller than that of top and bottom plates. This is because when the critical surface of the defect is perpendicular to the test surface (web condition), the transverse dimension of the fault is much smaller when the transverse size of the defect is parallel (top and bottom state); when the frequency drift rate of the thickness of the plate is more significant, the transverse dimension of the defect (the depth of the defect at the top of the pipeline) is more meaningful, and vice versa, and the difficulty of detection is increased.

Through comparative analysis of the results of 7-10 in Table 3 and c and d in Figure 4, it can be found that the frequency of plate thickness shifts. When the prestressed steel bundle is located on the top of the pipe, the reflection frequency of the steel bundle can be detected, which are 8781.0 kHz and 8692.0 kHz, respectively, which are close to the theoretical value 8463.1 kHz, and the reflection frequency of the steel bundle cannot be measured when the upper hole appears. However, the measurement of the depth frequency of the defect will not be disturbed. In addition, it is found that when the steel bundle is laid at the bottom of the pipeline, the reflection frequency of the steel bundle can easily overlap with the frequency of plate thickness under the condition of dense grouting, and the peak frequency cannot be displayed.

4. Field Tests

4.1. Specimen Preparation. In order to validate the findings of the finite element modeling investigation, three C40 concrete slab specimens were fabricated outdoors. The plate

was 1.6 m × 1 m × 0.3 m in size (length × width × height) (1 piece) and 0.8 m × 1 m × 0.3 m in size (length × width × height) (2 pieces). The former was used to validate the effect of pipe material and defect size on the influence law. The latter was utilized to validate the influence law between the position of a trapped critical surface and a prestressing steel beam. Each specimen has 4 orifices. The pipe diameter is set to $\phi 80$ mm; the center of the pipe is 110 mm from the surface of the sample, and in the third plate, another $\phi 8$ standard reinforcement is arranged with a spacing of 5 cm. $3\phi 16$ standard reinforcement bundles are selected instead of the prestressing steel bundles, and the dimensional diagram of specimen 1 is shown in Figure 5(a), and the field specimen is shown in Figure 5(b). The longitudinal arrangement of specimens 2 and 3 is the same as that of specimen 1. The transverse dimensions of the grouting are as described in Table 2.

4.2. Testing Process. The concrete slab surface corresponding to the longitudinal axis of each pipeline is selected as the test line of pipeline grouting with a diameter of 6 mm. The test spacing is 10 cm in the longitudinal direction without considering the edge point and the midpoint of the specimen. There are 14 test points in specimen 1, 7 test points in specimens 2 and 3, and the distance between the test point and the impact point should be less than 0.4 h (h is the distance between the top of the bellows and the test surface). 3 cm was selected in this experiment. Firstly, the wave velocity of each specimen is calibrated by SPC-MATS, and each sample is averaged by selecting several measuring points.

4.3. Test Results. The results of wave velocity calibration are as follows: specimen 1 is 3956.5 m/s, specimen 2 is 3988.3 m/s, and specimen 3 is 4000.2 m/s. The frequency of each measuring point is measured, and the corresponding thickness frequency drift rate and defect depth drift rate are calculated. The results



FIGURE 5: Schematic diagram of specimen 1. (a) Specimen size drawing. (b) On-site test piece diagram.

of points 3, 4, and 9, 10 in the No. 1 board are compared and analyzed. The results are shown in Figure 6. From Figure 6(a) and calculation, it can be seen that with the increase of defect size, the corresponding plate thickness frequency decreases gradually, and the drift rate increases slowly. In metal pipes, the drift rate of measuring point 3 is from 4.4% to 20.8%, and the drift rate of measuring point 4 is from 3.9% to 21.2%; in PVC pipes, the drift rate of measuring point 9 is from 7.5% to 27.6%, and the drift rate of measuring point 10 is from 6.5% to 27.3%; but for the defect degree error, the drift rate of measuring point 3 is calculated. The nominal defect depth is shown in Table 4. The error rate of metal bellows is between 4% and 5.5%, while PVC tubes are between 6% and 8.1%. It shows that the test result of the metal tube is more accurate.

For the metal pipelines under the vertical working conditions of No. 2 and No. 3 in the No. 2 plate, relevant data of 3 and 4 measuring points are taken. The results are shown in Table 4.

It can be seen from Table 4 that under the same defect size conditions as the top and bottom plates, the measured frequency drift rate of plate thickness is less than that under the top and bottom conditions. The error of defect depth is more significant than that of roof and floor, and there are no data at some detection points, which shows that under the same conditions, it is more difficult to detect the defect when the critical surface of the fault is perpendicular to the test surface (web condition) than when the transverse dimension of the defect is parallel (top and bottom conditions).

The plate thickness frequency and defect frequency of the measured points are counted as shown in Figure 7.

From Figure 7 and calculation, it can be found that the drift rate of plate thickness frequency is low. The drift rate of plate thickness in working conditions 7 and 8 is between 4% and 6.3%, the drift rate of plate thickness in working conditions 9 and 10 is between 15% and 18%, and the frequency of defect depth can be detected in working conditions 9 and

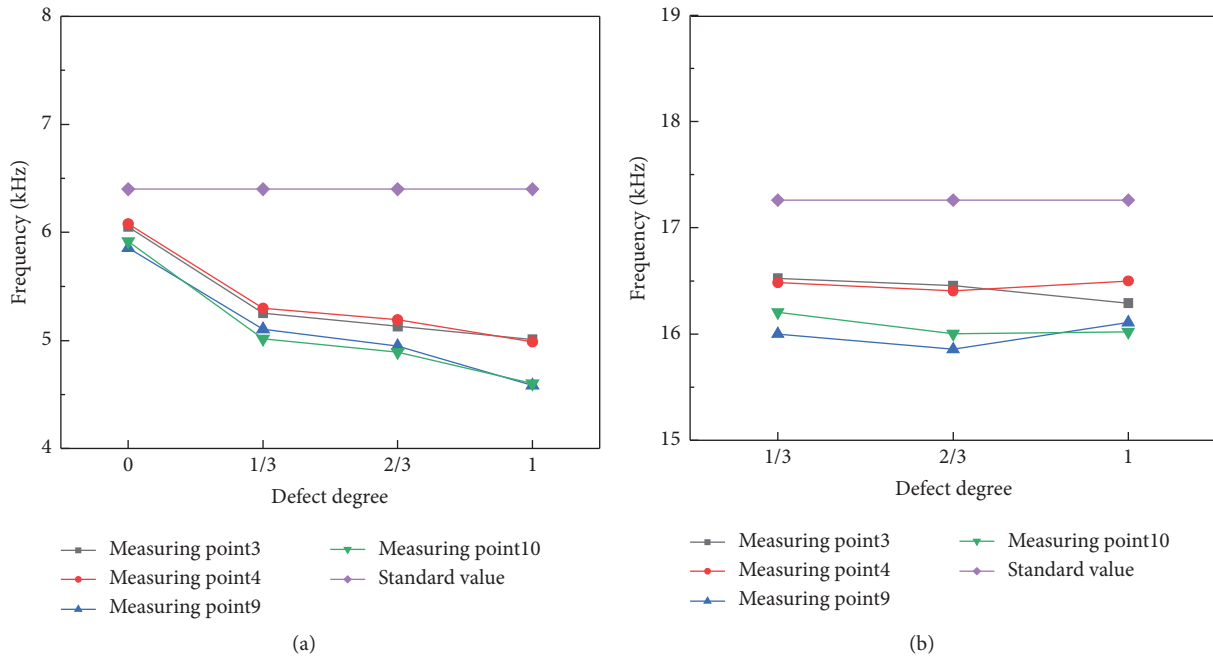


FIGURE 6: Frequency diagram of measuring points on the plate 1# (a) Plate thickness frequency chart (b) Defect frequency chart.

TABLE 4: Measurement point results of plate No. 2.

Measuring point	Working condition	f_{test}	f_{theory}	Δf (%)	F_{test}	F_{theory}	ΔF (%)
3	1/3	5409	6381	15.2	16280	17403	6.5
	2/3	5882		7.8	18943		8.8
4	1/3	5304		16.8	15986		8.1
	2/3	5943		6.9	15874		8.7

Notes. The above frequency unit is kHz. f_{test} —the test value of plate thickness frequency. f_{theory} —the theoretical value of plate thickness frequency. F_{test} —the test value of defect frequency. F_{theory} —the theoretical value of defect frequency.

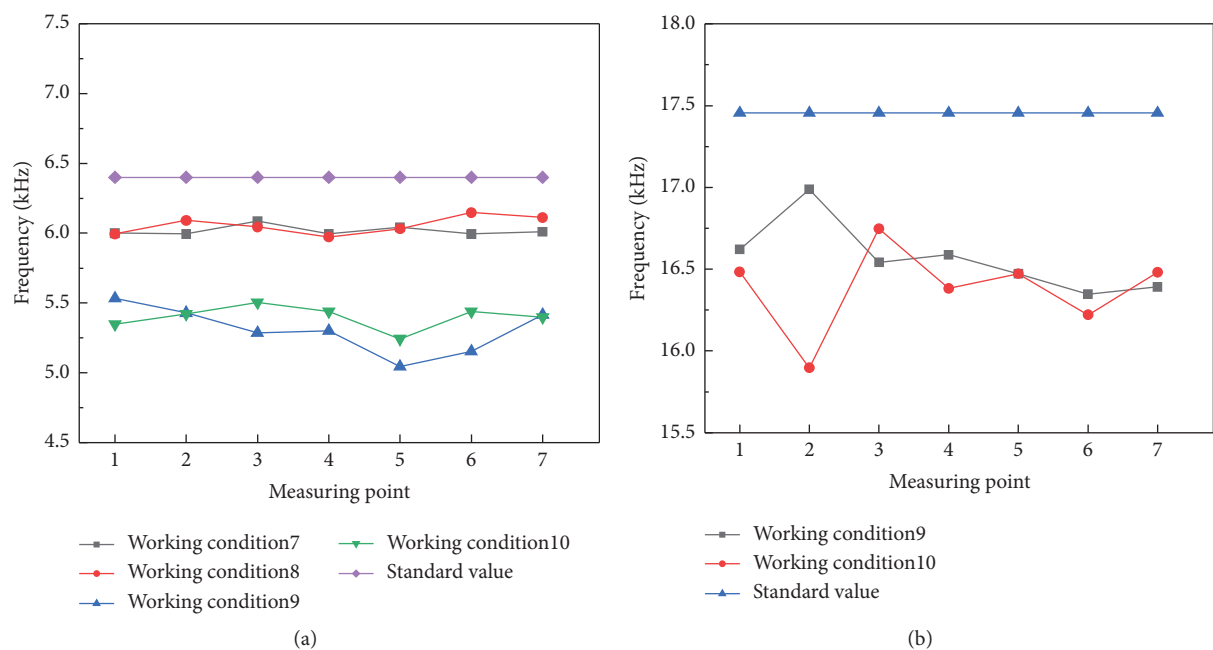


FIGURE 7: Frequency diagram of measuring points on the 3# board. (a) Board thickness frequency chart. (b) Defect frequency chart.

10, and most of the errors are between 4.2% and 7.1%. In addition, the reflection frequency rate of the steel bundle is concentrated between 8972 kHz and 9372 kHz at condition 7 and detected. The error is between 1.8% and 10.6% compared with the theoretical value of 8814 kHz, which shows that the steel bundle does not affect the detection of grouting defects by the impact-echo method.

5. Conclusion

Through the mutual verification of finite element analysis and field test, the following conclusions can be drawn:

- (1) The impact echo method can effectively measure the location and depth of defects, and the pipeline material has an impact on the test results. The effects of metal bellows are smaller than that of PVC pipes, and the accuracy is higher. In addition, the larger the frequency drift rate of plate thickness is, the larger the transverse size of the defect is. Therefore, the defect depth can be quantitatively judged by combining the frequency drift rate of plate thickness with the measured defect depth.
- (2) The critical surface of the defect and the testing surface influence the test results. When they are perpendicular to each other, it is not easy to detect them. And the detection error of defect depth is significant.
- (3) When the longitudinal reinforcement is small, the reflection signal of the longitudinal support can hardly be detected, so it does not influence the detection of the main test signals such as defects and prestressing tendons. It is difficult for the prestressing steel bar to detect the beam signal when there is a defect, but it does not affect the defect depth signal test.

Data Availability

The data are included within the article.

Conflicts of Interest

The authors declare that there are no conflicts of interest regarding the publication of this paper.

References

- [1] R. Woodward, L. Blake, W. Sketch et al., "Discussion. Collapse of ynys-y-gwas bridge, west glamorgan," *Proceedings - Institution of Civil Engineers*, vol. 86, no. 6, pp. 1177–1191, 1989.
- [2] B. Mathy, R. Demars, F. Roisin, and M. Wouters, "Wouters. Investigation and strengthening study of twenty damaged bridges: a Belgium case history," in *Proceedings of the 3rd International Conference on bridge Management*, pp. 658–666, Guildford, UK, 1996.
- [3] G. F. Xing, Z. X. Wang, J. H. Liu et al., "Research on compactness testing technology of box girder prestressed pore slurry," *Highway Traffic Science and Technology*, vol. 27, no. S1, pp. 114–117+121, 2010.
- [4] H. Liu, C. Chen, Z. Guo, Y. Xia, X. Yu, and S. Li, "Overall grouting compactness detection of bridge prestressed bellows based on RF feature selection and the GA-SVM model," *Construction and Building Materials*, vol. 301, Article ID 124323, 2021.
- [5] H. Liu, Y. Qi, Z. Chen, H. Tong, C. Liu, and M. Zhuang, "Ultrasonic inspection of grouted splice sleeves in precast concrete structures using elastic reverse time migration method," *Mechanical Systems and Signal Processing*, vol. 148, Article ID 107152, 2021.
- [6] T. Maruyama, "Harmonic balance-boundary element and continuation methods for steady-state wave scattering by interior and surface-breaking cracks with contact acoustic nonlinearity," *International Journal of Solids and Structures*, vol. 210–211, pp. 310–324, 2021.
- [7] M. Janku, P. Cikrle, J. Grosek et al., "Comparison of infrared thermography, ground-penetrating radar and ultrasonic pulse echo for detecting delaminations in concrete bridges," *Construction and Building Materials*, vol. 225, no. 20, pp. 1098–1111, 2019.
- [8] N. J. Carino and M. Sansalone, "Detection of voids in grouted ducts using the impact-echo method," *Materials Journal*, vol. 89, no. 3, pp. 296–303, 1992.
- [9] M. Hill, J. McHugh, and J. D. Turner, "Cross-sectional modes in impact-echo testing of concrete structures," *Journal of Structural Engineering*, vol. 126, no. 2, pp. 228–234, 2000.
- [10] P.-L. Liu, L.-C. Lin, Y.-Y. Hsu, C.-Y. Yeh, and P.-L. Yeh, "Recognition of rebars and cracks based on impact-echo phase analysis," *Construction and Building Materials*, vol. 142, no. Jul.1, pp. 1–6, 2017.
- [11] J. M. Kang, S. Song, D. Park, and C. Choi, "Detection of cavities around concrete sewage pipelines using impact-echo method," *Tunnelling and Underground Space Technology*, vol. 65, pp. 1–11, 2017.
- [12] W. Jiang, Y. Xie, J. Wu, J. Guo, and G. Long, "Identifying bonding interface flaws in CRTS III type ballastless track structure using the impact-echo method," *Engineering Structures*, vol. 227, Article ID 111429, 2021.
- [13] L. Yin, B. Ye, Z. Zhang et al., "A novel feature extraction method of eddy current testing for defect detection based on machine learning," *NDT & E International*, vol. 107, no. Oct., Article ID 102108, 2019.
- [14] O. Abraham and P. Cote, "Impact-echo thickness frequency profiles for detection of voids in tendon ducts," *ACI Structural Journal*, vol. 99, no. 3, pp. 239–248, 2002.
- [15] C. Colla, "Improving the accuracy of impact-echo in testing post-tensioning ducts," *AIP Conference Proceedings*, vol. 657, no. 1, pp. 1185–1192, 2003.
- [16] R. Muldoon, A. Chalker, M. C. Forde, M. Ohtsu, and F. Kunisue, "Identifying voids in plastic ducts in post-tensioning prestressed concrete members by resonant frequency of impact-echo, SIBIE and tomography," *Construction and Building Materials*, vol. 21, no. 3, pp. 527–537, 2007.
- [17] S. Dorafshan and H. Azari, "Evaluation of bridge decks with overlays using impact echo, a deep learning approach," *Automation in Construction*, vol. 113, Article ID 103133, 2020.

Research Article

Study on Deformation Evolution Characteristics of Reverse-Dip Rock Slope under the Influence of Rainfall

Jiabing Zhang,¹ Liangfu Xie ^{1,2}, Xuejun Liu,³ Yongjun Qin,^{1,2} and Liming Wu¹

¹College of Civil Engineering and Architecture, Xinjiang University, Urumqi 830046, China

²Xinjiang Civil Engineering Technology Research Center, Urumqi 830046, China

³Xinjiang Academy of Architectural Science (Limited Liability Company), Urumqi 830046, China

Correspondence should be addressed to Liangfu Xie; xieliangfu@xju.edu.cn

Received 3 September 2021; Accepted 25 October 2021; Published 6 December 2021

Academic Editor: Nan Zhang

Copyright © 2021 Jiabing Zhang et al. This is an open access article distributed under the Creative Commons Attribution License, which permits unrestricted use, distribution, and reproduction in any medium, provided the original work is properly cited.

In Southwestern China, there exists deep river valleys and abundant rainfall, which leads to a large number of reverse-dip rock slopes. In order to investigate the evolution characteristics of toppling deformation of reverse-dip slope under the influence of rainfall, and a typical reverse-dip slope was taken as an engineering case. Firstly, the temporal and spatial evolution nephogram of toppling displacement under different rainfall was obtained based on the discrete surface displacement monitoring data of bank slope. Then, taking bank slope, gully buffer zone, and development degree of bank slope as development characteristics based on geological field survey, afterward, the evolution characteristics in different strong deformation zones were analyzed by superimposing the development characteristic partition and the spatial and temporal displacement nephogram. The results showed that the horizontal displacement mainly occurred on the right front and middle rear of the bank slope while large vertical displacement occurred on the middle of the bank slope under the influence of rainfall. As the rainfall increased to the maximum, the toppling deformation reached the peak, and vertical displacement was more sensitive to the rainfall than horizontal displacement. After the superposition, the largest strong deformation zone was located in the middle and rear part of the bank slope, which is characterized by medium and high slope and mature stage and 50 m gully buffer zone. This paper explores the deformation and failure process of reverse-dip rock slope considering the change of rainfall through real displacement monitoring data and focuses on the real deformation evolution law of each characteristic zone combined with different development characteristics partition.

1. Introduction

Toppling deformation is a kind of phenomenon that the reverse-dip rock mass bends and breaks to the free face under the coupling function of gravity and in situ stress. In the southwest of China, there exists deep river valleys and complex topographic and geological conditions, which leads to many high and steep reverse-dip rock slopes under the function of the uplift of Qinghai Tibet Plateau, and it is counted that about 33% of the slope deformation occur in the anti-inclined slope [1, 2]. Scholars mainly qualitatively describe the toppling deformation and failure based on the actual cases [3–13]. Caine [14] surveyed the cliff collapse on the edge of Tasmania plateau and pointed out that this failure was caused by the toppling of rock stratum. Besides,

some scholars classify rock slopes according to toppling failure types. Based on practical engineering cases, Goodman and Bray [15] categorized toppling failure into three types, including flexural toppling, blocky toppling, and block-flexural toppling. Nichol et al. [4] classified toppling failure into brittle fracture toppling and flexible bending toppling according to the hardness and development conditions of the rock. Alejano et al. [16] analyzed the failure mechanism of open-pit mine and interpreted the toppling and cyclic failure of rock slope as a composite toppling failure mode. Huang et al. [17] analyzed the mechanism of slope toppling deformation and divided its process into shallow toppling and deep toppling.

There are many factors inducing slope toppling deformation and failure, and scholars analyze the conditions of

causing toppling deformation mainly with theory [18–21], numerical simulation [22–24], and centrifugal model test [25–28]. Some researchers conduct the centrifugal model test to study the bending deformation and analyze the influence of rock layer inclination, tensile strength, internal friction angle, and joint spacing on slope toppling deformation and failure [18, 29]. Brideau and Stead [30] analyzed the effects of the dipping direction and angle of the structural plane and internal friction angle on the toppling deformation by 3DEC. The tensile strength was considered to be the main factor of bending toppling deformation [31]. Some scholars thought that periodic fluctuation of reservoir water and long-term immersion in the water were the important factors that resulted in toppling failure [32, 33]. Yu et al. [34] numerically simulated a rock slope model with complex joints and exhibited the progressive failure processes. Some scholars simulated the excavation process of reverse-dip slope and analyzed the influence of rock thickness, slope inclination, and lithology on toppling deformation [35–37].

At present, many factors affecting the toppling deformation of rock slope are mentioned and studied. However, the toppling deformation of rock slope under the effect of rainfall is rarely considered and the slope is always regarded as integrity to analyze its toppling deformation and failure characteristics. Besides, many scholars generally studied the toppling deformation characteristics of the slopes by establishing engineering geological models but giving up mechanical models by which satisfying results can be yielded based on proper constitutive relations or limit equilibrium theory; in addition, it should be noticed that the mechanical model is difficult to be applied to bank defacement cases because of lacking monitoring data, and the influencing mechanism of external factors such as rainfall and reservoir water cannot be well solved by mechanical models. Therefore, considering that in situ deformation data is the most objective criterion for evaluating various mechanical models, a typical anti-inclined rock slope was adopted in this study to explore the toppling displacement evolution characteristics of bank slope under rainfall based on discrete actual displacement monitoring data, which is valuable to further understand the deformation and failure characteristics of anti-inclined slope and provide the reference for similar anti-inclined slope cases.

1.1. Project Overview. Xiaodongcao bank slope is located in the right bank of the upstream side of Xixi River, Zhongliang Town, Wuxi County, Chongqing, and is 1.2 km away from Zhongliang reservoir; its elevation ranges from 540 m to 1183 m, the longitudinal length is about 900 m, the width ranges from 400 to 650 m, the inclination is 345° , and the vegetation is well developed (Figure 1). The middle and front of the slope are steep and the terrain slope is $45^\circ\sim 68^\circ$ with some parts nearly vertical, while the rear edge is relatively flat and the terrain slope ranges from 11° to 18° . The rock mass of the bank slope is mainly the lower Triassic Jialingjiang formation (T1j) and Daye Formation (T1D). Jialingjiang formation (T1j) is dolomitic limestone, which is located in the middle and front of the bank slope, and Daye Formation

(T1D) is argillaceous limestone, which is mainly located in the middle and rear of the bank slope.

Gullies are relatively developed; there are five large gullies flowing into Zhongliang reservoir mainly from north to south; the valleys are V-shaped, and the bottom of the valley where the slope angle is $40^\circ\sim 60^\circ$ is steep and the width ranges from 5 to 25 m, and groove cutting depth is from 20 to 50 m. In the research area, the rainfall is abundant and the average annual rainfall is 1333 mm; the rainy season is from April to October and accounts for 90% of the annual rainfall; the rainfall in January is the lowest and accounts for about 1%. After the rainstorm and continuous heavy rainfall, Gullies G1 and G4 collapsed in different degrees, and their toppling deformation increased significantly.

1.2. Surface Displacement Monitoring System. To monitor the displacement of the Xiaodongcao bank slope, 22 surface displacement monitoring points were evenly distributed throughout the study area; among them, 17 monitoring points were arranged on the bank slope and 5 were arranged outside the bank slope. The monitoring period is from January to December 2017, and the research area can be divided into five cross sections and three longitudinal sections according to the layout of the monitoring system (Figure 2).

1.3. Monitoring Results of Ground Displacement

1.3.1. Longitudinal Displacement. The monitoring results of the longitudinal section of the bank slope midline 2-2' showed that the horizontal displacement (Figure 3(a)) gradually developed from the front to the rear edge of the bank slope and increased with the amount of rainfall; the vertical displacement (Figure 3(b)) developed from the front to the back of the bank slope with larger displacement in the middle and first increased and then decreases; when the rainfall reached the peak, the trailing edge went upward, which was mainly manifested as the bending and toppling deformation of the reverse-dip rock slope.

1.3.2. Horizontal Displacement. The monitoring results of the C-C' cross section in the middle of the bank slope (Figure 4) show that the horizontal displacement on the right side of the bank slope was greater than that on the left side while the vertical displacement shows the opposite trend. The vertical displacement in the middle was larger than other sides and increased with the amount of rainfall; it reached the peak when the rainfall was the maximum. It can be concluded that the right side of the bank slope is dominated by horizontal displacement and the middle part is dominated by vertical displacement.

1.4. Superposition Partition Based on Development Characteristic Factors. Hypsometric Integral (HI) is an important indicator that reflects the degree of landform erosion by counting the surface elevation of the watershed and thereby reveals the morphology and development characteristics of

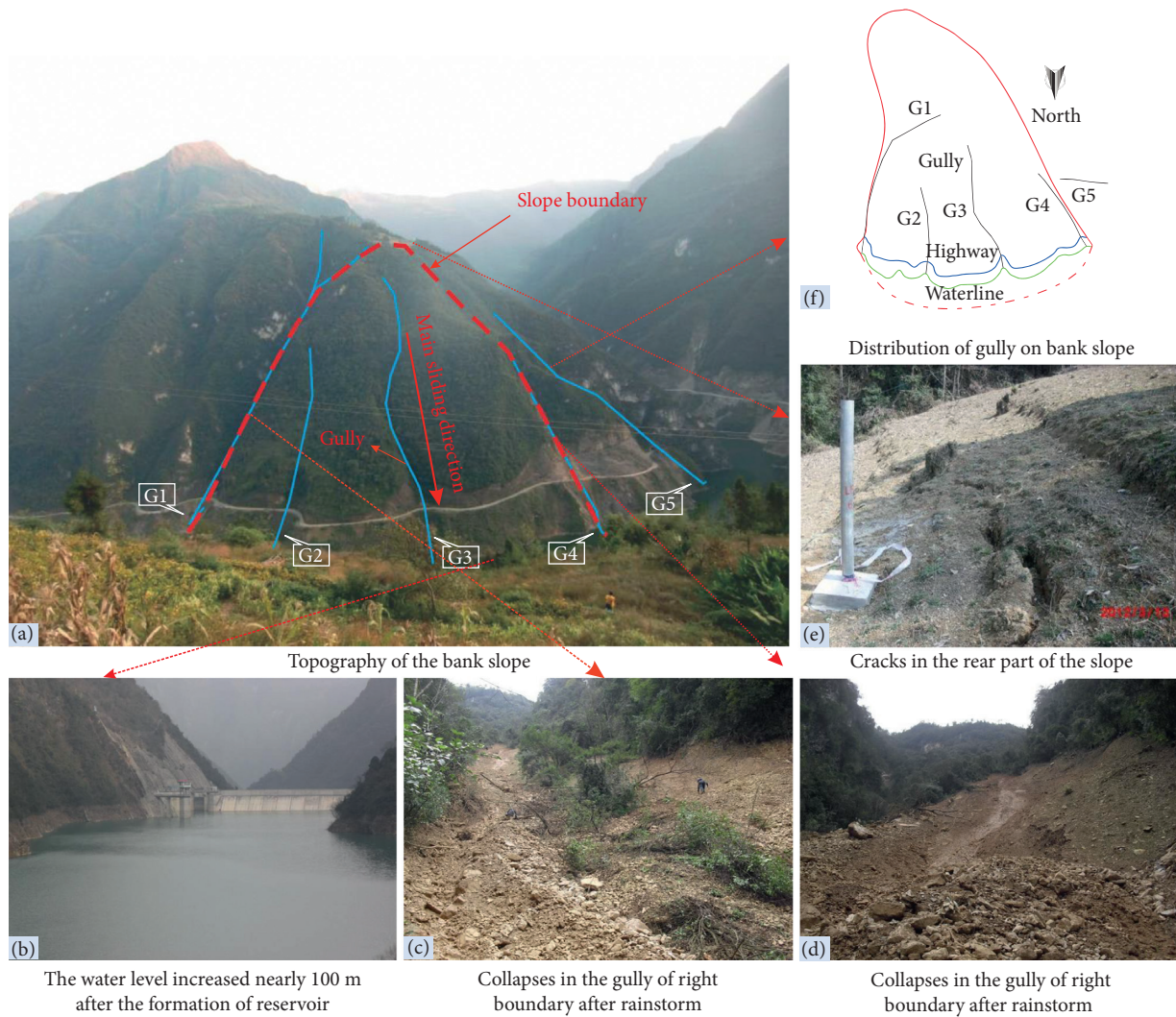


FIGURE 1: Toppling deformation and failure of the slope after the rainstorm. (a) Topography of the bank slope, (b) the water level increased nearly 100 m after the formation of the reservoir, (c) collapses in the gully of right boundary after a rainstorm, (d) collapses in the gully of right boundary after a rainstorm, (e) cracks in the rear part of the slope, and (f) distribution of gully on bank slope.

the watershed. In the 1950s, geomorphologists [38] applied the area integral curve to independent small watersheds to quantify the W. Davies landform development model [39]. According to the area-elevation integral value, they divided the landform development process into three stages: young stage ($HI > 0.6$), mature stage ($0.35 < HI < 0.6$), and old age stage ($HI < 0.35$). The calculation process is as follows: $X = a/A$, $Y = h/H$, X , and Y are within $[0, 1]$ (A is the area of the whole watershed, a is the area above some contour line in the watershed, h is the height difference between the contour line and the lowest point of the watershed, and H is the height difference between the highest and lowest point of the watershed); the area-elevation curve can be drawn with X as the abscissa and Y as the ordinate, and the area between the abscissa and the curve is defined as the area-elevation integral value. Based on the engineering geological survey of bank slope, the flow direction and flow of the bank slope were analyzed using the ArcGIS hydrological analysis tool, and the number of bank slope watersheds and the

corresponding area-elevation integral values under different confluence accumulations were obtained. As shown in Figure 5, most areas of the bank slope were in young and mature stages. Due to the vertical and horizontal cutting of bank slope valleys and the development of gullies, buffer zones with different distances of 10 m, 30 m, and 50 m were formed. Besides, the overall terrain of the bank slope is steep, and the terrain slope of most areas is greater than 40° , except that the trailing edge is relatively flat (the terrain slope angle is from 0 to 31°).

Therefore, by taking the slope of the bank, gully buffer zone, and the HI value of the watershed as the development characteristic factors, geometric superposition characteristic zones of the bank slope can be obtained by ArcGIS layer superposition based on Table 1 and the bank slope was finally divided into 104 characteristic zones (Figure 5).

The area of every characteristic zone in Figure 6 was calculated by ArcGIS geometry, the total area was 96999.12 m^2 , the influence of characteristic zones with a

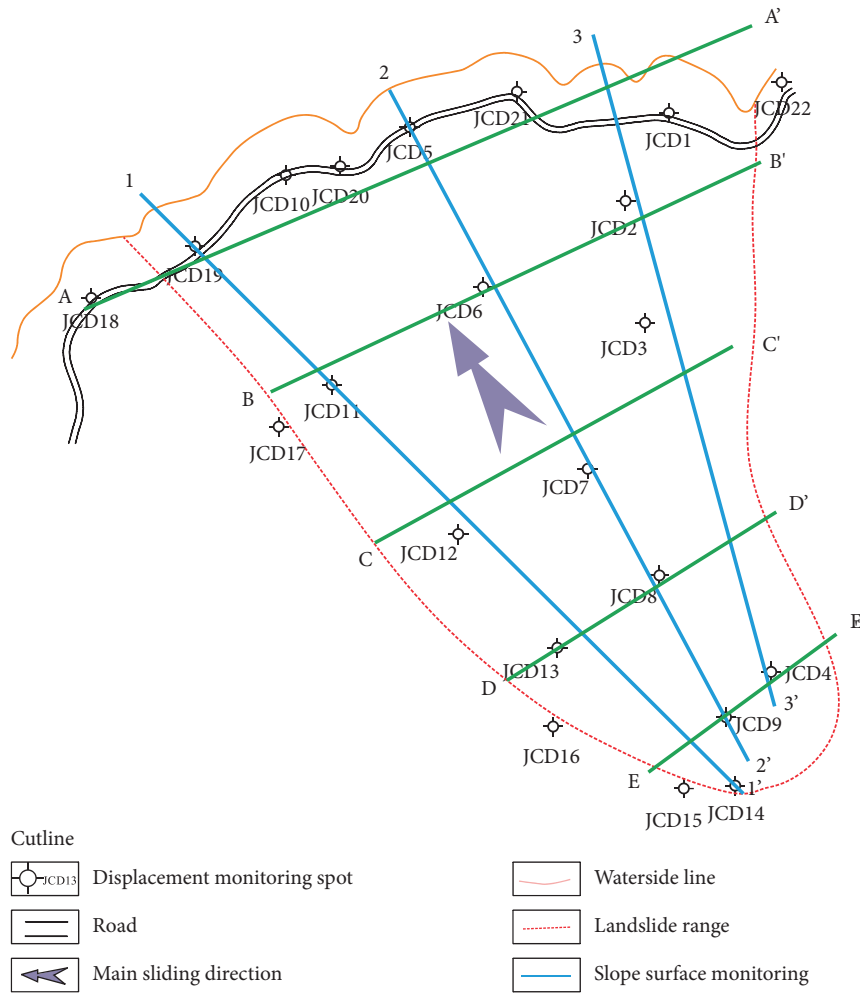


FIGURE 2: Layout of monitoring points of the slope.

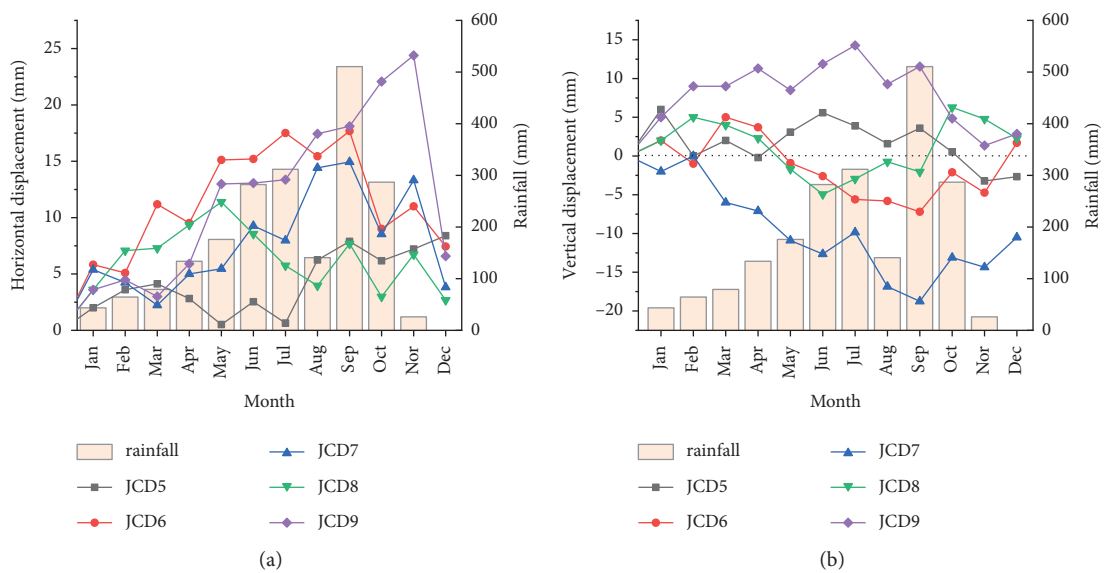


FIGURE 3: Monitoring curve of surface displacement with the rainfall of 2-2' longitudinal section of bank slope.

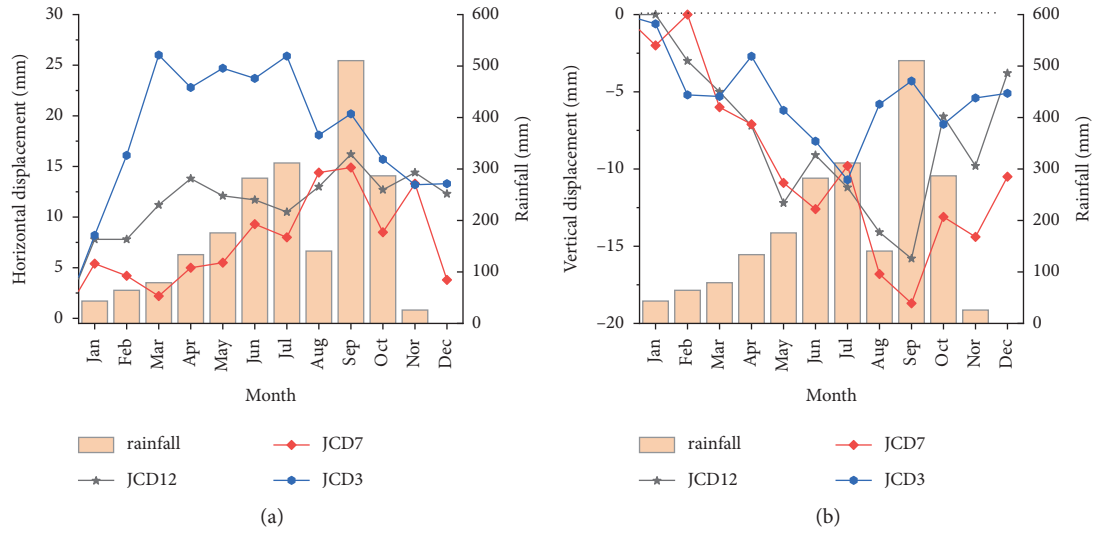


FIGURE 4: Monitoring curve of surface displacement with the rainfall of the C-C' cross section of bank slope.

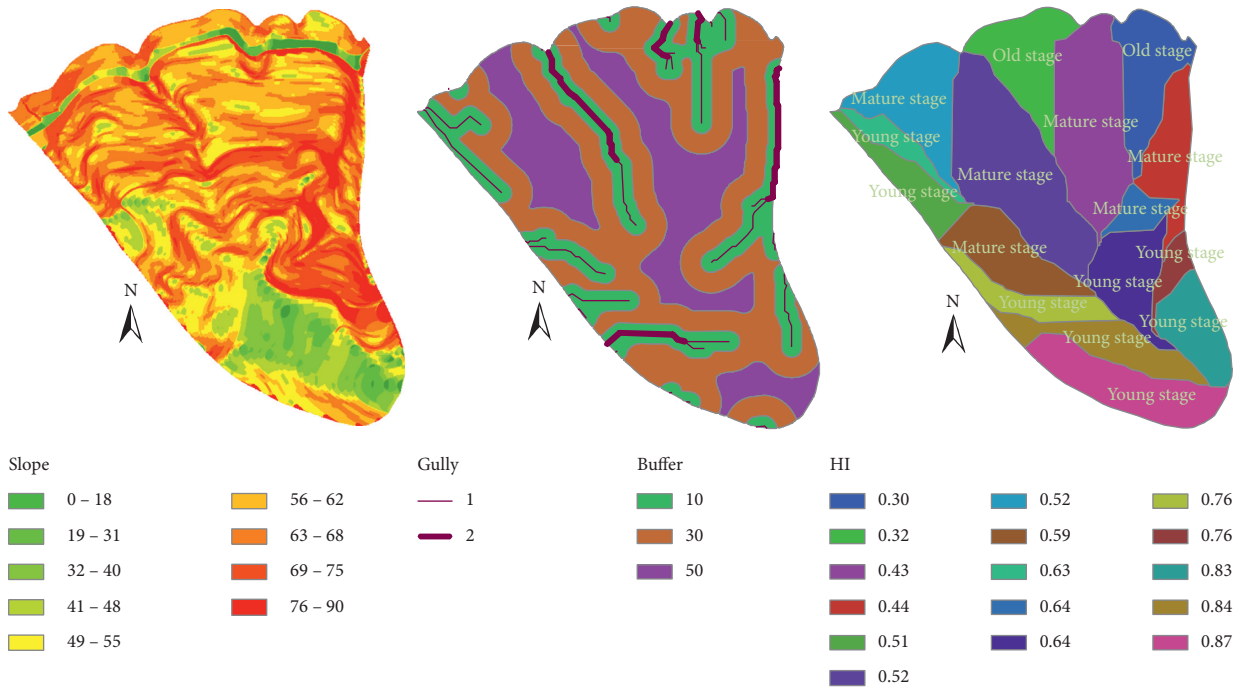


FIGURE 5: Distribution of the slope, buffer, and hypsometric integral.

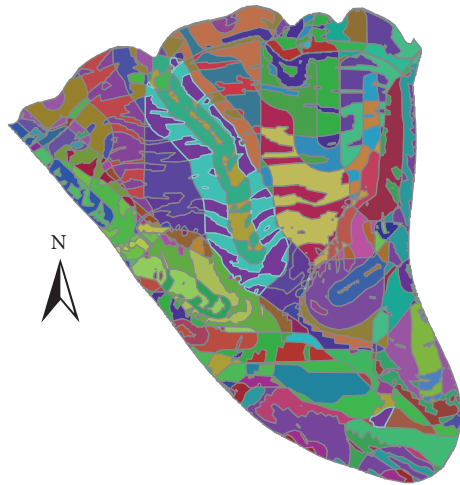
small area can be ignored, and the cumulative area of characteristic zones whose area is larger than 1500 m^2 accounts for 64.48%. Zone 232 with a high slope (the highlight zone in Figure 6), which forms a 10 m buffer zone and is at the mature stage, is located in gully G3 and holds the largest area (3761.32 m^2) among all the characteristic zones (Figure 7).

1.5. Spatial and Temporal Evolution Nephogram of Toppling Displacement. Due to the abundant rainfall, especially rainstorms or continuous heavy rainfall in the flood season,

gullies G1 and G4 collapsed in different degrees, and their collapse deformation was significantly intensified with water infiltration through cracks. The annual rainfall in 2017 is 2054.34 mm , which is the maximum in the last nine years (Figure 8), and the cumulative rainfall of each month is calculated and shown in Table 2. It can be seen that the rainy season was from May to October, and the rainfall in July was 510.60 mm and the highest, accounting for 24.85% of the annual rainfall, but there was no rain in December. For a brief description, all the months are numbered in Table 2. The bank slope toppling deformation was real-time monitored, the distance inverse weighting method was used to

TABLE 1: Basis for the geometrical zone of bank slope.

Type	Slope	Buffer	HI
Level	1: 0°-40°	1: 10 m	Assign values according to the value of HI from small to large; for example, if the value of HI is 0.3, it is represented by 1
	2: 41°-62°	2: 30 m	
	3: 63°-90°	3: 50 m	
Number	Hundred	Decade	Unite



Legend

111	135	221	242	327
112	136	222	243	328
113	137	223	244	329
114	138	224	245	330
115	139	225	246	331
116	140	226	311	332
117	141	227	312	333
119	142	228	313	334
120	143	229	314	335
121	144	230	315	336
122	145	231	316	337
123	211	232	317	338
124	212	233	318	339
125	213	234	319	340
126	214	235	320	341
127	215	236	321	342
129	216	237	322	343
131	217	238	323	344
132	218	239	324	345
133	219	240	325	346
134	220	241	326	

FIGURE 6: Partition map of the slope based on the geometrical conditions.

interpolate the displacement nephogram under different rainfalls based on the discrete displacement monitoring data on the surface, and then the evolution characteristics of the

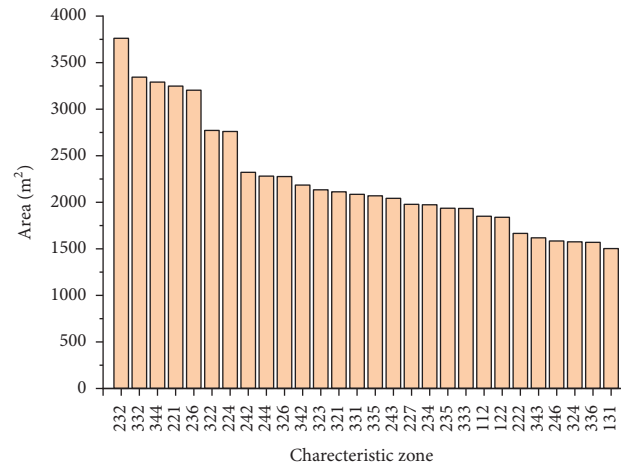


FIGURE 7: Bank slope geometric partitioning unit area of statistical results.

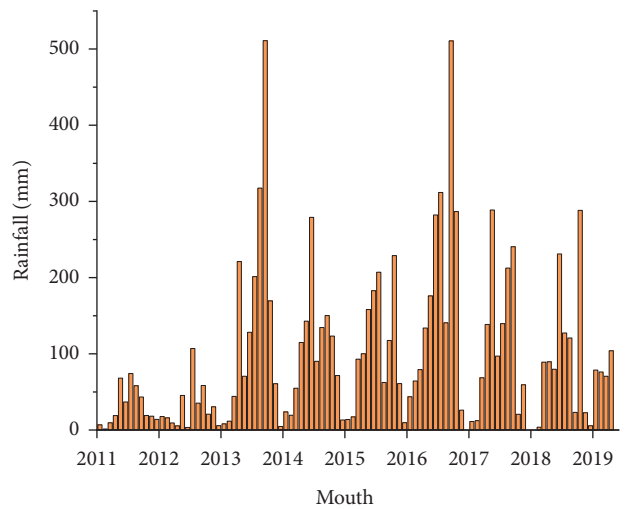


FIGURE 8: Cumulative monthly rainfall in recent nine years of bank slope.

horizontal, vertical, and total displacement spatial-temporal evolution nephogram were analyzed.

1.6. *Spatial-Temporal Evolution Nephogram of Horizontal Displacement.* Figure 9 is the cloud map of the horizontal displacement under the condition of different rainfalls. The natural breaks (Jenks) method [40] was used to classify the horizontal displacement into ten grades and the zones where the horizontal displacement is greater than 16.03 mm were defined as the obvious horizontal deformation zone.

TABLE 2: Cumulative monthly rainfall in 2017.

Month	Jan	Feb	Mar	Apr	May	Jun	Jul	Aug	Sep	Oct	Nor	Dec	Total
Rainfall (mm)	43.5	64.3	79.1	133.7	175.97	282.2	311.67	140.6	510.6	286.7	26	0	2054.34
Number	A	B	C	D	E	F	G	I	J	K	L	M	N

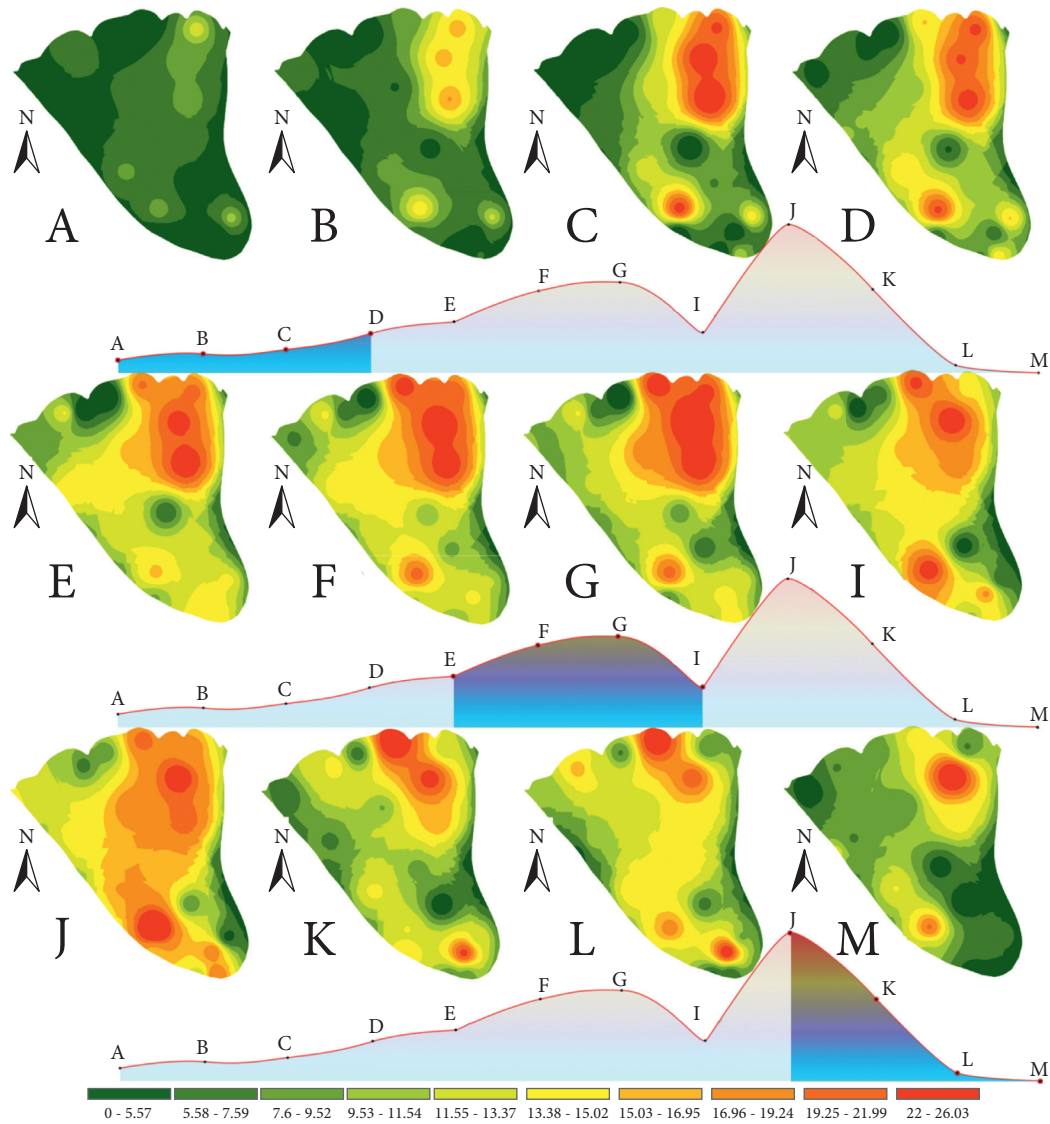


FIGURE 9: Temporal and spatial evolution characteristics of horizontal displacement of bank slope toppling (mm).

Obvious horizontal deformation zones were mainly located in the right front of the bank slope, and some were on the left side of the trailing edge of the bank slope. The change of horizontal displacement mainly extended from the right front to the middle and the left of the trailing edge, forming an “S” shape, and the maximum horizontal displacement occurred in the middle front between gullies G1 and G2. As shown in Figure 10, the horizontal deformation of the bank slope was sensitive to the rainfall and increased with the amount of rainfall. The area of the obvious horizontal deformation zones reached the peak value of 34286.85 m² when the rainfall was the highest value of 510.60 mm in July; this value was 4815.49 m² in December without rainfall. In

flood season, the total area of obvious horizontal deformation zones was 126654.10 m² and accounts for 74.61%, which is larger than that in the nonflood season with an area of 43083.64 m².

1.7. Spatial-Temporal Evolution Nephogram of Vertical Displacement. Figure 11 shows the cloud map of vertical displacement under the condition of different rainfalls. The natural breaks (Jenks) method was used to classify the vertical displacement into ten grades and the zones where the vertical displacement is smaller than -6.88 mm were defined as the obvious vertical deformation zones. Obvious

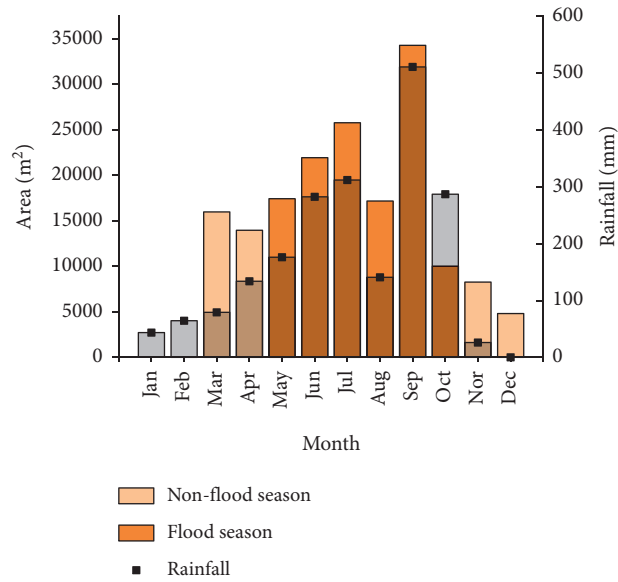


FIGURE 10: Area variation of obvious horizontal deformation zones.

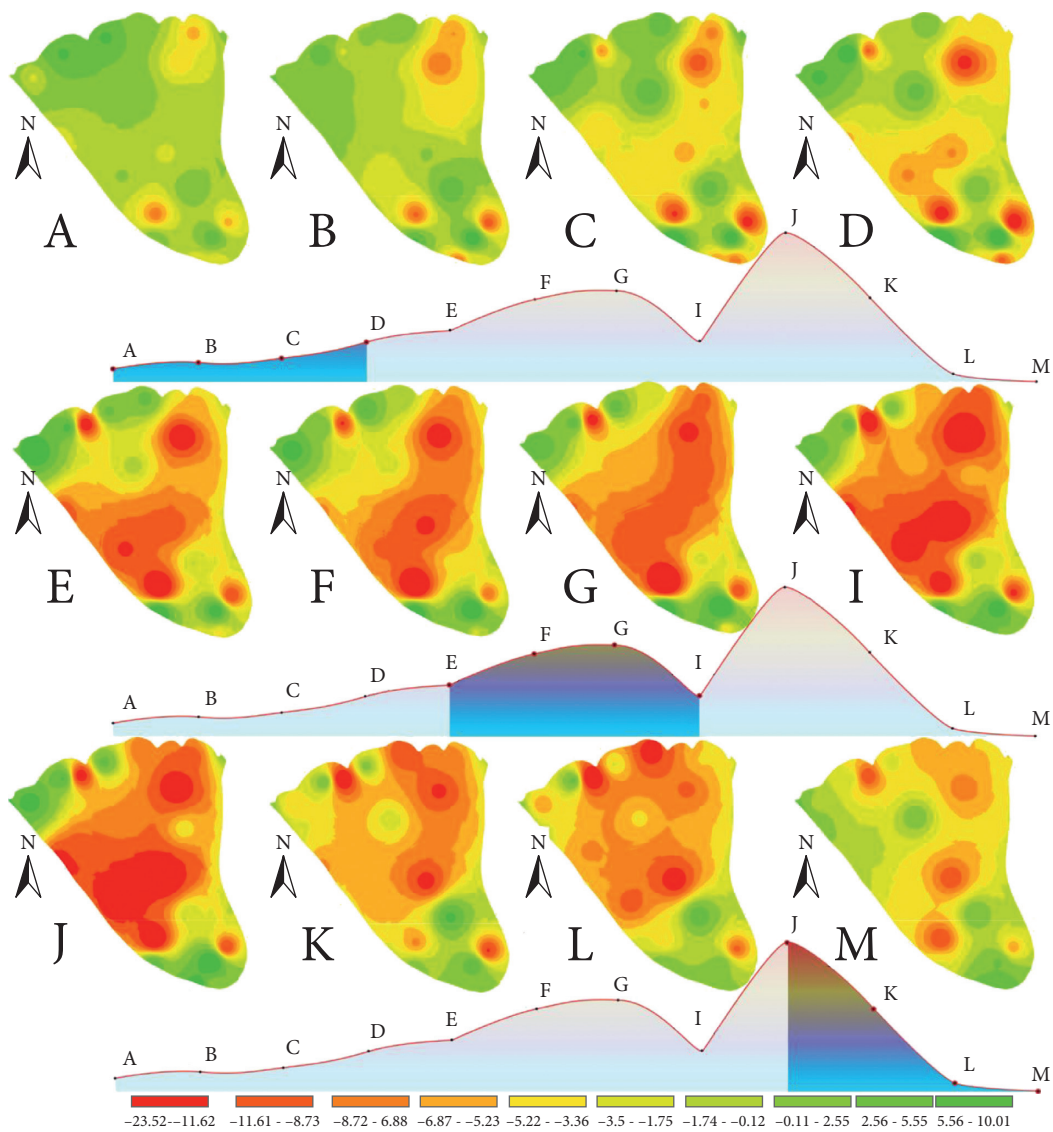


FIGURE 11: Temporal and spatial evolution characteristics of vertical displacement of bank slope toppling (mm).

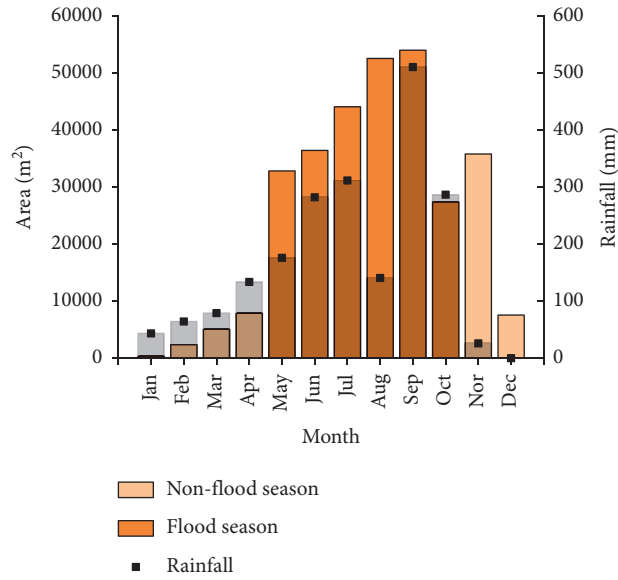


FIGURE 12: Area variation of obvious vertical deformation zones.

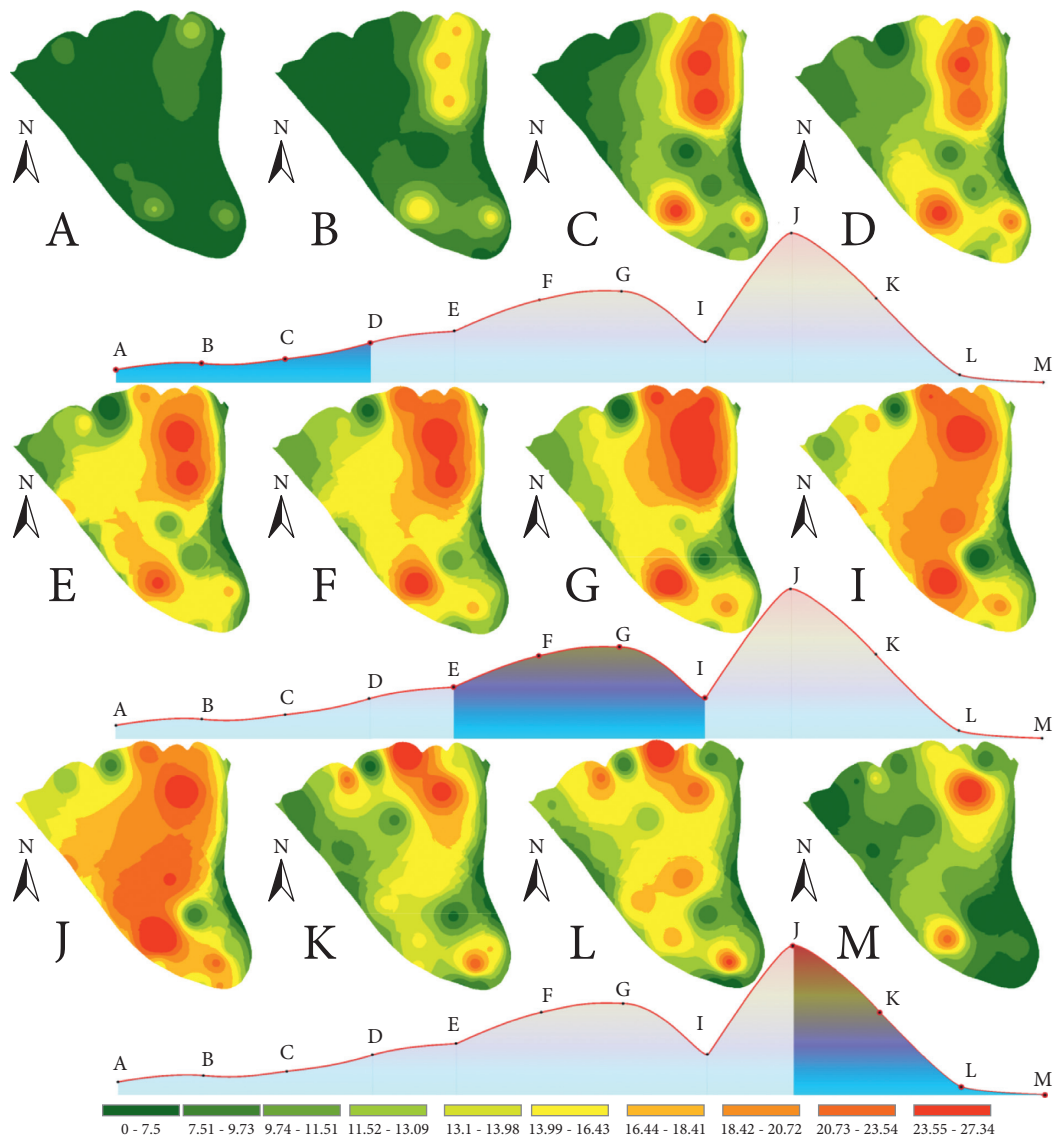


FIGURE 13: Temporal and spatial evolution characteristics of the total displacement of bank slope toppling (mm).

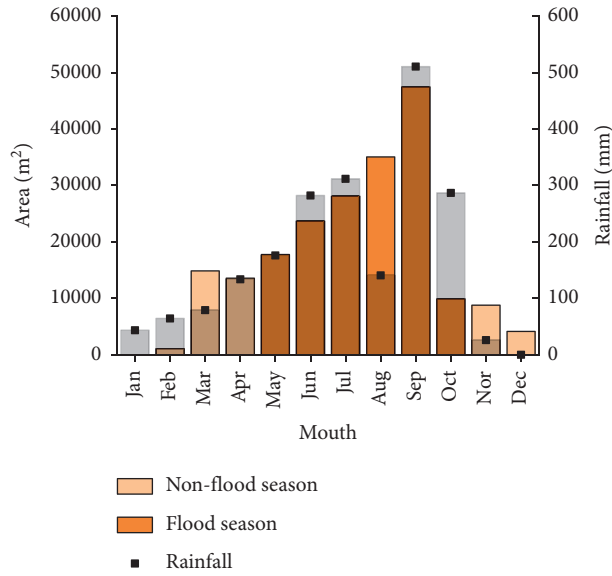


FIGURE 14: Area variation of obvious total deformation zones.

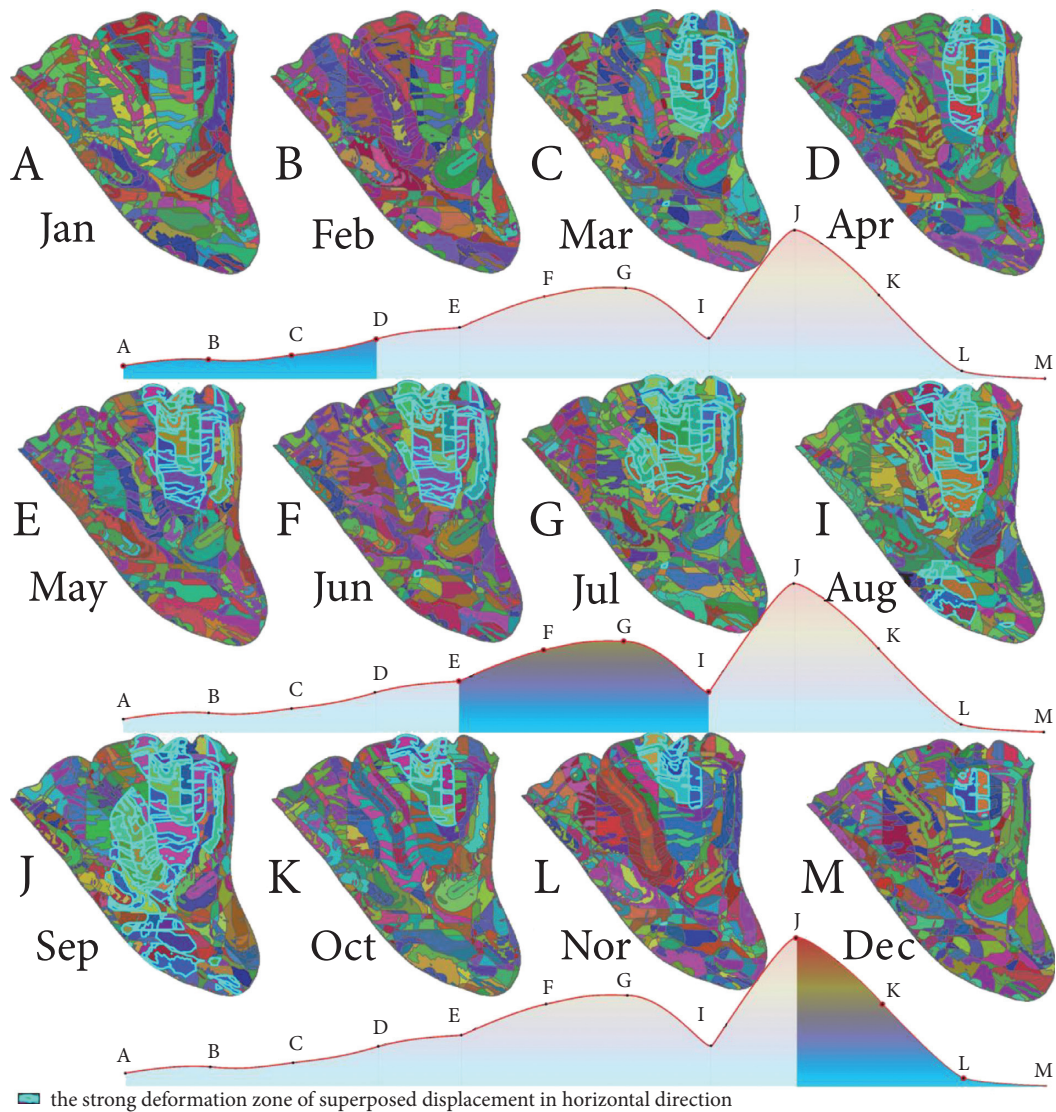


FIGURE 15: Evolution of the superposed displacement in the horizontal direction based on the development characteristic partition.

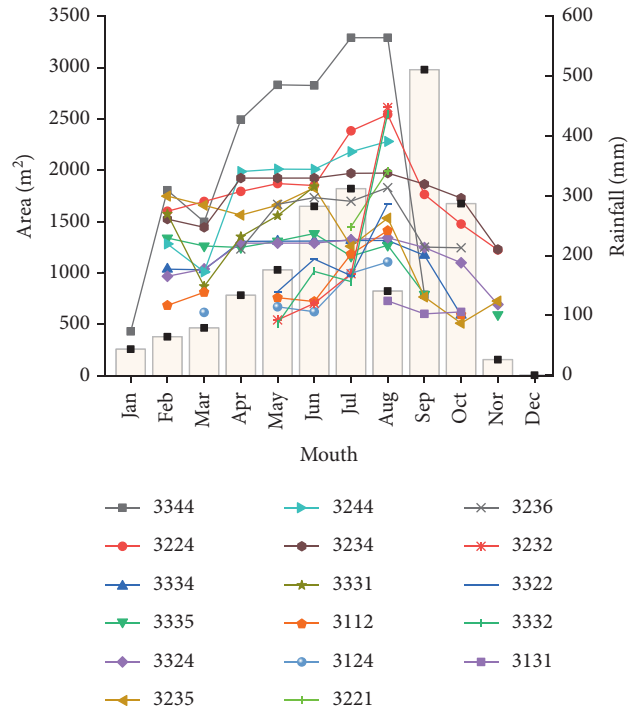


FIGURE 16: Area variation of the characteristic zone of strong deformation of superposed displacement in the horizontal direction under different rainfalls.

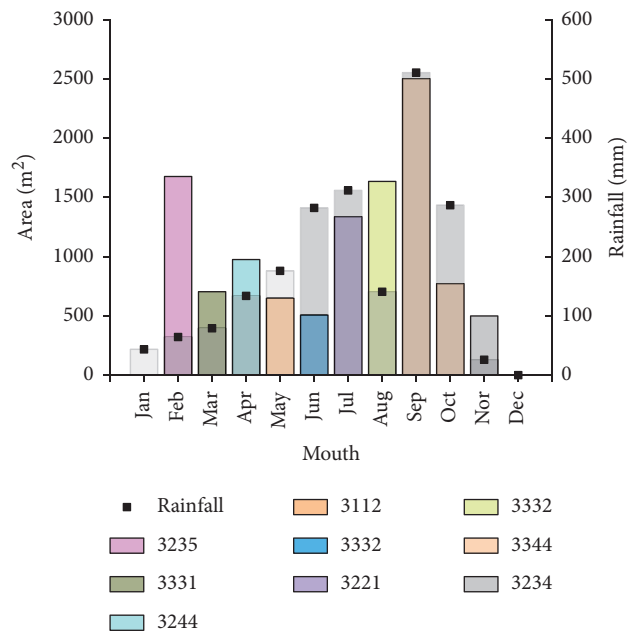


FIGURE 17: Diagram of the area of active characteristic zone in relation to the superposed displacement in the horizontal direction.

vertical deformation zones were mainly located in the middle of the bank slope, and the maximum vertical displacement occurred on the right side of the middle of the bank slope. As shown in Figure 12, the vertical displacement increased with the amount of rainfall. From January to September, the area of zones with obvious vertical deformation which extends from the right front of the bank slope

to the middle gradually increased with the amount of rainfall and reached the maximum value of 54031.06 m^2 in September when the rainfall was the highest and 510.60 mm . After September, this area gradually decreased to 7561.79 m^2 in December without rainfall. In flood season, the area of the zone with obvious vertical deformation was 247417.77 m^2 and accounted for 80.07% ; it was larger than 59023.42 m^2 in

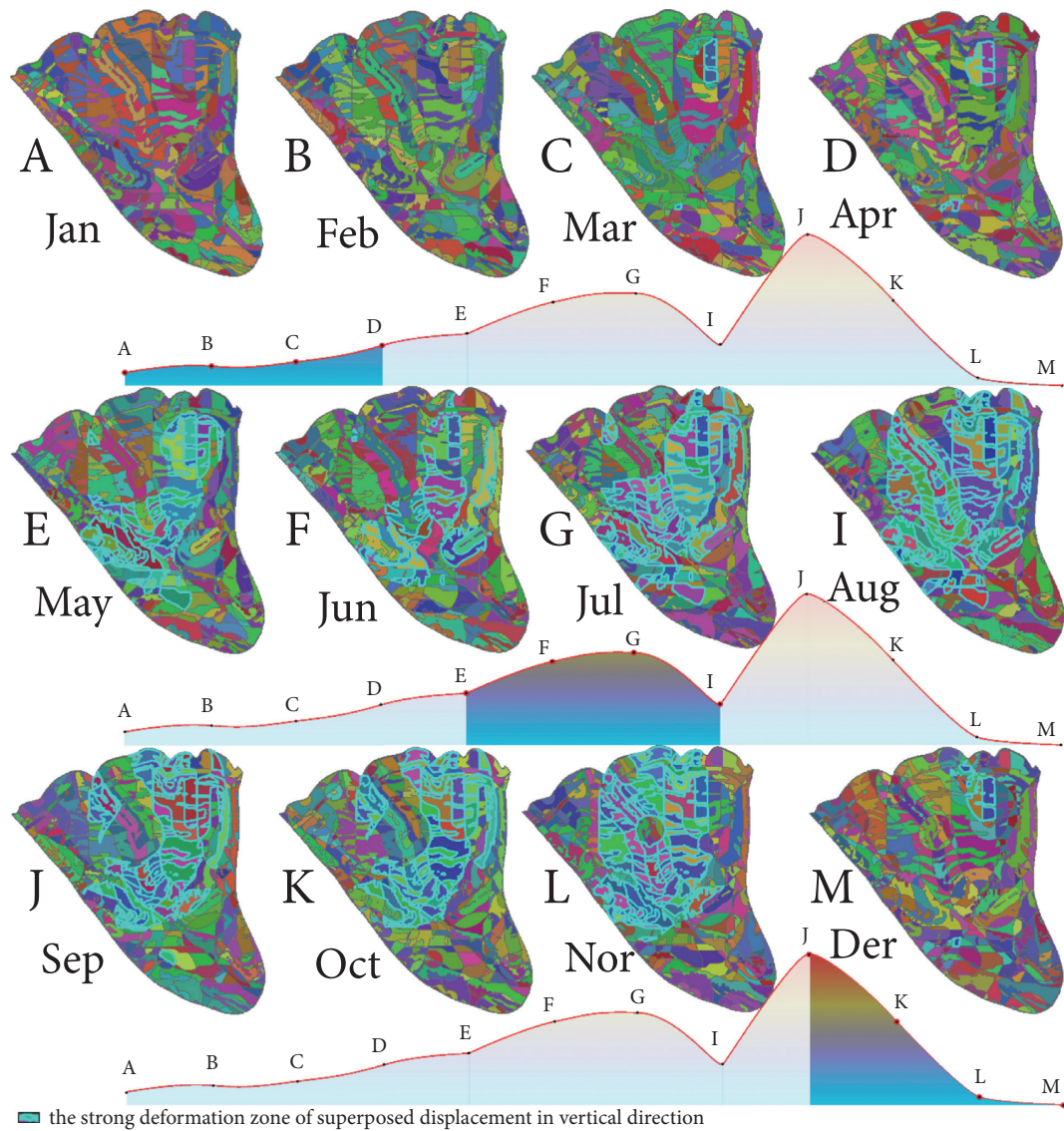


FIGURE 18: Evolution of the superposed displacement in the vertical direction based on the development characteristic partition.

the nonflood season, so it can be inferred that the vertical displacement is more sensible to rainfall than horizontal displacement.

1.8. Spatial-Temporal Evolution Nephogram of Total Displacement. Figure 13 shows the cloud map of total displacement under the condition of different rainfalls. The natural breaks (Jenks) method was used to classify the total displacement into ten grades and the zones where the total displacement is greater than 18.42 mm were defined as the obvious deformation zone. Obvious deformation zones were mainly located in the right front and middle rear of the bank slope. The area of obvious deformation zones reached the maximum value of 47455.16 m² when the rainfall was the highest and decreased to 4141.94 m² in December without rainfall (Figure 14). The total displacement distribution is similar to the horizontal displacement and S-shape in the front and rear edge of the bank slope while the total

displacement distribution is similar to vertical displacement in the middle of the bank slope, which means that the middle features vertical displacement and the front and rear edge features horizontal displacement.

1.9. Toppling Displacement Evolution Characteristic Based on Development Characteristic Partition

1.9.1. Analysis of Horizontal Toppling Evolution. The horizontal displacement nephogram under the condition of different rainfalls was classified into three grades using the Jenks natural breaks method: weak horizontal deformation zone where the horizontal displacement is smaller than 9.42 mm is represented by 1, medium horizontal deformation zone where the horizontal displacement ranges from 9.42 mm to 14.53 mm is represented by 2, and strong horizontal deformation zone where the horizontal displacement is larger than 14.53 mm is represented by 3. Based

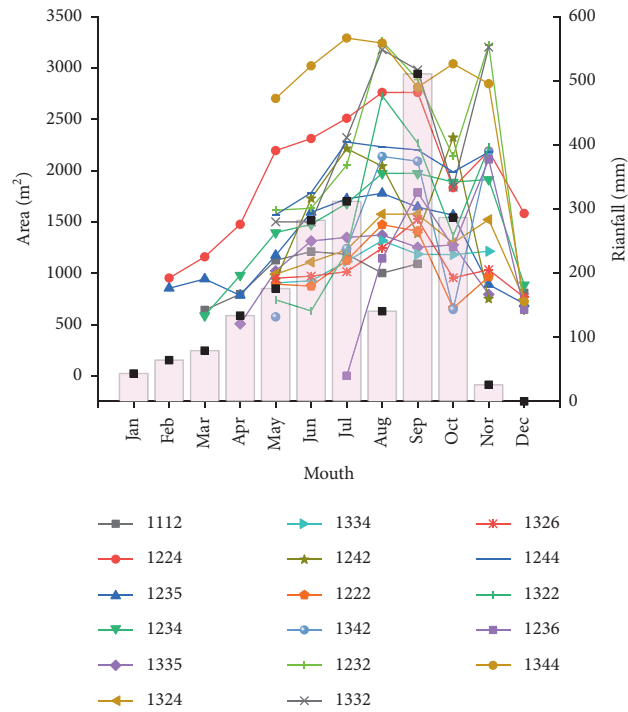


FIGURE 19: Area variation of the characteristic zone of strong deformation of superposed displacement in the vertical direction under different rainfalls.

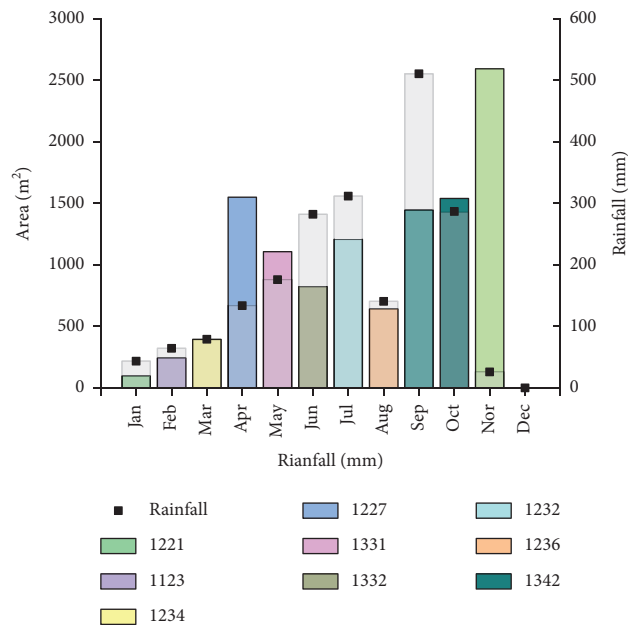


FIGURE 20: Diagram of the area of active characteristic zone concerning the superposed displacement in the vertical direction.

on the development characteristics partition (Figure 6), the evolution nephogram of the horizontal displacement based on geometric features was obtained through the superposition of ArcGIS raster layers (Figure 15).

The strong deformation zones of superposed displacement in the horizontal direction can be obtained through GIS in Figure 15. The influence of a zone with a small area is ignored, the strong deformation zones with an area larger

than 1000 m² are counted, and the zones with an area change rate greater than 15% are selected. As shown in Figure 16, under different amounts of rainfall, the variation of the area of strong deformation zones was analyzed, and it can be found that the area increased with the amount of rainfall and reached the peak when the rainfall was the highest value of 510.60 mm and then decreased with rainfall reducing. Zone 3344 was the largest strong deformation zone where the area

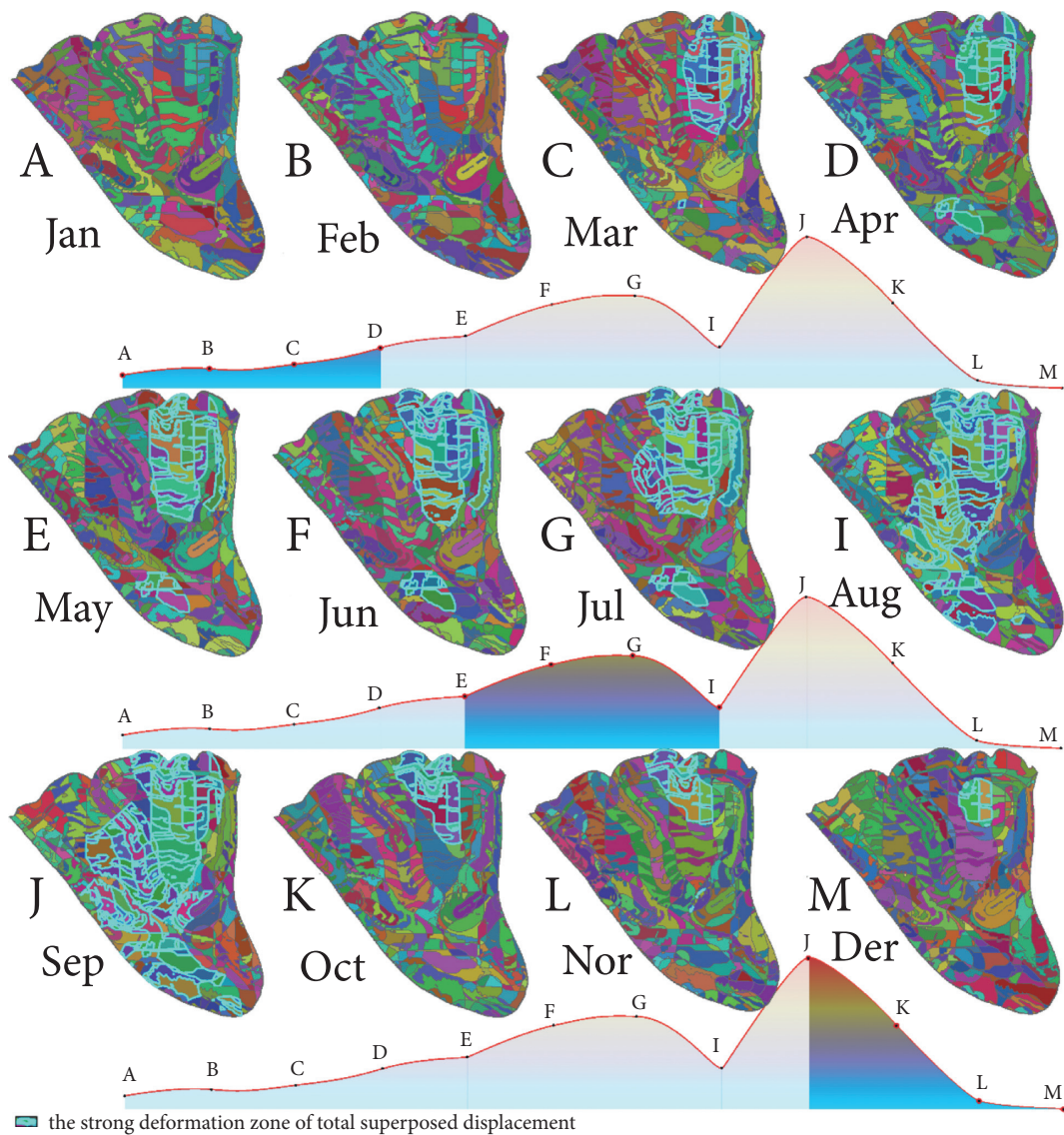


FIGURE 21: Evolution of the superposed displacement in the total direction based on the development characteristic partition.

was 3290 m^2 and the peak rainfall was 510.60 mm ; at the same time, it is featured by medium to high slope and mature stage and formed a 50 m buffer zone. Under different rainfalls, the strong deformation zone accompanying the largest area change was defined as the displacement prone zone. As shown in Figure 17, when the rainfall decreased from 510.60 mm to 286.70 mm , the area change of Zone 3344 was 2502.23 m^2 with an area changing rate of 76.5% .

1.9.2. Analysis of Vertical Toppling Evolution. Similarly, the vertical displacement nephogram under the condition of different rainfalls was classified into three grades using the Jenks best natural fracture method: weak vertical deformation zone where the vertical displacement is greater than -1.77 mm is represented by 1; medium vertical deformation zone where the vertical displacement ranges from -4.82 mm to -1.77 mm is represented by 2; strong vertical deformation zone where the vertical displacement is smaller than

-4.81 mm is represented by 3. Based on the geometrical partition (Figure 6), the evolution nephogram of the vertical displacement based on geometric features was obtained through the superposition of ArcGIS raster layers (shown in Figure 18).

The strong deformation zones of superposed displacement in the vertical direction can be obtained through GIS in Figure 18. The influence of a zone with a small area was ignored, the strong deformation zones with an area larger than 1000 m^2 were counted, and the zones with an area change rate greater than 15% were selected. As shown in Figure 19, the area variation of strong deformation zones under different rainfalls is explored, and it can be seen that the area of every strong deformation zone increased with the rainfall amount and reached the maximum when the rainfall was the peak value of 510.60 mm and then decreased. Zone 1344 had the largest area of 3290 m^2 , was featured by medium and high slope and mature stage, and formed a 50 m buffer zone. As shown in Figure 20, Zone 1232 located in the

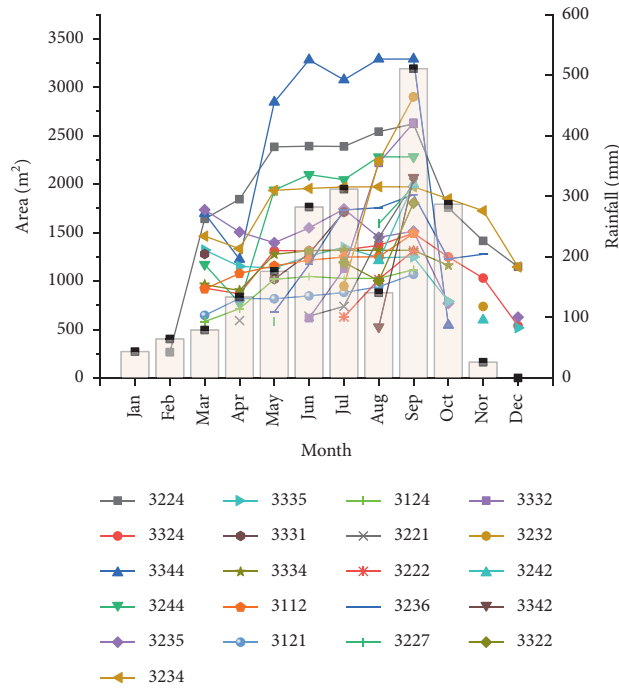


FIGURE 22: Area variation of the characteristic zone of strong deformation of total superposed displacement under different rainfalls.

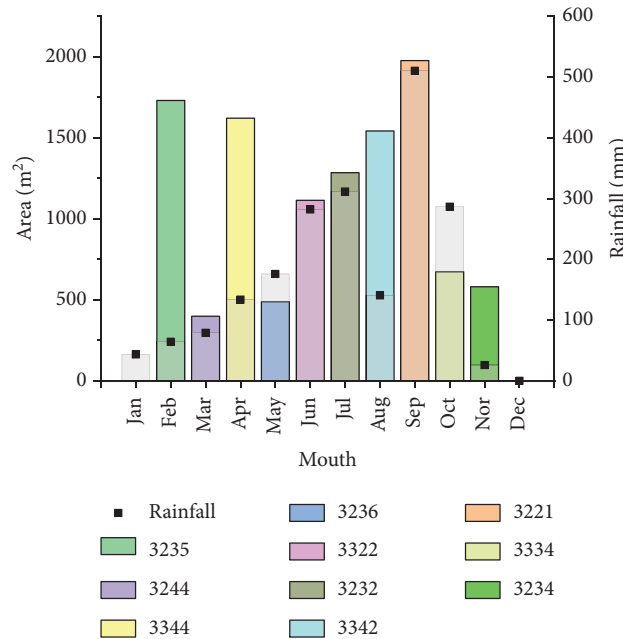


FIGURE 23: Diagram of the area of active characteristic zone concerning the total superposed displacement.

right rear of the bank slope and featured by high slope and the young stage was the vertical displacement prone area and formed a 10 m buffer zone; when the rainfall decreased from 26 mm to 0 mm, its area change was 2593.59 m² with an area changing rate of 80.4%.

1.9.3. Analysis of Total Toppling Evolution. Similarly, under the condition of different rainfalls, the total displacement

nephogram was classified into three grades using the Jenks best natural break method [41–48]: weak total deformation zone where the total displacement is smaller than 11.68 mm is represented by 1; medium total deformation zone where the total displacement ranges from 11.69 mm to 18.13 mm is represented by 2; strong total deformation zone where the total displacement is greater than 27.33 mm is represented by 3. Based on the geometrical partition (Figure 6) and geometric features, the evolution nephogram of the total

displacement was obtained through the superposition of ArcGIS raster layers (Figure 21).

The strong deformation zones of superposed total displacement can be obtained through GIS in Figure 21. The influence of zones with a small area was ignored, the strong deformation zones with an area larger than 1000 m² were counted, and the zones with an area change rate greater than 15% were selected. As shown in Figure 22, the area variation of strong deformation zones under different rainfalls is explored, and it can be seen that the area of every strong deformation zone increased with the rainfall amount and reached the maximum when the rainfall was peak value of 510.60 mm and then decreased. Zone 3344 holds the largest area of 3290 m² and was featured by medium and high slope and mature stage and formed a 50 m buffer zone. As shown in Figure 23, when the rainfall decreased from 510.60 mm to 286.70 mm, the area change of Zone 3221 located in the right front and left rear of bank slope and formed a 10 m buffer zone was 1977.56 m² with an area changing rate of 98.26%; it was featured by medium-high slope and young stage and was the total displacement prone area.

2. Conclusions

Based on discrete surface displacement monitoring data and different geological divisions, this paper explored the toppling deformation evolution law of each zone in a typical reverse-dip rock slope under the condition of different rainfalls; this research can provide some reference for monitoring, advance warning, and prevention of similar anti-inclined slopes. The main research results are as follows:

- (1) Taking the bank slope, gully buffer zone, and erosion degree as the development characteristic factors, the bank slope is divided into 104 development characteristic zones, and the largest characteristic zone is featured by high slope and mature stage and forms a 10 m buffer zone.
- (2) The horizontal displacement mainly occurs on the right front and middle rear of the bank slope while the vertical displacement mainly occurs on the middle of the bank slope; when the rainfall increases to the maximum, the toppling deformation reaches the peak; higher rainfall intensity increases the displacement while vertical displacement is more sensitive to the rainfall than horizontal displacement since the obvious vertical deformation area is 247417.77 m² and accounts for 80.07% in flood season while obvious horizontal deformation area is 43083.64 m² and accounts for 74.61%.
- (3) Under the influence of rainfall, the development characteristic partition is superimposed with the spatial and temporal evolution nephogram of toppling displacement. When the rainfall increases, the maximum area of displacement superposition strengthening deformation zone is 3290 m², which is characterized by medium and high slope and mature stage and 50 m gully buffer zone. When the rainfall decreases, the area change of the most prone zone of

displacement superposition in the horizontal direction is 2502.23 m², with a change rate of 76.5%, which is located in the middle and rear of the bank slope. The area change of the most prone zone of displacement superposition in the vertical direction is 2593.59 m², with a change rate of 80.4%, which is located at the right rear of the bank slope. The area change of the most prone zone of total displacement superposition is 1977.56 m², and its change rate is 98.26%, which is mainly located in the right front and left rear of the bank slope.

Data Availability

The processed data required to reproduce these findings cannot be shared at this time as the data also form part of an ongoing study.

Conflicts of Interest

The authors declare no conflicts of interest.

Acknowledgments

This project was supported by the National Natural Science Foundation of China (52068066 and 51908482) and the Scientific Research Program of the Higher Education Institution of Xinjiang (XJEDU2018Y008).

References

- [1] R. Huang, "Large-scale landslides and their sliding mechanisms in China since the 20th century," *Chinese Journal of Rock Mechanics and Engineering*, vol. 26, pp. 433–454, 2007.
- [2] R. Huang, "Geodynamical process and stability control of slope development," *Chinese Journal of Rock Mechanics and Engineering*, vol. 27, pp. 1525–1544, 2008.
- [3] D. C. Wyllie, "Toppling rock slope failures examples of analysis and stabilization," *Rock Mechanics Felsmechanik Mcanique des Roches*, vol. 13, no. 2, pp. 89–98, 1980.
- [4] S. L. Nichol, O. Hungr, and S. G. Evans, "Large-scale brittle and ductile toppling of rock slopes," *Canadian Geotechnical Journal*, vol. 39, no. 4, pp. 773–788, 2002.
- [5] X. Tu, F. Dai, X. Lu, and H. Zhong, "Toppling and stabilization of the intake slope for the Fengtan Hydropower Station enlargement project, Mid-South China," *Engineering Geology*, vol. 91, no. 2–4, pp. 152–167, 2007.
- [6] E. Eberhardt, "Twenty-ninth Canadian Geotechnical Colloquium: the role of advanced numerical methods and geotechnical field measurements in understanding complex deep-seated rock slope failure mechanisms," *Canadian Geotechnical Journal*, vol. 45, no. 4, pp. 484–510, 2008.
- [7] Z. Zhang, G. Liu, S. Wu et al., "Rock slope deformation mechanism in the cihaxia hydropower station, northwest China," *Bulletin of Engineering Geology and the Environment*, vol. 74, no. 3, pp. 943–958, 2014.
- [8] M. Liu, F.-z. Liu, R.-q. Huang, and X.-j. Pei, "Deep-seated large-scale toppling failure in metamorphic rocks: a case study of the Erguxi slope in southwest China," *Journal of Mountain Science*, vol. 13, no. 12, pp. 2094–2110, 2016.
- [9] L. Xie, E. Yan, J. Wang, G. Lu, and G. Yu, "Study on evolutionary characteristics of toppling deformation of reverse-dip

- layered rock slope based on surface displacement monitoring data,” *Environmental Earth Sciences*, vol. 77, no. 4, 2018.
- [10] J.-c. Cai, N.-p. Ju, R.-q. Huang et al., “Mechanism of toppling and deformation in hard rock slope: a case of bank slope of Hydropower Station, Qinghai Province, China,” *Journal of Mountain Science*, vol. 16, no. 4, pp. 924–934, 2019.
- [11] S. Gschwind, S. Loew, and A. Wolter, “Multi-stage structural and kinematic analysis of a retrogressive rock slope instability complex (Preonzo, Switzerland),” *Engineering Geology*, vol. 252, pp. 27–42, 2019.
- [12] S. Sardana, A. K. Verma, R. Verma, and T. N. Singh, “Rock slope stability along road cut of Kulikawn to Saikhamakawn of Aizawl, Mizoram, India,” *Natural Hazards*, vol. 99, no. 2, pp. 753–767, 2019.
- [13] D. Shaunik and M. Singh, “Bearing capacity of foundations on rock slopes intersected by non-persistent discontinuity,” *International Journal of Mining Science and Technology*, vol. 30, no. 5, pp. 669–674, 2020.
- [14] N. Caine, “Toppling failures from alpine cliffs on ben Lomond, Tasmania,” *Earth Surface Processes and Landforms*, vol. 7, no. 2, pp. 133–152, 1982.
- [15] R. E. Goodman and J. W. Bray, “Toppling of rock slopes, specialty conference on rock engineering for foundations and slopes,” *Engineering*, vol. 8, 1976.
- [16] L. R. Alejano, I. Gómez-Márquez, and R. Martínez-Alegría, “Analysis of a complex toppling-circular slope failure,” *Engineering Geology*, vol. 114, no. 1-2, pp. 93–104, 2010.
- [17] R. Huang, L. Yusheng, and Y. Ming, “The implication and evaluation of topping failure in engineering geology practice,” *Journal of Engineering Geology*, vol. 25, pp. 1165–1181, 2017.
- [18] D. P. Adhikary and A. V. Dyskin, “Modelling of progressive and instantaneous failures of foliated rock slopes,” *Rock Mechanics and Rock Engineering*, vol. 40, no. 4, pp. 349–362, 2007.
- [19] M. Amini, A. Majdi, and M. A. Veshadi, “Stability analysis of rock slopes against block-flexure toppling failure,” *Rock Mechanics and Rock Engineering*, vol. 45, no. 4, pp. 519–532, 2012.
- [20] A. Majdi and M. Amini, “Analysis of geo-structural defects in flexural toppling failure,” *International Journal of Rock Mechanics and Mining Sciences*, vol. 48, no. 2, pp. 175–186, 2011.
- [21] D. Roy and P. Maheshwari, “Probabilistic analysis of rock slopes against block toppling failure,” *Indian Geotechnical Journal*, vol. 48, no. 3, pp. 484–497, 2017.
- [22] D. Huang, D. Cen, G. Ma, and R. Huang, “Step-path failure of rock slopes with intermittent joints,” *Landslides*, vol. 12, no. 5, pp. 911–926, 2014.
- [23] J.-J. Lian, Q. Li, X.-F. Deng, G.-F. Zhao, and Z.-Y. Chen, “A numerical study on toppling failure of a jointed rock slope by using the distinct lattice spring model,” *Rock Mechanics and Rock Engineering*, vol. 51, no. 2, pp. 513–530, 2017.
- [24] P. Sikora and M. Wesolowski, “Numerical assessment of the influence of former mining activities and plasticity of rock mass on deformations of terrain surface,” *International Journal of Mining Science and Technology*, vol. 31, no. 2, pp. 209–214, 2021.
- [25] Z. Chen, W. Gong, G. Ma et al., “Comparisons between centrifuge and numerical modeling results for slope toppling failure,” *Science China Technological Sciences*, vol. 58, no. 9, pp. 1497–1508, 2015.
- [26] W.-C. Huang, K.-C. Li, J.-Y. Hsieh, M.-C. Weng, and W.-Y. Hung, “Deformation behaviors of dip slopes considering the scale effect and their geological properties,” *Bulletin of Engineering Geology and the Environment*, vol. 79, no. 3, pp. 1605–1617, 2019.
- [27] Z. Tao, Y. Shu, X. Yang, Y. Peng, Q. Chen, and H. Zhang, “Physical model test study on shear strength characteristics of slope sliding surface in Nanfen open-pit mine,” *International Journal of Mining Science and Technology*, vol. 30, no. 3, pp. 421–429, 2020.
- [28] Y. Ye, Z. Guangcheng, C. Hongjie, W. Mingfei, B. Liulei, and C. Zheng, “Study on the failure mechanism of rock slope with layered cataclastic structure,” *Chinese Journal of Rock Mechanics and Engineering*, vol. 40, pp. 365–381, 2021.
- [29] D. P. Adhikary, A. V. Dyskin, R. J. Jewell, and D. P. Stewart, “A study of the mechanism of flexural toppling failure of rock slopes,” *Rock Mechanics and Rock Engineering*, vol. 30, no. 2, pp. 75–93, 1997.
- [30] M.-A. Brideau and D. Stead, “Controls on block toppling using a three-dimensional distinct element approach,” *Rock Mechanics and Rock Engineering*, vol. 43, no. 3, pp. 241–260, 2010.
- [31] A. K. Alzo’ubi, C. D. Martin, and D. M. Cruden, “Influence of tensile strength on toppling failure in centrifuge tests,” *International Journal of Rock Mechanics and Mining Sciences*, vol. 47, no. 6, pp. 974–982, 2010.
- [32] D. Gu and D. Huang, “A complex rock topple-rock slide failure of an anaclinal rock slope in the Wu Gorge, Yangtze River, China,” *Engineering Geology*, vol. 208, pp. 165–180, 2016.
- [33] D. Huang and D. M. Gu, “Influence of filling-drawdown cycles of the Three Gorges reservoir on deformation and failure behaviors of anaclinal rock slopes in the Wu Gorge,” *Geomorphology*, vol. 295, pp. 489–506, 2017.
- [34] S. Yu, X. Ren, J. Zhang, H. Wang, and Z. Sun, “An improved form of smoothed particle hydrodynamics method for crack propagation simulation applied in rock mechanics,” *International Journal of Mining Science and Technology*, vol. 31, no. 3, pp. 421–428, 2021.
- [35] N. Bar, M. Kostadinovski, M. Tucker et al., “Rapid and robust slope failure appraisal using aerial photogrammetry and 3D slope stability models,” *International Journal of Mining Science and Technology*, vol. 30, no. 5, pp. 651–658, 2020.
- [36] M. Dong, F. Zhang, J. Lv, Y. Fei, and Z. Li, “Study of stability influencing factors of excavated anti-dip rock slope,” *KSCE Journal of Civil Engineering*, vol. 24, no. 8, pp. 2293–2303, 2020.
- [37] Z.-y. Wang, D.-m. Gu, and W.-g. Zhang, “Influence of excavation schemes on slope stability: a DEM study,” *Journal of Mountain Science*, vol. 17, no. 6, pp. 1509–1522, 2020.
- [38] A. N. Strahler, “Hypsometric (Area-Altitude) analysis of erosional topography,” *The Geological Society of America Bulletin*, vol. 63, 1952.
- [39] W. M. Davis, *The Geographical Cycle*, Macmillan Education, UK, 1973.
- [40] J. Chen, S. T. Yang, H. W. Li, B. Zhang, and J. R. Lv, “Research on geographical environment unit division based on the method of natural breaks (Jenks),” *The International Archives of the Photogrammetry, Remote Sensing and Spatial Information Sciences*, vol. XL-4/W3, pp. 47–50, 2013.
- [41] Z. Leng, Y. Fan, Q. Gao, and Y. Hu, “Evaluation and optimization of blasting approaches to reducing oversize boulders and toes in open-pit mine,” *International Journal of Mining Science and Technology*, vol. 30, no. 3, pp. 373–380, 2020.
- [42] I. Vennes, H. Mitri, D. R. Chinnasane, and M. Yao, “Large-scale distress blasting for seismicity control in hard rock

- mines: a case study,” *International Journal of Mining Science and Technology*, vol. 30, no. 2, pp. 141–149, 2020.
- [43] A. I. Lawal, S. Kwon, O. S. Hammed, and M. A. Idris, “Blast-induced ground vibration prediction in granite quarries: an application of gene expression programming, ANFIS, and sine cosine algorithm optimized ANN,” *International Journal of Mining Science and Technology*, vol. 31, no. 2, pp. 265–277, 2021.
- [44] X. Liu, S. Song, Y. Tan et al., “Similar simulation study on the deformation and failure of surrounding rock of a large section chamber group under dynamic loading,” *International Journal of Mining Science and Technology*, vol. 31, no. 3, pp. 495–505, 2021.
- [45] R. Kumar, P. K. Mandal, A. Narayan, and A. J. Das, “Evaluation of load transfer mechanism under axial loads in a novel coupler of dual height rock bolts,” *International Journal of Mining Science and Technology*, vol. 31, no. 2, pp. 225–232, 2021.
- [46] Y. Zhou, D. Zhao, B. Li, H. Wang, Q. Tang, and Z. Zhang, “Fatigue damage mechanism and deformation behaviour of granite under ultrahigh-frequency cyclic loading conditions,” *Rock Mechanics and Rock Engineering*, vol. 54, no. 9, pp. 4723–4739, 2021.
- [47] J. Ma, X. L. Li, J. G. Wang et al., “Experimental study on vibration reduction technology of hole-by-hole presplitting blasting,” *Geofluids*, vol. 20, 2021.
- [48] J. Wang, T. Zuo, X. Li, Z. Tao, and J. Ma, “Study on the fractal characteristics of the pomegranate biotite schist under impact loading,” *Geofluids*, vol. 22, 2021.

Review Article

Research Progress on Corrosion of Equipment and Materials in Deep-Sea Environment

Sheng Chen ^{1,2,3}, Liping Qiu ¹, Shaofang Sun,¹ Junyi Yang ², Qinghua Meng,² and Weibo Yang³

¹School of Chemistry and Chemical Engineering, University of Jinan, Jinan, Shandong 250000, China

²School of Mechanical Engineering, Hangzhou Dianzi University, Hangzhou, Zhejiang 310018, China

³Anji ChangHong Chain Manufacturing Limited Company, Huzhou, Zhejiang 313300, China

Correspondence should be addressed to Liping Qiu; lipingqiu@ujn.edu.cn and Junyi Yang; [junyiyang@hdu.edu.cn](mailto:junyi yang@hdu.edu.cn)

Received 25 September 2021; Accepted 5 November 2021; Published 3 December 2021

Academic Editor: Nan Zhang

Copyright © 2021 Sheng Chen et al. This is an open access article distributed under the Creative Commons Attribution License, which permits unrestricted use, distribution, and reproduction in any medium, provided the original work is properly cited.

The deep sea is the frontier of materials research in the 21st century. Owing to the particularity of pressure (15–120 MPa), hydrothermal temperature (90–400°C), and explosive fluid (strong H₂S) in the deep-sea hydrothermal field environment, the research on the corrosion mechanism of service materials in this environment under the coupling action of many harsh factors is almost blank. It has become the bottleneck of equipment and material research and development for China to explore the deep sea. This paper reviews the research progress of corrosion mechanisms of deep-sea environmental materials at home and abroad, and forecasts the research trend and difficulties in this field, especially in the deep-sea hydrothermal field. At the same time, it points out the urgency of the construction of harsh environment materials platform and its relevance to the discipline construction of marine college.

1. Introduction

Oceans account for about 71% of the Earth's surface area and are the largest potential resource base on the planet that has not been fully recognized and utilized by mankind. In addition to offshore oil and gas resources and coastal ores, there are also known metallic mineral resources such as polymetallic nodules, cobalt-rich crusts, and polymetallic sulfides that have commercial exploitation value on the seabed. These minerals are rich in nickel, cobalt, copper, manganese, and gold and silver metals, and the total reserves are tens to thousands of times higher than the corresponding reserves on land. With the increasing demand for metal resources and the exhaustion of land mineral resources, seabed mineral resources will become the replacement resources of mankind in the 21st century. These seabed mineral resources are often referred to as deep-sea mineral resources because they are located at depths of thousands of meters under water. According to the latest statistics in the 2020 InterRidge database (<https://www.interridge.org/>), more than 700 hydrothermal fields were found on a global

scale, including 660 active hydrothermal activity fields and 55 inactive hydrothermal activity areas (Figure 1).

In the deep-sea hydrothermal area (Figure 2), seawater, which penetrates the lithosphere through oceanic crust fissures, is heated by a heat source (surrounding rock or magma chamber) and reacts with the surrounding rock, resulting in changes in the properties of the surrounding rock and seawater itself, and seawater turning into hydrothermal fluid in this process. As it continues to percolate and be heated, the hydrothermal fluids (temperatures of 300–400°C and density of 0.7 g/cm³) rise back to the seafloor under buoyant force, forming sulfide-rich hydrothermal fluids that erupt at several meters per second and form “black chimneys”; (rich in H₂S, H₂, CH₄, metal sulfides, oxides, metal particles, and so on).

Owing to the high temperature near the vents in the submarine hydrothermal area, a special temperature and pressure field coupled with various extreme factors is formed, with the hydrothermal vent temperature (350–400°C) at the center, the mineral seawater temperature (50–90°C) in the nearby area, and seawater temperature

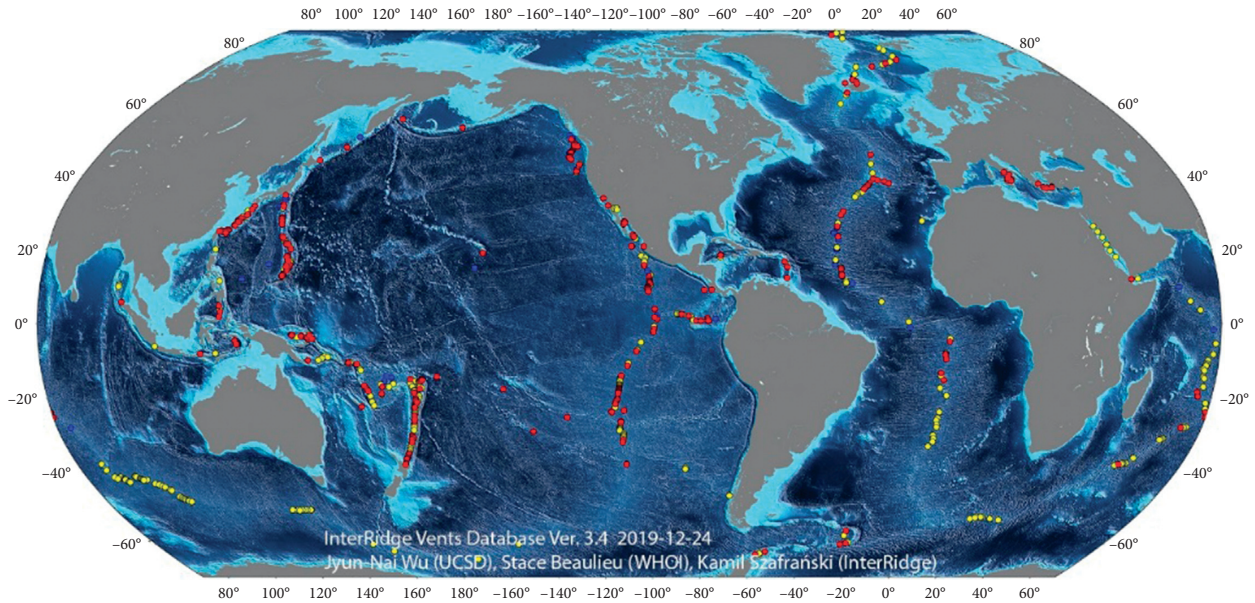


FIGURE 1: Distribution of hydrothermal activities globally (<https://doi.org/10.1594/PANGAEA.917894>).

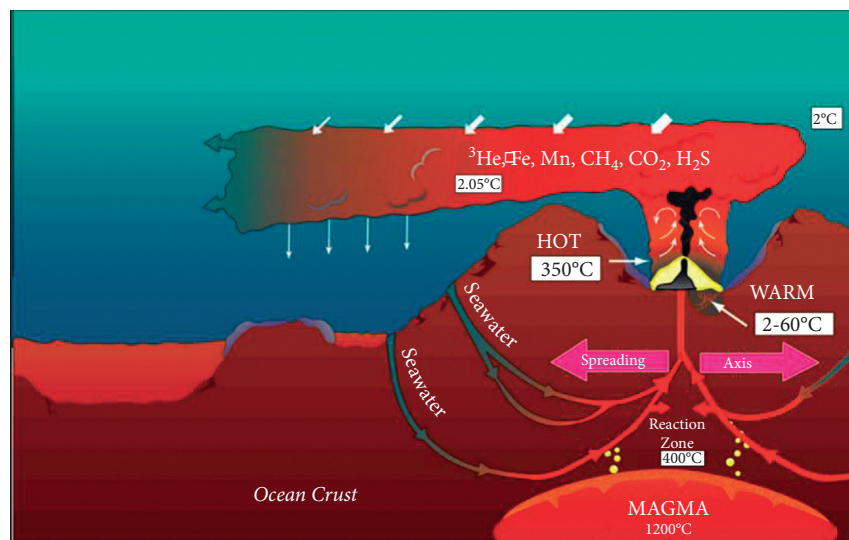


FIGURE 2: Schematic of hydrothermal activity and hydrothermal plume (figure from Schmidt Ocean Institute).

(0–4°C) in the outer edge. The in-depth study and exploration of this area will not only provide a new breakthrough direction for potential energy exploitation in the future but also have great theoretical and engineering value for the study of the origin of life and biological evolution. In addition, seafloor hydrothermal activity is a cyclic mechanism of heat and material exchange between the ocean and the seafloor lithosphere [1]. It is a window for human to understand the process of deep earth movement, and its scientific significance and resource potential have become one of the most promising areas for human exploration of nature in the 21st century.

The outline of the 14th Five-Year Plan points out that China should actively expand the space for the development of marine economy, strengthen the national strategic

scientific and technological force, and strengthen the deployment of high-tech in deep space, deep earth, and polar exploration. This is not only because the deep-sea contains rich seabed mineral resources but also with the progress of science and technology and the exhaustion of earth resources, the exploitation and exploration of deep-sea oil and gas, mineral resources, deep-sea engineering construction, and the exploitation and application of deep-sea equipment will become the focus of the development of marine economy in various countries.

However, China's deep-sea equipment manufactured materials for a long time to rely on imports, delaying the pace of China's entry and management of the deep sea. Therefore, it is urgent to accelerate the research on the preparation science and protection technology of materials

adapted to the deep-sea field in China (especially the extreme environment of the submarine hydrothermal field).

Since the 1960s, material researchers have carried out continuous and effective experimental research in the natural environment corrosion of deep-sea (deep-sea hanging plates) and laboratory simulation corrosion.

2. Tests in the Deep-Sea Environment

Starting in the 1960s, some countries have successively carried out material deep-sea environment corrosion aging research to promote the development of their own deep-sea exploration technology, deep-sea resources exploitation technology, space utilization technology, deep-sea environmental protection technology, and equipment manufacturing technology in the deep-sea area, improving its competitiveness in the field of marine technology [2, 3].

Between 1962 and 1970, the Civil Engineering Laboratory, Naval Construction Battalion Center, Port Hueneme, California, exposed approximately 20,000 specimens of about 475 different alloys in the Pacific Ocean. These specimens were exposed at the surface and at nominal depths of 2,500 and 6,000 feet for periods of time varying from 123 to 1064 days [4, 5]. Figure 3 is a schematic diagram of the deep-sea corrosion test device used. The test apparatus, which used a bottom-sitting sample frame, was dropped on the sea floor after reaching the deep-sea test site. During recovery, the anchorage on the seabed was disconnected through acoustic release device, and the connecting rope was brought up to the upper buoy, and finally, the sample frame was lifted. The study found that the effect of depth (seawater pressure) cannot be generalized for different materials. Taking aluminum alloy as an example, the degree of pitting and corrosion cracking in deep-sea environment was much higher than that in shallow sea environment and the corrosion damage was more serious.

At the same time, the United States Lockheed company in 1968–1972 carried out deep-sea tests using seven kinds of coating aluminum alloy and various stainless steel materials; the samples were placed in the Pacific Ocean and the Atlantic Ocean at depths of 1798 m and 1234 m, respectively. By comparing the corrosion morphology of stainless steel, it is found that the maximum corrosion cracking depth of the two samples is 5.0 mm and 2.5 mm, respectively. The authors suggest that the oxygen content of the Pacific sample site is lower than that of the Atlantic sample site, which inhibits the passivation of stainless steel and leads to a higher corrosion cracking rate.

In the 1970s, the former Soviet Union carried out deep-sea corrosion tests (Figure 4). On carbon steel, stainless steel, copper, brass, aluminum alloy, and other materials in the Pacific Northwest and the Sargasso Sea [6, 7]. The duration of the experiments was 20, 40, and 70 days. Corrosion of stainless steel and aluminum alloys is correlated with temperature and changes appreciably to a depth of 300 m. Below this level (from 300 to 5500 m), the corrosion is practically constant. Corrosion of carbon steel depends on the oxygen and silica contents and temperature. India National Institute of Oceanography selected four types of metals (mild steel, brass, aluminum, and stainless

steel) for exposure tests during the period November 1987 to November 1988 at depths exceeding 1000 m in the Arabian Sea, to assess their behavior with respect to corrosion. The results indicated an increase of the corrosion rate of mild steel and brass with increased depth, whereas in the case of stainless steel and aluminum, the corrosion rate decreased with increased depth. This difference in behavior with respect to depth could be attributed to the characteristic way that metals and alloys react with the dissolved oxygen present in the water column [8, 9]. In addition, it was also pointed out that although macroscopic biocontamination was minimal in deep-sea conditions, the growth of microbial films on the sample surface and the corrosion induced by microorganisms could not be ignored, although the inhibition effect of high pressure in the deep sea on the growth of many microbial communities was limited [10].

In recent years, the latest advances in deep-sea corrosion testing have come from European research teams (Figure 5). This study aims to investigate the deep-sea environment effects on the corrosion of Al, Fe, and Cu alloys, employed in the KM₃NeT project, a deep-sea infrastructure designed to host a neutrino telescope [11–14]. Alloys commonly used in seawater, as well as less widely employed materials, were studied. Samples were immersed at the NEMO site (located off Capo Passero, Italy; 3365 m depth) for consecutive time periods of 6, 12, and 18 months. A representative set of samples was recovered, and laboratory tests were performed to evaluate the type and degree of corrosion attack. Stainless steel reported the best performance in terms of the weight loss, corrosion rate, and corrosion morphology. However, also Al 5093 and Al 6082 performed satisfactorily in terms of the weight loss and corrosion rate. This prescreening will be partially employed in selecting building materials for the KM₃NeT structure. Some studies have pointed out [11] that deep-sea conditions will also change the corrosion products of aluminum alloys. The corrosion products of 6000 series aluminum alloy are Al(OH)₃ in the shallow seawater environment at 1 atmosphere pressure, while the corrosion products in the deep-sea environment are mainly aluminite (Al₂O₃·H₂O).

In 2008, CSIC 725 Research Institute took the lead in carrying out large-scale aging test of material corrosion in deep-sea natural environment in China, successfully breaking through several key technologies such as low-power long-term self-sustaining design of deep-sea test devices, simulation, and analysis of underwater stress state of large depth deep-sea test device, and in-situ corrosion detection of deep-sea [15, 16]. The deep-sea environmental tests at different depths have been carried out in the South China Sea, and more than 13 000 deep-sea corrosion data of 9 categories and more than 40 kinds of different materials and different periods have been accumulated. The first deep-sea corrosion aging database of materials in China was established. The environmental factors such as sea temperature, salinity, dissolved oxygen, and current velocity in the test area were measured and collected, and the relationship between material corrosion and environmental factors was discussed, which promoted the systematic study of material properties in the deep-sea environment in China [17, 18].

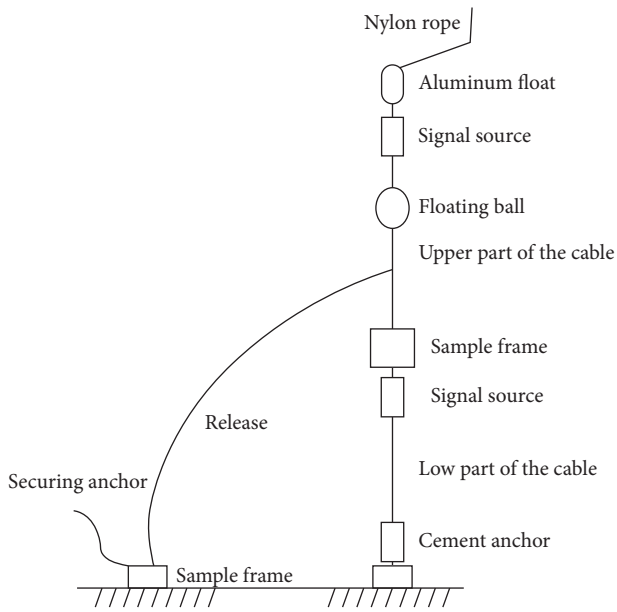


FIGURE 3: Seated bottom type deep-sea corrosion test device (figure from [5]).

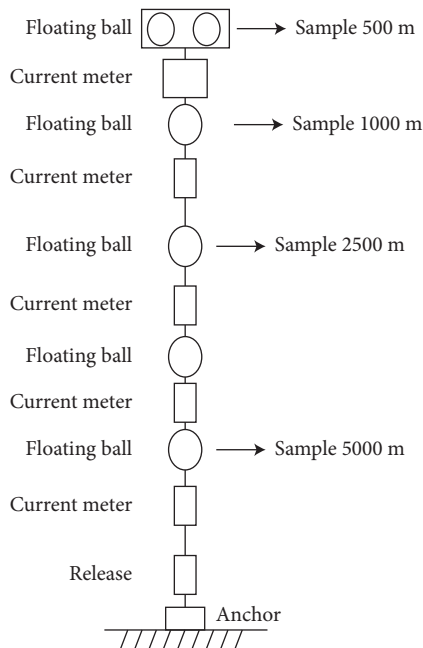


FIGURE 4: Bunch-style testing system (figure from [5]).

With the manned submersible “Jiaolong” and the semisubmersible deep-water drilling platform “Haiyang Shiyou 981”, which were designed and integrated by our country, reaching the depth of 7 000 m and entering the South China Sea to carry out deep-water operations, the problem of erosion of deep-sea equipment in deeper waters and more demanding environment has become increasingly prominent. The harshness of the deep-water environment results in severe corrosion hazards [4, 19–21], which may even become the technological bottleneck for the development of deep-sea resources, utilization of deep-sea space,

and construction of deep-sea engineering, thus affecting the smooth research and development of China’s Marine economy and deep-sea equipment.

It is also pointed out [22] that under deep-sea conditions, stainless steel components will be subjected to great static pressure, stress corrosion sensitivity will sharply increase, and mechanical properties will continue to deteriorate, which will seriously threaten the service safety of deep-sea structures and equipment. The corrosion properties of titanium alloy in deep-sea environment were studied and tested, and the results show that it has excellent corrosion resistance and pitting resistance, and almost no corrosion occurs at low temperature in deep sea.

3. Laboratory Simulation Corrosion

Although the results of deep-sea sling-plate test are real and direct, the experiment cost is expensive, the experiment cycle is long, and the continuous reliability of the experiment is difficult to guarantee because of the harsh deep-sea environment conditions. Therefore, it is increasingly urgent to simulate deep-sea environment conditions and carry out laboratory corrosion experiments. The simulated accelerated corrosion method in the laboratory is to study the main factors and laws of material corrosion by chemical or electrochemical accelerated methods by simulating the deep-sea environment using small samples and an artificial seawater medium.

Pohjanne studied the corrosion behavior of aluminum-magnesium alloy 5083-H116, aluminum-silicon magnesium alloy 6082-T6, and aluminum-zinc magnesium alloy 7020-T5 in a simulated deep-sea environment by a laboratory experiment [23]. The test results indicated that the pitting corrosion resistance of aluminum alloys decreased as the depth increased, but the effect depended much on the alloy. The deterioration in corrosion resistance is caused by the changes in the chemical composition of the sea water and the hydrostatic pressure.

Norway and India have carried out electrochemical measurements of deep-sea corrosion of metals, but their methods and emphases are different. In India, the exposure test was carried out in the Indian Ocean at a depth of 5 000 m, while seawater was collected from 500 m to 1200 m deep and sent to the laboratory as a medium for polarization detection of steel samples. Although the test results obtained cannot be completely reliable but, as a relative comparison, are feasible. During 1982–1984, the Norwegian Ship Research Institute conducted deep-sea cathodic protection measurements of materials at various sites in the North Norwegian Sea, ranging from 400 m to 1200 m, and obtained the protection current density of steel at different depths off Norway. Researchers developed a deep-sea corrosion potential and galvanic current multichannel test devices for metal materials (Figure 6), which can monitor the corrosion process of dozens of metal materials in situ, providing strong technical support for the study on deep-sea corrosion mechanisms of metal materials, as well as the specific material compatibility application in deep-sea environment [24].

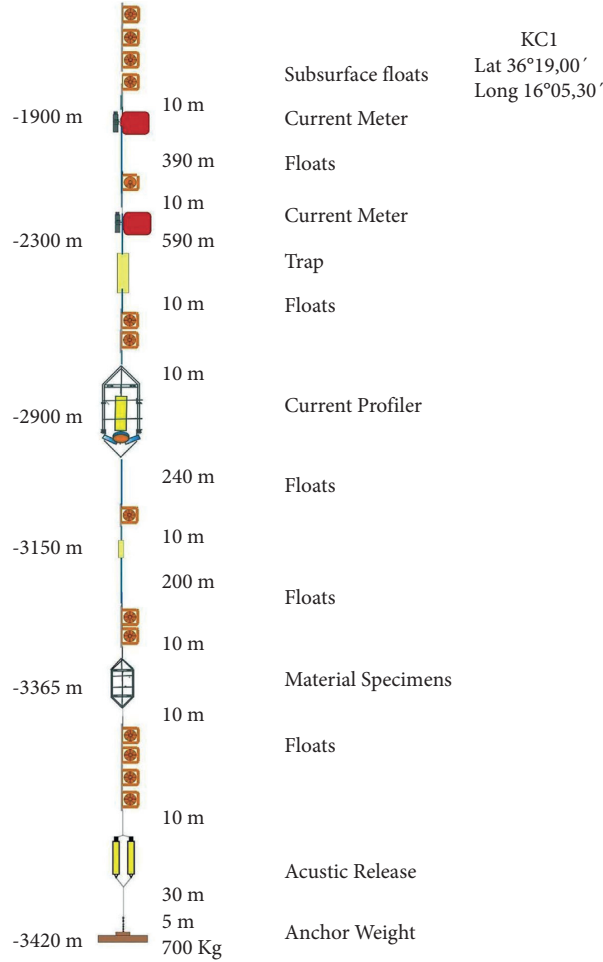


FIGURE 5: Outline of the KCL mooring line (from [11] located at the NEMO site).

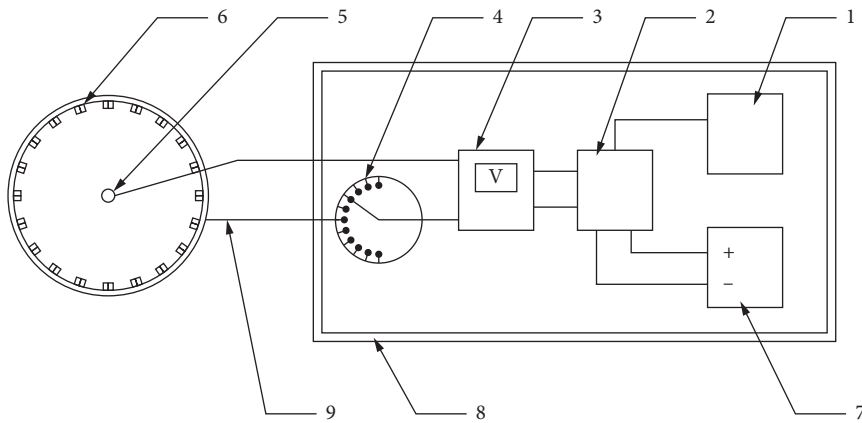


FIGURE 6: Schematic diagram of assembly structure principle of invention device (from [24]. 1-Data Storage, 2- General control device, 3-potentiometer, 4- transverter, 5- reference electrode, 6- under test sample, 7-battery, 8- pressure hull, 9- pressure resistant multicore wire.)

The China University of Petroleum designed a water-tight electronic chamber (Figure 7) that can conduct various corrosion electrochemical online monitoring operations in a water depth of 300 m [25]. CSIC 725 Research Institute, the University of Science and Technology, the Beijing Ocean University of China, the Institute of Metals, the Chinese Academy

of Sciences, and other domestic research institutes have carried out fruitful research work and obtained a lot of important data in the field of deep-sea materials laboratory corrosion [16, 26]. Yuan focused on the main characteristics of the marine environment, which include temperature, dissolved oxygen, and static and dynamic load; the effects on the electrochemical

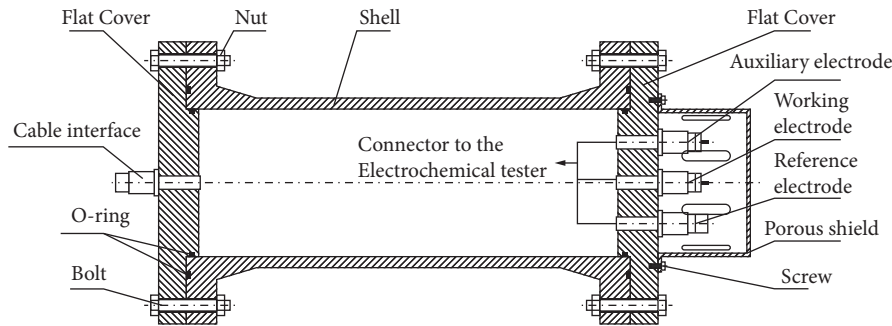


FIGURE 7: Shell structure of the watertight electronic cabin (figure from [25]).

corrosion behavior and hydrogen embrittlement under cathodic protection of X80 pipeline steel in $\text{pH} = 7.7 \pm 0.2$, 3.5wt.% Na Cl simulated seawater were studied, and the influence law and mechanism of various marine environmental factors were discussed for providing basic data and theoretical guidance to the application and protection of X80 pipeline steel in marine engineering [27]. At present, most of the research focuses on the following aspects:

3.1. Simulation Prediction. Researchers studied the influence of environmental factors such as the pH value and calcium and magnesium ion deposition on the corrosion behavior of materials in the deep seas [28, 29]. On this basis, a database and simulation prediction model related to seawater corrosion parameters and corrosion velocity are established. Hou et al. predicted the corrosion velocity of A3 steel at different depths in the South China Sea using the function expression between corrosion velocity of A3 steel and marine environmental parameters based on systematically summarizing the characteristics and variation rules of environmental factors of deep-sea corrosion such as dissolved oxygen, temperature, and salinity.

Jia Wang and his team from the Ocean University of China studied the corrosion behavior of five kinds of marine engineering steels above 5 000 m deep-sea environment using electrochemistry, artificial neural network, and database methods [30]. The results showed that temperature, dissolved oxygen, salinity, and the pH value were the main factors which affect the corrosion behavior of the five steels in seawater. Two databases, MCM-CORRDB03 and MCM-GOCEANDB03, were established and used to predict the corrosion rate of related steels in different deep-sea environments. It is pointed out that the deep-sea corrosion behavior of different metal materials is very different, and the main environmental factors are different. It was confirmed that the minimum corrosion rate of the behavior was appeared at a depth of 5000 meters, and the content of dissolved oxygen has the greatest effect on the corrosion behavior of the steels in deep ocean.

3.2. Stress Corrosion. Most of the alloy in the deep-sea environment is not sensitive to stress corrosion; however, the deep-sea environment determines the must usage of the high-strength alloy with high stress corrosion sensitivity; therefore,

the role of hydrogen in the deep-sea stress corrosion mechanism research should not be ignored. High hydrostatic pressure by influencing the process of stripping, absorption, and penetration may change the material stress corrosion sensitivity. The crack growth rate of stress corrosion failure is generally between 10^{-6} and $10^{-3} \text{ mm s}^{-1}$, which is much higher than the corrosion rate without stress. Stress corrosion cracking usually has no obvious symptoms, but it often results in catastrophic results [31]. At present, only a few countries in the world have carried out deep-sea environmental corrosion tests of materials. The United States (Hueneme Port test station), the former Soviet Union, Japan (Kitakyushu test site and Beppu test site), the United Kingdom, and other countries began to conduct deep-sea environmental corrosion test studies of materials in the 1960s, followed by Norway, India, and other countries [4].

3.3. Temperature. Temperature can not only directly affect the corrosion behavior of materials but also intensify (coupling) the influence of other corrosion factors. The increase of temperature will accelerate the reaction rate of cathodic and anodic processes, increase the diffusion rate of oxygen, increase the conductivity of seawater, and promote the corrosion process. Research shows that when the temperature is around 23°C , the corrosion rate is the largest, while the deep ocean water temperature is lower than 23°C ; the corrosion rate for carbon steel and low alloy steel will decline with the increase of depth. The study from Yuan [27] provided more detailed information about the effect of temperature. The promoting effect of temperature in corrosion was realized by accelerating anodic dissolution. The cathode process was closely related to the concentration of dissolved oxygen, and the Evans diagram was obtained (Figure 8). With the decrease of the concentration of dissolved oxygen, the corrosion rate decreased significantly. However, in the deep-sea environment, high-temperature factors (such as seafloor hydrothermal area) on the material of the coupling corrosion mechanism exploration are almost blank [30].

3.4. Velocity of Sea Water. Seawater flow can scour the corrosion products, weaken the blocking effect of corrosion product deposition on the corrosion reaction, and accelerate the corrosion reaction. Corrosion of deep-sea equipment is usually much less affected by velocity in the deep sea than that at the surface [4, 32].

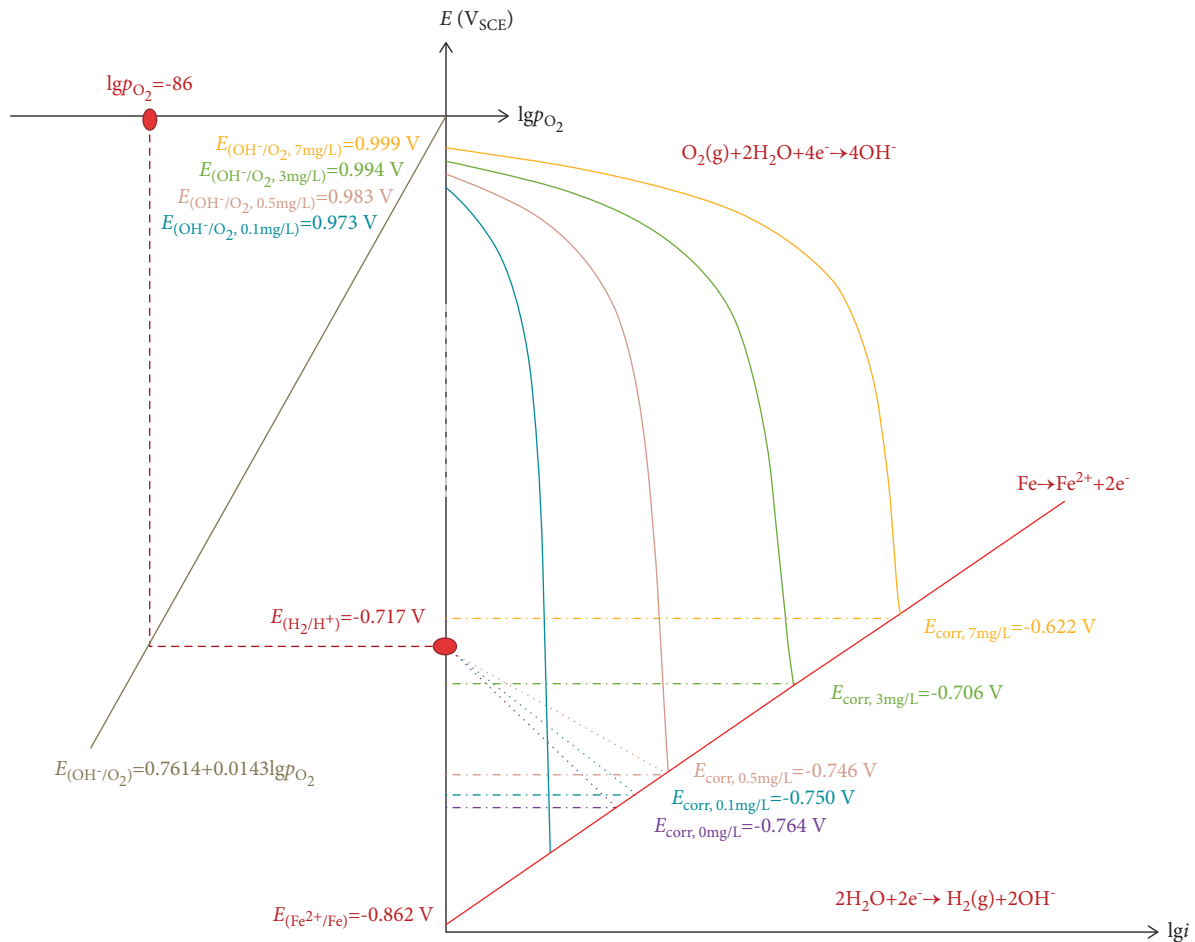


FIGURE 8: Evans diagram for the corrosion of X80 pipeline steel in the 3.5% NaCl solution with different dissolved oxygen concentrations (from [27].)

Tang et al. compared the corrosion rates of Q235 carbon structural steel (A3 steel) in static and flowing seawater by indoor and deep-sea weight loss tests, and tested the corrosion rates of Q235 carbon structural steel (A3 steel) by the potentiodynamic method, as well as the environmental parameters in seawater with different flow rates [33]. The results show that the seawater flow can accelerate the corrosion rate of Q235 carbon structural steel in seawater, especially in the initial stage of corrosion.

Researchers studied the corrosion behavior of five kinds of aluminum alloys in flowing seawater [34]. The results show that aluminum alloys are more resistant to corrosion than carbon steel and copper, especially Al-Mg-Al alloys and Al-Mg-Mn alloys. Because Al-Cu and Al-Zn-Mg alloys have obvious peeling corrosion sensitivity in flowing seawater, they should not be used in flowing seawater environment. These experimental results are only suitable for shallow sea experiments under atmospheric environment or low pressure. In addition, eddy-induced vibration is easily caused by ocean current, which causes fatigue damage to slender structural parts such as columns, pile legs, and submarine pipelines, affecting the safety of marine engineering structures [31].

3.5. Pitting. Pitting is the phenomenon of corrosion holes with deep development in local areas of the metal surface and no corrosion or slight corrosion in other areas. The application of cyclic stress can promote pitting initiation. SEM observation results show that the increase of hydrostatic pressure increases the metastable pitting and increases the sensitivity of average corrosion performance of Ni-Cr-Mo-V steel [2, 35, 36].

As mentioned above, decades of systematic exploration laid the experimental and theoretical foundation for the subsequent in-depth research and development of deep-sea materials. However, owing to the lack of research platforms and means and the low degree of perfection, especially the field of research starts late in China, it left a lot to be explored and perfected.

4. Development Trends and Difficulties

4.1. Shortcomings of Deep-sea Material Corrosion Test Research. Owing to the limitation of depth and real-time detection in deep-sea environment, previous deep-sea corrosion tests were only carried out in the deep-sea environment of about 6000 m for a variety of metal materials,

while the data of material corrosion in the deeper sea are scattered and lack of systematic.

During the test of corrosion and aging of materials (bolt) in the deep natural environment, the domestic and foreign experts measured and collected the environment factors such as seawater temperature, salinity, dissolved oxygen, current velocity, and probes into the relationship between the environmental factors and the material corrosion. However, in experimental design, pressure (depth) is usually taken as a variable factor, while other ocean factors are basically considered constant or with small variation range, and there is a lack of effective means to systematically test and detect the corrosion of materials under the coupling effect of multiple factors in deeper waters and more demanding environments. Owing to the single influencing factor, or the lack of multiple factors, coupling and alternating to exert a significant impact on material corrosion (such as seawater flow under deep pressure and temperature rise influence on material corrosion law and superimposed effect) results detection; therefore, it is difficult to provide an accurate theoretical description and guidance for material design and equipment protection in more complex and harsh environment (such as hydrothermal field environment) in deep sea.

Given the limitations of natural deep-sea corrosion experiments, although experts developed a multichannel device to test the potential and galvanic current of metal materials during corrosion in the deep-sea environment, designing and developing one electrochemical test device, which could tolerate deeper water pressure, is resistant to outside interference, and could integrate with electrochemical data acquisition, storage, and remote (wireless) transmission, is still difficult. Therefore, the corrosion mechanism of deep-sea environmental materials remains to be further studied.

In addition, the previous theoretical research and discussion of corrosion are mostly focused on the surface protection technology of materials, while the research on the design theory and preparation science of materials is less, resulting in the long-term lag in the research and development of key materials in this field and becoming the bottleneck of China's entry into the deep sea and exploration of the deep sea.

4.2. Experimental Research Trend of Deep-Sea Material Corrosion. The research on the corrosion mechanism of deep-sea materials is the basis of the research and development of deep-sea equipment and materials. Only by conducting an overall and comprehensive research on the corrosion mechanism in the deep-sea environment can the targeted design, protection, and selection of equipment and materials be carried out according to the deep-sea service environment. Based on this, further research on the corrosion of environmental materials in the deeper sea is carried out to complement the corrosion tests in the deep-sea area. It will be the direction and trend of the research and development of the corrosion mechanism of deep-sea materials and their adaptive materials in the future to design

and establish the environment simulation corrosion platform of deep-sea hydrothermal zone and carry out the corrosion mechanism research of materials in this field.

To realize the deep sea, especially near hydrothermal area, the coupling corrosion environment influence the mechanism of the key factors in the process of repeatability test, an urgent need to design and manufacture of deep-sea environment experiment simulator, with in situ observation and real-time measurement on the basis of the following functions: (1) safe injection or controllable generation of the harmful gases under a high-pressure and high-temperature environment; (2) in the high-pressure and harmful gas test environment, ensure the smooth matching of pressure in the heating process; (3) in the test environment, material corrosion information is collected smoothly and has good repeatability.

To select and design high-strength metal materials for deep-sea use, metal materials (such as precipitated hardened stainless steel) that are expected to be suitable for such harsh environments (such as near the hydrothermal zone) should be selected for three types of experiments. That is, no load, elastic load, and plastic deformation of the deep-sea hydrothermal zone environmental coupling corrosion experiment.

On this basis, the multifactor coupling corrosion mechanism of high-strength metal materials is explored, which will promote the design and preparation of deep-sea extreme environment simulation devices and carry out innovative experimental research.

4.2.1. Multifactor Coupling Corrosion In the Deep-sea Environment. In the deep-sea hydrothermal area environment (Pressure: 15–120 MPa, temperature of hydrothermal vent: 90–400°C), multisystem, multifactor (the strong H₂S and other harmful gases, intense upwelling of ocean currents (seafloor storm) caused by temperature changes) interweave and superimpose each other and act together on the service equipment and materials in this environment. The strong coupling effect may magnify the influence degree of a factor by several or tens of times.

4.2.2. Design of the Total Element Deep-Sea Simulation Experiment Device. The designed and prepared deep-sea extreme environment corrosion simulation device should meet the full-depth pressure (120 MPa) condition within the known deepest ocean. The maximum operating temperature of 430°C can cover all the found hydrothermal zones and the surrounding ambient temperature. Flexible safe injection and extraction function of gas, microorganisms, corrosive gas, and liquids can ensure the implementation and detection of multifactor coupling corrosion process. The design of a continuous and precisely controlled agitation system in the range of 0–2 000 r/min will simulate the state of deep-sea current inrush to simulate the seabed inrush velocity in the range of 0–15 m/s. The simulation device with the aforementioned design conditions will be able to simulate the harshest environment of the deep sea to the greatest extent.

4.2.3. Fill the Blank Of the Deep-Sea Integral Corrosion Test. The experiment of material corrosion in deep-sea hydrothermal zone will improve the overall corrosion mechanism of deep-sea materials and fill in the blank of material corrosion mechanism in this area. The structure, composition, morphology, and distribution of each component phase or microstructure in the microstructure of materials subjected to multifactor coupling corrosion were studied. The mechanochemical effect mechanism of materials in an extremely harsh (near hydrothermal field) environment is revealed at macro and phase scales. In the future, it will be one of the important innovative research directions for the cross-penetration of deep-sea engineering and material engineering to combine the corrosion mechanism of materials with the change of microstructure and adaptive design of materials, to select, protect, and design equipment and materials for service in the extremely harsh deep-sea corrosive environment.

5. The Urgency of R&D Platform and Team Building

5.1. Support of National Development Strategy. Marine harsh environment refers to the extreme environment in the deep sea, harsh ocean conditions in the far sea, the alternation of temperature difference, polar ice water, deep cold, and so on, which is summarized as the “;four poles”; of the ocean. With the expansion of national resources exploration and drilling to the sea areas with more complex geological conditions and physical environment, the equipment and materials in service will certainly suffer from wear and corrosion in the harsh and extreme environment. However, owing to the blank material test platform, it is difficult to organize a special research team, which makes it impossible to start the research on the erosion mechanism of equipment and materials in service in extreme environment, especially in the South China Sea, deep sea, open sea, polar, and other harsh environments. As a result, the selection of engineering materials, research and development, and large-scale application greatly lag the strong expectation of the demands in this field and become the bottleneck of national energy drilling and ocean engineering development.

In the 21st century, mankind has entered a period of large-scale exploitation and utilization of the oceans. Marine undertakings are related to the survival and development of the nation and the rise and fall of the country. Zhejiang is not only a large province of marine resources, but also a strong province of marine economy. During the 13th Five-Year Plan period, the provincial Party Committee and government actively promoted the development of marine economy, and formed a good pattern of marine economic development led by the construction of world-class marine ports, driven by the construction of a modern marine industrial system, and supported by strengthening the construction of marine science and education and ecological civilization. To further promote the province's marine economy comprehensive strength and modernization level, to better support the construction of a powerful province of marine, Zhejiang province specially formulates 14th five-year

plan of Marine economy development, attaches importance to and promotes breakthroughs in key technologies, carries out “double sharp double collar” plan. Centering on marine resources, disaster prevention and mitigation, marine new materials, marine engineering equipment, and high-tech ships, scientific research projects are set up in provincial key research and development programs to overcome several key technologies, fully highlighting the economic, ecological, and sustainable capabilities of marine resources development and engineering construction. However, the harsh and complex deep-sea environment seriously restricts and threatens the exploitation of resources and the service safety of marine equipment.

Due to historical reasons, the research on corrosion and protection of marine equipment and materials serving in the harsh marine environment in China is still not thorough, which is very inconsistent with the national strategy and development plan. Therefore, around the regional economic and technological development, strategic target for deep harsh environment in the process of the development of key materials preparation and erosion protection of scientific problems and the corresponding experimental platform construction and exploration, to research and develop the basic theory and form new series which is suitable for the demanding deep and complicated environment adaptability of materials and erosion protection technology. It is of great significance for the development of national strategy and location to build a first-class material research and development and erosion protection team to serve the national overall marine strategy, resource development, and national defense construction and to promote the transformation of China from a major maritime country to a maritime power and Zhejiang from a large province of marine resources to a strong province of marine economy.

The ways to break the bottleneck of service equipment and material corrosion in harsh marine environment are as follows: (1) reasonable material selection and key material development on the basis of the accumulation of a large amount of material environmental corrosion data and research of regularity; (2) establish safety evaluation and life prediction methods for materials in service in harsh environments (deep-sea hydrothermal zone, high humidity and heat in south China Sea, polar cold, etc.); (3) provide reasonable and effective protection technology. The key to link these three aspects is the rapid establishment of a research platform for the corrosion regularity and mechanism of marine engineering materials under harsh environments.

Timely proposed establishment of marine harsh environment materials research and development and protection platform, which is of great significance to improve the layout of Zhejiang Provincial Key laboratory of Marine materials and scientific research and discipline construction of related institutes.

The construction of the platform and the research on the mechanism of material corrosion will highlight the interdisciplinary and integration of various disciplines (life science, environmental science, chemistry and chemical engineering, marine geology, marine physics, etc.). The construction of the platform and the research on the

mechanism of material corrosion will highlight the interdisciplinary and integration of various disciplines (life science, environmental science, chemistry and chemical engineering, marine geology, marine physics, etc.). The establishment of a key laboratory for the research and development of material erosion mechanisms and protection technology in marine extreme environment is the first in China, which will highlight the creativity of the research field. It will benefit Zhejiang province to lead the fierce competition trend of international energy exploitation to march into the deep sea and support the strategy of strong ocean province, to promote the strategic needs of national and provincial marine science and technology development, and to fill the blank of Zhejiang Province's harsh marine environment materials basic research and adaptive materials research platform.

5.2. Platform and Talent Team Construction. Zhejiang province attaches great importance to the development of marine strategy. Aiming at the development of science and technology in the field of marine, it has carried out a relevant advanced layout of the key laboratory of Marine science and technology. Related institutes, respectively, set up MNR Key Laboratory of Submarine Geoscience, State Laboratory of Satellite Ocean Environment Dynamics (SOED), Ocean Engineering Survey, Design and Research Institute, Polar Deep-Sea Technology Institute, Key Laboratory of Marine materials and Related technologies, CAS, Zhejiang Provincial Key Laboratory of Marine Geotechnical Engineering and Materials, Zhejiang Greater Bay Area (Wisdom Ocean) Innovation and Development Center, Zhejiang Provincial Science and technology innovation Service platform for sea trial, and so on. Especially in the Key Laboratory of Marine materials and Related technologies, CAS, guided by the national Marine strategy and regional Marine industry needs, focuses on basic research, process technology integration, and engineering application of marine new materials; studies the interaction between materials and the marine environment; targets on three major marine material damage problems, such as electrochemical coupling corrosion, biological fouling and mechanical-chemical interaction wear; and accelerates the core collaborative capability research and development of failure mechanism and application technology, gradually improving the design and preparation of new marine materials, new coupling damage mechanism, and engineering technology innovation system, becoming a bridge and link for industrial transformation and national defense application of marine new materials.

5.3. The Latest Research Direction of Marine Service Materials in Harsh Environment

5.3.1. Erosion Interface and Erosion Process Dynamics. According to the seawater environment in deep-sea hydrothermal area, we systematically study the corrosion failure behavior of metal materials (nickel base alloy, copper alloy material), nonmetallic ceramic materials, and composite materials in the mechanical and chemical interaction

of high temperature, high pressure, and strong corrosive medium seawater. On this basis, aiming at the characteristics of the deep-sea energy mining equipment, such as serious erosion phenomenon, short service life, low safety, and high cost, by adjusting the microcomposition and surface protection of materials, improved the corrosion resistance, and mechanical properties of materials, enhancing the safety of deep-sea energy exploitation.

5.3.2. Microbial Adhesion Corrosion Process and Protection Technology. Biological fouling is a prominent marine material damage problem faced by marine engineering and equipment. Reveal the interface binding mechanism of marine fouling organisms attached to the surface of materials (especially the lush biological environment in the high humidity and heat of the South China Sea and the submarine hydrothermal zone) and develop antifouling bare engineering materials or adaptive protective materials, which lay a good foundation for solving the problem of biological fouling on the surface of engineering equipment materials in the high humidity and heat (and deep-sea hydrothermal area) sea area in the South China Sea. Previous research is limited to the interface and surface formed between inanimate materials, while the interface and surface formed between the marine material and microbial activity is half of life, and half of the unique compound interface, with the common organizational structure characteristics of the composite interface, and the unique structural characteristics of dynamic development and both "active" biochemical reaction, therefore, making the interface study of marine materials (especially those serving in harsh marine environment) have remarkable novelty.

5.3.3. Erosion Mechanism of Ship Materials in Polar and Open Sea Environments. Study the corrosion resistance, abrasion resistance, crack arrest, welding repair, and coating performance of steel used for arctic icebreakers in a special environments. Establish the testing standards, laying a foundation for the quantification and theoretical study of abrasion phenomenon. Study the key problems in the design of ships sailing in the ice region. Study the spatial distribution characteristics and the determination method of ice load. Study the ultimate bearing capacity of ship hull structure in ice region. Combined with these, the study of marine harsh environment materials can be condensed into three important research directions which are interrelated and characteristic.

6. Conclusion

In this paper, based on the data accumulation and shortcomings of the study on the mechanism of corrosion of deep-sea environmental materials, the establishment of the deep-sea hydrothermal zone environmental materials research platform is proposed to promote the improvement of the theoretical study of deep-sea material corrosion and the research and development of adaptive materials. On this basis, the research scope of deep-sea material corrosion

mechanism is extended to the high humidity and heat of the South China Sea, the research and development of equipment and materials for ocean transportation and marine transportation, and the research and development of corrosion protection technology for ship engineering materials in polar environments.

Data Availability

The data used to support the findings of this study are available from the corresponding author upon request.

Conflicts of Interest

The authors declare that there are no conflicts of interest regarding the publication of this paper.

Acknowledgments

This work was funded by Zhejiang Provincial Key Research and Development Program, Grant/Award Number: 2021C03013; Fundamental Research Funds for the Provincial Universities of Zhejiang, Grant/Award Number: GK199900299012-026; National Natural Science Foundation of China, Grant/Award Number: 42006167; and Natural Science Foundation of Zhejiang Province, Grant/Award Numbers: LQ19D060008 and LZ21E050002.

References

- [1] C. R. German and K. L. Von Damm, "Hydrothermal processes," *Treatise on geochemistry*, vol. 6, p. 625, 2003.
- [2] W. Guo, M. Sun, Ri Qiu, and X. Li, "Research progress on corrosion and aging of materials in deep-sea environment," *Corrosion Science and Protection Technology*, vol. 29, no. 3, pp. 313–317, 2017.
- [3] W. M. Guo, W. Li, and G. Z. Chen, "Corrosion testing in the deep ocean," *Equipment Environment Enquiring*, vol. 3, no. 1, pp. 10–15, 2006.
- [4] M. Schumacher, *Seawater Corrosion Handbook*, Noyes data corporation, Park Ridge, New Jersey, USA, 1979.
- [5] L. K. Xu, W. J. Li, and G. Z. Chen, "Deep sea corrosion test technique," *Marine Sciences*, vol. 29, no. 7, pp. 1–3, 2005.
- [6] I. Ulanovskii and V. Egorova, "Metal corrosion at different depths in the sea," *Proteus*, vol. 14, pp. 137–139, 1978.
- [7] I. Ulanovskii, "Corrosion of metals in the Atlantic Ocean," *Proteus*, vol. 15, pp. 563–566, 1979.
- [8] S. S. Sawant, K. Venkat, and A. B. Wagh, "Corrosion of metals and alloys in the coastal and deep waters of the Arabian Sea and the Bay of Bengal," *Indian Journal of Technology*, vol. 31, no. 12, pp. 862–866, 1993.
- [9] S. S. Sawant and A. B. Wagh, "Corrosion behaviour of metals and alloys in the waters of the Arabian Sea," *Corrosion Prevention and Control*, vol. 36, pp. 154–157, 1990.
- [10] C. Wang, H. Wu, and H. Y. Yang, "Electrochemical behavior of organic coatings in simulated deep ocean environment," *Corrosion Science and Protection Technology*, vol. 21, no. 4, pp. 351–353, 2009.
- [11] P. Traverso and E. Canepa, "A review of studies on corrosion of metals and alloys in deep-sea environment," *Ocean Engineering*, vol. 87, no. 1, pp. 10–15, 2014.
- [12] E. Canepa, R. Stifanese, L. Merotto, and P. Traverso, "Corrosion behaviour of aluminium alloys in deep-sea environment: a review and the KM3NeT test results," *Marine Structures*, vol. 59, pp. 271–284, 2018.
- [13] B. J. Little and J. S. Lee, "Microbiologically influenced corrosion: an update," *International Materials Reviews*, vol. 59, no. 7, pp. 384–393, 2014.
- [14] G. Luciano, P. Letardi, and P. Traverso, "Corrosion behavior of Al, Cu, and Fe alloys in deep sea environment," *La Metallurgia Italiana*, vol. 105, no. 1, pp. 21–29, 2013.
- [15] J. Hou, W. Guo, and C. Deng, "Influences of deep sea environmental factors on corrosion behavior of carbon steel," *Equipment environment engineering*, vol. 5, no. 6, pp. 85–87+104, 2008.
- [16] W. Peng, J. Hou, and W. Guo, "Research progress on the corrosion of Aluminum Alloy in deep ocean," *Development and Application of Materials*, vol. 25, no. 1, pp. 59–62, 2010.
- [17] J. Liu, X. Li, and J. Wang, "EIS characteristic of organic coating with artificial defects in simulated deep-sea environment," *Corrosion Science and Protection Technology*, vol. 22, no. 4, pp. 333–337, 2010.
- [18] J. Zhou, X. Li, X. Cheng, and C. Dong, "Research progress on corrosion of metallic materials in deep sea environment," *Corrosion Science and Protection Technology*, vol. 22, no. 1, pp. 47–51, 2010.
- [19] J. Chen, X. Jiang, Ze Zhang, and Yi Wang, "Review on environmental influence factors of submarine optical fiber cable," *Electronic product reliability and environmental testing*, vol. 36, no. S1, pp. 242–246, 2018.
- [20] J. Liu, X. Li, and J. Wang, "Effect of hydrostatic pressure on the corrosion behaviors of two low alloy steels," *Acta Metallurgica Sinica*, vol. 6, pp. 697–705, 2011.
- [21] H. Sun, Li Liu, and Li Ying, "Corrosion behavior of a high strength low alloy steel under hydrostatic pressure in deep ocean," *Journal of Electrochemistry*, vol. 19, no. 5, pp. 418–424, 2013.
- [22] Y. Yang, T. Zhang, Y. Shao, and G. Meng, "Effect of hydrostatic pressure on the corrosion behavior of Ni-Cr-Mo-V high strength steel," *Corrosion Science*, vol. 52, no. 8, pp. 2697–2706, 2010.
- [23] P. Pohjanne, "Effect of deep sea environment on corrosion of some aluminum alloys," *Finland VTT Offsetpaino: Espoo Research Reports*, vol. 724, p. 17, 1991.
- [24] W. Guo, C. Deng, and W. Li, "Testing method and apparatus for deep sea corrosion potential of metallic materials," CN101074917, 2007.
- [25] L. I. Qiang and L. I. Yan, "A design of watertight electronic cabin for in-situ electrochemical measurement under deep sea condition," *Marine Science*, vol. 37, no. 11, pp. 64–68, 2013.
- [26] W. Wang, W. Guo, and H. Zhang, "Research on the corrosion of stainless steel in deep sea," *Equipment Environmental Engineering*, vol. 7, no. 5, pp. 79–83, 2010.
- [27] W. Yuan, *Effect of marine Service Environment on Electrochemical Corrosion Behavior and Hydrogen Embrittlement under Cathodic protection of X80 Steel*, Wuhan University of Science and Technology, Wuhan, China, 2020.
- [28] Y. Huang, C. Cao, and H. Lin, "Investigation on SCC and SCCinhibition of AISI 316L stainless steel in acidic chloride solution," *Corrosion Science and Protection Technology*, vol. 5, no. 3, pp. 192–196, 1993.
- [29] B. Liu, "Study on the evaluation technique for the performance of anticorrosion coatings under deep sea environment," *Shanghai Coatings*, vol. 49, no. 5, pp. 34–36, 2011.

- [30] J. Wang, J. Meng, X. Tang, and W. Zhang, "Assessment of corrosion behavior of steel in deep ocean," *Journal of Chinese Society for Corrosion and Protection*, vol. 27, no. 1, pp. 1–7, 2007.
- [31] L. K. Xu, *Material Failure and protection in Ocean Engineering*, Chemical Industry Press, Beijing, 2014.
- [32] R. Venkatesan, *Studies on Corrosion of Some Structural Materials in Deep Sea Environment*, India Department of Metallurgy India Institute of Science, Bengaluru, 2000.
- [33] X. Tang, J. Wang, and Li Yan, "Effect of flow velocity of seawater on corrosion rate for A3 steel," *Marine Science*, vol. 7, pp. 26–29, 2005.
- [34] Y. Wang, "Corrosion behavior of aluminum alloy in flowing seawater," *Equipment environmental Engineering*, vol. 2, no. 6, pp. 72–78, 2005.
- [35] K. Ding, L. Fan, and W. Guo, "Deep sea corrosion behavior of typical metal materials and research hotspot discussion," *Equipment environmental engineering*, vol. 16, no. 1, pp. 107–113, 2019.
- [36] Z. Cui, S. Chen, Y. Dou et al., "Passivation behavior and surface chemistry of 2507 super duplex stainless steel in artificial seawater: Influence of dissolved oxygen and pH," *Corrosion Science*, vol. 150, pp. 218–234, 2019.

Research Article

Experimental Investigation on the Influence of Ambient Temperature on the Test Accuracy for the Differential Pressure Hydrostatic Levelling System

Li Bo,¹ Chen Guo,^{1,2} and Wu Qi ²

¹Advanced Road and Bridge Maintenance Engineering Technology Research Center of Jiangsu Province, China Design Group Co., Ltd., Nanjing 210000, China

²Institute of Geotechnical Engineering, Nanjing Tech University, Nanjing 210009, China

Correspondence should be addressed to Wu Qi; qw09061801@163.com

Received 19 September 2021; Accepted 8 November 2021; Published 28 November 2021

Academic Editor: Lingkun Chen

Copyright © 2021 Li Bo et al. This is an open access article distributed under the Creative Commons Attribution License, which permits unrestricted use, distribution, and reproduction in any medium, provided the original work is properly cited.

Hydrostatic levelling system (HLS) is widely used to monitor the settlement of major projects, such as high-speed railways, bridges, tunnels, dams, and nuclear power plants; ambient temperature is the most important influencing factor in the actual engineering settlement detection process. In order to systematically study the influence of ambient temperature T_A on the test accuracy of the HLS, a test platform was built in the ambient temperature laboratory, and the influence of factors, including the amount of T_A change, the rate of increase/decrease of T_A , the expansion coefficient of the connecting pipe, and the distance of the measuring point, on the HLS test accuracy was quantitatively analyzed. The test results show that the elevation of a single HSL case has a linear correlation with the ambient temperature; when the temperature rise rate is greater than $0.1^\circ\text{C}/\text{min}$, the measured data are distorted due to incomplete development of material expansion. The temperature influence coefficient of a single HSL case is linearly related to the expansion coefficient deviation between the refrigerant and pipe; the test error of the double HLS case caused by T_A is attributed to the expansion coefficient deviation of the pipe and the refrigerant between the base station and the measuring point. The relative temperature influence coefficient increases as distance measurement increases, and the HLS test error caused by T_A will maintain a constant value when the distance measurement exceeds a certain value.

1. Introduction

With the rapid socioeconomic development and urbanization, major national infrastructure projects, such as high-speed railways, large-span bridges, ultralong tunnels, high-rise buildings, integrated pipeline corridors, and dams, are increasing; their uneven settlement, deformation, and foundations are a precursor to the engineering failure [1, 2]. Therefore, the accurate measurement for the settlement or deformation is crucial and can provide a scientific reference for the design, construction, and operation of major foundation projects; moreover, reliable data for numerical engineering analysis and long-term deformation prediction can be provided [3–5].

Settlement monitoring methods include geometric levelling, trigonometric levelling, GPS measurement, CCD

optical imaging measurement, laser convergence measurement, hydrostatic levelling, and fibre grating measurement [6, 7]. Among them, geometric levelling and trigonometric levelling are costly and inaccurate; besides, they are limited by topographical fluctuations and challenging to realize real-time monitoring [7, 8]. The accuracy of GPS measurement for plane relative positioning has reached $0.1\text{--}1 \times 10^{-6}$, but its elevation measurement accuracy is only 10^{-2} , which cannot meet some projects' accuracy requirements, and GPS is expensive [9]. Although the CCD optical imaging sensors, laser convergence sensors, and fibre grating sensors have the advantages of high accuracy, strong modality to the terrain, and a high degree of automation [10], the construction and maintenance costs are relatively high, and their anti-interference performance is poor [6]. Because of the simple

structure, high accuracy, strong stability, and little influence from the external environment [11], hydrostatic levelling is widely used in the subsidence monitorization of major projects such as subways [12, 13], bridges [14], tunnels [11, 15–18], dams, and nuclear power plants [19].

The basic principle of the hydrostatic levelling system (HLS) is the liquid connector, which means that, by measuring the relative change of the liquid level in the levelling bowl at different positions, the settlement or uplift of each monitoring point relative to the base point can be determined [19]. However, the accuracy of the HLS is disturbed by factors, including temperature changes, pressure differences, earth tides, and gravity anomalies. [20]. Among them, the earth tides and gravity anomaly can only be filtered under constant temperature, and their influence can be ignored for nonprecision engineering because of the micron-level effect. The influence of pressure difference can be eliminated using equal-pressure pipes. In actual engineering, the temperature change is considered the most important influencing factor during settlement detection. Chen Jihua [21] thought that the uneven temperature would lead to uneven liquid density in the HLS, which leads to the test error; he also proposed a preliminary approach to eliminate temperature impact. Xu Shaofeng [22] investigated the influence of temperature and pressure change on the accuracy of HLS testing and proposed a temperature correction model considering the pipe's expansion coefficient. By installing a temperature sensor in the magnetostatic level bowl, Li Deqiao [9] analyzed the influence of temperature on HLS testing accuracy and verified the temperature correction model proposed by Xu Shaofeng. Based on field test data, Chen et al. [2] proposed a temperature gradient model, and it is suitable for the HLS test system.

In summary, there have been preliminary studies on temperature-induced HLS test errors, but it needs to be noted that most current research studies only focused on a single HLS case, and the temperature changes are concentrated in the order of 10^{-1} [17, 18]. However, during actual settlement monitoring, the annual ambient temperature basically varies from -10 to 30°C . In addition, the existing temperature correction model, based on the water medium, no longer has practical engineering significance, especially in the subzero state; also, there are certain differences in the HLS measuring point spacing arrangement and pipe materials in the actual project.

In this paper, a differential pressure hydrostatic levelling platform was built in the ambient temperature laboratory to systematically study the impact of ambient temperature on HLS testing accuracy. The high-precision temperature sensor was used to collect the temperature data, the change of T_A , the increase/decrease rate of T_A , the expansion coefficient of the connecting pipe, and the distance of the measuring point on the HLS testing accuracy which is quantitatively analyzed. Furthermore, an evaluation method for the influence of ambient temperature on the HLS testing accuracy was developed.

2. Test Platform Construction and Test Program

2.1. Test Equipment and Materials. The Rosemount 3051S differential pressure hydrostatic levelling system was selected in this test because of the advantages of high sensitivity, wide frequency, lightweight, small size, and reliable operation, and its technical parameters are shown in Table 1. The platinum resistance temperature sensor was used to measure the ambient temperature. In order to ensure that the signals of the HLS and temperature sensor can be collected simultaneously and avoid time lag, a full-function collect instrument was selected. The closed-loop controlled ambient temperature chamber in the State Key Laboratory of Materials-Oriented Chemical Engineering of Nanjing Technology University was used to control the temperature changing rate and temperature difference. This equipment can precisely and linearly control the ambient temperature in the range of -40 – 150°C with a fluctuation of less than 0.1°C . The detailed performance parameters of the test chamber are shown in Table 2.

Because the liquid medium of “deionized water + antifreeze” is likely to cause flocculation at low-temperature conditions and the thermal expansion coefficient of water increases with the increase of temperature, dimethicone was selected as the liquid medium in this test. The density of dimethicone is 1.03 g/cm^3 (20°C), and its effective operating temperature range is -60 – 160°C ; the expansion coefficient in the operating temperature range is basically fixed at the value of 6.3×10^{-4} . To study the influence of the expansion coefficient of different connecting pipe materials on the HLS test accuracy, four kinds of connecting pipes with different expansion coefficients, including PU plastic pipe, polypropylene pipe, PTFE pipe, and 204 stainless steel pipe, were selected. The corresponding expansion coefficients are 3.35×10^{-4} , 1.32×10^{-4} , 1.45×10^{-4} , and 6.43×10^{-5} , respectively.

2.2. Test Platform Installation. Figure 1 shows the layout of the test platform. It can be seen that, in the ambient temperature test chamber, all HLS liquid pipes are connected, and one end is connected to the liquid storage tank; besides, all air pipes are connected, and one end is connected to the upper air section of the tank through a drying pipe. It should be pointed out that the pressure difference of a single HLS measuring point comes from the difference between the liquid pressure and the air pressure, which is an absolute value; the liquid/gas pressure difference between the HLS datum point and the test point is used to calculate the relative settlement between the measured point and the datum point, which is a relative value. The RT-1Q temperature sensor was arranged next to every HLS measuring point, and then the output signal of the HLS and temperature sensor can be collected by the VW-102E full-function reader. The technical parameters of the RT-1Q temperature sensor are shown in Table 3.

TABLE 1: Technical parameters of the Rosemount 3051S hydrostatic levelling system.

Index	Value
Input voltage	24 Vdc
Input current	200 mA
Power	0.9 W
Output current (signal)	4–20 mA
Effective pressure range	0–60 kPa
Effective operating temperature	–50–65°C

TABLE 2: Ambient temperature test chamber parameter performance index.

Index	Value
Temperature range (°C)	–40–150
Temperature fluctuation (°C)	<0.1
Temperature rising rate (°C/min)	<3–5
Temperature falling rate (°C/min)	<0.7–1.5
Temperature sensor	Platinum resistance PT100

2.3. Test Scheme. The influence of the ambient temperature on the test accuracy of the HLS usually can be reflected by the measurement error caused by temperature change. Considering the complex change of the annual ambient temperature of the detected structure, especially in winter and summer, two types of test platforms, including single HLS case (only single differential pressure hydrostatic levelling point) and double HLS cases (test base station + test point), were built in a laboratory with the standard ambient temperature to study the influence of the change of T_A ($-10^\circ\text{C} \rightarrow 30^\circ\text{C} \rightarrow -10^\circ\text{C}$) and the rate of increase/decrease of T_A on the accuracy of HLS test quantitatively. At the same time, combined with the actual engineering conditions and the environmental temperature change, the influence of the connecting pipe length between the base station and the test point (the distance between the test points) and the expansion coefficient of the connecting pipe (with obvious material differences) on the HLS test accuracy was comprehensively considered. The test conditions are shown in Table 4.

3. Test Results and Analysis

3.1. The Influence of the Ambient Temperature Rising/Falling Mode on the HLS Test Accuracy. In order to investigate the influence of the rising/falling mode of the ambient temperature on the HLS test accuracy, by converting the vertical pressure of the liquid medium, the settlement difference of case C1 caused by the temperature rising and falling was compared and analyzed. At the beginning of the test, the settlement of the HLS was recorded as zero for the convenience of analysis.

It can be seen from Figure 2 that, as ambient temperature T_A linearly increased from -10°C to 30°C , the corresponding settlement H_E of the HLS linearly decreased to 3.04 mm; when T_A linearly decreased from 30°C to -10°C , H_E linearly rose from 3.04 mm to 0.03 mm. The temperature influence coefficient $P_t = \Delta H_E / \Delta T_A$ was defined to quantitatively

characterize the effect of ambient temperature on the HSL test accuracy; under the rising/falling mode of case C1, P_t of the HLS was $-0.0774 \text{ mm}/^\circ\text{C}$ and $-0.0731 \text{ mm}/^\circ\text{C}$, respectively, and their relative deviation was 5.8%, indicating that the rising or falling mode of ambient temperature had no significant effect on P_t .

3.2. The Influence of Temperature Rising Rate on the HLS Test Accuracy. Because these two ambient temperature changing modes have no significant effect on P_t , there is no need to conduct the falling mode test for cases C2, C3, and C4. Figure 3 shows the influence of the rising rate of temperature on the test accuracy of the single HSL. When the rising rate was 0.05 and $0.02^\circ\text{C}/\text{min}$, H_E and T_A of the HLS were strongly linearly correlated, and P_t of cases C1 and C4 was $-0.0774 \text{ mm}/^\circ\text{C}$ and $-0.0777 \text{ mm}/^\circ\text{C}$, respectively. When the rising rate was $0.1^\circ\text{C}/\text{min}$, H_E decreased as T_A increased, but it needs to be noticed that the linear correlation between T_A and H_E was significantly weakened, and the data fluctuation became large. When the rising rate was $0.2^\circ\text{C}/\text{min}$, as T_A linearly increased, H_E increased with a decreasing rate. When $T_A > 10^\circ\text{C}$, H_E nearly did not increase as T_A increased; this is because the excessive rising rate of ambient temperature led to the incomplete expansion of materials and liquid media, resulting in data distortion and failing to reflect the impact of T_A on the HLS test accuracy.

The relationship between P_t and the temperature rising rate is shown in Figure 4. Combined with Figure 3, it can be seen that when the temperature rising rate was 0.02 or $0.05^\circ\text{C}/\text{min}$, the HLS worked normally, and P_t was consistent. When the rising rate was greater than or equal to $0.1^\circ\text{C}/\text{min}$, the material expansion was not complete, and the data were distorted. In general, the temperature reached the lowest at 0 a.m., and the temperature reached the highest at 13:00. The maximum temperature difference during this period basically did not exceed 30°C . Therefore, under natural conditions, the temperature changing rate was less than $0.04^\circ\text{C}/\text{min}$. Besides, considering the effectiveness of data collection and the test progress, the temperature changing rate was decided to be $0.05^\circ\text{C}/\text{min}$ for other test cases.

3.3. The Influence of Pipe Expansion Coefficient on the HLS Test Accuracy. In order to investigate the influence of the pipe expansion coefficient γ_{pi} on the single HSL test accuracy, a series of single-point test platforms were built with the PU plastic pipe, PTFE pipe, polypropylene pipe, and 204 stainless steel pipe, respectively. The test was carried out under a temperature rising rate of $0.05^\circ\text{C}/\text{min}$. As shown in Figure 5, H_E decreased linearly with the increase of T_A for PU plastic pipes, while H_E increased linearly with the increase of T_A for PTFE pipes, polypropylene pipes, or 204 stainless steel pipes. This is because γ_{pi} of PU plastic pipes is greater than that of dimethicone, and the liquid level of simethicone decreased with the increase of T_A , leading to a decrease in elevation; by contrast, for PTFE pipes, polypropylene pipes, and 204 stainless steel pipes, γ_{pi} is obviously

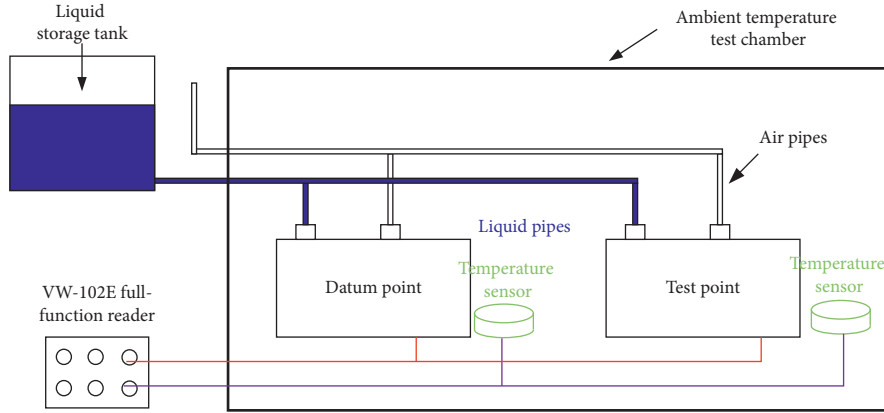


FIGURE 1: Schematic diagram of the working layout for the typical hydrostatic levelling system.

TABLE 3: Technical parameters of the RT-1Q temperature sensor.

Index	Value
Effective operating temperature	-40–80°C
Level of sensitivity	±0.005°C
Temperature measurement accuracy	±0.01°C
Water pressure resistance	≥0.5 MPa
Insulation resistance	≥50 MΩ
Storage humidity	≤80% RH
Storage temperature	-30–70°C

smaller than that of dimethicone, and the liquid level of simethicone rose with the increase of T_A , increasing H_E .

Furthermore, it was found that smaller γ_{pi} would not deliver the influence of T_A on the single HSL measuring point. It is necessary to study the relationship between P_t and the difference between the liquid medium expansion coefficient γ_{di} and the pipe expansion coefficient γ_{pi} . As shown in Figure 6, P_t increased with the increase of $\gamma_{di}-\gamma_{pi}$, showing a linear relationship.

$$P_t = 0.04553(\gamma_{di} - \gamma_{pi}) - 0.0103. \quad (1)$$

It can be known that if γ_{pi} and γ_{di} are close, the influence of T_A on the test accuracy of the single HSL measuring point can be ignored.

In order to study the effect of γ_{pi} on the double HSL test accuracy, the double HSL measuring point test platform was built with PU plastic pipes, PTFE pipes, and polypropylene pipes; HSL was used as a base station, and the other one was used as the measuring point. The test was carried out under the temperature raising rate of 0.05°C/min. Figure 7 shows the test data of the base station and the measuring point for case C8. It can be seen that H_E of the base station and the measuring point increased with T_A , but the increasing rate of the elevation of the base station was apparently less than that of the measuring point, and P_t presented a significant difference, which was 0.213 mm/°C and 0.231 mm/°C, respectively.

Figure 8(a) shows the relative elevation ΔH_E between the base station and the measuring point caused by T_A 's increasing for case C8. The relative temperature influence coefficient ΔP_t is defined as the difference in P_t between the

base station and the measuring point. For case C8, ΔP_t was 0.018 mm/°C, which is significantly smaller than that of C1–C7, suggesting that the measurement error caused by T_A on the “liquid medium box-connecting pipe-base station” did not affect the relative elevation between the base station and the measuring point. The elevation difference was caused by the expansion difference between the connecting pipe and the refrigerant that connects the base station and the measuring point. Figures 8(b) and 8(c) show ΔH_E between the base station and the measuring point for cases C9 and C10, which was caused by the increase of T_A . Similar to the single test point results, for polypropylene pipes, ΔH_E increased with T_A but decreased for PU plastic pipes. However, similar to case C8, ΔP_t of cases C9 and C10 was also obviously smaller than that of the single-point test, and when the connecting pipe was a PU plastic, ΔP_t was negative. It should be pointed out that although the connecting pipe material had a significant effect on ΔP_t , it was related to the length of the connecting pipe between the base station and the measuring point combined with the test results of cases C1–C9.

3.4. The Effect of Measuring Distance on the HLS Test Accuracy. According to the analysis above, when the connecting pipe material was fixed, the test error of the double or multiple HSL measurement points, which was induced by T_A changing, was mainly determined by the distance of the measurement points. To systematically explore the effect of the distance between measurement points D_{test} (the length of the connecting pipe) on the test accuracy of double HSL test points, PTFE pipes were used to construct the double measurement points' test platform, and the distance between the base station and the test point was set as 0.5 m, 1 m, 5 m, and 10 m. Figure 9 shows the relationship between ΔH_E and T_A . It can be seen that when D_{test} increased to 1 m and 5 m, ΔH_E also increased with the increase of T_A , but under the same T_A , the larger D_{test} was, the larger ΔH_E was, which was consistent with the test results of case C8. Besides, ΔP_t of the double HLS test points was significantly smaller than P_t of the base station under each working condition.

Figure 10 shows the relationship between D_{test} and ΔP_t ; ΔP_t increased with the increase of D_{test} . However, the increasing rate

TABLE 4: The influence of ambient temperature on the measurement accuracy of the HLS.

ID	Test platform	Pipe material	D_{test} (m)	T_A (°C)	T_A rate (°C/min)	Test purpose
C1	Single HLS	PU plastic pipe	—	-10→30→-10	0.05	The effect of temperature rising/falling rate on the HSL test error
C2					0.1	
C3					0.2	
C4					0.02	
C5	Single HLS	PU plastic pipe	—	-10→30	0.05	The effect of pipe material on the single HSL test error
C6		204 stainless steel pipe				
C7		Polypropylene pipe				
C8	Double HLS	PTFE pipe	0.5	-10→30	0.05	The effect of pipe material on the double HSL test error
C9		Polypropylene pipe				
C10		PU plastic pipe				
C11	Double HLS	PTFE pipe	1	-10→30	0.05	The effect of measuring distance on the single HSL test error
C12			5			
C13			10			

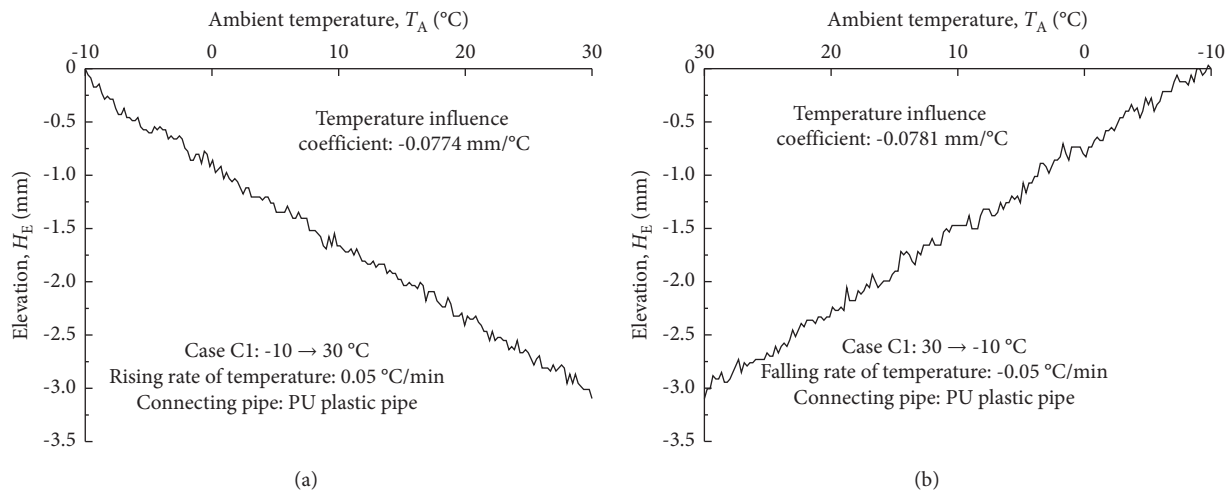


FIGURE 2: The influence of temperature rise/fall rate on the measurement accuracy of the HLS. (a) Ambient temperature rising. (b) Ambient temperature falling.

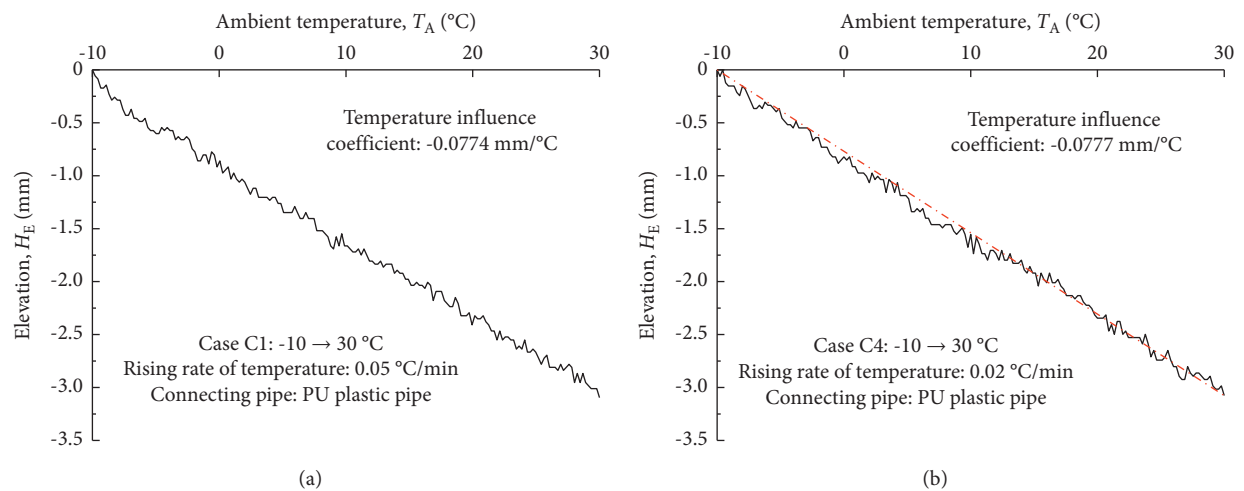


FIGURE 3: Continued.

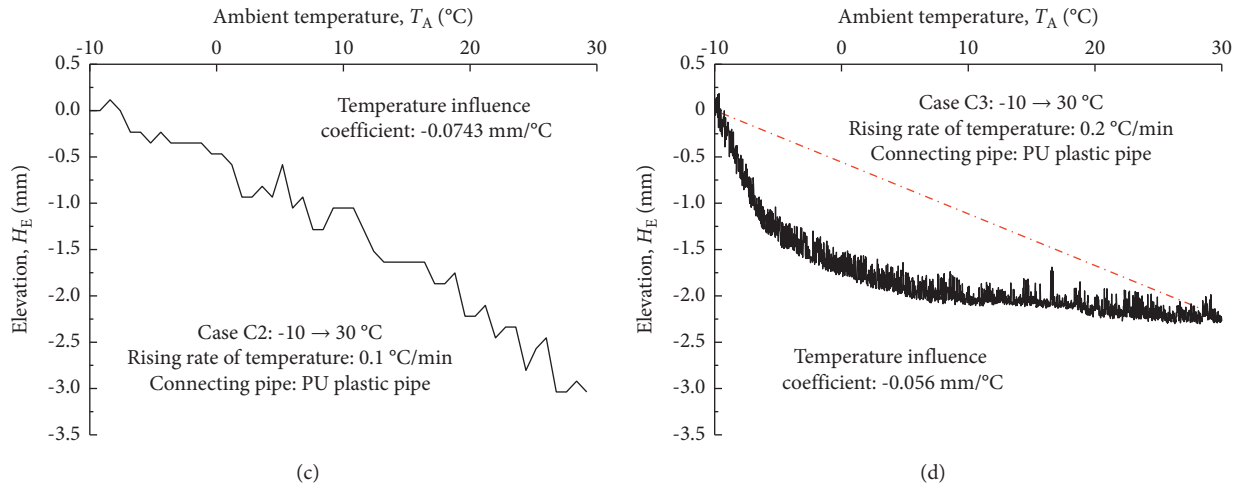


FIGURE 3: The influence of temperature rise rate on the measurement accuracy of the single HSL test point. (a) Case C1. (b) Case C4. (c) Case C2. (d) Case C3.

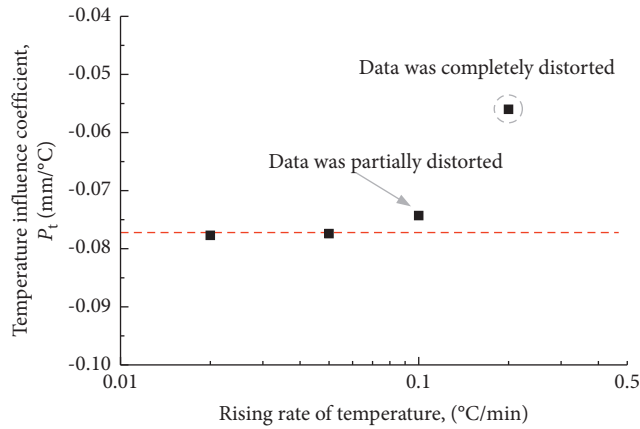


FIGURE 4: The relationship between temperature influence coefficient and temperature rise rate.

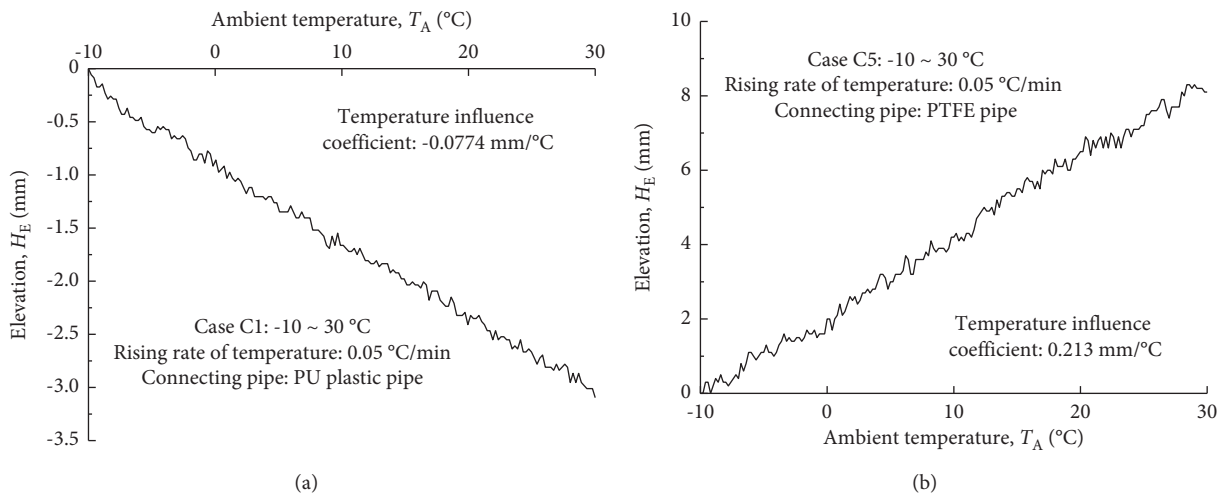


FIGURE 5: Continued.

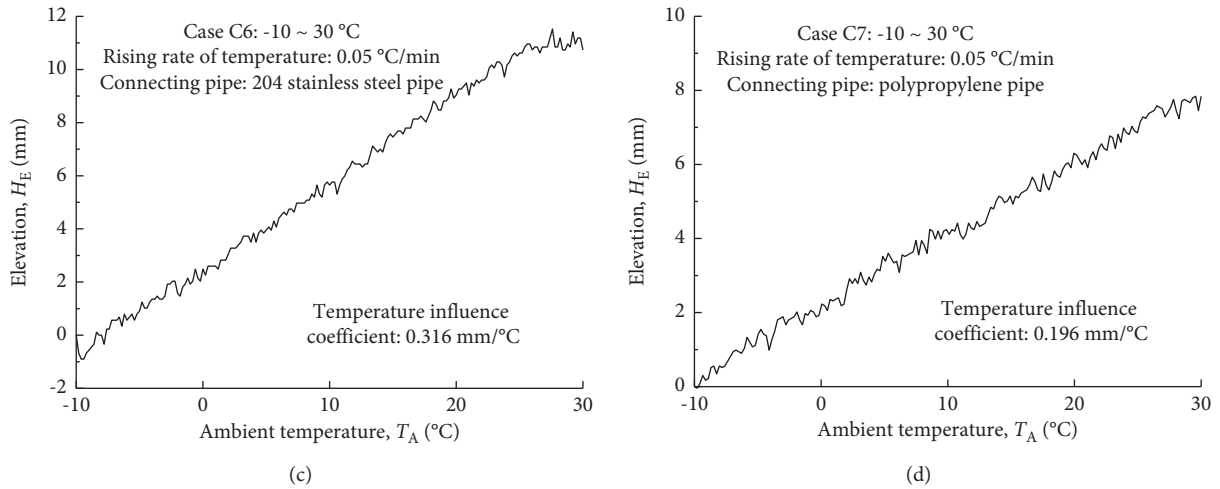


FIGURE 5: The influence of pipe expansion coefficient on the measurement accuracy of the single HSL test point. (a) PU plastic pipe. (b) PTFE pipe. (c) 204 stainless steel pipe. (d) Polypropylene pipe.

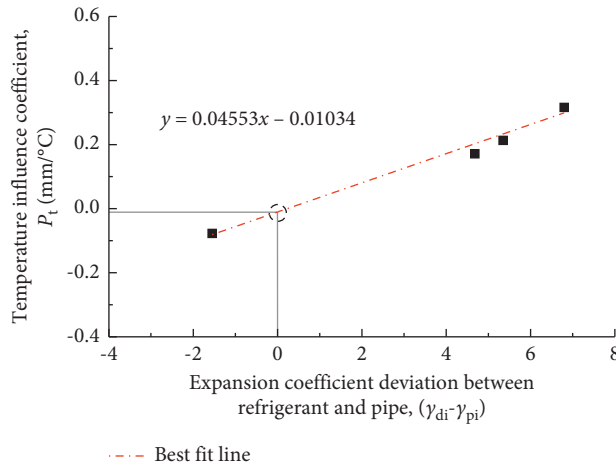


FIGURE 6: The relationship between the temperature influence coefficient and the expansion coefficient deviation between the refrigerant and pipe.

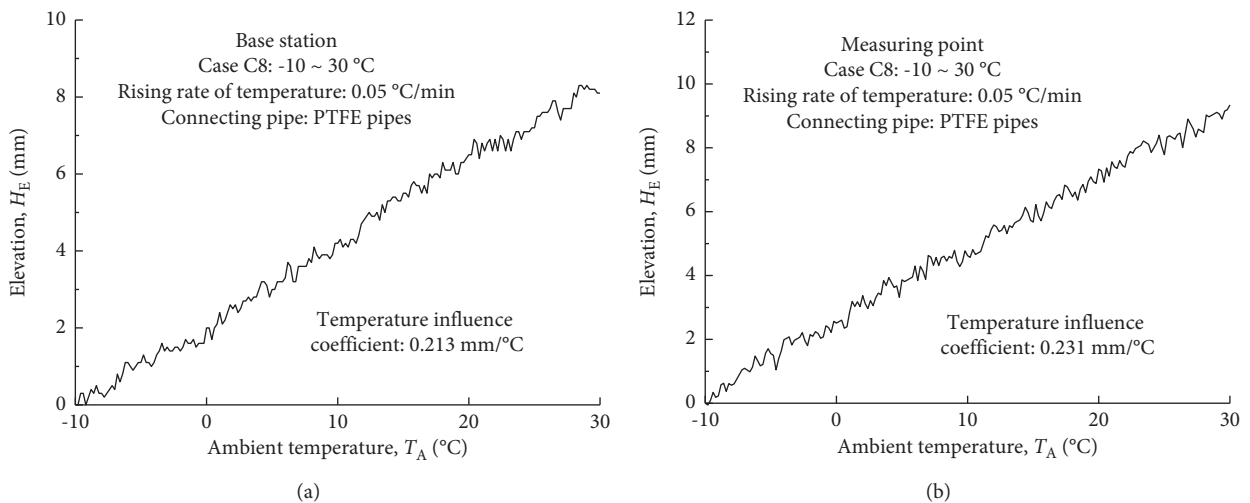


FIGURE 7: The relationship between ambient temperature and elevation of the base station and test point HSL for case C8. (a) Base station. (b) Measuring point.

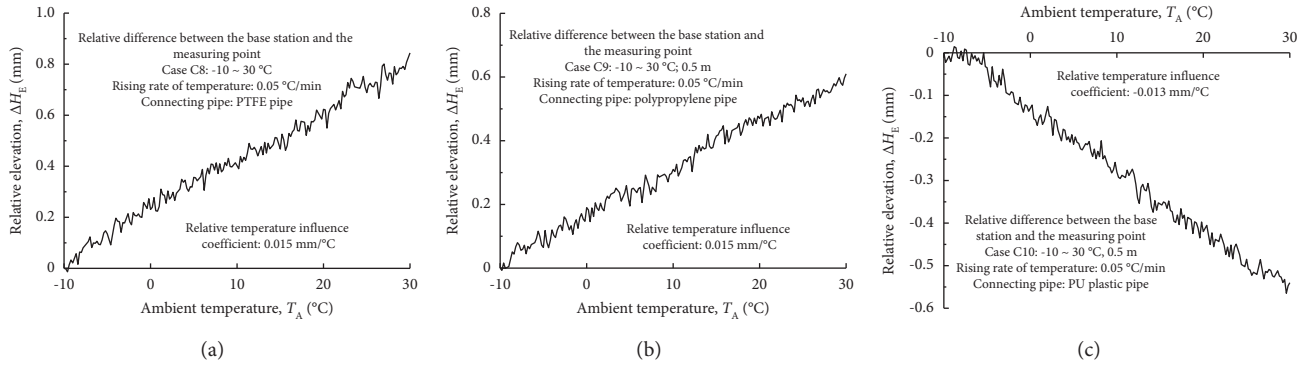


FIGURE 8: The relative elevation between the base station and test point HLS versus ambient temperature for cases C8–C10. (a) PTFE pipe. (b) Polypropylene 204 pipe. (c) PU plastic pipe.

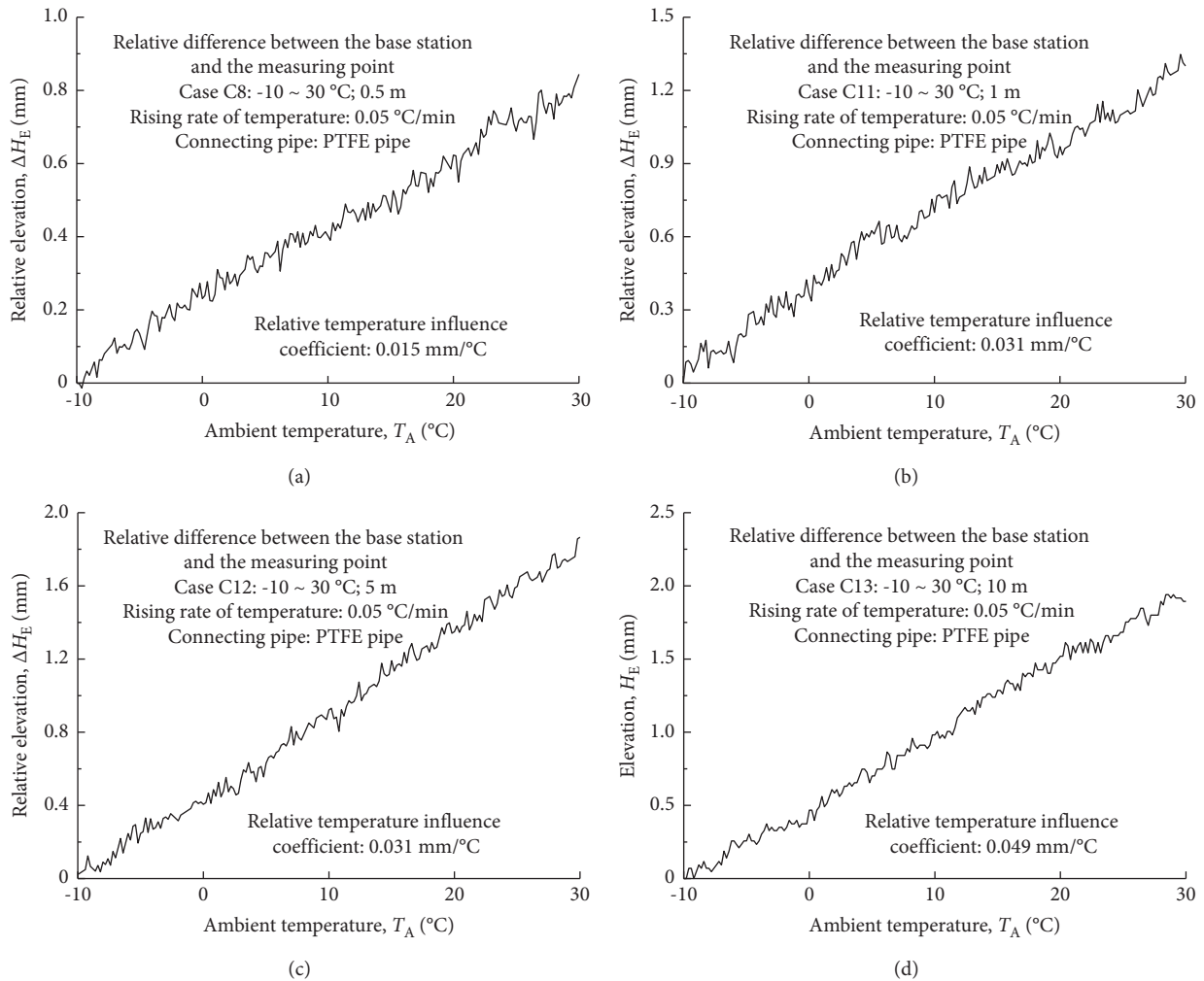


FIGURE 9: The relationship between relative elevation and ambient temperature under different measuring distances. (a) Case C8. (b) Case C11. (c) Case C12. (d) Case C13.

of ΔPt appears gradually decreased, and it can be inferred that when D_{test} exceeds a certain value, ΔP_t may be maintained at a fixed value, but under larger D_{test} conditions, the precise

environmental temperature control is difficult to be achieved due to the limited test conditions. D_{test} and ΔP_t present a power function relationship as follows:

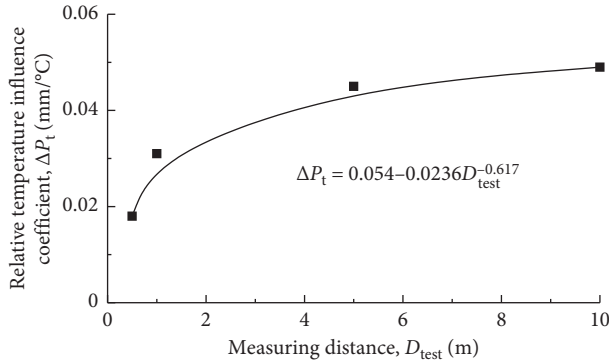


FIGURE 10: The relationship between measuring distance and relative temperature influence coefficient.

$$\Delta P_t = 0.054 - 0.0236D_{\text{test}}^{-0.617}. \quad (2)$$

Incorporating with the definition of ΔP_t , under the ambient temperature considering the influence of D_{test} , the ambient temperature evaluation model of the HLS measuring points can be established:

$$\begin{aligned} \text{Set}_{\text{true}} &= \text{Set}_{\text{test}} - \Delta H_E, \\ \Delta H_E &= (0.054 - 0.0236D_{\text{test}}^{-0.617}) \times \Delta T_E, \end{aligned} \quad (3)$$

where Set_{true} is the actual settlement of each HLS measuring point to eliminate the influence of temperature effect and Set_{test} is the test settlement of each HLS measuring point.

4. Conclusions and Discussion

In this paper, a test platform with differential pressure hydrostatic levelling was installed in the ambient temperature laboratory. The high-precision temperature sensors were adopted to collect the temperature of each measurement point of the HLS, and the influence of factors, such as the ambient temperature, the increasing/decreasing rate of the ambient temperature, the expansion coefficient of the connecting pipe, and the distance of the measuring point, on the HLS test accuracy was quantitatively analyzed. The relevant conclusions can be drawn as follows:

- (1) The elevation of the single HSL measuring point showed a single correlation with the ambient temperature. When the ambient temperature increasing rate was 0.02 or 0.05°C/min, the ambient temperature influence coefficient was consistent, and the test results were valid. When the increasing rate was greater than or equal to 0.1°C/min, the material expansion was not complete, and the data were distorted.
- (2) The single HSL measuring point's temperature influence coefficient was linearly related to the difference in the expansion coefficient between the liquid medium and the pipe. When the expansion coefficient of the selected pipe was close to the expansion coefficient of the liquid medium, the effect of the temperature on single HSL test accuracy can be ignored.

- (3) The test error of the double HLS measuring points caused by ambient temperature was attributed to the expansion difference between the connecting pipe and the liquid medium. The connecting pipe material and the length of the connecting pipe had a significant effect on the relative temperature influence coefficient.
- (4) The relative temperature influence coefficient increased with the increase of the measurement distance, while the increase rate of the relative temperature influence coefficient gradually decreased, which preliminarily indicated that when the measurement distance exceeded a certain value, the HLS test error caused by the environmental temperature basically remains constant.

Data Availability

The data are generated from experiments and can be made available from the corresponding author upon request.

Conflicts of Interest

The authors declare that there are no conflicts of interest regarding the publication of this paper.

Acknowledgments

This work was supported by the National Science Foundation of China (52008206) and Institute of Crustal Dynamics, China Earthquake Administration (no. ZDJ2018-11).



References

- [1] N. F. Li and Y. F. Zhao, "Application of hydrostatic leveling system in XIANGJIABA hydropower station," *Journal of Geodesy and Geodynamics*, vol. 33, pp. 181–185, 2013.
- [2] L. H. Chen, G. L. Guo, X. J. Zhu, and Q. Guo, "Precision analysis of deformation monitoring by hydrostatic level system," *Safety In Coal Mines*, vol. 46, no. 3, pp. 201–204, 2015.
- [3] S. T. Liu and H. F. Zhang, "Research progress on deformation monitoring technology of surrounding rock of tunnel structure," *Highway*, vol. 9, pp. 262–268, 2013.
- [4] H. Y. Zhuang, X. Yu, C. Zhu, and D. Jin, "Shaking table tests for the seismic response of a base-isolated structure with the SSI effect," *Soil Dynamics and Earthquake Engineering*, vol. 67, pp. 208–218, 2014.
- [5] H. Zhuang, J. Fu, X. Yu, S. Chen, and X. Cai, "Earthquake responses of a base-isolated structure on a multi-layered soft soil foundation by using shaking table tests," *Engineering Structures*, vol. 179, no. 15, pp. 79–91, 2019.
- [6] X. Wang, Y. Liu, and J. Yuan, "Development and application of settlement intelligent monitoring and evaluation system of high-speed railway," *Journal of Railway Engineering Society*, vol. 247, no. 4, pp. 20–25, 2019.
- [7] J. Wei, P. Wei, and D. Q. Li, "Development and study on settlement remote monitoring and controlling system based on general packet radio service," *China Civil Engineering Journal*, vol. 48, no. S2, pp. 332–336, 2015.
- [8] Z. L. Zhang, Y. Deng, C. L. Luo, and X. Hu, "Research on precise triangulated height surveying in place of first order

- leveling,” *Geomatics and Information Science of Wuhan University*, vol. 31, no. 1, pp. 5–8, 2006.
- [9] D. Q. Li, *Studies on the Remote Settlement Monitoring System Based on Magnetostrictive Hydrostatic Leveling*, Beijing JiaoTong University, China, Beijing, 2015.
- [10] G. Y. Hou, Z. X. Li, T. Hu et al., “Study of tunnel settlement monitoring based on distributed optic fiber strain sensing technology,” *Rock and Soil Mechanics*, vol. 41, no. 9, pp. 3148–3158, 2020.
- [11] J. Jia and T. Zhang, “Application of high accuracy static level automatic system in bridge deformation monitoring,” *Highway Engineer*, vol. 43, no. 2, pp. 172–176, 2018.
- [12] F. Liu, M. D. He, L. Yu, and Y. Liu, “Measurement on the separation of monolithic roadbed from tunnel by hydrostatic leveling sensor,” *China Civil Engineering Journal*, vol. 48, no. S2, pp. 356–360, 2015.
- [13] C. P. Zhang, D. L. Zhang, J. J. Luo, and M. S. Wang, “Remote monitoring system applied to the construction of metro station undercrossing existing metro tunnel,” *Rock and Soil Mechanics*, vol. 30, no. 6, pp. 1861–1866, 2009.
- [14] Z. Liu, S. F. Zhang, and S. R. Cai, “Experimental study on deflection monitoring scheme of steep gradient and high drop bridge,” *Journal of Highway and Transportation Research and Development*, vol. 32, no. 11, pp. 88–93, 2015.
- [15] Z. G. Liu, H. W. Huang, Y. H. Zhao et al., “Immersed tube tunnel real-time health monitoring system,” *Hinese Journal of Underground Space and Engineering*, vol. 4, no. 6, pp. 1110–1115, 2008.
- [16] H. Q. Yang, J. C. Li, and Z. N. Chen, “Investigation on longitudinal ground subsidence caused by shallow tunnel excavation,” *Journal of Nanjing Tech University (Natural Science Edition)*, vol. 30, no. 3, pp. 56–60, 2008.
- [17] W. Gang, X. J. Qin, D. Han, and Z. Liu, “Study on seepage and deformation characteristics of coal microstructure by 3D reconstruction of CT images at high temperatures,” *International Journal of Mining Science and Technology*, vol. 31, no. 02, pp. 175–185, 2021.
- [18] C. D. Su, J. D. Qiu, Q. H. Wu, and L. Weng, “Effects of high temperature on the microstructure and mechanical behavior of hard coal,” *International Journal of Mining Science and Technology*, vol. 30, no. 05, pp. 643–650, 2020.
- [19] Q. Zhang, X. Y. He, Z. Tang, and W. Wang, “Comparison of hydrostatic leveling system and wire position sensor for position monitoring in particle accelerator,” *Atomic Energy Science and Technology*, vol. 51, no. 8, pp. 1532–1536, 2017.
- [20] X. Y. He, “Application of hydrostatic leveling system in key scientific engineering and its developing tendency,” *Chinese Journal of Nuclear Science and Engineering*, vol. 26, no. 4, pp. 332–336, 2006.
- [21] J. H. Chen, “The influence of temperature unevenness on the accuracy of hydrostatic level,” *Geotechnical Investigation & Surveying*, vol. 55, no. 1, pp. 51–57, 2000.
- [22] S. F. Xu, *Studies on Accuracy Theory and Validation of HLS Used in Particle Accelerators*, University of science and Technology of China, Anhui, China, 2014.

Research Article

Study on Deep and Large Foundation Pit of a National First-Class Key Tomb Protection Project

Jiagang Zhang ¹, Zhimin Chen ^{1,2}, Mingzhu Hu,^{3,4,5} and Zhaoguo Wu⁶

¹School of Civil Engineering, Lanzhou Jiaotong University, Lanzhou 730070, China

²National and Provincial Joint Engineering Laboratory of Road & Bridge Disaster Prevention and Control, Lanzhou 730070, China

³Northwest Research Institute Co., Ltd. of C.R.E.C, Lanzhou 730000, China

⁴Grottoes and Engineering Application Research on Integration and State Administration of Cultural Heritage of Cultural Relics Protection Key Research Base, Lanzhou 730000, China

⁵Geotechnical Cultural Relics Protection Research Center of Gansu Province, Lanzhou 730000, China

⁶CCCC First Highway Consultants, Xi'an 710075, China

Correspondence should be addressed to Zhimin Chen; 0219162@stu.lzjtu.edu.cn

Received 13 August 2021; Accepted 28 September 2021; Published 23 November 2021

Academic Editor: Qinghua Zhang

Copyright © 2021 Jiagang Zhang et al. This is an open access article distributed under the Creative Commons Attribution License, which permits unrestricted use, distribution, and reproduction in any medium, provided the original work is properly cited.

For the support engineering of the deep and large foundation pit (DLFP) due to tomb protection, there are still no clear standards. The construction of DLFP will introduce large-range transverse and longitudinal disturbance on the stratum; therefore, it should be reinforced. In this paper, the reinforcement of the deep and large foundation pit of a national first-class key tomb protection project is studied. By comparing the existing supporting scheme and the stress conditions of the reinforced tomb, the combination reinforcement scheme by bored pile and pile slab retaining wall is found to be safe and feasible. Furthermore, according to the simulated bending moment, displacement, and axial force of the tomb by numerical analysis, an economic and reasonable mixed anchor support scheme is selected. In order to ensure the stability of the tomb during the supporting process of the foundation pit, a maximum value of 10 mm for the overall settlement of the tomb can be treated as the control benchmark based on the support and anchorage schemes in each specification and the in-site measured settlement values of the tomb. The determined support, anchorage schemes, and the control benchmark can provide certain technique guidance and research significance for the protection of similar ancient buildings in the future.

1. Introduction

From the twenty-first century, relative specifications put forward clear requirements on the support effects of the foundation pit and their influence on the surrounding environment, and the conventional design calculation for general foundation pit support is already mature. However, there are still no detailed standards and requirements on the ancient buildings with cultural relics protection value. Besides, the conventional single support type is difficult to meet the design requirements of the foundation pit of ancient tombs, which have complex surrounding environment, strict support effect demand, and large depth and area.

Nowadays, the controlled settlement due to repair of the ancient buildings, ancient tombs, and other cultural heritages protected by the state is mainly based on the experience of experts. The control benchmark of settlement is higher and higher, and some key protection projects even require zero settlement. The increment of the benchmark can better provide the cultural relic from destroying, but it also increases construction difficulty and cost. Wang [1] analyzed the monitoring data of the engineering project of the Line 2 Town God's Temple Station of Ningbo Rail Transit and determined the controlled displacement benchmark, requirement, and detailed protection measurements for protection of the ancient buildings in Town God's Temple, which accumulated experiences for similar projects.

According to the protection requirements of isolated ancient buildings in soft soil deep foundation pit engineering, Gong et al. [2] simulated various construction conditions of foundation pit excavation by using PLAXIS finite element software and determined the support mode that can effectively control the deformation of isolated ancient buildings. Besides, Wang et al. [3] compared and analyzed the stress distribution of the foundation pit of an ancient building under original and modified design conditions, which can provide information for the dynamic design of the foundation pit. In addition, Qiu et al. [4] made a detailed analysis on the design and construction of a super deep and super large foundation pit near the subway. Yooc et al. [5–13] made conducted many researches and discussions on this area. Chen [14] optimized the supporting system and the reinforcement scheme of the pit bottom through the characteristics of the ancillary structure of the station close to the old City God Temple of the historical building. According to this scheme, the deformation of the old City God Temple has been effectively controlled to ensure the smooth progress of the project. Dan et al. [15] provided a new design theory for the complex foundation pit support of the ancient buildings in the old city site. On the analysis of the foundation pit adjacent to key ancient architectural relics, Wang et al. [16] formulated a monitoring scheme, and the feasibility of this scheme is verified by systematically monitoring the foundation pit supporting structure, buildings, groundwater level around foundation pit, and soil mass.

The Dingtao Han Tomb locates in Dingtao County, and there exists earthen ruins outside the tomb, beside the main tomb. The excavation perimeter of the foundation pit is 149 m in the north-south direction and 110 m in the east-west direction. The burial depth of the tomb is 6 m, and the range is a 22.8 m × 22.8 m square. The buried depth of the earthen site is 6 m, and the range is a 50 m × 50 m square, as shown in Figure 1.

In order to ensure the safety of the foundation pit and the site not be damaged during excavation, the proper enclosing structure of the foundation pit and support structure of the earthen ruins should be selected, and the proper water stop curtain should be selected to avoid the damage of the antiquities due to excessive settlement.

2. Analysis on Foundation Pit Reinforcement of the Ancient Tomb

Based on the project characteristics and construction conditions, several possible used support schemes are analyzed and compared technically and economically.

The excavation area of the foundation pit is very large, which can reach 16,390 m², and its depth is 16 m belonging to the deep foundation pit project. There are cultural relics under special state protection in the foundation pit; their high requirements are imposed on its settlement. Many soil layers with different properties exist in the excavation depth of the foundation pit, especially the 8th layer, which contains a lot of confined water and has a great impact on the tomb.

2.1. Comparison of Foundation Pit Support Schemes of the Ancient Tomb Chamber. The bored pile is selected as the support structure.

The construction of the bored pile as the support structure of the foundation pit is convenient, and its cost is low as the construction is mature. Steel support has the advantages of fast, easy assembly, and repeated use. In order to enhance the support force, prestress can be applied to the steel support in advance. Therefore, the support structure has certain economic efficiency and safety. However, the bored pile cannot form a connected successive wall; thus, the waterproof performance is extremely bad; and the water stop curtain shall be set additionally.

The main body of the support structure adopts a diaphragm wall with steel support. When the diaphragm wall is used for construction, the noise and vibration are both very small, which shows great advantages in urban construction. The wall support has great stiffness and good impervious performance; thus, waterproof cloth is not needed. The diaphragm wall can be used as both an enclosure structure and a part of the main structure. Besides, it occupies a small land area. But it also has some disadvantages, such as the high cost. Besides, the construction site must have mud treatment conditions because improper treatment of waste mud will cause serious environmental pollution. In addition, the commonly occurred tank wall collapse in construction can induce the settlement of the tomb and the earthen ruins, and it can also cause exceeded quantity of concrete, which will increase the engineering cost.

The second scheme has the advantage of low noise and small land occupation; thus, it is suitable for urban construction. However, the studied tomb locates in the wild, which has a wide site and no limitations space, noise, and construction disturbance, indicating that the second scheme has no apparent superiority on the present project, and also its cost is very high. In addition, the waterproof curtain has been set outside the foundation pit, and it is a little redundant in terms of the waterproof if the diaphragm wall is made. Compared with the second scheme, bored cast-in-place pile has the advantages of easy construction, low cost, repeated use for many times, and imposing prestress in advance before construction; thus, it has higher cost performance. Considering various factors, the support structure of the bored cast-in-place pile and internal support is finally determined.

2.2. Comparison of Supporting Materials for Foundation Pit of the Ancient Tomb Chamber. In the support system of the deep foundation pit, the support systems can be divided into steel support, reinforced concrete support, and reinforced concrete steel tube mixed support. Among them, the reinforced concrete supporting structure has good integrity, large strength, and small deformation, which can ensure construction safety and reliability. However, its construction technique is more complex than steel support, and the demolition is also relatively difficult, inducing a low material recovery rate. The steel support is the most commonly used structure in foundation pit engineering projects because it is

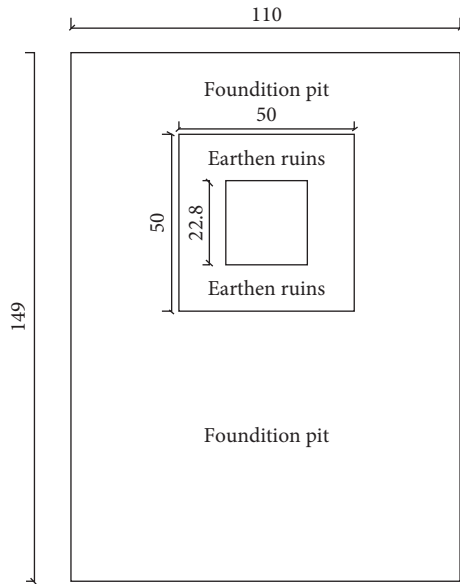


FIGURE 1: Location plan of the ancient tomb.

convenient to be installed and removed. The dosage ratio of steel can improve the support capacity by applying prestress, which can effectively control the deformation of the foundation pit. In the meanwhile, the erection of the steel support is very quick, which can save time and increase the construction efficiency. Besides, the recovery rate of the steel support is high, which can reduce a lot of waste and save cost.

2.3. Comparison of Reinforcement Schemes of the Ancient Tomb Room Soil Sites. The earthen ruins belong to the key cultural relics protected by the state; thus, the support structure should have enough strength to protect this structure. Moreover, the construction technology should not only be simple but also fast, and the disturbance to earthen ruins and Han Tombs should be minimal. As the anchor bolt and anchor plate retaining wall have certain damage on the earthen ruins; thus, they can be excluded first. Compared with the pile slab retaining wall, as other retaining walls have no hanging plate, the earthen ruins cannot be protected well. Therefore, combined with the engineering characteristics, existing technologies, economic conditions, and construction period, the pile plate retaining wall is finally selected to strengthen the earth site as shown in Figure 2.

In addition, pile slab retaining wall also has the following obvious advantages: (1) it not only can prevent the overall sliding of the earthen ruins but also can provide well protection because the hanging plate can prevent the local displacement of the earthen ruins; (2) at present, the construction method of the pile plate retaining wall is mature, and the construction team is experienced; therefore, the construction quality and progress can be guaranteed; and (3) the construction of square pile retaining wall has no high requirements on the site conditions; thus, it is convenient to construct, and it has little disturbance to the main body of earthen sites and Han Tombs.

3. Comparison of Settlement Control Standards

During the excavation stage of the deep and large foundation pit, there is particularity and high requirements on the protection of the cultural relic architecture. The different standards are shown in Tables 1–3. Therefore, in the design process of the present project, various specifications and reports are referred to, and their deformation control standards and requirements for buildings are preliminarily analyzed. Finally, the deformation control standards of the ancient buildings are determined from the perspective of strict control.

The settlement of the foundation pit can be determined by the soil characteristics, design results, and local experience (Table 2). The soil layer of the tomb is mainly composed of silt, silty clay, and silty sand mixed with silt, and the hydrogeological condition is simple; thus, the soil layer of the tomb is simple. The surrounding tombs are national key protected cultural relics, and the grade of the foundation pit is class I. As the soil layer is simple, the suggested settlement value of the foundation pit is mainly designed based on the grade of the foundation pit and local experience. Besides, the building importance is sensitive to the surrounding environment, the foundation pit of grade 1 adopts the most strict control, and the settlement value is controlled in 10 mm.

4. Result Analysis of Different Anchor Support Schemes

The support plan is shown in Table 4.

4.1. Result Analysis of Mixed Anchor Support Scheme. The earth pressure under various working conditions and in the pile body of bored cast-in-place pile is calculated by using Lizheng system. The calculation results are as follows.

Figure 3 shows the internal force and displacement of the excavation to 6.90 m. After excavation to the depth of 6.90 m, the appearance of the maximum earth pressure locates at 24 m under the ground, and the pressure value is 500.2 kN/m, while the minimum earth pressure locates at 15 m under the ground with a value of 0 kN/m. The displacement of the pile top is 0, and that of the pile bottom is the largest with a value of 4.9 mm. The maximum bending moment is 783.7 kN·m, which appears at about 22 m under the ground, and the maximum shear stress is 455.3 kN, which appears at about 24 m under the ground.

Figure 4 shows the internal force and displacement after excavation to 6.9 m with support. After imposing the first bracing, the appearance of the maximum earth pressure locates at 24 m under the ground, and the pressure value is 500.2 kN/m, while the minimum earth pressure locates at 15 m under the ground with a value of 0 kN/m. The displacement of the pile top is 0, and that of the pile bottom is the largest with a value of 4.9 mm. The maximum bending moment is 783.7 kN·m, which appears at about 22 m under the ground, and the maximum shear stress is 455.3 kN, which appears at about 24 m under the ground.

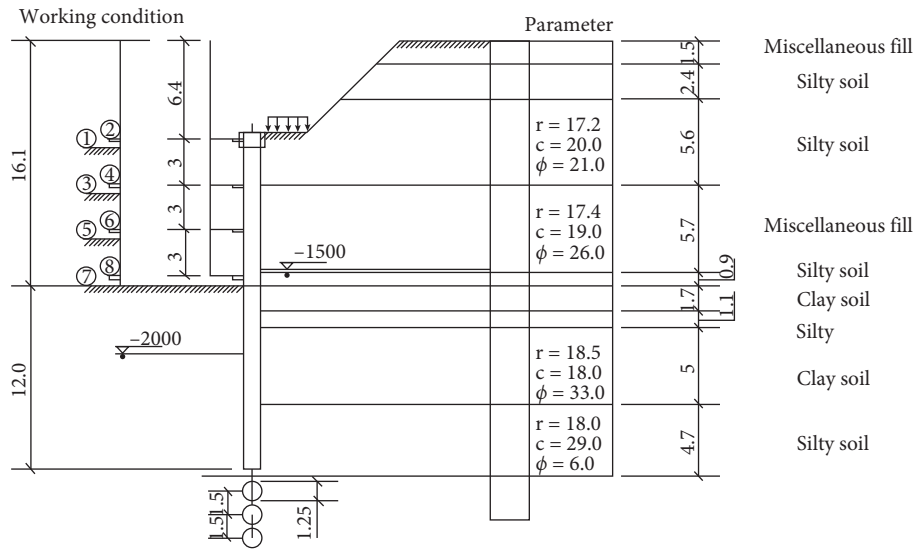


FIGURE 2: Schematic diagram of pile slab retaining wall (unit: m).

TABLE 1: Comparison of building protection standards.

Monitoring items	Building foundation pit monitoring technical specifications (GB50497—2009)	Shanghai standard: code for construction monitoring of foundation pit engineering (DG/TJ08—2001—2006)	Monitoring alarm value in report and suggestions on cultural relics of Jun temple	Recommended design value
Building settlement	Settlement value 10~60 mm	Settlement value, 10~60 mm Change rate, 1~3 mm/d	Settlement value, 15 mm Change rate, 1.5 mm/d	Settlement value, 10 mm Change rate, 1.5 mm/d

TABLE 2: Settlement values of different foundation pit grades.

Monitoring items	Support structure type	Foundation pit type		
		I Cumulative value (mm)	II Cumulative value (mm)	III Cumulative value (mm)
Settlement around foundation pit		10~35	50~60	60~80

TABLE 3: Complexity of soil layer.

Foundation complexity	Foundation soil properties, degree of weakness, and hydrological conditions
Complex	There is large super weak muddy clay within 2H depth; there is silt or sand with large thickness at the bottom of the pit, and the water curtain cannot be separated; there is a large area of thick fill and hidden pond distribution; hydrogeological conditions: it is adjacent to rivers and has hydraulic connection; there are aquifers with high permeability and microconfined water or confined water
Moderate	There is mucky cohesive soil or silt within 2H depth; hydrogeological conditions: there is a certain distance from the river, and there is no hydraulic connection
Simple	The soil property within 2H excavation depth is good; no dark pond distribution; hydrogeological conditions are simple

Figure 5 shows the internal force and displacement of the excavation to 9.90 m. After excavation to the depth of 9.90 m, the appearance of the maximum earth pressure locates at 24 m under the ground, and the pressure value is 498.90 kN/m, while the minimum earth pressure locates at 15 m under the ground with a value of 0 kN/m. The displacement of the pile top is 0, and that of the pile bottom is the largest with a

value of 5.6 mm. The maximum bending moment is 867.8 kN·m, which appears at about 22 m under the ground, and the maximum shear stress is 478.1 kN, which appears at about 24 m under the ground.

Figure 6 shows the internal force and displacement after excavation to 9.90 m with support. After imposing the second bracing, the appearance of the maximum earth

TABLE 4: Different anchor support schemes.

Number	Working condition	Depth (m)	Mixed anchor	Reinforced concrete anchor	Steel pipe anchor
1	Excavation	6.900			
2	Supporting	6.400	Internal bracing by reinforced concrete	Internal bracing by reinforced concrete	Inner support by steel pipe
3	Excavation	9.900			
4	Supporting	9.400	Inner support by steel pipe	Internal bracing by reinforced concrete	Inner support by steel pipe
5	Excavation	12.900			
6	Supporting	12.400	Inner support by steel pipe	Internal bracing by reinforced concrete	Inner support by steel pipe
7	Excavation	15.900			
8	Supporting	15.400	Inner support by steel pipe	Internal bracing by reinforced concrete	Inner support by steel pipe
9	Excavation	16.000			

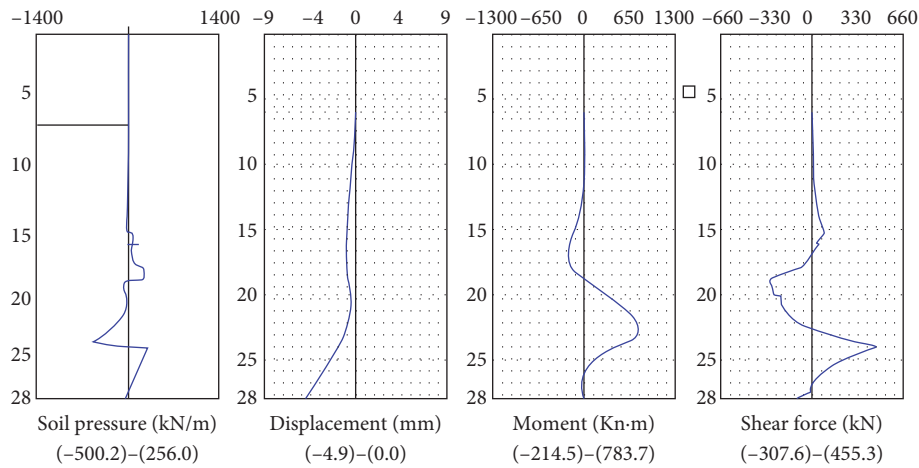


FIGURE 3: Internal force-displacement diagram of the first bracing.

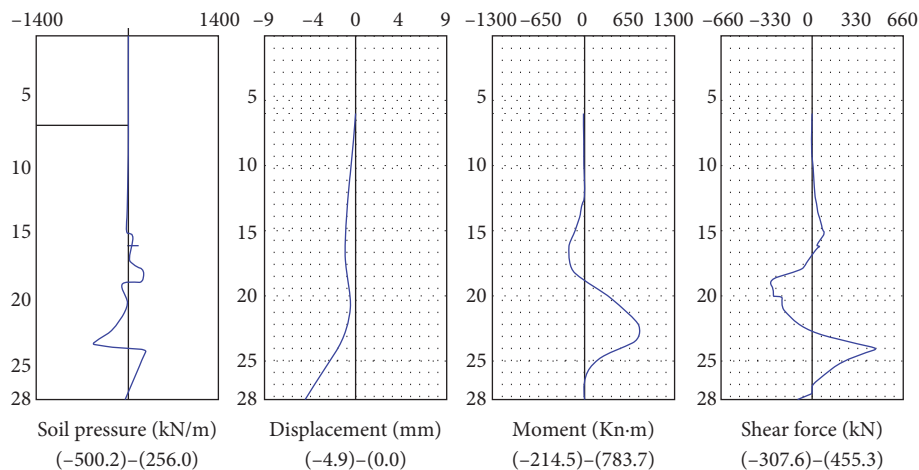


FIGURE 4: Internal force-displacement diagram of the first excavation.

pressure locates at 24 m under the ground, and the pressure value is 498.9 kN/m, while the minimum earth pressure locates at 15 m under the ground with a value of 0 kN/m. The displacement of the pile top is 0, and that of the pile bottom

is the largest with a value of 5.6 mm. The maximum bending moment is 867.5 kN-m, which appears at about 22 m under the ground, and the maximum shear stress is 478.1 kN, which appears at about 24 m under the ground.

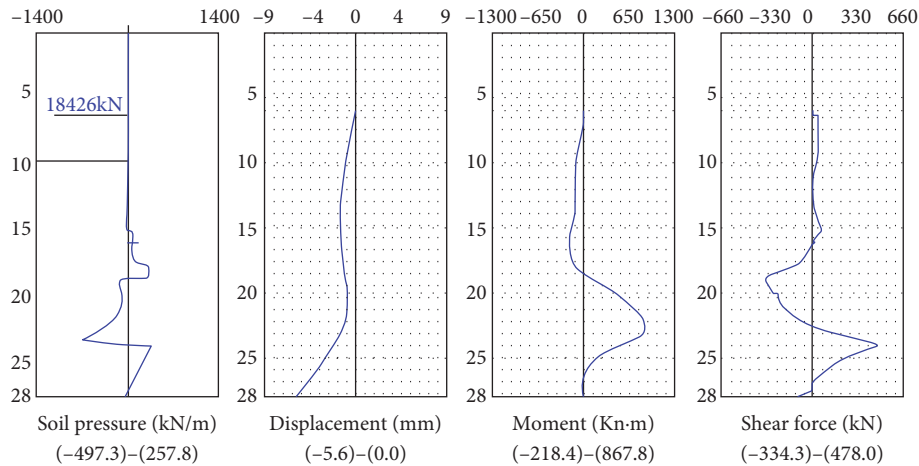


FIGURE 5: Internal force-displacement diagram of the first bracing.

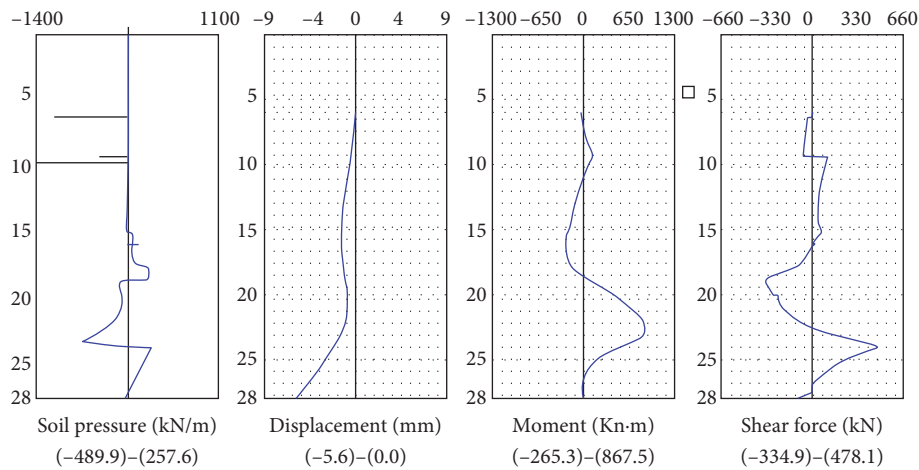


FIGURE 6: Internal force-displacement diagram of the second excavation.

Figure 7 shows the internal force and displacement of the excavation to 12.90 m. After excavation to the depth of 12.90 m, the appearance of the maximum earth pressure locates at 24 m under the ground, and the pressure value is 491.6 kN/m, while the minimum earth pressure locates at 10 m under the ground with a value of 0 kN/m. The displacement of the pile top is 0, and that of the pile bottom is the largest with a value of 6.6 mm. The maximum bending moment is 1,015.5 kN·m, which appears at about 22 m under the ground, and the maximum shear stress is 516 kN, which appears at about 24 m under the ground.

Figure 8 shows the internal force and displacement after excavation to 12.90 m with support. After imposing the third bracing, the appearance of the maximum earth pressure locates at 24 m under the ground, and the pressure value is 596.7 kN/m, while the minimum earth pressure locates at 10 m under the ground with a value of 0 kN/m. The displacement of the pile top is 0, and that of the pile bottom is the largest with a value of 6.6 mm. The maximum bending moment is 995.0 kN·m, which appears at about 22 m under the ground, and the maximum shear stress is 512.2 kN, which appears at about 24 m under the ground.

Figure 9 shows the internal force and displacement of the excavation to 15.90 m. After excavation to the depth of 15.90 m, the appearance of the maximum earth pressure locates at 24 m under the ground, and the pressure value is 513.0 kN/m, while the minimum earth pressure locates at 10 m under the ground with a value of 0 kN/m. The displacement of the pile top is 0, and that of the pile bottom is the largest with a value of 7.77 mm. The maximum bending moment is 1,198.2 kN·m, which appears at about 22 m under the ground, and the maximum shear stress is 572.5 kN, which appears at about 24 m under the ground.

Figure 10 shows the internal force and displacement after excavation to 12.90 m with support. After imposing the fourth bracing, the appearance of the maximum earth pressure locates at 24 m under the ground, and the pressure value is 514.2 kN/m, while the minimum earth pressure locates at 10 m under the ground with a value of 0 kN/m. The displacement of the pile top is 0, and that of the pile bottom is the largest with a value of 7.8 mm. The maximum bending moment is 1,169.9 kN·m, which appears at about 22 m under the ground, and the maximum shear stress is 559.4 kN, which appears at about 24 m under the ground.

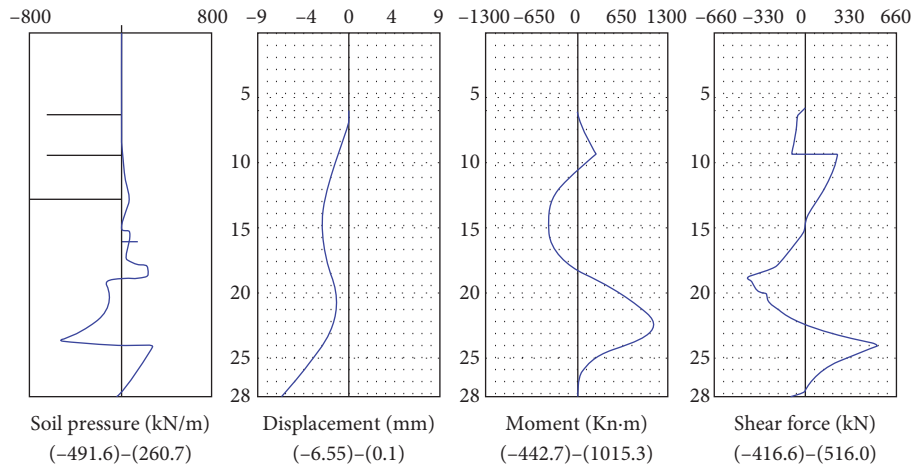


FIGURE 7: Internal force-displacement diagram of the third bracing.

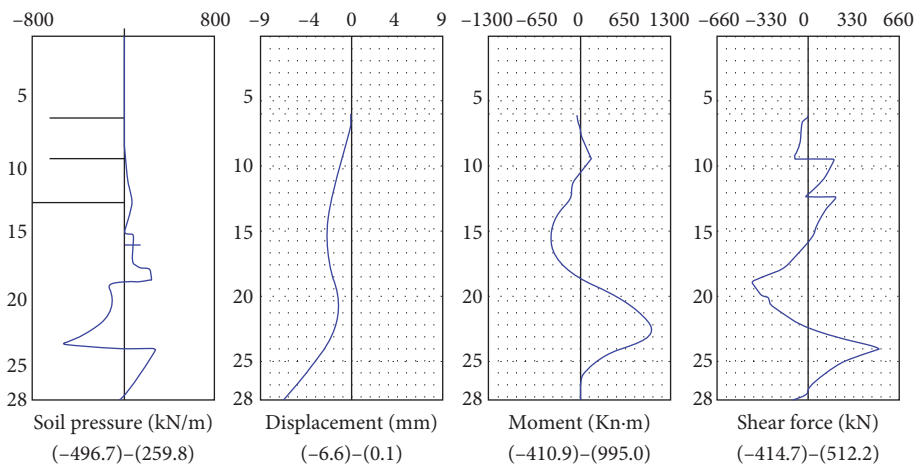


FIGURE 8: Internal force-displacement diagram of the third excavation.

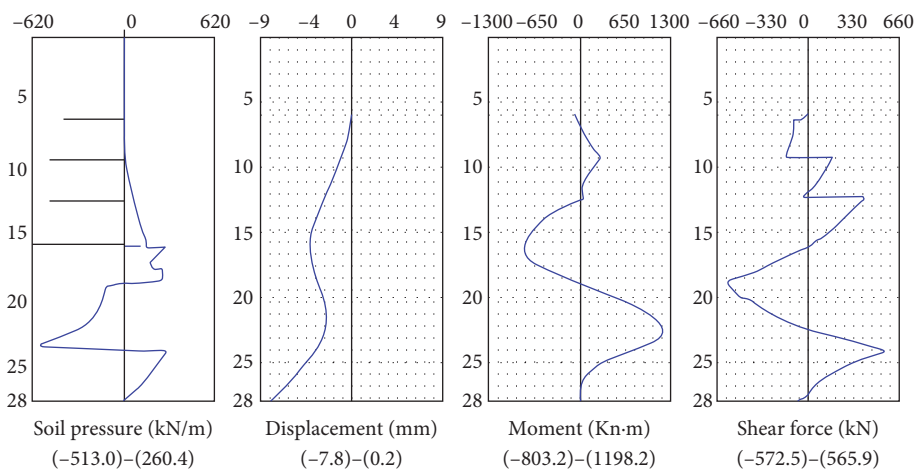


FIGURE 9: Internal force-displacement diagram of the fourth bracing.

Figure 11 shows the internal force and displacement of the excavation to 16.00 m. After excavation to the depth of 16.00 m, the appearance of the maximum earth pressure

locates at 24 m under the ground, and the pressure value is 515.9 kN/m, while the minimum earth pressure locates at 10 m under the ground with a value of 0 kN/m. The

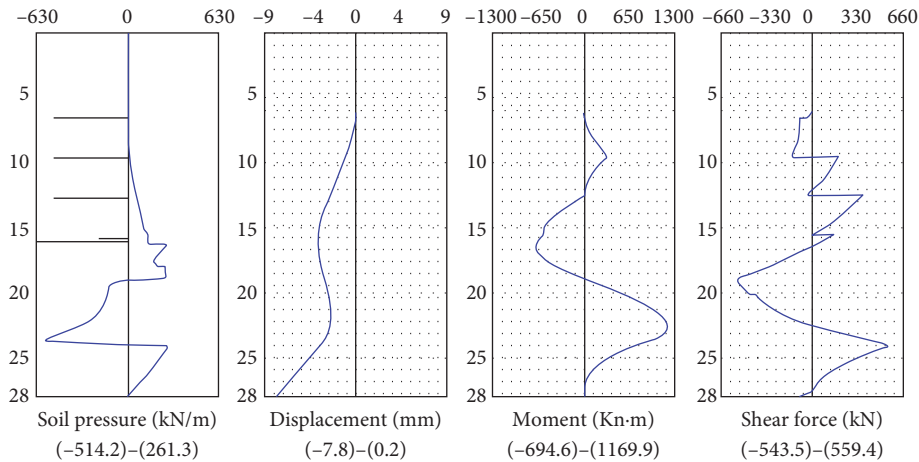


FIGURE 10: Internal force-displacement diagram of the fourth excavation.

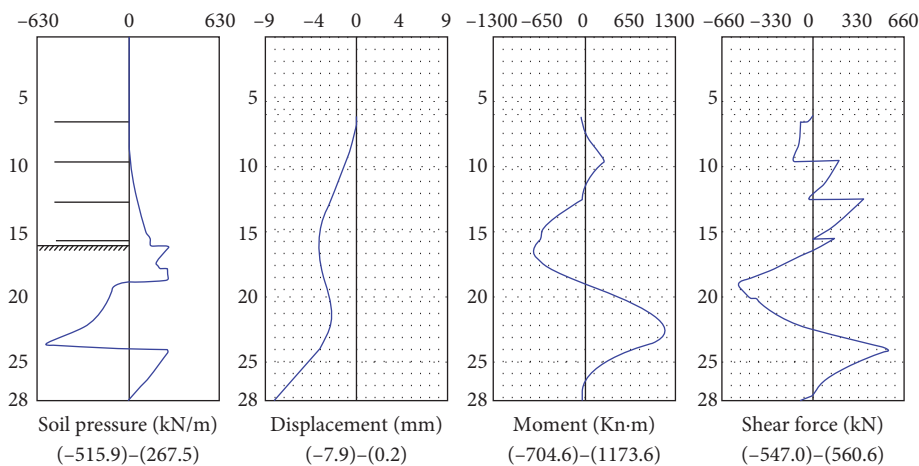


FIGURE 11: Internal force-displacement diagram of the fifth excavation.

displacement of the pile top is 0, and that of the pile bottom is the largest with a value of 7.87 mm. The maximum bending moment is 1,173.6 kN·m, which appears at about 22 m under the ground, and the maximum shear stress is 560.6 kN, which appears at about 24 m under the ground.

The system offers three methods for calculating settlement: triangle method, exponential method, and parabola method. In these methods, the triangle method and exponential method only consider the influence of the lateral displacement area of supporting structure and surface settlement range of retaining structure, but the parabola method also considers the influence of the top and bottom displacements of the supporting structure; therefore, its calculation result is more accurate. Here, the parabola method is adopted for calculating settlement, and the results are plotted in Figure 12.

The settlement of different anchor schemes is shown in Table 5. The maximum settlement is 4 mm, which appears at 6 m away from the foundation pit, and the minimum influence locates at 20 m away from the boundary of the foundation pit. Therefore, it can be deemed that there is no settlement at the place with a distance exceeding 20 m.

The settlement value of the mixed anchor scheme and reinforced concrete anchor scheme is 5 mm at least, but the reinforced concrete anchor scheme is expensive and uneconomical. Therefore, from the perspective of settlement control and economical efficiency, the mixed anchor scheme is the best choice.

4.2. Results Comparison of Different Anchor Support Schemes.

Figures 13–15 show the comparison of displacement, shear force, and bending moment of different support schemes. Through the comparison of the results of the three schemes, it can be seen that their displacements are close to each other, which are nearly the same, and their bending moments are also similar. For the shear force, the result of scheme 3 is larger than the other two schemes. In total, the support effects of the three schemes have little difference, and they can all ensure the safety of the tomb.

The reinforced concrete support structure has the advantages of good integrity, small displacement, and feasible construction safety. But its construction technology is more complex than steel support, and the demolition is also

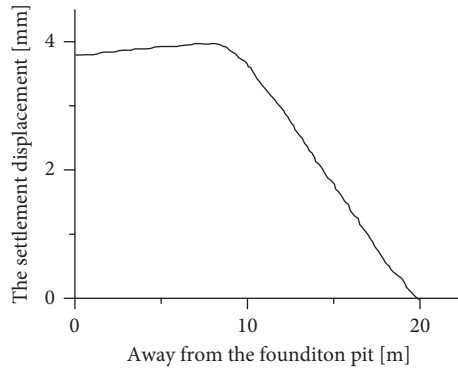


FIGURE 12: The settlement displacement.

TABLE 5: Settlement values of different anchor schemes.

	Mixed anchor	Reinforced concrete anchor	Steel pipe anchor	Double row pile anchor	Required settlement value
Settlement value (mm)	6	5	8	10	10

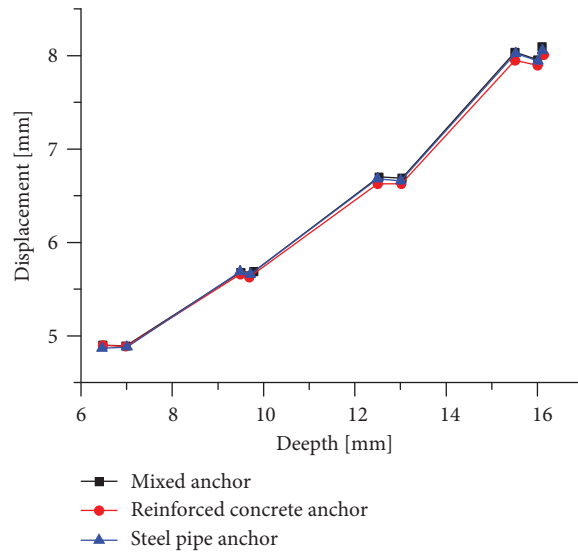


FIGURE 13: The comparison of displacement.

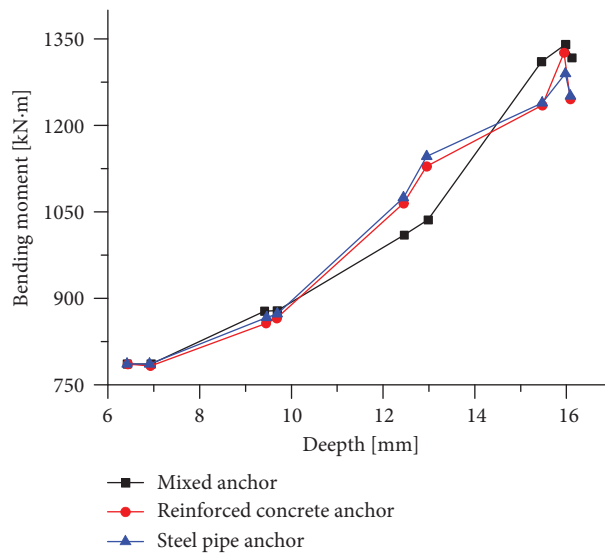


FIGURE 14: The comparison of bending moment.

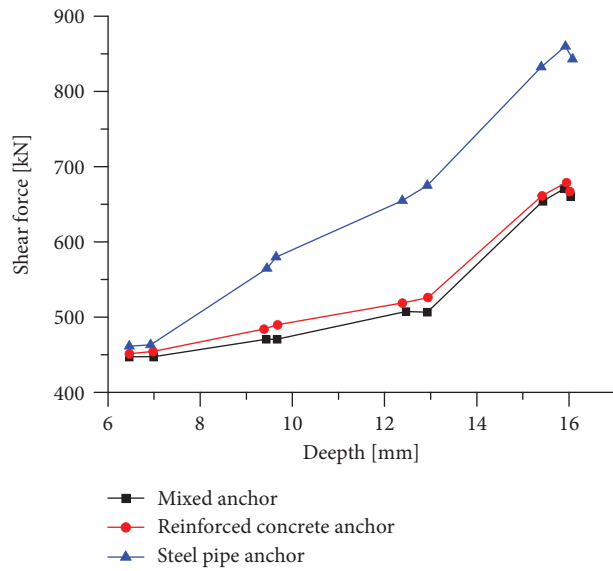


FIGURE 15: The comparison of shear force.

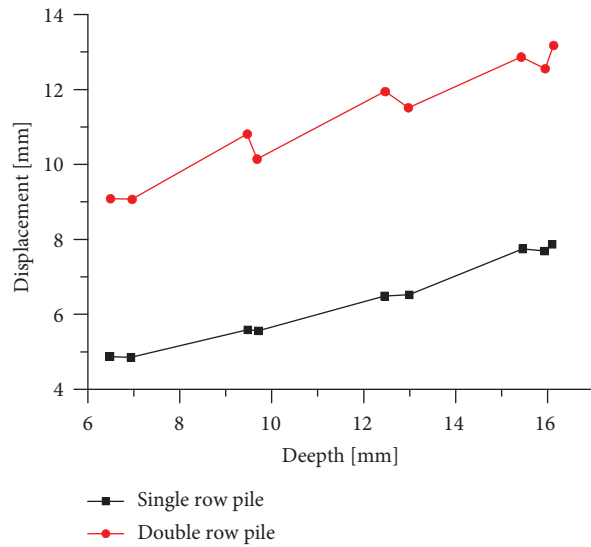


FIGURE 16: The comparison of displacement.

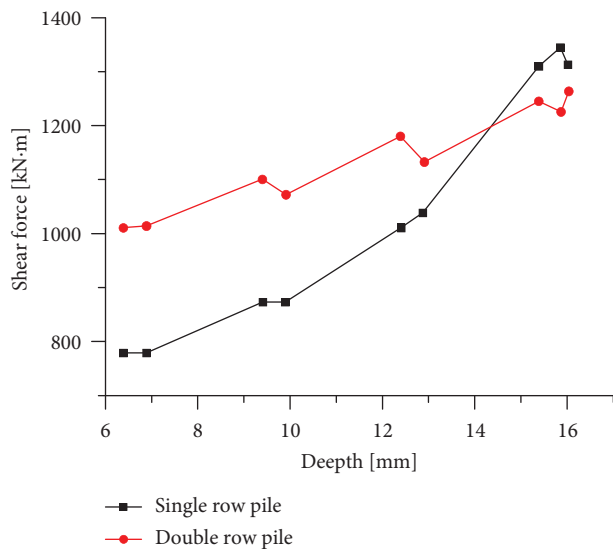


FIGURE 17: The comparison of bending moment.

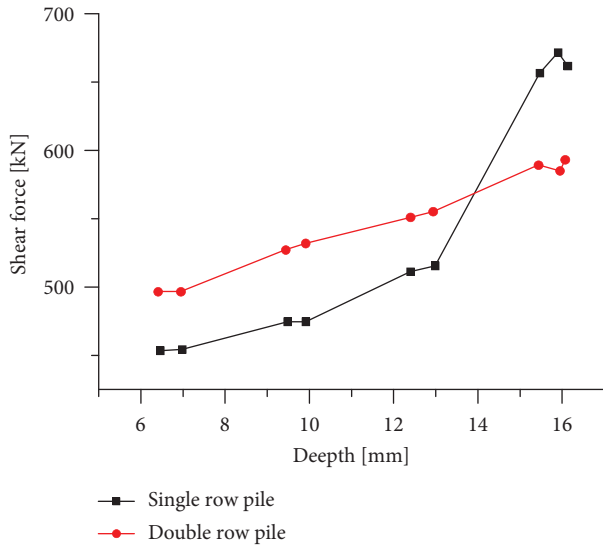


FIGURE 18: The comparison of shear force.

difficult, which induces a low rate of recovery. Due to the advantages of easy installation and demolition, steel support is most widely used in foundation pit engineering.

According to the above analysis, on the premise of safety and economy, scheme 1 is the most consistent with the project.

4.3. Results Comparison of Different Support Types. The results of adopting double row pile and single row pile are compared as shown in Figures 16–18.

From the comparison of the results of the two-pile row scheme, it can be seen that their displacement and bending moment are quite different, and the results of the double-row pile are both larger than the single row pile, but their shear forces are similar.

According to the actual situation and economic efficiency, to ensure the safety of the tomb, the first bracing should adopt the reinforced concrete structure, and the 2th, 3th, and 4th bracing should adopt steel pipe support.

5. Conclusions

Take the ancient tomb protection project as the research case, based on the geological conditions and surrounding environment of the foundation pit, along with the requirements of Building Technical Specification of Protection of Foundation Pit (JGJ120 - 2012), the excavation and support scheme of the foundation pit are designed. The following conclusions can be drawn:

- (1) The support scheme of the bored cast-in-place pile with internal support and the pile slab retaining wall for tomb reinforcement is most suitable for tomb construction. Compared with the scheme of the underground continuous wall with steel support, the scheme of a bored cast-in-place pile with internal support has the advantages of high efficiency, easy construction, low cost, mature technique, and good

stability. Compared with other reinforcement schemes, the pile plate retaining wall has the advantages of the mature technique, convenient construction, and small disturbance to the main body of the tomb, which can effectively prevent the overall sliding of the earth site.

- (2) The suggested value of the controlled settlement of the tomb is 10 mm. As the soil layer of the tomb is simple, it is no need to consider its effect. The more sensitive the building's importance to the surrounding environment, the smaller the controlled value, and the most restrict value is 10 mm.
- (3) The displacement of the mixed anchor scheme is the smallest, and its cost is low. By analyzing the results of four schemes, it is found that the displacement of the double row pile anchor scheme is twice of the mixed anchor scheme. The displacement of the reinforced concrete anchor scheme and steel pipe anchor scheme only has little difference. But the reinforced concrete anchor scheme has a high cost, and the steel pipe anchor scheme cannot ensure the safety of the tomb.
- (4) The greater the strength of the anchor structure, the smaller the settlement is. The settlement value of the reinforced concrete anchor shall be 5 mm at least, and that of the mixed anchor shall be 6 mm. However, considering the economic factor, the mixed anchor support scheme is selected [17–25].

Data Availability

The processed data required to reproduce these findings cannot be shared at this time as the data also form part of an ongoing study.

Conflicts of Interest

The authors declare no conflicts of interest.

References

- [1] J. Wang, "Analysis of protective effect of foundation pit of metro station on ancient buildings," *Construction & Design for Engineering*, vol. 16, no. 7, pp. 62–65+69, 202016.
- [2] D. Gong, C. Wu, J. Zeng, and W. Ye, "Example for the protection of isolated island type ancient architecture in soft soil deep foundation pit excavation," *Building Structure*, vol. 46, no. 8, pp. 95–99, 2016.
- [3] X. Wang, B. Zhu, and B. He, "Monitoring and numerical analysis of deep foundation excavation near the ancient architecture," *Construction Technology*, vol. 43, no. 17, pp. 39–42, 2014.
- [4] J. Qiu, W. Gao, and Z. Zhou, "Influence analysis and countermeasures for extra-deep foundation pit and extra-large digging piles construction ON adjacent metro," *Chinese Journal of Rock Mechanics and Engineering*, vol. 31, no. 6, p. 1081, 2013.
- [5] C. Yoo, D. Lee, "Deep excavation-induced ground surface movement characteristics-a numerical investigation," *Computers and Geotechnics*, vol. 35, no. 2, pp. 231–252, 2008.

- [6] M. Son, E. J. Cording, Estimation of building damage due to excavation-induced ground movements,” *Journal of Geotechnical and Geoenvironmental Engineering*, vol. 131, no. 2, pp. 162–177, 2005.
- [7] C. F. Wu and C. H. Li, “Filed test studies on internal force of pile in pile-anchor supporting system for deep foundation pit,” *Construction Technology*, vol. 383-390, pp. 7713–7717, 2012.
- [8] M. A. Feng-Hai, Z. Yan, and Y. Fan, “Research on deformation prediction method of soft soil deep foundation pit,” *Journal of Coal Science and Engineering*, vol. 14, no. 4, pp. 637–639, 2008.
- [9] X. K. Bao and M. H. Que, “A certain foundation pit support design and construction in baotou,” *Applied Mechanics and Materials*, vol. 580-583, pp. 539–543, 2014.
- [10] X. Y. Liu, W. P. Cai, J. Zhou, and X. Y. Wang, “Finite element study on ring-beam supporting structure of deep foundation pit in coastal soft soil area,” *Applied Mechanics and Materials*, vol. 256-259, pp. 1908–1911, 2013.
- [11] X. D. Zhang, Z. Liu, and X. J. Liu, “The stability analysis of deep foundation pit engineering support and field testing research,” *Applied Mechanics and Materials*, vol. 105-107, pp. 1456–1459, 2012.
- [12] Q. H. . Huang, “Geotechnical engineering practice of multi-forms of composite support of deep foundation pit,” *Advanced Materials Research*, vol. 838-841, pp. 690–696, 2014.
- [13] H. Sun, Y. Chen, J. Zhang, and T. Kuang, “Analytical investigation of tunnel deformation caused by circular foundation pit excavation,” *Computers and Geotechnics*, vol. 106, pp. 193–198, 2019.
- [14] S. Chen, “Optimization of construction scheme of deep excavation pit adjacent to historic buildings,” *Underground Engineering and Tunnels*, vol. 23, no. 3, pp. 20–22+51, 2015.
- [15] R. Dan, M. Zhang, H. Zhou, N. Yang, and Z. Huang, “The theory and practice on deep excavation closing to ancient architectures,” *Construction & Design for Project*, vol. 40, no. 1, pp. 145–147, 2014.
- [16] Y. Wang, “Monitoring of foundation ditch construction of the fujian market of wanmucaotang in guangzhou city,” *Mine Surveying*, vol. 92, no. 2, pp. 29–31+78, 2006.
- [17] National Standards of the People’s Republic of China, *Technical Specification for Retaining and Protection of Building Foundation Excavations(JGJ120-2012)*, pp. 16–28, China Construction Industry Press, China Academy of Building Sciences, Beijing, China, 2012.
- [18] National Standards of the People’s Republic of China, *Technical Code for Building Pile Foundations(JGJ94-2008)*, China Academy of Building Sciences, Beijing, China, 1995.
- [19] National Standards of the People’s Republic of China, *Code for Quality Acceptance of Building Foundation Engineering (GB50202-2002)*, China Academy of Building Sciences, Beijing, China, 2002.
- [20] National Standards of the People’s Republic of China, *Code for Design of concrete Structures (GB50010-2002)*, China Academy of Building Sciences, Beijing, China, 2002.
- [21] National Standards of the People’s Republic of China, *Technical Specifications for Foundation Pits Excavation for Buildings(YB9258-97)*, Metallurgical Industry Press, Beijing, China, 1997.
- [22] National Standards of the People’s Republic of China, *Code for Investigation of Geotechnical Engineering(GB50021-2009)*, China Academy of Building Sciences, Beijing, China, 2009.
- [23] National Standards of the People’s Republic of China, *Code for Design of Building Foundations(GB5007-2011)*, China Academy of Building Sciences, Beijing, China, 2011.
- [24] C.-Y. Ou, J.-T. Liao, and W. Cheng, “Building response and ground movements induced by a deep excavation,” *Géotechnique*, vol. 50, no. 3, pp. 209–220, 2000.
- [25] Oucy, P. G. Hsieh, and Chioudc, “Characteristics of ground surface settlement during excavation,” *Canadian Geotechnical Journal*, vol. 30, no. 5, pp. 758–767, 1993.

Research Article

Fracture Modeling of the Bi-Block Ballastless Track System Resulting from Early-Aged Relative Humidity during the Construction Process

Shihao Cao ¹, Wang Hui ², Shufang Zhai ¹, Kui Hu ¹, Yujing Chen ¹,
and Junqi Chen ¹

¹College of Civil Engineering, Henan University of Technology, Zhengzhou 450001, China

²School of Civil Engineering and Architecture, Hainan University, Haikou 570228, China

Correspondence should be addressed to Wang Hui; huiwang@hainanu.edu.cn

Received 8 September 2021; Accepted 12 October 2021; Published 25 October 2021

Academic Editor: Qinghua Zhang

Copyright © 2021 Shihao Cao et al. This is an open access article distributed under the Creative Commons Attribution License, which permits unrestricted use, distribution, and reproduction in any medium, provided the original work is properly cited.

Drying-induced cracks are an important issue for bi-block ballastless track system consisting of foundation, precast sleepers, and cast-in-place track slab, which not only significantly affects the comfortableness and safety of rapid transit railway but also reduces the service life of ballastless track. In order to explore its damage mechanism, this work presents an evolution model of relative humidity (RH) in the CRTS I bi-block ballastless track system by considering the actual construction sequence and environmental conditions to simulate the crack propagation induced by nonuniform RH field. Firstly, based on the node coupling technique, a three-step transfer process of RH is designed to separately investigate the influence of the construction sequence on the early humidity field in the foundation, sleepers, and cast-in-place track slab, and then the nonuniform distribution of early humidity field in the ballastless track system is determined. Subsequently, the formation mechanism of shrinkage crack in the system is analyzed, and the crack propagation path is predicted by using the mixed-mode fracture criterion. The results show that the maximum relative humidity gradient (RHG) appears at the interface between the track slab and the sleeper after concreting the cast-in-place track slab, which causes the maximum principal stress due to the drying shrinkage property of concrete materials. When the maximum principal stress exceeds the tensile strength of the interface, an interface crack will be generated and converted to a splayed crack with an initial angle of about 45° at the sleeper corner, which will be further propagated under the action of drying shrinkage deformation and finally forms a transverse through-wall crack in the track slab. The simulated crack propagation path agrees with the observed one at the site well, and thus the results are beneficial to understand the formation mechanism of through-wall crack in the track slab and further guide the construction design of the bi-block ballastless track system.

1. Introduction

Since the operation of Beijing-Tianjin intercity high speed railway in 2008, Chinese rapid transit railway has made a rapid development and remarkable achievement [1]. Ballastless track has become the main structural type of rapid transit railway because of its good stability and less maintenance. By the end of April 2021, the total mileage of rapid transit railway has reached about 38,000 kilometers in China [2, 3]. As the most widely used type of ballastless track, the CRTS (Chinese Railway Track System) I bi-block ballastless track has been applied on more than 44 rapid transit railways

such as Wuhan-Guangzhou, Xi'an-Chengdu, and Lanzhou-Xinjiang lines [4]. According to the difference of structures built on the subgrade, bridge, and tunnel, the CRTS I bi-block ballastless track can be divided into three types. The schematic diagram of CRTS I bi-block ballastless track in tunnel is shown in Figure 1, which consists of rail, fastener, sleeper, track slab, and tunnel foundation [5]. However, the ballastless track, as the basis for rapid transit railway, is directly exposed to the atmosphere and eroded by the complex environment factors. These influencing factors make the component materials of the ballastless track in a continuous deterioration process [6–8]. Through the field

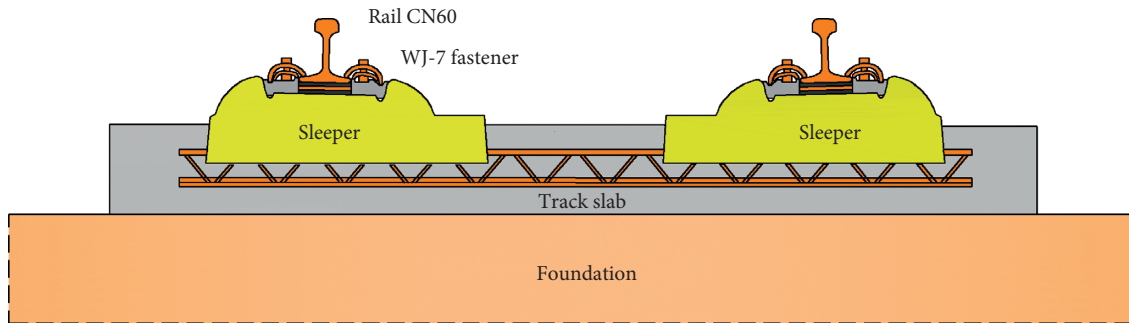


FIGURE 1: Diagram of CRTS I bi-block ballastless track in tunnel.

investigation, it is found that the early cracks are more likely to occur on the surface of track slab due to the bad construction and inadequate design, and then these cracks would rapidly develop into obvious water diseases in abundant rain or poor drainage areas, as shown in Figures 2(c) and 2(d).

The bi-block ballastless track has large contact area with the external environment, and thus the transport of moisture from concrete to environment is significantly affected by the environmental humidity. After concreting the track slab, the hydration of concrete materials will lead to the overall decrease of relative humidity inside the structure. Then, the higher humidity diffuses from track slab to sleepers and ambient dry air, as shown in Figure 2(b). Due to the slow transport rate of moisture in concrete materials, the nonlinear humidity gradient is formed in the ballastless track by the difference of low surface humidity and high internal humidity. On account of the wetting expansion and drying contraction of concrete materials, the shrinkage deformation and stress will occur under the nonlinear humidity gradient. Once the stress is greater than the ultimate tensile strength of concrete, the early cracks will form in the structure, as shown in Figure 2(c).

Figure 3 shows the distribution of early cracks on the track slab of bi-block ballastless track, which was discovered during the investigation of a new bi-block ballastless track. Combined with existing reports [9], the characteristics of cracks on the track slab of bi-block ballastless track can be described as follows: (1) the majority of cracks occurred at the age of 2~3 days or 2 months after the initial setting of track slab; (2) the splayed crack first appeared at the corner of sleeper, and its initial angle is about 40° ; (3) the crack angle decreases with the propagation of crack and gradually tends to 0° ; (4) the cracks at corner of adjacent sleepers would be coalesced and finally form a transverse through-wall crack in the track slab. Currently, the formation mechanism of early drying-induced cracks on the track slab is not clear.

In view of the causes of early cracks in the ballastless track, Wang [9] firstly conducted a statistical analysis of the early crack characteristics on the track slab under construction and pointed out that the temperature and drying shrinkage deformation could be the main reasons for the early cracks. Over the next decade, the related researches [10, 11] mainly focus on the strength and stability caused by temperature load and seldom consider the influence of

shrinkage deformation resulting from internal relative humidity. Based on the heat-moisture-deformation coupling analysis, Chen [12] found that the shrinkage deformation of concrete with a 1% drop in humidity is equivalent to a 2°C drop in temperature. The research results of Li et al. [4] and Yang et al. [6] indicate that the maximum humidity gradient on the surface of the concrete in a dry environment is dozens of times the temperature gradient. That is, the drying shrinkage deformation is much greater than the temperature deformation. Han et al. [13] believe that the contribution of drying shrinkage deformation to early crack can reach 80%. In the control of early-age cracks of track slab, the addition of anticrack steel bars can reduce the early splayed cracks, while the film-forming moisture curing can effectively reduce the irregular cracks [14]. The crack resistance test of concrete slab indicates that adding the 6% TK-ICM anticrack materials in cementitious materials can maintain the internal humidity of concrete for a long time and reduce the risk of cracking [15].

As a main component material of ballastless track, the influence of water on concrete is first reflected in its internal moisture distribution. At present, the moisture transfer model based on Fick's law is widely used to describe the moisture exchange between concrete and environment [16]. Liu et al. [17] used the finite difference method to conduct the concrete humidity. By programming the finite element program, Akika et al. [18] analyzed the humidity field of solid structure with a simplified boundary. In the aspect of experimental research, Parrott [19] fitted the formula for calculating the humidity field in a unilateral drying condition based on experimental data. Combining the theoretical and test results, Gao [20] proposed a calculation model for the concrete humidity field under dry-wet cycles. For the problem of humidity distribution in complex environment, Wang et al. [21] qualitatively analyzed the problem of parameter values affecting the calculation accuracy of humidity field. Subsequently, Gao and Wei [22] put forward the quantitative analysis method of humidity gradient in concrete slab by comprehensively considering the influencing factors such as water/cement ratio, ambient air humidity, and moisture diffusion property of concrete material. To predict the relative humidity of early-age concrete under sealed and unsealed conditions, the models for early-age relative humidity are proposed in consideration of water/cement ratio, critical time, and age of concrete [23]. In view

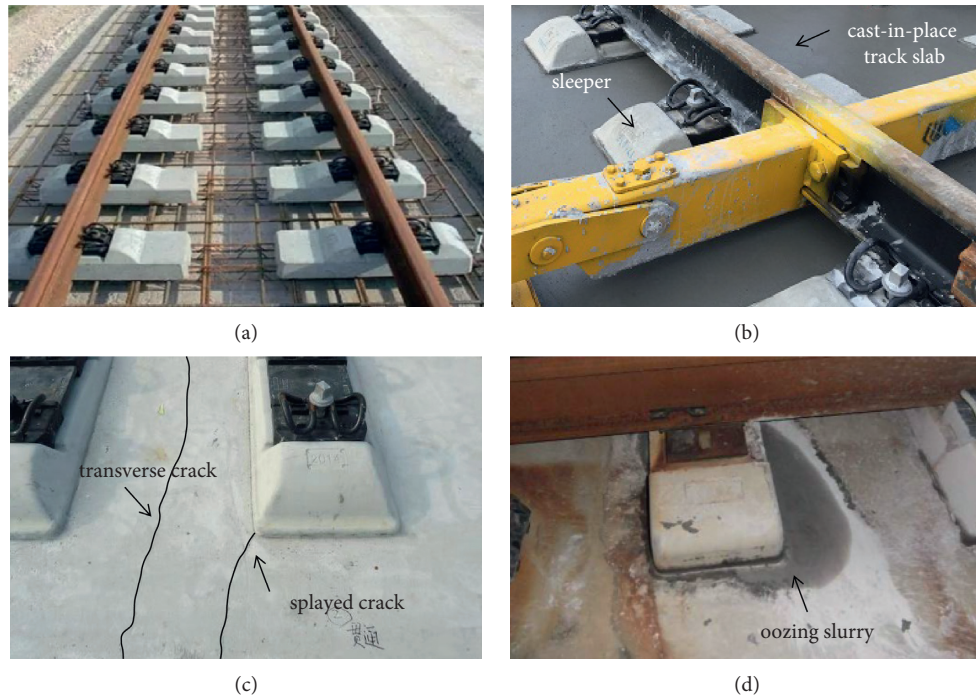


FIGURE 2: State of bi-block ballastless track at different stages. (a) Accurately adjusted and positioned sleepers [4]. (b) Cast-in-place track slab. (c) Early cracks. (d) Oozing slurry.



FIGURE 3: Distribution of cracks on the surface of track slab. (a) Initial crack. (b) Crack coalescence.

of the disadvantages of the complex numerical calculation method of humidity field which is not conducive to engineering application, Wang et al. [24] proposed a conventional method to calculate the concrete humidity field based on the temperature field module by comparing the differential equation, initial and boundary conditions of the temperature, and humidity fields. Although the scholars have studied the distribution characteristics of humidity field in concrete materials, these research results can neither consider the influence of construction characteristics of ballastless track on humidity field nor satisfy the complex humidity environment acting on ballastless track. Up to now, there are few reports on the research of early humidity field of ballastless track. To realize the early humidity analysis of the bi-block ballastless track, the following obstacles need to be resolved firstly: (1) after concreting the track slab, the three separated layers of bi-block ballastless

track bond to adjacent layers, (2) affected by the construction sequence, the initial humidity field of each layer is inconsistent, and (3) the initial humidity conditions of sleepers and foundation are unknown. Therefore, the early humidity prediction presents a considerable challenge when construction sequence is taken into consideration.

In this paper, a finite element computational model of humidity distribution in ballastless track was established by introducing the complex environmental influence and construction process. Based on the node coupling technique, a three-step calculation process including one steady-state and two transient analyses was designed to realize the influence of the construction sequence on the early humidity field. Then according to the construction sequence, the early humidity field of each layer of bi-block ballastless track was analyzed, and the effects of controlling parameters related to external ambient air drying, internal hydration self-

desiccation, and local wetting time on early humidity distribution in ballastless track were analyzed. The distribution characteristics and development law of early humidity field of bi-block ballastless track were defined. Moreover, the formation mechanism of shrinkage crack was analyzed on the basis of strength theory, and the crack propagation path was predicted by using the mixed-mode fracture criterion. The research results can provide theoretical basis for optimizing track structure design and improving track construction technology.

2. Computational Model of Humidity Field in Concrete

In the complex environment, the internal relative humidity field of the ballastless track is in a state of dynamic equilibrium under the combined action of wetting on the bottom, moisture exchange between the exposed surface and the ambient air, internal moisture diffusion from high humidity region to low humidity region, and self-desiccation due to hydration of cement. To serve the practical analysis of the ballastless track, here the computational theory of humidity field is firstly reviewed.

Assuming that the RH at the position (x, y, z) and time t is $H(x, y, z, t)$, the moisture change within a closed domain Ω caused by the RH variation from $H(x, y, z, t_1)$ to $H(x, y, z, t_2)$ is

$$Q_1 = \int_{t_1}^{t_2} \left[\iiint_{\Omega} \frac{\partial H}{\partial t} dV \right] dt. \quad (1)$$

Considering the effect of self-desiccation of material, the moisture change from time t_1 to t_2 is

$$Q_2 = - \int_{t_1}^{t_2} \left[\iiint_{\Omega} G(x, y, z, t) dV \right] dt, \quad (2)$$

where $G(x, y, z, t)$ is the function of hydration self-desiccation of material, and the relationship between the hydration self-desiccation and the water-cement ratio w/c can be described as follows [24]:

$$G(t) = \frac{0.002 \cdot \exp[-(w/c)/0.3068]}{(1 + 0.43t)^{1.2}}. \quad (3)$$

The moisture in the structure will diffuse from high humidity region to low humidity region under the action of humidity gradient, and the moisture diffused through a tiny surface is proportional to the time dt , surface area dA , and humidity gradient along the surface normal direction; that is,

$$dQ_3 = -D(x, y, z, t) \frac{\partial H}{\partial n} dA dt, \quad (4)$$

where $\partial H/\partial n$ is the change rate of humidity along the normal direction of surface and $D(x, y, z, t)$ is the coefficient of moisture diffusion which is a function of the internal RH [22]:

$$D(H) = D_1 \left[\alpha + \frac{1 - \alpha}{1 + (1 - H/1 - H_c)^\beta} \right]. \quad (5)$$

In equation (5), D_1 is the maximum moisture diffusion coefficient, α is the ratio of minimum to maximum moisture diffusion coefficient, H_c is the relative humidity when $D(H) = 0.5D_1$, and β is the material constant.

Therefore, the total amount of water diffused through the closed surface from time t_1 to t_2 can be written as

$$Q_3 = \int_{t_1}^{t_2} \left[\iiint_{\Omega} D \nabla^2 H dV \right] dt. \quad (6)$$

According to the law of conservation of mass, $Q_1 = Q_2 + Q_3$, we have

$$\int_{t_1}^{t_2} \left[\iiint_{\Omega} \frac{\partial H}{\partial t} dV \right] dt = - \int_{t_1}^{t_2} \left[\iiint_{\Omega} G(x, y, z, t) dV \right] dt + \int_{t_1}^{t_2} \left[\iiint_{\Omega} D \nabla^2 H dV \right] dt. \quad (7)$$

The humidity boundary condition for the ballastless track can be divided into the following two categories.

- (1) The humidity on the material surface is a known function related to time; that is,

$$H_m = H(t). \quad (8)$$

- (2) The moisture exchange coefficient between the exposed surface and ambient air is known; then,

$$-D \frac{\partial H}{\partial n} = a_m (H_m - H_s), \quad (9)$$

where H_s is the RH of the ambient air, H_m is the RH of the exposed surface, and a_m is the moisture exchange coefficient.

In order to verify the correctness of the computation model of concrete early humidity field, a concrete specimen from casting to curing stage is considered, as shown in Figure 4. A serial of monitoring points A, B, C, D, and E were set in the calculation model, and the corresponding distance to the upper surface is 2, 8, 15, 25, and 28 cm, respectively. The calculation conditions were set as follows: within 28 days after casting the concrete specimen, the upper surface of specimen is exposed to the ambient air with a RH of 65%. After this, the bottom is in contact with water directly.

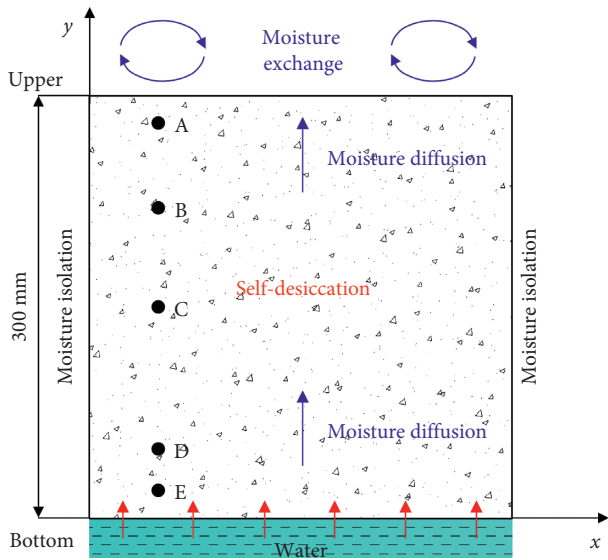


FIGURE 4: Early humidity field calculation model of concrete specimen ($w/c=0.4$).

Furthermore, both the left and right sides of the concrete specimen keep isolated from the ambient air. Using ANSYS Workbench 18.0, the concrete specimen is discretized by 900 elements. The resulting humidity distribution in the specimen is shown in Figures 5 and 6.

As can be seen from Figure 5, since the monitoring point A is close to the upper surface and greatly affected by the dry ambient air, the relative humidity declines rapidly over time. For the deeper monitoring point B and below, due to the slow rate of moisture diffusion in the concrete material, the declining rate and amplitude of humidity are significantly smaller than those at monitoring point A, and the humidity reduction is mainly caused by the hydration self-desiccation. At the age of 28 days, the specimen bottom is beginning to contact with the water directly, and the relative humidity of monitoring points adjacent to the bottom increases to a different degree. Due to the fast rate of capillary water absorption, the relative humidity at monitoring point E increases rapidly, while the relative humidity at monitoring point D increases with a delay amplitude and slow rate but still shows a rising trend. From Figures 6 and 7, it can be seen that, under the combined action of upper drying air, bottom wetting environment, and internal hydration self-desiccation, the moisture variation in the concrete specimen can be divided into three regions along depth: (1) the influence area of the ambient drying air is about 8 cm away from the upper surface; (2) the influence area of the wetting environment is within 7.5 cm from the bottom; (3) the influence area of hydration self-desiccation is the intermediate region with a uniform humidity distribution. In addition, the numerical calculation value of relative humidity is in good agreement with the test result, so it can be considered that the transient calculation model of humidity field established in this paper can be used to predict the humidity distribution of ballastless track under the complex environment.

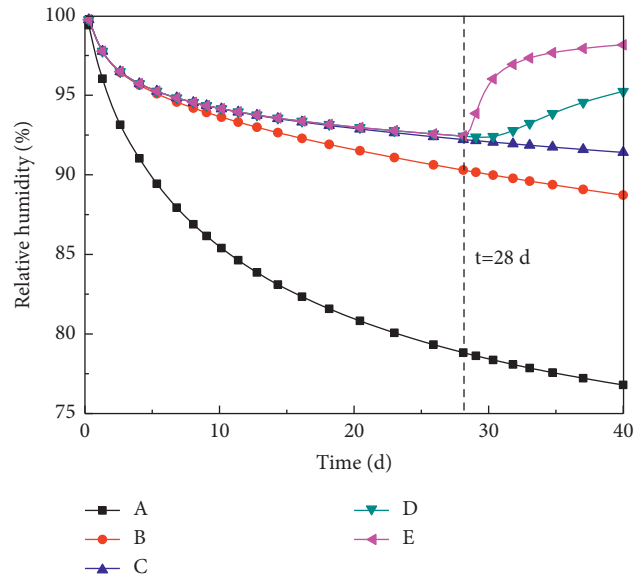


FIGURE 5: Variations of RH at different monitoring points.

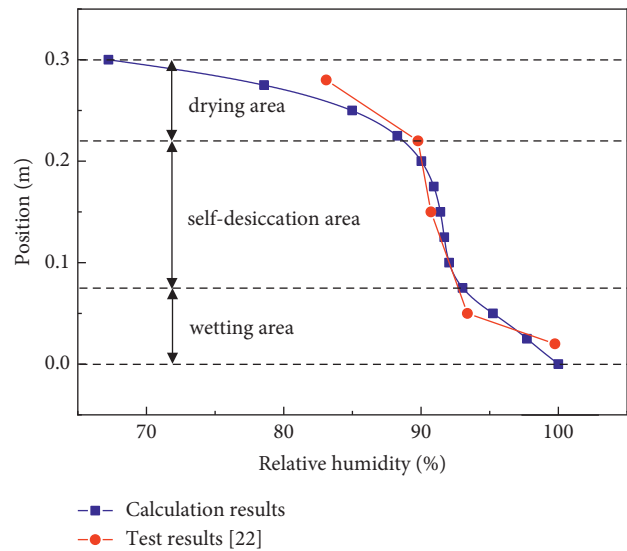


FIGURE 6: RH distribution along the vertical direction ($t=40$ d).

3. Early Humidity Field Calculation Model and Process of Ballastless Track

3.1. Calculation Model. In this paper, the CRTS I bi-block ballastless track in tunnel is focused on to establish the humidity field calculation model, as shown in Figure 8. The model consists of bi-block sleepers ($800\text{ mm} \times 140\text{ mm} \times 300\text{ mm}$), track slab ($2800\text{ mm} \times 260\text{ mm} \times 6250\text{ mm}$), and foundation ($5800\text{ mm} \times 2000\text{ mm} \times 6250\text{ mm}$). The corresponding material parameters are shown in Table 1 [20, 22, 25]. In order to solve the unsteady moisture diffusion problem, the internal moisture source with negative value is used to control the hydration self-desiccation of early-age concrete, as shown in equation (3). Meanwhile, the convective moisture flux is applied on the exterior boundaries of ballastless track to realize the moisture

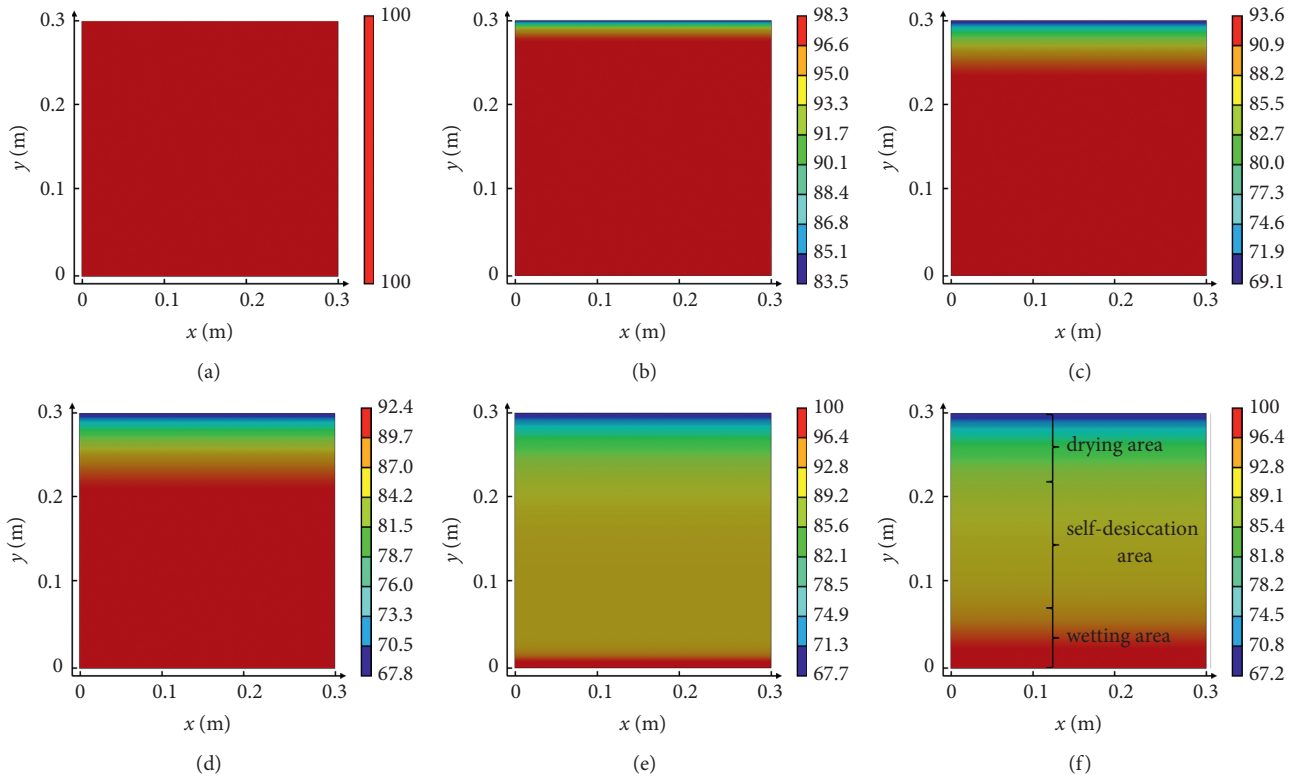


FIGURE 7: RH contour of concrete specimen at different times. (a) $t=0$ d, (b) $t=1$ d, (c) $t=14$ d, (d) $t=28$ d, (e) $t=29$ d, and (f) $t=40$ d.

exchange between exterior boundaries and ambient air. The external ambient relative humidity is set to be 65%, and the moisture transfer coefficient a_m is listed in Table 1. In addition, the wet boundary is specified as constant relative humidity of 100%.

3.2. Calculation Process. CRTS I bi-block ballastless track is a kind of track structure which is one-time cast-in-place after assembling the prefabricated bi-block sleepers into track panels. It is important to notice that the three separated layers of bi-block ballastless track will be bonded to adjacent layer after concreting the track slab. Meanwhile, the initial humidity conditions of three layers are nonuniform and inconsistent. In order to overcome the above technical obstacles, based on the node coupling technique, the three-step calculation process including one steady-state and two transient analyses was designed to realize the influence of the construction sequence on the early humidity field, as shown in Figure 9.

- (1) Step 1: Under the long-term action of groundwater infiltration and external ambient air drying, the humidity field of foundation is in equilibrium. First, the steady humidity field of foundation is obtained by conducting a steady-state humidity field analysis. This steady result will be used as the initial humidity condition of foundation for the transient humidity field analysis of ballastless track in step 3.

- (2) Step 2: The sleepers are precast at the factory and maintained to $t=60$ d. In this case, their humidity distribution is mainly affected by the external ambient air drying and internal hydration self-desiccation. In this step, the variation of humidity field is obtained by carrying out a transient humidity field analysis of sleepers. The last-time result is used as the initial humidity condition of sleepers for the transient humidity field analysis of ballastless track in step 3.
- (3) Step 3: To control the interface state transition before and after concreting the track slab, the node coupling technique is applied at the interfaces between track slab and sleepers, track slab and foundation, as shown in Figure 10. Before concreting the track slab, the node coupling technique is deactivated, and the interface state keeps separated. After concreting the track slab, the node coupling technique is activated, and the interface state translates from separated state to bonded state. Then, the initial high humidity will diffuse from track slab to sleepers and foundation through the bonded interfaces.

According to the above calculation process, the early humidity distribution characteristics of CRTS I bi-block ballastless track can be defined. The initial conditions, boundary conditions, and result analysis of the above three steps are described in detail in Section 4.

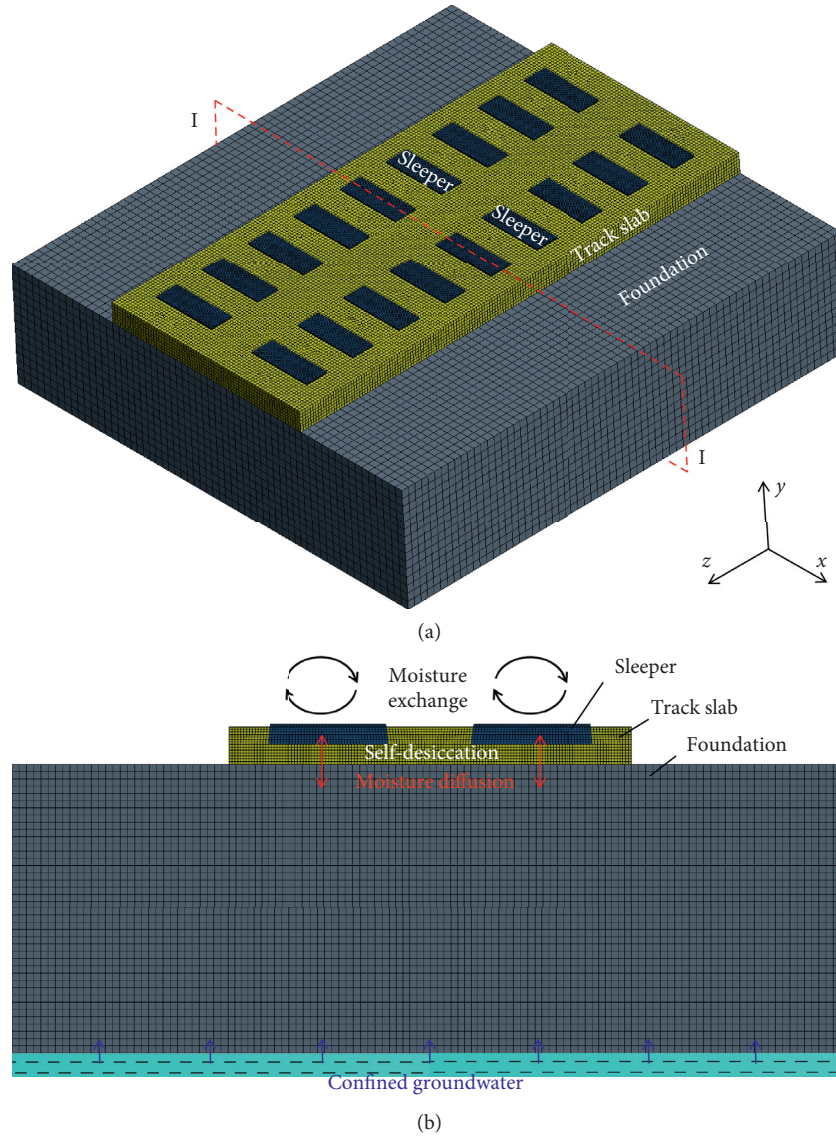


FIGURE 8: Early humidity field calculation model of CRTS I bi-block ballastless track. (a) Overall FE model and (b) local schematic for the cross section I-I.

TABLE 1: Material parameters.

Component	E_{28} (GPa)	ν	w/c	f_t (MPa)	$D_1 \times 10^{-10}$ ($\text{m}^2 \cdot \text{s}^{-1}$)	α	β	H_c (%)	a_m ($\text{m} \cdot \text{d}^{-1}$)
Sleeper	36.0	0.2	0.3	1.54	0.25	0.018	1.3	98	0.0038
Track slab	32.5	0.2	0.4	2.39	0.5	0.022	1.1	98	0.0055
Foundation	25.5	0.2	0.6	2.74	2.02	0.071	0.8	98	0.0105

4. Early Humidity Analysis in the Ballastless Track

4.1. Steady-State Humidity Analysis of Foundation. In the tunnel, it is assumed that the groundwater exists at a depth of 2 m, and the relative humidity of the ambient air is 65%. Under the long-term action of groundwater and ambient air, the steady humidity distribution of tunnel foundation was calculated by steady-state analysis, as shown in Figures 11 and 12.

Up to now, the linear interpolation is still a common approach used to deal with the initial conditions of sub-structures such as tunnel foundation and subgrade bed during a transient physical field analysis of ballastless track [26]. However, in view of the nonlinear relationship between moisture diffusivity and humidity, the steady humidity distribution along the depth follows a cubic polynomial, as shown in Figures 11 and 12. The relative humidity of the upper surface is about 65.1%, which is very close to that of the ambient air in tunnel. At the depth of 1 m, the maximum

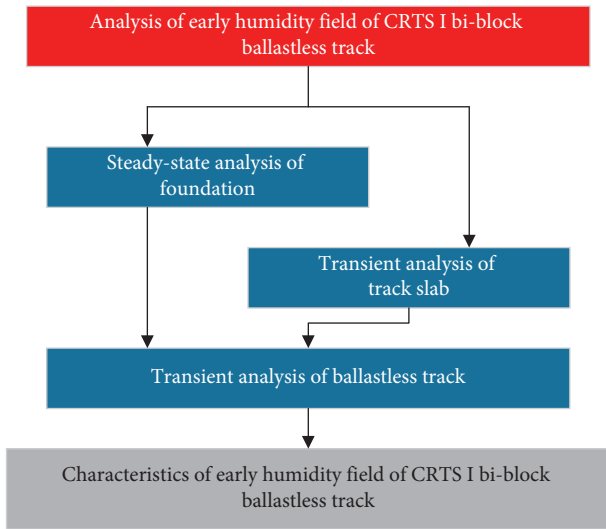


FIGURE 9: Early humidity field calculation process of CRTS I bi-block ballastless track.

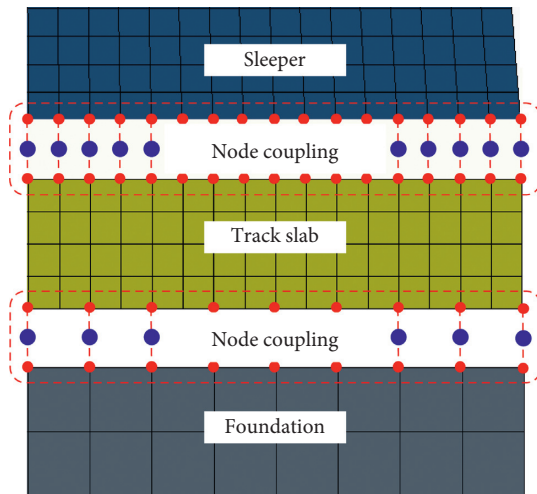


FIGURE 10: Node coupling technique applied at the interfaces.

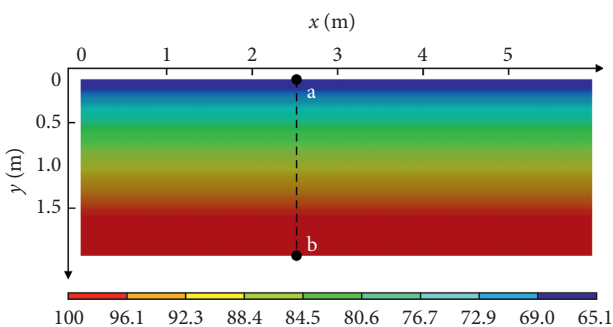


FIGURE 11: Steady RH contour of foundation.

difference between numerical result and linear interpolation is 7.5%. Therefore, the steady-state humidity analysis of foundation is essential, and the steady result will be as the initial humidity condition of foundation for the transient humidity field analysis of ballastless track in Section 4.3.

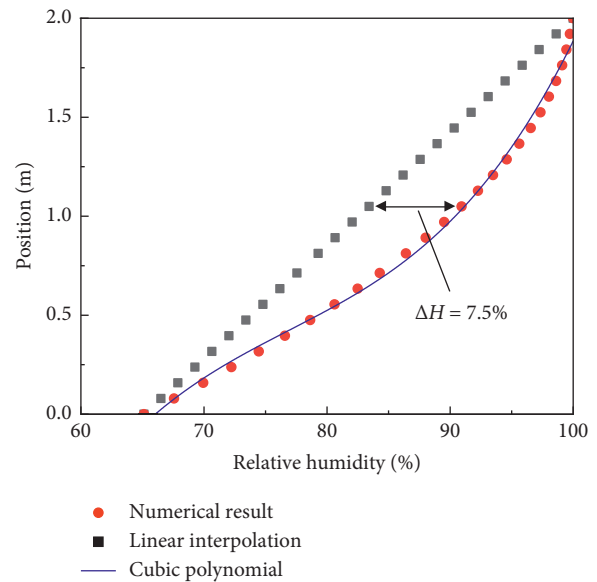


FIGURE 12: Distribution of RH along the path ab.

4.2. *Transient Humidity Analysis of Sleeper.* After concreting sleepers at the factory, the sleepers were stored in the ambient air with an average RH of 65% and RH amplitude of 50%, as shown in Figure 13, and kept for 60 days. Under the action of external ambient air drying and internal hydration self-desiccation, the humidity distribution of sleeper was calculated, as shown in Figures 14–16.

Figure 14 shows that, under the coupling effect of external air drying and internal hydration self-desiccation, the relative humidity in the sleeper shows a steady decline. On the 60th day after the sleepers have been precast, the surface relative humidity decreases to 66.6%, and the intermediate relative humidity decreases to 80.1%. The relative humidity of the surface layer of the sleeper is mainly affected by the ambient air, while the interior of the sleeper is mainly controlled by hydration self-desiccation. In order to further study the distribution of sleeper’s relative humidity, the relative humidity and relative humidity gradient (RHG) along line ab shown in Figure 14(b) were calculated, as shown in Figures 15 and 16, respectively.

According to Figures 15 and 16, it is found that the typical nonlinear relative humidity gradient is formed inside the sleeper due to the slow transfer of moisture in concrete materials, which can also be approximated by a five-segment linear distribution. As a result of diurnal fluctuations of ambient relative humidity, the maximum relative humidity gradient appears around 6 mm beneath the surface of sleeper, and the limit influence depth of diurnal fluctuations of ambient relative humidity is about 8 mm. In this section, the last-time transient result will be as the initial humidity condition of sleepers for the transient humidity field analysis of ballastless track in Section 4.3.

4.3. *Transient Humidity Analysis of Ballastless Track.* Sixty days after the sleepers had been precast, the sleepers were transported to the construction site. Then, the track slab was poured after the sleepers had been assembled into

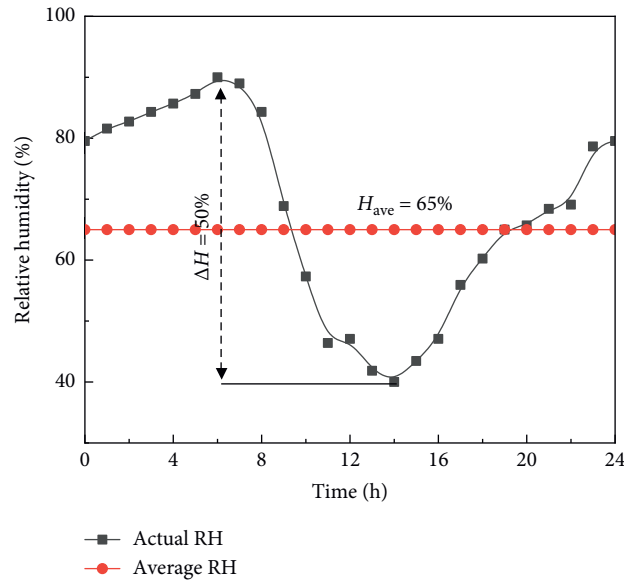


FIGURE 13: Daily periodic fluctuations of ambient relative humidity applied on the surface of sleeper.

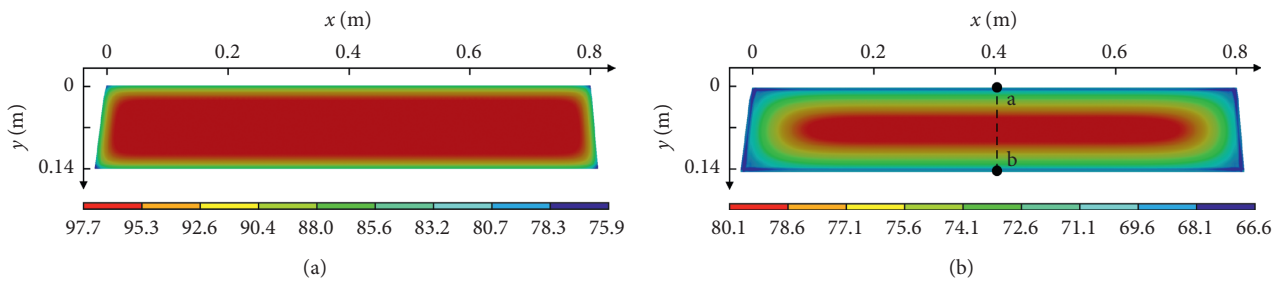


FIGURE 14: RH contour of sleeper at different times. (a) $t = 1$ d and (b) $t = 60$ d.

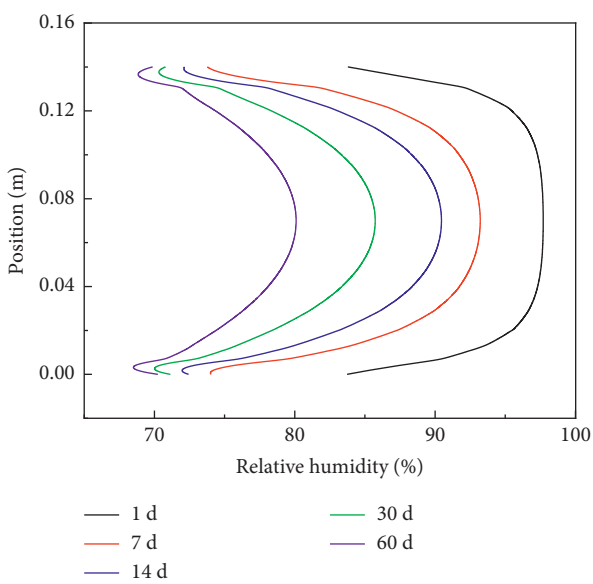


FIGURE 15: Distribution of RH along the path ab.

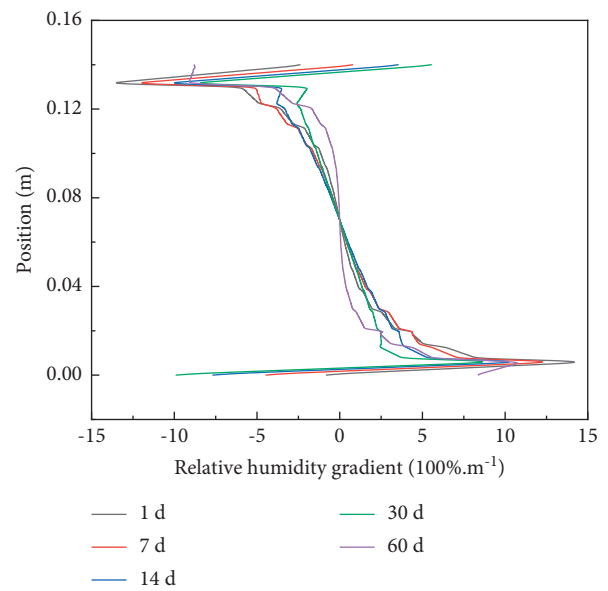


FIGURE 16: Distribution of RHG along the path ab.

track panels and maintained for 90 days. In this transient analysis, the initial humidity state of ballastless track is shown in Figures 17(a) and 17(b). The initial humidity of foundation used the steady-state result in Section 4.1, the initial humidity of track slab was set to be 100%, and the initial humidity of sleepers adopted the transient result in Section 4.2. In the first seven days, the exposed surfaces of ballastless track were specified as wet boundaries ($H = 100\%$) according to the construction requirements and replaced by a convective moisture flux condition ($H = 65\%$) in the days that followed. Under the water wetting, external ambient air drying, and internal hydration self-desiccation, the humidity distribution of the ballastless track was calculated, as shown in Figure 17.

It can be seen from Figure 17 that, at the initial phase after concreting the track slab, the significant difference of humidity forms on both sides of the interface. Under the driving action of humidity difference, the moisture in the structure diffuses from high humidity to low humidity areas and forms a higher relative humidity gradient at the interface, as shown in Figures 17(c), and 17(d). Subsequently, the relative humidity field inside the whole ballastless track gradually becomes stable under the continuous effect of moisture diffusion, as shown in Figures 17(c), 17(e), and 17(g). Finally, the maximum relative humidity gradient of each region appears at the surface interface, shown as points A and B in Figure 17(h). In order to further study the humidity distribution at the interface, the relative humidity and relative humidity gradient along the line ab shown in Figure 17(h) were calculated, as shown in Figures 18 and 19. Interface 1 represents the interface between sleeper and track slab, and interface 2 represents the interface between track slab and foundation.

From Figures 18 and 19, a large relative humidity gradient will occur at the interface between track slab and sleeper or the track slab and foundation. On the 1st, 3rd, 7th, 14th, 30th, 45th, 60th, and 90th days after concreting the track slab, the relative humidity gradients at the interface between the track slab and sleeper are 24.46, 14.45, 8.69, 4.17, 2.26, 1.65, 1.39, and $1.09 \times 100\%/m$, respectively. The results show that the relative humidity gradient decreases rapidly in the first week after concreting the track slab, and then the descending rate tends to be slow over time.

5. Crack Formation

5.1. Cracking Criterion. Due to the apparent characteristics of wetting expansion and drying contraction of concrete materials, the cracks in concrete structures may be caused by the nonuniform internal relative humidity. Based on the beam warping test, the relation between drying-induced strain ε and internal relative humidity H in concrete can be written as follows [27]:

$$\varepsilon = 8.14 \times (1 - H) \times 10^{-4}, \quad (10)$$

from which it is found that the nonuniform RH field leads to the nonuniform strain and then stress.

Besides, as a key parameter that affects the deformation of material, the elastic modulus of concrete increases with

age, and the increase rate in early age is higher than that in the later age. In this paper, the constant elastic modulus E_{28} of sleeper and foundation listed in Table 1 is adopted, and the elastic modulus of track slab is described by exponential formula [28]:

$$E(t) = E_{28} \times [1 - \exp(-0.4t^{0.34})], \quad (11)$$

where t is the time in day and E_{28} is the elastic modulus of the concrete at the equivalent age of 28 days.

For brittle materials such as concrete, its failure is mainly caused by the maximum tensile stress. The cracking risk of concrete can be defined as the ratio of the maximum principal stress to the tensile strength [29]; that is,

$$\zeta = \frac{\sigma_{1,\max}}{f_t}, \quad (12)$$

where ζ is the cracking risk, $\sigma_{1,\max}$ is the maximum principal stress, and f_t is the tensile strength.

Considering the fluctuating characteristics of the mechanical properties of concrete materials, it is generally believed that the crack will be caused when the cracking risk reaches 0.7 [30].

5.2. Results and Analysis. After concreting the track slab, the distributions of maximum principal stress at different times were calculated without taking into account wet curing, as shown in Figure 20.

It can be seen from Figure 20 that, in the curing stage of track slab, a certain tensile stress will be generated due to the drying shrinkage property of concrete materials, and the stresses that occur at the interface between sleeper and track slab are greater than those at other areas. When the stress exceeds the tensile strength of the interface, the interface crack will be generated.

After the interface crack between sleeper and track slab has been generated, shown as white lines ab and cd in Figure 20(b), the released energy of interface crack will be transferred to the corner of sleeper and intensifies the stress concentration effect. When the maximum principal stress exceeds the tensile strength of the track slab, the splayed crack with an initial angle of about 45° will be generated at the sleeper corner. Finally, the cracks at corner of adjacent sleepers would be coalesced and form a transverse through-wall crack of track slab, as shown in Figures 3(b) and 20(b).

6. Crack Propagation

6.1. Mixed-Mode Fracture Criterion. In order to clarify the propagation mechanism of track slab crack, the mixed-mode fracture criterion was selected to predict the propagation direction of track slab crack by considering the combined effect of tensile and shear stresses. The previous studies have shown that the maximum circumferential tensile stress criterion is in good agreement with the test data of brittle materials such as concrete and rock. Therefore, this criterion is often used to analyze the fracture mechanism of concrete structures. For the mixed-mode crack, the equivalent stress

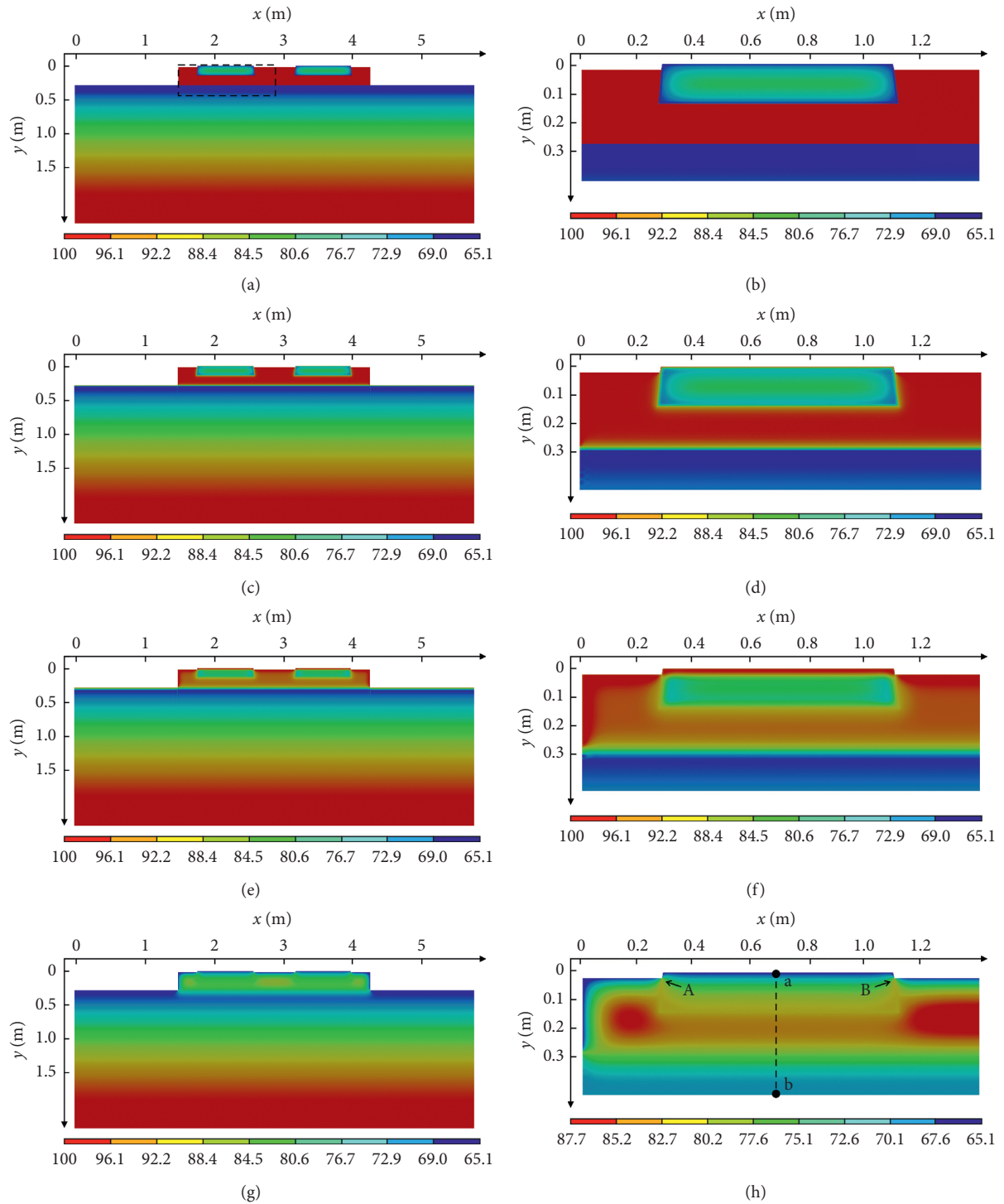


FIGURE 17: RH contour of ballastless track at different times. (a) $t = 0$ d, entire contour; (b) $t = 0$ d, local contour; (c) $t = 1$ d, entire contour; (d) $t = 1$ d, local contour; (e) $t = 7$ d, entire contour; (f) $t = 7$ d, local contour; (g) $t = 60$ d, entire contour; (h) $t = 60$ d, local contour.

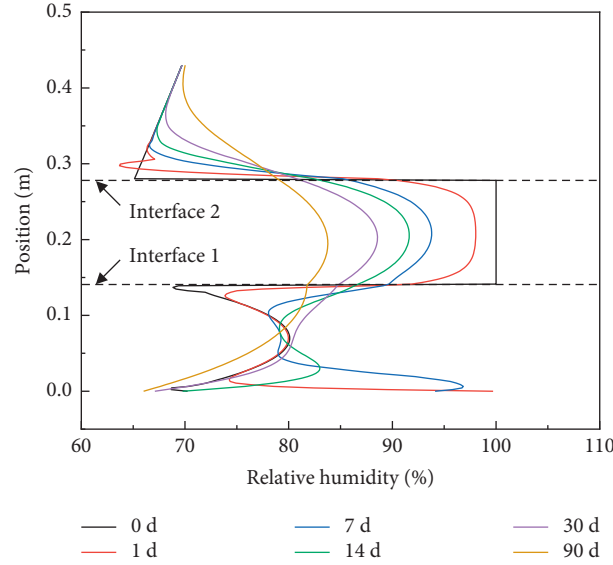


FIGURE 18: Distribution of RH along the path ab.

intensity factor K_{eff} can be evaluated by the following equation [31]:

$$K_{eff} = \sqrt{(K_I + K_{II})^2 + \frac{1}{1-2\nu} K_{III}^2}, \quad (13)$$

where ν is Poisson's ratio and K_I , K_{II} , and K_{III} are the stress intensity factors in modes I, II, and III, respectively, which can be computed based on the displacement extrapolation method [32]; that is,

$$\begin{cases} K_I = \frac{G(\nu_c - \nu_e)}{\kappa + 1} \sqrt{\frac{2\pi}{r}}, \\ K_{II} = \frac{G(u_c - u_e)}{\kappa + 1} \sqrt{\frac{2\pi}{r}}, \\ K_{III} = \frac{G(w_c - w_e)}{\kappa + 1} \sqrt{\frac{2\pi}{r}}. \end{cases} \quad (14)$$

G is the shear modulus, κ is the coefficient related to Poisson's ratio, r is the element length, and u , v , and w are the node displacements in the x , y , and z directions, respectively, as shown in Figure 21.

When the equivalent stress intensity factor K_{eff} exceeds the fracture toughness K_C , the crack will lose the stability and fracture rapidly. The fracture condition can be expressed as

$$K_{eff} \geq K_C. \quad (15)$$

The maximum circumferential tensile stress criterion assumes that the crack propagates along the direction of the maximum circumferential tensile stress [33]:

$$\theta = 2 \tan^{-1} \left[\frac{1}{4} \frac{K_I}{K_{II}} + \frac{1}{4} \sqrt{\left(\frac{K_I}{K_{II}} \right)^2 + 8} \right], \quad (16)$$

where θ is the turning angle of the crack, as shown in Figure 21.

The fracture models described above have been implemented in the ANSYS Workbench 18.0, and the flowchart of numerical procedure for the fatigue crack growth simulation is shown in Figure 22.

6.2. Results and Analysis. Based on the maximum circumferential tensile stress criterion, the propagation path of crack with an initial length $L_{in} = 0.1$ m and angle $\theta_{in} = 45^\circ$ was predicted, as shown in Table 2 and Figure 23. The results show that, under the action of drying shrinkage deformation of early-age concrete, the initial crack tip is subject to the combined action of tensile and shear stresses. In this case, the initial crack belongs to a mixed-mode crack, and the ratio of K_{II} and K_{III} to K_I is 31.37% and 7.6%, respectively. Under the combined action of stress intensity factors including K_I , K_{II} , and K_{III} , the initial crack direction will turn an angle of 30.06° , as shown in Figure 23(b). After the propagation path of initial crack has been turned, the ratio of K_{II} to K_I drops to 1.34%, and then the crack propagation path further turns an angle of 1.53° , as shown in Figure 23(c). Due to the continuous turning of crack propagation path, the final propagation path tends to be along the transverse direction of track slab, and the corresponding failure mode gradually transforms from mixed-model into pure opening-mode. When there are initial cracks at the corner of adjacent sleepers, the cracks would be coalesced

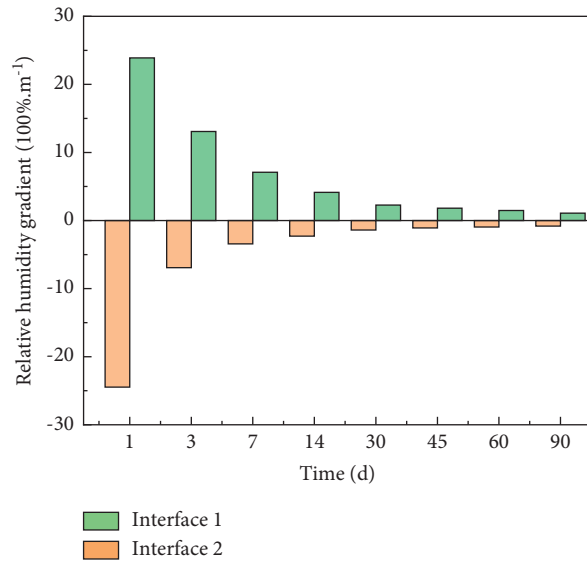
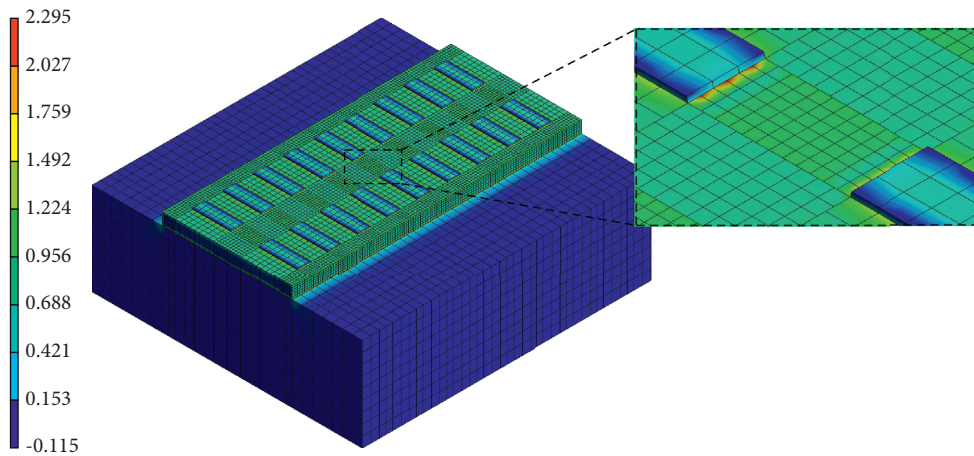


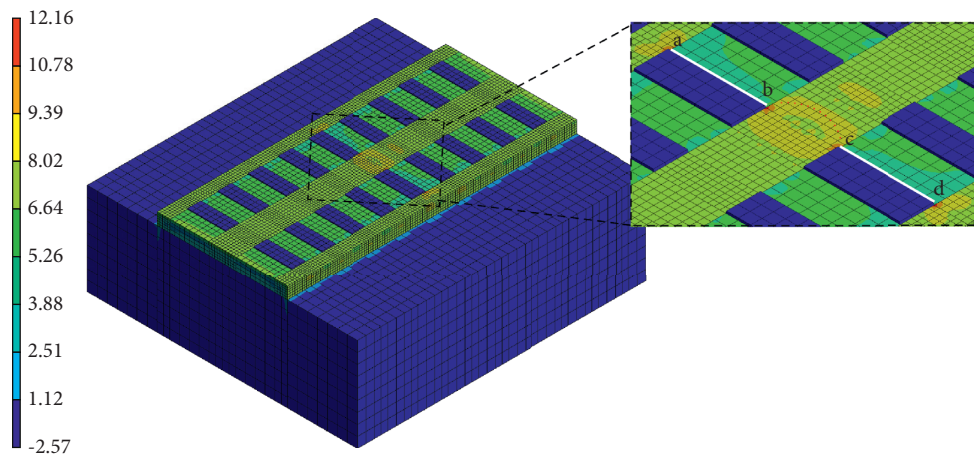
FIGURE 19: RHG at the interfaces.

TYPE: Maximum principal stress
 Unit: MPa
 Time: 1 d



(a)

TYPE: Maximum principal stress
 Unit: MPa
 Time: 90 d



(b)

FIGURE 20: Maximum principal stress contour of ballastless track. (a) $t=1$ d and (b) $t=90$ d.

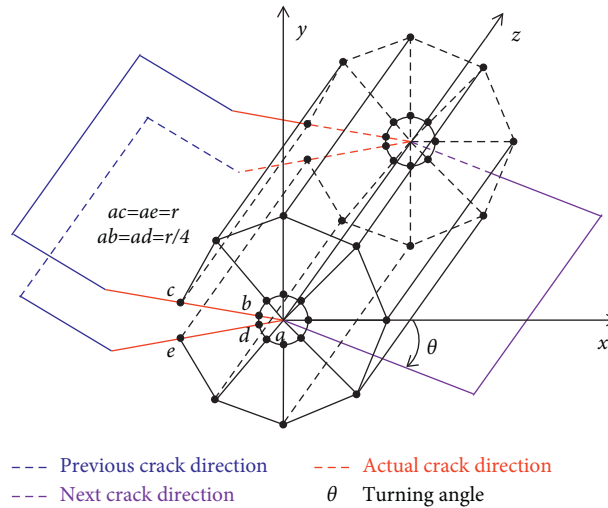


FIGURE 21: Singularity elements at the crack tip and crack propagation path.

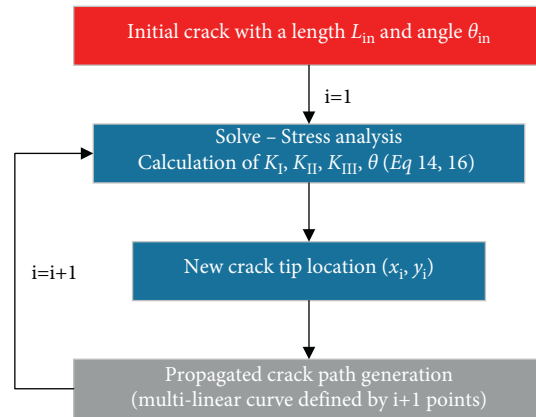


FIGURE 22: Numerical procedure for the fatigue crack growth simulation.

TABLE 2: Turning angle of the crack propagation path.

Crack length (m)	K_I (MPa.m ^{0.5})	K_{II} (MPa.m ^{0.5})	K_{III} (MPa.m ^{0.5})	K_{eff} (MPa.m ^{0.5})	Initial angle (°)	Previous angle (°)	Actual angle (°)	Turning angle (°)
0.1	3.8659	1.2128	0.2960	5.0930	45	—	45	30.06
0.2	5.2919	0.0709	0.0072	5.3637	45	45	14.94	1.53
0.3	5.4932	0.1268	0.0009	5.6200	45	14.94	13.41	2.65

and further form the transverse through-wall crack of track slab, as shown in Figures 3(b) and 23(d). The transverse through-wall crack not only significantly

affects the comfortableness and safety of rapid transit railway, but also reduces the service life of ballastless track.

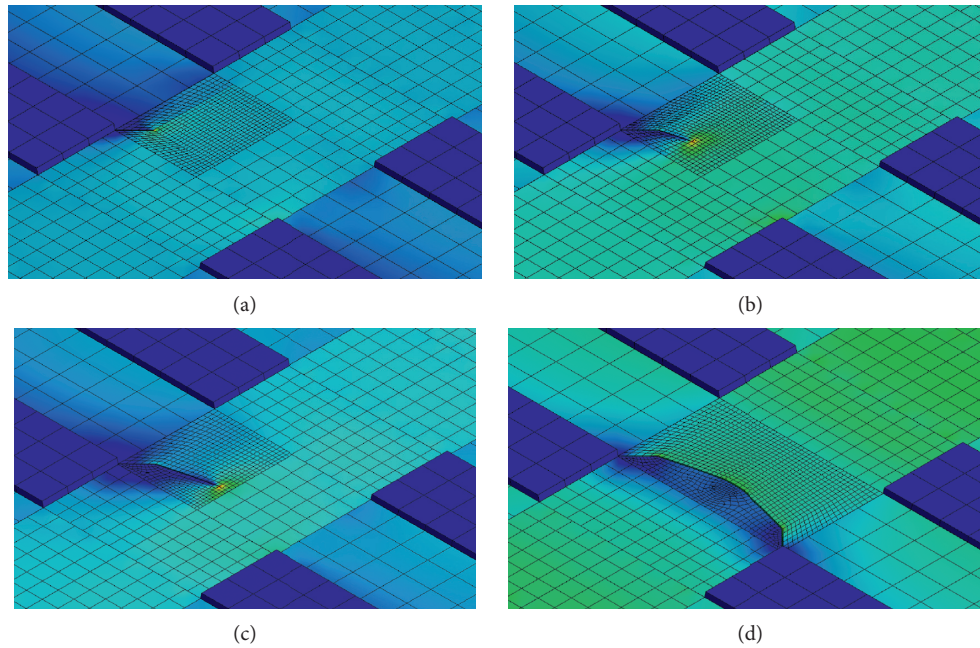


FIGURE 23: Predicted propagation paths of the crack with an initial angle of 45° . (a) $\theta = 30.06^\circ$, (b) $\theta = 1.53^\circ$, (c) $\theta = 2.65^\circ$, and (d) crack coalescence.

7. Conclusions

This paper focuses on the drying-induced crack mechanism of the CRTS I bi-block ballastless track system induced by early-aged internal relative humidity. Considering the construction sequence and environmental conditions of the ballastless track system, the RH distribution in the system is simulated, and the crack propagation induced by the nonuniform RH is predicted. The following conclusions can be drawn:

- (1) Under the long-term action of groundwater infiltration and external ambient air drying, the steady humidity of foundation along the depth obeys a cubic polynomial distribution. The steady result can provide an accurate initial humidity condition of foundation for the transient humidity field analysis of ballastless track relative to the linear interpolation method.
- (2) After precasting the sleeper, the nonuniform humidity field is formed inside the sleeper. The surface relative humidity of sleeper is mainly affected by the ambient air drying, and the interior relative humidity is mainly controlled by the hydration self-desiccation. The transient result can provide a nonuniform initial humidity condition of sleepers for the transient humidity field analysis of ballastless track.
- (3) After concreting the track slab in the site, the high humidity diffuses from track slab to sleepers and foundation through the bonded interfaces, and the maximum relative humidity gradient appears at the interface between track slab and sleeper. The maximum value rapidly decreases from $24.46 \times 100\%/m$

to $8.69 \times 100\%/m$ in the first week, and then the descending rate tends to be slow over time.

- (4) Due to the drying shrinkage property of concrete materials, the stresses that occur at the interface between sleeper and track slab are greater than those at other areas. When the maximum principal stress exceeds the ultimate tensile strength of the track slab, the splayed crack with an initial angle of about 45° will be generated at the sleeper corner.
- (5) Under the action of drying shrinkage deformation of early-age concrete, the initial splayed crack belongs to a mixed-mode crack, and the direction of crack tip turns an angle of 30.06° . Then, the final propagation path tends to be along the transverse direction of track slab due to the continuous turning of crack propagation path, and the corresponding failure mode gradually transforms from mixed-model into pure opening-mode. When there are initial cracks at the corner of adjacent sleepers, the cracks would be coalesced and further form the transverse through-wall crack of track slab. The transverse through-wall crack not only significantly affects the comfortableness and safety of rapid transit railway, but also reduces the service life of ballastless track.

Data Availability

All data used to support this study are available from the corresponding author upon reasonable request.

Conflicts of Interest

The authors declare that there are no conflicts of interest regarding the publication of this paper.

Acknowledgments

This project was supported by the National Natural Science Foundation of China (Grant nos. 51908197, 12072107, and 41907249), the Tackle Key Problems in Science and Technology Project of Henan Province, China (Grant no. 202102310262), the Key Research Project of Higher Education Institutions of Henan Province, China (Grant no. 20B580001), and Cultivation Programme for Young Backbone Teachers in Henan University of Technology (21420100).




References

- [1] W. Zhai, K. Wang, Z. Chen, S. Zhu, C. Cai, and G. Liu, "Full-scale multi-functional test platform for investigating mechanical performance of track-subgrade systems of high-speed railways," *Railway Engineering Science*, vol. 28, no. 3, pp. 213–231, 2020.
- [2] Q. Luo, M. Wei, Q. Lu, and W. Tengfei, "Simplified analytical solution for stress concentration ratio of piled embankments incorporating pile-soil interaction," *Railway Engineering Science*, vol. 29, no. 2, pp. 1–12, 2021.
- [3] J. Zhu, H. Hu, Z. He, X. Guo, and W. Pan, "A power-quality monitoring and assessment system for high-speed railways based on train-network-data center integration," *Railway Engineering Science*, vol. 29, no. 1, pp. 30–41, 2021.
- [4] X. Li, J. Ren, J. Wang, Y. Rongshan, S. Luhui, and L. Xueyi, "Drying shrinkage of early-age concrete for twin-block slab track," *Construction and Building Materials*, vol. 243, pp. 1–9, 2020.
- [5] S. Yan, L. Ding, and S. Wang, "Key construction technology for CRTS I double-block ballastless track in tunnel," *Journal of Railway Engineering Society*, vol. 12, no. 11, pp. 13–16, 2009.
- [6] R. Yang, J. Li, W. Kang, L. Xueyi, and C. Shihao, "Temperature characteristics analysis of the ballastless track under continuous hot weather," *Journal of Transportation Engineering, Part A: Systems*, vol. 143, no. 9, pp. 1–10, 2017.
- [7] Z. Chen, J.-L. Xiao, X.-K. Liu, X.-Y. Liu, R.-S. Yang, and J.-J. Ren, "Effects of initial up-warp deformation on the stability of the CRTS II slab track at high temperatures," *Journal of Zhejiang University-Science*, vol. 19, no. 12, pp. 939–950, 2018.
- [8] P. Zhao, C. Ding, L. Guo, Y. A. Zhang, and X. Liu, "A prototype fatigue test for slab track subjected to the coupling action of wheel load, temperature variation, and water erosion," *Proceedings of the Institution of Mechanical Engineers-Part F: Journal of Rail and Rapid Transit*, vol. 233, no. 5, pp. 566–579, 2019.
- [9] S. Wang, R. Yang, X. Liu, P. Wang, and Z. Qian, "Discussion on ballastless track about the bring cause of crack and renovation measure," *Railway Engineering*, vol. 47, no. 9, pp. 76–79, 2007.
- [10] Z. Zeng, Z. Huang, H. Yin, M. Xiaobai, W. Weidong, and W. Jundong, "Influence of track line environment on the temperature field of a double-block ballastless track slab," *Advances in Mechanical Engineering*, vol. 10, no. 12, pp. 1–16, 2018.
- [11] S. Zhu, J. Luo, M. Wang, and C. Cai, "Mechanical characteristic variation of ballastless track in high-speed railway: effect of train-track interaction and environment loads," *Railway Engineering Science*, vol. 28, no. 4, pp. 408–423, 2020.
- [12] D. Chen, "Multi-physical field coupling simulation of hygro-thermal deformation of concrete," *Journal of Southeast University (Natural Science Edition)*, vol. 43, no. 3, pp. 582–587, 2013.
- [13] Y. Han, J. Zhang, and Q. Yue, "Review on shrinkage of modern concrete," *Concrete*, vol. 29, no. 2, pp. 1–12, 2019.
- [14] C. He, G. Miao, and X. Li, "Control measures for crack on ballastless track bed slab of plateau railway," *Railway Engineering*, vol. 61, no. 4, pp. 129–132, 2021.
- [15] Y. Tan, Y. Zheng, and L. Kang, "Crack resistance performance of cast-in-situ concrete for double-block ballastless track," *Railway Engineering*, vol. 61, no. 2, pp. 91–94, 2021.
- [16] J. Li, F. Xie, G. Zhao, and L. Li, "Experimental and numerical investigation of cast-in-situ concrete under external sulfate attack and drying-wetting cycles," *Construction and Building Materials*, vol. 249, Article ID 118789, 2020.
- [17] P. Liu, W. Yu, W. Wang, and C. Ying, "Moisture transmission boundary condition between concrete and artificial simulation environment," *China Journal of Highway and Transport*, vol. 28, no. 5, pp. 108–116, 2015.
- [18] H. Akita, T. Fujiwara, and Y. Ozaka, "A practical procedure for the analysis of moisture transfer within concrete due to drying," *Magazine of Concrete Research*, vol. 49, no. 179, pp. 129–137, 1997.
- [19] L. J. Parrott, "Moisture profiles in drying concrete," *Advances in Cement Research*, vol. 1, no. 3, pp. 164–170, 1988.
- [20] Y. Gao, "Studies on shrinkage and shrinkage induced stresses of concrete under dry-wet cycles," Dissertation, Tsinghua University, Beijing, China, 2013.
- [21] J. Wang, H. Dai, and C. Gu, "Summary on numerical calculation of moisture transfer in concrete," *Journal of Hydroelectric Engineering*, vol. 24, no. 2, pp. 85–89, 2015.
- [22] X. Gao and Y. Wei, "Modeling and analysis of moisture gradients in concrete pavements," *Engineering Mechanics*, vol. 31, no. 8, pp. 183–188, 2014.
- [23] D. Shen, B. Zhou, M. Wang, Y. Chen, and G. Jiang, "Predicting relative humidity of early-age concrete under sealed and unsealed conditions," *Magazine of Concrete Research*, vol. 71, no. 22, pp. 1151–1166, 2019.
- [24] Y. Wang, Y. Jia, and R. Zhao, "Calculation of internal humidity field of concrete based on ANSYS," *Journal of Southwest Jiaotong University*, vol. 52, no. 1, pp. 54–60, 2017.
- [25] S. F. Wong, T. H. Wee, S. Swaddiwudhipong, and S. L. Lee, "Study of water movement in concrete," *Magazine of Concrete Research*, vol. 53, no. 3, pp. 205–220, 2001.
- [26] W. Kang, S. Chen, and C. Wei, "Temperatures of ballastless track and effect of continuous hot weather," *Journal of the China Railway Society*, vol. 41, no. 7, pp. 127–134, 2019.
- [27] Y. Wei, W. Hansen, J. J. Biernacki, and E. Schlangen, "Unified shrinkage model for concrete from autogenous shrinkage test on paste with and without ground-granulated blast-furnace slag," *ACI Materials Journal*, vol. 108, no. 1, pp. 13–20, 2011.
- [28] G. Liu, "The mechanical analysis of CRST I Bi-block Track's process," Dissertation, Southwest Jiaotong University, Chengdu, China, 2015.
- [29] J. H. Hattel and J. Thorborg, "A numerical model for predicting the thermomechanical conditions during hydration of early-age concrete," *Applied Mathematical Modelling*, vol. 27, no. 1, pp. 1–26, 2003.
- [30] Y. Gao, J. Zhang, and D. Hou, "Calculation of moisture induced stresses and evaluation of crack risk in early-age concrete," *Engineering Mechanics*, vol. 29, no. 2, pp. 121–128, 2012.

- [31] D. Xu and X. Fu, "Study on fracture criterion for I-II mixed mode crack by using four-point shearing specimen," *Journal of Hydraulic Engineering*, vol. 15, no. 9, pp. 63–69, 1984.
- [32] J. M. Alegre and I. I. Cuesta, "Some aspects about the crack growth FEM simulations under mixed-mode loading," *International Journal of Fatigue*, vol. 32, no. 7, pp. 1090–1095, 2010.
- [33] J. Li, "Experimental investigation on initial cracking criterion for I-II Mixed in concrete," Dissertation, Dalian University of Technology, Dalian, China, 2009.

Research Article

Optimization of VEDs for Vibration Control of Transmission Line Tower

Guoping Huang ^{1,2}, Jianhua Hu ³, Yuzhu He,² Haibo Liu ³ and Xiugui Sun⁴

¹College of Civil Engineering, Hunan City University, Yiyang 413000, China

²College of Civil Engineering, Hunan University, Changsha 410082, China

³Hunan Communication & Water Conservancy Group Ltd., Changsha 410008, China

⁴Hunan Provincial Communications Planning Survey & Design Institute Co, Ltd., Changsha 410200, China

Correspondence should be addressed to Jianhua Hu; master_hjh@163.com and Haibo Liu; 17120365@qq.com

Received 30 August 2021; Accepted 7 October 2021; Published 19 October 2021

Academic Editor: Nan Zhang

Copyright © 2021 Guoping Huang et al. This is an open access article distributed under the Creative Commons Attribution License, which permits unrestricted use, distribution, and reproduction in any medium, provided the original work is properly cited.

This paper investigates the optimization of viscoelastic dampers (VEDs) for vibration control of a transmission line tower. Considering the stiffness of the steel brace connected to a VED, the mechanical model of the VED-brace system was established. Subsequently, the additional modal damping ratio of the transmission line tower attached with VEDs was obtained analytically. Furthermore, the finite element model of a two-circuit transmission line tower with VEDs was built in ANSYS software, and the influences of installation positions and parameters of VEDs on the additional modal damping ratio were clarified. In addition, the control performance of VEDs on the transmission line tower subjected to wind excitations was emphatically illustrated. The results show that the stiffness of the steel brace connected to a VED has a significant effect on the maximum additional modal damping ratio of the VED-brace system provided for the transmission line tower and the optimal parameters of the VED. Meanwhile, the installation positions of VEDs dramatically influence the additional modal damping ratio. Moreover, the increase of the brace stiffness and the loss factor is beneficial to improve the control performance of VEDs. Besides that, the VEDs present superior control performance on the top displacement of the transmission line tower as well as the transverse bending vibration energy.

1. Introduction

Transmission line tower is one of the typical high-rise structures, which is widely used throughout the world for energy supplying [1, 2]. The transmission line tower is vulnerable to suffering from wind-induced vibrations owing to its high flexibility and low inherent damping characteristics [3–5]. Frequent and excessive vibration could potentially induce damage and even collapse of the transmission line tower and have adverse effects on the serviceability of the whole transmission tower-line system [6–8]. Considerable investigations focused on theoretical [9–11], experimental [12–14], and field measurement [15] have been carried out in recent decades, which is devoted to mitigating the dynamic responses of the line transmission

tower. To guarantee the normal operation of the transmission line tower, several measures have been proposed for the vibration control of the transmission line tower, which mainly include increasing the stiffness of the transmission line tower [16, 17] and attaching energy dissipation devices on the transmission line tower.

Attaching energy dissipation devices is a commonly used method for mitigating vibrations of the transmission line tower [18–20]. The tuned mass damper (TMD) is a typical energy dissipation device, which has been commonly utilized for mitigating vibrations of high-rise structures [21, 22]. It has been found that the application of TMDs helps reduce the dynamic responses of the transmission line tower [23–25]. However, the disadvantage is that several additional masses should be installed on top of a

transmission tower, which requires the occupancy of the structural space. To overcome the shortcomings of the TMD, several energy-dissipating dampers were further proposed to enhance the vibration control performance of the transmission line tower. The magnetorheological (MR) damper has been successfully used on suppressing the wind-induced response of a real transmission line tower [26]. It has shown that the MR damper with optimally designed parameters has some advantages in controlling the wind-induced response of the transmission line tower. Nevertheless, the MR damper is quite complicated, and the requirement in the additional energy supply during the vibration control process is unrealistic while accepting strong excitations. Besides that, the passive friction dampers have been used in a finite element tower model with lumped mass, which is further applied in a real transmission line tower for verifying its superior control performance [27]. In addition, the use of viscoelastic dampers (VEDs) for the wind-resistant design of the transmission line tower has also been proposed [28]. Note that the optimal design of VEDs for vibration control of the transmission line tower has not been investigated.

This paper investigates the optimal design of VEDs for vibration control of a transmission line tower subjected to wind excitations. The paper is organized as follows. Firstly, the mechanical model of the VED-brace system was established. Subsequently, the maximum additional modal damping ratio of the transmission line tower attached with VEDs was calculated. Next, based on the finite element model of a two-circuit transmission line tower with VEDs, the influences of installation positions and parameters of VEDs on the additional modal damping ratio were clarified. Finally, the control performance of VEDs on the transmission line tower subjected to wind excitations was numerically demonstrated.

2. Model of VED-Brace System and Optimal Design of VED

2.1. Mechanical Model of the VED-Brace System. A coupled system combined with a viscoelastic damper and a supported steel brace, also denoted as VED-brace system, is shown in Figure 1. The VED is represented by a parallel spring (with stiffness K_d) and damper (with damping coefficient C_d), while the supported steel brace, connected to the VED and primary structure, is modeled by a spring with stiffness K_b and in series with the VED. Assuming that a sinusoidal displacement $u(t) = u_0 \sin \omega t$ with amplitude u_0 and natural frequency ω is applied on the VED, its output force is given as

$$F_d(t) = K_d u(t) + C_d \dot{u}(t), \quad (1)$$

where $\dot{u}(t)$ denotes the first-order derivative of $u(t)$ with time t .

Introducing the energy dissipation stiffness of VED as $K'_d = C_d \omega$, the output force of the VED can be rewritten as

$$F_d(t) = K_d u_0 \sin(\omega t) + K'_d u_0 \cos(\omega t). \quad (2)$$

Supposing that the displacement of the VED-brace system is represented by $u_A = u_a \sin \omega t$, the displacement of the VED and the brace can be expressed as

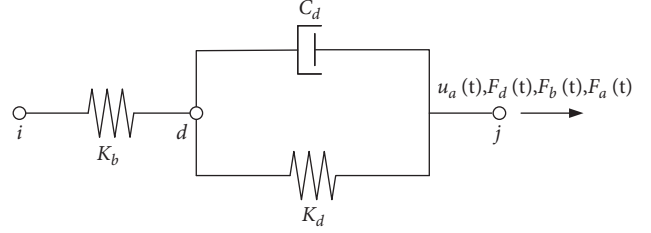


FIGURE 1: Mechanical Model of the VED-brace system.

$$\begin{aligned} u_D &= u_d \sin(\omega t - \varphi), \\ u_B &= u_A - u_D, \end{aligned} \quad (3)$$

where φ is the displacement phase difference between the VED and the brace.

Based on the equality of internal force for the series system, we obtain

$$\begin{aligned} F_b(t) &= F_d(t) \\ &= F_a(t) \\ &= K_a u_a \sin \omega t + K'_a u_a \cos \omega t, \end{aligned} \quad (4)$$

where

$$K_a = \frac{(K_b + K_d)K_b K_d + K_b (K'_d)^2}{(K_b + K_d)^2 + (K'_d)^2}, \quad (5)$$

$$K'_a = \frac{K_b^2 K'_d}{(K_b + K_d)^2 + (K'_d)^2}. \quad (6)$$

The ratio of the relative displacement amplitude at both ends of the VED to the relative displacement amplitude at both ends of the VED-brace system is expressed as

$$\begin{aligned} \beta &= \frac{u_d}{u_a} \\ &= \frac{K_b}{\sqrt{(K_b + K_d)^2 + (K'_d)^2}}. \end{aligned} \quad (7)$$

According to equation (7), it is straightforward to see that the ratio β approaches 1 if the brace stiffness K_b is sufficiently large. Otherwise, the effect of the limited stiffness of the steel brace must be included during vibration control analysis. For the convenience of analysis, the nondimensional parameters are introduced here:

$$\begin{aligned} \eta &= \frac{K'_d}{K_d}, \\ \alpha &= \frac{K_b}{K_d}, \\ \alpha_1 &= \frac{K_a}{K_d}, \\ \alpha_2 &= \frac{K'_a}{K_d}, \end{aligned} \quad (8)$$

where α denotes the ratio of the brace stiffness to the damper stiffness; α_1 is the ratio of the energy storage stiffness of the VED-brace system to the energy storage stiffness of the VED; α_2 denotes the ratio of the energy dissipation stiffness of the VED-brace system to the energy storage stiffness of the VED; η denotes the loss factor of the VED, and its typical value ranges from 0.2 to 5.0.

Figure 2 shows the variations of β , α_1 , and α_2 with respect to the stiffness ratio α . It can be seen from Figure 2(a) that β increases with α and will eventually converge to 1, which means that increasing the brace stiffness is beneficial to improve the energy dissipation efficiency of the VED. As shown in Figure 2(b), when α is greater than 2, α_1 will be greater than 1, and K_a finally converges to K_d as K_b continues to increase. In this case, the brace can be regarded as a rigid rod, indicating that the energy storage stiffness of the VED-brace system is equal to the energy dissipation stiffness of the VED. It can be found in Figure 2(c) that α_2 increases with α . Moreover, K'_a finally converges to K_d as α grows, which can be considered that the energy dissipation stiffness of the VED-brace system is also equal to that of the VED.

2.2. Optimal Design of VED. The simplified model of the tower segment with the VED-brace system is depicted in Figure 3. Note that the VED-brace system is connected in parallel to the main member of the transmission line tower.

Assume the relative displacement of both the i end and j end of the tower segment as

$$u(t) = u_{\max} \sin \omega t. \quad (9)$$

For the tower segment coupled with the VED-brace system, the output force becomes

$$\begin{aligned} F(t) &= F_f(t) + F_a(t) \\ &= (K_f + K_a)u_{\max} \sin \omega t + K'_a u_{\max} \cos \omega t. \end{aligned} \quad (10)$$

The equivalent damping ratio for the tower segment may be obtained as

$$\begin{aligned} \xi_a &= \frac{E_d}{4\pi E_s} \\ &= \frac{K'_a}{2(K_f + K_a)}. \end{aligned} \quad (11)$$

By defining the additional stiffness ratio $\alpha_a = K_a/K_f$, equation (10) can be rewritten as

$$F(t) = u_{\max} K_f (1 + \alpha_a) \sin(\sin \omega t + 2\xi_a \cos \omega t), \quad (12a)$$

where

$$\alpha_a = \alpha_b \alpha_d \frac{\alpha_b \eta + (1 + \eta^2) \alpha_d}{(\alpha_b \eta + \alpha_d)^2 + \eta^2 \alpha_d^2}, \quad (12b)$$

$$\xi_a = \frac{1}{2} \frac{\alpha_b^2 \eta^2 \alpha_d}{(\alpha_b \eta + \alpha_d)(\alpha_b \eta + \alpha_b \alpha_d + \alpha_d) + (1 + \alpha_b) \alpha_d^2 \eta^2}, \quad (12c)$$

where $\alpha_b = K_b/K_f$ represents the ratio of the brace stiffness to the tower segment stiffness; $\alpha_d = K'_d/K_f$ represents the energy dissipation stiffness ratio of the VED.

From equations (12a) to (12c), it is shown that α_a and ξ_a are dependent on α_b , α_d , and η . Again, η is taken as 1.4. Figure 4 shows the variations of the stiffness ratio α_a with respect to α_d under various α_b . It is apparent that the stiffness ratio α_a increases with the increase of α_d and approaches α_b for a large α_d . This is because extremely large damper stiffness will lock the damper, which causes the damper to fail to dissipate the vibration energy. The variations of the equivalent damping ratio ξ_a with respect to α_d under various α_b are further illustrated in Figure 5. Note that the equivalent damping ratio ξ_a firstly increases with the increase with α_d , reaching the maximum value when the α_d reaches a certain value, and then decreases with the increase of α_d .

By taking the derivatives of the damping ratio ξ_a with respect to α_d , there is

$$\xi_a = \frac{1}{2} \frac{\alpha_b^2 \eta^2}{(1 + \eta^2)(1 + \alpha_b) \alpha_d + \alpha_b^2 \eta^2 / \alpha_d + \alpha_b^2 \eta + 2\alpha_b \eta}. \quad (13)$$

By defining $f(\alpha_d) = (1 + \eta^2)(1 + \alpha_b) \alpha_d + \alpha_b^2 \eta^2 / \alpha_d$ and letting $\partial f(\alpha_d) / \alpha_d = 0$, we obtain

$$\alpha_d = \frac{\alpha_b \eta}{\sqrt{(1 + \eta^2)(1 + \alpha_b)}}. \quad (14)$$

Substituting equations (14) into equation (12c), the peak damping ratio is derived as

$$\xi_{a,\text{peak}} = \frac{1}{4} \frac{\alpha_b \eta}{\sqrt{(1 + \alpha_b)(1 + \eta^2)} + 1 + \alpha_b / 2}. \quad (15)$$

The variations of the peak damping ratio $\xi_{a,\text{peak}}$ with respect to the stiffness ratio α_b for $\eta = 1.4$ and loss factor η for $\alpha_b = 0.2$ are illustrated in Figure 6. As shown in Figure 6, the peak damping ratio $\xi_{a,\text{peak}}$ increases with the increase of stiffness ratio α_b and loss factor η . In summary, equation (15) describes peak damping ratio for the tower segment when equation (14) is fulfilled. These two equations constitute the optimal parameter design for VEDs in the transmission line tower.

After the brace stiffness K_b and the loss factor η of the VED are determined, the damping ratio of the energy dissipation system reaches the maximum value. The ratio of the equivalent

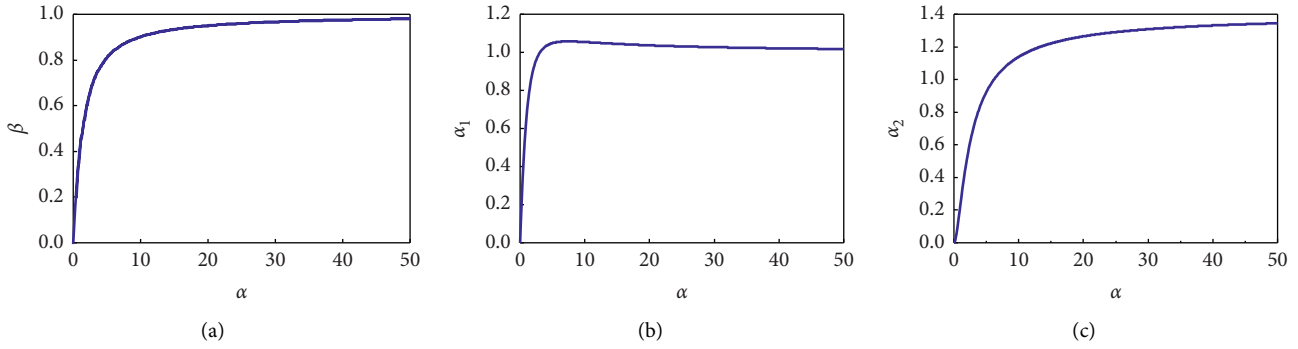


FIGURE 2: Variations of β , α_1 , α_2 with the stiffness ratio α for $\eta = 1.4$.

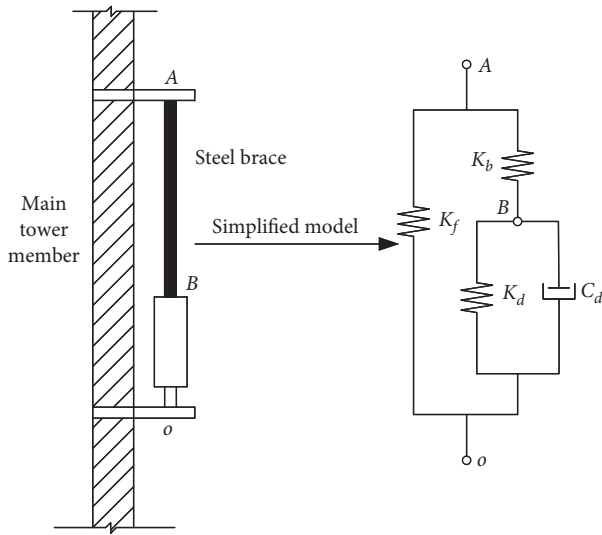


FIGURE 3: Simplified model of the tower segment with the VED-brace system.

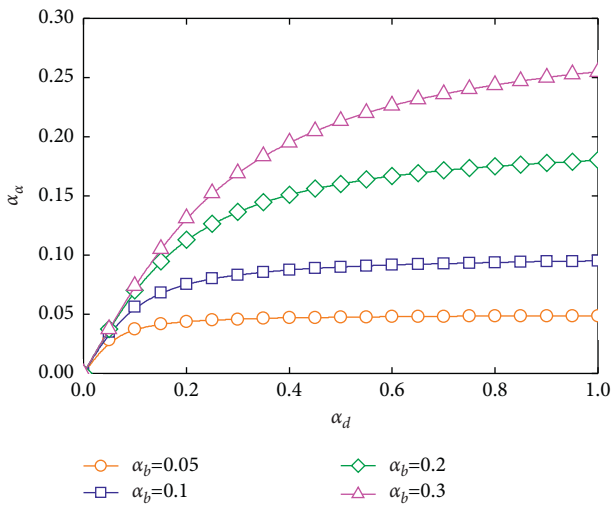


FIGURE 4: Variations of the stiffness ratio α_a with respect to α_d under various α_b .

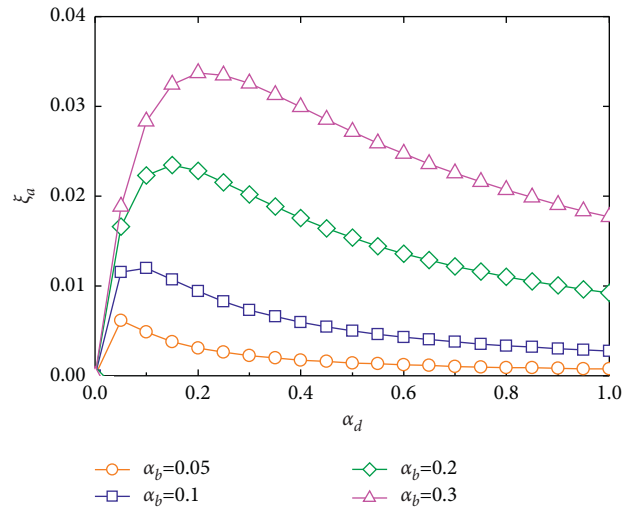


FIGURE 5: Variations of the equivalent damping ratio ξ_a with respect to α_d under various α_b .

energy storage stiffness K_d of the VED to the brace stiffness K_b can be calculated by the following formula as

$$\lambda = \sqrt{\frac{1}{(1 + \eta^2)(1 + \alpha_b)}} \tag{16}$$

It should be noted that when the additional modal damping ratio of the VED-brace system reteaches maximum, its energy dissipation efficiency is also the largest. Thus, the optimal parameters of the VED-brace system can be determined by equations (14) and (16), and the maximum additional modal damping ratio of the tower section can be calculated by equation (15).

3. Numerical Simulation of a Transmission Line Tower with VEDs

3.1. Finite Element Model of Transmission Line Tower. To investigate the vibration control performance of VEDs for a transmission line tower, a three-dimensional finite element

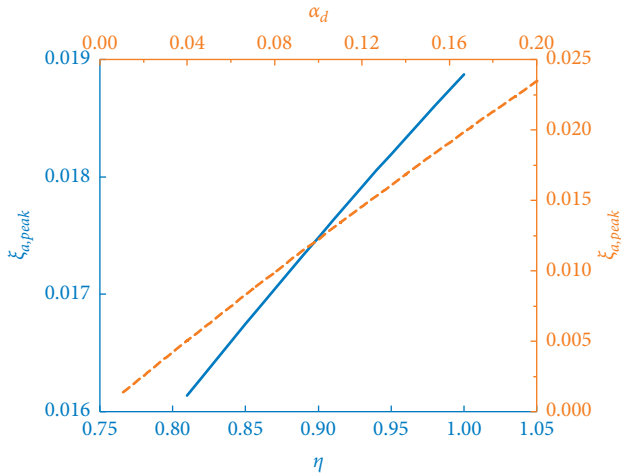


FIGURE 6: Variations of the peak damping ratio $\xi_{a,peak}$ with respect to α_b and η .

model of a two-circuit transmission line tower shown in Figure 7 is built in ANSYS software. The transmission line tower height is 103.6 m, and two cross arms are symmetrically arranged at the heights of 57 m, 78.2 m, and 99.6 m above the ground. The end of the cross arm is 16.6 m, 17.6 m, and 20.22 m away from the center of the transmission tower, respectively. The main structure of the transmission line tower is composed of steel pipes and connected with high-strength bolts. The cross section of the steel pipe is varied with height of the transmission line tower. The most important stressed components are the four tower columns, and their cross-sectional area decreases from bottom to top. The main material parameters of members are as follows: elastic modulus 206 GPa, density 7850 kg/m³, and Poisson's ratio 0.3.

The spatial beam element BEAM188 is used for each member, without considering the coupling vibration of the conductor, ground wire, and transmission tower. The transmission line tower without control consists of 527 nodes and 1406 elements in total. The overall coordinate system is divided into the horizontal X axis, the forward Y axis, and the Z axis along with the tower height. The origin of coordinates is at the midpoint of the bottom of the tower. The first three mode shapes of the transmission tower are obtained by modal analysis, as illustrated in Figure 8. The first mode shape is the bending vibration mode perpendicular to the conductor direction, the second mode shape is the bending vibration mode along the conductor direction, and the third mode shape is the torsional vibration mode rotating around the centerline of the tower. Based on the finite element model of the transmission tower, the modal analysis of the transmission tower is carried out, and the properties of the transmission line tower shown in Table 1 are further obtained.

3.2. The Installation Position of VED. Figure 9 presents the strain energy distribution in the transmission tower for the first second mode. It can be seen from Figure 9(a) that the first modal strain energy of the primary members is much

greater than that of the inclined bars and the cross arms, and the first modal strain energy of the lower part of the tower legs is also greater than that of the upper parts. As shown in Figure 9(b), the distribution law of the second modal strain energy in the transmission tower is consistent with that of the first modal strain energy. Thus, the VEDs should be installed on the lower primary members with the largest possible modal strain energy, which helps to efficiently control the vibration of the transmission line tower for the first two modes.

The main tower columns with the same function are recorded as a unit, and there are 72 main tower column units numbered from bottom to top of the transmission line tower. The axial deformation of each main tower column for the first mode is shown in Table 2. The variations of the axial deformation with the unit number are further illustrated in Figure 10. Note that the large deformation occurs at the 1, 2, 3, 4, 21, 22, 23, 25, and 49 units of the transmission line tower. To effectively control the bending and the axial deformation of the transmission line tower, the installation positions of VEDs need to be taken into account in combination with the data in Table 2 and Figure 10. There are mainly two installation schemes: scheme 1 is to install VEDs on the tower column unit with large axial deformation, and scheme 2 is to install the same number VEDs with the same parameters as scheme 1 on the tower column unit from the bottom to top of the transmission line tower. 44 VEDs used in installation scheme 1 are installed in parallel on the four main tower columns of the transmission tower, and 44 VEDs used in installation scheme 2 are installed on the tower column unit from bottom to top of the transmission line tower. Note that the unit numbers of VEDs corresponding to installation scheme 1 and installation scheme 2 are shown in Table 3.

3.3. The Optimal Parameters of VED. The outer diameters of the circular steel pipes of the main tower columns of the transmission tower vary from 109.5 mm to 213 mm, and the wall thickness of the steel pipes varies from 6 mm to 10 mm. $K = EA/L$ is the axial stiffness of the tower column unit, A is the area of steel pipe, and L is the unit length. The stiffness of the tower column unit installed with VEDs is shown in Table 4.

For the convenience of calculation and analysis, the ratio of the stiffness between each brace and each tower column is taken as 0.2, and the loss factor of the VED is taken as 1.4. Then, the ratio of the equivalent energy storage stiffness of the VED to brace stiffness λ can be calculated by equation (16), and the additional modal damping ratio ξ_a of the transmission line tower installed with VEDs can be further gained. The stiffness of the i th tower segment, the energy storage stiffness of the i VED, and the energy dissipation stiffness of the i VED are defined as

$$K_{bi} = \alpha_{bi} K_{fi}, \quad (17)$$

$$K_{di} = \lambda_i K_{bi}, \quad (18)$$

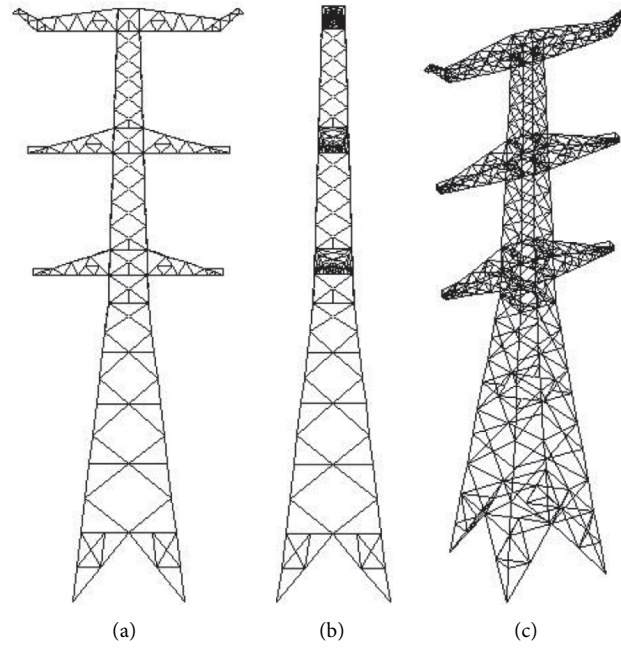


FIGURE 7: Finite element model of the transmission line tower: (a) X-Z plane; (b) Y-Z plane; (c) X-Y-Z space.

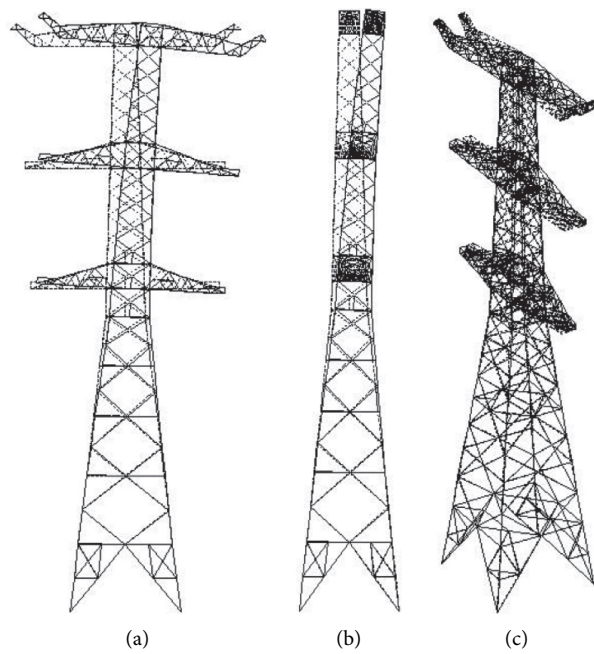


FIGURE 8: The first three mode shapes of the transmission line tower: (a) the first mode; (b) the second mode; (c) the third mode.

TABLE 1: Properties of the transmission line tower.

Modal order	Frequency f (Hz)	Modal strain energy W_s (N·m)	Generalized mass m (ton)	Characteristics of vibration mode
1	0.832	341896	25.00	Transverse bending
2	0.849	337865	23.74	Vertical bending
3	1.411	193149	4.91	Torsion

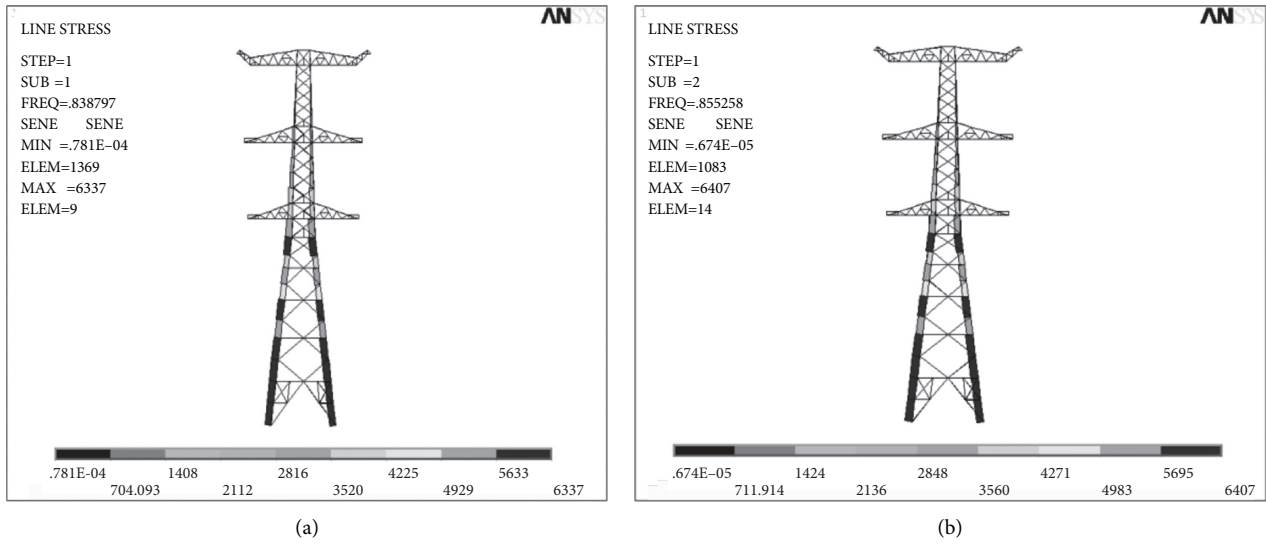


FIGURE 9: Strain energy distribution: (a) the first mode; (b) the second mode.

TABLE 2: Axial deformation of each main tower column for the first mode.

Unit number	Unit length (m)	Axial strain	Axial deformation (mm)
1	6.08	0.000616955	3.75
2	6.08	0.000619991	3.77
3	6.08	0.000636258	3.87
4	6.11	0.000646764	3.95
5	5.04	0.000648939	3.27
21	5.61	0.000667406	3.75
22	4.53	0.000670219	3.04
23	4.48	0.000685088	3.07
24	3.63	0.000688744	2.50
25	5.07	0.000693175	3.52
41	5.00	0.000678386	3.40
42	4.40	0.000627275	2.76
49	4.20	0.000754969	3.17
50	4.20	0.000667704	2.81
57	4.20	0.000623425	2.62
58	4.20	0.000503736	2.12
65	4.40	0.000589224	2.60
66	3.40	0.000540314	1.84
73	3.40	0.000544409	1.85
74	3.40	0.000397533	1.35
75	3.40	0.000261701	0.89
76	3.40	0.000105639	0.36
77	4.00	5.09371E - 06	0.02

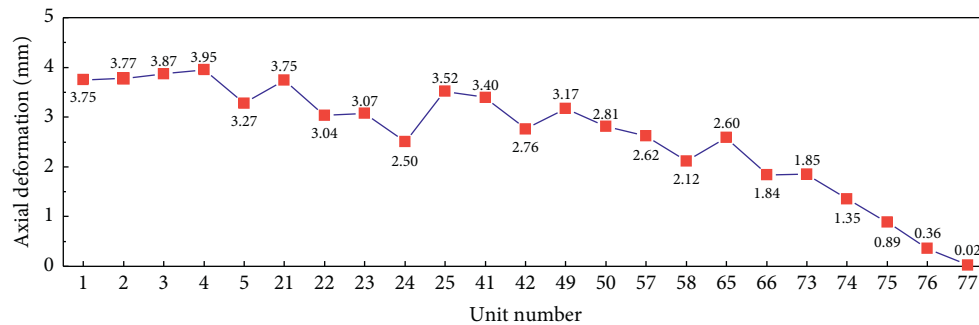


FIGURE 10: Variations of the axial deformation with the unit number for the first mode.

TABLE 3: Installation scheme of VEDs.

1# tower column	Unit number of the main tower column				Axial deformation of the tower column (mm)	Installation scheme 1	Installation scheme 2
	2# tower column	3# tower column	4# tower column				
1	6	11	16	3.75	w/installed	w/installed	
2	7	12	17	3.77	w/installed	w/installed	
3	8	13	18	3.87	w/installed	w/installed	
4	9	14	19	3.95	w/installed	w/installed	
5	10	15	20	3.27	w/installed	w/installed	
21	26	31	36	3.75	w/installed	w/installed	
22	27	32	37	3.04	w/installed	w/installed	
23	28	33	38	3.07	w/installed	w/installed	
24	29	34	39	2.50	w/o installed	w/installed	
25	30	35	40	3.51	w/installed	w/installed	
41	43	45	47	3.40	w/installed	w/installed	
42	44	46	48	2.76	w/o installed	w/o installed	
49	51	53	55	3.18	w/installed	w/o installed	
50	52	54	56	2.81	w/o installed	w/o installed	
57	59	61	63	2.62	w/o installed	w/o installed	
58	60	62	64	2.12	w/o installed	w/o installed	
65	67	69	71	2.60	w/o installed	w/o installed	
66	68	70	72	1.84	w/o installed	w/o installed	
73	78	83	88	1.85	w/o installed	w/o installed	
74	79	84	89	1.36	w/o installed	w/o installed	
75	80	85	90	0.90	w/o installed	w/o installed	
76	81	86	91	0.40	w/o installed	w/o installed	
77	82	87	92	0.02	w/o installed	w/o installed	

TABLE 4: Stiffness of the main tower column unit installed with VEDs.

1# tower column	Unit number of the main tower column				Unit stiffness (N/m)
	2# tower column	3# tower column	4# tower column		
1	6	11	16	442038825	
2	7	12	17	442038825	
3	8	13	18	442038825	
4	9	14	19	440236029	
5	10	15	20	533066110	
21	26	31	36	456295733	
22	27	32	37	565187787	
23	28	33	38	571298462	
24	29	34	39	705064904	
25	30	35	40	504937712	
41	43	45	47	474209703	
42	44	46	48	538877694	
49	51	53	55	428210759	

$$K'_{di} = \eta \lambda_i K_{bi}, \quad (19)$$

$$C_a = \frac{K'}{\omega}. \quad (20)$$

where a_{bi} denotes the ratio of the brace stiffness to the tower column unit stiffness; K_{fi} denotes the axial stiffness of the tower column; λ_i denotes the ratio of the energy storage stiffness of the VED to the corresponding brace stiffness.

Equations (17)–(19) require that the parameters of VEDs in each tower section be different, which increases the difficulty of manufacturing dampers. Thus, the VEDs with the same parameters are used in this paper. Furthermore, the equivalent damping coefficient of the VED-brace system can be defined as

3.4. Calculation Method of Supplemental Modal Damping Ratio. There are mainly two methods used in calculating the additional modal damping ratio of the transmission line tower installed with VEDs: the modal strain energy method and the complex mode calculation method. The modal strain energy method is regarded as a simple method, which assumes that the tower frequency and vibration mode show less variation before and after installing VEDs. When the modal strain energy method is adopted, the additional

modal damping ratio of the transmission line tower provided by VEDs can be expressed as

$$\begin{aligned}\xi_a &= \frac{E_d}{4\pi E_s} \\ &= \frac{\pi\omega \sum_{i=1}^{n_d} C_{di}u_i}{4\pi E_s},\end{aligned}\quad (21)$$

where E_d denotes the consumed energy by all VEDs in one cycle; n_d is the number of VEDs; u_i is the elongation at both ends of the VED; E_s is the modal strain energy of the tower in one vibration cycle. It can be seen from equation (21) that the modal damping ratio can be calculated by the parameters of the VED and modal parameters such as the vibration mode and frequency of the transmission line tower.

When using the complex modal analysis method, it is necessary to establish the finite element model of the tower-VED-brace system. The VED-brace system is regarded as a mechanical model with equivalent stiffness and equivalent damping, which is simulated with COMBIN14 element in ANSYS software. A total of 44 COMBIN14 elements are attached to both ends of the main tower column units of the transmission line tower. In the establishment of the COMBIN14 element, only one COMBIN14 element is needed to be added to the transmission tower node with VEDs, and the program automatically defaults that the two elements are in parallel mode. Accordingly, it is very convenient for establishing the finite element model of the tower-VED-brace system. In addition, the modal damping ratio can be further obtained by the complex modal analysis method. And the r th vibration circular frequency and modal damping ratio of the transmission tower are computed as

$$\begin{aligned}\omega_r &= \text{Im}(\lambda_r), \\ \xi_r &= \frac{-\text{Re}(\lambda_r)}{\text{Im}(\lambda_r)}.\end{aligned}\quad (22)$$

3.5. Influence of Installation Position and Parameters of VEDs on the Additional Modal Damping Ratio. The brace stiffness is taken as 0.1 to 0.2 times the tower column unit stiffness, and the loss factor η of the VED is taken as 1.4. The ratio of the equivalent energy storage stiffness of the VED to brace stiffness λ is calculated as 0.531 by equation (16). Based on the modal strain energy method and the complex modal analysis method, the variations of the first additional modal damping ratio ξ_1 with α_b provided by VEDs under two installation schemes are presented in Figure 11. It can be seen from Figure 11 that the first additional modal damping ratio ξ_1 of provided by VEDs installed in accordance with installation scheme 1 is greater than that provided by VEDs installed in accordance with installation scheme 2. Hence, since installation scheme 1 is superior to installation scheme 2, installation scheme 1 will be used in the following research.

The brace stiffness K_b is taken as 0.2 times of the axial stiffness of the tower column unit, and the loss factor η of the

VED is taken as 1.4. The ratio of the equivalent energy storage stiffness of the VED to brace stiffness λ is calculated as 0.531 by equation (16), and the value of λ is further varied from 0.491 to 0.631. Based on the modal strain energy method and the complex modal analysis method, the variations of the first additional modal damping ratio ξ_1 with λ are illustrated in Figure 12. It can be found in Figure 12 that when the brace stiffness K_b is a setting value, and the ratio of the equivalent storage of the VED to the brace stiffness is taken as the calculated value of equation (16), the first additional modal damping ratio ξ_1 of the transmission line tower obtained by the complex modal analysis method reaches the maximum value. Note that the first additional modal damping ratio ξ_1 predicted by the complex modal analysis method is greater than that of the modal strain energy method, and the value of the λ corresponding to the first maximum additional modal damping ratio ξ_1 calculated by the complex modal analysis method is less than that of the first maximum additional modal damping ratio ξ_1 calculated by the modal strain energy method. In addition, the first additional modal damping ratio of the transmission line tower can be improved by increasing the bracing stiffness K_b .

The variations of the second additional modal damping ratio ξ_2 with λ are further depicted in Figure 13. It is noteworthy that the variation of the second additional modal damping ratio ξ_2 with λ is consistent with that of the first additional modal damping ratio ξ_1 with λ . It means that lower-order vibration control of the transmission line tower can be realized by controlling the first-order modal vibration of the transmission tower. Hence, the influences of the ratio of brace stiffness to tower column unit stiffness α_b and the loss factor η on the first additional modal damping ratio ξ_2 of the transmission line tower are emphatically investigated in the following research.

The loss factor η of the VED is taken as 1.4, and the ratio of the equivalent energy storage stiffness of the VED to brace stiffness λ is calculated by equation (16). Based on the modal strain energy method and the complex modal analysis method, the variations of the first additional modal damping ratio ξ_1 with the ratio of brace stiffness to tower column unit stiffness α_b are shown in Figure 14. As shown in Figure 14, the first additional modal damping ratio ξ_1 increases linearly with the increase of the α_b . In addition, the first additional modal damping ratio ξ_1 predicted by the complex modal analysis method is also greater than that of the modal strain energy method.

The ratio of brace stiffness to tower column unit stiffness α_b is taken as 0.2, and the ratio of the equivalent energy storage stiffness of the VED to brace stiffness λ is calculated by equation (16). Based on the modal strain energy method and the complex modal analysis method, the variations of the first additional modal damping ratio ξ_1 with the loss factor η of the VED are shown in Figure 15. Note that the first additional modal damping ratio ξ_1 increases linearly with the increase of the η . Consistent with the result of Figure 14, the first additional modal damping ratio ξ_1 predicted by the complex modal

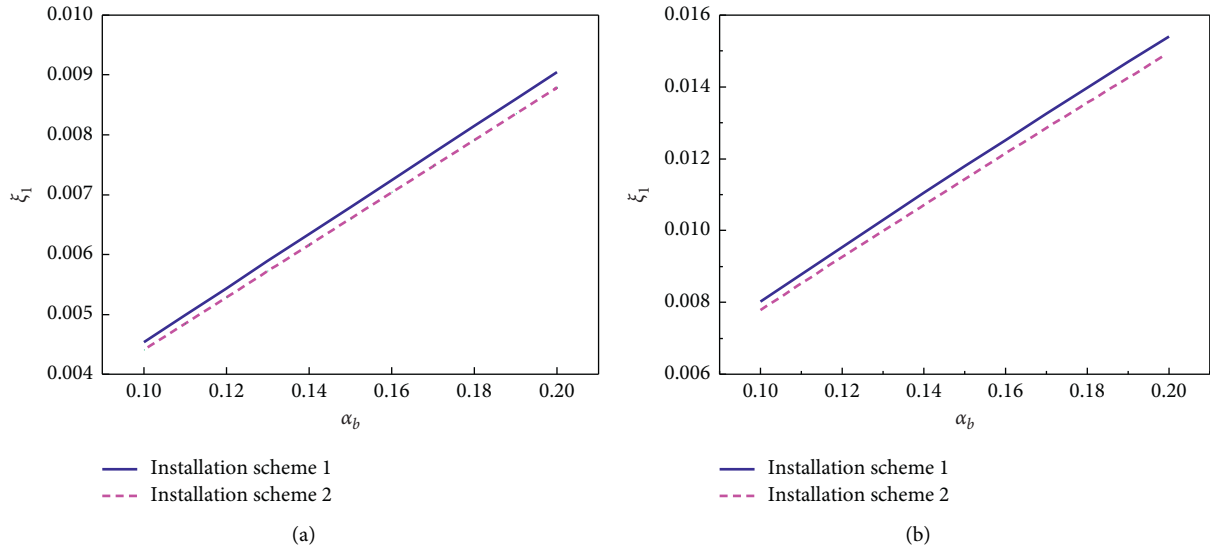


FIGURE 11: Variations of the first additional modal damping ratio ξ_1 with α_b under two installation schemes: (a) the modal strain energy method; (b) the complex modal analysis method.

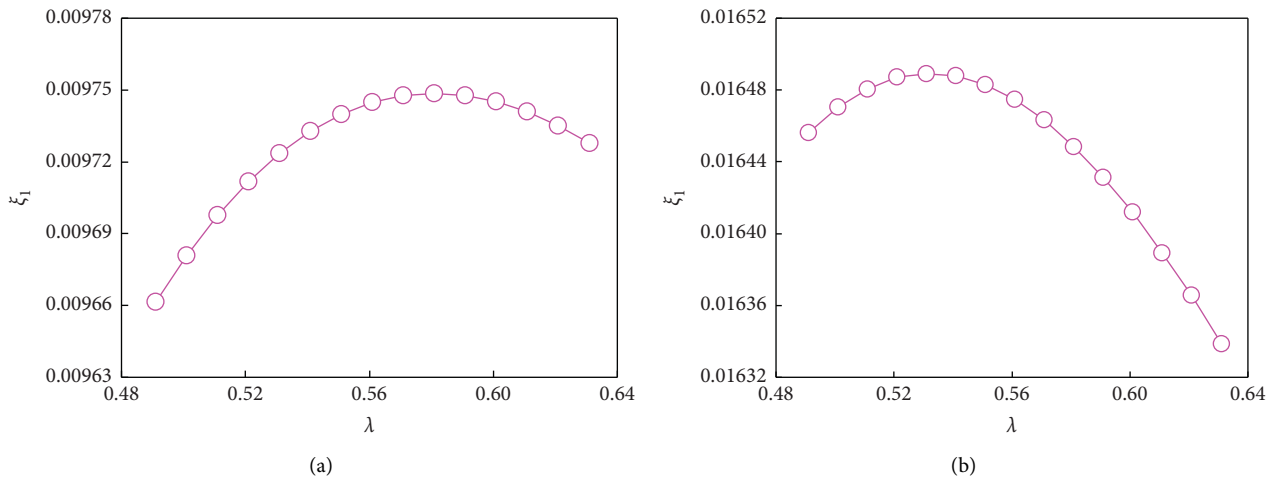


FIGURE 12: Variations of the first additional modal damping ratio ξ_1 with λ : (a) the modal strain energy method; (b) the complex modal analysis method.

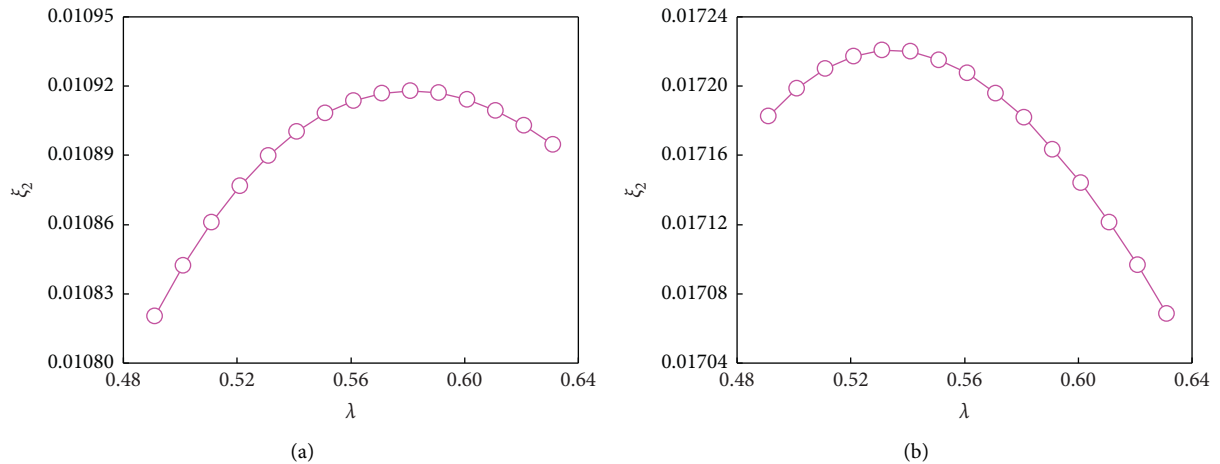


FIGURE 13: Variations of the second additional modal damping ratio ξ_2 with λ : (a) the modal strain energy method; (b) the complex modal analysis method.

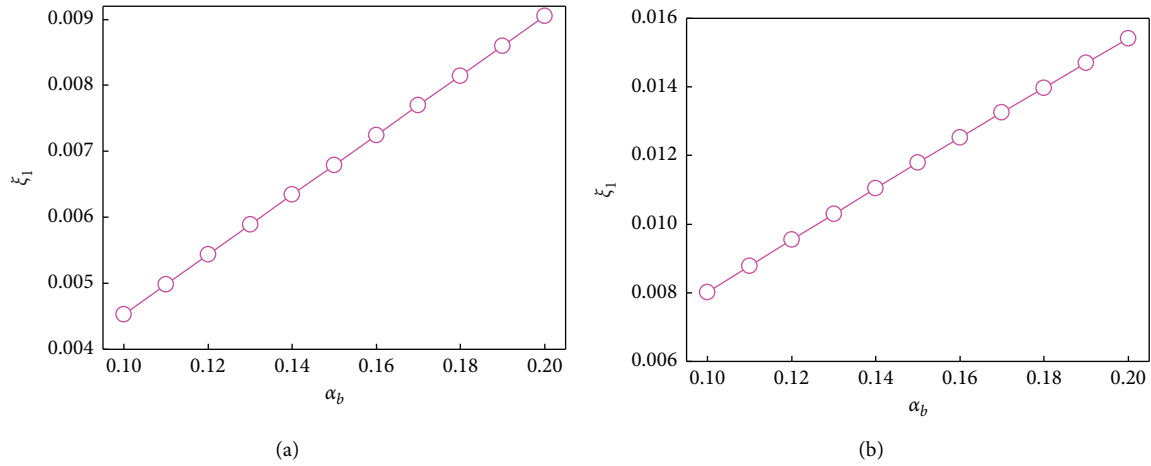


FIGURE 14: Variations of the first additional modal damping ratio ξ_1 with α_b : (a) the modal strain energy method; (b) the complex modal analysis method.

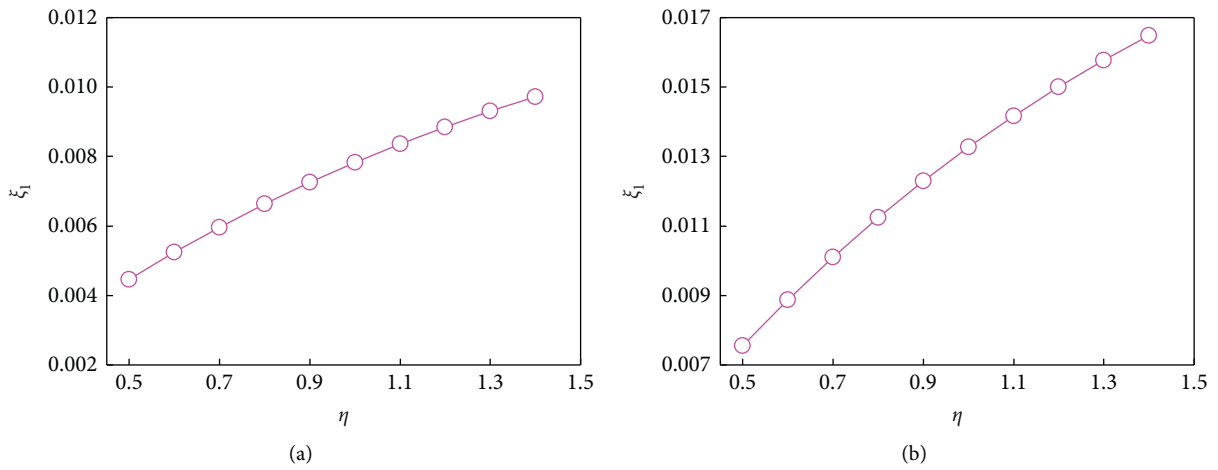


FIGURE 15: Variations of the first additional modal damping ratio ξ_1 with η : (a) the modal strain energy method; (b) the complex modal analysis method.

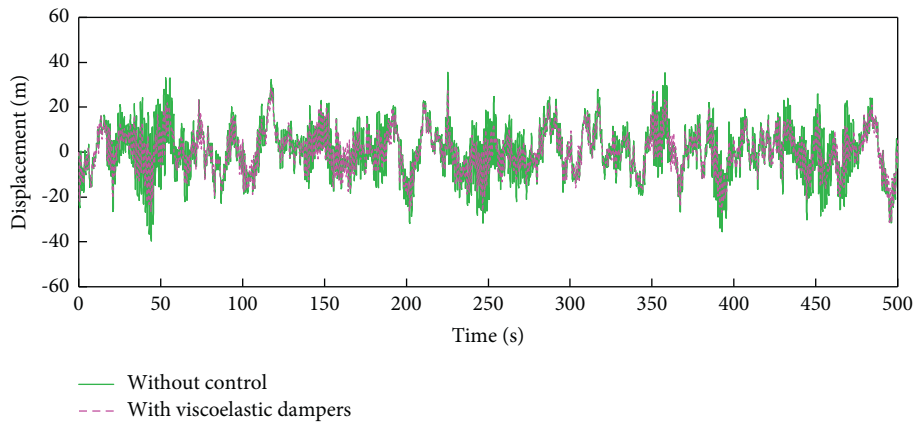


FIGURE 16: Time history response of the top displacement of the transmission line tower.

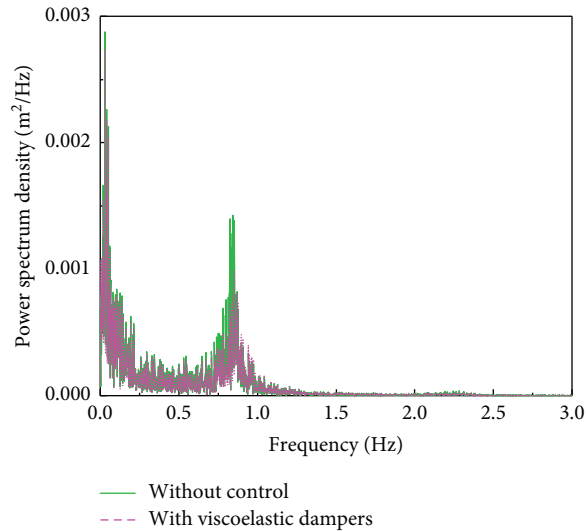


FIGURE 17: Power spectrum density of the displacement response.

analysis method is also greater than that of the modal strain energy method.

4. Control Performance of VEDs for Wind-Induced Excitations

The wind load in the vertical direction is applied to the transmission line tower without control and controlled by VEDs, respectively. The basic wind speed at 10 mm elevation is 30 m/s, and the site type is class B. The wind speed corresponding to each elevation is different, and the fluctuating wind speed time history at each height of the transmission line tower is simulated according to the harmonic synthesis method. In ANSYS, the buffeting force-time history is input along the main tower column of the transmission line tower, and the time domain response of the buffeting displacement is calculated by the time history integration method. The first two natural modal damping ratios of the transmission line tower are 0.02. The transmission line tower is subjected to random vibration under fluctuating wind load in the range of 0 s to 500 s.

Figure 16 illustrates the time history response of the displacement of the 481 nodes on the top of the transmission line tower along the wind direction without control and controlled by VEDs. The mean square value of the displacement on the top of the transmission line tower control by VEDs is 0.0091 m, which is 18.9% lower than that of the transmission line tower without control 0.1124 m. The power spectrum density of the displacement response of the transmission line tower without control and controlled by VEDs is shown in Figure 17. Compared with the transmission line tower without control, the transverse bending vibration energy of the transmission line tower control by VEDs presents a significant decrease.

5. Conclusions

This paper investigates the optimization of VEDs for vibration control of a transmission line tower subjected to wind excitations. The mechanical model of the VED-brace

system was first established, and the maximum additional modal damping ratio of the transmission line tower attached with VEDs was calculated. Based on the finite element model of a two-circuit transmission line tower with VEDs, the influences of installation positions and parameters of VEDs on the additional modal damping ratio were clarified. In the end, the control performance of VEDs on the transmission line tower subjected to wind excitations was numerically demonstrated. The main conclusions are summarized as follows:

- (1) The stiffness of the steel brace connected to a VED has a significant effect on the maximum additional modal damping ratio of the VED-brace system provided for the transmission line tower and the optimal parameters of the VED, which indicates that the stiffness of the steel brace cannot be ignored for the refined theoretical analysis and numerical simulation.
- (2) The installation positions of VEDs dramatically influence the additional modal damping ratio of the transmission line tower. Studies indicate that the first additional modal damping ratio provided by VEDs installed in accordance with installation scheme 1 is greater than that provided by the VED installed in accordance with installation scheme 2. Hence, installation scheme 1 is superior to installation scheme 2. Besides that, the first additional modal damping ratio predicted by the complex modal analysis method is greater than that of the modal strain energy method.
- (3) The increase of the brace stiffness and the loss factor helps to improve the vibration control performance of the transmission line tower with VEDs. The equivalent additional modal damping ratio provided by VEDs is increased with the brace stiffness and the loss factor, which presents a significant advantage in carrying out the optimal design of VEDs for mitigating tower vibrations.
- (4) The VEDs present superior control performance on the top displacement of the transmission line tower as well as the transverse bending vibration energy. The mean square value of the displacement on the top of the transmission line tower control by VEDs is 0.0091 m, which is 18.9% lower than that of the transmission line tower without control 0.1124 m.

Data Availability

The data used to support the findings of this study are included within the article.

Conflicts of Interest

The authors declare no conflicts of interest.

Acknowledgments

This study was sponsored by Hunan Provincial Natural Science Foundation of China (Grant no. 2021JJ50143) and by Hunan Science and Technology Talent Promotion Project in China (Grant no. 2019TJ-Y08), which are greatly acknowledged.

References

- [1] T. Okamura, T. Ohkuma, E. Hongo, and H. Okada, "Wind response analysis of a transmission tower in a mountainous area," *Journal of Wind Engineering and Industrial Aerodynamics*, vol. 91, no. 1-2, pp. 53–63, 2003.
- [2] E. P. U. S. Salunkhe and Y. M. Ghugal, "Analysis and design of three legged 400kV double circuit steel transmission line towers," *International Journal of Civil Engineering & Technology*, vol. 4, no. 3, pp. 197–209, 2013.
- [3] R. C. Battista, R. S. Rodrigues, and M. S. Pfeil, "Dynamic behavior and stability of transmission line towers under wind forces," *Journal of Wind Engineering and Industrial Aerodynamics*, vol. 91, no. 8, pp. 1051–1067, 2003.
- [4] Y. Ming, Z. H. He, Y. C. Zhang, Y. C. Liu, J. Yang, and Z. Y. Zhang, "Dynamic response of transmission lines crossing high-speed railway," *IEEE Transactions on Power Delivery*, vol. 2021, Article ID 3104902, 2021.
- [5] M. Zhang, G. F. Zhao, L. Wang, and J. Li, "Wind induced coupling vibration effects of high voltage transmission tower line systems," *Shock And Vibration*, vol. 2017, Article ID 1205976, 34 pages, 2017.
- [6] B. Asgarian, S. Dadras Eslamlou, A. Mehr, and M. Mehr M, "Progressive collapse analysis of power transmission towers," *Journal of Constructional Steel Research*, vol. 123, pp. 31–40, 2016.
- [7] X. Fu and H.-N. Li, "Uncertainty analysis of the strength capacity and failure path for a transmission tower under a wind load," *Journal of Wind Engineering and Industrial Aerodynamics*, vol. 173, pp. 147–155, 2018.
- [8] H. Patil, G. Doshi, N. P. Rao, D. Lakhpati, and V. Subramanian, "Failure analysis of transmission line tower: a case study," *The IUP Journal of Structural Engineering*, vol. 3, no. 1, pp. 20–27, 2010.
- [9] F. G. A. Albermani and S. Kitipornchai, "Numerical simulation of structural behaviour of transmission towers," *Thin-Walled Structures*, vol. 41, no. 2-3, pp. 167–177, 2003.
- [10] B. Eltaly, A. Saka, and K. Kandil, "FE simulation of transmission tower," *Advances in Civil Engineering*, vol. 2014, pp. 343–355, Article ID 258148, 2014.
- [11] E. Veg, M. Regodic, A. Joksimovic, and N. Gubeljak, "Development of the transmission tower virtual 3D model for structural analysis in ANSYS," *FME Transaction*, vol. 45, no. 2, pp. 232–235, 2017.
- [12] H.-N. Li, S.-Y. Tang, and T.-H. Yi, "Wind-rain-induced vibration test and analytical method of high-voltage transmission tower," *Structural Engineering & Mechanics*, vol. 48, no. 4, pp. 435–453, 2013.
- [13] J. H. Park, B. W. Moon, K. W. Min, S. K. Lee, and C. K. Kim, "Cyclic loading test of friction-type reinforcing members upgrading wind-resistant performance of transmission towers," *Engineering Structures*, vol. 29, no. 11, pp. 435–453, Article ID 31853196, 2007.
- [14] H. Z. Deng, S. Y. Zhu, Y. Chen, and Z. M. Wang, "Study on wind-induced vibration control of long span transmission line system," *Journal of Building Structures*, vol. 24, no. 4, pp. 60–64+75, 2003, in Chinese.
- [15] H. Z. Deng, R. J. Si, X. Y. Hu, and C. Y. Duan, "Wind tunnel study on wind-induced vibration responses of a UHV transmission tower-line system," *Advances in Structural Engineering*, vol. 16, no. 7, pp. 1175–1185, 2013.
- [16] L. Tian, Q. Wang, Q. Yu, and N. Xu, "Wind-induced vibration optimal control for long span transmission tower-line system," *The Open Civil Engineering Journal*, vol. 7, no. 1, pp. 159–163, 2013.
- [17] Q. Xie and L. Sun, "Failure mechanism and retrofitting strategy of transmission tower structures under ice load," *Journal of Constructional Steel Research*, vol. 74, pp. 26–36, 2012.
- [18] B. Chen, W. H. Guo, P. Y. Li, and W. P. Xie, "Dynamic responses and vibration control of the transmission tower-line system: a state-of-the-art review," *Science World Journal*, vol. 2014, Article ID 538457, 20 pages, 2014.
- [19] D. M. Lima, P. A. L. Yanez, and M. A. Pareira Ma, "Vibration control device for steel tubular towers of horizontal axis wind turbines," *Latin American Journal of Solids and Structures*, vol. 16, no. 6, pp. 1–21, 2019.
- [20] S. Roy and C. K. Kundu, "State of the art review of wind induced vibration and its control on transmission towers," *Structure*, vol. 29, pp. 254–264, 2021.
- [21] L. Suresh and K. M. Mini, "Effect of multiple tuned mass dampers for vibration control in high-rise buildings," *Practice Periodical on Structural Design and Construction*, vol. 24, no. 4, Article ID 04019031, 2019.
- [22] F. Rahimi, R. Aghayari, and B. Samali, "Application of tuned mass dampers for structural vibration control: a state-of-the-art review," *Civil Engineering Journal*, vol. 6, no. 8, pp. 1622–1651, 2020.
- [23] L. Tian and Y. Zeng, "Parametric study of tuned mass dampers for long span transmission tower line system under wind loads," *Shock and Vibration*, vol. 2016, Article ID 4965056, 11 pages, 2016.
- [24] X. Lei, W. P. Xie, M. Nie, H. W. Niu, J. L. Chen, and Y. X. Wang, "Development and application of a new type of TMD in transmission tower vibration reduction," *Journal of Vibration and Shock*, vol. 38, no. 13, pp. 73–80, 2019, in Chinese.
- [25] B. Zhao, D. Wu, and Z. Lu, "Shaking table test and numerical simulation of the vibration control performance of a tuned mass damper on a transmission tower," *Structure and Infrastructure Engineering*, vol. 17, no. 8, pp. 1110–1124, 2021.
- [26] B. Chen, J. Zheng, and W. Qu, "Control of wind induced response of transmission tower line system by using magnetorheological dampers," *International Journal of Structural Stability and Dynamics*, vol. 9, no. 4, pp. 661–865, 2009.
- [27] B. Chen, X. Xiao, P. Li, and W. Zhong, "Performance evaluation on transmission tower-line system with passive friction dampers subjected to wind excitations," *Shock And Vibration*, vol. 2015, Article ID 310458, 13 pages, 2015.
- [28] C. Zeng, D. X. Hao, and L. Q. Hou, "Research on calculation of equivalent damping ratio of electrical transmission tower-line system with viscoelastic dampers," *Advanced Materials Research*, vol. 1064, pp. 115–119, 2014.

Research Article

Design of Constructive Controller of Nonlinear System Based on Polynomial Function Growth Condition and Its Application in Deep Subsea Energy Mining and Production Control System

Longchuan Guo ^{1,2}, Chuanping Zhou,^{1,2} Xiaoqing Tian,¹ Huawei Ji,¹ and Yudong Peng¹

¹School of Mechanical Engineering, Hangzhou Dianzi University, Hangzhou 310018, China

²Department of Computer Information Engineering, National Technical University of Ukraine, Kyiv 03056, Ukraine

Correspondence should be addressed to Longchuan Guo; glc1988@126.com

Received 14 August 2021; Accepted 16 September 2021; Published 7 October 2021

Academic Editor: Nan Zhang

Copyright © 2021 Longchuan Guo et al. This is an open access article distributed under the Creative Commons Attribution License, which permits unrestricted use, distribution, and reproduction in any medium, provided the original work is properly cited.

This paper mainly studies the output feedback control problem of the stochastic nonlinear system based on loose growth conditions and applies the research results to the valve control system of underwater oil and gas pipelines, which can improve the speed and stability of the equipment system. First, the concept of randomness is introduced to study the actual tracking control problem of output feedback of stochastic nonlinear systems, remove the original harsher growth conditions, make it meet the more general polynomial function growth conditions, and propose a combination of static and dynamic output feedback practices. The design of the tracking controller makes all the states of the system meet boundedness and ensures that the tracking error of the system converges to a small neighborhood of zero. Second, the system is extended to the parameter-uncertain system, and the output feedback tracking controller with complete dynamic gain is constructed by proving the boundedness of the system state and gain. Further, the time-delay factor is introduced, and the nonlinear term of the system satisfies the more relaxed power growth condition, combined with the inverse method to cleverly construct a set of Lyapunov functions and obtain the output controller to ensure that the system is asymptotically probabilistic in the global scope. Stability. Finally, through the ocean library in the Simulation X simulation software, the controller design results are imported into the underwater electro-hydraulic actuator model to verify the effectiveness of the controller design.

1. Introduction

Stability and robustness are two important basic concepts in system and control science. However, there is a difference between the two. Stability describes the ability of the system to maintain relative to changes in the initial state, while robustness describes the ability of the system to maintain relative to changes in the external environment or the system itself. The robustness analysis and control law design of the control system are the main aspects of the research problems in robust control theory [1–3]. Robustness analysis mainly studies the stability and dynamic performance of the control system in the presence of uncertainty or external interference. The main research of control law design is the need to design an effective control law to make the system with

uncertainty and external interference more robust. After more than 30 years of development, robust control theory has achieved a series of results, and it has become one of the most active fields in the research content of control theory [4–6].

In the 1990s, the authors in [3] first proposed a sliding mode variable structure control method, and the authors in [5, 6] further developed sliding mode variable structure control theory. In 2010, the research on sliding mode variable structure in [7] attracted widespread attention from the control community. Since then, scholars have begun to study sliding mode variable structure control in depth and formed a complete system, and sliding mode variable structure control has also begun. It is applied to complex systems such as discrete systems, uncertain

systems, time-delay systems, nonlinear systems, and switching systems. Sliding mode variable structure control is a control strategy of variable structure control systems. Its fundamental difference from conventional control lies in the discontinuity of control, that is, a switching characteristic that makes the “structure” of the system change over time. Sliding mode variable structure control can force the system to move along a prescribed state trajectory under certain characteristic conditions. Since the sliding mode can be designed and has nothing to do with the parameters and disturbances of the system, all systems in sliding mode motion have good robustness.

In [8], the author introduced the development history of sliding mode variable structure, the definition and mathematical expression of sliding mode, and so on. Combined with the introduction in the article, we focus on the introduction of discrete-time system sliding mode variable structure control. For discrete systems, sliding mode variable structure control cannot produce an ideal sliding mode but can only produce a quasi-sliding mode [9]. Discrete sliding mode variable structure control mainly discusses three basic issues: the existence, accessibility, and stability of sliding modes.

Based on this, uncertain nonlinear time-delay systems are an important class of nonlinear systems. At present, there have been many mature research results for the control design theory of uncertain nonlinear time-delay systems or single uncertain nonlinear systems under strong constraints. However, in practical engineering problems, most uncertain nonlinear time-delay systems need to meet relatively loose constraints, and some engineering conditions are even unconstrained. It is particularly worth noting that in the field of deep-sea oil and gas development, due to the influence of different components in pipeline, the opening process model of underwater electro-hydraulic valve satisfies the Hölder constraint condition; at the same time, the electronic integrated modules of underwater electro-hydraulic systems generally use chaotic circuits containing piecewise linear memristors (piecewise linearization of nonlinearities is also one of the important methods for studying nonlinear systems) [10–12]. Based on the above analysis, the system characteristics of the two engineering problems include nonlinearity, uncertainty, and piecewise linearity, and the good control of the underwater electro-hydraulic valve actuator and its electronic module determines the overall speed, stability, and real-time and reliability of oil and gas pipeline operation, which are related to the overall safety and reliability of offshore oil and gas production.

Combining the above research and analysis, the main innovative contributions of this paper are as follows:

- (1) Different from the research object in [13–16], the state equation of the control object we studied in this chapter contains both a time-delay term and an uncertain parameter, including a nonlinear function term of the state and time delay. Among them, the uncertainty includes the uncertainty of the state and time delay, the uncertainty of the disturbance,

and the uncertainty of the Hölder condition nonlinear function.

- (2) From the description in [17], we can see that many robust controller designs for uncertain nonlinear time-delay systems are based on the known state of the system. A state observer is established to obtain the state estimate, and further a robust controller is designed.
- (3) Simulation X optimization tool is an important and effective method in optimal control. The optimal control performance mentioned in [18] can be obtained by solving LMIs. In this paper, by establishing a new Lyapunov–Krasovskii functional, the Lyapunov stability theorem and Simulation X method will be applied to the design of robust controllers for nonlinear systems based on observers.
- (4) The nonlinear term in the nonlinear system is assumed to satisfy the Hölder condition described in [19, 20].
- (5) This chapter introduces and models an electro-hydraulic valve position control system and applies the designed observer and controller to the system. The model includes uncertain parameter disturbances, hydraulic transmission time lag, and non-uniformity that meets Hölder’s conditions, linear friction, and so on.

2. Description of Valve Control System Model of Offshore Gas Transportation Pipeline

Electro-hydraulic control systems are widely used in aerospace systems, vehicle systems, artillery launch base control and oil extraction, and so on and have a wide range of applications in actual production and processes. In this section, we consider an application to the offshore oil and gas production process. The electro-hydraulic valve position control system [21–24] mainly focuses on the output practical tracking controller design for a class of complex stochastic nonlinear systems with unknown control coefficients. As the technical accumulation of paper [24], a solution is provided for increasing the nonlinear constraint conditions for this paper, and it is just suitable for underwater control valve systems.

The electro-hydraulic composite valve position control system studied in this section has been applied in actual offshore engineering such as oil and gas exploration and production, especially in the field of deep-sea oil and gas development. Its core hub part-underwater hydraulic actuators, due to the influence of different component substances in pipelines, the system presents uncertain and nonlinear characteristics, and for underwater hydraulic actuators, fast response time and good tracking performance are two extremely important indicators in actual oil and gas production applications because they determine the speed, stability, real-time, and reliability of the operation of the entire oil and gas pipeline and are related to the overall safety and reliability of offshore oil and gas production.

The electro-hydraulic compound valve position control system is composed of a water equipment part and an underwater equipment part (as shown in Figure 1). The water part includes liquid supply unit, hydraulic station, other power units, and other control units; the underwater part includes electromagnetic reversing valve, hydraulic actuator, and the electronic control unit that controls the electromagnetic reversing valve; the inside of the electronic control unit is the controller logic design.

In actual marine engineering applications, in order to ensure the stability, reliability, and safety of the system, the response speed of the valve position control needs to be stable, accurate, and timely; during the valve position opening/closing process, it is also affected by the hydraulic driving force, spring restoring force, and the force generated by the fluid medium inside the oil and gas pipeline during the opening process of the actuator.

Combined with the existing research results, the electro-hydraulic compound valve position control system model in the process of valve position opening is considered as follows:

$$\begin{aligned} p(S - S_1) + \rho g H S_1 &= m \frac{d^2 \tau}{dt^2} + \left(\rho g H + \frac{128 \mu l_p Q}{\pi d_p^4} \right) (S - S_2) \\ &+ k(L_0 + \tau) + f\left(\tau, \frac{d\tau}{dt}\right) + w(t), \\ Q_h &= v(S - S_1) \left(2 * \frac{(P_1 - P_2)}{\rho_h} \right). \end{aligned} \quad (1)$$

According to the characteristics of offshore oil and gas transportation pipelines, we generalize the pipeline transportation model to obtain a broad mathematical model with unknown control directions as follows:

$$\begin{aligned} dx_i &= g_i(t, x) x_{i+1} dt + f_i(t, x, u) d\omega, \quad (i = 1, \dots, n-1), \\ dx_n &= g_n(t, x) u dt + f_n(t, u, x) d\omega, \\ y &= x_1 - y_r(t), \end{aligned} \quad (2)$$

where $x = (x_1, \dots, x_n)^T \in R^n$, $u \in R$, and $y \in R$ are the states, input, and output of system; corresponding to this, y_r is a given unmeasurable output trajectory. Here, we introduce a stochastic process for the system: ω is an m -dimensional standard Wiener process defined on the complete probability space (Ω, Γ, P) with Ω being a sample space, Γ being a filtration, and P being a probability measure. $g_i(t, x)$ ($i = 1, \dots, n$) is the control coefficient and is bounded; furthermore, the control coefficient is unknown, and the first variable is continuous, and the second variable is local Lipschitz. Nonlinear term $f_i: R^+ \times R \times R^n \rightarrow R^n$, $i = 1, \dots, n$, is continuous for t and locally Lipschitz in (u, x) .

At present, there have been some results related to the stability analysis of Hölder nonlinear systems, but there are

no relevant results in the research on the control problems of uncertain nonlinear time-delay systems that meet such conditions, and they also include uncertainties and time delays. Nonlinear systems with complex factors and other complex factors have certain practical application research value; further, it is necessary to consider the design of state observers when state variables are unmeasurable and the design of robust controllers based on state observers. In order to achieve the control objectives, the system and reference signals are required to satisfy following assumptions.

Assumption 1. There exists positive integer p and known positive constant c_0 such that the following inequality holds:

$$|f_i(t, x, u)| \leq c_0 (1 + |x_1|^p) (|x_1| + \dots + |x_i|) + c_0, \quad i = 1, \dots, n. \quad (3)$$

Based on this assumption, system (2) is dominated by an output polynomial function growth rate system.

Assumption 2. The symbol of $g_i(t, x)$, ($i = 1, \dots, n$) is defined as the control direction of system (3), and control direction in this system is unknown. $g_i(t, x)$ takes the value on the unknown interval $[\xi_i, \zeta_i]$ in which ξ_i and ζ_i are the upper and lower bounds of the determined constant interval.

Assumption 3. The reference output trajectory y_r of system (3) is continuously differentiable and satisfies the following inequality:

$$\max(|y_r|, |\dot{y}_r|) \leq c_1, \quad (4)$$

where c_1 is the known positive constant.

According to the characteristics and constraints of the above system, it leads to the objective of this paper: for any constant $\delta > 0$, all the states of stochastic nonlinear system (3) are well defined and bounded. In addition, there exists a finite time $T > 0$ such that for any $t > T$, it can get

$$|y(t)| = |x_1(t) - y_r(t)| \leq \delta. \quad (5)$$

Remark 1. There have been some research studies on this type of system, and some results have been obtained. For example, in [23, 25, 26], the random impulse control problem of the system under Hölder conditions is analyzed. Among the problems studied in this chapter, compared with previous studies, the described nonlinear system conditions have a stronger scope of application. On the basis of the nonlinear system analysis method, considering the problem of robust sliding mode controller design for piecewise linear discrete time-delay systems with state lag and uncertain parameters, applying sliding mode control theory to piecewise linear time-delay systems can make the system state move along a given "sliding mode" motion trajectory and apply the sliding mode variable structure control theory to the electro-hydraulic compound valve position control system, which has practical significance in the control theory and application of the piecewise linear system.

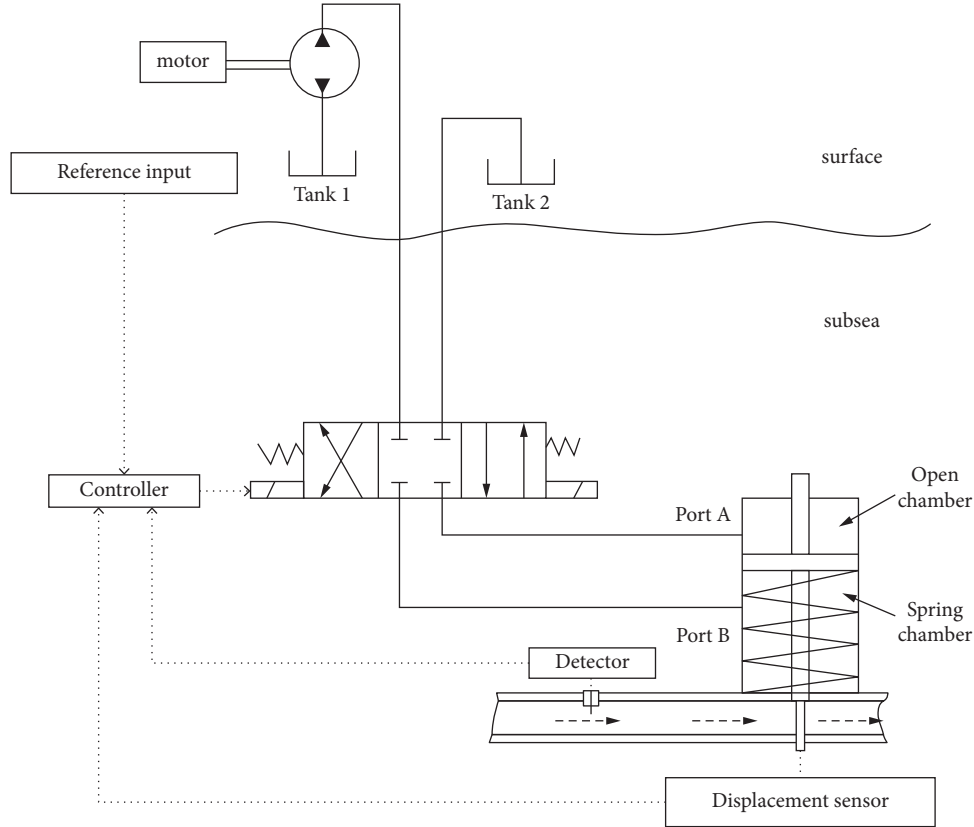


FIGURE 1: Underwater electro-hydraulic composite valve position control system.

3. Complex Tracking Control Design

According to the description of the stochastic nonlinear system with unknown control coefficients (1) and Assumptions 1–3, we can get

$$|f_i(t, x, u)| \leq c(1 + |y|^p)(|x_1| + \dots + |x_i|) + c, \quad (6)$$

where $c = c_0 \max(1 + 2^{p-1}c_1^p, 2^{p-1})$ is a known constant.

For the sake of convenience of calculation and formula derivation, the following simple states transformation is introduced and then it can obtain the updated stochastic nonlinear system:

$$\begin{aligned} dz_i &= g_i(t, z)z_{i+1}dt + F_i(t, u, z)d\omega, \\ dz_n &= g_n(t, z)udt + F_n(t, u, z)d\omega, \\ y &= z_1. \end{aligned} \quad (7)$$

Based on the simplicity of formula derivation, especially introducing state transitions:

$$\begin{aligned} z_1 &= x_1 - y_r, \\ z_i &= x_i, \quad (i = 2, \dots, n), \end{aligned} \quad (8)$$

definition $F_i(t, u, z)$ is as follows:

$$F_i(t, u, z) = g_i f_i(t, u, z_1 + y_r, z_2, \dots, z_n). \quad (9)$$

States observer of system (3) is established as follows:

$$\begin{aligned} \hat{z}_i &= \hat{z}_{i+1} + K^i l_i (z_1 - \hat{z}_1), \quad (i = 1, \dots, n-1), \\ \hat{z}_n &= u + K^n l_n (z_1 - \hat{z}_1), \end{aligned} \quad (10)$$

where $l_i > 0$ ($i = 1, \dots, n$) is the coefficient of the Hurwitz polynomial with $s^n + l_1 s^{n-1} + \dots + l_{n-1} s + l_n$. $K = RT(t)$ is a high-order gain term which consists of a constant R and a variable $T(t)$ as follows:

$$\dot{T} = -\alpha_1 T^2 + \alpha_2 (1 + |y|^p)^2 T, \quad T(0) = 1. \quad (11)$$

Define the system error states as $e_i = z_i - \hat{z}_i$ ($i = 1, \dots, n$), and then by (6)–(9), the error system can be obtained:

$$\begin{aligned} de_i &= \|\xi\| \cdot \|\zeta\| e_{i+1} dt - K^i l_i e_1 dt + F_i(t, u, z) d\omega, \\ de_n &= -\|\xi\| \cdot \|\zeta\| K^n l_n e_1 dt + F_n(t, u, z) d\omega. \end{aligned} \quad (12)$$

Remark 2. On the basis of designing observers for nonlinear systems, scholars have launched the observer-based controller design. Among them, the controller design of the observer combining the Lyapunov stability theorem and the LMIs method has achieved certain research results. In [23], the author studied the robust controller design of the state observer for uncertain time-delay systems. From the above research results, it can be obtained that robust control has a wide range of applications, and it also reflects the degree of attention paid to the research of uncertain nonlinear systems with time delays. However, on the other

hand, most of the research results mentioned at present are the study of time-delay nonlinear systems, state-uncertain nonlinear systems, or both time-delay characteristics and parameter-uncertain nonlinear systems. There are relatively few research studies on observers of time delay, state uncertainty, and time-delay uncertainty, as well as observers of nonlinear discrete systems that include state variables and nonlinear functions of time-delay variables and robust control based on observers.

Transformation of estimated states \hat{z}_i and error states e_i is introduced to further simplify subsequent controller design issues:

$$\begin{aligned} \varepsilon_i &= \frac{e_i}{K^{b+i-1}}, \quad (i = 1, \dots, n), \\ \tau_i &= \frac{\hat{z}_i}{K^{b+i-1}}, \quad (i = 1, \dots, n), \end{aligned} \quad (13)$$

where $0 \leq b \leq (1/p)\|\xi\|\|\zeta\|$ is the known constant. Further, by (12), systems (7)–(9) can be converted into the following:

$$\begin{aligned} d\varepsilon &= KL\|\xi\|\|\zeta\|\varepsilon dt - \frac{\dot{K}}{K}C_b\varepsilon dt + G(z, K)d\omega, \\ \dot{\tau} &= KL^T\tau\|\xi\|\|\zeta\| + K\varepsilon_1 - \frac{\dot{K}}{K}C_b\tau, \end{aligned} \quad (14)$$

where

$$\begin{aligned} L &= \begin{pmatrix} -I_1 & 1 & \dots & 0 \\ \vdots & \vdots & \ddots & \vdots \\ -I_{n-1} & 0 & \dots & 1 \\ -I_n & 0 & \dots & 0 \end{pmatrix}, \\ L^T &= \begin{pmatrix} 0 & 1 & \dots & 0 \\ \vdots & \vdots & \ddots & \vdots \\ 0 & 0 & \dots & 1 \\ -I_1 & -I_2 & \dots & -I_n \end{pmatrix}, \\ C_b &= \text{diag}(b, b+1, \dots, b+n-1), \end{aligned} \quad (15)$$

$$G(z, K) = \left(\frac{F_1}{K^b}, \dots, \frac{F_n}{K^{b+n-1}} \right)^T.$$

According to the system description and definition in the second section, it is concluded that the closed-loop system has a unique solution in interval $[0, t_T)$. Moreover, if T is maximum value of t_f , then $0 < T \leq \infty$.

Next, we need to discuss the boundedness of the various states and parameter variables of the system. Appropriate parameters r_1, r_2, r_3 , and r_4 are chosen such that positive definite matrix P, Q and matrix L, L^T, C_b satisfy the following relation:

$$\begin{aligned} r_1 I_n &\leq C_b P + P C_b \leq r_2 I_n, \\ r_3 I_n &\leq C_b Q + Q C_b \leq r_4 I_n. \end{aligned} \quad (16)$$

Define the following Ito Lyapunov function $V(\varepsilon, \tau) = \varepsilon^T P \varepsilon + \tau^T Q \tau$, and then it can get the trajectory of (16) along the Ito differentiation for system (13) as follows:

$$\begin{aligned} LV &= -K|\varepsilon|^2\|\zeta\|\|\xi\| + 2\varepsilon^T P G - \frac{\dot{K}}{K}\varepsilon^T (C_b P + P C_b)\varepsilon - 2K|\tau|^2\|\zeta\|\|\xi\| \\ &\quad + 2K\tau^T \varepsilon_1 h - \|\zeta\|\|\xi\| \frac{\dot{K}}{K}\tau^T (C_b Q + Q C_b)\tau - \frac{\dot{K}}{K}\tau^T (C_b P + P C_b)\varepsilon \\ &\leq r_4 \alpha_1 B \|\zeta\|\|\xi\|\|\tau\|^2 - r_3 \alpha_2 (1 + |y|^p)^2 |\tau|^2, \end{aligned} \quad (17)$$

where

$$|G| = \left(\left(\frac{F_1}{K^b} \right)^2 + \dots + \left(\frac{F_n}{K^{b+n-1}} \right)^2 \right)^{1/2}, \quad (18)$$

where (17) can be magnified to

$$\begin{aligned} &(\|P\| + \|G\|)(c(1 + |y|^p)(\sqrt{n}(|\varepsilon| + |\tau|) + c_1) + c + c_1)^2, \\ &\leq (\|P\| + \|G\|) \cdot (nc^2(1 + |y|^p)^2(|\varepsilon|^2 + |\tau|^2) \\ &\quad + 4c^2\|\zeta\|\|\xi\|c_1^2 + 2(c + c_1)^2). \end{aligned} \quad (19)$$

By inequality scaling principle, parameter α_2 can be chosen as follows:

$$\alpha_2 \geq \frac{\|\zeta\|\|\xi\|c\|P\|(1 + c_1) - nc^2(\|P\| + \|Q\|)}{r_3}. \quad (20)$$

Since $T \geq 1$, parameter R needs to satisfy the following relationship:

$$R \geq \frac{\|\zeta\|\|\xi\|\|P\|(nc + c + c_1) + r_2 \alpha_1}{1 - \|\zeta\|\|\xi\|\|I\|^2} \geq 1. \quad (21)$$

According to the above for the choice of parameters, then (22) can be translated into the following:

$$\begin{aligned} LV &\leq -\frac{R}{\max(\lambda_{\max}(P) + \lambda_{\max}(Q))} \cdot V + \|\zeta\|\|\xi\|\|P\|(cc_1 + c + c_1) \\ &\quad + (c^2(1 + |y|^p\|\zeta\|\|\xi\|)^2 c_1^2 + (c + c_1)^2)(\|P\| + \|Q\|). \end{aligned} \quad (22)$$

By using other variables instead of the above derivation results, we can get

$$E_1 = \frac{R}{\max(\lambda_{\max}(P) + \lambda_{\max}(Q))}, \quad (23)$$

$$E_2 = \|\zeta\|\|\xi\|\|P\|(cc_1 + c + c_1) + ((1 + |y|^p)^2 c_1^2 + 1).$$

Since the closed-loop system has a unique solution in interval $[0, \infty)$, by (21)–(23), we can obtain

$$V(\varepsilon(t), \tau(t)) \leq V(\varepsilon(0), \tau(0))e^{-(E_1/A)t} + \frac{E_2}{E_1}, \quad t \in [0, T], \quad (24)$$

such that states $\varepsilon(t)$ and $\tau(t)$ of stochastic nonlinear system (7)–(9) and (13) are well defined and bounded on $[0, T]$.

Correspondingly, by $y = z_1 = (\varepsilon_1 + \tau_1)K^b$ and $|y| \leq (RT)^b(|\varepsilon_1| + |\tau_1|)$, we can get $|y| \leq (AB)^b E_3$. According to the boundedness of ε and τ on $[0, T]$, combined with the above obtained $|y| \leq (RT)^b E_3$ and $b \in (0, (1/p)\|\zeta\|\|\xi\|)$, we can obtain

$$T(t) \leq \frac{\alpha_2^2 \|\zeta\|\|\xi\| (1 + E_3^{2p} \sqrt{R})^2}{\alpha_1^2}. \quad (25)$$

Through the above analysis, we can prove that the system gain $T(t)$ is well defined and bounded on $[0, T]$ with $T = \infty$.

Through the above analysis, it can be concluded that the system is essentially bounded. Then, we give the theorem of output feedback practical tracking controller.

Theorem 1. *By choosing appropriate parameters a_i, l_i, α_1 , and α_2 , the following output feedback practical tracking controller can be designed:*

$$u = -(K^n a_1 \hat{z}_1 + K^{n-1} a_2 \hat{z}_2 + \dots + K a_n \hat{z}_n), \quad (26)$$

where K is defined by (10) and $a_i > 0$ is the coefficient of Hurwitz polynomial. Since the closed-loop stochastic nonlinear system satisfies locally Lipschitz condition, it is concluded that the closed-loop system has a unique solution in interval $[0, t_T]$. Moreover, if T is maximum value of t_f , then $0 < T \leq \infty$. There exists a time $T = T_1$ such that

$$V(\varepsilon(t), \tau(t)) \leq \frac{2E_2}{E_1}, \quad t \geq T = T_1. \quad (27)$$

According to (19)–(25), we can conclude that

$$\lambda_{\min}(P)|\varepsilon|^2 + \lambda_{\min}(Q)|\tau|^2 \leq V(\varepsilon(t), \tau(t)). \quad (28)$$

Further squaring formula (28), we can get

$$\varepsilon_1^2(t) + \tau_1^2(t) \leq \frac{E_4}{R}. \quad (29)$$

By using $|y| \leq (AB)^b E_3$ and (27)–(29), we can get

$$|y| \leq A^b B^b \|\xi\|\|\zeta\| (|\varepsilon_1(t)| + |\tau_1(t)|) \leq \sqrt{\frac{\|\xi\|\|\zeta\| E_4}{A}}. \quad (30)$$

Simultaneously, combined with (30), we can get further

$$y^2(t) \leq \frac{\|\xi\|\|\zeta\| E_4}{A}. \quad (31)$$

Remark 3. In the control design program, the design problem of the controller is transformed into a parameter construction problem by introducing the appropriate coordinate transformation, and the forward push and

saturation control design method based on the iterative program is not used. The controller gain obtained by the iterative design method may become too small during multiple iterations. The obtained controller is theoretically effective, but it is difficult to achieve in engineering practice, and when the dimensionality of the system is relatively high, the multiple iteration procedures will greatly increase the difficulty and complexity of the design. The controller designed in this project has a simple form and moderate dynamic/static gain strength, so it is easier to apply to engineering practice. In this article, we take the underwater electro-hydraulic valve system as an example and apply the robust controller designed above to verify the effectiveness of the controller.

4. Offshore Gas Pipeline Valve Transportation Model Example

The underwater electro-hydraulic compound valve position control system is used in actual marine engineering such as oil and gas exploration and production, especially in the field of deep-sea oil and gas development. Its core hub part—underwater hydraulic actuator is affected by different components in the pipeline. The system presents uncertainties and nonlinear characteristics. The electro-hydraulic composite valve position control system is composed of aquatic equipment part and an underwater equipment part (as shown in Figure 1). The water part includes liquid supply unit, hydraulic station, other power units, and other control units; underwater part includes electromagnetic reversing valve, hydraulic actuator, and the electronic control unit for controlling the electromagnetic reversing valve, and the inside of the electronic control unit is the controller logic design.

Combining existing research results [27, 28], the model of the electro-hydraulic composite valve position control system during the valve position opening process is obtained as follows:

$$\begin{aligned} p(S - S_1) + \rho g H S_1 &= m \frac{d^2 \tau}{dt^2} + \left(\rho g H + \frac{128 \mu l_p Q}{\pi d_p^4} \right) \\ &\cdot (S - S_2) + k(L_0 + \tau) + f\left(\tau, \frac{d\tau}{dt}\right) + w(t), \\ Q_h &= v(S - S_1) \left(2 * \frac{(P_1 - P_2)}{\rho_h} \right). \end{aligned} \quad (32)$$

In the above formula, the physical meaning of each parameter is shown in Table 1.

Due to the pressure instability of the oil and gas medium and the sand and other components in the formation, it will cause certain interference in the opening process of the electro-hydraulic composite valve position, and the viscosity coefficient of the control fluid changes with temperature, and there are factors such as vibration in the hydraulic system. The resistance during the opening process has the characteristics of satisfying the Hölder condition. According

TABLE 1: Variable description.

Variable	Meaning	Variable	Meaning
p	Valve opening cavity supply pressure	H	Working water depth
τ	Valve position	L_0	Spring precompression displacement
S	Piston area	S_1	Piston rod area
S_2	Stem area	m	Piston rod quality
ρ	Sea water density	μ	Control fluid viscosity
k	Spring coefficient of elasticity	g	Acceleration of gravity
d_p	Inner diameter of pilot hole	f	Resistance during opening of the actuator
Q_h	Control fluid flow	Q_p	Flow rate of fluid medium in pipeline
P_1	Control fluid inlet pressure	P_2	Control fluid outlet pressure
v	Control fluid flow rate	ρ_h	Control liquid density
σ	Pressure coefficient	l_p	Control the length of the liquid guide hole
v_p	Flow rate of fluid medium in pipeline	η	Valve opening

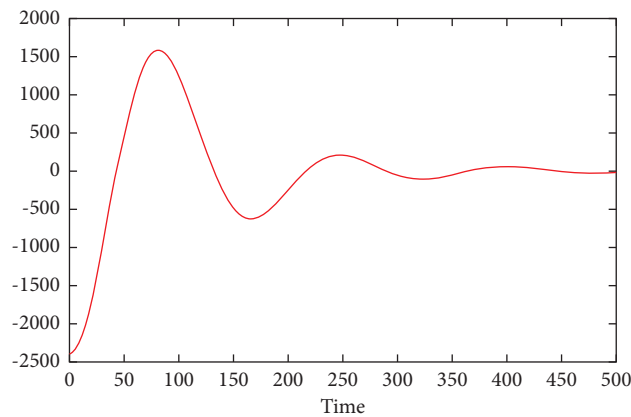


FIGURE 2: The trajectory of system output $y = x_1 - y_r$.

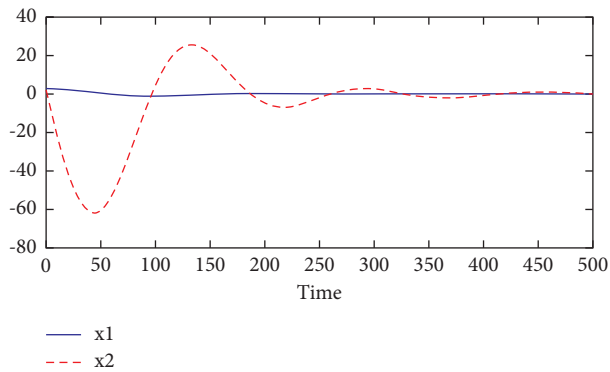


FIGURE 3: The trajectory of system state x_1 and x_2 .

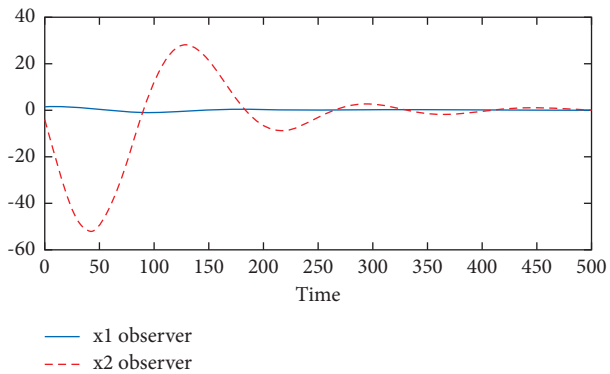


FIGURE 4: The trajectory of system observer state x_1 and x_2 .

to the decomposition of the actual model and the comparative study, we can completely believe that the control system model of the marine pipeline valve is completely matched with the theoretical control law and control model obtained above:

$$\begin{aligned}x_1 &= \tau, \\x_2 &= \frac{d\tau}{dt}, \\dx_1 &= x_2 dt + dx_1^{p(x)} \sin x_2 d\omega, \\dx_2 &= u dt + d(x_1^{p(x)} + x_2^{(x)}) d\omega, \\y &= x_1.\end{aligned}\quad (33)$$

Here, we set the initial value as

$$[x_1(0), x_2(0), \hat{z}_1(0), \hat{z}_2(0)] = [2.5, 1, 1.5, -5]. \quad (34)$$

Figures 2–4 show the response curve of the closed-loop system 1. Observed by the simulation diagram, the state of the two-dimensional systems (1)–(3) is bounded and gradually converges, and the system can also be observed. The output tracking error gradually converges and finally adjusts to near zero. The simulation results verify the effectiveness of the designed output feedback actual tracking controller.

5. Concluding and Future Prospects

In this paper, we study the design of the system observer under the condition that the state of the system is unmeasurable and the design of the system controller based on the observer. The system has uncertain parameter disturbances, time-delay terms, and nonlinear terms. By introducing the error between the observation value and the actual value, the error equation and the closed-loop loop of the observer-based control system are combined, using the Lyapunov method for stability analysis, and finally the relevant theorems obtained from the stability analysis are combined to design the observer and the controller. The Simulation X is used to solve the robust controller under the given parameters; finally, the electro-hydraulic compound valve position control model is established, and the valve position of its actuator through the controller designed is analyzed in this paper. In this paper, we study the design of system observer and controller when state variables are unmeasurable based on the stability theorem. The nonlinear system studied includes uncertain parameter disturbances and time-delay terms.

However, in the actual research process, there is a class of nonlinear systems that can be piecewise linearized. The system model is a piecewise linear model; that is, a nonlinear system is composed of finite or infinite linear subsystems [29–32]. Piecewise linear systems are widely used in practice. In the life and production process, the piecewise linear system is also an important approximation method for the nonlinear system. The nonlinear system can be described by

the piecewise linear system. Therefore, it is necessary to study the control problem of the piecewise linear system.

Data Availability

The data generated or analyzed during this research are included in this paper.

Conflicts of Interest

The author declares that there are no conflicts of interest regarding the publication of this paper.

Acknowledgments

This work was supported by the National Natural Science Foundation of China under Grant 61807010, Key R&D Program of Zhejiang Province under Grant 2021C03013, Zhejiang Provincial Natural Science Foundation of China under Grant LZ21E050002, Fundamental Research Funds for Provincial Universities of Zhejiang under Grants GK199900299012-026 and GK219909299001-309.

References

- [1] Y. Mizuta and T. Shimomura, “Sobolev’s inequality for Riesz potentials with variable exponent satisfying a log-Hölder condition at infinity,” *Journal of Mathematical Analysis and Applications*, vol. 311, no. 1, pp. 268–288, 2005.
- [2] J.-Q. Li, Y.-S. Zhang, C.-M. Ji, A.-J. Wang, and J. R. Lund, “Large-scale hydropower system optimization using dynamic programming and object-oriented programming: the case of the Northeast China Power Grid,” *Water Science and Technology*, vol. 68, no. 11, pp. 2458–2467, 2013.
- [3] Q. Liu and Z. Liang, “Global stabilisation of a class of feed-forward systems with distributed delays,” *IET Control Theory & Applications*, vol. 9, no. 1, pp. 140–146, 2015.
- [4] R. Raoufi, H. J. Marquez, and A. S. I. Zinober, “ \mathcal{H}_∞ sliding mode observers for uncertain nonlinear Lipschitz systems with fault estimation synthesis,” *International Journal of Robust and Nonlinear Control*, vol. 20, no. 16, pp. 1785–1801, 2010.
- [5] M. Abbaszadeh and H. J. Marquez, “LMI optimization approach to robust H ∞ observer design and static output feedback stabilization for discrete-time nonlinear uncertain systems H infinity observer design and static output feedback stabilization for discrete-time nonlinear uncertain systems,” *International Journal of Robust and Nonlinear Control*, vol. 19, no. 3, pp. 313–340, 2009.
- [6] X. Chen, X. Zhang, C. Zhang, and L. Chang, “Global asymptotic stabilization for input-delay chained nonholonomic systems via the static gain approach,” *Journal of the Franklin Institute*, vol. 355, no. 9, pp. 3895–3910, 2018.
- [7] D. Soudry, D. Di Castro, A. Gal, A. Kolodny, and S. Kvatinsky, “Memristor-based multilayer neural networks with online gradient descent training,” *IEEE transactions on neural networks and learning systems*, vol. 26, no. 10, pp. 2408–2421, 2015.
- [8] P. Kokotovic and M. Arcak, “Constructive nonlinear control: a historical perspective,” *Automatica*, vol. 37, no. 5, pp. 637–662, 2001.
- [9] T. Chen and J. Huang, “A small gain approach to global stabilization of nonlinear feedforward systems with input

- unmodeled dynamics,” *Automatica*, vol. 46, no. 6, pp. 1028–1034, 2010.
- [10] M. Krstic, “Feedback linearizability and explicit integrator forwarding controllers for classes of feedforward systems,” *IEEE Transactions on Automatic Control*, vol. 49, no. 10, pp. 1668–1682, 2004.
- [11] L. Long and J. Zhao, “Global stabilization for a class of switched nonlinear feedforward systems,” *Systems & Control Letters*, vol. 60, no. 9, pp. 734–738, 2011.
- [12] X. Ye, “Adaptive stabilization of time-delay feedforward nonlinear systems,” *Automatica*, vol. 47, no. 5, pp. 950–955, 2011.
- [13] H. Ye, “Saturated delayed controls for feedforward nonlinear systems,” *IEEE Transactions on Automatic Control*, vol. 59, no. 6, pp. 1646–1653, 2014.
- [14] B. Bao, F. Hu, and Z. Liu, “Mapping equivalent approach to analysis and realization of memristor-based dynamical circuit,” *Chinese Physics B*, vol. 23, no. 7, pp. 303–310, 2014.
- [15] M. Pai, “RBF-based discrete sliding mode control for robust tracking of uncertain time-delay systems with input nonlinearity,” *Complexity*, vol. 21, 2015.
- [16] L. Praly and Z. P. Jiang, “Linear output feedback with dynamic high gain for nonlinear systems,” *Systems & Control Letters*, vol. 53, no. 2, pp. 107–116, 2004.
- [17] M.-S. Koo, H.-L. Choi, and J.-T. Lim, “Global regulation of a class of uncertain nonlinear systems by switching adaptive controller,” *IEEE Transactions on Automatic Control*, vol. 55, no. 12, pp. 2822–2827, 2010.
- [18] X. Zhang and Y. Lin, “Global adaptive stabilisation of feedforward systems by smooth output feedback,” *IET Control Theory & Applications*, vol. 6, no. 13, pp. 2134–2141, 2012.
- [19] X. Zhang, H. Gao, and C. Zhang, “Global asymptotic stabilization of feedforward nonlinear systems with a delay in the input,” *International Journal of Systems Science*, vol. 37, no. 3, pp. 141–148, 2006.
- [20] H.-W. Jo, H.-L. Choi, and J.-T. Lim, “Observer based output feedback regulation of a class of feedforward nonlinear systems with uncertain input and state delays using adaptive gain,” *Systems & Control Letters*, vol. 71, pp. 44–53, 2014.
- [21] L.-C. Guo, X. Zuo, J.-W. Liu, and H.-Q. Liang, “Output-feedback control of a class of stochastic nonlinear systems with power growth conditions,” *International Journal of Control, Automation and Systems*, vol. 12, no. 2, pp. 274–282, 2014.
- [22] L.-C. Guo and J.-W. Liu, “Improved backstepping control for stochastic high-order nonlinear time delay system with a constructive mechanical system,” *Transactions of the Institute of Measurement and Control*, vol. 40, no. 15, pp. 4115–4124, 2018.
- [23] X. Chen and X. Zhang, “Output-feedback control strategies of lower-triangular nonlinear nonholonomic systems in any prescribed finite time,” *International Journal of Robust and Nonlinear Control*, vol. 29, no. 4, pp. 904–918, 2019.
- [24] L. Guo and X. Fang, “Bounded analysis and practical tracking control of complex stochastic nonlinear systems with unknown control coefficients,” *Complexity*, vol. 2, Article ID 1502065, 2021.
- [25] X. Chen, X. Zhang, and C. Zhang, “A time-varying high-gain approach to feedback regulation of uncertain time-varying nonholonomic systems,” *ISA Transactions*, vol. 98, pp. 110–122, 2020.
- [26] X. Chen, X. Zhang, and Q. Liu, “Prescribed-time decentralized regulation of uncertain nonlinear multi-agent systems via output feedback,” *Systems & Control Letters*, vol. 137, Article ID 104640, 2020.
- [27] A. Benabdallah, M. Hammami, and J. Kallel, “Robust stability of uncertain piecewise-linear systems: LMI approach,” *Nonlinear Dynamics*, vol. 63, no. 1, pp. 183–192, 2011.
- [28] C. Briat, “Stability analysis and control of a class of LPV systems with piecewise constant parameters,” *Systems & Control Letters*, vol. 82, pp. 10–17, 2015.
- [29] P. Krishnamurthy and F. Khorrami, “Feedforward systems with ISS appended dynamics: adaptive output-feedback stabilization and disturbance attenuation,” *IEEE Transactions on Automatic Control*, vol. 53, no. 1, pp. 405–412, 2008.
- [30] X. Zhang, Q. Liu, L. Baron, and E.-K. Boukas, “Feedback stabilization for high order feedforward nonlinear time-delay systems,” *Automatica*, vol. 47, no. 5, pp. 962–967, 2011.
- [31] X. Zhang, L. Baron, Q. Liu, and E.-K. Boukas, “Design of stabilizing controllers with a dynamic gain for feedforward nonlinear time-delay systems,” *IEEE Transactions on Automatic Control*, vol. 56, no. 3, pp. 692–697, 2011.
- [32] W. Zha, J. Zhai, and S. Fei, “Global output feedback control for a class of high-order feedforward nonlinear systems with input delay,” *ISA Transactions*, vol. 52, no. 4, pp. 494–500, 2013.
- [33] Z. Liang and Q. Liu, “Design of stabilizing controllers of upper triangular nonlinear time-delay systems,” *Systems & Control Letters*, vol. 75, pp. 1–7, 2015.